

Modelling of Oceanic Vortices

Royal Netherlands Academy of Arts and Sciences
P.O. Box 19121, 1000 GC Amsterdam, the Netherlands

Proceedings of the Colloquium
'Modelling of Oceanic Vortices',
Amsterdam, 11-13 May 1993

Koninklijke Nederlandse Akademie van Wetenschappen
Verhandelingen, Afd. Natuurkunde, Eerste Reeks, deel 43

Modelling of Oceanic Vortices

Edited by G.J.F. van Heijst

North-Holland, Amsterdam/Oxford/New York/Tokyo, 1994

Preface

Coherent vortex structures are common features of quasi-geostrophic or two-dimensional turbulence. In the oceans and in the planetary atmospheres, vortices are abundant: the high and low-pressure areas on weather maps are in fact huge vortices embedded in the global zonal atmospheric currents, and satellite observations have revealed the occurrence of large- and mesoscale vortices in virtually all parts of the world's oceans. Because of their relative longevity it is obvious that these vortex structures play an important role in the transport of physical properties such as mass, momentum and heat (and in the ocean also salt and biochemical components). For this reason the dynamics of geophysical vortices have attracted the attention of an increasing number of meteorologists and physical oceanographers during the last two decades or so.

Under typical atmospheric and oceanic conditions the quasi two-dimensionality of the motion on the larger scales is governed by the planetary rotation and/or the density stratification and, in addition, by dynamical constraints imposed by the 'flatness' of the domain itself. Two-dimensionality of motion can also be established in other ways, for example by external magnetic forces or by simply enclosing the fluid in an essentially two-dimensional domain. Such situations are encountered in magneto-hydrodynamic flows, in certain plasma configurations (tokamaks), in accretion disks of neutron stars, and also in soap films. Therefore, studying the dynamics of coherent vortex structures is not only relevant to geophysical fluid dynamics, but also to other fields of physics, such as plasma physics and astrophysics.

In 1983 Prof. Benoit Cushman-Roisin took the initiative to organize a colloquium on 'Modelling of Oceanic Vortices' at the Florida State University, Tallahassee (USA). The purpose of this meeting was to bring together the various scientists involved in modelling and observational studies of oceanic vortices in order to discuss and summarize recent developments and to exchange ideas for future work. The meeting appeared to fill a gap, and was followed by similar colloquia in 1985, 1987, 1988 and 1990, the latter two at the University of Liège (Belgium) and at Dartmouth College, Hannover (USA), respectively. Through the years the number of participants from outside the USA, in particular from Europe, steadily increased and it seemed appropriate to organize the next colloquium in the series again somewhere on the 'other' side of the Atlantic Ocean. On 11-13 May 1993, under the auspices of the Royal Netherlands Academy of

Arts and Sciences, the sixth colloquium on 'Modelling of Oceanic Vortices' was held in Amsterdam, in the Academy building. This time the meeting was organized by a committee consisting of Benoit Cushman-Roisin (Dartmouth College, USA), David G. Dritschel (University of Cambridge, UK), GertJan F. van Heijst (Eindhoven University of Technology, The Netherlands) and Gordon E. Swaters (University of Alberta, Canada), and gathered over 50 mainly North-American and European participants with backgrounds in physical oceanography, dynamical meteorology, plasma physics and theoretical physics.

This book contains a collection of extended abstracts of most of the presentations at the Amsterdam colloquium. At the present stage of research on oceanic vortices, efforts seem equally divided between the general study of the behaviour of vortices *per se* (e.g., stability, interaction, merger), on one hand, and the investigation of their role in the overall chain of oceanic processes (e.g., geostrophic turbulence, oceanic circulation), on the other. These two lines of research are reflected in the oral and poster presentations at the colloquium. It is hoped that this collection of contributions may serve as a useful description of the state-of-the-art, not only for physical oceanographers, but for anybody interested in coherent vortex structures.

GertJan F. van Heijst
Eindhoven, March 1994

The Colloquium on Modelling of Oceanic Vortices was organized under the auspices of the Royal Netherlands Academy of Arts and Sciences, which also provided financial support.

Additional financial support was obtained from the Department of Technical Physics, Eindhoven University of Technology; the Dorgelo Foundation, Eindhoven; and the J. M. Burgers Centre for Fluid Mechanics.

Index

- A.R. Robinson
Vortices and jets: dynamics, interactions and forecasts 1
- J.C. McWilliams
Statistical dynamics and coherent vortices in two-dimensional and planetary turbulence 15
- E.G. Pavia, M. Lopèz and P. Ripa
Axisymmetrization of warm oceanic vortices 25
- C. Shi and D. Nof
Eddy splitting along boundaries 31
- J. Sommeria
Organized vortices as maximum entropy structures 37
- B. Legras and D.G. Dritschel
Vortex stripping 51
- D. Etling and S. Raasch
Formation of vortices in rotating thermal convection 61
- R. Verzicco, J.B. Flór, G.J.F. van Heijst and P. Orlandi
Interaction of dipoles with cylinders: experiments and numerical simulations 67
- V.T. Grinchenko, V.S. Maderich and V.I. Nikishov
Mixing and restratification in stably stratified fluids 75
- M.A. Spall
Mixing and transport in the Mediterranean salt tongue 85
- G.G. Sutyrin
Nonlinear Rossby waves and vortices 93
- W.T.M. Verkley
A contour dynamics approach to large-scale atmospheric flow 101
- E.C. Neven
Determination of the linear stability of modons on a sphere by high-truncation time integrations 113

- B. Cushman-Roisin and M. T. Özgökmen
A new look at the role of eddies in the general circulation 123
- X.J. Carton and C. Bertrand
The influence of environmental parameters on two-dimensional vortex merger 125
- J. Verron and S. Valcke
Scale-dependent merging of baroclinic vortices 135
- D.G. Dritschel, J. Nycander and G.G. Sutyrin
A Hamiltonian approach to the dynamics of long, nonlinear frontal waves 145
- P. Ripa
Hamiltonian dynamics, conservation laws and the vortex stability-instability problem 151
- R.C. Kloosterziel and G.F. Carnevale
Stability of 2-D circular vortices 161
- P. Orlandi, R. Verzicco and G.J.F. van Heijst
Stability of shielded vortex dipoles 169
- J. Nycander
Dynamics of dipole vortices 177
- O.U. Velasco Fuentes and G.J.F. van Heijst
Laboratory experiments on dipolar vortices in a rotating fluid 187
- B.E. Cremers and O.U. Velasco Fuentes
Chaotic advection by dipolar vortices on a topographic β -plane 197
- G.E. Swaters
The February 1989 Pacific block as a coherent structure 207
- G.F. Carnevale and R.C. Kloosterziel
Stability of isolated compound vortices 217
- B.W. van de Fliert
Characterization and numerical calculation of plane vortex structures 231
- G.J.F. van Heijst and O.U. Velasco Fuentes
Topography-induced modulation of a tripolar vortex in a rotating fluid 241
- J.R. Bidlot and M.E. Stern
Maintenance of continental boundary layer shear through counter-gradient vorticity flux in a barotropic model 251
- B.L. Lipphardt, R.P. Mied, A.D. Kirwan, J.R. and G.J. Lindemann
Evolution of a rotating barotropic modon in a primitive equation model 259

- V.V. Meleshko and A.A. Gurzhi
Stirring of an inviscid fluid by interacting point vortices 271
- D.C. Montgomery, X. Shan and W.H. Matthaeus
Entropies for 2D viscous flows 283
- R.A. Pasmarter
On long-lived vortices in 2D viscous flows and most probable states of inviscid 2D flows 289
- D.B. Olson, G. Peng, G.R. Halliwell and C. Forbes
Evolution of turbulence as a function of initial flows on a β -plane 297
- F.M. Selten and J.D. Opsteegh
Toward an optimal description of atmospheric flow 311
- S.P. Beerens
Chaotic mixing in tidal residual vortices 317
- J.B. Flór and G.J.F. van Heijst
Decay of monopolar vortices in a stratified fluid 325
- Y. Morel
The effect of topography on the motion of coherent structures 335
- J. Nuijten and O.U. Velasco Fuentes
Merging of cyclonic vortices in a rotating fluid 345

Vortices and Jets: Dynamics, Interactions and Forecasts

Abstract

This review is concerned with the estimation of physical fields in the use of such fields in interdisciplinary research and modeling. Field estimates via data assimilation meld observations and dynamics and provide an efficient means of representing the physical processes which influence biogeochemical, ecological, acoustical and other processes in the sea. Dynamically adjusted fields can be differentiated and thus allow the influence of dynamical processes from observations via the quantitative study of energy and vorticity budgets, productivity rates, etc. A general discussion of processes and methodology is followed by a detailed review of the ocean forecast system developed at Harvard University. The model sets and algorithms are first overviewed, and then the issues are illustrated by nowcasts, forecasts and simulations carried out in various locations in the world ocean.

1. Introduction

This lecture summarizes research on the dynamics of realistic oceanic vortices. The approach adopted is to simulate synoptic realizations of the ocean via real ocean data assimilation into oceanic dynamical models. Process studies are then carried out by balance of terms studies for the vorticity and energy balances. General processes are then approached by inference from the synthesis and statistics of a number of synoptic realizations and by regional intercomparisons. The system used by the Harvard group for realistic simulations, and real time nowcasts and forecasts is shown in Figure 1. It is a modular, flexible and portable system which has been utilized in eleven locations throughout the world ocean during the past several years. Two examples will be presented. The first is the general circulation of the Eastern Mediterranean Sea which is comprised of a number of multiscale interactive jets and vortices. The second is the physical, biological and chemical dynamics of the spring bloom in the northeast Atlantic Ocean. During and after the bloom, physical dynamics of interacting vortices can control biological effects of primary production and carbon uptake, with implications for climate change processes. The remaining material in this note is excerpted from a submitted manuscript entitled 'Physical Processes, Field Estimation and Interdisciplinary Modeling' by this author.

HARVARD OCEAN FORECAST SYSTEM

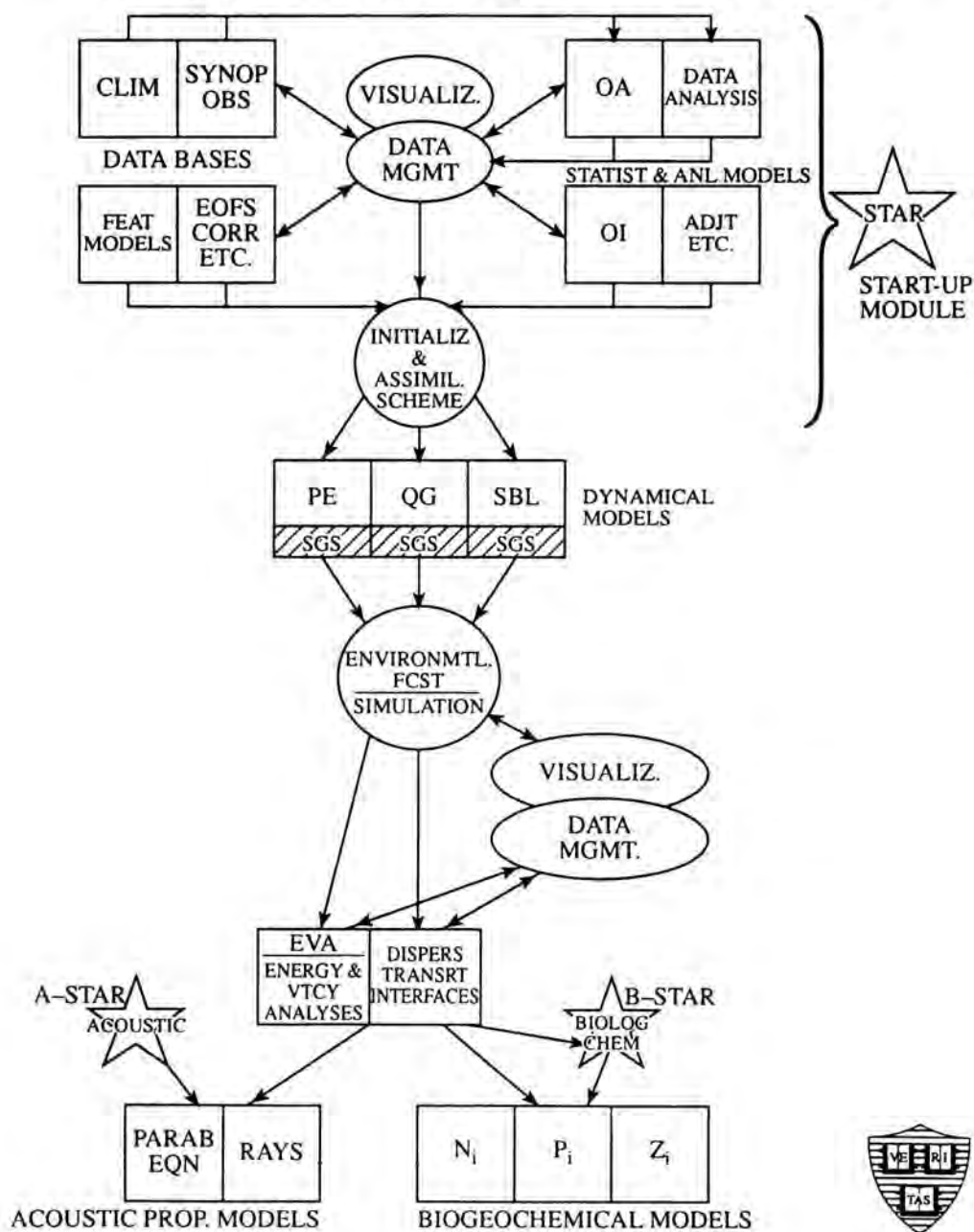


Fig. 1. Schematic of the forecast system.

2. The Eastern Mediterranean

The Eastern Mediterranean is interesting in its own right, but also serves as a test basin for ocean circulation and climate dynamics studies, for forecasting research and the development of operational models, and for the development of the 'arbitrary regional approach' to include subregions of interest within a full-scale basin. In this section we: demonstrate the real data initialization of the QG model in domains with islands and with irregular coastlines which are partially open and partially closed, illustrate dynamical adjustment and interpolation, and illustrate the concept of embedded subregional domains for dynamical process studies.

The set of domains so far studied in the Eastern Mediterranean is shown on Figure 2a. The Eastern Mediterranean upper thermocline general circulation is now known to be constituted from subbasin scale cyclonic and anticyclonic gyres linked by free and boundary jet segments and filaments (Robinson *et al.*, 1991). Thus the five domains of Figure 2a, full basin, Levantine half basin, Sicily Straits region, Rhodes gyre and Mersa-Matruh gyre were chosen for interest, data-availability, subbasin gyre dynamical studies and sensitivity studies.

The international cooperative research program for the Physical Oceanography of the Eastern Mediterranean (POEM Group, 1992) has collected and pooled four (three half-basin, one almost full basin) high resolution general circulation data sets. Robinson and Golnaraghi (1993) have performed data driven simulations and dynamical process studies (Golnaraghi, 1993) based on these data. Figure 2b shows respectively quasisynoptic objective analysis initialization field in the main thermocline from late-March/early-April 1986 and Figure 2c shows the dynamically adjusted fields twenty days after initialization. The dynamical adjustment process is nearly completed in five days in the main thermocline and in twenty days in the deep water (not shown). Topographic vortex stretching has been found to be essential for the dynamical maintenance of the subbasin scale circulation features. An interesting process of ring formation from the interaction of the Mid-Mediterranean set with the Mersa-Matruh gyre takes place a few days into the simulation, which has been dynamically analyzed by the EVA scheme by Golnaraghi (1993). The ring forms from the extended meander seen in Figure 2c. The EVA analysis region indicated on Figure 2b is shown larger on Figure 2d. The three phase process of ring formation is summarized in the cartoons of Figures 2e,f,g. The process is unusual and involves a large burst of (finite-amplitude) baroclinic instability (Figure 2f). However, another analyzed ring formation event involving the same jet and sub-basin scale gyre observed in November 1985 occur via the diffuser-like mechanism known for Gulf-Stream ring formations.

A full basin, quasisynoptic nowcast for late-August/early-September with mesoscale resolution is illustrated in Figure 3. It is to our knowledge, the first high resolution full basin synoptic circulation estimate that has been obtained. One-half degree of latitude and longitude nominal sampling produced the expected error map of Figure 3a. The bold masking contour is at 80% expected error.

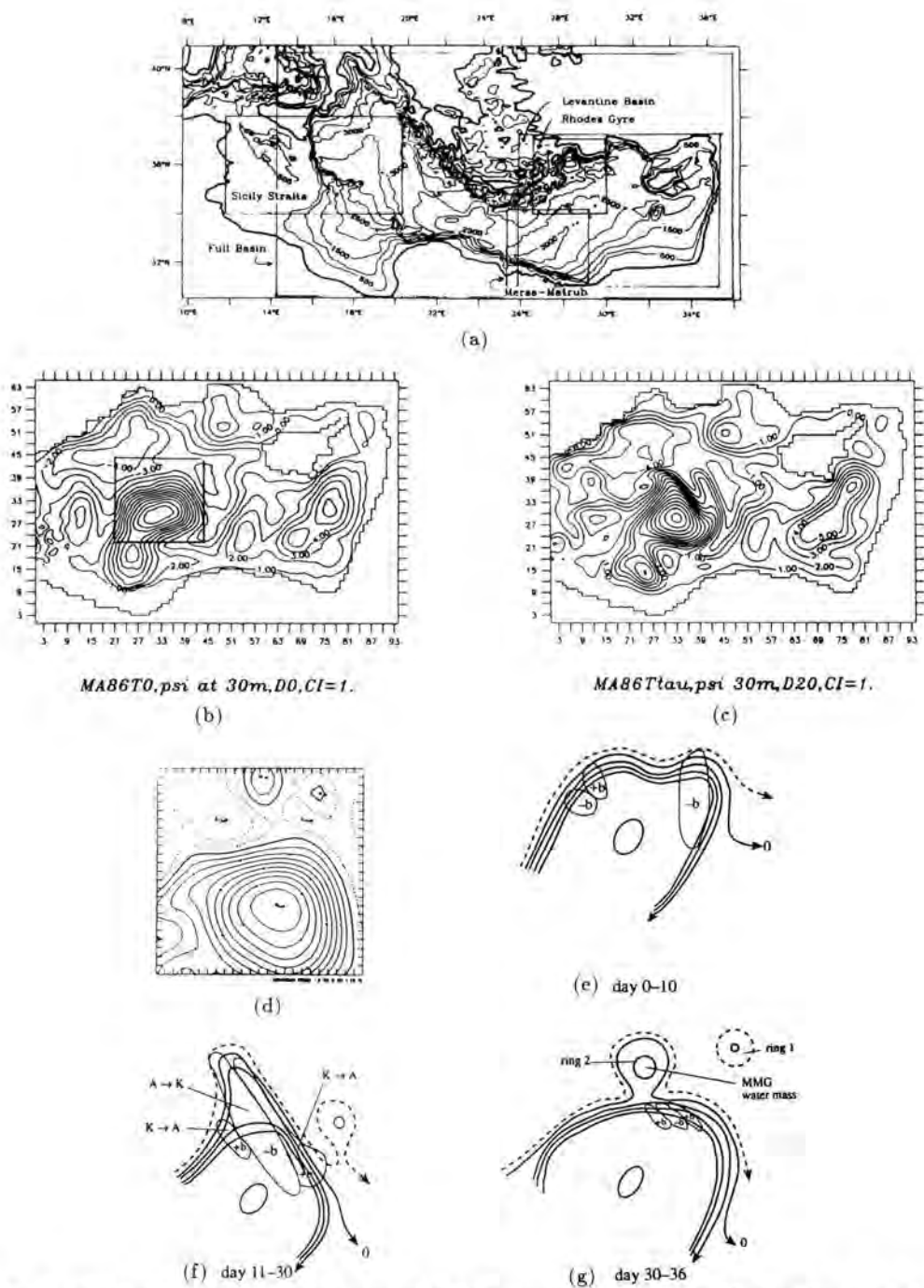
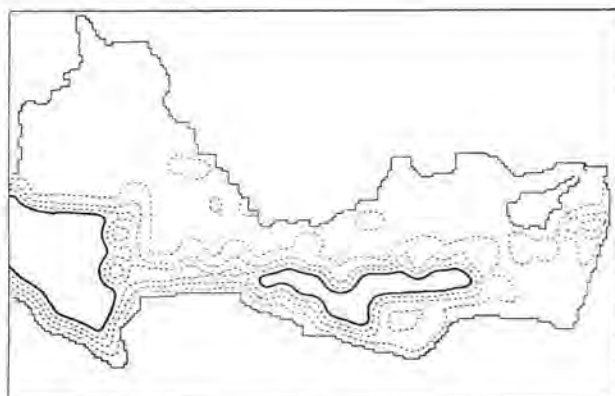
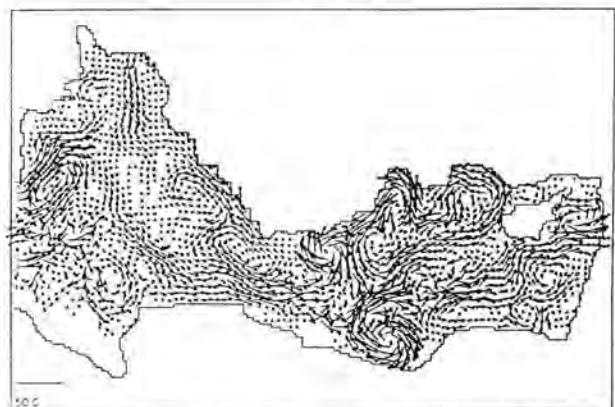


Fig. 2. a) Modeling domain over topography; b) stream function map at 30 m on day zero; c) as b) for day 20; d) zoom on ring formation; e-f) schematic of formation dynamics.

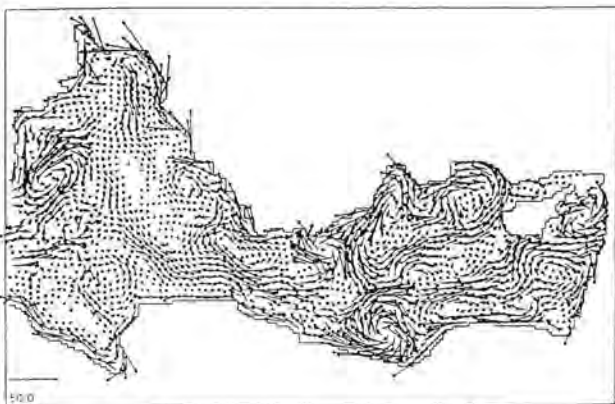


(a)



(b)

Day 0



(c)

Day 5

Fig. 3. a) Expected error of the objective analysis, contour interval of 20%; b) map of associated surface velocity; c) five day forecast.

There is a data gap due to instrument failure in the southeast Levantine and a larger data gap in the southeast Ionian where no ship voyaged. The coastal objective analysis technique employed introduces along the effective coastal boundary, the shelf/break at 600 m depth, a horizontally uniform set of density profiles inferred from near coastal data (Robinson *et al.*, 1991; Milliff and Robinson, 1992). This prohibits geostrophic flow into the coast and provides a coastal anisotropy in the objective analysis. However, it is the coastal 'pseudodata' that provides the apparent low error right along the coast on Figure 3a. The initialization objective analysis field is shown on Figure 3b and the five-day initially dynamically adjusted field on Figure 3c. The dynamical interpolation results in the flow fields sketched in Figure 3d, which also depicts the synthesized features—permanent, transient and recurrent—indicated in all of the POEM data sets. In August/September 1987 the Ionian Atlantic Stream entering through the Straits of Sicily is seen to have three filaments which feed the Mid-Mediterranean Jet.

3. The Northeast Atlantic

This oceanic region appears to be populated with energetic midocean mesoscale eddies with radii typically in the range of 50–100 km and time scales of months. The upper ocean can be acted upon by vigorous atmospheric forcing. Studies will be reviewed from the 1989 JGOFS North Atlantic Spring Bloom Experiment centered at $\sim 47^\circ\text{N}$ 19°W . Issues to be illustrated include: the initialization of the eddy resolving model via remotely sensed data and the use of feature models only; the coupling of the surface boundary layer model to the deep ocean model; the use of dynamical hindcasts and simulations to produce realistic vertical and horizontal transport fields for biological studies, and the coupling of the physical and biogeochemical models for productivity and cycling research.

Nowcasts were provided in real time (Robinson *et al.*, 1992) for the JGOFS experiment based on sea surface height information obtained from the Geosat satellite borne radar altimeter (Douglas and Cheney, 1990). The domain was 540 km by 750 km with the pattern of satellite ground tracks spaced about 1.5 degrees longitude apart. Each track was repeated every 17 days. It is not possible to locate unambiguously the local undisturbed sea level ($z = 0$) height from altimeter data alone (Glenn *et al.*, 1991) and the zero level was set to depict the cyclones with additional information from some AXBTs which indicated the presence of cold core eddies. From this information and from past knowledge of eddies in the general area (Kupferman *et al.*, 1986; Groupe Tourbillion, 1988), the indices of eddy feature models (radius, depth of the thermocline, maximum sound speed, etc.) were evaluated which were used to initialize the QG model. Dynamical adjustment and dynamical interpolation then provide a consistent estimation of the mesoscale fields throughout the domain. This also provides the mesoscale environment for estimation and study of all the physical and related fields in the upper ocean. The evolution of the physical fields is shown on Fig. 4

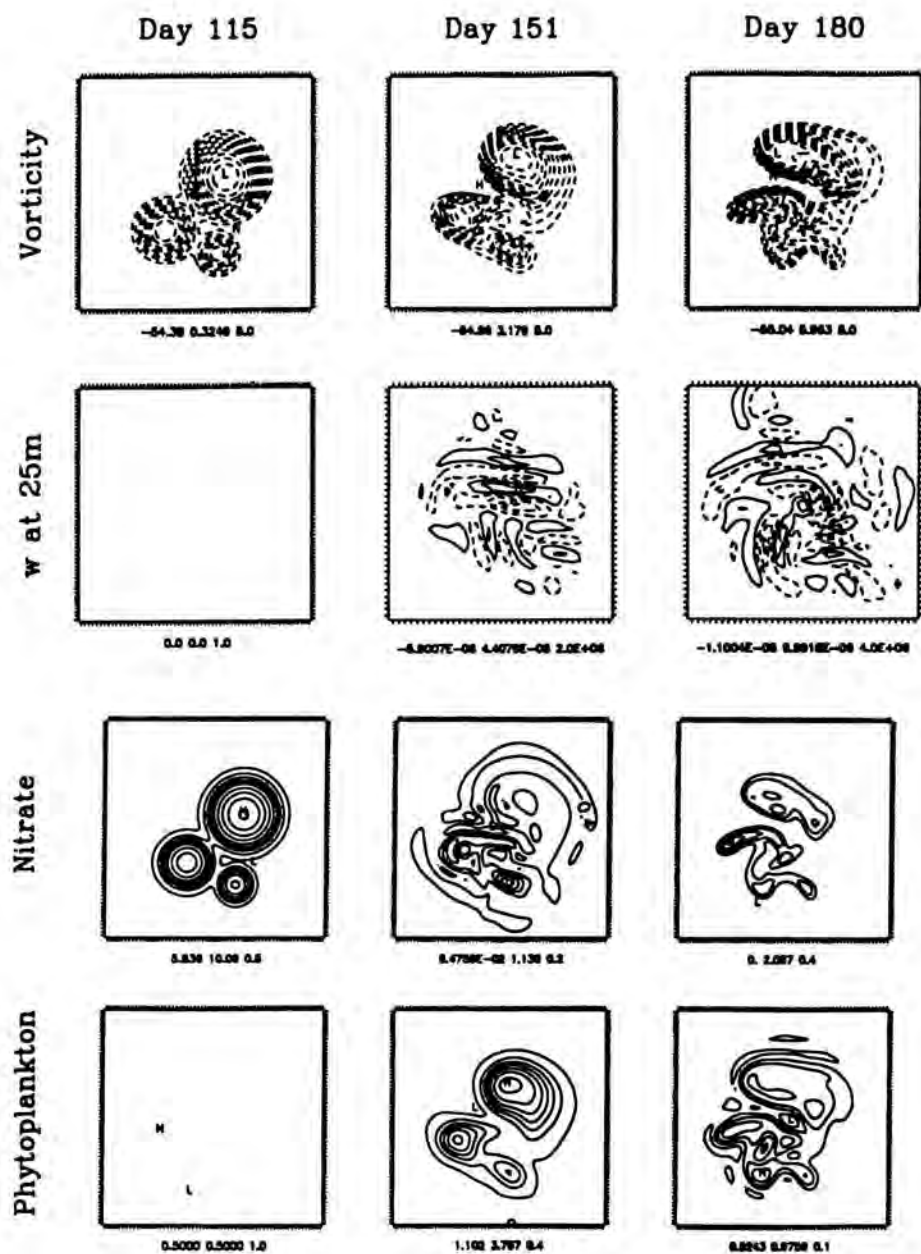


Fig. 4. Vorticity, vertical velocity, nutrient and phytoplankton concentration at the start and end of the bloom and postbloom.

in terms of the vorticity field. The eddies first persist, begin to interact and distort. The interaction between the Standard and Small eddies, for example, elongates and then begins to break up Small. These interactions provide the basis for significant nutrient transports into the upper ocean. Year day 115 is near the start of the bloom, 151 at the end of the bloom, and 181 is well into normal summertime conditions.

The coupled surface boundary layer model was attached and driven by forecast and/or shipboard estimates of the atmospheric wind, heat, and fresh water fluxes. Some estimate is required also for initial mixed layer temperature and depth. For the hindcast illustrated, a constant initial mixed layer depth based on climatology was chosen and an initial mixed layer temperature was obtained from the adjustment of a surface extrapolated QG model temperature profile with heat conservation. The SBL rapidly achieves equilibrium with the surface flux and mesoscale eddy forcings. In this case there was an initial period of light winds and shallow mixed layer followed by a storm which markedly altered the temperature characteristics of the near surface ocean by deepening and cooling the mixed layer (Robinson *et al.*, 1992). The three-dimensional SBL run provides the vertical and horizontal transport fields required for OBCE model hindcasts. The biological results (McGillicuddy, 1993) are shown on Figure 4.

Nutrient enhancement due to original and prior doming of the isopycnal and isonutrient surfaces in the cyclonic eddies is apparent in the nitrate initial condition on day 115; the phytoplankton is uniform and low at the end of the winter. The vertical velocity of the feature-model initialization is zero. Between days 115 and 151, a bloom occurs that removes nearly all of the nitrate from the mixed layer. The phytoplankton biomass distribution reflects the initial nitrate distribution in that the enhanced nitrate within the eddies has allowed the bloom to proceed much further there. Note the eddy-eddy interactions as shown in the vorticity field. Particularly, the small eddy has interacted vigorously with the standard eddy resulting in transport processes which have significantly increased the nutrient concentration in the center of the small eddy via entrainment. Between days 151 and 180, the increased nutrient in the center of the small eddy gives rise to a local maximum in phytoplankton biomass. The continued eddy-eddy interactions have now produced a nutrient enhancement within the standard eddy which is an order of magnitude greater than the background concentration outside of the eddies. The nutrient transports due to eddy-eddy interactions are in this case much larger than the submesoscale enhancements previously hypothesized to be the most important biological effects of mesoscale motions (Woods, 1988).

Acknowledgements

The research on the Eastern Mediterranean was carried out in collaboration with Dr. Maryam Golnaraghi and Mr. Wayne G. Leslie and the research on the bloom was carried out with Dr. Dennis J. McGillicuddy and Professor James

J. McCarthy. Dr. Hernan Arango has contributed significantly to the development of the forecast system. Research was supported by the Office of Naval Research under grant No. N00014-90-J-1612 to Harvard University.

References

- Auer, S.J., 1987 - Five-year Climatological Survey of the Gulf Stream System and its Associated Rings, *Journal of Geophysical Research* **92**, 11709–11726.
- Akima, H., 1970 - A New Method of Interpolation and Smooth Curve Fitting Based on Local Procedures, *J. Assoc. Comp. Mach.* **17**, 589–602.
- Arango, H.G., A. Gangopadhyay and A.R. Robinson, 1992 - Feature Models for the Western North Atlantic I: Currents, Subbasin and Mesoscale Features in the GSMR Region. Harvard University, Reports in Meteorology and Oceanography No. 43, Division of Applied Sciences, Cambridge, MA 02138.
- Botseas, G., D. Lee and K.E. Gilbert, 1983 - IFD: Wide Angle Capability, NUSC Technical Report 6905.
- Botseas, G., D. Lee and W.L. Siegmann, 1989 - IFD: Interfaced with Harvard Open Ocean Model Forecasts, NUSC Technical Report 8367.
- Bryan, K. and M.D. Cox, 1967 - A Numerical Investigation of the Oceanic General Circulation, *Tellus*, 54–80.
- Calman, J. and L.P. Manzi, 1990 - Real-time Satellite Altimetry, *Johns Hopkins APL Digest* **10**(4), 380–385.
- Carman, J.C., 1991 - Oceanographic and Topographic Interactions in Underwater Acoustic Propagation, with Regional Applications. Ph.D. Thesis, Harvard University, Reports in Meteorology and Oceanography No. 39, Division of Applied Sciences, Cambridge, MA 02138.
- Carman, J.C., 1992a - Oceanographic and Sediment Interactions in Deep Water Acoustic Propagation: Part I; Sediment Effects on Water Column Propagation Patterns. *Journal of the Acoustical Society of America*, submitted.
- Carman, J.C. and A.R. Robinson, 1992b - Oceanographic and Sediment Interactions in Deep Water Acoustic Propagation: Part II; Gulf Stream Simulations. *Journal of the Acoustical Society of America*, submitted.
- Carter, E.F. and A.R. Robinson, 1987 - Analysis Models for the Estimation of Oceanic Fields, *Journal of Atmospheric and Oceanic Technology* **4**(1), 49–74.
- Charney, J.G., R. Fjortoft and J. von Neumann, 1950 - Numerical Integration of the Barotropic Vorticity Equation, *Tellus* **2**, 237–254.
- Choubert, G. and A. Faure-Muret, 1987 - *Geological World Atlas*, UNESCO.
- Cornillon, P. and D.R. Watts, 1987 - Satellite Thermal Infrared and Inverted Echo Sounder Determinations of the Gulf Stream Northern Edge, *Journal of Atmospheric and Oceanic Technology* **4**, 7212–7232.
- Cornuelle, B., 1990 - Some Practical Aspects of Ocean Acoustic Tomography, in: *Oceanographic and Geophysical Tomography*, (Desaubies, Tarantola and Zinn-Justin, eds.), North-Holland, Amsterdam.

- DeMey, P. and the AthenA Group, 1992 - AthenA-88: An Investigation of the Regional Structure of Mesoscale Fields in the Northeast Atlantic involving In-situ Observations and Satellite Altimetry. *Oceanologica Acta*, in press.
- Denbo, D.W. and A. R. Robinson, 1988a - Harvard Gapcast; A Progress Report: Regional Forecasting, Processes and Methodology in the Iceland-Faeroe Island Gap. Part I: Data Forecast and Hindcast Experiments, *Harvard Open Ocean Model Reports* 32, Reports in Meteorology and Oceanography, Harvard University, Cambridge, MA, December 1988.
- Denbo, D.W. and A. R. Robinson, 1988b - Harvard Gapcasts; A Progress Report: Regional Forecasting, Processes and Methodology in the Iceland-Faeroe Island Gap. Part II: GFD and Process Experiments, *Harvard Open Ocean Model Reports* 33, Reports in Meteorology and Oceanography, Harvard University, Cambridge, MA, December 1988.
- Douglas, B.C. and R.E. Cheney, 1990 - Geosat: Beginning a New Era in Satellite Oceanography, *Journal of Geophysical Research* 95 C3, 2833-2837.
- Evans, J.C., D.B. Haidvogel and W.R. Holland, 1987 - A Review of Numerical Ocean Modeling (1983-1986): Midlatitude Mesoscale and Gyre-scale, *Review of Geophysics* 25, 235-244.
- Fofonoff, N.P. and R.C. Millard, Jr., 1983 - Algorithms for Computation of Fundamental Properties of Seawater, UNESCO Technical Papers in Marine Science.
- Frisk, G.F., J.A. Doult and E.E. Hays, 1986 - Geoacoustic Models for the Icelandic Basin, *Journal of the Acoustical Society of America* 80(2), 591-600.
- Garwood, R.W., 1977 - An Oceanic Mixed-Layer Model Capable of Simulating Cyclic States, *Journal of Physical Oceanography* 7, 455-471.
- Glenn, S.M. and A.R. Robinson, 1990 - Nowcasting and Forecasting of Oceanic Dynamic and Acoustic Fields, in: *Computational Acoustics II*, (D. Lee, A. Cakmak and R. Vichnevetsky, eds.), 117-128, Elsevier Science Publishers, Amsterdam.
- Glenn, S.M. and A.R. Robinson, 1991 - A Continuous Temperature and Salinity Model Across the Gulf Stream, *Harvard Open Ocean Model Reports*, 38, Reports in Meteorology and Oceanography, Harvard University, Cambridge, MA.
- Glenn, S.M., D.L. Porter and A.R. Robinson, 1991 - A Synthetic Geoid Validation of Geosat Mesoscale Dynamic Topography in the Gulf Stream Region, *Journal of Geophysical Research-Oceans*, 96(64), 7145-7166.
- Haidvogel, D.B. and A.R. Robinson, eds., 1989 - Special issue on Data Assimilation, *Dynamics of Atmospheres and Oceans* 13(3-4), 171-517.
- Haidvogel, D.B., A.R. Robinson and E.E. Schulman, 1980 - The Accuracy, Efficiency and Stability of Three Numerical Models with Application to Open Ocean Problems, *Journal of Computational Physics* 34, 1-53.
- Halkin, D.H. and H.T. Rossby, 1985 - The Structure and Transport of the Gulf Stream at 73 West, *Journal of Physical Oceanography* 15, 1439-1452.
- Hallock, Z.R., 1985 - Variability of Frontal Structure in the Southern Norwegian Sea, *Journal of Physical Oceanography* 15, 1245-1254.

- Hamilton, E.L., 1980 - Geoacoustic Modeling of the Sea Floor, *Journal of the Acoustical Society of America* **68**(5), 1313-1340.
- Holloway, G., 1989 - Subgrid scale representation. In: *Oceanic Circulation Models Combining Data and Dynamics*, (D.L.T. Anderson and J. Willebrand, eds.), 513-593, Kluwer Academic Publishers, Dordrecht, Netherlands.
- Jensen, F. B., G. Dreini and M. Prior, 1991 - Acoustic Effects of the Iceland-Faeroe Front, in: *Ocean Variability and Acoustic Propagation*, (J. R. Potter and A. Warn-Varnes, eds.), 359-374, Kluwer Academic Publishers, Dordrecht, Netherlands.
- Johannessen, O.M., 1986 - Brief Overview of the Physical Oceanography, in: *The Nordic Seas*, (B.G. Hurdle, ed.), 102-127, Springer-Verlag, New York.
- Johns, E., D.R. Watts and H.T. Rossby, 1989 - A Test of Geostrophy in the Gulf Stream, *Journal of Geophysical Research* **94**, 3211-3222.
- Knobles, D.P. and P.J. Vidmar (1986). Simulation of Bottom Interacting Waveforms, *Journal of the Acoustical Society of America* **79**(6), 1760-1766.
- Kupferman, S., G. Becker, W. Simmons, U. Schauer, M. Marietta and H. Nies, 1986 - An Intense Cold Core Eddy in the North-east Atlantic, *Nature* **319**, 474-477.
- Le Groupe Tourbillion, 1983 - The Tourbillion Experiment: A Study of a Mesoscale Eddy in the Eastern North Atlantic, *Deep Sea Research* **30**, 475-511.
- Lee, D. and G. Botseas, 1982 - IFD: An Implicit Finite-Difference Computer Model for Solving the Parabolic Equation, NUSC Technical Report 6659.
- Lee, D., G. Botseas and J.S. Papadakis, 1981 - Finite-Difference Solution to the Parabolic Wave Equation, *Journal of the Acoustical Society of America* **70**(3), 795-800.
- Lee, D., G. Botseas, W.L. Siegmann, and A.R. Robinson, 1989 - Numerical Computations of Acoustic Propagation through Three-Dimensional Ocean Eddies, in: *Numerical and Applied Mathematics*, (W.F. Ames, ed.), 317-321, J.C. Baltzer AG, Scientific Publishing Co.
- Lee, D. and S.T. McDaniel, 1988 - *Ocean Acoustic Propagation by Finite Difference Methods* (Pergamon Press).
- Lee, D. and J.S. Papadakis, 1979 - Numerical Solutions of Underwater Acoustic Wave Propagation Problems, NUSC Technical Report 5929.
- Levitus, S., 1982 - NOAA, Climatological Atlas of the World Ocean, Professional Paper No. 13, Rockville, Maryland.
- Lozano, C.J. and A.R. Robinson, 1991 - 88 Surface Boundary Layer Model —Model Description and Numerics. Unpublished Manuscript.
- Lybanon, M., R.L. Crout, C.H. Johnson and P. Pistek, 1991 - Operational Altimeter-derived Oceanographic Information: The NORDA Geosat Ocean Applications Program, *Journal of Atmospheric and Oceanic Technology*, in press.
- Malanotte-Rizzoli, P. and A.R. Robinson, 1988 - POEM: Physical Oceanography of the Eastern Mediterranean, *EOS The Oceanography Report* **69**(14), 194-203.

- Mellberg, L.E., A.R. Robinson and G. Botseas, 1990 - Modeled Time Variability of Acoustic Propagation through a Gulf Stream Meander and Eddies, *Journal of the Acoustical Society of America* **87**(3), 1044-1054.
- Mellberg, L.E., A.R. Robinson and G. Botseas, 1991 - Azimuthal Variation of Low Frequency Acoustic Propagation through Asymmetric Gulf Stream Eddies, *Journal of the Acoustical Society of America*, **89**(5), 2157-2167.
- Miller, R.N., A.R. Robinson and D.B. Haidvogel, 1983 - A Baroclinic Quasi-geostrophic Open Ocean Model, *Journal of Computational Physics* **50**, 38-70.
- Milliff, R.F., 1990 - A Modified Capacitance Matrix Method to Implement Coastal Boundaries in the Harvard Open Ocean Model, *Mathematics and Computers in Simulations* **31**, 541-564.
- Milliff, R.F. and A.R. Robinson, 1992 - Structure and Dynamics of the Rhodes Gyre System and its Dynamical Interpolation for Estimates of the Mesoscale Variability, *Journal of Physical Oceanography*, in press.
- Munk, W.H. and C. Wunsch, 1979 - Ocean Acoustic Tomography: A Scheme for Large-scale Monitoring, *Deep Sea Research* **26**, 123-161.
- Nihoul, J.C.J. and B.M. Jamart, eds., 1987 - *Three Dimensional Ocean Models of Marine and Estuarine Dynamics*, (Elsevier Scientific Publishing, Amsterdam).
- O'Brien, J.J., ed., 1986 - *Advanced Physical Oceanographic Numerical Modeling*, (R. Reidel Publishing Co., Dordrecht, The Netherlands).
- Ozsöy, E., C.J. Lozano, and A.R. Robinson, 1992 - Consistent Baroclinic Quasigeostrophic Ocean Model in Multiply Connected Ocean Domains, *Mathematics and Computers in Simulation*, in press.
- Pedlosky, J., 1987 - *Geophysical Fluid Dynamics* (Springer-Verlag, New York).
- Pinardi, N. and A.R. Robinson, 1986 - Quasigeostrophic Energetics of Open Ocean Regions, *Dynamics of Atmospheres and Oceans* **10**(3), 185-221.
- Pinardi, N. and A.R. Robinson, 1986 - Dynamics of Deep Thermocline Jets in the POLYMODE Region, *Journal of Physical Oceanography*, **17**, 1163-1188.
- Porter, D. L., A.R. Robinson, S.M. Glenn and E.B. Dobson, 1989 - The Synthetic Geoid and the Estimation of Mesoscale Absolute Topography from Altimeter Data, *Johns Hopkins APL Digest* **10**(4), 369-379.
- Rhines, P.B., 1979 - Geostrophic Turbulence, *Annual Review of Fluid Mechanics* **11**, 401-441.
- Robinson, A.R., ed., 1983 - *Eddies in Marine Science*, (Springer-Verlag, New York, NY).
- Robinson, A.R., 1992 - Shipboard Prediction with a Regional Forecast Model, *The Oceanography Society Magazine*, in press.
- Robinson, A.R., S.M. Glenn, W.L. Siegmund, D. Lee and G. Botseas, 1991 - Environmental Sensitivity Studies with an Interfaced Ocean-Acoustics System, in: *Ocean Variability and Acoustic Propagation*, (J.R. Potter and A. Warn-Varnas, eds.), 545-560, Kluwer Academic Publishers, Dordrecht, Netherlands.
- Robinson, A.R., S.M. Glenn, M.A. Spall, L.J. Walstad, G.M. Gardner and W.G. Leslie, 1989 - Forecasting Gulf Stream Meanders and Rings, *EOS The Oceanography Report* **70**(45), 1464-1473.

- Robinson, A.R. and M. Golnaraghi, 1991 - Progress in Understanding of the Eastern Mediterranean, Proceedings of ICSEM Symposium, Perpignan, Oct. 1990.
- Robinson, A.R., M. Golnaraghi, W.G. Leslie, A. Artegiani, A. Hecht, E. Lazzoni, A. Michelato, E. Sansone, A. Theocharis and U. Unluata, 1991 - The Eastern Mediterranean General Circulation: Features, Structure and Variability, *Dynamics of Atmospheres and Oceans* **15**(3-5), 215-240.
- Robinson, A.R. and W.G. Leslie, 1985 - Estimation and Prediction of Oceanic Fields, *Progress in Oceanography* **14**, 485-510.
- Robinson, A.R., P. Malanotte-Rizzoli, A. Hecht, A. Michelato, W. Roether, A. Theocharis, U. Unluata, N. Pinardi and the POEM Group, 1992 - General Circulation of the Eastern Mediterranean, *Earth - Science Reviews*, in press.
- Robinson, A.R., D.J. McGillicuddy, J. Calman, H. Ducklow, M.J.R. Fasham, F.E. Hoge, W.G. Leslie, J.J. McCarthy, S. Podewski, D.L. Porter, G. Saure and J.A. Yoder, 1992 - Mesoscale and Upper Ocean Variabilities during the 1989 JGOFS Bloom Study Region, *Deep Sea Research*, in press.
- Robinson, A.R., M.A. Spall and N. Pinardi, 1988 - Gulf Stream Simulations and the Dynamics of Ring and Meander Processes, *Journal of Physical Oceanography* **18**(12), 1811-1853.
- Robinson, A.R. and L.J. Walstad, 1987 - The Harvard Open Ocean Model: Calibration and Application to Dynamical Process, Forecasting, and Data Assimilation Studies, *Applied Numerical Mathematics* **3**(1-2), 89-131.
- Scott, J.C., N.R. Geddes, N.M. Lane and A.L. McDowell, 1988 - Thermal Structure and Remote Sensing Measurements in a Major Frontal Region, *Advances in Underwater Technology Ocean Science and Offshore Engineering* **16**, 59-68.
- Semtner, A.J., 1974 - An Oceanic General Circulation Model with Bottom Topography, *UCLA Dept. of Meteorology Technical Report* **9**.
- Shapiro R., 1971 - The Use of Linear Filtering as a Parameterization for Atmospheric Diffusion, *Journal of Atmospheric Science* **29**, 523-531.
- Siegmann, W.L., M.J. Jacobson, D. Lee, G. Botseas, A.R. Robinson and S.M. Glenn, 1990 - Interfacing Mesoscale Ocean Prediction and Parabolic Acoustic Propagation Models, in: *Computational Acoustics II*, (D. Lee, A. Cakmak and R. Vichnevetsky, eds.), 155-168, Elsevier Science Publishers, Amsterdam.
- Spall, M.A. and A.R. Robinson, 1989 - A New Open Ocean, Hybrid Coordinate Primitive Equation Model, *Mathematics and Computers in Simulation* **31**, 241-269.
- Spall, M.A. and A.R. Robinson, 1990 - Regional Primitive Equation Studies of the Gulf Stream Meander and Ring Formation Region, *Journal of Physical Oceanography* **20**(7), 985-1016.
- Smart, J.H., 1984 - Spatial Variability of Major Frontal Systems in the North Atlantic-Norwegian Sea Area: 1980-81, *Journal of Physical Oceanography* **14**, 185-192.
- Vidmar, P.J., 1980 - Ray Path Analysis of Sediment Shear Wave Effects on Bottom Reflection Loss, *Journal of the Acoustical Society of America* **68**(2), 639-648.

- Walstad, L.J., 1987 - Modeling and Forecasting Deep Ocean and Near Surface Mesoscale Eddies: Hindcasting and Forecasting with, and Coupling a Surface Boundary Layer Model to, the Harvard Quasigeostrophic Model. PhD Thesis, Harvard University, Cambridge, MA. Reports in Meteorology and Oceanography, **23**.
- Walstad, L.J. and A.R. Robinson, 1992 - A Coupled Surface Boundary Layer-Quasigeostrophic Ocean Model, *Dynamics of Atmospheres and Oceans*, in press.
- Warren, B.A. and C. Wunsch, eds., 1981 - *Evolution of Physical Oceanography* (MIT Press, Cambridge, MA).

Division of Applied Sciences
Department of Earth and Planetary Sciences
Harvard University

Statistical Dynamics and Coherent Vortices in Two-Dimensional and Planetary Turbulence

Abstract

Results are presented for initial-value problems in two-dimensional flows and three-dimensional, rotating, stably stratified (i.e., planetary-scale) flows with small diffusivities. The domains and initial conditions are spatially homogeneous and isotropic (though only in a particular sense for the latter problem). In each problem the evolution is dominated by coherent vortices that spontaneously emerge around the time of maximum dissipation. The vortex populations evolve by a lengthy sequence of combinatorial interactions until non-chaotic end-state configurations are achieved. In the three-dimensional flow, the vortices effect a significant departure from the isotropy prediction of Charney (1971).

Two-dimensional turbulence

Two-dimensional turbulence has been investigated quite extensively, in certain aspects more so than any other type or regime of turbulent flow. To be brief I will not attempt to review the literature here, other than to refer the reader to the review papers by Kraichnan and Montgomery (1980) and McWilliams (1983)—plus other articles in the same issue of *Journal de Mécanique*—written near the end of the “classical” period prior to the discovery of the importance of coherent vortices, and to a recent paper by Weiss and McWilliams (1993), from whose references some of the “modern” period can be explored.

The primary attractions in examining two-dimensional turbulence are twofold: (1) by having one fewer spatial dimension than natural fluid motions, it is more accessible to numerical and at least some kinds of theoretical calculations, and (2) by having only two components of velocity, it provides an archetype for anisotropic turbulence of various types commonly found in planetary fluid motions (see below).

The velocity incompressibility condition in two dimensions is

$$\frac{\partial u}{\partial x} + \frac{\partial v}{\partial y} = 0, \quad (1)$$

for velocity components (u, v) and coordinates (x, y) . This permits a representation in terms of a streamfunction ψ ,

$$u = -\frac{\partial\psi}{\partial y}, \quad v = \frac{\partial\psi}{\partial x}. \quad (2)$$

The governing equation is

$$\frac{\partial q}{\partial t} + \frac{\partial\psi}{\partial x} \frac{\partial q}{\partial y} - \frac{\partial\psi}{\partial y} \frac{\partial q}{\partial x} = -\nu \nabla^4 q, \quad (3)$$

where q is the vorticity field,

$$q = \nabla^2 \psi, \quad (4)$$

and ν is a small hyperviscosity (see, e.g., Sadourny and Basdevant, 1981). Among the inviscid invariants of (3) are the energy and enstrophy,

$$E = \frac{1}{2} \int [(\nabla\psi)^2 \mathbf{d}\mathbf{x}], \quad V = \frac{1}{2} \int q^2 \mathbf{d}\mathbf{x}. \quad (5)$$

I offer the following summary of the most important properties of freely evolving, spatially homogeneous two-dimensional turbulence at large Reynolds number. The first four items are classical, and the last four are modern.

- As $\nu \rightarrow 0$, the dissipation rate of E vanishes, while that for V remains finite.
- The characteristic time for nonlinear (i.e., turbulent) evolution is $\sim V^{-1/2}$ and for significant enstrophy dissipation is $\sim V^{-1/2} \log [1/\nu]$.
- $\psi(x, y)$ and $q(x, y)$ evolve towards a state of statistical isotropy from nearly all initial conditions.
- There is a preferential transfer of energy towards larger spatial scales and of enstrophy towards smaller ones, hence towards its dissipation.
- Coherent vortices spontaneously emerge from random initial conditions on the time scale of enstrophy dissipation and subsequently dominate the statistical dynamics for as long as they remain chaotic (see below). The principal means of their non-conservative evolution is merger of close, like-sign vortices.
- A vortex-based dynamical system successfully mimics key aspects of the statistical dynamics of the turbulence; it is called “punctuated Hamiltonian dynamics”, where intervals of conservative mutual advection of vortices are punctuated by abrupt, dissipative transformations, representing mergers.
- There exist fundamental solutions in which the coherent vortex population exhibits self-similar evolution in spatial size and/or time (i.e., scaling behavior).
- After the occurrence of all possible mergers, the nonlinear, chaotic evolution nearly always ends in a final dipole vortex configuration (a modon).

I believe that the preceding comprises a fairly mature understanding of the statistical dynamics of two-dimensional turbulence. With this perspective, therefore, we now turn to its most plausible three-dimensional analogue — homogeneous, rotating, stratified turbulence. We are not yet ready, of course, to make such a broad summary of its dynamics.

Planetary turbulence

Planetary fluid motions commonly evolve under the influences of planetary rotation and stable density stratification. A long-standing theoretical prediction (Charney, 1971; Rhines, 1979; Herring, 1980) is that the flow evolves to have isotropic spatial dependence; furthermore, previous numerical assessments (Hua and Haidvogel, 1986; McWilliams, 1989), based upon sparse and anisotropic computational grids, have appeared to confirm this prediction. Here we test this prediction with a dense, fully isotropic computational grid in a spatially homogeneous domain. The results can be summarized as follows. The solution exhibits significant anisotropy associated with the emergence of long-lived (coherent), spatially intermittent vortex structures that control the flow evolution. This, I believe, is generic behavior that has particular manifestations in, for example, the phenomena of Jupiter's Red Spot, tropospheric cyclones, stratospheric polar vortices, and oceanic Gulf Stream Rings. Over a very long time scale, the coherent vortices undergo successive combinatorial interactions until reaching an approximate evolutionary end-state consisting of two vertical columns containing vortex cores of common sign. A more formal presentation of these results (and with better graphics) is made in McWilliams *et al.* (1993).

An asymptotic regime relevant to planetary-scale motions is defined by small viscosity, incompressibility, rapid rotation rate Ω , and strongly stable ambient density stratification $\frac{d\rho}{dz}$. The characteristic frequencies for rotation and stratification are $f = 2\Omega$ and $N = \sqrt{-\frac{g}{\rho} \frac{d\rho}{dz}}$. In this regime, f and N are large compared to fluid recirculation rates. It follows that the velocity is anisotropic in the sense that the vertical component w (parallel to the gravitational vector) is weak compared to horizontal components u and v . Thus, u, v are nearly non-divergent in x, y and can be represented approximately by a streamfunction ψ : $u = -\frac{\partial\psi}{\partial y}$ and $v = \frac{\partial\psi}{\partial x}$. The theoretical prediction of isotropy applies to the spatial dependence of ψ in a stretched coordinate frame $(x, y, \frac{N}{f}z)$.

The governing equation is

$$\frac{\partial q}{\partial t} + \frac{\partial\psi}{\partial x} \frac{\partial q}{\partial y} - \frac{\partial\psi}{\partial y} \frac{\partial q}{\partial x} = -\nu \nabla^4 q, \quad (6)$$

where q is the potential vorticity field,

$$q = \frac{\partial^2\psi}{\partial x^2} + \frac{\partial^2\psi}{\partial y^2} + \frac{f^2}{N^2} \frac{\partial^2\psi}{\partial z^2}, \quad (7)$$

∇ is now the three-dimensional spatial gradient operator, and ν is a small hyperviscosity. Note the formal similarities with (3)-(4). We solve (6)-(7) in a periodic domain of non-dimensional extent $2\pi \times 2\pi \times \frac{f}{N} 2\pi$. The initial condition in ψ is a Gaussian random realization of an isotropic wavenumber spectrum peaked at scales intermediate between the domain and grid-resolution. The initial energy, $E = \frac{1}{2} \int [(\frac{\partial \psi}{\partial x})^2 + (\frac{\partial \psi}{\partial y})^2 + (\frac{f}{N} \frac{\partial \psi}{\partial z})^2] d\mathbf{x}$, is one, which defines the time-scale of the evolution. The equations are discretized by finite differences, and the numerical integration is by a fully implicit multigrid method (see Yavneh and McWilliams, 1993). To achieve the large grid dimension of 320^3 , we developed an efficient parallel algorithm for the Cray C-90 supercomputer.

The initial stage of evolution is a broadening of the spectrum. Energy is transferred preferentially towards larger scales and thus away from the smaller scales at which dissipation occurs. In contrast, potential enstrophy, $V = \frac{1}{2} \int q^2 d\mathbf{x}$, is transferred towards smaller scales, resulting in its dissipation (Charney, 1971; Rhines, 1979; Herring, 1980). These effects are seen in Fig. 1, where E decreases by only 4% over the integration but V decreases by nearly two orders of magnitude. The rate of enstrophy dissipation reaches a maximum at $t \approx 1$, after several nonlinear advection times (of order $V^{-1/2}$). Thereafter the rate of spec-

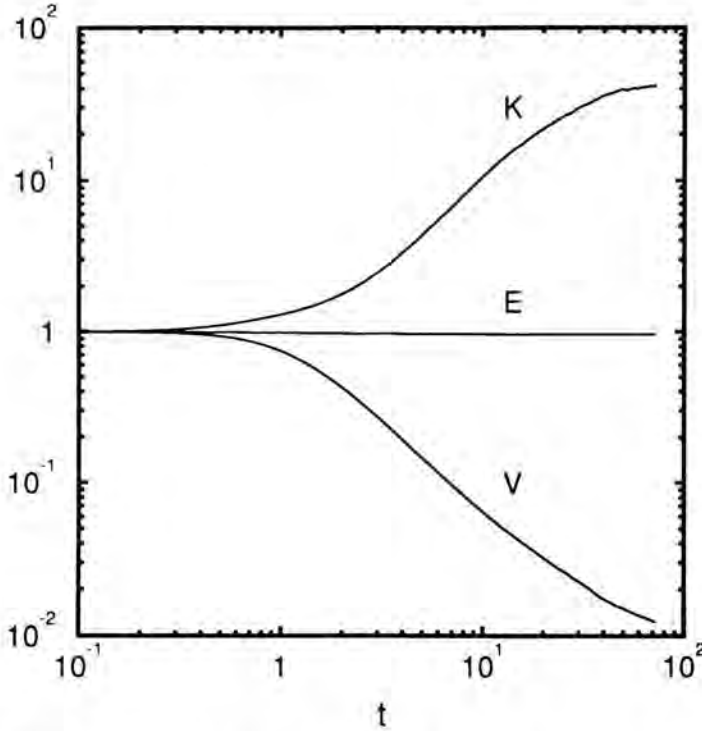


Fig. 1. Time series of the energy E , potential enstrophy V , and kurtosis K . All quantities are normalized by their initial values.

trum broadening diminishes, and the flow develops substantial intermittency; in particular, the kurtosis of q , $K = \int q^4 d\mathbf{x} / [\int q^2 d\mathbf{x}]^2$, grows monotonically from its initial Gaussian value and eventually reaches very large values (Fig. 1).

Figure 2 shows the isotropic wavenumber spectrum for q : $S(\kappa)$, $\kappa = \sqrt{k_x^2 + k_y^2 + (\frac{f}{N} k_z)^2}$. Only near the time of maximum enstrophy dissipation does $S(\kappa)$ approach the κ^{-1} inertial-range form previously predicted (Charney, 1971); it is also quite broad-band and has a steep decay in the dissipation range at very large κ . Its subsequent evolution is slow movement of its centroid towards smaller κ and further steepening at large and intermediate κ .

The spectrum anisotropy can be measured by

$$A(k) = \frac{2S_z(fk/N)}{[S_x(k) + S_y(k)]}, \quad (8)$$

where the 1D q spectra, $S_\eta(k_\eta)$, $\eta = x, y, z$, are integrals over the plane of wavenumbers perpendicular to their wavenumber argument k_η . Our solution shows significant departures from isotropy (i.e., $A \equiv 1$): at small k , $A < 1$,

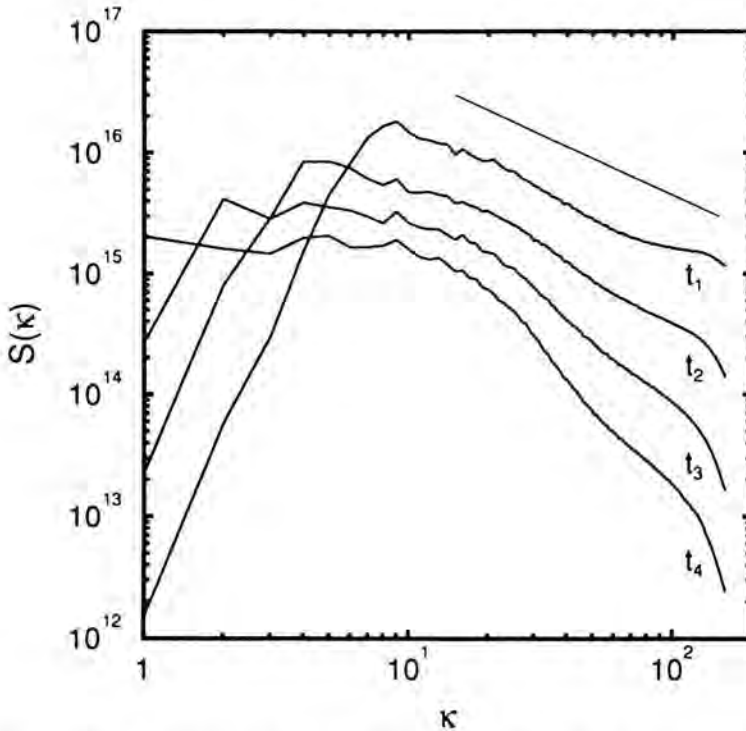


Fig. 2. Wavenumber spectra $S(\kappa)$ at $t_1 = 2.2$, $t_2 = 5.0$, $t_3 = 10.0$, and $t_4 = 20.4$. $S(\kappa)$ is the squared modulus of the 3D Fourier transform of q integrated over wavenumber shells of constant wavenumber magnitude. The reference line represents a function $\propto \kappa^{-1}$.

whereas at intermediate and large k , $A > 1$ in two distinct wavenumber bands (Fig. 3). The former is in the inertial range, where the theoretical prediction of isotropy applies, and the latter is in the dissipation range. The degree of inertial-range anisotropy grows systematically after the time of maximum dissipation rate.

The rate of spectrum migration and the increases in intermittency and anisotropy are associated with the emergence of coherent vortices (McWilliams, 1989), which are isolated concentrations in q (Fig. 4). Their shape, at the time of emergence, is roughly spherical in $(x, y, \frac{1}{N}z)$ with monotonic decay from the central extremum. They move by mutual advection in an essentially conservative fashion, except during close approaches when dissipative transformations occur. The most important of these are *merger* (e.g., Melander *et al.*, 1988) and *attachment* (McWilliams, 1989); these are horizontal and vertical combinations of like-sign vortices. As a consequence of these transformations, the population of vortices decreases and their average size increases in all dimensions. However, the merger and attachment events cause dissimilar transformations in vortex shape: merger involves mixing of fluid parcels in horizontal planes and thus a complete combination of the q fields of the component vortices, whereas attachment

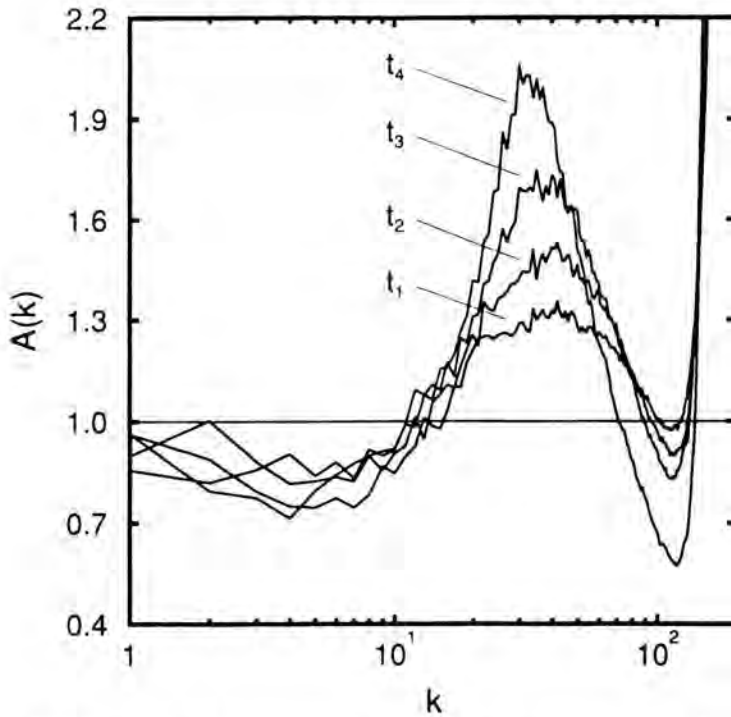


Fig. 3. Spectrum anisotropy $A(k)$ at the same times as in Fig. 2.

involves no vertical parcel exchange (because of velocity anisotropy) and thus retains the distinct extrema of the component vortices. In both events the transformed vortex is approximately axisymmetric about a vertical axis, and its q field is everywhere of one sign and decays monotonically in x, y but not necessarily in z . Each such vortex is, by itself, a stable, stationary state of the inviscid dynamics that results from the organizing processes of horizontal *axisymmetrization* (Melander *et al.*, 1987) and vertical *alignment* (McWilliams, 1989; Polvani, 1991; Dritschel and Saravanan, 1993).

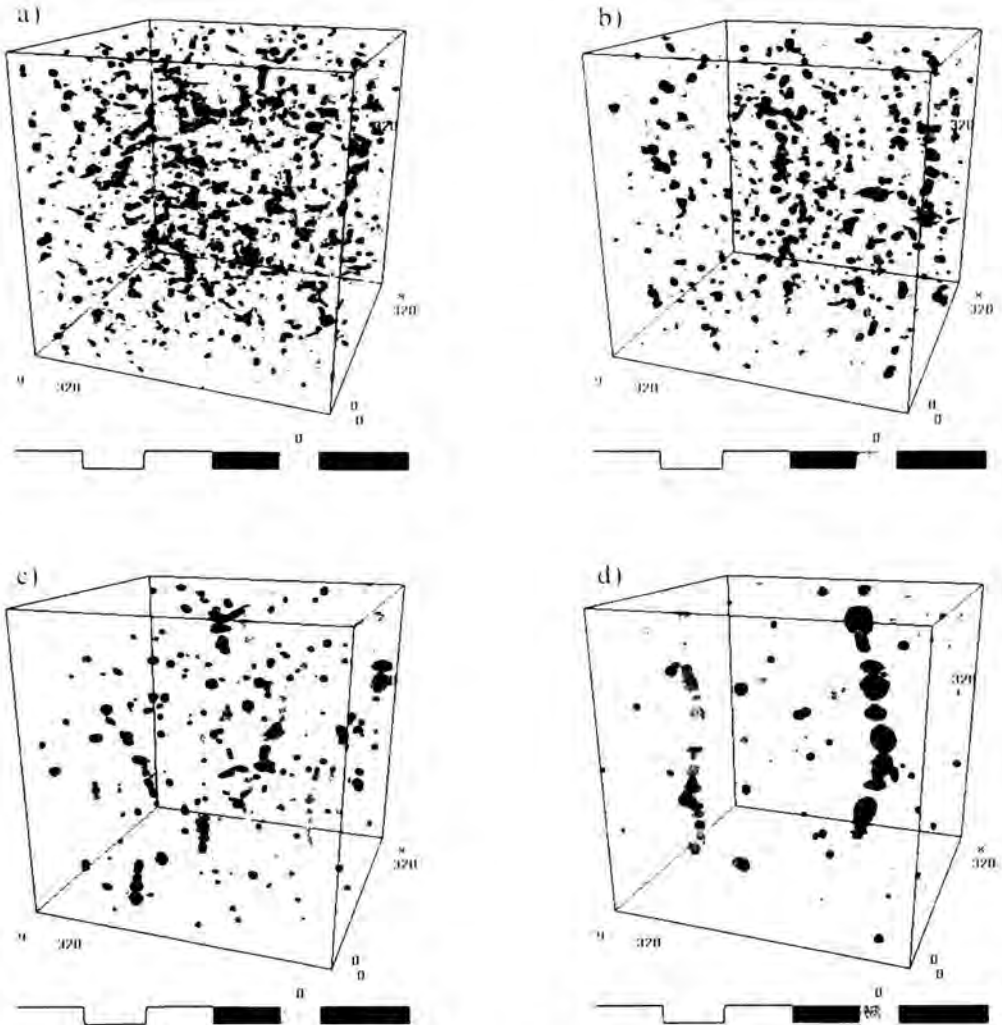


Fig. 4. Potential vorticity $q(x, y, Nz/f)$ at (a) $t = 5.0$, (b) $t = 10.0$, (c) $t = 25.6$, and (d) $t = 72.1$. The curves beneath the images show the opacity (left) and grey-scale hue (right) as a function of q , centered about $q = 0$.

Over a very long time scale, the chaotic mutual advection leads to a succession of mergers and attachments, resulting in a configuration of coherent vortices that is a global stationary state of the inviscid dynamics. Thereafter the only non-conservative evolution is very slow diffusion, and $S(\kappa)$ is equally slow in its evolution. This “final” configuration consists of two, opposite-sign, axisymmetric vertical columns each containing many vortex cores of common sign; the final time in Fig. 4 approaches this configuration, although as yet not all the mergers and attachments have occurred.

The behavior of coherent vortices and their roles in the statistical dynamics of turbulence are fundamental processes we are just beginning to understand, but it is clear that they are of great importance in planetary circulations.

Acknowledgements

This research was sponsored by the National Science Foundation through the National Center for Atmospheric Research and the Pittsburgh Supercomputing Center. I thank Nancy Norton, Jeffrey Weiss, and Irad Yavneh for their partnership in this work.

References

- Charney, J.G., 1971 - Geostrophic turbulence. *J. Atmos. Sci.* **28**, 1087–1095.
- Dritschel, D., and R. Saravanan, 1993 - Three-dimensional quasi-geostrophic contour dynamics, with application to stratospheric vortex dynamics. *Q. J. Roy. Met. Soc.*, submitted.
- Herring, J., 1980 - Statistical theory of quasi-geostrophic turbulence. *J. Atmos. Sci.* **37**, 969–977.
- Hua, L.B., and D.B. Haidvogel, 1986 - Numerical simulations of the vertical structure of quasi-geostrophic turbulence. *J. Atmos. Sci.* **43**, 2923–2926.
- Kraichnan, R., and D. Montgomery, 1980 - Two-dimensional turbulence. *Progress in Physics* **43**, 547–619.
- McWilliams, J.C., 1983 - On the relevance of two-dimensional turbulence to geophysical fluid motions. *J. de Mécanique Numero Special*, 83–97.
- McWilliams, J.C., 1989 - Statistical properties of decaying geostrophic turbulence. *J. Fluid Mech.* **198**, 199–230.
- McWilliams, J.C., J.B. Weiss, and I. Yavneh, 1993 - Anisotropy and coherent vortex structures in planetary turbulence. *Nature*, submitted.
- Melander, M.V., J.C. McWilliams, and N.J. Zabusky, 1987 - Axisymmetrization and vorticity gradient intensification of an isolated two-dimensional vortex. *J. Fluid Mech.* **178**, 137–159.
- Melander, M.V., N.J. Zabusky, and J.C. McWilliams, 1988 - Symmetric vortex merger in two dimensions: causes and conditions. *J. Fluid Mech.* **195**, 303–340.

- Polvani, L., 1991 - Two layer geostrophic vortex dynamics. Part 2. Alignment and two-layer V-states. *J. Fluid Mech.* **225**, 241–270.
- Rhines, P.B., 1979 - Geostrophic turbulence. *Ann. Rev. Fluid Mech.* **11**, 401–441.
- Sadourny, R., and C. Basdevant, 1981 - Une classe d'opérateurs adaptés à la modélisation de la diffusion turbulente en dimension deux. *C.R. Acad. Sci. Paris* **39**, 2138–2143.
- Weiss, J.B., and J.C. McWilliams, 1993 - Temporal scaling behavior of decaying two-dimensional turbulence. *Physics of Fluids A* **5**, 608–621.
- Yavneh, I., and J.C. McWilliams, 1993 - Efficient multigrid solution of the shallow-water balance equations. *J. Comp. Phys.*, submitted.

Geophysical Turbulence Program
 National Center for Atmospheric Research
 P.O. Box 3000
 Boulder, Colorado 80307, USA

Axisymmetrization of Warm Oceanic Vortices

Abstract

Previous studies have shown that in many cases eccentric vortices become axisymmetric. In this work we report the results of a numerical experiment performed with the shallow-water, reduced-gravity model for elongated warm eddies. The evolution of these eddies is invariably toward less-eccentric states and, often, includes the shedding of a small portion of mass. An attempt is made to characterize this process by defining an intensive quantity.

Introduction

Warm eddies are common and important features in the oceans, because their properties are both distinct and persistent. Satellite imagery allows us to witness the generation and evolution of many oceanic vortices. For example, it has been observed that Gulf Stream meanders often break off to form long-lasting eddies, which carry away warm waters to colder regions. The evolution of these eddies, in turn, plays a significant role in determining the characteristics of wide areas in the ocean.

In this work we analyze the evolution of oceanic eddies similar to those mentioned above, by utilizing a primitive equation numerical model. Such a model is used because: one, we are able to study a series of eddies with very different eccentricities and strengths; and two, the ensuing states of the initially prescribed model eddies can be easily tracked. We expect a wide variety of eddy-behaviors, since previous works (e.g. Ripa, 1987) have shown that many of these vortices are unstable, particularly the most eccentric ones. Previous studies using approximate models (e.g. McCalpin, 1987) indicate that *weak* elliptical vortices evolve toward a circular state, a process known as axisymmetrization. But, do elongated eddies (unstable, but not necessarily weak) become axisymmetric in order to achieve a more stable state? If so, it would be desirable to be able to characterize this process.

The next section outlines the model used and the form of the initial conditions.

The model

The shallow-water, reduced-gravity ocean model is written here as a pair of Lagrangian momentum equations:

$$\frac{Du}{Dt} = fv - g' \frac{\partial h}{\partial x}, \quad (1)$$

$$\frac{Dv}{Dt} = -fu - g' \frac{\partial h}{\partial y}, \quad (2)$$

where u and v are the velocity components in the x and y directions, respectively, t is time, f is the constant Coriolis parameter, g' is the reduced gravity, and h is the thickness of the active layer. The latter vanishes at the eddy's edge and, since resolving this frontal line is crucial for this study, we will use a particle-in-cell (PIC) method to solve (1)–(2). This requires one more pair of Lagrangian equations, namely

$$\frac{Dx}{Dt} = u, \quad (3)$$

$$\frac{Dy}{Dt} = v, \quad (4)$$

making it [system (1)–(4)] a four-by-four system for each of the N particles' positions and velocities ($x_i, y_i, u_i, v_i, i = 1, 2, 3, \dots, N$). The initial particle distribution yields the initial h -field and their prescribed velocities should correspond to the initial velocity fields [see (5)–(7) ahead]. The numerical integration of (1)–(4) by the PIC method assures conservation of mass; thus the continuity equation $h_t + (hu)_x + (hv)_y = 0$ complements (1)–(2), but it is not explicitly solved. The reader is referred to previous works for details and examples of the use of the same PIC model as employed here (e.g. Pavia and Cushman-Roisin, 1990).

An exact solution of the above described system, consisting of an elliptical clockwise rotating, anticyclonic vortex, was first given by Cushman-Roisin *et al.* (1985) and called the Rodon solution. Ripa (1987) transformed variables and equations to a frame rotating at the same rate as the eddy, Ω , so that the h contours become stationary, thereby obtaining a steady version of the Rodon. We will use another form of the latter version of the solution to prescribe the initial conditions of the model, namely:

$$u_0 = \left[1 + \frac{a}{b} \left(\frac{f - \Omega}{\Omega} \right)^{1/2} \right] \Omega y, \quad (5)$$

$$v_0 = \left[1 + \frac{b}{a} \left(\frac{f - \Omega}{\Omega} \right)^{1/2} \right] \Omega x, \quad (6)$$

$$h_0 = H \left[1 - \left(\frac{x}{a} \right)^2 - \left(\frac{y}{b} \right)^2 \right], \quad (7)$$

where a and b are the minor and major semiaxes, respectively, and

$$H = \left(\frac{ab}{2g'} \right) (f - 2\Omega) [\Omega(f - \Omega)]^{1/2}, \quad (8)$$

is the center depth of the eddy. This vortex is fully characterized by two intensive parameters which are the aspect ratio, $r = a/b$, and the ratio of the clockwise rotation of the vortex to the Coriolis parameter, $S = \Omega/f$ [or by the Rossby number, $Ro \equiv S + (S - S^2)^{1/2}$]; as well as one extensive parameter (say the total volume), and three geometrical parameters: the position of the center of mass and the initial orientation. The instability of elliptical eddies to infinitesimal perturbations for the whole range of values of the parameters

$$0 < r \leq 1 \quad 0 < S < 0.5, \quad (9)$$

was studied by Ripa (1987).

In the next section, the evolution of a series of widely diverse eddies will be investigated by means of a numerical experiment.

The numerical experiment

The main numerical experiment consists of a series of runs with eddies whose initial conditions correspond to all cases varying S from $S = 0.05$ to $S = 0.45$, every 0.05, and the aspect ratio from $r = 0.1$ to $r = 0.9$, every one tenth. These 81 cases include a wide range of the parameter space (9). Each run is time-integrated until $t = 500f^{-1}$, which is considered long term in all cases. The resulting h -field was fitted with a second order polynomial of the form

$$h \approx A - Bx^2 - Cy^2 + 2Dx + 2Ey + 2Fxy, \quad (10)$$

which, after some manipulation of the six coefficients, yields the $x - y$ coordinates of the center of the eddy, its orientation (θ), the maximum depth (H), and the minor (a) and major (b) semiaxes (mean radius [$R = (ab)^{1/2}$] and aspect ratio [$r = a/b$] can be calculated from these last two). The theoretical rotation rate of the vortex, assuming the eddy passes adiabatically through a series of Rodon-like states, is obtained using the numerical values of R and H to solve for Ω in (8). In doing so we make the transformation $\Omega = f(1 - \cos \alpha)/2$, $0 < \alpha < \pi/2$, so that (8) becomes $H = (Rf)^2 \sin(2\alpha)/8g'$. This theoretical rotation rate is compared with the measured one $d\theta/dt$.

We consider this procedure (10) to be successful if its root-mean-square (*rms*) error is less than 20%. Larger *rms* errors indicate that the original eddy has broken up into two or more parts, so that the resulting *h*-field is not appropriately fitted by (10). The results, therefore, must be discarded. Not surprisingly, this is the situation for several of the most eccentric eddies, while the less eccentric ones showed the smaller *rms* errors. Furthermore, in the cases with *rms* error of less than 20% the difference between the parameters of the original eddy (prescribed) and those of the final (fitted) eddy seemed proportional to the eccentricity of the original eddy. This difference is mainly in aspect ratio, *r*, and to a lesser extent in *S*. A general result is that in all cases the evolution was toward greater *r* (all eddies "axisymmetrize" somewhat), and expel mass (the estimated volume of the final eddy was smaller than the volume of the original one). In contrast, changes in *S* seemed to depend on the sign of the potential vorticity, *q*; i.e. for $q < 0$, the value of *S* increased and for $q \geq 0$, *S* decreased, changed little or not at all.

A couple of typical examples include:

a. Evolution of a highly elongated eddy

The evolution of an eddy whose initial parameters are $r = 0.2$ and $S = 0.15$ is examined at $\Delta t = f^{-1}$ intervals; i.e. the least-squares procedure (10) is performed every $ft = 1$. This particular case is chosen because it exhibited one of the most dramatic parameter changes during the main experiment.

To help us visualize the nature of the step-by-step parameter change, we define an intensive quantity

$$\mu \equiv q_0 V^{1/2} = f(S, r), \quad (11)$$

where q_0 and *V* are the potential vorticity of the center and the volume of the eddy, respectively. We expect this quantity to be approximately conserved because the system conserves potential vorticity, and we assume the eddy to conserve most of its mass. If potential vorticity and all the mass is conserved in one single blob, and if the eddy were to change its position in parameter space, then it should move along a particular isoline of μ . The evolution may be divided into two stages. During the first stage, characterized by rapid changes, the eddy departs from its original isoline, and apparently does not conserve μ . This is so because the least-squares procedure overestimates the size of the eddy when it undergoes distortion and shedding of mass. During the second stage, the eddy regains an almost elliptical shape and, despite high-frequency inertial oscillations, the trajectory closely follows its μ -isoline. This is a particularly dramatic case, which we examined in detail in order to check the results of the numerical experiment.

b. Evolution of a stable eddy

The evolution of an eddy with $r = 0.6$ and $S = 0.05$ is similarly examined, it moves relatively little within the parameter space. The small movement is mainly

toward greater r with even smaller change in S . In contrast with the previous case, this eddy is selected because its initial position in parameter space is located within the stable region of all the stability diagrams considered. [The eigenperturbations of the eddy's linear stability analysis are n -order polynomials, all eddies are stable for $n < 3$, and Ripa's (1987) diagrams include $n > 3$ up to $n = 6$. The corresponding stability diagrams for $n = 7$ and $n = 8$ present new instability areas suggesting that perhaps the high Ro region is full of higher-order instability tongues; but the eddy-parameters of this case remain outside of them.] From time series of r and other parameters we observe that besides a small axisymmetrization, inertial oscillations are the only action taking place. Other minor changes are more likely due to numerical dissipation than stability reasons.

Acknowledgements

This research was sponsored by the *Consejo Nacional de Ciencia y Tecnología* of Mexico [Grants 1002-T9111 (E.G.P.), D1112-904342 (M.L.), and 1282-T9204 (P.R.)], and by the *Universidad Nacional Autónoma de México* through time granted on its Cray YMP supercomputer. Additional supercomputer time was kindly provided by Prof. J. J. O'Brien at Florida State University.

References

- Cushman-Roisin, B., W.H. Heil, and D. Nof, 1985 - Oscillations and rotations of elliptical warm-core rings. *J. Geophys. Res.*, **90**, 11756–11764.
- McCalpin, J.D., 1987 - On the adjustment of azimuthally perturbed vortices. *J. Geophys. Res.*, **92**, 8213–8225.
- Pavia, E.G., and B. Cushman-Roisin, 1990 - Merging of frontal eddies. *J. Phys. Oceanogr.*, **20**, 1886–1906.
- Ripa, P., 1987 - On the stability of elliptical vortex solutions of the shallow-water equations. *J. Fluid Mech.*, **183**, 343–363.

Centro de Investigación Científica y de Educación Superior de Ensenada (CICESE), A.P. 2732, Ensenada, B.C. 22800, Mexico.

E-mail: epavia@cicese.mx

Eddy Splitting along Boundaries

Abstract

This paper addresses the question of what happens to an eddy that is forced “violently” against a boundary by an advective current or another vortex. The detailed temporal evolution of such a collision on an f -plane is examined using a barotropic model, a one-and-a-half-layer contour dynamics model and an isopycnic, primitive equation model. Our calculations show that an eddy splits into two along the wall: a cyclone to the right and an anticyclone to the left (looking offshore).

Introduction

Collision of eddies with boundaries is inevitable mainly because of two processes. First, the variation of the Coriolis parameter with latitude forces eddies toward the western boundaries of the ocean. Second, advection by main currents or propulsion induced by neighboring eddies also force eddies toward the ocean walls. The former process causes a “soft” and “gentle” impact with the western wall because of the β -induced westward speed is relatively small [$O(1 \text{ km day}^{-1})$] so that it takes many days [$O(\beta R_d)^{-1}$, where R_d is the Rossby radius] for a significant fraction of the eddy (i.e., a distance comparable to the eddy diameter) to be pushed into the wall. The latter processes, on the other hand, can be of a more “explosive” and “violent” nature as advection [$O(10\text{--}100 \text{ km day}^{-1})$] can push an eddy into the wall so rapidly that gross distortions in the eddy shape (and structure) can occur in a matter of days. The “gentle” eddy-wall interaction process has been studied extensively in Shi and Nof (1993) and the present article focuses on the more “explosive” and “violent” collision. Shi and Nof (1993) have shown that a soft collision is typically associated with (1) a small leakage from the eddy rim which forms a thin jet along the wall, and (2) a transformation of the eddy into a half-circular structure that migrates steadily along the wall (a wodon). We shall show in the present study that a violent collision causes more drastic effects. In particular, the eddy will not only migrate along the wall but will also split into *two* eddies with an opposing sense of rotation.

In this study, an eddy is conceptually cut by a wall at $t = 0$ (as if the advection

forced violently the eddy into the wall). Our aim is to explain the subsequent development of the eddy-wall collision. We shall first use the so-called contour dynamics method, which will be applied to an eddy on an f -plane. We shall then investigate this process using a constant potential vorticity eddy in an isopycnic model (noting that the contour dynamics method is a Lagrangian approach, whereas the isopycnic model is a Eulerian method). We shall show that both of these studies point to a new counter-intuitive eddy splitting process. We speak here about a counter-intuitive process because intuitively we would expect that an eddy that is cut by a wall would simply leak along the wall until its outer rim leaks out completely and its core is merely "kissing" the wall (Nof, 1988). It turns out, however, that such a benign state is never reached and that instead both the core and the leaked fluid are forced farther and farther into the wall.

A contour dynamics model

In the following discussion, we present the contour dynamics results of a barotropic model. Earlier studies have shown that, in an open ocean, a barotropic eddy with $b < 2$ is linearly unstable (Flierl, 1988). Therefore, for the barotropic model, we shall focus on the evolution of a linearly stable eddy ($b > 2$) colliding with a wall. Before presenting the detailed evolution of the eddy-wall collisions, it is recalled that the evolution of a barotropic cyclone is the mirror image of its anticyclone counterpart. Therefore, it is sufficient to present only a cyclonic (or anticyclonic) evolution.

For the case of the linearly stable eddy-wall collision in a barotropic model (Fig. 1), there are two stages in the evolution process. In the first stage ($t = 0-120$) the stable eddy leaks fluid along the wall and the eddy's outer radius decreases (and eventually reduces to less than 2). In the second stage ($t > 120$), the eddy is unstable. The annulus fluid is peeled quickly off the parent eddy because the interior fluid advects the annulus fluid toward the wall. For $t > 160$, a new, large anticyclonic eddy detaches from the parent eddy. This new, anticyclonic, eddy consists of all the original annulus fluid. Another important evolution process is that, during this eddy-wall collision, the interior of the eddy is forced toward the wall by the leaked vortex on the left (looking offshore). As the interior is continuously forced toward the wall, its shape changes from a circle to a near-semicircle. It moves to the right (whereas the offspring eddy moves to the left) due to the image effect. As time goes on, the mutual advection of an anticyclone on the left and a cyclone on the right leads both eddies farther toward the wall. Eventually, we see a new anticyclonic eddy on the far left and a cyclonic eddy on the far right. It is also worth pointing out that, during the splitting process, outside fluid slowly intrudes into the new eddy through a streamer. Our calculations show that, once detached from its parent eddy, the new anticyclonic eddy moves to the left at a constant speed, and that the remaining cyclonic core migrates to the right at a different constant speed.

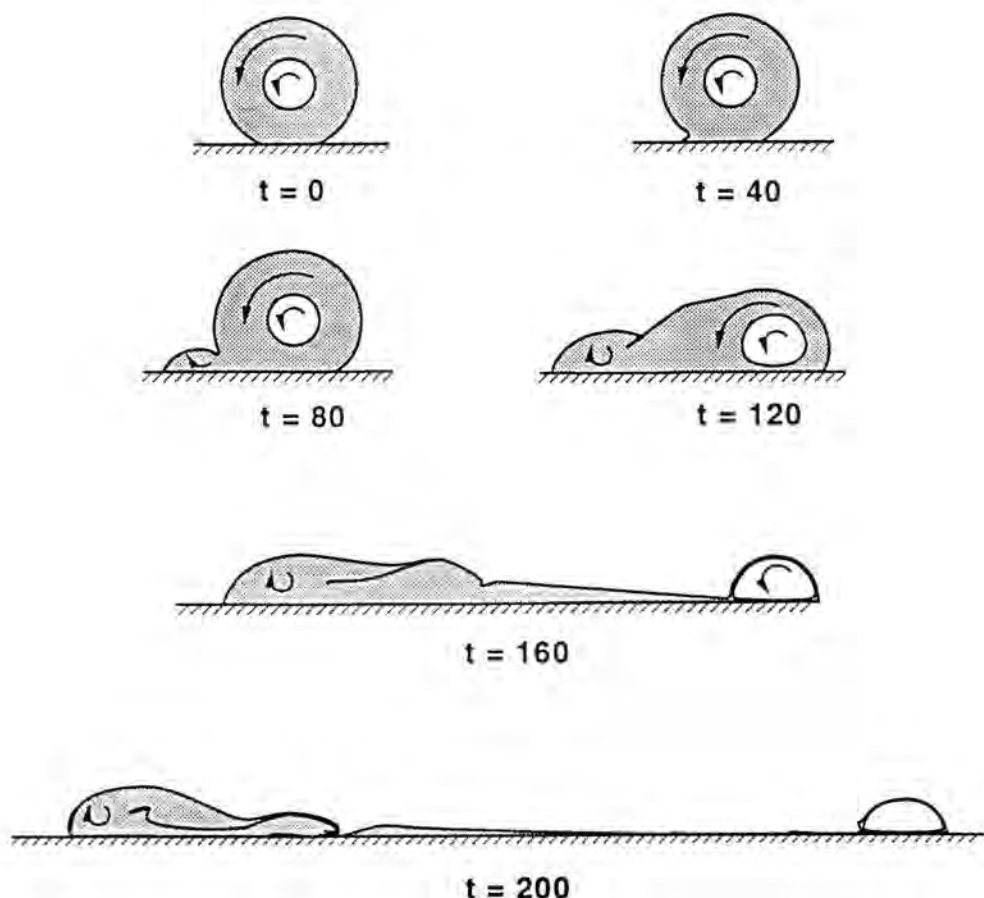


Fig. 1. The temporal evolution of the inner and outer fronts of an initially stable barotropic eddy from $t = 0$ to $t = 200$. The cyclonic eddy leaks its annulus fluid (shaded area) to the left and the leakage gradually forms an anticyclonic eddy moving to the left (looking offshore). The cyclonic interior of the parent eddy moves toward the wall and migrates steadily to the right.

An isopycnic, primitive equation model

To verify the new eddy splitting process presented earlier, we now use an isopycnic, primitive equation model described in Shi and Nof (1993). This Bleck and Boudra (1986) isopycnic model uses an Eulerian method, whereas the contour dynamics model uses a Lagrangian method. Since the isopycnic model is a primitive equation model, it includes more dynamical processes than are contained in the contour dynamics model. For example, Kelvin waves are generated in an isopycnic model but such waves are not present in a contour dynamics model. Fig. 2 illustrates an anticyclonic eddy collision corresponding to such an

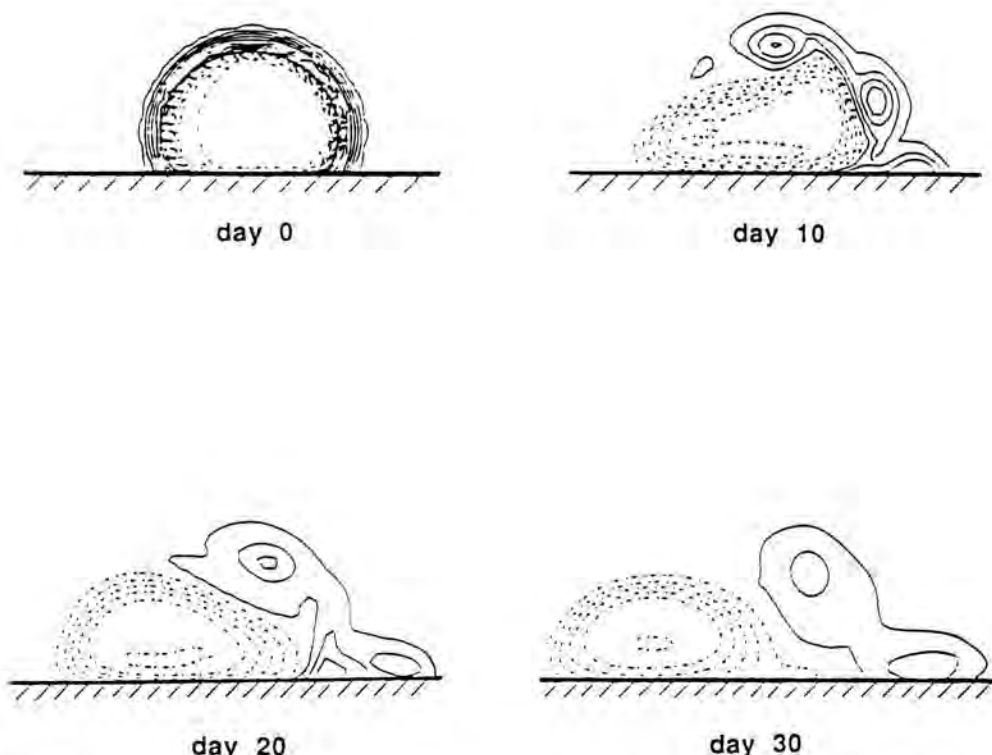


Fig. 2. Contours of the potential vorticity anomaly of an anticyclonic eddy colliding with a wall. The annulus fluid is advected anticyclonically to form a weak cyclonic eddy migrating to the right. The original eddy becomes half-circular and moves at a constant speed to the left.

eddy that is suddenly cut off by a vertical wall. From $t = 0$ day to $t = 20$ days, the interior anticyclonic fluid advects the annulus anticyclonic fluid to the right, and this process is compatible with that of Fig. 1. At $t = 10$ days, due to instability of the eddy, the shape of the interior is deformed. On day 20, the cyclonic annulus fluid is pushed farther to the right by both the interior and the image effect. At $t = 30$ days, this anticyclonic-wall collision produces a new cyclone to the right along the wall. Similar to the result of the contour dynamics study shown in Fig. 1, the newly formed cyclonic eddy is weak compared to its anticyclonic counterpart. This new, weak, cyclonic eddy moves slowly to the right. The area of the new eddy in Fig. 2 is approximately 100% of that of the initial annulus, which is identical to the final area of the new eddy in Fig. 1.

Interactions of the interior with the annulus force the interior to move farther into the wall. Then, the initial constant potential vorticity eddy is transformed into a half-circular wodon-like eddy (e.g., Shi and Nof 1993). In a fashion similar to the result shown Fig. 1, the present numerical calculation shows that the remaining parent eddy migrates to the left at a constant speed of

4.2 km day⁻¹. By using the wodon solution of Shi and Nof (1993), we obtain an analytical speed of 4.0 km day⁻¹, which agrees well with the numerical calculation. The isopycnic model also shows that eddy-wall collisions generate a Kelvin wave propagating along the wall. Such a wave was, of course, not present in the contour dynamics model because the contour dynamics technique filters these waves out.

Comparison with oceanic observations

One of the most comprehensive surveys of eddy-wall collisions is that of Vidal *et al.* (1992) who examined Loop Current rings. They identified the collision from temperature, salinity and dynamic topography distributions. As suggested by our models, they found that, when the anticyclonic eddy collided with the continental slope, the eddy translated to the left. During the collision process, the anticyclonic ring shed approximately one third of its volume to the right. They also found that a cyclonic ring was formed to the *right* of the parent ring as suggested by our model. Because of the relatively large amount of mass that was lost from the parent eddy, we speculate that the actual collision was similar to our collision processes, all of which have been termed "violent" collision.

While the above observations compare favorably with our model, the following data do not necessarily support our model predictions. Vukovich and Waddell (1991) used data from XBT/hydrographic cruises in the Gulf of Mexico and from satellite images to study collisions of a warm-core ring with the western slope. They indicated that the collisions of the anticyclonic ring with the continental slope induced a large-scale flow to the left in the upper layer near the slope. There was a cyclonic ring to the *left* of the Loop current warm-core ring along the slope. The line-up is the cyclone to the left and the anticyclone to the right, which is different from both our model results and the observations of Vidal *et al.* (1992). We speculate that the cyclonic ring of Vukovich and Waddell (1991) could have been generated by shelf water being pushed to deep regions by the anticyclonic ring. This process is, of course, absent from our analysis as our boundaries were taken to be vertical.

Acknowledgments

Comments by M.E. Stern, W.K. Dewar and S. Meacham were very helpful. This study was supported by the Office of Naval Research grant number N00014-89-J-1606 and by the National Science Foundations grants number OCE-9012114 and OCE-9102025 as well as by a postdoctoral fellowship of the University of Maryland, Horn Point Environmental Laboratory.

References

- Bleck, R. and D. Boudra, 1986 - Wind-driven spin-up in eddy-resolving ocean models formulated in isopycnic and isobaric coordinates. *J. Geophys. Res.* **91**, 7611–7621.
- Flierl, G.R., 1988 - On the instability of geostrophic vortices. *J. Fluid Mech.* **197**, 349–388.
- Nof, D., 1988 - Draining vortices. *Geophys. Astrophys. Fluid Dynamics*, **42**, 187–208.
- Shi, C. and D. Nof, 1993: The destruction of lenses and generation of wadons. accepted by *J. Phys. Oceanogr.*
- Vidal, V., F. Vidal and J. Perez-Molero, 1992 - Collision of a Loop Current anticyclonic ring against the continental shelf slope of the western Gulf of Mexico. *J. Geophys. Res.* **97**, 2155–2172.
- Vukovich, F. and E. Waddell, 1991 - Interactions of a warm ring with the western slope in the Gulf of Mexico. *J. Phys. Oceanogr.* **21**, 1062–1074.

* Horn Point Environmental Lab,
University of Maryland, P.O. Box 775
Cambridge, MD 21613-0775 USA

+ Department of Oceanography B-169
and Geophysical Fluid Dynamics Institute,
Florida State University,
Tallahassee, FL 32306-3048 USA

Organized Vortices as Maximum Entropy Structures

Abstract

A theory of equilibrium statistical mechanics for two-dimensional perfect fluids is summarized. It predicts the organization of a turbulent flow into a steady final structure. In the limit of low energy, the final structure is explicitly obtained as an expansion in the successive moments of the probability distribution function for the initial vorticity field. The previous results of point vortex statistics and selective decay into minimum enstrophy structures appear as special limits of this theory.

A good agreement is obtained with direct numerical computations and some experimental results. Applications to isolated vortex structures (monopoles and modons) are particularly developed here.

1. Introduction

The formation of coherent structures in strongly turbulent regimes is a remarkable property of two-dimensional turbulence. Such organization is observed in large scale oceanic or atmospheric flows, and can be reproduced in laboratory experiments. A general explanation of this long time organization has been proposed by Onsager (1949), in terms of equilibrium statistical mechanics for a set of point vortices. This is a remarkable anticipation since observations were very scarce at that time. This idea has been developed then by Montgomery & Joyce (1974), who have obtained explicit predictions by a mean field approximation. The result appears as a relationship between locally averaged vorticity and stream function, which characterizes a steady solution of the Euler equations (possibly in a rotating or translating frame of reference). However, the modeling of a continuous vorticity field by a set of point vortices can lead to inconsistencies: in particular the maximum vorticity is not bounded by the initial maximum, as it should for the two-dimensional Euler equations.

This contradiction is resolved by a new theory proposed by Robert (1990), Robert & Sommeria (1991), and independently by Miller (1990). This equilibrium statistical theory is performed directly on the continuous Euler equations. Then, the standard procedure for Hamiltonian systems of particles is not available, but still the method is justified (on a weaker basis) by a set of rigorous

properties (Robert 1990, Robert 1991). The result is again a steady solution of the Euler equation, on which fine scale vorticity fluctuations are superimposed. The relationship between vorticity and stream function is different than in Montgomery & Joyce (1974), and it is now quite consistent with the properties of the continuous Euler equations. Nevertheless, the relationship of Montgomery & Joyce is recovered in what we call the dilute limit, for which non-zero vorticity occupies only a small area of the domain. Another interesting limit is the case of low energy, in which the minimum enstrophy states (Leith, 1984) can be obtained.

A brief overview of the theory is given in section 2, referring to the original papers for a more thorough discussion and justification. The general properties of the resulting equilibrium structures are discussed in section 3, with emphasis on the important limit of low energy, for which the results can be linearized and expanded as a function of the energy. The application to isolated vorticity structures is emphasized in this paper: the case of monopole is studied in section 5, while the case of modons is discussed in section 6.

2. Principle of the statistical theory

The Euler equations are known to develop very complex vorticity filaments, and a deterministic description of the flow would require a rapidly increasing amount of information as time goes on. However, the conservation laws of the system bring important constraints to the evolution, and an essential property of the present theory is to take into account all the known conservation laws for the Euler equation (unlike the truncated spectral models, Kraichnan, 1975). In addition to the energy, the vorticity of each fluid particle is conserved, which results in the conservation of any function of the vorticity. It is often convenient (but not necessary) to approximate the vorticity field by patches with uniform vorticity level. Then the area of each level is conserved. Additional conservation laws for angular or linear momentum are also obtained in specific geometries.

In spite of these constraints, the vorticity field can still take many configurations, especially as the filaments become finer and finer. The idea of the statistical description is to give the same weight to all these possible configurations, called the microscopic states. Nevertheless we have to consider only the possible configurations which have the right values of the conserved quantities. Then it is remarkable that, if we introduce a coarse grain (macroscopic) description, most of the microscopic state will be close to a given macroscopic state. Thus, this optimal state is very likely to be reached if the vorticity configuration is chosen at random.

More specifically, a macroscopic state is defined as the field of probability $p_i(\mathbf{r})$ of finding the level a_i in a small neighbourhood of the point \mathbf{r} . The most probable macroscopic state is obtained by maximizing the entropy

$$S = \int_D s(p) d^2\mathbf{r}, \quad \text{where } s(p) = -\sum_i p_i \text{Log } p_i, \quad (1)$$

with the constraints brought by the conserved quantities. These are the energy, the total area

$$F_i = \int_D p_i d^2\mathbf{r}$$

of each vorticity level i , and the linear or angular momentum if these quantities are conserved (due to specific symmetries of the fluid domain). The energy E is expressed in terms of the vorticity field $\omega(\mathbf{r})$ and the associated stream function $\psi(\mathbf{r})$ defined by

$$-\Delta\psi = \omega, \quad \psi = \text{const. on boundaries}, \quad (2)$$

$$E\{\omega\} = \frac{1}{2} \int_D \psi \omega d^2\mathbf{r}. \quad (3)$$

The energy can be also expressed in terms of the macroscopic state by replacing $\omega(\mathbf{r})$ in (3) by the locally averaged vorticity $\bar{\omega}(\mathbf{r})$, and using the corresponding stream function Ψ , defined by

$$\bar{\omega}(\mathbf{r}) = \sum a_i p_i(\mathbf{r}), \quad -\Delta\Psi = \bar{\omega} \quad (4)$$

(the vorticity has fine-scale fluctuations, but these fluctuations are smoothed out for the quantities obtained as integral of the vorticity, like the stream function or the energy).

The variational problem is treated by introducing the Lagrange parameters corresponding to the conserved quantities, so that the first variations satisfy

$$\delta S - \sum \alpha_i \delta F_i - \beta \delta E = 0 \quad (5)$$

As a consequence, the optimal probability $p_i(\mathbf{r})$ is related to the equilibrium stream function Ψ by the relationship (see Robert & Sommeria, 1991).

$$p_i(\mathbf{r}) = \frac{e^{-\alpha_i - \beta a_i \Psi}}{Z(\Psi)}, \quad \text{with } Z(\Psi) = -\sum_i e^{-\alpha_i - \beta a_i \Psi}. \quad (6)$$

Then the locally averaged vorticity $\bar{\omega}(\mathbf{r})$ is expressed by (4) as a function $f_{\alpha,\beta}$ of the stream function Ψ . The resulting flow can be calculated in a self-consistent way by solving the corresponding partial differential equation. A steady Euler flow is characterized in general by the existence of a relationship between vorticity and stream function, so the function $f_{\alpha,\beta}$ selects a particular steady inviscid flow. We notice that in the absence of the energy constraint, i.e. $\beta=0$, p_i is uniform so that the mixing is complete. In general, the energy constraint prevents complete mixing and a flow structure remains.

This structure depends on the Lagrange parameters, which are not directly given. (We do not know about the possibility of a thermal bath that could set the temperature of the system, like in usual thermodynamics). Generally the available information is rather integral quantities, like the energy and the other

conserved quantities known from the initial condition (but other kinds of integral constraints can be obtained in forced cases). In summary, the stream function Ψ , together with the Lagrange parameters, are obtained by solving the system of equations resulting from (4), (6) and the integral constraints

$$-\Delta\Psi = f_{\alpha,\beta}(\Psi) = \frac{\sum_{i=1}^n a_i e^{\alpha_i - \beta a_i \Psi}}{Z(\Psi)} \quad (7a)$$

$$\Psi = \text{const. at the boundaries} \quad (7b)$$

$$\int_D \frac{e^{-\alpha_i - \beta a_i \Psi}}{Z(\Psi)} d^2\mathbf{r} = F_i, \quad i = 1, n-1 \quad (7c)$$

$$1/2 \int_D (-\Delta\Psi) \Psi d^2\mathbf{r} = E. \quad (7d)$$

The general case of a continuous distribution of vorticity levels is a straightforward generalization of (7). The final state depends then on the energy and the continuous probability distribution function $g(a)$ of the vorticity levels, given by the initial condition: $g(a) da$ is the fraction of the domain with vorticity between a and $a + da$. The terms $e^{-\alpha_i}$ are then replaced by a continuous function $\lambda(a) \geq 0$, so that

$$p(a, \mathbf{r}) = \lambda(a) \frac{e^{-\beta a \Psi}}{Z(\Psi)}, \quad \text{with } Z(\Psi) = \int_{-\infty}^{+\infty} \lambda(a) e^{-\beta a \Psi} da$$

and the system (7) becomes

$$-\Delta\Psi = f_{\alpha,\beta}(\Psi) = \int_{-\infty}^{+\infty} a \lambda(a) \frac{e^{-\beta a \Psi}}{Z(\Psi)} da \quad (8a)$$

$$\Psi = \text{const. at the boundaries} \quad (8b)$$

$$\int_D \lambda(a) \frac{e^{-\beta a \Psi}}{Z(\Psi)} d^2\mathbf{r} = \frac{g(a)}{|D|} \quad (8c)$$

$$1/2 \int_D \Psi (-\Delta\Psi) d^2\mathbf{r} = E. \quad (8d)$$

3. Methods of determination and general properties of the equilibrium states

The solution of the problem (7) must be generally obtained by a numerical method. It requires much less spatial resolution than solving the initial Euler equations, since the fine-scale vorticity structures have been filtered out by the statistical averaging. Nevertheless, the problem is still difficult because it generally involves bifurcations with several parameters, and the Lagrange parameters α_i, β are only indirectly determined by the n integral constraints.

A direct attack to this problem is presented by Thess & Sommeria (1993), and applied to the organization of a jet in a channel: (7) is discretized on N grid points (by a finite difference method), which yields a set of $N + n$ algebraic equations, that can be solved by the Newton's method. The different branches of solution are then followed by continuity: Starting from a known solution, the parameters are varied by small steps, and the previous solution is used as the initial guess for the Newton's method. Equilibrium states can be obtained also as the final state of relaxation equations (Robert & Sommeria, 1992) which conserve all the constants of the motion, while entropy monotonically increases. Notice finally that a new method of relaxation has been proposed by Turkington & Whitaker (1993), and applied to a shear layer with great efficiency.

Useful information can be also obtained from the theory without solving the problem (7) or (8). Indeed the function $f_{\alpha,\beta}(\Psi)$ has general properties discussed in Robert & Sommeria (1991). It is always a monotonous function bounded by the minimum and maximum initial vorticity levels a_i (this function is strictly increasing when $\beta < 0$, and strictly decreasing when $\beta > 0$). The mean field approximation of Joyce & Montgomery (1974) for point vortices can be recovered from (7) in the limit $Z(\Psi) \rightarrow 1$. This limit is obtained when most of the domain is filled by the zero vorticity level, and vorticity patches occupy a very small area, which is reasonable for a point vortex model.

There is another interesting special limit when the argument $\beta a \Psi$ is small and the results can be expanded in powers of this quantity. This will appear to correspond to the limit of low energy. We shall restrict the analysis to vorticity distributions which are symmetric with respect to a , and remain so in the equilibrium state, i.e. the function $\lambda(a)$ is also symmetric. In this restricted case, the expansion of $p(a, \mathbf{r})$ and the set of equations (7) yields

$$p(a, \mathbf{r}) = \lambda(a) \left[1 - \beta a \Psi + \frac{a^2 - A_2}{2} (\beta \Psi)^2 - \frac{3a^3 - A_2 a}{2} (\beta \Psi)^3 + \dots \right] \quad (9)$$

$$-\Delta \Psi = -A_2 \beta \Psi - \frac{3A_4 - A_2^2}{6} (\beta \Psi)^3 - \dots \quad (10)$$

$$\lambda(a) = g(a) \left[1 + \beta a \langle \Psi \rangle - \frac{a^2 - \langle a^2 \rangle}{2} \beta^2 \langle \Psi^2 \rangle + \dots \right] \quad (11)$$

$$E = -|D| \frac{\langle a^2 \rangle \beta}{2} (\langle \Psi^2 \rangle - \langle \Psi \rangle^2) + \dots \quad (12)$$

The integral constraints associated with the conservation of the global probability distribution of vorticity have been inverted to give explicitly $\lambda(a)$ by the expansion (11), as a function of the spatial averages $\langle \Psi^n \rangle$. The successive momenta of the function $\lambda(a)$ are denoted

$$A_n = \int_{-\infty}^{+\infty} a^n \lambda(a) da$$

At the lowest order, $\lambda(a) = g(a)$, so that A_n is equal to the moment

$$\langle a^n \rangle = \int_{-\infty}^{+\infty} a^n g(a) da$$

of the global vorticity distribution. However, differences appear at higher orders as indicated by (11). The partial differential equation (10) can be solved by successive approximations, together with the conditions (11) and (12).

At the lowest order, the vorticity is an eigenfunction of the Laplacian with eigenvalue βA_2 , which must be negative (i.e. $\beta < 0$), as a consequence of the positivity of energy in (12). Then each eigenfunction of the Laplacian initiates a branch of solutions, but we can check that the branch corresponding to the lowest eigenvalue has always the maximum entropy, and must be selected. The result of the statistical theory then corresponds to the minimum enstrophy structure in this limit. The eigenvalue of the Laplacian $\langle a^2 \rangle \beta$ is of the order $1/|D|$, so that, using the energy value (12), $(\beta a \Psi)^2$ is of order

$$\frac{E}{(a^2 |D|) |D|}.$$

Therefore the expansion is indeed valid for low energy. More precisely, the ratio of the energy over the initial enstrophy defines an initial scale of motion, and the expansion is valid when this initial scale is sufficiently small in comparison with the size of the domain.

The deviation from this linear approximation can be obtained by solving (10) by a perturbation method. The corrective term in Ψ^3 has the sign of $(Ku - 3)$, where Ku is the Kurtosis of $\lambda(a)$, i.e. $Ku = A_4/A_2^2$, which is equal to the Kurtosis of the vorticity distribution $g(a)$ in first approximation. Therefore, in the domain of validity of the expansion (i.e. low energy), we can predict the behaviour of the function $f_{\alpha, \beta}(\Psi)$ from the successive momenta of the initial probability distribution function of vorticity. For instance, in the case of two non-zero vorticity levels a and $-a$ which occupy a total area F , $Ku = |D|/F/F$. If $F > |D|/3$, the coefficient of the cubic term Ψ^3 in (10) is negative ($f_{\alpha, \beta}(\Psi)$ behaves like a \tanh), while if $F < |D|/3$, the coefficient is positive ($f_{\alpha, \beta}(\Psi)$ behaves like a \sinh). Notice that a similar expansion can be obtained from the results of Joyce & Montgomery (1974), but the coefficient of the cubic term is then only $A_4/2$, which is always positive. This result is recovered in the new theory when the Kurtosis is very large, which is indeed obtained in the dilute case, for which the area of the initial vorticity patches is small.¹ Notice finally that when $\lambda(a)$ is a

¹ This expansion should apply to typical computations of two-dimensional turbulence, with initial state at small scale, predicting a nearly linear relationship between vorticity and stream function. However the time of evolution is long before reaching a final state, so that small viscosity effects can modify the distribution of vorticity levels, leading to a high Kurtosis. Therefore the behaviour in \sinh obtained by Montgomery *et al.* (1992) can be explained, at least qualitatively.

gaussian, $Ku = 3$, so the cubic term vanishes. Moreover, it is then easily shown by the exact calculation of $f_{\alpha,\beta}(\Psi)$, that all the higher order terms also vanish: the relation between vorticity and stream function is linear (however, the corresponding vorticity distribution function $g(a)$ depends on the energy and is generally not gaussian).

Coming back to the general case, $f_{\alpha,\beta}$ appears obviously as a single-valued function. However the method of Lagrange multipliers leading to (7) or (8) allows only to find solutions p_i of extremal entropy which are continuous. Discontinuous solutions may also exist, as in the case of the modons discussed in section 6. Then, if the optimal functions p_i are continuous and strictly positive on some open connected subset $D' \subset D$, the same argument on Lagrange multipliers works on D' and shows that the representation (7) or (8) of this solution holds on D' . Therefore the function $f_{\alpha,\beta}$ could take several values, on different subsets D' , separated by discontinuities of at least one of the p_i . Moreover, it can be proved that if one of the optimal functions p_i is strictly equal to zero at some point, then the solution p_i is discontinuous.

4. Tests and applications of the theory

The result of the theory has been found in good agreement with direct numerical computations of the Navier-Stokes equations at high Reynolds number in several configurations. One of the simplest geometries is a channel with periodic boundary conditions in x and impermeable transverse boundaries. The case of a shear layer in a channel with stream-wise periodic boundary conditions has been investigated by Sommeria *et al.* (1991). Good agreement is also obtained for a jet in the same domain by Thess & Sommeria (1993). We shall present similar comparisons in the next section, for the problem of vortex merging in a large domain.

Different kinds of fluid systems can be described by a two-dimensional dynamics, mostly in Geophysical Fluid Dynamics and plasma physics. The extension of the theory to quasi-geostrophic systems is straightforward, even in multilayer cases, by replacing the vorticity by the potential vorticity. Therefore, a new way of understanding and predicting the organization of atmospheric and oceanic systems can be developed. For instance, it is possible to predict the formation of coherent jets and vortices like the Great Red Spot of Jupiter, as shown by Sommeria *et al.* (1991) and Michel *et al.* (1994).

The dynamics of an electron plasma in a magnetic field can be described by the 2D Euler equations, as shown by the beautiful experiments of Fine *et al.* (1991), and Peurrung & Fajans (1993). In this context the point vortex statistics has been applied to a circular domain by Pointin & Lundgren (1976) and Smith & O'Neill (1990), and the difference with the present theory remains to be tested. The similar flow of a liquid metal in a uniform magnetic field has been experimentally studied by Denoix *et al.* (1993), and a good fit with the present theory is obtained. However, such flows are strongly confined by the fluid

domain, and possible boundary layer detachments make the problem more complex. I shall discuss here the case of vorticity structures in a very large domain, for which boundary effects are not important (but the ergodicity of such an open system and its possibility to really reach a statistical equilibrium are more questionable).

5. Application to the vortex merging and the organization of a monopole

To apply the statistical theory, we need first to note the conserved quantities associated with the specific symmetries. In an unbounded domain, the two components of the linear momentum \mathbf{P} are conserved, as well as the angular momentum M :

$$\mathbf{P} = \int_D \omega \times \mathbf{r} d^2\mathbf{r}$$

$$M = \int_D \omega \mathbf{r}^2 d^2\mathbf{r}$$

(these quantities depend on the choice of the origin of the position vector \mathbf{r}). The corresponding Lagrange multipliers have to be introduced in (5). The modification is straightforward and leads to equilibrium states of the form

$$\omega = f(\Psi - \mathbf{U} \cdot \mathbf{r} - \gamma \mathbf{r}^2),$$

i.e. steady Euler flows in a translating or rotating frame of reference. There are two cases, depending on the total circulation

$$\Gamma = \int_D \omega d^2\mathbf{r}.$$

For the case of monopoles that we consider in this section, $\Gamma \neq 0$, while the case $\Gamma = 0$ (dipoles) is postponed to next section. If $\gamma \neq 0$, the term $\mathbf{U} \cdot \mathbf{r}$ can always be suppressed by a change of the coordinate origin, taking $\mathbf{r}' = \mathbf{r} + \mathbf{U}/2\gamma$. Then a purely rotating structure is obtained, and the linear momentum, calculated with the new origin, must vanish: otherwise it would rotate with the structure and would not be conserved. This means that the centre of the rotation must be the centre of mass of the vorticity distribution² (If $\gamma = 0$, the structure is translating with velocity \mathbf{U} , but since the centre of mass cannot move, we must have $\mathbf{U} = 0$, this is just a regular limit of the case $\gamma \neq 0$).

The equilibrium state has been obtained by Delbende *et al.* (1994) as the final evolution of the relaxation equations proposed by Robert & Sommeria (1992). A turbulent diffusion term increases the entropy, while keeping constant all the

² However, this is only possible if the centre of mass is defined, i.e. if $\Gamma \neq 0$. Otherwise, \mathbf{P} does not depend on the origin of the coordinates: then if $\mathbf{P} \neq 0$, we must have $\gamma = 0$, and get a translating structure.

conserved quantities, until a maximum entropy state is reached. From a numerical point of view, it is necessary to have boundaries, and a circular domain, centred at the centre of mass of the vorticity field, would be appropriate to keep the conservation laws. However, for practical reasons, we have used instead a square domain while still imposing the conservation of angular momentum. Since the domain is much wider than the size of the vorticity distribution, this brings only weak perturbations.

The equilibrium state depends on the vorticity distribution function $g(a)$, the total vorticity area F , the angular momentum M , and the energy E . We restrict ourselves to the case of initial vorticity patches with a single non-zero vorticity level $\omega = a$ with total area F . The equilibrium vorticity structure still depends on the two non-dimensional parameters $M/(aF^2)$ and $E/(aF)^2$, while the area F and vorticity a determine the size and typical vorticity of the structure. We have still restricted the problem to an initial state with two circular vortices of radius R whose axis are separated by a distance d . This is the classical problem of symmetric vortex merging, and the final structure depends only on a single parameter d/R .

In this problem, the final equilibrium state appears to be always axisymmetric, with exponentially decreasing vorticity at large distance. The radial structure of the vorticity depends on the parameter d/R , but the central core has always a very similar vorticity profile, shown in fig. 1a. For high values of the angular momentum (large d), a small proportion of the total vorticity is expelled at fairly large distances, with little change in the central core. Therefore merging is not prevented by the conservation of angular momentum, and we have never obtained equilibrium states with two separated vortices. This is the case even for ratios $d/R > 3.3$, for which it is not supposed to occur (see for instance, Christiansen & Zabusky 1973). The two vortex system with large separation may be a particular set of stable states which cannot initiate the mixing process³. However, when a complex vortex distortion is initiated, we can explain the merging process and its final axisymmetric organization by the tendency of the system to increase its entropy, with the constraints of the conservation laws.

Quantitative agreement with direct numerical computations of the Navier-Stokes equations is indeed obtained. Although we are interested in the inviscid dynamics, a small viscosity must be introduced to avoid the development of fine-scale noise (and the vorticity field must be smoothed at the edge of the patches). For applying the theory to a real flow, *it is essential to assume that viscosity has no significant effect on the distribution of the vorticity levels, during the time of formation of the final equilibrium structure*: then the only effect of viscosity is to suppress the local fluctuations of the equilibrium state, leading to a vorticity field equal to the local average of the inviscid theory $\bar{\omega}(\mathbf{r})$. We use a pseudo-spectral code in a periodic domain with symmetry conditions in x and y , so that

³ Nevertheless, further investigation of possible two vortex equilibrium states has still to be performed, with a rigorous test for bifurcations, and the search for possible discontinuous equilibrium states.

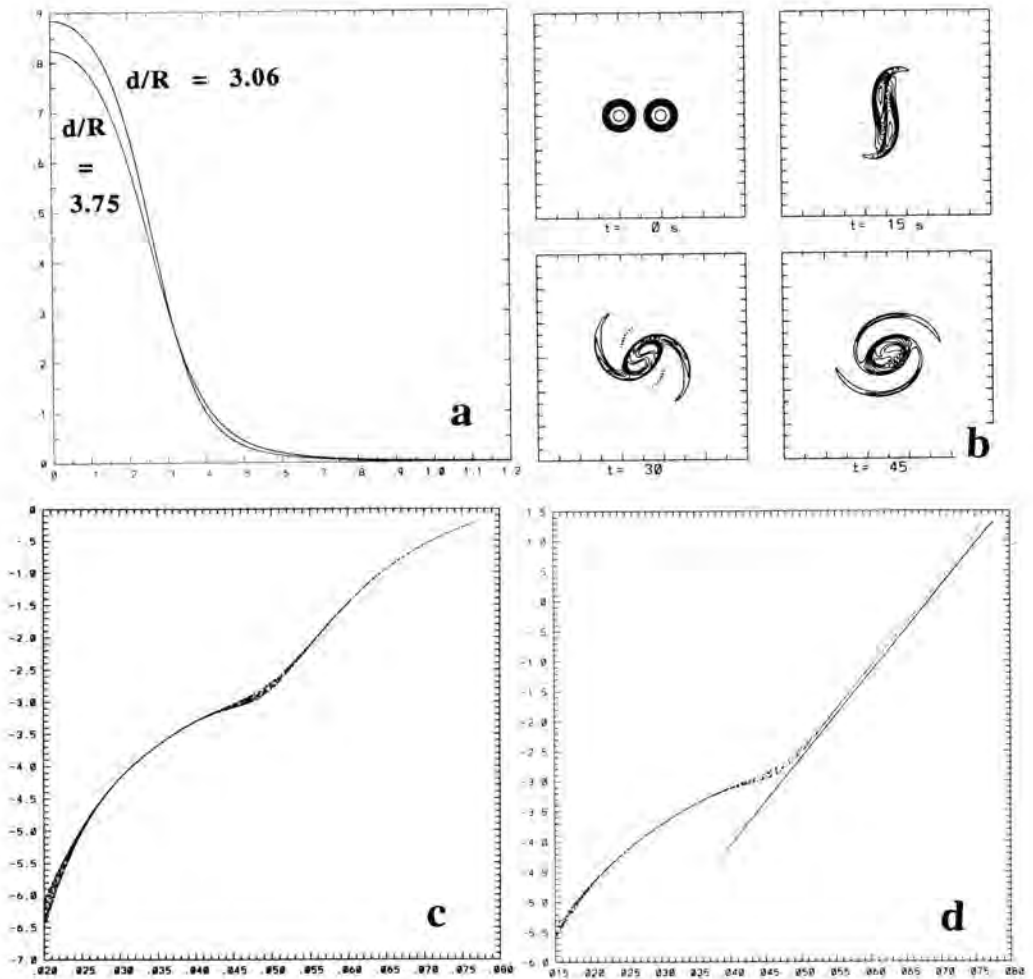


Fig. 1. Vortex merging and final equilibrium state (2 initial vortices of radius $R = 1/16$, vorticity $a = 1$, resolution 256^2 , viscosity $\nu = 2 \cdot 10^{-5}$); (a) Radial vorticity profile of the predicted equilibrium state for two ratios d/R ; (b) Snapshots from a direct numerical computation of the merging ($d/R = 3.18$); (c) Representation of $\text{Log}(\omega)$ versus stream function Ψ after organization into an axisymmetric state ($t = 274$); (d) Representation of $\text{Log}[\omega/(a - \omega)]$ versus Ψ for the same points as in (c); the linear behavior predicted by the theory is checked in the vortex core.

the square $[0,1] \times [0,1]$ has impermeable boundaries. The merging process is illustrated by the snapshots of Fig. 1b. At the end of the merging process, we can distinguish two regions: a strongly mixed central core, and spiral arms which roll up around the core. A final axisymmetric vortex structure is obtained at $t = 200$ (with a very slow decay due to viscosity).

The quantitative agreement with theory is best checked by plotting vorticity versus stream function from the final state of the numerical computation. Two representations are given in Fig. 1c, d (at $t = 274$). We first observe that all the

points nearly collapse on a single curve, an indication for a steady solution of the Euler equations. The point vortex statistics predicts an exponential function which should be represented by a straight line on Fig. 1c. There is clearly a discrepancy, especially near the vorticity maximum. By contrast, the present theory predicts a straight line for the representation of Fig. 1d, which is indeed well verified in the core of the vortex. However discrepancy appears in the spiral region. This result can be interpreted as the consequence of strong mixing in the core but only incomplete mixing outside. Indeed the filaments are in the first approximation stretched by the irrotational axisymmetric flow induced by the vortex core. This is an organized motion, rather than a complete mixing process. There is here a fundamental alternative: does the mixed core extend more and more in the limit of long times and vanishing velocity? Instead, does a barrier to mixing, or a complex set of barriers, remain in the inviscid limit? Limitations to mixing appear also in other cases, for instance in the partial merging of two unequal vortices (Dritschel & Waugh, 1992). In any case, the completely mixed state predicted by the theory is clearly a good starting point to study the merging process.

6. Maximum entropy solutions for a modon

Now let us consider the organization of an initial state with zero total vorticity $\Gamma=0$, surrounded by an infinite irrotational fluid. The linear momentum \mathbf{P} is now an important conserved quantity, while the angular momentum only determines the position of the structure: we choose the origin such that it vanishes. We then define the x axis parallel to \mathbf{P} , and use the usual polar coordinates r, θ . At large distance from the vorticity region, the stream function is the dipolar field

$$\Psi = \frac{P \sin \theta}{2\pi r}$$

(obtained as an expansion of the Biot-Savart formula).

We first notice that a continuous maximum entropy solution in the whole domain is now impossible (except for the degenerate case $\beta=0$, with zero energy). Indeed, each probability p_i would be a function of $(\Psi - Uy)$. Since $\Psi \rightarrow 0$ at large distance, the argument is then dominated by Uy ($U \neq 0$), which takes all the values between $-\infty$ to $+\infty$, so that the probability could not vanish everywhere at large distance. Therefore the equilibrium probabilities cannot decay smoothly in the whole domain, *and for each vorticity level, we must have a discontinuity, beyond which $p=0$* (The same result holds for $U=0$, although the justification is a little less simple). We shall make the hypothesis that all the probabilities are continuous inside a domain D , and drop to zero on the same line: the boundary of D . Inside this domain, the flow must be steady in the frame of reference translating at a velocity U . Therefore the line of prob-

ability discontinuities must keep the same shape, and the whole domain D translates at constant speed U : the boundary of D is a streamline in the translating frame of reference.

Outside D , the flow is irrotational, and is therefore uniquely determined by the boundary of D and its velocity U . This velocity can be related to the momentum P and a boundary integral, using an integration by parts

$$P = U|D| + \oint y \mathbf{u} \cdot d\mathbf{l} \equiv C_D U|D|.$$

The velocity on the boundary depends only on the outside flow, so that the coefficient C_D depends only on the shape of the domain D . It is convenient to use the non-dimensional variables \mathbf{r}' , a' and the stream function Φ in the translating frame or reference

$$\mathbf{r} = R\mathbf{r}', \quad \text{with } \pi R^2 = |D|, \quad a = a_0 a', \quad \Psi(\mathbf{r}) - Uy = a_0 R^2 \Phi(\mathbf{r}'),$$

where a_0 is a characteristic vorticity of the initial condition. We can write the energy as the sum of the internal energy and the translation energy

$$E = (a_0 R^2)^2 \frac{1}{2} \int_D \Phi(-\Delta\Phi) d^2\mathbf{r}' + \frac{P^2}{2\pi C_D R^2}.$$

In fact, because of the continuity of the velocity at the boundary of D , the two terms must be of the same order, which imposes a strong constraint on the domain area $\pi R^2 \approx P^2/E$. Then, the determination of the equilibrium states requires to solve a non-dimensional version of (8), with the new integral conditions (denoted by primes):

$$g'(a') = \frac{Fa_0}{R^2} g(a_0 a'), \quad E' = (a_0 R^2)^{-2} \left[E - \frac{P^2}{2\pi C_D R^2} \right].$$

The probability distribution $g(a)$ is relative to the initial area F where the vorticity is non-zero (the value $a=0$, for which $g(a)$ is not defined must be excluded of all the integrals involving a). We have again the impermeable boundary condition $\Phi=0$, but also an imposed velocity on the boundary, by continuity with the outside flow. The necessity for these two conditions will determine the shape of the boundary, and the value of R .

Therefore the shape and structure of the modon is in principle predicted by the statistical theory in terms of the conserved quantities, although the general problem is difficult. However we can use the expansion presented in section 3. At the first order, we get the classical modon, translating at velocity $U = U/P$, with the vorticity confined to a circular domain with $R = P/(2\pi E)^{1/2}$. The internal stream function

$$\Psi - Uy = \sqrt{\frac{2E}{\pi}} \frac{J_1(x_1 r') \sin\theta}{-x_1 J_0(x_1)}$$

is expressed in terms of the Bessel functions J_0 and J_1 . x_1 must be a zero of J_1 , and the condition of highest entropy selects the first zero ($x_1 \approx 3.83$). Indeed, the expansion of the entropy gives at this order

$$S = \text{const} - \frac{x_1^2 E'}{2\langle a^2 \rangle} + \dots$$

The next order correction can be obtained by a perturbation method, and the shape of the domain must be corrected together with the function Φ . Such an expansion is valid if

$$\frac{E}{a_0^2 F R^2} \ll 1 \quad \left(\text{with } R^2 = \frac{P^2}{E} \right) \quad (13)$$

which is true if the scale R of the modon is sufficiently large. In the opposite limit, the area R^2 defined by P^2/E may become smaller than the initial vorticity area F . A possible organization in that case is the formation of two modons with partly opposing directions, such that the momentum of each individual modon is greater than the initial one, allowing a larger scale P^2/E . In any case, such a system of two modons occupies a wider area, and it has clearly a higher entropy than a single modon. Therefore, we can understand that the condition (13), and the corresponding linear relationship between vorticity and stream function is a quite common feature.

Part of this work is supported by the European network "Two-dimensional turbulence, vortices and geophysical flows" (grant ERBCHRXCT920001).

References

- Christiansen, J.P. & N.J. Zabusky, 1973 - Instability, coalescence and fission of finite area vortex structures, *J. Fluid Mech.* **61**, 219-243.
- Delbende, I., J. Sommeria & C. Staquet, 1994 - Vortex merging interpreted as entropy maximization, to appear.
- Denoix, M.A., 1992 - Etude expérimentale de structures stables en turbulence bidimensionnelle, comparaison avec une théorie de mécanique statistique, thèse (Inst. Nat. Polytechnique Grenoble).
- Denoix, M.A., J. Sommeria & A. Thess, - Two-dimensional turbulence: the prediction of coherent structures by statistical mechanics, Proceeding of the 7th Beer-Sheva Seminar on M.H.D. Flow and Turbulence, Jerusalem, 14-18 Feb 1993.
- Dritschel, D.G. & D.W. Waugh, 1992 - Quantification of the inelastic interaction of unequal vortices in 2D vortex dynamics, *Phys. Fluids A* **4**, 1737-1744.
- Fine, K.S., C.F. Driscoll, J.H. Malmberg, & T.B. Mitchel, 1991 - Measurements of symmetric vortex merger, *Phys. Rev. Lett.* **67**, 588-591.
- Kraichnan, R.H., 1975 - Statistical dynamics of two-dimensional flow, *J. Fluid Mech.* **67**, 155-175.

- Leith, C.E., 1984, - Minimum enstrophy vortices, *Phys. Fluids* **27**, 1388–1395.
- Michel, J., R. Robert & J. Sommeria, 1994 - Statistical mechanics of the quasi-geostrophic model: application to the Great Red Spot of Jupiter, to appear.
- Miller, J., 1990 - Statistical mechanics of Euler equations in two dimensions, *Phys. Rev. Lett.* **65**, 2137–2140.
- Montgomery, D. & G. Joyce, 1974 - Statistical mechanics of negative temperature states, *Phys. Fluids* **17**, 1139–1145.
- Montgomery, D., W. Matthaeus, W. Stribling, D. Martinez & S. Oughton, 1992 - Relaxation in two dimensions and the sinh-Poisson equation, *Phys. Fluids A* **4**, 3–6.
- Onsager, L., 1949 - Statistical hydrodynamics, *Nuovo Cimento Suppl.* **6**, 279–287.
- Peurrung, A.J. & J. Fajans, 1993 - Experimental dynamics of an annulus of vorticity in a pure electron plasma, *Phys. Fluids A* **5**, 493–499.
- Pointin, Y.B. & T.S. Lundgren, 1976 - Statistical mechanics of two-dimensional vortices in a bounded container, *Phys. Fluids* **19**, 1459–1470.
- Robert, R., 1990 - Etat d'équilibre statistique pour l'écoulement bidimensionnel d'un fluide parfait, *C.R. Acad. Sci. Paris*, **311**, Série I, 575–578.
- Robert, R., 1991 - Maximum entropy principle for two-dimensional Euler equations, *J. Stat. Phys.* **65**, 531–551.
- Robert, R. & J. Sommeria, 1991 - Statistical equilibrium states for two-dimensional flows, *J. Fluid Mech.* **229**, 291–310.
- Robert, R. & J. Sommeria, 1992 - Relaxation towards a statistical equilibrium state in two-dimensional perfect fluid dynamics, *Phys. Rev. Lett.* **69**, 2776–2779.
- Smith, A.R. & T.M. O'Neil, 1990 - Nonaxisymmetric thermal equilibria of a cylindrically bounded guiding-center plasma or discrete vortex system, *Phys. Fluids B* **2**, 2961–2975.
- Sommeria, J., C. Staquet & R. Robert, 1991 - Final equilibrium state of a two-dimensional shear layer, *J. Fluid Mech.* **233**, 661–689.
- Sommeria, J., C. Nore, T. Dumont & R. Robert, 1991 - Statistical theory of the Great Red Spot of Jupiter, *C.R. Acad. Sci. Paris* **312**, Série II, 999–1005.
- Sommeria, J., S.D. Meyers. & H. L. Swinney, 1991 - Experiments on vortices and Rossby waves in eastward and westward jets, Proceeding of the Varenna Summer School "Non-linear Topics in Ocean Physics", (Ed. Osborne A.R.), North Holland, p. 227–269.
- Thess, A. & J. Sommeria, 1993 - Inertial organization of a jet in two dimensions. preprint.
- Turkington, B. & N. Whitaker, 1993 - Statistical equilibrium computations of coherent structures in turbulent shear layers. preprint.

Laboratoire de Physique
Ecole Normale Supérieure de Lyon
46 al. d'Italie, 69 364 Lyon Cedex 07
France

Vortex Stripping

Abstract

We examine below the process of “stripping”, the sharp removal of peripheral vorticity from vortices in a two-dimensional flow when the critical points of the global stream function field penetrate the vortex. We show that arbitrarily sharp vorticity gradients can be produced at the vortex edge and that the stripped filaments may undergo Hamiltonian mixing. A theory which allows detailed quantification is possible in several simple but relevant cases. We also show that the combination of stripping and diffusion or eddy-viscosity leads to surprisingly rapid vortex decay, with hyperviscosity leading to additional spurious effects. As regards the enstrophy cascade concept for 2D flows, we find that the process of stripping short-circuits this cascade, thereby putting into question long-held beliefs.

Keywords: vortex dynamics – coherent structures – two-dimensional turbulence

1. Introduction

Two-dimensional turbulence is often considered a useful paradigm for geophysical fluid dynamics. Extensive numerical experiments have led to the conclusion that two-dimensional turbulence is dominated by long-lived coherent vortices moving through a sea of quasi-passive filamentary structures [1].

These filaments are generated by the straining of vorticity structures in the velocity field mainly controlled by the large vortices. The saddle points of the stream function field are characterised by a deformation tensor having two real eigenvalues, one positive and one negative, and are consequently the places where vorticity structures are compressed in one direction while being elongated in the direction of straining [8, 16]. This mechanism is very effective when a small structure is strongly deformed on a much shorter time-scale than that associated with significant changes of the deformation field along a Lagrangian trajectory. In this case, vorticity gradients intensify and are only bounded by dissipation effects.

A second generation mechanism of vorticity filaments—which has been largely overlooked in the literature on two-dimensional turbulence—is wave breaking

on the periphery of vortices. Two phenomena are involved here. The first is the formation of nonlinear critical layers, to which classical analytical treatment may be applied to study the initial stages of perturbation development on a weakly unstable vorticity profile [14]. When a sharp vorticity interface is involved, the instability can be investigated using the modern numerical method of contour surgery [4], and it can be shown [2] that a cascade of folding occurs which generates an extremely complicated structure of embedded filaments on the vorticity interface. There exist, however, nonlinear stability bounds which restrict the growth of such perturbations [3]. In particular, the mean-square displacement of the interface is conserved, and it is believed, on the basis of many numerical experiments, that the filaments remain close to the initial location of the vorticity interface. This phenomenon, known as "filamentation", is certainly important in determining an effective turbulent diffusion acting on the vorticity profile of a coherent vortex, but as just noted probably injects little material into the background flow.

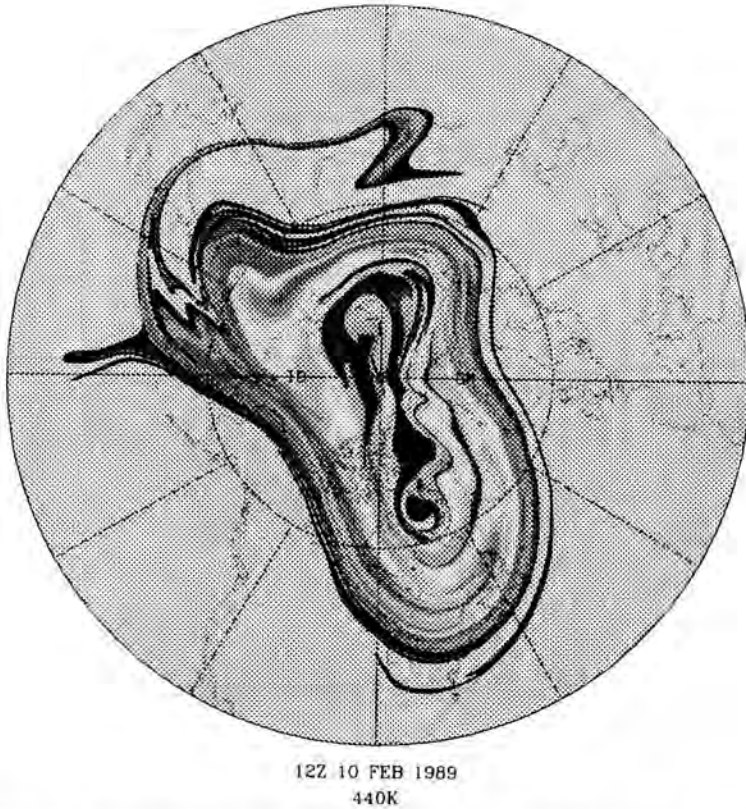


Fig. 1. Reconstruction of the potential vorticity on the isentropic surface $\theta = 440K$ on 10 February 1989, using contour advection with surgery [15].

The second phenomenon, that we denote as “stripping”, is associated with the deformation of a vortex by an external straining field produced by other vortices (or any imposed non-uniform flow). The superposition of a vortex having closed streamlines and an external straining field (i.e. $u = \gamma x - \Omega y$, $v = -\gamma y + \Omega x$) yields a total stream function field having two critical points, often located inside the vortex, and associated separatrices passing through these critical points, capable of transporting fluid to large distances from the vortex into the background flow. For some combinations of γ and Ω , the vortex may be destabilized, resulting in tearing, folding and appreciable filament generation [5].

These phenomena are particularly relevant to the dynamics of the stratospheric polar vortex which forms during winter over the Arctic and the Antarctic. The polar vortex persists during most of the winter season and it acts as a barrier to subtropical air masses. The consequent isolation of cold polar air in turn favours the chemical reactions responsible for ozone destruction [12]. During spring, the vortex is torn apart and ozone loss is propagated to lower latitudes. The final tearing (called the “final warming” in the meteorological literature) is, however, preceded by progressively more violent events such as that shown in Fig. 1 where we see how a broad filament is emitted from the vortex and carried to lower latitudes while thinner structures remain glued to the vortex edge.

2. Stripping

With these motivations in mind, we now focus on the phenomenon of stripping. We consider the simple but in many ways generic case of a single vortex (or a row of vortices) under uniform adverse shear in a pure two-dimensional framework.

2.1. Critical points

When a finite adverse shear is applied at $t = 0$ to a circular vortex, the vortex reacts by rapidly elongating, then by differentially rotating, and finally by ejecting a tongue of peripheral vorticity along the direction of the shear (see Fig. 2a). The instantaneous stream function exhibits two symmetrically-placed critical points (zero velocity points) just within the region dividing the core-bound vorticity from the escaping vorticity tongue. At a later stage (see Fig. 2b) the expelled tongue elongates into a filament attached to the vortex through an exceedingly thin section at the very location of the critical point. Stripping has then reached a quasi-equilibrium in which the vortex is nearly a stationary solution of the Euler equations. This can be demonstrated by plotting the stream function versus the vorticity and verifying that a functional relationship is

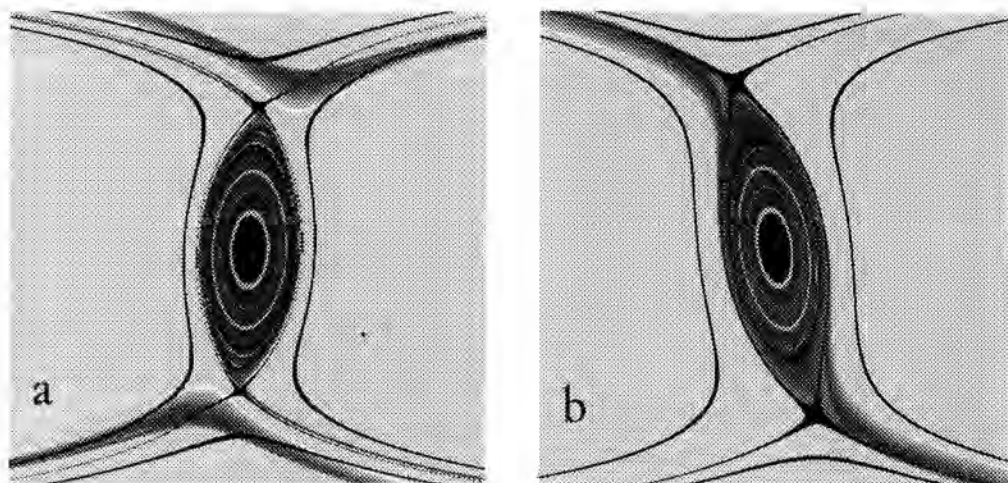


Fig. 2. Vorticity chart of a vortex within a row of vortices submitted to a uniform adverse shear. (a): early time. (b): quasi-equilibrium stage. Four streamline contours, in black, are superimposed on each view to locate the critical points and to outline the stream function field.

closely satisfied within the vortex. This nearly stationary situation persists only for an isolated vortex ; for a vortex street, the flow continues to evolve as vorticity filaments produced by one vortex interact with neighbouring vortices [10].

2.2. *Mixing and sharpening of the vortex edge*

Upon passing close to a critical point, filaments are folded and split into two parts, one continuing its journey towards a neighbouring vortex and the other one sweeping along the vortex edge (see Fig. 3). Iterating this process leads to Hamiltonian mixing, a subject which has been well-studied when the velocity field varies periodically in time [13]. Here, however, the oscillations of the vortex are induced by the filaments themselves, so the velocity field is aperiodic; yet, the observed mixing bears the main characteristics of Hamiltonian chaos. It differs totally from a down-gradient vorticity diffusion. Instead, the vorticity gradient increases dramatically on the edge of the vortex as demonstrated by the cross-section shown in Fig. 3. This is simply a consequence of stripping removing the periphery of the vortex while leaving the interior intact. The filaments may, however, crowd in the vicinity of the vortex edge and reduce the steepness of the profile by diffusive smoothing of the transverse structure as soon as viscous scales are reached. But when they are carried away, the sharp edge remains. A sharp edge is indeed observed at the periphery of the polar vortex by in-situ aircraft measurements [15] and is found to be most pronounced follow-

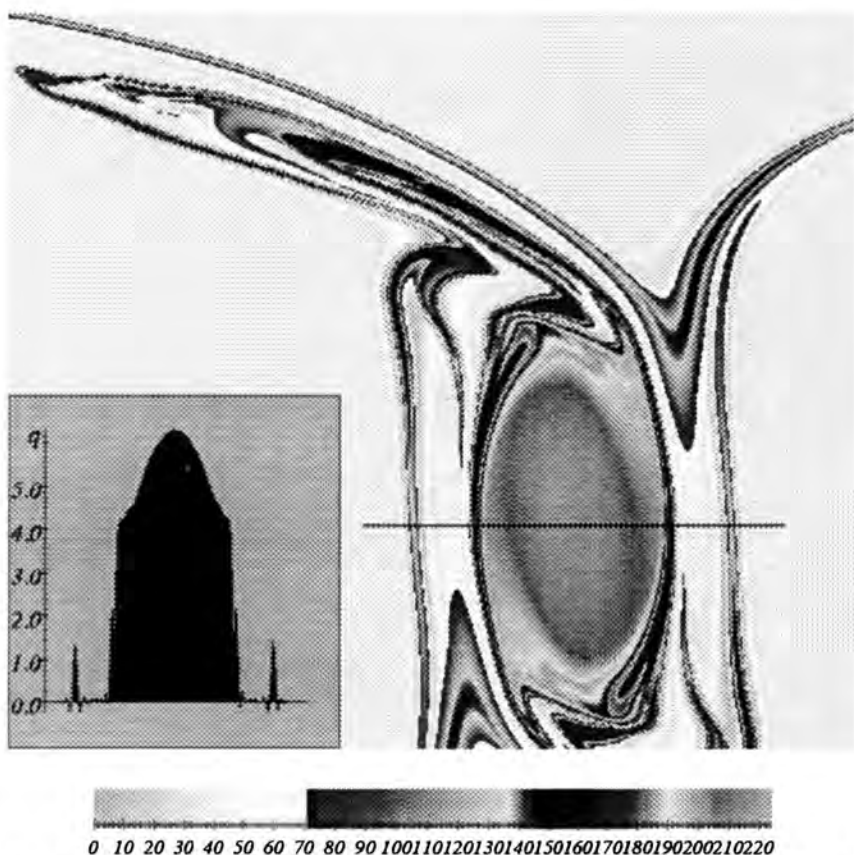


Fig. 3. Same vortex as in figure 2 at a later stage of its evolution after several foldings of the expelled filaments. The vorticity cross-section is taken along the segment shown on the figure.

ing a strong perturbation of the vortex, in agreement with our analysis. One of the main difficulties of numerical weather forecast models is their inability to resolve such structures. We will come to this point below.

3. Quasi-adiabatic stripping

A more quantitative understanding of stripping is attainable in the case of slowly-changing external flow. It can be shown [11] that when an initially circular, monotonic, isolated vortex is submitted to a slowly growing external shear, it evolves along a quasi-equilibrium path (through states resembling that shown in Fig. 2b) while progressively eroding until the shear is strong enough to indefinitely stretch the small remaining core. A principal result is that the critical value of the shear (for the final vortex tearing) depends almost exclusively on the ratio A/ω_{max} of the shear to the maximum vorticity within the

vortex; that is there is little dependence on the vorticity profile. This critical value is $\Lambda = \Lambda_c = 0.135\omega_{\max}$ for pure adverse shear. The universality comes from the fact that a distributed vortex generically has, to leading order, a parabolic core profile and that higher-order corrections to this profile shape have an increasingly negligible effect as the radius of the eroding vortex decreases.

In addition, it has been observed that during the whole evolution the vorticity contours within the vortex exhibit only small deviations from a pure elliptical shape. As a consequence, we can use the results of the elliptical model [9] in which a vortex is represented by a nested stack of elliptical disks of vorticity. By taking the continuous limit of this model for an initially axisymmetric vorticity profile $\omega(r)$ bounded by a sharp edge at the vorticity level $\omega = \omega(R)$, we obtain the following integral equation for the equilibrium:

$$0 = 2 \frac{\sigma(r)(1-\sigma(r))}{r^2(1+\sigma(r))} \int_0^r s^2 \omega'(s) ds - \frac{(1-\sigma(r))^2}{r^4} \int_0^r s^4 \frac{\sigma(s)}{1-\sigma^2(s)} \omega'(s) ds \\ + \Lambda - \omega(r) - \frac{1+\sigma^2(r)}{(1+\sigma(r))^2} \int_r^R (1+\sigma(s)) \omega'(s) ds + \frac{1+\sigma^2(R)}{1+\sigma(R)} \omega(R), \quad (1)$$

where $\sigma(r)$ is the eccentricity of the vorticity contour $\omega(r)$, and $0 \leq r \leq R$. In addition to (1), we need an extra condition for quasi-stationary stripping which allows one to determine R . This condition is that the critical point is located at the tip of the vortex. More accurately, since we know that the separatrices form a right angle at this point, we may demand that the sides of this angle are tangent to the outermost ellipse. This condition is:

$$0 = \int_0^R \frac{\omega' s^2}{X_R + \sqrt{X_R^2 - 4 \frac{\sigma(s)s^2}{1-\sigma^2(s)}}} ds - \frac{1}{2} R \omega(R) \sqrt{1-\sigma^2(R)} + \Lambda x_R, \quad (2)$$

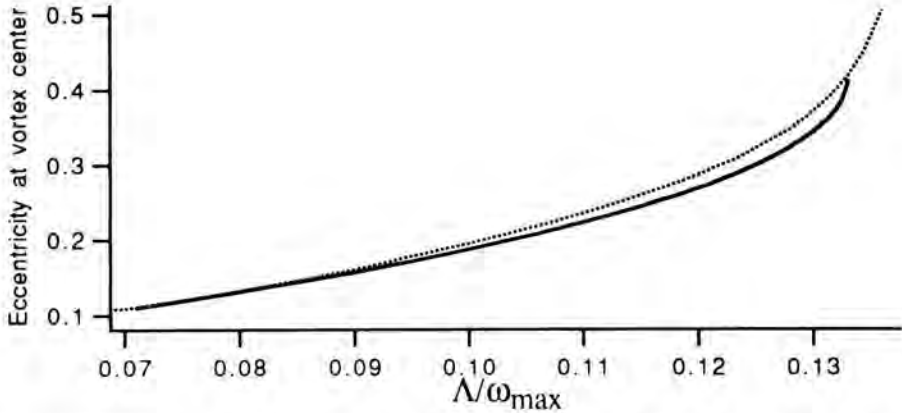


Fig. 4. Eccentricity at the vortex center as a function of Λ/ω_{\max} . Dotted line : numerical simulation of the Euler equations by contour dynamics. Solid line : the prediction obtained from solving (1) and (2).

with $x_R = \sqrt{2R} \sqrt{(1 + \sigma^2(R))/(1 - \sigma^2(R))}$. These equations can be reduced to a single second-order differential equation for $\sigma(r)$ which can be solved numerically or by Padé approximation. Fig. 4 compares the results of this approximate method with that of a direct numerical simulation, for the stripping of the initial profile $\omega(r) = \frac{1}{2}(1 + \cos(\pi r))$. We obtain an accurate prediction of the erosion up to the final tearing, with an error of less than 3% in the critical shear.

A progressive growth of external shear seems to be a more realistic condition than an abrupt application of it. Nevertheless, we have seen in Fig. 2b that even in this later case the vortex can reach a state of quasi-equilibrium after being strongly deformed. It is thus likely that the above results characterise a broad range of cases. The extension to more general combinations of strain and rotation will be presented elsewhere. It is also feasible to incorporate higher-order deformations in a perturbative way to deal with cases of non-uniform straining fields such as those encountered during the inelastic interaction of two vortices [7].

4. Diffusive effects

We have so far neglected the effect of diffusion and have studied stripping as an inviscid mechanism except in assuming that the filaments dissipate when they get very thin. This latter effect is, however, a consequence rather than an ingredient of stripping. Diffusion plays a significant role in stripping when the scale of the vortex is small enough (how small will be seen below) and/or when one uses an artificial eddy viscosity to represent unresolved dynamics in large-eddy simulations (like in the current generation of general circulation models of the atmosphere and the ocean).

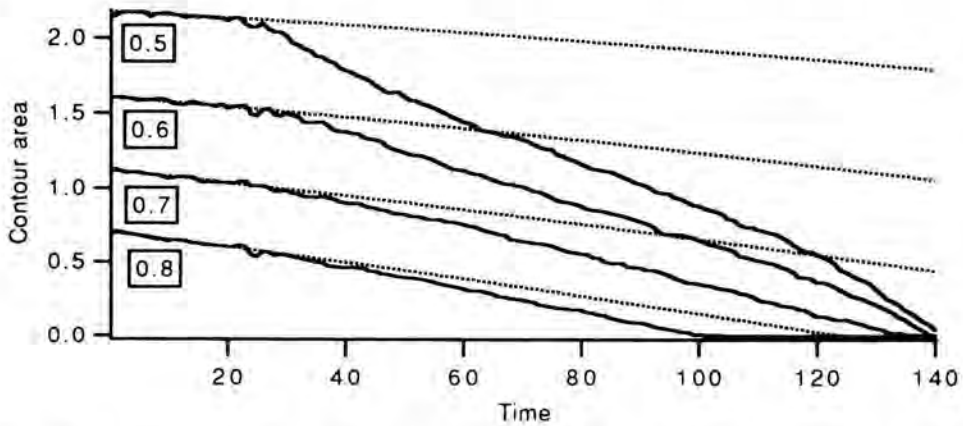


Fig. 5. Evolution of the area of vorticity contours as a function of time, with and without shear, at $Re = 12500$ for a Gaussian vorticity profile with $\omega_{\max} = 1$ at $t = 0$. Vorticity contours are $\omega = 0.5, 0.6, 0.7$ and 0.8 . Dotted line : pure diffusive decay. Solid line : convective-diffusive decay with $A = 0.1$.

Let's see what we get when diffusion is coupled with stripping. Qualitatively, we can understand that there will be an accelerated decay of the vortex when one balances the diffusive flux of vorticity (accentuated by the presumed tight gradients along the vortex edge) across the separatrices of the stream function with the advection away by the external flow. We expect a fast linear decay. Fig. 5 compares the decrease of the area of several interior vorticity contours, for the initial Gaussian profile $\omega(r) = \exp(-\frac{r^2}{2a^2})$, in the presence and absence of adverse shear at Reynolds number $Re = \omega_{max} a^2 / \nu = 6250$. In this example, the edge is located at approximately $\omega = 0.5$. The enhancement of diffusion is obvious, the more so for the contours which are close to the edge, but it also increases (by 20%) for the most interior level. As a consequence, the vorticity maximum ω_{max} also decreases much faster than in the absence of shear. Fig. 6 shows the evolution of ω_{max} for various values of Re . The decay is linear until the critical value of vortex tearing is reached, and then there is a sharp exponential decay as the vortex is extended as a filament. We see that tearing always occurs for the same critical value of ω_{max} , independent of Re , corresponding to $A = A_c$, the critical shear value for inviscid stripping. For a given profile, the tearing time (not shown) is approximately proportional to the Reynolds number.

In large-eddy simulations, one may expect from the above observations that the combined effect of eddy viscosity and strain leads both to a premature disappearance of small-scale eddies and to an enhanced erosion of large-scale structures [17], as conjectured previously in [6]. It is a mechanism which may explain why some coherent patterns like atmospheric blocking anticyclones are not properly maintained during the integration of numerical weather forecast models.

It must be added that the use of hyperviscosity (i.e. using $\nu_p (-1)^p \nabla^{2p} \omega$ instead of $\nu \nabla^2$), a common parameterisation of eddy-viscosity, may delay some

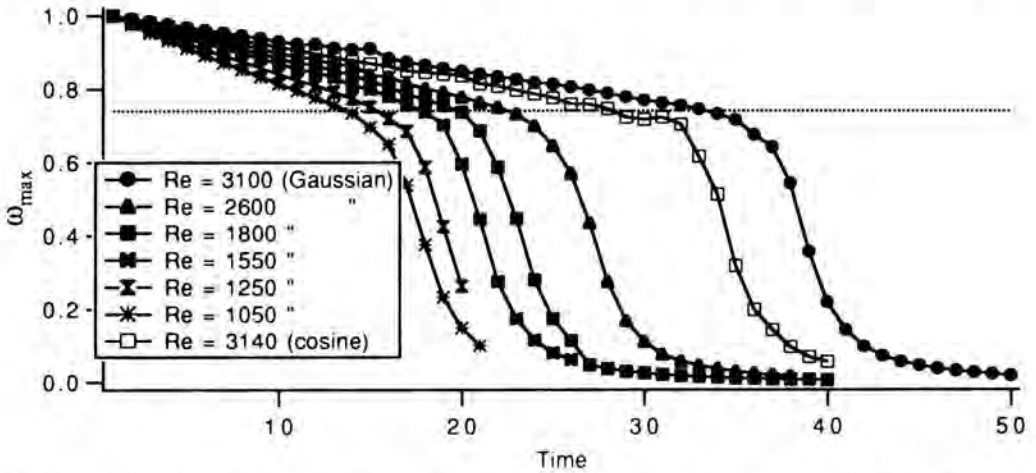


Fig. 6. Evolution of ω_{max} as a function of time for various values of Re , as indicated on the figure, with $A = 0.1$. Dotted line : critical value of ω_{max} for tearing.

what the final tearing since the maximum vorticity decays more slowly than in the case of normal diffusion. But there are also some spurious effects. Hyperviscosity is not a diffusive operator: artificial oscillations develop across a sharp edge leading to an up-gradient pumping of vorticity inside the vortex. This violates vorticity conservation, of course, and can enhance maxima by 20% above their initial value (or more if $p > 2$). The consequences of this result for forced simulations require further analysis. We can say, however, that it casts doubt on the statistics of small-scale vortices in experiments using hyperviscosity (see [6] for further remarks) and on the reported occurrences of cusp-shaped vortices in low-resolution experiments.

5. Stripping and the enstrophy cascade

We remark that the ability of stripping to produce in one step and in approximately an eddy-turnaround time structures at the dissipation scale from initially large-scale vorticity gradients goes against the classical cascade concept. The latter assumes the existence of an inertial range in which the fluctuations are statistically independent of both the large-scale flow and dissipation. We see here that, on the contrary, we cannot assume any homogeneity or isotropy of the small scales since they are fully dependent on the large-scale flow. It remains to be seen whether the kind of Hamiltonian chaos we have encountered above is able to restore, at least partially, statistical independence for small-scale fluctuations. Any effort to restore the classical theory will, however, have to contend with a very recent result (R. Benzi, personal communication) that the Kolmogorov relation on third-order correlations, which can be derived exactly from the Navier-Stokes equations on the sole assumption of statistical homogeneity and isotropy, is never satisfied by known data on two-dimensional turbulence, unless conditions that forbid coherent vortices are imposed.

Acknowledgements

We thank D. Waugh and A. Plumb for authorising the reproduction of unpublished results in Fig. 1. Calculations for Fig. 2 have been performed at CCVR. The results shown in Figs. 4-6 have been obtained by F. Bonjean and A. Mariotti.

References

1. Babiano, A., C. Basdevant, B. Legras, and R. Sadourny., 1987 - Vorticity and passive scalar dynamics in two-dimensional turbulence. *J. Fluid. Mech.* **183**, 379-397.
2. Dritschel, D.G., 1988 - The repeated filamentation of two-dimensional vorticity interfaces. *J. Fluid. Mech.* **194**, 511-547.

3. Dritschel, D.G., 1988 - Nonlinear stability bounds for inviscid, two-dimensional, parallel or circular flows with monotonic vorticity, and the analogous three-dimensional quasi-geostrophic flows. *J. Fluid. Mech.* **191**, 575–581.
4. Dritschel, D.G., 1989 - Contour dynamics and contour surgery: numerical algorithms for extended, high-resolution modelling of vortex dynamics in two-dimensional, inviscid, incompressible flows. *Computer Phys. Rep.* **10(3)**, 77–146.
5. Dritschel, D.G., 1989 - Strain-induced vortex stripping. In R.E. Caflisch, editor, *Mathematical aspects of vortex dynamics*, pages 107–119. SIAM.
6. Dritschel, D.G., 1993 - Vortex properties of two-dimensional turbulence. *Phys. Fluids A* **5(4)**, 984–997.
7. Dritschel, D.G. and B. Legras, 1991 - The elliptical model of two-dimensional vortex dynamics. Part II: Disturbance equations. *Phys. Fluids A* **3**, 855–869.
8. Elhmaïdi, D., A. Provenzale, and A. Babiano, 1993 - Elementary topology of two-dimensional turbulence from a Lagrangian viewpoint and single-particle dispersion. *J. Fluid Mech.* **257**, 533–558.
9. Legras, B. and D.G. Dritschel, 1991 - The elliptical model of two-dimensional vortex dynamics. Part I: The basic state. *Phys. Fluids A* **3**, 845–854.
10. Legras, B. and D.G. Dritschel, 1993 - A comparison of the contour surgery and pseudo-spectral methods. *J. Comput. Phys.* **104(2)**, 287–302.
11. Legras, B. and D.G. Dritschel, 1993 - Vortex stripping and the generation of high vorticity gradients in two-dimensional flows. *Applied Scientific Research* **51**, 445–455.
12. McIntyre, M.E., 1989 - On the Antarctic ozone hole. *J. Atmos. Terr. Phys.* **51**, 29–43.
13. Ottino, J.M., 1989 - *The Kinematics of Mixing: stretching, Chaos and Transport*. Cambridge U.P., Cambridge UK.
14. Warn, T. and H. Warn, 1978 - The evolution of a nonlinear critical level. *S.I.A.M.* **59**, 37–71.
15. Waugh, D.W., R.A. Plumb, R.J. Atkinson, M.R. Schoeberl, L.R. Lait, P.A. Newman, M. Lowenstein, D.W. Toohey, L.M. Avallone, C.R. Webster, and R.D. May, 1993 - Transport of material out of the stratospheric Arctic vortex by Rossby wave breaking. *J. Geophys. Res.*, to appear.
16. Weiss, J., 1991 - The dynamics of enstrophy transfer in two-dimensional hydrodynamics. *Physica D* **48**, 273–294.
17. Yao, H.B., D.G. Dritschel and N.J. Zabusky, 1993 - The simulation of high gradients in 2D vortex interactions. *Phys. Fluids A*, submitted.

* Laboratoire de Météorologie Dynamique du CNRS, École Normale Supérieure, 24 rue Lhomond, 75231 Paris CEDEX 05, France

+ Department of Applied Mathematics and Theoretical Physics
University of Cambridge
Silver Street, Cambridge CB3 9EW, England

Formation of Vortices in Rotating Thermal Convection

Abstract

We have investigated the problem of thermal convection subject to background rotation by means of a three-dimensional, non-hydrostatic numerical model. In accordance with the set up of laboratory experiments, a fluid layer in solid rotation is heated by applying a constant heat flux at the lower boundary. In the non-rotating case, more or less random convection cells develop after the heated layer has reached a certain critical height. If background rotation is applied, these cells are replaced by vortices with vertical axis, whose strength and dimensions depend on the applied heat flux and on the background rotation rate.

Introduction

Turbulent thermal convection is manifested in many geophysical flow systems. Examples are the mixed layer in the ocean or the convective boundary layer (CBL) in the atmosphere. The convective atmospheric boundary layer has been treated extensively through field experiments and numerical simulations during the last decade.

Although atmospheric and oceanic convective boundary layers are developing on a rotating Earth, only little attention has been given to the influence of background rotation on turbulent convection. This may stem from the observational fact that the typical time-scale in the atmospheric CBL of about 30 minutes is much shorter than the inertial time scale of about 15 hours for mid latitudes. Nevertheless, recent laboratory experiments on rotating turbulent convection (e.g. Boubnov and Golitsyn, 1990; Fernando *et al.*, 1991; Maxworthy and Narimousa, 1991) have been performed with respect to geophysical applications. In addition to this work, results of numerical simulations on the rotating convection problem will be presented here.

Rotating turbulent convection

In order to compare field observations, laboratory experiments and numerical simulations it is necessary to define characteristic values for the convective

boundary layer. In the case of vanishing mean wind the CBL can be fully described by the surface kinematic heat flux $w'\theta'_0$ and the inversion height h . With $w'\theta'_0$ and h , a characteristic velocity w_* can be defined by:

$$w_* = \left(\frac{g}{\bar{\theta}} w'\theta'_0 h \right)^{1/3} \quad (1)$$

where g is the acceleration due to gravity and $\bar{\theta}$ a mean temperature of the CBL.

In a rotating CBL we need the angular frequency Ω of the rotation as an additional scaling factor. It is usual to use the Coriolis parameter $f = 2\Omega$ for this purpose. For application to oceanic or atmospheric problems $f = 2\Omega \sin \varphi$, where φ is geographic latitude and Ω the Earth's angular frequency, as usual. A characteristic non-dimensional number may now be formed from the governing parameters h , w_* and f by

$$Ro_c = \frac{w_*}{fh} \quad (2)$$

which we may call a "convective" Rossby number. We will use Ro_c for evaluation of our numerical simulations of rotating turbulent convection.

The influence of background rotation on the CBL has been investigated with a three-dimensional LES model, similar to the approach used e.g. by Moeng (1984). The model equation and the numerical techniques are described in detail in Raasch and Etling (1991) and will therefore not be repeated here. The principle setup of the experiments is as follows.

All runs start with an atmosphere at rest. The initial temperature stratification is neutral up to a height of 800 m with a stable layer of 1 K/100 m aloft, in order to allow a rapid growth of the CBL in the beginning of the simulation. The boundary layer is heated by imposing a constant uniform surface heat flux of 0.1 K ms^{-1} (about 125 W m^{-2}). At the start of the simulation, convection is enforced by a vertical velocity perturbation applied in the lower part of the neutral layer.

Model results

From model runs, no difference in the CBL structure has been found for non rotating case and cases with coriolis parameter typical for the earth ($f = 10^{-4} \text{ s}^{-1}$). Therefore f was increased artificially ("fast rotating planet") and the simulations were repeated for fixed surface heat flux but different rotation rates.

Numerical simulations have been performed for a non-rotating case ($f = 0$) and three fast rotating cases ($f = 0.01, 0.03, 0.05 \text{ s}^{-1}$). The related values of the convective Rossby number are $Ro_c = \infty, 0.16, 0.053, 0.03$ respectively. Without

going into further details, the model results might be summarized as follows concerning vertical profiles of horizontally-averaged quantities:

- mean temperature gradient increases with increasing rotation rate. No well mixed CBL like in the non-rotating case is found.
- Vertical heat flux due to resolved scale motions is decreased for increasing rotation, subgrid-scale heat flux is increased at the same time.
- Variances of vertical and horizontal velocity components are decreased with increasing rotations. The ratio of vertical to horizontal variance is also decreasing to near isotropic conditions.

Marked changes in the flow structure can be also observed when the background rotation is increased. This is illustrated in figures 1 and 2, where streaklines of the horizontal flow patterns are displayed. For the non-rotating case (Fig. 1), convergence lines, marking the boundaries of convective cells, exhibit little rotation. If background rotation is applied, these cells are modified by vortices with vertical axis as can be seen in Fig. 2. Strength and dimensions of these vortices depend on the applied heat flux and on the background rotation rate. The scale of convective cells (updrafts and downdrafts) is decreased for increasing rotation.

These type of vortices have also been observed in laboratory experiments on rotating convection by Boubnov and Golitsyn (1990), Fernando *et al.* (1991) and Maxworthy and Narimousa (1991).

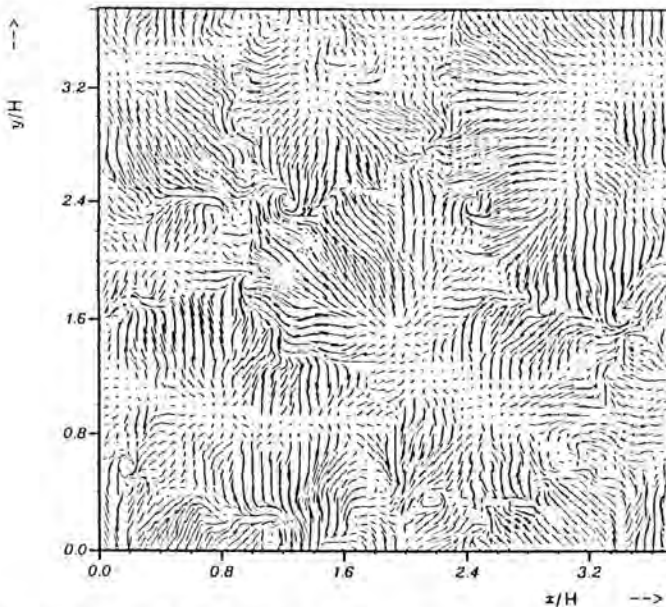


Fig. 1. Streaklines of horizontal motions in a non-rotating CBL. Horizontal cross section at $z = 0.05 h$.

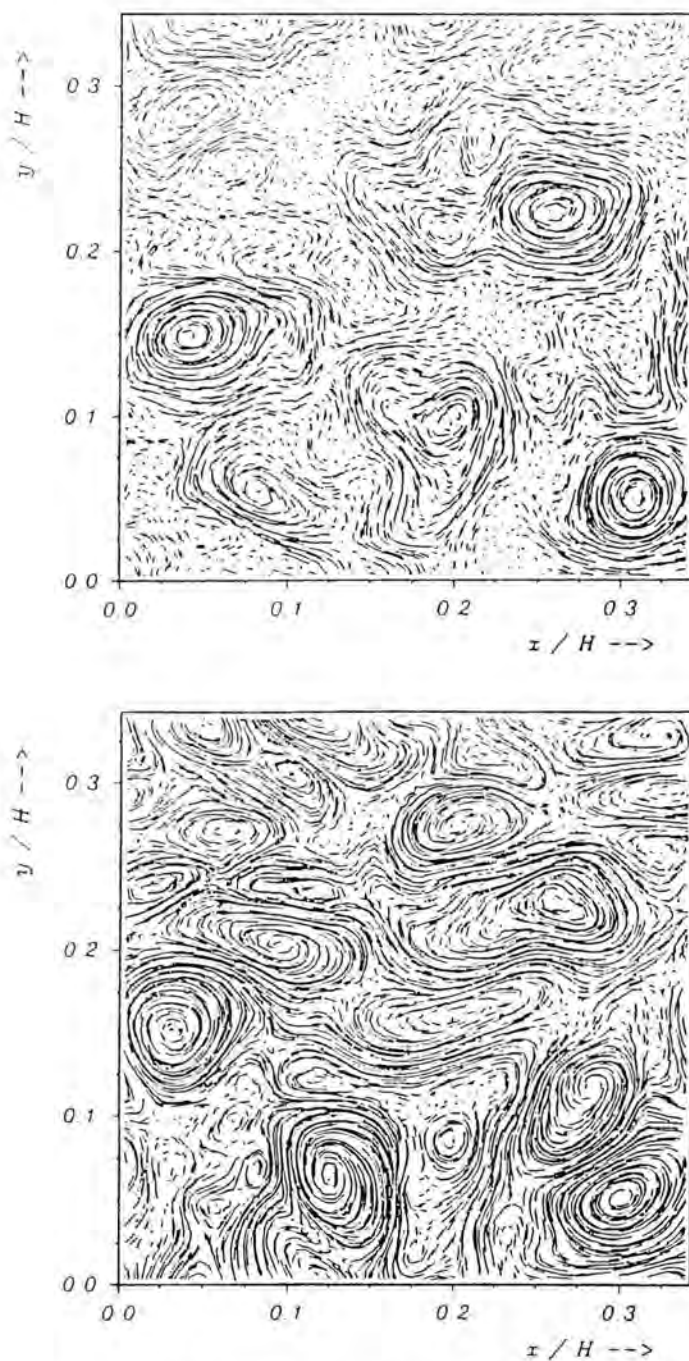


Fig. 2. Streaklines of horizontal motions in a rotating CBL ($f = 0.03 \text{ s}^{-1}$, $Ro_\tau = 0.053$). Horizontal cross section at $z = 0.5 h$ (top) and $z = 0.07 h$ (bottom).

Conclusions

Through numerical simulations we have shown, that background rotation has a marked influence on turbulence characteristics and flow morphology of a convective boundary layer. But for typical surface heat flux, as observed in the atmospheric CBL, we had to increase the Coriolis parameter up to a factor of 100 compared to situation on earth in order to obtain small Rossby numbers. With $f = 10^{-4} \text{ s}^{-1}$, as usual for geophysical applications, small values of Ro_c can be only obtained for deep convection in the ocean. In this case, the buoyancy flux $q_0/\rho c$ is in the order of $10^{-8} \text{ m}^2 \text{ s}^{-3}$ for $q_0 = 100 \text{ W m}^{-2}$ at the ocean-atmosphere boundary. If we take $h \approx 2 \text{ km}$, as observed for deep ocean convection, we obtain $Ro_c \approx 0.4$. Hence it is very likely, that the Earth's background rotation is much more important in oceanic situations than for the atmospheric CBL. Indeed recent field observations (e.g. Schott and Leaman, 1991) and numerical simulations (Jones and Marshall, 1993) on deep convection in the ocean have revealed vortex-like structures like those displayed in Fig. 2, but some more field data are necessary in order to check our numerical results against geophysical observations.

References

- Boubnov, B.M. and G.S. Golitsyn, 1990 - Temperature and velocity field regimes of convective motions in a rotating plane fluid layer. *J. Fluid Mech.* **219**, 215–239.
- Fernando, H.J.S., R. Chen and D.L. Boyer, 1991 - Effects of rotation on convective turbulence. *J. Fluid Mech.* **228**, 513–547.
- Jones, H. and J. Marshall, 1993 - Convection with rotation in a neutral ocean; a study of open-ocean deep convection. *J. Geophys. Res.* in Press.
- Maxworthy, T. and S. Narimousa, 1991 - Vortex generation by convection in a rotating fluid. *Ocean Modelling* **92**, 1037–1040.
- Moeng, C.-H., 1984 - A large-eddy-simulation for the study of planetary boundary layer turbulence. *J. Atmos. Sci.* **41**, 2052–2062.
- Raasch, S. and D. Etling, 1991 - Numerical Simulation of Rotating Turbulent Thermal Convection. *Contr. Atmos. Phys.* **64**, 185–199.
- Schott, F. and K.D. Leaman, 1991 - Observations with moored acoustic doppler current profilers in the convection regime in the Golfe du Lion. *J. Phys. Oceanogr.* **21**, 558–574.

Institut für Meteorologie und Klimatologie
Universität Hannover, Herrenhäuser Str. 2
30419 Hannover, Germany

Interactions of Dipoles with Cylinders: Experiments and Numerical Simulations

Abstract

Flow visualizations and numerical simulations of the centred collision between a dipole and a circular cylinder have shown that the main feature is the formation of oppositely signed vorticity at the cylinder wall. The thin layer of wall vorticity rolls-up in two compact patches, which couple with the primary lobes and, by self-induced motion, move away from the cylinder along curved trajectories. The diameter of the cylinder (D_c) plays an important role in the dynamics of the collision. As D_c decreases the wall vorticity increases but, since a larger dissipation is a fundamental topic which also occurs in a number of practical situations, the secondary lobe becomes less pronounced. Measurements of the vorticity distribution before and after the collision have shown that the primary lobes preserve their original relationship $\omega = f(\psi)$ and that the secondary vorticity tends to organize into structures with a similar $\omega = f(\psi)$. The differences between advection of vorticity and of passive markers have been also analysed.

Introduction

The interaction of vortices with (solid) boundaries is a fundamental fluid dynamic topic which also occurs in a number of practical situations. The interaction with the ground of the trailing vortices of an airplane during take-off, or the free surface signature by the trailing vortices of submarines are two examples of the wide range of phenomena in which these flows are involved. The case of a pair of rectilinear vortices impinging on a solid flat wall has been investigated numerically and experimentally by a number of authors (e.g. van Heijst & Flór (1989), Orlandi (1990)) and the generation of secondary vorticity at the wall was found to play a fundamental role in the interaction process.

For the interaction of a dipole with a circular cylinder, the curvature of the body adds the radius as a new parameter that makes the flow more complex. A recent numerical study by Orlandi (1993) considers the interaction for no-slip and free-slip boundary conditions. In the ideal latter case, after the collision, the dipole conserves its original shape and ω - ψ scatter plots confirm that a linear

relationship is attained again. On the other hand with the no-slip condition the secondary vorticity, interacting with the primary vortex, forms two dipolar structures that move along circular trajectories. Even in this case scatter plots present a clear tendency to attain the linear relationship eventually.

The simulations by Orlandi (1993) were limited to interactions with very small cylinders since for comparison only the experiments by Homa *et al.* (1988) were available. The present study describes laboratory and computer experiments in a large range of cylinder radii. The main goal is the comprehension of the physics of the interaction process, in particular, with respect to the effect of the diameter of the cylinder. The results indicate that the smaller the diameter of the cylinder the higher is the peak vorticity at the wall. These high peak values produce large vorticity gradients and a large dissipation. As a final result the secondary lobes have a reduced intensity.

Scatter-plots between vorticity and streamfunction have been finally analysed to investigate the distribution of the vorticity inside primary and secondary vortices. Experimental results have partially confirmed those obtained by Orlandi (1992): both vortices attain the same relationship but while in the numerical simulation it is linear, in the experiments the function $\omega = f(\psi)$ has a sinh-like shape.

Numerical method

The numerical code is the same as described by Orlandi (1993), and is here summarized briefly. Although the model has the possibility to solve the 2D Navier-Stokes equations in terms of ω and ψ in general curvilinear coordinates, it is simplified by introducing a polar coordinate system with a clustering of computational points near the cylinder. Non-uniform coordinates are mandatory to accurately describe the generation and the diffusion of wall vorticity that is the leading process of the flow. For the same reason the vorticity at the cylinder wall has been obtained by differencing the vorticity definition in the radial direction. In this way the vorticity at the wall is connected with the vorticity inside the field. The external boundary was located at 4 dipole radii where the condition $\omega = 0$ was imposed.

A finite difference scheme second order-accurate in space and in time has been used to solve the equations. The nonlinear terms have been discretized by the Arakawa (1966) scheme that, in the inviscid limit, conserves energy and enstrophy. This conservation property ensures not only the stability of the calculation but also the correct energy transfer.

The advancement in time has been obtained by a third-order Runge-Kutta scheme which calculates the nonlinear terms explicitly and the viscous terms implicitly. The large stability limit ($CFL \leq \sqrt{3}$) allows a large Δt and a consequent CPU saving.

Experimental set-up

The experimental set-up was the same as that of van Heijst & Flór (1989) and only the main features are described. The experiments were carried out in a plexiglass tank $90 \times 115 \times 30$ cm, with a working depth of 21 cm, filled with a linearly-stratified salt solution. The vertical variation in density was obtained by using a two-tank system. In the experiments described here the final density profile was linear with the corresponding buoyancy frequency $N \simeq 1.88 \text{ rad s}^{-1}$.

The dipole generator consisted of a remote controlled injection mechanism which injected the fluid horizontally, at the level of its equilibrium density ρ_s , through a circular orifice submerged in the tank. The fluid was visualized by the thymol-blue pH-indicator. After the collapse of the turbulent region and the subsequent emergence of the dipolar structure a thin-walled plexiglass cylinder of diameter D_c was placed in the tank to realize a centred collision between the dipole and the cylinder. The positioning of the cylinder was done most carefully in order to avoid the generation of internal waves that would disturb the motion of the dipole. The evolving flow was then recorded photographically at several times by a camera fixed over the centre of the tank.

In order to get quantitative information about the flow evolution a second set of experiments was carried out by adding polystyrene particles of uniform density and injecting the fluid at the level of these particles. Streak photography and digital image analysis enable to reconstruct the velocity field to determine the associated distributions of the vorticity and the stream function.

Results

Experiments

When the fluid is pushed out of the orifice it forms a 3D turbulent jet ($Re \sim O(10^3)$) that, being discharged in a stratified fluid, collapses within a time of the order of one eddy turnover-time, resulting in a 2D structure at the level of its equilibrium density (van Heijst & Flór (1989), Voropayev *et al.* (1991)). The resulting structure is a large-scale dipole, of diameter D_D , whose relationship between ω and ψ is nonlinear, possibly of a sinh-like shape (Flór & van Heijst (1994)). When the formation process is completed it is argued, from flow visualizations, that most of the initial vorticity is concentrated in the dipole and only very weak patches are left behind in the wake. The dipole moves along a straight trajectory with a constant velocity and, apart from viscous diffusion, the structure of the dipole does not change in time. The cylinder was placed after the formation of the dipole, when the direction of translation was evident.

When the dipole is close to the cylinder a thin layer of oppositely signed vorticity is generated at the wall. This vorticity diffuses in the field and is entrained by the two dipole halves, which advect it far from the cylinder. As a result, layers of vorticity are continuously peeled from the surface and this process continues

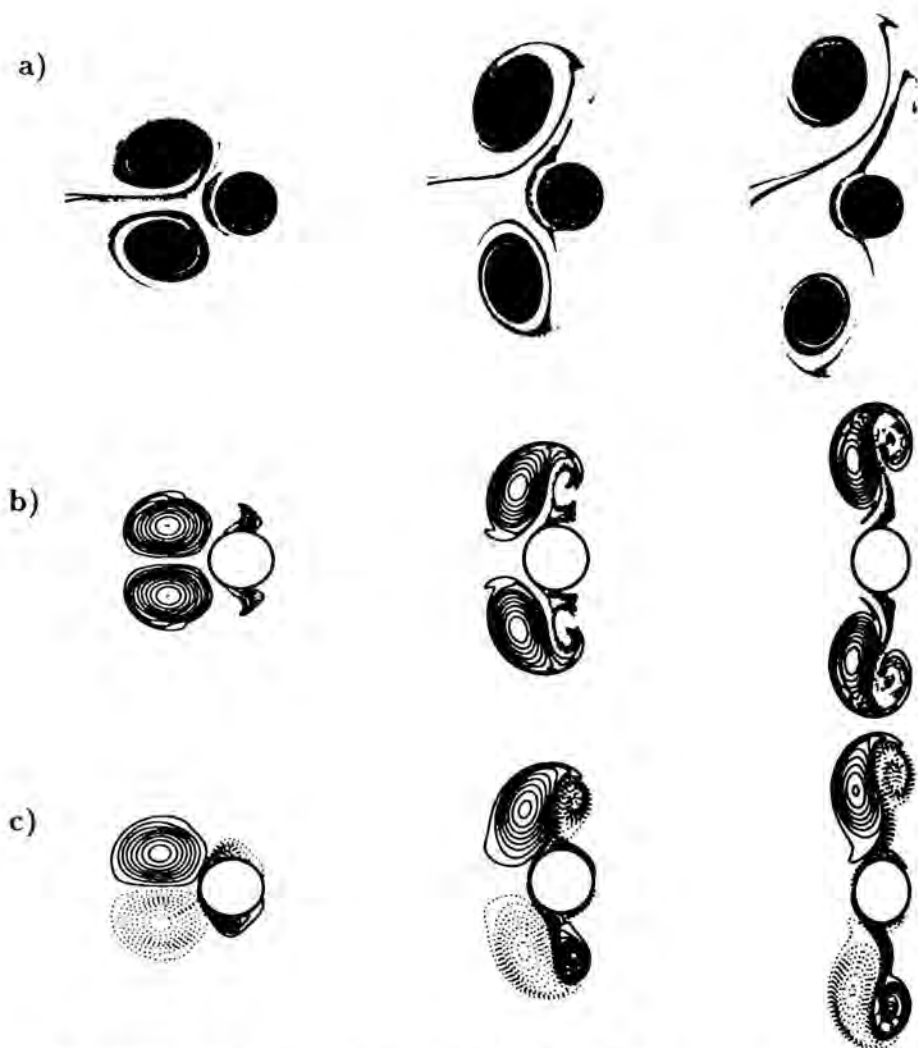


Fig. 1. Time evolution of the centred collision between a dipole and a circular cylinder, $D_D = 2D_C$, $Re = 500$. (a) Experimental results. Numerical results: (b) passive scalars released in the dipole (solid lines) and at the cylinder surface (shaded contours), (c) vorticity contour plots (solid lines for positive values, dotted for negative values). The distortion of the circular cylinder as visible in (b, c) is a graphical artifact.

even when primary structures have moved from the body. This mechanism has been evidenced by putting some fluorescein at the surface of the cylinder (Fig. 1a).

Thin layers of vorticity are very unstable and tend to roll-up to organize themselves into compact patches. Each lobe of the primary dipole couples with those patches to form asymmetric pairs moving along a curved trajectory. This

phenomenon has been observed in all experiments for different values of D_c . In particular it was observed that as D_c decreases the vortex pairs cover a larger distance downstream the cylinder and their trajectories have a smaller radius of curvature. These results agree with the numerical simulations by Orlandi (1993) who performed simulations with $D_c = 0.03 D_D$. Voropayev *et al.* (1992) also showed, by experimental visualizations, that it is possible to find a suitable D_c (with $D_c \ll D_D$) such that at the final stage of the interaction a new dipole with a reduced intensity is found beyond the cylinder. This last result has been investigated numerically in more detail.

A fundamental question concerning the dynamics of coherent structures is the relationship between the vorticity ω and the stream function ψ . On short time scales viscous effects can be neglected and the structure is stationary, in a frame co-moving with the vortex. Then the Navier-Stokes equation reduces to $J(\hat{\omega}, \hat{\psi}) = 0$ with $\hat{\omega}$ and $\hat{\psi}$ the vorticity and the stream function evaluated in the co-moving frame. Provided that the function f is integrable, any $\hat{\omega} = f(\hat{\psi})$ satisfies $J(\hat{\omega}, \hat{\psi}) = 0$, showing that a large class of solutions f are possible. In the present work the function f has been evaluated by the velocity field obtained from the digitization of the streak photographs. In Fig. 2 scatter plots of $\hat{\omega}$ and $\hat{\psi}$ are shown before (Fig. 2a) and some time after the collision (Fig. 2b). After the collision the lobe of the main structure maintains its coherence while the vorticity generated at the cylinder organizes to form the second branch in the scatter-plot which has a different slope than the original one. The comparison between Fig. 2a and 2b provides evidence that after the collision the $\hat{\omega} = f(\hat{\psi})$ relaxes towards a relationship with a uniform slope which is approximately the same slope as that of the original vortex dipole.

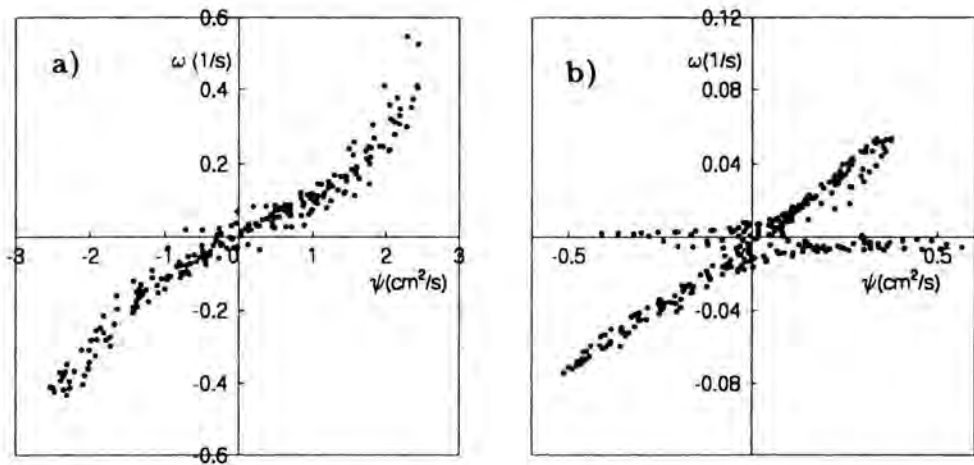


Fig. 2. Scatter plots of ω and ψ : (a) before the collision, (b) after the collision (only the upper half of the domain is considered).

To simulate the initial condition of experiments with a simple model, the Lamb (1932) solution ($\omega = k^2\psi$) has been modified with the vorticity peaks slightly displaced. The displacement of the peaks produces a shift in the positive and negative branches of the initial scatter plot resembling the sinh-like ω - ψ relationship of Fig. 2a.

Simulations with different cylinder diameters have shown that the smaller the value of D_C , the larger is the wall vorticity (since $\omega \sim V_1/R$, where V_1 is the tangential velocity and $R = D_C/2$) (Fig. 3). This high vorticity is confined within thin layers and, because of the intense gradients, a large dissipation occurs. As a consequence the secondary lobes are not intense like the high wall vorticity would suggest. The trajectories of the upper main lobe are shown in Fig. 4. As expected for large D_C , they do not present large curvatures, meaning that the positive and negative circulations are of the same order. In contrast, when $D_C \ll D_D$ the secondary lobe has a small circulation and tends to rotate around the primary lobe. The trajectory for $D_C = 0.01 D_D$ consists of a closed loop followed by a curve representing a translation of the structure beyond the cylinder. It means that for D_C below a certain value the dissipation is so strong that the secondary lobe is not intense enough to migrate with the primary. The primary dipole loses part of its vorticity and after the interaction a new weakened dipole forms beyond the cylinder.

In the present study attention is focussed on a collision with $D_C = 0.5 D_D$ and a Reynolds number of 500. The numerical results show the main features of the experimental observations and the vorticity contour plots (Fig. 1c) resemble the pictures of the evolving dye concentration (Fig. 1a).

The main difference between the experiment and the vorticity contours is the large dissipation of filaments of vorticity that survive for a shorter time than filaments of dye. This behaviour is characteristic of experiments with markers

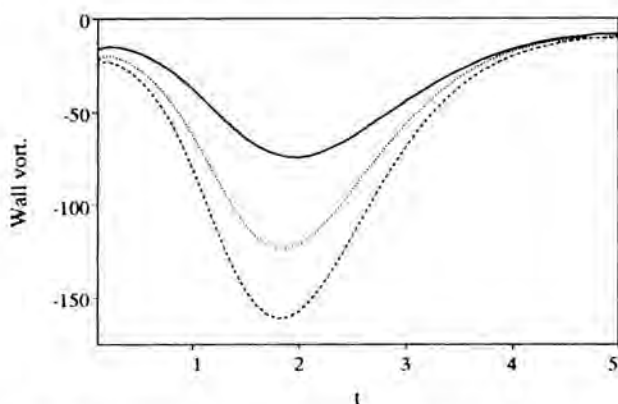


Fig. 3. Time evolution of the extremal value of the wall vorticity in the upper half plane: — $D_C = D_D$, ···· $D_C = 0.5 D_D$, — — $D_C = 0.25 D_D$.

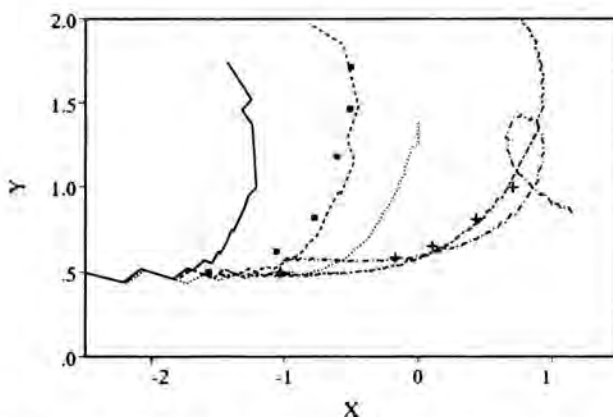


Fig. 4. Trajectories of the upper primary lobe: — $D_c = D_D$, --- $D_c = 0.5 D_D$, $D_c = 0.25 D_D$, -.- $D_c = 0.03 D_D$ (Orlandi (1992)), --- $D_c = 0.01 D_D$, + experiment by Homa *et al.* (1986) $D_c = 0.03 D_D$, ■ present experiment at $D_c = 0.5 D_D$.

and is due to the large Schmidt number which, from one side, prevents the advection of vorticity and dye to be the same but, on the other hand, allows to follow the history of the folding of layers of vorticity. For large-scale structures, where the effects of viscosity are negligible, patterns of dye and patches of vorticity behave in the same way. To evidence this behaviour the evolution of passive scalars released inside the dipole and at the cylinder surface (like the experiment of Fig. 1a) has been simulated (Fig. 1b). A Schmidt number $Sc = 10$ has been used. Although for the laboratory experiment the Schmidt number has a value $Sc \sim O(10^3)$, the numerical demonstration clearly demonstrated the effect of the reduced diffusivity. Numerical and experimental results show that, when the dipole approaches the cylinder, the shear determines the accumulation of the scalar on a small part of the cylinder surface. Subsequently the scalar is convected in the field. In contrast the vorticity is shed from a larger part of the surface, showing that the difference is due to the fact that the vorticity is continuously generated at the wall, while the passive scalar is not.

The structure of the vorticity inside the new dipoles has not been computed for this case but here we refer to results obtained by Orlandi (1993) for a similar case. The numerically determined scatter-plots show the same tendency as in the experiments: the primary lobe preserves its original relationship while the wall vorticity organizes in such a way that it attains a relationship similar to that of the primary structure.

Conclusions

Laboratory and computer experiments have been performed to investigate the dynamics of centred collisions of a dipole against a circular cylinder. In the whole range of D_c values considered, similar features have been observed, i.e. when the dipole collides with the cylinder it splits in two lobes and each one

couples with the wall vorticity to produce asymmetric dipoles moving along curved trajectories. The diameter of the cylinder has been seen to play a role in the generation of the wall vorticity and in the distance travelled, by the emerging pairs, beyond the cylinder. In particular as D_c increases the secondary lobes become more pronounced and the trajectories of the newly formed vortices become more and more orthogonal to the trajectory of the primary dipole. In contrast for small D_c ($D_c = O(10^{-2}) D_D$) the primary lobes, after moving along a closed loop, couple again beyond the cylinder. These observations are consistent with numerical simulations by Orlandi (1993).

The analysis of the distribution of the vorticity, before and after the collision, has confirmed that the primary lobes conserve their original relationship $\omega = f(\psi)$ while the secondary vorticity becomes concentrated in compact patches attaining the same f . Passive scalars and vorticity have been seen to be advected similarly in the larger structures, but quite differently in the elongated regions where the different diffusivities play an important role.

Acknowledgement

One of the authors (J.B.F.) gratefully acknowledges financial support from the Netherlands Foundation for Fundamental Research on Matter (FOM).

References

- Arakawa, A., 1966 - Computational design for long term numerical integration of the equations of fluid motion: Two-dimensional incompressible flow. Part I. *J. Comp. Phys.* **1**, 119–143.
- Flór, J.B. and G.J.F. van Heijst, 1994 - Experimental study of dipolar vortex structures in a stratified fluid. *J. Fluid Mech.* **279**, 101–134.
- Homa, J., M. Lucas and D. Rockwell, 1988 - Interaction of impulsively generated vortex pairs with bodies. *J. Fluid Mech.* **197**, 571–594.
- Lamb, H., 1932 - *Hydrodynamics*. Cambridge University Press.
- Orlandi, P., 1990 - Vortex dipole rebound from a wall. *Phys. Fluids A2*, 1429–1436.
- Orlandi, P., 1993 - Vortex dipoles impinging on circular cylinders. *Phys. Fluids A5*, 2196–2206.
- van Heijst, G.J.F. and J.B. Flór, 1989 - Dipole formation and collisions in a stratified fluid. *Nature* **340**, 212–215.
- Voropayev, S.I., Y.D. Afanasyef and I.A. Filippov, 1991 - Horizontal jet and vortex dipoles in a stratified fluid. *J. Fluid Mech.* **227**, 543–566.

* Università di Roma “La Sapienza”
Dipartimento di Meccanica e Aeronautica
Via Eudossiana 18, 00184 Rome, Italy

+ Fluid Dynamics Laboratory
Eindhoven University of Technology
P.O. Box 513, 5600 MB Eindhoven, The Netherlands

Mixing and Restratification in Stably Stratified Fluids

Abstract

The restratification effect on mixing is considered. The model of "blocking" collapse of the three-dimensional turbulent vortices explains the mixing efficiency dependence on the turbulent Richardson number. The "layered structure" mode of the decaying turbulence is identified alongside with known wave and vortical modes. It is shown that restratification can be determined essentially by molecular processes.

Introduction

Turbulent mixing is a general process of mass and energy transfer in geophysical flows. It is known that buoyancy forces result in a restriction of vertical scales of vortices in a stably stratified medium. A spatio-temporal intermittency of turbulent vortices leads to their collapse. This collapse causes a counter-gradient flux of mass that results in a partial restoring of the undisturbed stratification (restratification) and thus decreases the diapycnal transport.

For these reasons the structure of the collapsed state of turbulence is of considerable importance to the mixing process. The aim of this paper is to analyse some peculiarities of the dynamics and energetics of the restratification process. The results are considered with reference to mixing processes in the ocean.

The restratification effect on mixing efficiency

The mixing efficiency is a measure of the fraction of the available kinetic energy used to mix fluid. A number of laboratory experiments is known in which mixing was produced by a vertically or horizontally moving grid in a tank or in a stably stratified flow channel. In these cases the mixing efficiency can be described by an integral form of a flux Richardson number $Rf = \Delta\Pi/\Delta K$ (Linden, 1980). Here $\Delta\Pi$ is the layer potential energy increase, ΔK is the kinetic

energy of turbulent vortices available for mixing. The mixing efficiency is calculated as

$$Rf = \frac{\Delta \Pi}{\Delta K} = g \int_0^D z(\rho_f - \rho_s) dz / (C_D \rho_0 U^2 L_m / 2),$$

where ρ_s, ρ_f are the densities of fluid before and after mixing, respectively, z is the vertical coordinate directed upward, D is the height of the layer, U is the grid velocity, C_D is the drag coefficient of the grid, and L_m is the scale of vortices mixing the medium. In a first approach this scale is assumed to be proportional to the mesh length M , and the ratio $\lambda = L_m/M$ is considered as a constant. The mixing efficiency can be computed also by using measurements of the vertical buoyancy flux $g\rho'w'/\rho_0$ as

$$Rf = 2g \int_0^{t_L} \overline{\rho'w'} dt / (\rho_0 C_D U^2),$$

where $t = x/U$, x is the streamwise coordinate, $t_L = x_L/U$, and x_L is the length of work section.

The dependence of Rf on the influence of buoyancy forces is defined by the turbulent Richardson number $Ri_0 = M^2 N^2 / U^2$. The results of computations of $Rf(Ri_0)$ are shown in Fig. 1. Despite the significant data scatter it can be observed that with small Ri_0 the mixing efficiency increases with Ri_0 , whereas with large Ri_0 it decreases.

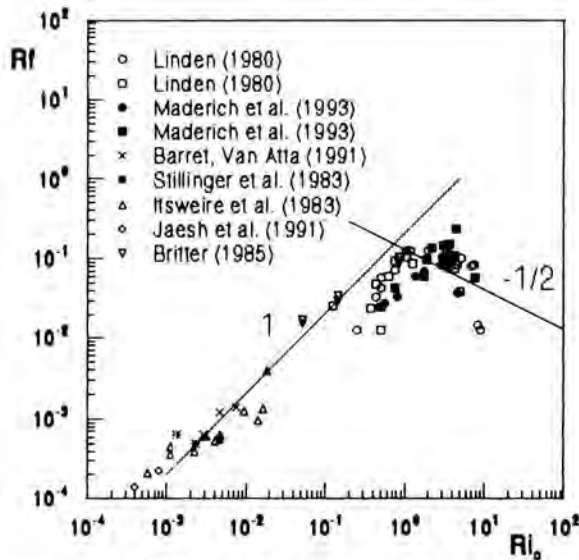


Fig. 1. Dependence of the flux Richardson number Rf on the turbulent Richardson number Ri_0 according to the experiments on turbulence decay.

Consider now the physical interpretation of these results. During the restratification process the potential energy of a three-dimensional vortex transforms into kinetic energy associated with the collapse and with the radiating internal waves. The collapse processes are prevented when vortices are packed closely enough. Thus, a portion of the potential energy is seized and is non-available for transformation into kinetic energy.

Let us evaluate these "blocking" effects in the case of an initial two-layer stratification with a density difference $\Delta\rho$ and buoyancy $\Delta b = g\Delta\rho/\rho_0$, where ρ_0 is the undisturbed value of the density in the lower layer. For simplicity it is assumed that a regular system of spherical turbulent vortices is generated behind a moving grid. The distance between their centres is M . In the initial stage of evolution the turbulent vortices expand isotropically with time t as $l/M = (Ut/M)^{1/2}$. The buoyancy forces put a limit to the vertical growth of the vortex. Its maximal vertical size l_{max} is achieved for $t = t_c$, when the buoyancy forces are balanced by the inertial ones, thus

$$l_{max}/M = \text{Ri}_0^{-1/4} (N_1 t_c)^{1/2}, \quad (1)$$

where $N_1^2 = \Delta b/M$. It is assumed that $N_1 t_c \approx 1$ by the analogy with the linear stratification case (Maderich *et al.*, 1988). We may expect that the picture of mixing depends on the ratio l_{max}/M .

If $l_{max} \gg M$, the process of gravitational collapse of vortices is not developed and the final thickness H_f of the mixed layer is $H_f/M \sim \lambda$, whereas the mixing efficiency

$$\text{Rf} \sim \lambda \text{Ri}_0 \quad (2)$$

according to Fig. 1 increases with the growth of Ri_0 .

When $l_{max} \ll M$, the collapse of vortices starts after reaching l_{max} . It ceases when the horizontal vortex size becomes comparable with M . It is supposed that the volume of the vortex, $l_{max}^3 \approx l_v l_H^2$, is conserved since as $t > t_c$ entrainment abruptly diminishes so that in first approximation it is negligible. Here l_v , l_H are the vertical and horizontal scales of the vortex, respectively. Then the final thickness of the mixed layer with $l_H \approx M$ is $H_f/M \sim \text{Ri}_0^{-3/4}$. The efficiency of mixing is

$$\text{Rf} \sim H_f^2 \text{Ri}_0 / M^2 \lambda \sim \lambda^{-1} \text{Ri}_0^{-1/2}. \quad (3)$$

As can be seen from Fig. 1 this dependence is not contradicted by the experimental data for large Ri_0 .

The mechanism of restratification described by (2)-(3) affects the mixing processes of a large class of the turbulent flows. The results of a number of experiments (Linden, 1979; Maderich *et al.*, 1993) also indicate the reduction of the mixing efficiency with larger Richardson number Ri_0 .

The coexistence of the internal waves, quasi-horizontal vortices and layered structures in the collapsed turbulence was clearly demonstrated in the experiments on turbulence decay. A linear analysis of these motions was carried out by Pearson and Linden (1983). They showed the existence of persistent viscous motions, which were driven by buoyancy forces. A scaling analysis of the Boussinesq equations without the dissipative terms was provided by Riley *et al.* (1981) and Lilly (1983). It was shown that the velocity field of collapsed turbulence can be decomposed into internal waves and quasi two-dimensional turbulence. Table 1 summarizes the scaling amplitudes of time t , pressure p , horizontal velocity V_H , vertical velocity w and buoyancy b for this isotropic scaling, depending on the Froude number $F = V_H/l_V N$ for large Reynolds number $Re = V_H l_V/\nu$. Here $\delta = l_V/l_H$ is the aspect ratio; l_V, l_H are the vertical and horizontal scales of motion, respectively, and N is the Väisälä frequency.

We extended this scaling to include the layered structure dynamics that is driven by the buoyancy field with amplitude b_0 and with conditions of strong anisotropy ($\delta \ll 1$) and small Re and F . The results are included in Table 1. The corresponding dimensionless Boussinesq system of equations for linearly stratified undisturbed fluid is then

$$9F^2(\partial \mathbf{V}_H/\partial t + \mathbf{V} \cdot \nabla \mathbf{V}_H) = -\nabla_H p + \partial^2 \mathbf{V}_H/\partial z^2 + \delta^2 \nabla_H^2 \mathbf{V}_H, \quad (4)$$

$$9\delta^2 F^2(\partial w/\partial t + \mathbf{V} \cdot \nabla w) = -\partial p/\partial z + b + \delta^2(\partial^2 w/\partial z^2 + \delta^2 \nabla_H^2 w), \quad (5)$$

$$\nabla_H \cdot \mathbf{V}_H + \partial w/\partial z = 0, \quad (6)$$

$$\partial b_T/\partial t + 9\mathbf{V} \cdot \nabla b_T + w = \varepsilon_T(\partial^2 b_T/\partial z^2 + \delta^2 \nabla_H^2 b_T), \quad (7)$$

$$\partial b_S/\partial t + 9\mathbf{V} \cdot \nabla b_S + w = \varepsilon_S(\partial^2 b_S/\partial z^2 + \delta^2 \nabla_H^2 b_S). \quad (8)$$

Table 1. Amplitude scales for flows

Flows	t	$\frac{p}{\rho_0}$	\mathbf{V}_H	w	b
Turbulence ($Re \gg 1, F \gg 1, \delta \sim 1$)	$l_0 V_0^{-1}$	V_0^2	V_0	V_0	$l_0 N^2$
Waves ($Re \gg 1, F \ll 1, \delta \sim 1$)	N^{-1}	$V_g^2 F^{-1}$	V_g	V_g	$V_g N$
Vortices ($Re \gg 1, F \ll 1, \delta \sim 1$)	$l_H V_H^{-1}$	V_H^2	V_H	$V_H F^2 \delta$	$V_H^2 l_V^{-1}$
Layered structures ($Re < 1, F \ll 1, \delta \ll 1$)	$\nu l_V^{-2} N^{-2} \delta^{-2}$	$l_V^2 N^2 g$	$l_V^3 N^2 \nu^{-1} \delta g$	$l_V^3 N^2 \nu^{-1} \delta^2 g$	b_0

Here b_T and b_S are the temperature and salinity components of the buoyancy $b = b_T + b_S$,

$$\varepsilon_T = \frac{\nu \chi_T l_H^2}{N^2 l_V^6}, \quad \varepsilon_S = \frac{\nu \chi_S l_H^2}{N^2 l_V^6}, \quad \vartheta = \frac{b_0}{l_V N^2},$$

χ_T is the temperature conductivity, χ_S is the diffusivity. The parameters $\varepsilon_T, \varepsilon_S$ describe the relation between effects of diffusion and buoyancy forces, whereas ϑ is a measure of the mixing degree of the collapsing density inhomogeneities. The main terms in the equations are underlined.

In the case of a one-component fluid ($\varepsilon_T = \varepsilon$) and ($\text{Re} \ll 1, F \ll 1, \delta \ll 1$) the system of equations (4)-(8) can be reduced to a single equation in the auxiliary function $Q(x, y, z, t)$:

$$\frac{\partial^5 Q}{\partial t \partial z^4} + \vartheta \left[J_{xz} \left(\frac{\partial^4 Q}{\partial z^4}, \frac{\partial Q}{\partial x} \right) + J_{yz} \left(\frac{\partial^4 Q}{\partial z^4}, \frac{\partial Q}{\partial y} \right) \right] - \nabla_H^2 Q = \varepsilon \frac{\partial^6 Q}{\partial z^6}, \quad (9)$$

where V_H, w, b , are expressed in terms of Q by

$$V_H = \nabla \left(\frac{\partial Q}{\partial z} \right), \quad w = -\nabla_H^2 Q, \quad b = \frac{\partial^4 Q}{\partial z^4}. \quad (10)$$

Here J_{xz}, J_{yz} are Jacobians. The value of the nondimensional parameter $\varepsilon = 1$ yields the relation between the vertical and horizontal scales of the most slowly decaying mode given by Pearson and Linden (1983). Equation (9) can be useful in the modelling of large classes of intrusion-like currents.

Consider now the solutions of (9) describing the dynamics of weakly mixed ($\vartheta \ll 1$) isolated axisymmetrical intrusion. The solution of linearized equation (9) by the Fourier transform method can be written as

$$Q(r, z, t) = \frac{1}{(2\pi)^2} \int_{-\infty}^{\infty} \exp(ik_3 z - \varepsilon k_3^2 t) F(k_3) dk_3, \\ F(k_3) = \int_0^{\infty} \hat{Q}_0(m, k_3) J_0(mr) \exp\left(-\frac{k^2 \tau}{k_3^4} t\right) m dm,$$

where \hat{Q}_0 is the Fourier representation of the initial distribution Q_0 , and $m^2 = k_1^2 + k_2^2$. Asymptotics for large t and moderate z gives $w \sim t^{-9/2}$ for $\varepsilon = O(1)$, $w \sim t^{-11/4}$ for $\varepsilon \ll 1$, whereas $w \sim t^{-6/5}$ (Maderich *et al.*, 1988) for a strongly mixed patch ($\vartheta = O(1), \varepsilon \ll 1$). Thus the effects of partial mixing and diffusion accelerate the process of restratification.

Effect of diffusion on layered structure decay

In this section we consider the evolution of layered structures in a temperature and salinity stratified fluid. It is assumed that double-diffusion instability effects

are absent. The linearized system of the equations (4)-(8) can be reduced to a single equation for the vertical velocity:

$$L_1 L_2 L_3 \Delta w + N_T^2 L_3 \Delta_H w + N_S^2 L_2 \Delta_H w = 0, \quad (11)$$

$$L_1 = \frac{\partial}{\partial t} - \nu \Delta, \quad L_2 = \frac{\partial}{\partial t} - \chi_T \Delta, \quad L_3 = \frac{\partial}{\partial t} - \chi_S \Delta.$$

The solutions are sought of the form

$$w = W_0 \exp(\sigma t + i \mathbf{k} \cdot \mathbf{r}). \quad (12)$$

The expressions for the decay rates are

$$\begin{aligned} \sigma_1 &= -\nu k^2 + \gamma_T \cdot n_T + \gamma_S \cdot n_S + \dots, \\ \sigma_2 &= -\chi_T k^2 + \gamma_T \cdot n_T + \gamma_T^2 \gamma_{TS} \cdot n_T n_S / \nu k^2 + \dots, \\ \sigma_3 &= -\chi_S k^2 + \gamma_S \cdot n_S + \gamma_S^2 \gamma_{ST} \cdot n_T n_S / \nu k^2 + \dots, \end{aligned}$$

where $\gamma_T = \text{Pr}/(\text{Pr} - 1)$, $\gamma_S = \text{Sc}/(\text{Sc} - 1)$, $\gamma_{TS} = \text{Pr}/(\text{PrSc}^{-1} - 1)$, $\gamma_{ST} = \text{Sc}/(\text{Pr}^{-1}\text{Sc} - 1)$, $n_T = N_T^2 m^2 / \nu k^4$, $n_S = N_S^2 m^2 / \nu k^4$, $m^2 = k_1^2 + k_2^2$, $k^2 = m^2 + k_3^2$, were found by series expansion in the parameter $\text{Re}_k^2 = (N_T^2 + N_S^2) m^2 / \nu^2 k^6 \ll 1$. This inequality characterizes the relation between the inertial and buoyancy effects. The first solution represents the viscous decay mechanism and others – the diffusion mechanism (thermal conduction and salt diffusion, respectively). The decay rates of the last solutions have the minimums defined by the balance of buoyancy, viscous and diffusion effects.

The presence of a salt stratification results in an enhancement of the decay of the second solution (σ_2) because the collapse effect increases. This effect causes the decrease of the perturbation vertical scale and the intensification of the diffusion process. Conversely, the decay rate of the third solution (σ_3) decreases when temperature stratification is involved. The small inhomogeneities of the temperature disappear due to thermal conduction and the temperature profile is quickly restored. However, the collapse of the salt inhomogeneities gives rise to temperature profile perturbations that oppose the collapse (“anticollapse”). Thus, the decay rate of the perturbations described by the third solution is less than that of the other ones.

Effect of shear current on layered structure decay

In the ocean a wide spectrum of shear flows exists, including quasi-horizontal vortices and internal waves. They influence the behaviour of layered structures. Some problems of the effects of viscosity and diffusivity on the velocity perturbation were studied by Criminale and Cordova (1985). In this section it is demonstrated that the decay of the velocity and scalar perturbations in the presence of shear is different.

The linearized equation for the vertical velocity perturbations in a shear flow ($\mathbf{U} = (0, 0, Gz)$) can be derived from the Boussinesq system of equations, yielding

$$L_1 L_2 \Delta w + N^2 \Delta_H w = 0, \quad (13)$$

where $L_1 = \partial/\partial t - \chi_T \Delta$, $L_2 = \partial/\partial t - \nu \Delta$, $G = \text{const.}$

Following Phillips (1966) we consider the solution in the next form

$$w = W(t) \exp[i(\mathbf{k} \cdot \mathbf{r} - k_1 Gz t)]. \quad (14)$$

By substitution in (13) we obtain the equation for the amplitude $W(t)$

$$d^2(\mu W)/d\tau^2 - A_2 d(\mu^2 W)/d\tau - A_3 \mu d(\mu W)/d\tau + A_2 A_3 \mu^3 W + A_1 W = 0, \quad (15)$$

where

$$\begin{aligned} \tau &= (k_3 - k_1 Gt)/k, & \mu &= a^2 + \tau^2, & a &= m/k. \\ A_1 &= m^2 N^2 / k_1^2 G, & A_2 &= \nu k^3 / k_1^2 G, & A_3 &= \chi_T k^3 / k_1^2 G. \end{aligned}$$

Three parameters (A_i , $i = 1, 2, 3$) defining the evolution of the layered structures are determined by the relations between buoyancy, shear velocity, viscosity and scalar diffusion. The system of solutions (modes) was found by an asymptotic method for the case of a dominant viscosity contribution ($A_2 \gg 1$):

$$W_1 = \mu^{-1} \exp[\phi_1(\tau) + o(A_2^{-1})], \quad (16)$$

$$W_2 = \mu^{-2} \exp[\phi_2(\tau) + o(A_2^{-1})], \quad (17)$$

where

$$\phi_1(\tau) = A_2 \int \mu d\tau - A_1 A_2^{-1} \int \mu^{-2} d\tau,$$

$$\phi_2(\tau) = A_3 \int \mu d\tau + A_1 A_2^{-1} \int \mu^{-2} d\tau.$$

The second solution decays more slowly than the first one. Here we have some analogy with the non-shear case (Pearson and Linden, 1983). The same solutions can be obtained for the perturbation amplitudes of the horizontal components of the velocity.

Evolution of buoyancy

The equation for the buoyancy perturbation can be derived in a similar manner, yielding

$$L_2 \Delta L_1 h + N^2 \Delta_\mu h = 0. \quad (18)$$

The buoyancy perturbation h has the same form (14) as w , viz.

$$h = B(t) \exp[i(\mathbf{k} \cdot \mathbf{r} - k_1 G t z)].$$

For the amplitude B we have the equation

$$d(\mu dB/d\tau)/d\tau - A_2 \mu^2 dB/d\tau - A_3 d(\mu^2 B)/d\tau + A_2 A_3 \mu^3 B + A_1 B = 0. \quad (19)$$

Unlike the case of the absence of mean shear, the equation for the amplitude B differs from the equation for the velocity amplitude. The solutions are

$$B_1 = \mu^{-2} \exp[\phi_1(\tau) + o(A_2^{-1})] \quad (20)$$

$$B_2 = \exp[\phi_2(\tau) + o(A_2^{-1})]. \quad (21)$$

The decay rate of the solution B_2 is less than that of B_1 , as it was with W_1 and W_2 . In distinction from the non-shear case the decay rates of the solutions W_2 and B_2 are different. The presence of shear flow implies a new energy exchange mechanism between velocity perturbations and basic flow. It causes the above-mentioned difference of the decay of the velocity and scalar perturbations.

Conclusions

The present study has produced the following results:

1. The performed analysis of experimental data and theoretical estimates demonstrates that the restratification is an effective mechanism that controls diapycnal transport in a stably stratified medium.
2. Whereas the process of mixing is carried out by turbulent vortices with large Reynolds and Peclet numbers, the non-turbulent stage of the mixing process (restratification) is essentially determined by molecular processes.
3. The presence of salinity stratification causes the enhancement of the decay rate of temperature inhomogeneities; however, the lifetime of the salinity inhomogeneities increases when the temperature stratification is involved.
4. The decay rate of the scalar (temperature, salinity) perturbations is less than that of the vertical velocity perturbations in shear flow in comparison to the case when the shear is absent.

References

- Barrett, T.K., C.W. Van Atta, 1991 - Experiments on the inhibition of mixing in stably stratified decaying turbulence using laser Doppler anemometry and laser-induced fluorescence. *Phys. Fluids A*, **3**, No.5, 1321-1332.
- Britter, R.E., 1985 - Diffusion and decay in stably-stratified turbulent flows. In: *Turbulence and Diffusion in Stable Environments*, (ed. J.C.R. Hunt) Clarendon press, Oxford, 3-14.
- Criminale, W.O., J.Q. Cordova, 1985 - Effect of diffusion in the asymptotics of perturbations in stratified shear flow. *Phys. Fluids* **29**, No.7, 2054-2060.
- Itsweire, E.C., K.N. Helland, C.W. Van Atta, 1986 - The evolution of grid generated turbulence in a stably stratified fluid. *J. Fluid Mech.* **162**, 299-338.
- Jaesh, S., K. Yoon, Z. Warhaft, 1991 - Turbulent mixing and transport in a thermally stratified interfacial layer in decaying grid turbulence. *Phys. Fluids A*, **3**, No.5, 1143-1155.
- Lienhard, J.H., C.W. Van Atta, 1988 - The decay of turbulence in thermally stratified flow. *J. Fluid. Mech.* **210**, 57-112.
- Lilly, D.K., 1983 - Stratified turbulence and mesoscale variability of the atmosphere. *J. Atm. Sci.* **40**, 749-761.
- Linden, P.F., 1979 - Mixing in stratified fluids. *Geophys. Astrophys. Fluid Dyn.*, No.1, 3-23.
- Linden, P.F., 1980 - Mixing across a density interface produced by grid turbulence. *J. Fluid Mech.*, **100**, 691-703.
- Maderich, V.S., V.I. Nikishov, A.G. Stetsenko, 1988 - *Dynamics of Internal Mixing in a Stratified Medium*. Kiev, Naukova Dumka, 239 pp (in Russian).
- Maderich, V.S., O.M. Konovalov, S.I. Konstantinov, 1993 - Mixing efficiency and processes of restratification in a stably stratified medium. *Morskoy Gidrofiz. Zh.*, N1, p. 23-28 (in Russian).
- Pearson, H.J., P.F. Linden, 1983 - The final stage of decay of turbulence in stably stratified fluid. *J. Fluid Mech.* **134**, 195-203.
- Phillips, O.M., 1966 - *The Dynamics of the Upper Ocean*. Cambridge University Press.
- Riley, J.J., R.W. Metcalfe, M.A. Weissman, 1981 - Direct numerical simulations of homogeneous turbulence in density-stratified fluids. In: *Proc. AIP Conf. Nonlinear Properties of Internal Waves*, (ed. B.J. West), 79-112.
- Stillinger, D.C., K.N. Helland, C.W. Van Atta, 1983 - Experiments on the transition of homogeneous turbulence to internal waves in a stratified fluid. *J. Fluid Mech.* **131**, 94-122.

Institute of Hydromechanics
Academy of Sciences of Ukraine
8/4, Zhelyabov Str., Kiev 252057, Ukraine

Mixing and Transport in the Mediterranean Salt Tongue

Abstract

The influences of time dependent motions on the mixing and transport of salt and heat in the Mediterranean salt tongue are considered. Two points of view are presented, the first considers salt as a passive tracer which is simply advected with the local flow while the second assumes salinity is dynamically active in determining the local velocity field and, hence, its own advection. The time dependent motion in this case is driven by baroclinic instability of the large scale flow. The results indicate that both mixing due to turbulent motions and eddy fluxes resulting from baroclinic instability are likely to be important in determining the large scale distribution of salinity in the Mediterranean salt tongue.

Introduction

The present study is motivated by recent Eulerian and Lagrangian observations near 1000 m in the Mediterranean salt tongue in the eastern North Atlantic. These data indicate that the low frequency motion within the salt tongue is zonally enhanced, has small meridional scales, and exceeds the mean velocities by more than an order of magnitude (Spall *et al.*, 1993). The nature of the observed variability is consistent with two distinct source mechanisms. Wave motions found to the south of the salt tongue are believed to be the signature of baroclinic Rossby waves generated at the meandering Cape Verde Front to the south (Spall, 1992). The low frequency zonal motions found within the salt tongue are consistent with the baroclinic instability of the large scale flow (Spall, 1993).

Turbulent mixing

The Lagrangian trajectories have been used to estimate the horizontal diffusivities in the vicinity of the salt tongue and the relative influences of turbulent mixing and mean advection on the dispersion of water parcels. The theory of mixing due to homogeneous, stationary turbulence (Taylor, 1921) is used to estimate mixing coefficients. The results indicate that mixing is non-

homogeneous with the zonally enhanced motions within the core of the salt tongue ($8\text{--}25 \times 10^6 \text{ cm}^2 \text{ s}^{-1}$) more effective at mixing than the wave motions which dominate the variability to the south of the salt tongue ($3\text{--}5 \times 10^6 \text{ cm}^2 \text{ s}^{-1}$). The mixing is also non-isotropic within the core of the salt tongue due to the zonal nature of the variability while the mixing to the south of the salt tongue is essentially isotropic. A comparison with mixing coefficients calculated directly from the dispersion of the floats gives the same result within 95% confidence limits, indicating that the floats are in a random walk regime and that dispersion is well represented by stationary homogeneous turbulence.

The relative influence of the time dependent motion on the dispersion of passive parcels may be estimated by the ratio of the root mean square displacement due to random mixing and the displacement due to the mean advection. This ratio is plotted in Figure 1 as a function of time for the zonal component (X) and meridional component (Y) of the wave-like floats (south of the salt tongue core) and zonal floats (within the salt tongue core). Because the contribution from the mean advection increases linearly with time and the mixing dispersion increases as the square root of time, the mean component will eventually dominate the dispersion. At the level of mixing estimated from the floats, however, the time dependent motion is still dominant over the mean after 5 years. Thus, over the time scale of the observations, the mixing of water parcels in the Mediterranean salt tongue is dominated by turbulent mixing. Additional data would probably result in weaker mean velocities and an even larger contribution due to the time dependent motion.

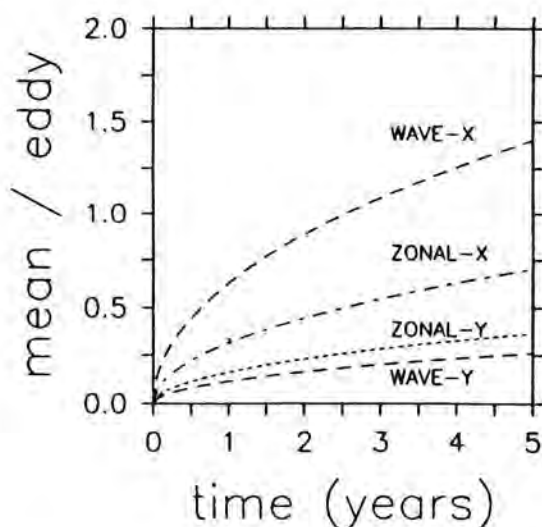


Fig. 1. Ratio of mean to eddy contributions for particle dispersion as a function of time. The turbulent motion dominates particle dispersion for both the zonal floats within the core of the salt tongue and the wave floats to the south.

A baroclinic instability mechanism

Traditional models of the large scale salt balance in the Mediterranean salt tongue have been based on the steady advection-diffusion equations. Numerical models allow for time dependent motion and an active salinity field but typically have either non-eddy resolving or marginally eddy-resolving resolution. While these prognostic models incorporate more realistic physics, basin scale computations prohibit extensive explorations of parameter space and local dynamics are often dependent on the basin scale circulation, making cause and effect difficult to sort out. We present here a simple theory which might account for observed characteristics of the low frequency variability within oceanic subtropical gyres, and demonstrates how an active salinity field might give rise to fluxes of heat and salt which are important in the overall budgets in the region of the salt tongue.

Linear theory

Linear quasigeostrophic stability theory is a useful starting point to illustrate the basic mechanism at work. The equations appropriate for non-zonal flows are derived from the conservation of quasigeostrophic potential vorticity by making use of a simple coordinate transformation (Pedlosky, 1979). The mean velocity profile used in the stability analysis is based on the hydrographic data of Saunders (1982) appropriate for the large scale flow in the North Atlantic east of the Mid-Atlantic ridge and within the core of the salt tongue, approximately 35 N to 45 N. The essential features of the mean state are southward flow in the upper 500 m, a reversal with northward flow between 500 m and 2000 m, and weak southward flow between 2000 m and the bottom. The background stratification is taken to be exponential.

The maximum growth rate as a function of the mean flow direction and the wave vector direction are shown in Figure 2. This preferentially zonal orientation of the perturbations results from the competition between maximal energy release for a wave vector oriented parallel to the mean flow and the beta effect, which stabilizes the flow for perturbations across the mean potential vorticity gradient (Pedlosky, 1979). This demonstrates that, for weak vertical shears typical of subtropical gyre interiors, the stabilizing influence of beta is sufficiently strong that the only perturbations which can efficiently extract energy from the mean flow are nearly zonal. This zonal enhancement of the low frequency variability is qualitatively consistent with observations found in many regions of the subtropical gyres.

The waves have periods of between 3 and 10 years so that the perturbations are essentially stationary during the growth period (0.5 to 1 year). The most unstable modes have wavelengths of approximately 75 to 100 km. The depths of the maximum and minimum eddy density fluxes may be directly related to the basic parameters which define the mean state. For a vertical velocity profile typical of the Canary Basin at latitudes of the salt tongue, the maximum positive

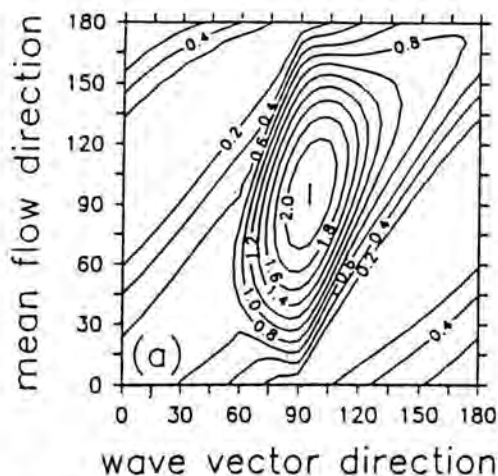


Fig. 2. Growth rate of the fastest growing wave (years^{-1}) as a function of mean flow direction and wave vector direction (0° is to the east). For mean flow angles between 20° and 160° the fastest growing waves propagate in a nearly north-south direction, resulting in zonal perturbations.

eddy density flux is centered near the core of the Mediterranean salt tongue and has a similar vertical scale of 1000 m. This similarity suggests that these eddy fluxes might contribute to the offshore flux of salt in this region.

Nonlinear regime

Although linear theory is very useful for understanding the underlying physics of the perturbations, a nonlinear model is required to investigate the large amplitude regime and to obtain a quantitative estimate of the salt flux carried by these waves. A random superposition of small perturbations between 50 km and 300 km wavelength were added to a uniform velocity profile at the center of a periodic channel (300 km in length) in a nonlinear primitive equation model (SPEM, Haidvogel *et al.*, 1991) and integrated for 700 days. After 250 days the initially uniform meridional flow has developed large amplitude zonal jets which then become unstable and break down into mesoscale eddies with amplitude $1\text{--}5 \text{ cm s}^{-1}$, close to the observed eddy kinetic energy in this region.

The zonal density flux on day 400 at the center of the channel is shown in Figure 3. The basic structure predicted by the simple linear theory carries over into the large amplitude interactive wave regime. There are a variety of scales which develop out of the initial conditions, however, the dominant meridional wavenumber is on the order of 100 km, in general agreement with linear theory. In this large amplitude regime, there is a significant transfer of energy from the low frequency, zonal regime of the growing waves to the more isotropic higher frequency mesoscale band as the jets become unstable. It is important to note that the mesoscale eddies which result from the instability of the early zonal jets do not prohibit the continued westward flux of density due to baroclinic instability of the large scale flow.

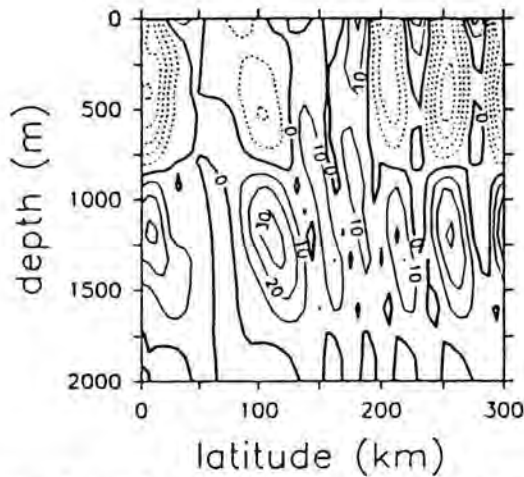


Fig. 3. Zonal perturbation density flux on day 400 from the primitive equation model, upper 2000 m only ($10^7 \text{ g cm}^{-2} \text{ s}^{-1}$). Note the positive flux (westward salt flux) over a depth range roughly corresponding to the depth of the Mediterranean salt tongue.

This is demonstrated in Figure 4, which shows the meridionally averaged zonal density flux as a function of time. The first 250 days are in the small amplitude linear regime, the fluxes are of the correct sign to release potential energy of the mean flow into kinetic energy of the growing waves. After 250 days the perturbations become large, an order of magnitude larger than the mean flow, and break down into meso scale eddies. After the first set of waves have become unstable (400 days), the mean state is still unstable and continues to flux density to the west in general agreement with linear theory. Two more wave

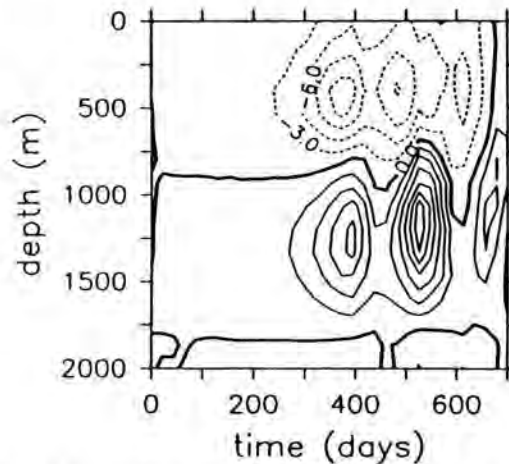


Fig. 4. Zonal perturbation density flux averaged over the meridional extent of the channel as a function of time. Three cycles of wave growth and instability are seen in the large amplitude, interactive regime.

cycles of growth and instability take place between days 400 and 700. The final cycle is much weaker than those previous because of the potential energy represented by the vertical shear in the mean state has essentially all been converted to the kinetic energy of the eddy field. Physics which are unresolved in the present simple model serve to maintain the observed mean large scale flow and provide an energy source for the continued eddy density flux.

Salt transport

The previous discussion has been in terms of the eddy density flux, however, as salinity makes an important contribution to the density of seawater within the salt tongue, these unstable waves also transport salt. An important parameter in relating density flux to salt flux is the horizontal density ratio R_H , which measures the relative influences of temperature and salinity to the zonal horizontal density gradient. A value of $R_H > 1$ indicates that the temperature gradient contributes more strongly to the density gradient than salinity. The climatological value of R_H within the core of the salt tongue increases from approximately 1.05 at 15° W to 1.25 at 27° W. The nonlinear primitive equation model was integrated using both temperature and salinity with a linear equation of state and $R_H = 1.2$. Integrating over the meridional extent of the salt tongue, approximately 10° of latitude, the average salt flux carried by these waves would be approximately $2 \times 10^6 \text{ m}^3 \text{ m}^{-1} \text{ ppt}$. The total anomalous flux of salt through the Strait of Gibraltar is estimated to be approximately $1.6 \times 10^6 \text{ m}^3 \text{ s}^{-1} \text{ ppt}$ (Bryden and Kinder, 1991).

It is likely that in the real ocean, which contains many processes not considered here, the present mechanism will be less effective at transporting salt than is found in this simple calculation. The main points in this analysis are that the theory is consistent with the observed variability, that the structure of the salt transported by the waves is very similar to the observed structure of the salt tongue, and that the waves are capable of transporting an amount of salt which may be important in the overall salt budget of the Mediterranean salt tongue. It would, of course, be interesting to investigate this mechanism in the context of a more complete ocean model, which includes frontal regions, mesoscale eddies, Meddies, external forcing, small scale mixing, and an explicit Mediterranean outflow.

References

- Bryden, H. and T.H. Kinder, 1991 - Steady two-layer exchange through the Strait of Gibraltar. *Deep Sea Res.* **38**, S445-S463.
Haidvogel, D.B., J.L. Wilkin, and R. Young, 1991 - A semi-spectral primitive equation ocean circulation model using vertical sigma coordinates and orthogonal curvilinear horizontal coordinates. *J. Comp. Phys.* **94**, 151-185.
Pedlosky, J., 1979 - *Geophysical Fluid Dynamics*. Springer Verlag, New York.

- Saunders, P.M., 1982 - Circulation in the eastern North Atlantic., *J. Mar. Res.* **40**, 641-657.
- Spall, M.A., 1992 - Rossby wave radiation in the Cape Verde Frontal Zone., *J. Phys. Oceanogr.* **22**, 796-807.
- Spall, M.A., 1993 - A mechanism for low frequency variability and salt flux within the Mediterranean salt tongue. Submitted to *J. Phys. Oceanogr.*
- Spall, M.A., P.L. Richardson and J.F. Price, 1993 - Advection and eddy mixing in the Mediterranean salt tongue. Submitted to *J. Mar. Res.*
- Taylor, G.I., 1921 - Diffusion by continuous movements. *Prod. Lond. Math. Soc.* **20**, 196-212.

Department of Physical Oceanography
 Woods Hole Oceanographic Institution
 Woods Hole, MA 02543
 USA

Nonlinear Rossby Waves and Vortices

Abstract

Interaction between planetary waves and vortices are analysed by decomposing into vortex and wave flow fields. The longtime evolution of a strong vortex is considered by assuming a quasi-stationary distribution of the potential vorticity inside the vortex core. The radial structure of the symmetric circulation in the vortex is described providing zero azimuthal velocity at the core boundary. The model describes weakening of the vortex, decreasing of its size, shrinking of the core and the development of a shielding annulus around the vortex core, depending only on the meridional position of the vortex center. The results are compared with numerical simulations using a semi-spectral quasigeostrophic model.

Introduction

Large-scale vortex structures, remaining coherent during many turnaround times, have been recognized to be typical in quasi-two-dimensional planetary flows. Such intense vortices, e.g. tropical cyclones in the atmosphere, frontal rings and lenses in the ocean, the Great Red Spot of Jupiter and other giant eddies occurring in the atmospheres of the outer planets, maintain their identities while traveling over distances much larger than their typical size. Thus, providing highly anisotropic transport of trapped fluid with different physical properties, coherent vortices are of fundamental interest for understanding the general atmospheric and oceanic circulations.

Over the past decade, observational programs, theoretical analyses, numerical simulations and laboratory experiments have improved increasingly our understanding of the structure and dynamics of planetary vortices. The results are summarized in books and reviews, e.g. Khain & Sutyrin, 1983; Kamenkovich *et al.* 1986; Flierl, 1987; Korotaev, 1988; McWilliams, 1991; Hopfinger & van Heijst, 1993; Nezlin & Sutyrin, 1994. In particular, substantial progress has been made on interaction of intense vortices with highly dispersive Rossby waves being generated due to the background gradient of the potential vorticity in planetary flows.

In analytical studies of steadily propagating anticyclones without Rossby

wave radiation (Nycander & Sutyrin, 1992) or of the initial acceleration of a monopolar vortex on the beta-plane (Sutyrin & Flierl, 1994), a symmetric circulation was prescribed. The problem was reduced to calculating the asymmetric circulation, the so-called beta-gyres, which modifies the vortex translation. Here we consider the nonlinear feedback between the vortex and the generated Rossby waves, thus allowing for the description of a change in the symmetric vortex structure due to the meridional drift of the vortex centre.

Decomposition into vortex and wave flows

We consider a localized vortex on the beta-plane using the equivalent-barotropic quasigeostrophic approximation which is a generic model for the quasi-two-dimensional planetary flows. A basic property of an inviscid flow is the material conservation of the potential vorticity (PV) in fluid particles. In the absence of a flow, PV depends only on the meridional coordinate, y , i.e. there are no closed isolines of PV. If a fluid perturbation of PV is strong enough, an area with closed isolines of PV exists. This area is considered to be a vortex core where Rossby waves propagating along the PV isolines are trapped.

To describe an interaction between the vortex and the Rossby waves we decompose the velocity into the vortex flow, $\vec{V} = \vec{k} \times \nabla \Psi$, corresponding to PV inside the vortex core, Q , and the wave flow field, $\vec{w} = \vec{k} \times \nabla \phi$, induced by the PV perturbation outside the core, ξ . Thus, inside the core the wave streamfunction, ϕ , obeys $\nabla^2 \phi - \phi = 0$, while the evolution of Q is described as follows

$$\frac{\partial Q}{\partial t} + \vec{V} \cdot \nabla Q = -\vec{w}^* \cdot \nabla Q, \quad (1)$$

$$\nabla^2 \Psi - \Psi = Q - Y_0 - r \sin \theta. \quad (2)$$

Here polar coordinates (r, θ) moving with the vortex center are used, $\vec{w}^* = \vec{w} - \vec{c}$ is the wave velocity relative to the vortex center, defined as an extremum of PV, $\vec{c} = \vec{v}_0 + \vec{w}_0$ is the drift velocity and $Y_0 = \int c_y dt$ is the meridional displacement of the vortex center. In the nondimensional Eqs. (1)-(2), the radius of deformation and the Rossby wave speed are used as spatial and velocity scales, respectively.

Outside the core $\nabla^2 \Psi - \Psi = 0$, whereas the wave perturbation of PV obeys

$$\frac{\partial \xi}{\partial t} + \vec{w}^* \cdot \nabla \xi + \vec{w} \cdot \nabla (r \sin \theta) = -\vec{V} \cdot \nabla (\xi + r \sin \theta), \quad (3)$$

$$\nabla^2 \phi - \phi = \xi. \quad (4)$$

This decomposition clearly shows that outside the core Rossby waves are forced by the vortex circulation, whereas inside the core the advection of PV by the vortex flow is accompanied by the feedback due to the wave field.

Evolution of the symmetric circulation

Now we separate the vortex flow into symmetric and asymmetric parts, denoting by $\langle \rangle$ the azimuthally averaged values

$$\vec{V} = \langle \vec{V} \rangle + \vec{v}, \quad \Psi = \langle \Psi \rangle + \psi, \quad Q = \langle Q \rangle + q.$$

Thus, the evolution of the symmetric vortex inside the core obeys

$$\frac{\partial \langle Q \rangle}{\partial t} = -\langle (\vec{v} + \vec{w}^*) \cdot \nabla q \rangle = \langle J(q, \psi + \phi^*) \rangle, \quad (5)$$

where $\phi^* = \phi + c_x r \sin \theta - c_y r \cos \theta$ describes the flow relative to the vortex center and J denotes the Jacobian.

The evolution of the asymmetric vortex circulation inside the core is described by

$$\frac{\partial q}{\partial t} = -\frac{\partial}{\partial \theta} [\Omega q - \Gamma(\psi + \phi^*)] + J(q, \psi + \phi^*) - \langle J(q, \psi + \phi^*) \rangle, \quad (6)$$

$$\Omega = \frac{\partial \langle \Psi \rangle}{r \partial r}, \quad \Gamma = \frac{\partial \langle Q \rangle}{r \partial r}$$

Here Ω is the angular rotational velocity and Γ is defined from the radial PV gradient.

For a strong vortex with a characteristic rotational frequency $\Omega_0 \gg 1$ there are three different time scales: the turnaround time $\simeq \Omega_0^{-1} \ll 1$, the typical wave time $\simeq 1$ and the vortex evolution time $\simeq \Omega_0$. Fast fluid rotation prevents growth in the amplitude of the vortex asymmetry and wave flow which remain at the order of unity ($q, \xi \simeq 1$). Unlike a linear wave packet, a strong vortex is long-lived since it changes its intensity on the order of unity at the wave time scale, which is much smaller than the vortex intensity, Ω_0 (Sutyrin, 1987).

In order to describe the long-time vortex evolution we introduce the slow time, $\tau = t\Omega_0^{-1}$, assuming that the flow does not depend on the fast turnaround time, $t\Omega_0$. Thus, considering the leading order terms, denoted by the capital letters in Eqs. (5)-(6), we conclude that $\langle Q \rangle = \langle Q \rangle_{int}$ and $\Omega q = \Gamma(\psi + \phi^*)$, such that using Eq. (2), we obtain

$$(\nabla^2 - 1) \langle \Psi \rangle = \langle Q \rangle_{int} - Y_0(\tau) \quad (7)$$

$$\left(\nabla^2 - 1 - \frac{\Gamma}{\Omega} \right) \psi = \frac{\Gamma}{\Omega} \phi^* - r \sin \theta \quad (8)$$

Eqs. (7)-(8) allow for an explicit expression of the vortex flow through the meridional displacement Y_0 and ϕ^* in the core by taking into account the assumption of no PV perturbation outside the core and provided the core boundary is known.

According to Eq. (7), the radial profile of the symmetric PV inside the core

changes independently on the radius due to the appears meridional displacement. As a result, the jump in the symmetric PV appears at the core boundary. Such an annulus with opposite radial PV gradient may lead to instability and to the appearance of a tripolar structure as shown in recent numerical simulations by Hesthaven *et al.* (1993). Rotating and oscillating satellites produce increased mixing and smoothing of PV near the core boundary.

In the leading order expansion we neglect this effect on the symmetric circulation and write the solution of Eq. (7) inside the core $r < r_c$

$$\begin{aligned} \langle \Psi \rangle = & Y_0 [1 - r_c K_1(r_c) I_0(r)] - K_0(r) \int_0^r I_0(r') \langle Q \rangle_{init} r' dr' \\ & - I_0(r) \int_0^{r_c} K_0(r') \langle Q \rangle_{init} r' dr'. \end{aligned} \quad (9)$$

Outside the core $\langle \Psi \rangle = F(Y_0, r_c) K_0(r)$, where

$$F = Y_0 r_c I_1(r_c) - \int_0^{r_c} I_0(r') \langle Q \rangle_{init} r' dr' \quad (10)$$

Thus, the symmetric circulation depends only on the meridional position, Y_0 , and the core radius, r_c

$$\begin{aligned} V_\theta = & -Y_0 r_c K_1(r_c) I_1(r) + K_1(r) \int_0^r I_0(r') \langle Q \rangle_{init} r' dr' \\ & - I_1(r) \int_r^{r_c} K_0(r') \langle Q \rangle_{init} r' dr' \quad r < r_c \end{aligned} \quad (11)$$

To satisfy Eq. (3) outside the core, the azimuthal velocity of the vortex must be zero in the leading order. This approximation has been used by Korotaev (1988) to describe the near stationary wave field outside the core and the associated vortex translation in the next order. Here we use the assumption $V_{\theta c} = 0$ at the core boundary for estimating the core radius by setting $F = 0$ in Eq. (10). Such an approach allows for a description of the long-time evolution of the symmetric vortex structure during its meridional displacement, Y_0 .

Calculations of the core radius, r_c , the radius of maximum azimuthal velocity, r_m , and the corresponding value of $V_{\theta m}$ for an initially Gaussian vortex with $Q_{init} = (6 - 2r^2) \exp(-r^2/2)$ are presented in the table below (the initial core radius is defined by $\Gamma(r_c) = 0$):

Y_0	r_c	r_m	$V_{\theta m}$
0.0	2.21	1.00	1.20
1.8	1.68	0.77	0.83
3.0	1.25	0.64	0.56
4.0	0.97	0.51	0.35

It shows that this simple model for the slow evolution of the symmetric circulation in the leading order displays such essential features as shrinking of the core, weakening of the vortex and decreasing of its size while the meridional displacement increases.

Semi-spectral model

To compare the results with the two-dimensional solution of the initial value problem we use a semi-spectral numerical model based on a decomposition of the flow field into azimuthal modes (Sutyrin, 1989),

$$\xi = \sum_{-M}^M \xi_m(r, t) e^{-im\theta}, \quad \phi = \sum_{-M}^M \phi_m(r, t) e^{-im\theta}.$$

Generally the translation of the vortex center, defined as the extremum of PV, is caused only by the flow with $m = 1$:

$$c_x + ic_y = \frac{r_c^2}{2} K_2(r_c) - 1 - i \int_0^{r_c} K_1(r) q_1 r dr - i \int_{r_c}^{\infty} K_1(r) \xi_1 r dr. \quad (12)$$

Here the first two terms describe the westward drift produced by the PV perturbation (the last term on the left-hand side of Eq. (8)) resulting from axisymmetrization of PV inside the vortex core. The next term arises due to the distortion of the vortex shape inside the core as it was considered by Sutyrin & Flierl (1994) for a vortex with piece-wise constant PV. The last term describes the translational feedback from the wave flow outside the vortex core.

The generation of the wave field outside the core is described by Eq. (3),

$$\frac{\partial \xi}{\partial t} = -\Omega \frac{\partial}{\partial \theta} (\xi + r \sin \theta) + J(\xi, \psi + \phi^*) + J(r \sin \theta, \psi + \phi). \quad (13)$$

By considering the dominant terms in Eq. (13), the initial development of an asymmetric spiral structure outside the core was described by Sutyrin (1987);

$$\xi = r \sin(\theta - \Omega t) - r \sin \theta, \quad \xi_1 = ir(e^{i\Omega t} - 1). \quad (14)$$

This solution allows for explaining the meridional and zonal acceleration of a strong vortex during many turnaround times ($\Omega_0 t \gg 1$).

The initial value problem was solved numerically for the same example of an initially Gaussian vortex as considered above. This vortex is not strong ($V_{0m} = 1.2$) and its trajectory deviates significantly from the theory of azimuthal mode $m = 1$ perturbation after $t \approx 2\pi$ due to the development of higher azimuthal modes and the change in the symmetric circulation. Nevertheless, calculations show that results of the semi-spectral model for $M = 8$ agree well with the high resolution (512x256) pseudo-spectral solution obtained by Sutyrin

et al. (1994) until $t \approx 40$. At this time the vortex decays and becomes essentially weaker than the generated wave flow field.

In this case of a rather weak monopole, a tripolar structure does not appear in spite of the initial presence of the annulus with the opposite radial gradient of PV. The vortex core gradually shrinks due to leaking of fluid near the separatrix in the PV distribution. However, the difference between the maximal azimuthal velocity, $V_{\theta m}$, as well as r_m , calculated from the semi-spectral model and from the simple model, presented in the table above, does not exceed 10%.

Conclusion

Decomposition into vortex and wave flows improves the understanding of their interaction. Planetary waves are generated by the vortex flow outside the core of closed isolines of potential vorticity. They produce a feedback resulting in the modification the vortex motion and as well as its structure.

For the long-time evolution of a strong vortex the dependence of the symmetric circulation on the meridional displacement is described by assuming zero azimuthal velocity at the core boundary. The model displays such characteristic features as shrinking of the vortex core, weakening of the vortex, decreasing size and developing of an annulus with opposite radial gradient of potential vorticity at the core boundary.

Numerical solutions using a semi-spectral model with only a few azimuthal modes agree well with the results of pseudo-spectral calculations with high resolution in two dimensions. Even for a rather weak initial vortex, the simple model of symmetric circulation is capable of reproducing well the vortex decay depending on the meridional displacement.

References

- Flierl, G.R., 1987 - Isolated eddy models in geophysics. *Ann. Rev. Fluid Mech.* **19**, 493–530.
- Hesthaven, J.S., J.P. Lynov, J. Juul Rasmussen & G.G. Sutyrin, 1993 - Generation of tripolar vortical structures on the beta-plane. *Phys. Fluids A* **5**, 1674–1678.
- Hopfner, E.J. & G.J.F. van Heijst, 1993 - Vortices in rotating fluids. *Ann. Rev. Fluid Mech.* **25**, 241–289.
- Kamenkovich, V.M., M.N. Koshlyakov & A.S. Monin, 1986 - *Synoptic Eddies in the Ocean*. D. Reidel Publ. Comp., Dordrecht.
- Khain, A.P. & G.G. Sutyrin, 1983 - *Tropical Cyclones and their Interaction with the Ocean* (in Russian), Gidrometeoizdat, Leningrad.
- Korotaev, G.K., 1988 - *Theoretical Simulation of the Synoptic Variability of the Ocean* (in Russian), Nauk. Dumka, Kiev.

- McWilliams, J.C., 1991 - Geostrophic vortices. *Nonlinear Topics in Ocean Physics*. Proceedings International School of Physics "Enrico Fermi", ed. A.R. Osborne, Elsevier Science Publ., 5-50.
- Nezlin, M.V. & G.G. Sutyrin, 1994 - Problems of simulation of large, long-lived vortices in the atmospheres of giant planets (Jupiter, Saturn, Neptune). *Surveys in Geophysics* **15**.
- Nycander, J. & G.G. Sutyrin, 1992 - Steadily translating anticyclones on the beta-plane. *Dyn. Atmos. Oceans* **16**, 473-498.
- Sutyrin, G.G., 1987 - The beta-effect and the evolution of a localized vortex. *Sov. Phys. Dokl.* **32**, 791-793.
- Sutyrin, G.G., 1989 - Forecast of intense vortex motion with an azimuthal modes model. *Mesoscale/synoptic Coherent Structures in Geophysical Turbulence*, J.C.J. Nihoul and B.M. Jamart Eds., Elsevier Oceanogr. Series **50**, 771-782.
- Sutyrin, G.G. & G.R. Flierl, 1994 - Intense vortex motion on the beta-plane: Development of the beta-gyres. *J. Atmos. Sci.* **51**, 773-790.
- Sutyrin, G.G., J.S. Hesthaven, J.P. Lynov, & J.Juul Rasmussen, 1994 - Dynamical properties of vortical structures on the beta-plane. *J. Fluid Mech.*, in press.

Russian Academy of Sciences,
P.P.Shirshov Institute of Oceanology, Moscow.

A Contour Dynamics Approach to Large-Scale Atmospheric Flow¹

Abstract

A simple model of the large-scale atmospheric circulation is studied. The model is based on the observation that the potential vorticity changes rapidly at the tropopause. We idealize the potential vorticity distribution on an isentropic surface (cutting through the tropopause) by taking it to be piecewise uniform with a discontinuity at the tropopause. If it is assumed that the time evolution of the atmosphere can be described by the equivalent barotropic vorticity equation, a dynamical system is obtained which can be formulated entirely in terms of the discontinuity. We first discuss a zonally symmetric flow to demonstrate that the model leads to quite realistic zonal velocity profiles. We then consider infinitesimal-amplitude (linear) waves superimposed on the basic zonal flow. It is found that these waves are neutral and move westward with respect to the basic zonal flow like Rossby-Haurwitz waves on a solid-body background flow. Using a numerical iteration procedure we also construct families of finite-amplitude (nonlinear) waves. The possible use of stationary waves of this kind as models for atmospheric blocking is discussed.

Introduction

The tropopause, the boundary between troposphere and stratosphere, is traditionally defined as the surface where the vertical gradient of potential temperature undergoes a large, discontinuous, change. It has been stressed by Shapiro (1980) that also the potential vorticity undergoes a large change at the tropopause. In fact he proposes to replace the traditional thermodynamic definition of the tropopause by Reed's (1955) dynamic definition in which the tropopause is identified with a surface of constant potential vorticity with a value in the range of rapid change. The fact that stratospheric values of potential vorticity are indeed much larger than tropospheric ones is illustrated by Fig. 1a. This figure shows a meridional cross-section through the atmosphere at the 45° east meridian. The dashed lines are isolines of potential temperature, the solid

¹ This contribution is an extended summary of the author's paper 'Tropopause dynamics and planetary waves', which will be published in the *Journal of the Atmospheric Sciences*.

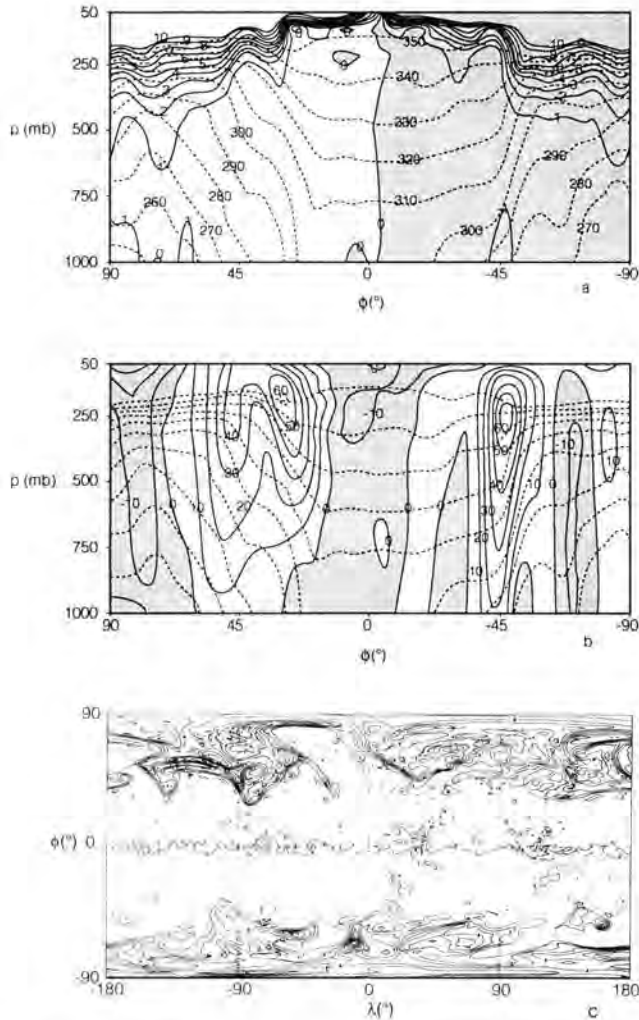


Fig. 1. (a) Meridional cross-section of the atmosphere at the 45° east meridian at January 27 1987, 12.00 GMT. Solid curves are isolines of potential vorticity in units of $10^{-6} \text{ m}^2 \text{ s}^{-1} \text{ K kg}^{-1}$ (PVU), dashed curves are isolines of potential temperature in K. The contour interval for potential vorticity is 1 PVU, the contour interval for potential temperature is 10 K. The region where potential vorticity is negative is shaded. (b) The same meridional cross-section but now with zonal velocity (in ms^{-1}) and potential temperature (in K). The contour interval for the zonal velocity is 10 ms^{-1} , the contour interval for potential temperature is 10 K. Regions with negative zonal velocity are shaded. (c) Isolines of potential vorticity on the 310 K isentropic surface for the same date and time as the cross-sections of (a) and (b). The contour interval for the potential vorticity is 1 PVU. Figs. 1a and 1b were prepared by dr. P. Berrisford, Fig. 1c by dr. T. Davies, both using archived meteorological fields from the European Centre for Medium Range Weather Forecasts (ECMWF).

lines are isolines of potential vorticity. The tropopause could, in Reed's definition, be placed at the +2 PVU level in the Northern Hemisphere and at the -2 PVU level in the Southern Hemisphere. (For the definition of one unit of potential vorticity (PVU) see the caption of Fig. 1a.) The potential vorticity involves both the vertical temperature gradient and the absolute vorticity, and usually both are involved in any change of its value. As a consequence one also finds the maximum velocities (the center of the jet stream) in the neighbourhood of the tropopause. This is illustrated by Fig. 1b, which shows the same meridional cross-section with isolines of potential temperature and zonal velocity.

Due to the large change in potential vorticity at the tropopause, its position determines, to a large extent, the structure of the potential vorticity distribution in the atmosphere. Its position therefore largely determines the state of the atmosphere as a consequence of the invertibility principle (assuming balanced flow and given the distribution of potential temperature at the ground, see Hoskins *et al.*, 1985). In this paper we wish to explore this fact to devise and study a simple model of the atmospheric large-scale circulation. Our first assumption is that we can limit ourselves to a single surface of constant potential temperature (isentropic surface) at a representative height in the atmosphere and such that it intersects the tropopause. Viewed from this perspective the tropopause emerges as a small band of closely packed isolines of potential vorticity, as illustrated by Fig. 1c. Our next assumption is that the large change at the tropopause is indeed the dominant feature of the potential vorticity distribution and that, on the isentropic surface, it can be assumed to be piecewise uniform. We then assume that large-scale atmospheric flow is adiabatic and frictionless, which means that both potential vorticity and potential temperature are conserved following the motion of fluid particles. This implies that the dynamics of potential vorticity is given by advection within each isentropic surface. To close the system we finally assume that the dynamics of potential vorticity is governed by the equivalent barotropic vorticity equation on a rotating sphere. Because potential vorticity only changes by advection, the dynamics reduces to the dynamics of a single line or contour. For this type of system a new theoretical and numerical technique has been developed recently which is called contour dynamics (see the review by Dritschel, 1989).

The model

As announced in the Introduction, we will consider the evolution of potential vorticity on a single isentropic surface, say the 310 K surface in Fig. 1. It is assumed that this surface does not intersect the earth and that the surface can be approximated by a sphere with radius $a = 6.371 \times 10^6$ m, rotating with the earth's angular velocity $\Omega = 7.292 \times 10^{-5} \text{ s}^{-1}$. Distances will be expressed in units a , time in units Ω^{-1} , and points \mathbf{r} on the sphere will be denoted by their geographical coordinates (λ, ϕ) .

We assume that the potential vorticity on an isentropic surface can be approximated by

$$q = \zeta + f - F\psi. \quad (1)$$

Here ζ is the relative vorticity, given by the vertical component of the curl of \mathbf{v} , where \mathbf{v} is the velocity field. The velocity field has components u and v along the unit vectors \mathbf{i} and \mathbf{j} and is assumed to be nondivergent. Therefore, \mathbf{v} can be written in terms of the stream function ψ ,

$$\mathbf{v} = \mathbf{k} \times \nabla\psi, \quad (2)$$

where \mathbf{k} is a unit vector pointing vertically upwards. This implies that the relative vorticity can be written as

$$\zeta = \nabla^2\psi. \quad (3)$$

The second contribution to the potential vorticity is the planetary vorticity f which, in the unit Ω , can be expressed as

$$f = 2 \sin \phi. \quad (4)$$

The last contribution to q is the 'stretching term' $-F\psi$. This term is an approximate way of taking into account the effects of vertical stratification. For the factor F in the stretching term we write

$$F = L_R^{-2}, \quad (5)$$

where L_R is the Rossby radius in units of a . We will take $L_R = 1/10$ which amounts to a Rossby radius of 637.1 km. (For a discussion of this particular choice we refer to the next section.) The fact that potential vorticity is conserved following the fluid motion thus leads to a single closed system in terms of the potential vorticity q

$$\frac{\partial q}{\partial t} + \mathbf{v} \cdot \nabla q = 0, \quad (6)$$

This equation is the equivalent barotropic vorticity equation.

Matters are simplified further by assuming that the q -field is piecewise uniform. We will thus assume that q has the constant value q_1 in a region R_1 (around the north pole) and another constant value q_0 in the rest of the sphere, denoted by R_0 . The boundary between R_1 and R_0 is assumed to be a single closed curve B , see Fig. 2.

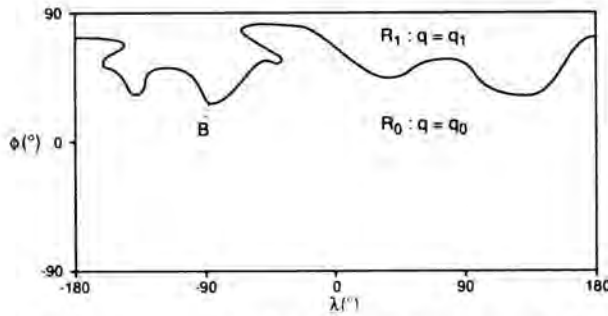


Fig. 2. Schematic picture (inspired by Fig. 1c) of the idealized potential vorticity distribution on an isentropic surface. The potential vorticity q has the constant value q_1 in the region R_1 and constant value q_0 in the region R_0 . The region R_1 is to be associated with the stratosphere, the region R_0 with the troposphere and the boundary B with the tropopause.

So the potential vorticity q is assumed to be of the form

$$q(\mathbf{r}) = q_0 + \begin{cases} q_1 - q_0 & \mathbf{r} \in R_1 \\ 0 & \mathbf{r} \in R_0 \end{cases} \quad (7)$$

It can then be demonstrated that the gradient of the stream function (from which the velocity follows according to (2)) is given by

$$\nabla\psi(\mathbf{r}) = \frac{\nabla f(\mathbf{r})}{F+2} + (q_1 - q_0) \oint_B d\ell' [\mathbf{n}' \cdot \mathbf{T}(\mathbf{r}; \mathbf{r}')] G(\mathbf{r}; \mathbf{r}'), \quad (8)$$

where $d\ell'$ is a line element along the boundary B and \mathbf{n}' is a unit vector locally perpendicular to the boundary and to \mathbf{k} and pointing away from R_1 . In this expression \mathbf{T} is a tensor defined by

$$\mathbf{T}(\mathbf{r}; \mathbf{r}') \equiv -\frac{\cos \phi'}{\cos \phi} \mathbf{i}'\mathbf{i} + \sin \phi' \sin(\lambda - \lambda') \mathbf{i}'\mathbf{j} - \cos(\lambda - \lambda') \mathbf{j}'\mathbf{j}. \quad (9)$$

and G is the Green's function of the Helmholtz operator for a sphere,

$$G(\mathbf{r}; \mathbf{r}') = -[4 \cosh(\pi\kappa)]^{-1} \times P_{-1/2 + i\kappa}^0(-\cos \theta''), \quad (10)$$

where $P_v^m(x)$ is a Legendre function with integer order m , real or complex degree v and real argument x . The order m of the Legendre function is 0 whereas the degree v is given by $-1/2 + i\kappa$. The parameter κ is related to F by

$$F = 1/4 + \kappa^2. \quad (11)$$

The argument x is $-\cos \theta''$ where θ'' is the angular distance between the points \mathbf{r} and \mathbf{r}' for which we have

$$\cos \theta'' = \sin \phi \sin \phi' + \cos \phi \cos \phi' \cos(\lambda - \lambda'). \quad (12)$$

It is also possible to derive an analogous expression for the stream function. We have

$$\psi(\mathbf{r}) = -\frac{q_0}{F} + \frac{f(\mathbf{r})}{F+2} - \frac{q_1 - q_0}{F} \frac{A_1}{4\pi} + \frac{q_1 - q_0}{F} \oint_B d\mathbf{l}' \cdot \mathbf{n}' \cdot \nabla' V(\mathbf{r}; \mathbf{r}'), \quad (13)$$

where V is a scalar defined by

$$V(\mathbf{r}; \mathbf{r}') \equiv G(\mathbf{r}; \mathbf{r}') - H(\mathbf{r}; \mathbf{r}'), \quad (14)$$

with

$$H(\mathbf{r}; \mathbf{r}') \equiv \frac{1}{4\pi} \ln \sin^2(\theta'/2). \quad (15)$$

By A_1 we mean the area of R_1 . These expressions give the stream function and its gradient (and therefore the velocity) in terms of the boundary B . The expression for the velocity allows us to determine the evolution of B in terms of B itself. Each point of B is advected by the velocity field at the corresponding point and this velocity is determined by the gradient of the planetary vorticity (the first term on the right-hand side of (8)) and a line integral over B (the second term on the right-hand side of (8)). This is the essence of what is called *contour dynamics*.

The material presented in this section is a straightforward application of known techniques in contour dynamics to the equivalent barotropic vorticity equation on a rotating sphere. Expression (8) was derived by Kimura and Okamoto (1987) for the barotropic vorticity equation on a sphere. A new element, according to the author's knowledge, is expression (13) for the stream function in terms of a line integral. Details of the derivations can be found in Verkley (1993).

Zonal flow

In order to check whether our model is capable of reproducing flows that resemble the global atmospheric circulation, we first discuss the flow resulting from a discontinuity in the q -field that coincides with a latitude circle. In other words, we first consider the case in which the region R_1 is separated from the rest of the sphere R_0 by a boundary B which is given by

$$\phi(\lambda) = \phi_B, \quad (16)$$

We note that although this is a highly idealized case, the corresponding velocity profile will serve as a first approximation of the velocity field associated with a contour of arbitrary shape.

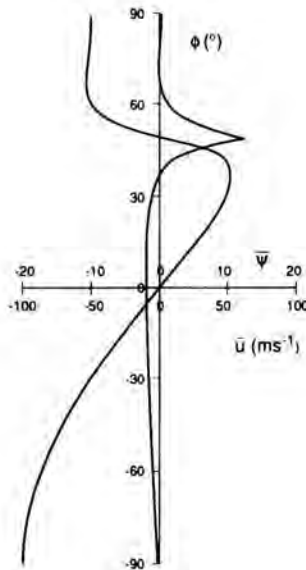


Fig. 3. An example of zonal flow profile, resulting from a piecewise uniform potential vorticity distribution. The value of ϕ_B is 50° and the value of $q_1 - q_0$ is 2.99. The value of q_0 is 0. The cusped line is the zonal velocity \bar{u} (in ms^{-1} , values below the horizontal axis), the smooth line is the nondimensional stream function $\bar{\psi}$ (multiplied by 1000, values above the horizontal axis). Note the sharp maximum of u at the tropopause $\phi(\lambda) = \phi_B$.

The velocity and stream function corresponding with a zonal contour can be calculated using (8) and (13). We used an alternative (simpler) way and the result of an example is given in Fig. 3. The value of ϕ_B is 50° and the value of q_0 is 0. For the difference in potential vorticity, $q_1 - q_0$, we have taken the value 2.99. This value is chosen such that a linear wave with zonal wavenumber 3 is stationary for this zonal flow, as will be seen in the next section. The figure shows the zonal velocity u (the cusped lines) and the zonal stream function ψ (the smooth lines) as a function of the latitude ϕ . The numbers below the horizontal axes are velocity in ms^{-1} , the numbers above the horizontal axis are nondimensional stream function values multiplied by 1000. The figure shows that the zonal velocity u has a sharp maximum at the tropopause. Around its maximum the wind is westerly and further away it is weakly easterly. The value of the velocity at the tropopause is in this case 63.09 ms^{-1} . It can be shown that the velocity at the tropopause depends mainly on the difference in potential vorticity between troposphere and stratosphere. The velocity at the tropopause is nearly independent of the latitude of the tropopause except when the tropopause lies close to the north pole. We remark that, in choosing the value of F , we were guided by the corresponding zonal velocity profiles. As can be seen from expression (8), the contribution of the Coriolis parameter to the velocity field is inversely proportional to $F + 2$. This means that if F becomes small this contribution becomes large. For $F = 0$, this contribution is so large that it is impossible to obtain a zonal flow profile that behaves realistically at all points on the sphere.

The barotropic vorticity equation, i.e., equation (6) without the 'stretching term' $-F\psi$ in the expression for q , would therefore be quite unacceptable as a basis for our contour dynamics model of the atmosphere.

Linear waves

In this section we consider linear waves, i.e., waves with infinitesimal amplitude on the basic zonal flows discussed in the previous boundary B . In the case of linear waves on a zonal background the contour B is written as

$$\phi(\lambda) = \phi_B + \delta\phi(\lambda) \quad (17)$$

with

$$\delta\phi(\lambda) = \text{Re}[\varepsilon \exp im(\lambda - \omega t)], \quad (18)$$

where Re denotes the real part, ε is a number with infinitesimally small absolute value, m is a nonnegative integer and ω is the angular velocity of the wave propagating along the basic zonal flow. Note that ε as well as ω can be complex.

It can be shown that wave solutions of the form above can indeed be found. It follows that for positive $q_1 - q_0$ the waves move westward with respect to the basic zonal flow. This can be understood qualitatively as follows. Fig. 4 shows, in addition to the perturbed contour, the corresponding stream function for $q_1 - q_0$ and ε equal to 1. Cells with positive values are marked with H , cells with negative values are marked with L . The arrows give the direction of maximum meridional velocity associated with the perturbation stream function. These arrows show that the perturbation stream function is such as to induce a

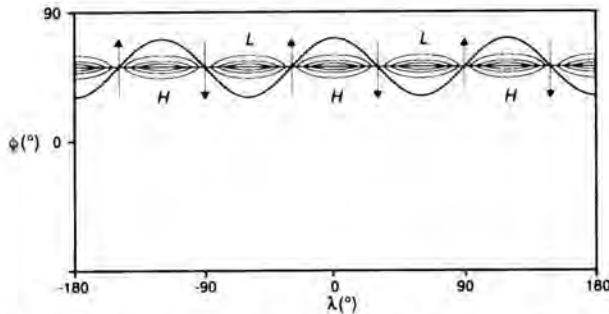


Fig. 4. The stream function associated with a linear wave. Both $q_1 - q_0$ and ε are given the value 1. Cells with positive values are marked by H , cells with negative values by L . The outer isoline of each cell has value ± 0.01 , the next isoline denotes a value of ± 0.02 and the third isoline has value ± 0.03 . The arrows denote the direction of the largest meridional velocity. The figure illustrates that the perturbed contour induces a westward phase velocity of the perturbation pattern.

westward motion of the wave pattern. In fact, the wave propagation mechanism encountered here is a specific example of the more general case discussed by Hoskins *et al.* (1985, p. 919).

Nonlinear waves

In this section we will investigate whether a system consisting of a single discontinuity in potential vorticity supports finite amplitude waves around an average zonal flow. We will restrict ourselves to stationary waves, i.e., waves of which the contours coincide with an isoline of the corresponding stream function. The approach of this issue is numerical and we therefore introduce a discrete label i , ranging from 1 to N , which labels the different points \mathbf{r}_i by which we represent any contour B . We then define the following functional K ,

$$K \equiv \frac{1}{N} \sum_{i=1}^N \frac{1}{2} [\psi(\mathbf{r}_i) - \psi_{av}]^2, \quad (19)$$

where ψ_{av} denotes the average value of ψ over B , which is defined as

$$\psi_{av} \equiv \frac{1}{N} \sum_{i=1}^N \psi(\mathbf{r}_i). \quad (20)$$

The functional K is nonnegative, and zero if and only if ψ is constant along the contour, i.e., if and only if the contour is stationary. If contours exist for which K is indeed zero we might expect to find them from appropriate first guesses by an adjustment process in which K is minimized. This is the basic idea of the method. For the minimization we used the routine E04KAF from the NAG Fortran Library, Mark 13, in double precision implementation, which is based on a quasi-Newton algorithm. We applied the numerical procedure to obtain families of stationary nonlinear waves on the basic zonal contour of which the velocity and stream function profiles are given in Fig. 3. We recall that the latitude of this basic zonal contour is $\phi_B = 50^\circ$ and that the value of $q_1 - q_0$ is chosen such that this contour supports a stationary linear wave with zonal wavenumber $m = 3$.

We will denote the positions of the k -th member of a family of stationary contours by (λ_i^k, ϕ_i^k) , where i runs from 1 to N and the first guess from which each member is obtained by (λ_i^0, ϕ_i^0) . Then the 0-th member of the family is the basic zonal contour represented by

$$\lambda_i^0 = -\pi + (i-1) \left(\frac{2\pi}{N} \right), \quad (21a)$$

$$\phi_i^0 = \phi_B. \quad (21b)$$

The first guess for contour (λ_i^1, ϕ_i^1) is of the form of a linear wave with a small but finite amplitude, i.e.,

$$\hat{\lambda}_i^1 = -\pi + (i-1) \left(\frac{2\pi}{N} \right), \quad (22a)$$

$$\phi_i^1 = \phi_B + \varepsilon \cos(m\hat{\lambda}_i^1), \quad (22b)$$

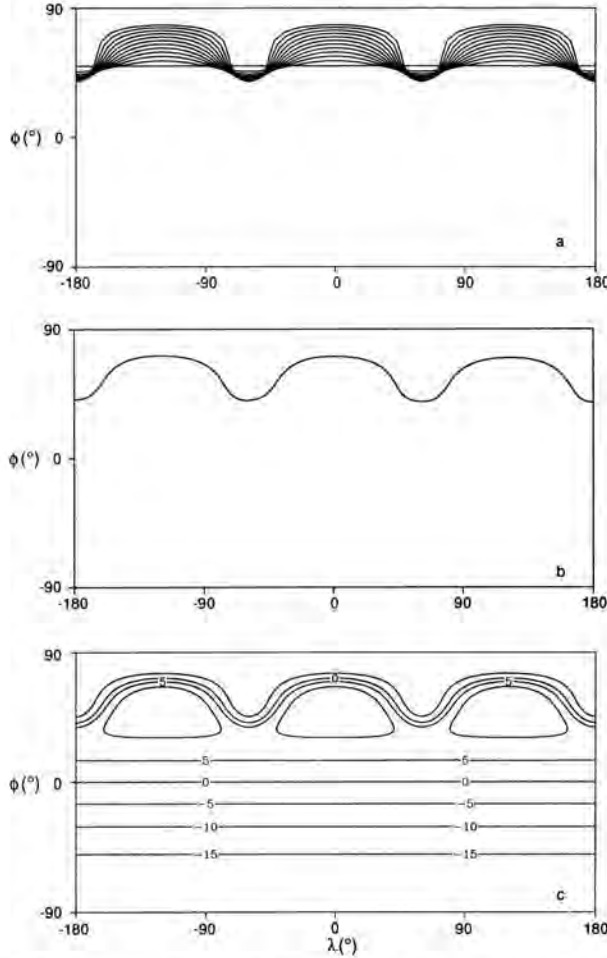


Fig. 5. (a) Families of stationary nonlinear waves on the basic zonal contour of which the stream function and velocity profiles are given in Fig. 3. In (a) we show the contours with $k=0, 2, 4, \dots, 22$ resulting from the numerical procedure described in the text. In (b) a representative member ($k=14$) is shown. In (c) we show the stream function corresponding with the contour of (b). The nondimensional values of the stream function are multiplied by 1000 and the contour interval is 5. The stream function is calculated on a regular grid of 144×72 points using a numerical discretization of expression (13).

where $\varepsilon = 2^\circ$. We build up a family of contours by using as a first guess for any new contour a linear extrapolation of the two previous contours. For the stationary contour (λ_i^k, ϕ_i^k) the first guess is thus taken to be

$$\hat{\lambda}_i^k = \lambda_i^{k-1} + [\lambda_i^{k-1} - \lambda_i^{k-2}], \quad (23a)$$

$$\hat{\phi}_i^k = \phi_i^{k-1} + [\phi_i^{k-1} - \phi_i^{k-2}]. \quad (23b)$$

For the number of points N we take $N = m \times 30$, i.e., 30 points for each wavelength.

For the basic zonal flow of Fig. 3 and $m = 3$ we could continue the process of finding stationary contours until $k = 22$. After this the obtained contours did not change appreciably but fell back to their predecessors. The average of the initial value of K for these 22 cases was 2.91×10^{-10} , the average of the final value of K was 8.63×10^{-13} . In Fig. 5a we show the contours for $k = 0, 2, 4, \dots, 22$. In Fig. 5b we show the contour for $k = 14$ from the family in Fig. 5a in isolation. The corresponding stream function, calculated by using a numerical discretization of (13), is shown in Fig. 5c. We observe that the isolines of the stream function are closely packed around the contour which signifies, of course, that the velocity field is sharply peaked at the tropopause. We also note that in the ridges of the waves closed cells of the stream function have formed.

We note that, although the procedure has brought us quite far into the realm of nonlinear stationary waves, it is quite likely that one can go much further. In the contours shown in Fig. 5a there is a tendency for the contours to touch upon themselves in the vicinity of the troughs, in much the same way as in the study of Pratt (1988). This suggests that, if the process were to be continued, a transition might occur in which the solution changes from a single contour into a combination of several isolated contours.

Summary and discussion

Our main finding is that the contour dynamics approach to large-scale atmospheric flow leads to a simple and concise picture of the atmosphere. First of all, the assumption of a single line of discontinuity representing the tropopause leads to a reasonable zonal flow profile. The velocity field is westerly and sharply peaked at the tropopause and falls off rapidly and becomes easterly away from the tropopause. Zonal flows of this form support linear neutral waves which, like Rossby-Haurwitz waves on a solid-body rotation, propagate westward with respect to the basic zonal flow. Also in analogy with Rossby-Haurwitz waves there exist families of nonlinear waves, although the form of the waves changes if the amplitudes increase. The nonlinear waves are obtained numerically using an iterative technique.

The results reported in the present paper only constitute a first step in the analysis of large-scale atmospheric phenomena from the viewpoint of the tropopause. In particular, the finite-amplitude waves we obtain can probably be

extended much further into the nonlinear domain. It should also be possible, we believe, to construct finite amplitude waves with a localized character in much the same way as modon solutions can be found. These waves, if they exist, would be an appropriate model of atmospheric blocking. The advantage of such a model would be that it quite naturally incorporates the basic finding of Illari (1984) and Crum and Stevens (1988), namely that in the blocking region the potential vorticity is relatively low and uniform.

References

- Crum, F.X., and D.E. Stevens, 1988 - A case study of atmospheric blocking using isentropic analysis. *Mon. Wea. Rev.* **116**, 223–241.
- Dritschel, D.G., 1989 - Contour dynamics and contour surgery: numerical algorithms for extended, high-resolution modelling of vortex dynamics in two-dimensional, inviscid, incompressible flows. *Computer Phys. Rep.* **10**, 77–146.
- Hoskins, B.J., M.E. McIntyre and A.W. Robertson, 1985 - On the use and significance of isentropic potential vorticity maps. *Quart. J. Roy. Meteor. Soc.* **111**, 877–946.
- Illari, L., 1984 - A diagnostic study of the potential vorticity in a warm blocking anticyclone. *J. Atmos. Sci.* **41**, 3518–3526.
- Kimura, Y., and H. Okamoto, 1987 - Vortex motion on a sphere. *J. Phys. Soc. Japan* **56**, 4203–4206.
- Pratt, L.J., 1988 - Meandering and eddy detachment according to a simple (looking) path equation. *J. Phys. Oceanogr.* **18**, 1627–1640.
- Reed, R.J., 1955 - A study of a characteristic type of upper-level frontogenesis. *J. Meteor.* **12**, 226–237.
- Shapiro, M.A., 1980 - Turbulent mixing within tropopause folds as a mechanism for the exchange of chemical constituents between the stratosphere and troposphere. *J. Atmos. Sci.* **37**, 994–1004.
- Verkley, W.T.M., 1993 - Tropopause dynamics and planetary waves. *J. Atmos. Sci.* (submitted).

Royal Netherlands Meteorological Institute (KNMI)
P.O. Box 201
3730 AE De Bilt, The Netherlands

Determination of the Linear Stability of Modons on a Sphere by High-Truncation Time Integrations¹

Abstract

The linear stability of modons on a sphere is determined from the growth of perturbations on an initial modon basic state. Numerical spectral time-integrations are performed for truncations T10-T43 and a few truncations up to T85. Three basic states are studied: a modon with an oscillatory exterior stationary in an eastward zonal flow, a modon with a decaying exterior stationary in a westward flow, and a Rossby wave. From the behaviour of the globally averaged energy and the relative vorticity at a particular point, the real and imaginary part of the eigenvalue of the fastest growing normal mode are obtained. Then from two stream function plots at different times, the real and imaginary part of this normal mode can be found. The modons and the Rossby wave are unstable: the decay time for the Rossby wave is 9 days, for the modons typically 5 days. The truncation runs confirm the results by Verkley (1987) who obtained the linear normal modes by solving the eigenvector problem up to T30. High-truncation runs show that the decay time slowly converges with truncation.

Introduction

The inviscid, unforced quasi-geostrophic equations possess a class of solutions known as modons. Modons are characterized by a multivalued relationship between potential vorticity and stream function in a comoving reference frame. Modons on the beta plane were introduced by Stern (1975) to describe Gulf Stream eddies and modons were put forward as models of atmospheric blocking by McWilliams (1980). The solutions have been extended to spherical geometry for several systems: dipole modon solutions for the barotropic vorticity equation by Verkley (1984, 1987, 1990), for the equivalent barotropic vorticity equation by Tribbia (1984), and for the two-layer quasi-geostrophic equations by Neven (1993). Quadrupole modon solutions are discussed in Neven (1992).

The decay of modons is an issue under discussion. On the beta plane, numerical stability analyses using time integrations were performed by Makino *et al.*

¹ This is a summary of the author's paper 'Stability of Modons on a Sphere,' submitted for publication to the *Journal of the Atmospheric Sciences*.

(1981) and McWilliams *et al.* (1981). On a sphere, the normal modes of the linearized barotropic vorticity equation were determined by solving the eigenvalue problem for truncations up to T30 (Verkley 1987, 1990). The analytical proofs of stability and instability known in literature are still inconclusive (Nycander, 1992).

The aim of this paper is to provide a reliable and accurate determination of the stability properties of modons. The linear stability of modons on a sphere is determined from the growth of perturbations on an initial modon basic state. For three basic state fields, numerical spectral time integrations are performed for truncations T10-T43 and a few truncations up to T85. The results from the time-integration method of this paper confirm the results of the eigenvector method. The advantage of the time-integration method is that for a spectral model on a sphere with truncation TN the memory space required is proportional to N^3 , whereas the eigenvector requires N^4 . This enables us to investigate higher truncations and to determine more accurately the stability properties of modons. Investigation of the convergence of eigenvalues in dependence of truncation provides an estimate of the accuracy of the results.

Dynamical equations

For an inviscid, incompressible, unforced, homogeneous fluid on a rotating sphere the conservation of potential vorticity q is expressed by the barotropic vorticity equation

$$\frac{\partial q}{\partial t} + J(\psi, q) = 0 \quad (1)$$

where ψ is the stream function. The velocity is $\mathbf{v} = \mathbf{k} \times \nabla \psi$ with \mathbf{k} the unit normal vector. With the radius of the earth $a = 6.371 \times 10^6$ m as the length scale, and the inverse of the angular velocity of the rotating earth $\Omega = 7.292 \times 10^{-5} \text{ s}^{-1}$ as the time scale, in spherical coordinates with longitude λ and latitude ϕ , the planetary vorticity $f = 2 \sin \phi$ and the potential vorticity $q = \nabla^2 \psi + f$.

A decomposition of the field into a basic state field and a perturbation field

$$\begin{aligned} \psi &= \bar{\psi} + \psi' \\ q &= \bar{q} + q' \end{aligned} \quad (2)$$

with

$$\begin{aligned} \bar{q} &= \nabla^2 \bar{\psi} + f \\ q' &= \zeta' = \nabla^2 \psi' \end{aligned} \quad (3)$$

leads to the linearized barotropic vorticity equation

$$\frac{\partial q'}{\partial t} + J(\bar{\psi}, q') + J(\psi', \bar{q}) = 0 \quad (4)$$

The normal mode solutions of (4) can be written as

$$\begin{aligned}\psi'(\lambda, \phi, t) &= \text{Re}[\xi(\lambda, \phi) e^{vt}] \\ \zeta'(\lambda, \phi, t) &= \text{Re}[p(\lambda, \phi) e^{vt}] \\ p(\lambda, \phi) &= \nabla^2 \xi(\lambda, \phi)\end{aligned}\quad (5)$$

with complex fields

$$\begin{aligned}\xi(\lambda, \phi) &= \xi_r(\lambda, \phi) + i\xi_i(\lambda, \phi) \\ p(\lambda, \phi) &= p_r(\lambda, \phi) + ip_i(\lambda, \phi)\end{aligned}\quad (6)$$

and complex eigenvalue

$$v = v_r + iv_i \quad (7)$$

Substitution of the fields (5) in the linearized equation (4) gives

$$vp + J(\bar{\psi}, p) + J(\xi, \bar{q}) = 0 \quad (8)$$

which is an eigenvalue problem with eigenvalue v and the harmonic coefficients of the field $p(\lambda, \phi)$ as the components of the eigenvector. The definition of the real and imaginary part of the complex fields contains an arbitrary global phase factor due to the choice of origin of time. The normal mode of which the eigenvalues have the largest real part determines the stability properties of the modon. For the eigenvalue corresponding to this fastest growing normal mode, the real part is related to the e-folding time of the mode

$$v_r = \frac{1}{\tau} \quad (9)$$

and the imaginary part is related to the oscillation time of the mode

$$v_i = \frac{2\pi}{T} \quad (10)$$

There are three cases. If v_r is negative all modes decrease exponentially and the stationary modon basic state solution is asymptotically stable. If $v_r = 0$ the modon is neutrally stable. If v_r is positive there is at least one exponentially growing mode and the modon is unstable.

Basic states

We have investigated three stationary basic states centred at midlatitude $(\lambda, \phi) = (270^\circ, 45^\circ)$. The Rossby wave is characterized by a single linear $q(\psi)$ -relationship with negative slope in the $q(\psi)$ -diagram. The wavenumber $n = 8$ and

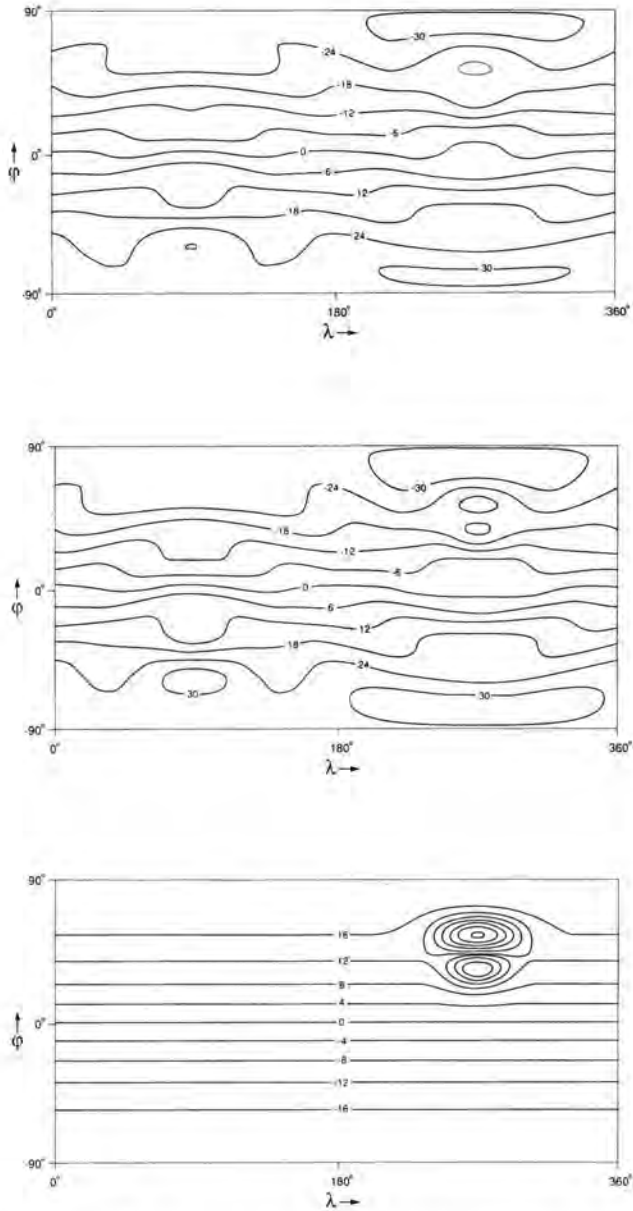


Fig. 1. The stream function for the stationary basic states (a) A Rossby wave with wavenumber $n=8$ in an eastward zonal flow. The contour interval is 0.006 (b) A wavelike modon with wavenumbers $\kappa_o=7.78$ and $\kappa_l=12.28$ in an eastward zonal flow. The contour interval is 0.006 (c) A localized modon with wavenumbers $\kappa_o=10$ and $\kappa_l=10$ in a westward zonal flow. The contour interval is 0.004.

there is a closed circular streamline at radius 15° from the centre. The modons have two regions separated by a boundary circle, and a piecewise linear $q(\psi)$ -relationship. For the wavelike modon (oscillatory behaviour in both regions) there is a negative slope in the $q(\psi)$ -diagram for both regions. We have investigated a wavelike modon with wavenumber in the outer region $\kappa_o = 7.78$ and wavenumber in the inner region $\kappa_i = 12.28$. For the localized modon (exponential decaying behaviour in the outer region) there is a positive slope in the $q(\psi)$ -diagram in the outer region, and a negative slope in the inner region. We have investigated a localized modon with wavenumber in the outer region $\kappa_o = 10$ and wavenumber in the inner region $\kappa_i = 10$. For both modons the radius is approximately 15° . The three basic states are shown in Fig. 1.

Evolution

The initial basic states were provided on a Gaussian grid. Extended time integrations of the linearized barotropic vorticity equation on a sphere using the spectral method were performed on the newly installed CRAY-C90 at the ECMWF. During the numerical integration, the global perturbation energy \mathcal{E} and the local perturbation relative vorticity ζ_p at a point in the inner region were observed. Two series of spectral runs were made: first, for each triangular truncation from T10 to T43 the time integration was performed over 256 days with timesteps of 15 minutes. Second, for the Rossby wave and wavelike modon a T85 run was made, whereas for the localized modon a truncation run for every other run from T75 to T85 was made. The time integration was performed over 128 days with timesteps of 5 minutes. The initial perturbation consisted of noise with energy 10^{-3} of the basic state. The perturbation field was rescaled to unity when its energy exceeded 100 times its initial energy.

The solution of the eigenvalue problem for a given spectral truncation yields a discrete set of eigenvalues. If the existence of a single eigenvalue with largest real part is assumed, then there is a single fastest growing normal mode. The behaviour of the system after some time in a time integration is dominated by this fastest growing normal mode. From substitution of (6) and (7) in (5) the stream function and relative vorticity are obtained in complex notation

$$\psi'(\lambda, \phi, t) = e^{v_r t} \cdot (\xi_r(\lambda, \phi) \cos v_i t - \xi_i(\lambda, \phi) \sin v_i t) \quad (11)$$

$$\zeta'(\lambda, \phi, t) = e^{v_r t} \cdot (p_r(\lambda, \phi) \cos v_i t - p_i(\lambda, \phi) \sin v_i t) \quad (12)$$

The real part of the eigenvalue of the fastest growing mode v_r is determined from the evolution of the globally averaged perturbation energy

$$\mathcal{E}(t) = \frac{1}{2} \int (\nabla \psi'(\lambda, \phi, t))^2 dS = -\frac{1}{2} \int \psi'(\lambda, \phi, t) \zeta'(\lambda, \phi, t) dS \quad (13)$$

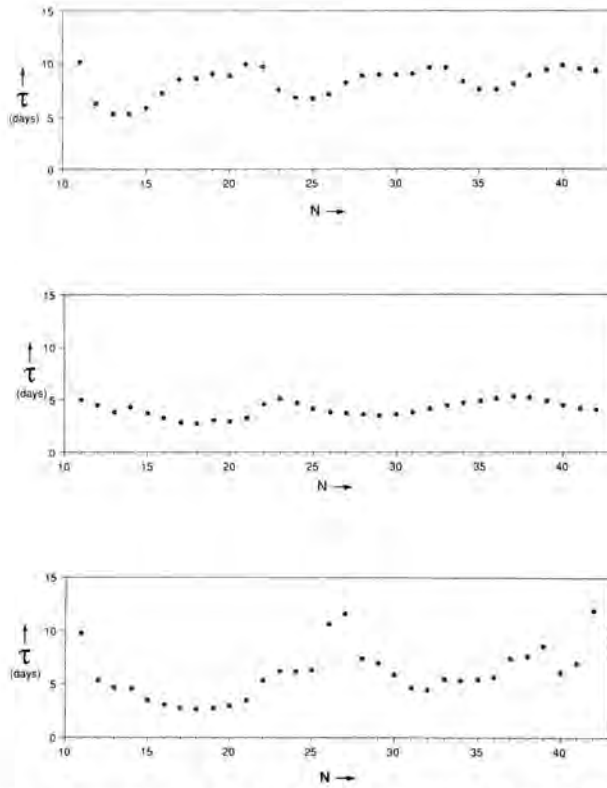


Fig. 2. The lifetime vs. truncation for (a) the Rossby wave (b) the wavelike modon (c) the localized modon.

After substitution of (11) and (12) in (13) we obtain

$$\mathcal{E}(t) = Ae^{2\nu_r t} (1 + \varepsilon \cos(2\nu_i t + \eta)) \quad (14)$$

with A , ε and η constants depending on the initial condition. The contribution to the time evolution of \mathcal{E} due to ε usually turns out to be small, and the global energy follows a nearly exponential curve. Then from an exponential fit over a long time series that includes several oscillations the real part of the eigenvalue ν_r and therefore the e-folding time τ can be obtained. The lifetime vs. truncation of the three basic states is shown in Fig. 2.

The imaginary part of the eigenvalue of the fastest growing mode ν_i is determined from the evolution of the perturbation relative vorticity at a particular point p on the sphere from (12)

$$\zeta'_p \equiv \zeta'(\lambda_p, \phi_p, t) = A_p e^{\nu_r t} \cos(\nu_i t + \eta_a(\lambda_p, \phi_p)) \quad (15)$$

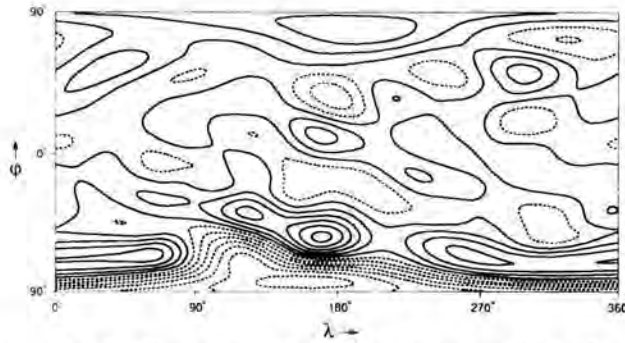


Fig. 3. For the Rossby wave the T38 perturbation stream function.

If the real part of the eigenvalue ν_r , obtained above is used, the exponential growth can be divided out from (15) and the result almost follows a sinusoidal curve. From a nonlinear fit over a long time series that includes several oscillations, the imaginary part of the eigenvalue ν_i and the oscillation time of the mode T can be obtained.

For the Rossby wave the T38 results are $\tau = 8.89$ days and $T = 36.8$ days, and the T85 results are $\tau = 8.62$ days and $T = 24.6$ days. For the wavelike modon the T30 results are $\tau = 3.59$ days and $T = 34.3$ days, and the T85 results are $\tau = 4.48$ days and $T = 37.3$ days. For the localized modon the T30 results are $\tau = 5.86$ days and $T = 2.12$ days, and the T85 results are $\tau = 4.01$ days and $T = 4.19$ days.

Normal mode fields

The normal mode fields $\xi_r(\lambda, \phi)$ and $\xi_i(\lambda, \phi)$ are obtained from the stream function fields at two different times t_1 and t_2 . For each point from the fields $\psi'_1 = \psi'(\lambda, \phi, t_1)$ and $\psi'_2 = \psi'(\lambda, \phi, t_2)$ the real part and the imaginary part can be obtained from (11)

$$\begin{aligned}\xi_r(\lambda, \phi) &= \frac{1}{\sin \nu_i(t_2 - t_1)} \cdot (e^{-\nu_r t_1} \sin \nu_i t_2 \cdot \psi'_1 - e^{-\nu_r t_2} \sin \nu_i t_1 \cdot \psi'_2) \\ \xi_i(\lambda, \phi) &= \frac{1}{\sin \nu_i(t_2 - t_1)} \cdot (e^{-\nu_r t_1} \cos \nu_i t_2 \cdot \psi'_1 - e^{-\nu_r t_2} \cos \nu_i t_1 \cdot \psi'_2)\end{aligned}\quad (16)$$

where the real part of the eigenvalue ν_r and the imaginary part of the eigenvalue ν_i are obtained as indicated above. This definition is not unique, since there is an arbitrary global phase factor related to the choice of origin of time. The stream function of the perturbation field at a particular instant in time for the Rossby wave is shown in Fig. 3.

A detail of the stream function for the fastest growing normal mode for the wavelike modon is given in Fig. 4, and for the localized modon in Fig. 5.

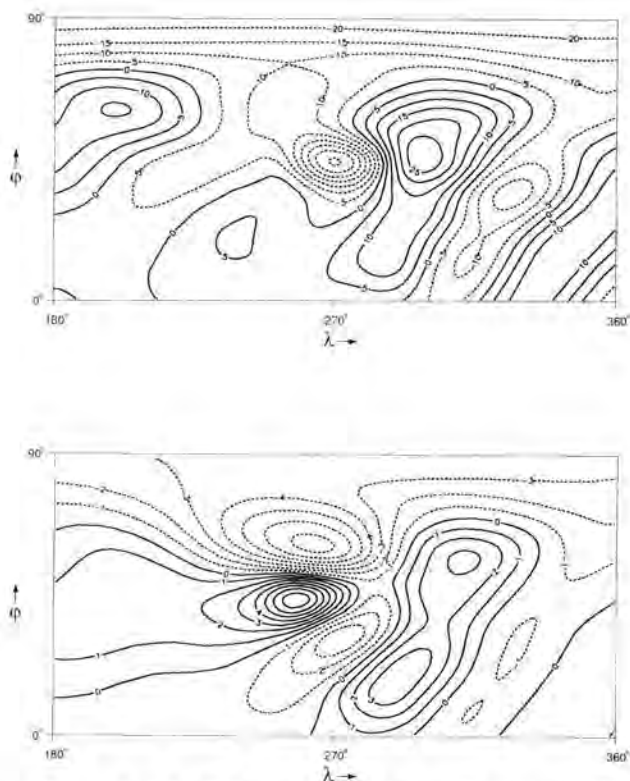


Fig. 4. For the wavelike modon the T30 perturbation stream function (a) the real part with contour interval 0.005 (b) the imaginary part with contour interval 0.01. The modulus of the perturbation relative vorticity field integrated over the sphere is normalized to unity.

The contour plots show that the fastest growing normal mode for the modons are localized in the inner region of the modon basic state, whereas for the Rossby wave the perturbation field is not localized in a particular region. These results agree with the comparison of modons with Rossby waves (Verkley, 1987). They also agree with barotropic instability being generated on gradients of potential vorticity. For a Rossby wave there is no concentrated potential vorticity in a particular region of the sphere, and normal modes in different regions of the sphere compete. A modon is characterized by concentrated potential vorticity in the inner region, so normal modes are likely to develop over the modon: a modon attracts a normal mode.

Since for a localized modon the total field is the sum of the dipole basic state field and the perturbation field, this suggests that in a nonlinear evolution the dipole shifts and tilts. This oscillation is observed if a normal mode field, with its energy normalized to a given fraction of the energy of the basic state field, is added to the basic state field. The behaviour of modons in an equivalent barotropic model on a beta plane can be modelled by a pair of point vortices

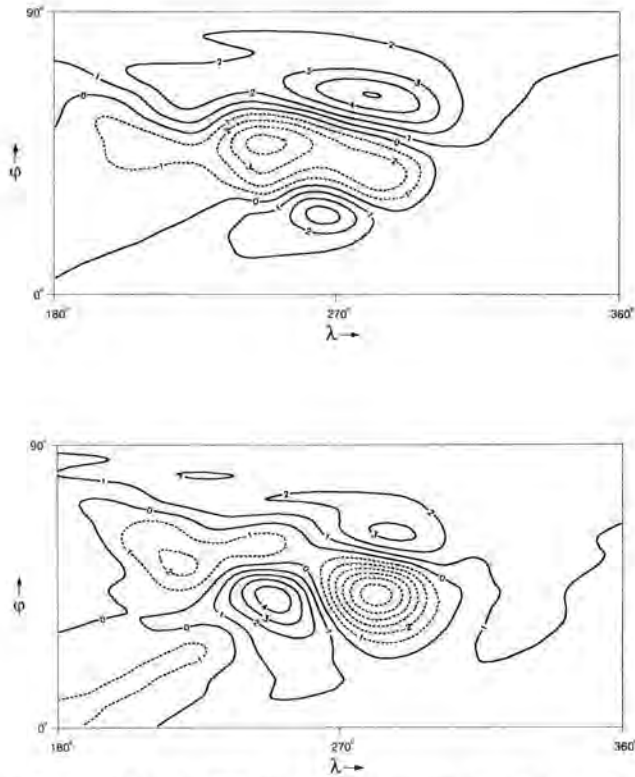


Fig. 5. For the localized modon the T38 perturbation stream function (a) the real part with contour interval 0.01 (b) the imaginary part with contour interval 0.01. The modulus of the perturbation relative vorticity field integrated over the sphere is normalized to unity.

(Aref, 1980; Hobson, 1991; Matsuoka and Nozaki, 1992). From a feedback argument the wobbling of a westward moving localized modon and the tumbling of the eastward wavelike modon in the absence of zonal flow was shown. We have shown that the localized modon is a much more rigid oscillator than the wavelike modon. During the lifetime of the localized modon the dipole wobbles, whereas the wavelike modon develops a tilt and disappears.

Conclusions

By performing numerical time integrations in a spectral model with high truncation, we have shown that both stationary wavelike and localized modon solutions of the barotropic vorticity equation on a sphere are linearly unstable.

References

- Aref, H., 1980 - Coherent features by the method of point vortices. *WHOI Tech. Rep.* **80-53**, 233-249.
- Hobson, D.D., 1991 - A point vortex dipole model of an isolated modon. *Phys. Fluids A* **3**, 3027-3033.
- Makino, M., T. Kaminura and T. Taniuti, 1981 - Dynamics of two-dimensional solitary vortices in as low- β plasma with convective motion. *J. Phys. Soc. Japan* **50**, 980-989.
- Matsuoka, C., and K. Nozaki, 1992 - Point vortex model of a modon solution. *Phys. Fluids B* **4**, 551-558.
- McWilliams, J.C., 1980 - An application of equivalent modons to atmospheric blocking. *Dyn. Atmos. Oceans*, **5**, 43-66.
- McWilliams, J.C., G.R. Flierl, V.D. Larichev and G.M. Reznik, 1981 - Numerical studies of barotropic modons. *Dyn. Atmos. Oceans* **5**, 219-238.
- Neven, E.C., 1992 - Quadrupole modons on a sphere. *Geophys. Astrophys. Fluid Dyn.* **65**, 105-126.
- Neven, E.C., 1993 - *Modons on a Sphere*. Ph.D. Thesis, Rijksuniversiteit Utrecht, Utrecht, 175 pp.
- Nycander, J., 1992 - Refutation of stability proofs for dipole vortices. *Phys. Fluids A* **4**, 467-476.
- Stern, M.E., 1975 - Minimal properties of planetary eddies. *J. Mar. Res.* **33**, 1-13.
- Tribbia, J.J., 1984 - Modons in spherical geometry. *Geophys. Astrophys. Fluid Dyn.* **30**, 131-168.
- Verkley, W.T.M., 1984 - The construction of barotropic modons on a sphere. *J. Atmos. Sci.* **41**, 2492-2504.
- Verkley, W.T.M., 1987 - Stationary barotropic modons in westerly background flows. *J. Atmos. Sci.* **44**, 2383-2398.
- Verkley, W.T.M., 1990 - Modons with uniform absolute vorticity. *J. Atmos. Sci.* **47**, 727-745.

Royal Netherlands Meteorological Institute (KNMI)
P.O. Box 201
3730 AE De Bilt
The Netherlands

A New Look at the Role of Eddies in the General Circulation

Abstract

It has been thought (at least since Holland, 1978) that the wind-driven circulation creates a reservoir of available potential energy (sloping thermocline) which, via baroclinic instabilities, generates eddies and that these, via a turbulent cascade, lead to mechanical dissipation. In other words, the eddy field is the unique link between the forced circulation and dissipation.

Although this paradigm has stimulated abundant numerical simulations and yielded countless publications, it nonetheless suffers from two important shortcomings. First, it provides no explanation whatsoever for the amounts and properties of the observed water masses (particularly the 18-degree Sargasso Sea water or its analogue in other ocean basins called the Subtropical Mode Water). Second, it leads to models in which the western boundary current (Gulf Stream) separates too far north. The obviously missing ingredient is the thermodynamics, alias the buoyancy effects. Indeed, with heat exchanges across the surface and within the water, water masses can change their characteristics, new kinds be formed, and amounts be adjusted. Further, as Huang (1987) and Chassignet (1991) showed, the amount of water in the upper thermocline establishes the latitude of separation of the western boundary current; less water brings this latitude southward.

As we all know (and engineers are most keenly aware of), heat fluxes anywhere are set by temperature differences; they are *in response to* a state of non-equilibrium. And so it is with the ocean. Therefore, theories in which heat fluxes are prescribed (Olson, 1985; Luyten & Stommel, 1986) are contrived and suspect. They, too, fail to explain the origins and amounts of water masses. As a remedy, the P.I. proposed a theory (Cushman-Roisin, 1987) in which the magnitude of the heat flux is not specified but instead controlled by the inhomogeneities produced by the circulation itself. (We shall call this type of flux a self-regulated heat flux.) And, the theory naturally leads to several important results. Without inclusion of any eddy dynamics, it allows for a purely inertial (i.e., non-dissipative) western boundary current, accounts for surface Ekman-pumping input by an equal rate of formation of deeper waters, explains the restoration of wind-modified potential vorticity, and provides a mechanism for a recirculation southeast of the western boundary current.

Obviously, eddies do play a role in circulation dynamics; they are observed,

they spontaneously emerge in numerical simulations, and they are ultimately necessary for mechanical dissipation. But, the above theory strongly suggests that eddying is not the exclusive mechanism that lies between the large-scale wind-driven currents and small-scale dissipation. Investigations that combine eddy dynamics and a self-regulated heat flux are clearly necessary.

Questions

The combination of eddy dynamics with heat exchanges immediately brings the following questions: What is the energy pathway? And, of what consists the recirculation? Indeed, being down the temperature gradient (or, equivalently, being of a relaxing type, Cushman-Roisin, 1987), the heat flux is dissipative in nature, affecting the amount of potential energy in the stratification; also, by its vertical mass flux, cooling generates motions at greater depths, thus affecting the distribution of kinetic energy in the vertical. Further, larger near-bottom velocities imply greater energy loss to bottom-drag dissipation and a correspondingly reduced need for lateral dissipation. Interestingly enough, Weatherly (1984) estimated from observations in the western North Atlantic that bottom friction can account for the entire dissipation of the wind-energy input and that this dissipation occurs in only about 20% of the areal extent of the subtropical gyre. It is therefore clear that, in the presence of heat fluxes, eddies have a much different job to accomplish than in purely wind-driven circulation models.

References

- Chassignet, E.P., 1991 - Influence of outcropping on mid-latitude jet separation. Part I: Wind-driven experiments. *Preprint*.
- Cushman-Roisin, B., 1987 - On the role of heat flux in the Gulf Stream - Sargasso Sea Subtropical Gyre system. *J. Phys. Oceanogr.* **17**, 2189-2202.
- Holland, W.R., 1978 - The role of mesoscale eddies in the general circulation of the ocean. Numerical experiments using a wind-driven quasigeostrophic model. *J. Phys. Oceanogr.* **8**, 363-392.
- Huang, R.X., 1987 - A three-layer model for wind-driven circulation in a subtropical-subpolar basin. Part II: The supercritical and hypercritical states. *J. Phys. Oceanogr.* **17**, 679-697.
- Luyten, J., and H. Stommel, 1986 - Gyres driven by combined wind and buoyancy flux. *J. Phys. Oceanogr.* **16**, 1551-1560.
- Olson, D.B., 1985 - Oceanic gyres forced by the wind and surface density fluxes. *J. Geophys. Res.* **90**, 3284-3292.
- Weatherly, G.L., 1984 - An estimate of bottom frictional dissipation by Gulf Stream fluctuations. *J. Mar. Res.* **42**, 289-301.

Thayer School of Engineering
Dartmouth College, Hanover, NH 03755, USA

The Influence of Environmental Parameters on Two-Dimensional Vortex Merger

Abstract

We numerically investigate the influence of several antagonistic effects on the merger of two identical piecewise-constant 2D vortices. First, on the f -plane, barotropic instability opposes vortex decay by breaking to their growth by merger. Secondly, on the β -plane, Rossby waves induce vortex dispersion and partial interactions. Finally, ageostrophic effects break the parity between cyclones and anticyclones.

Introduction

Vortices are central features of transient flows in the ocean where they play a key role in heat and momentum transfer, as well as in 2D free-decay turbulence for which they govern the dynamics of the flow (McWilliams, 1984). Merger of like-signed vortices can essentially account for their observed growth. It has been shown that a symmetric pair of Rankine vortices undergoes merger if the intercentroid distance d is initially less than 3.3 radii R (Melander *et al.*, 1988). The result is a vortex of size $\sqrt{2}R$ approximately (by conservation of vorticity and circulation), surrounded by orbiting filaments (by conservation of angular momentum). Vortex growth corresponds to the inverse energy cascade while the formation of filaments materializes the direct enstrophy cascade towards the small scales, where it is dissipated.

Some physical effects are known to influence two-dimensional vortex merger: it can be accelerated by diffusion, by the addition of random noise (Caperan and Verron, 1988) or by the presence of a free-surface in a rotating-tank experiment (Carnevale *et al.*, 1991). Asymmetry in the initial conditions results in a more complex phenomenology than pure merger or rotation (Melander *et al.*, 1987; Yasuda, 1991; Dritschel and Waugh, 1992).

In the framework of two-dimensional incompressible flows, we present the effects of barotropic instability (section 3), of Rossby wave dispersion (section 4) and of ageostrophy (section 5) on the merger of symmetric vortices with piecewise-constant potential vorticity. These cases are paradigms of ocean vortex dynamics.

Physical and numerical models

Incompressible two-dimensional flows obey the equation of vorticity conservation:

$$\frac{dq}{dt} = \partial_t q + J(\psi, q) = 0 \quad (1)$$

where q is the potential vorticity, ψ the stream function and J a Jacobian. For two-dimensional flows on the f -plane (section 3)

$$q = \nabla^2 \psi \quad \text{and} \quad \psi = p \quad (2)$$

where p is the pressure (in a first-order Rossby-number Ro truncation of the Navier-Stokes equations). On the β -plane (section 4), the vorticity also contains a contribution from the planetary vorticity gradient:

$$q = \nabla^2 \psi + \beta \psi \quad \text{and} \quad \psi = p \quad (3)$$

Finally, in section 5, we investigate flows with a larger Rossby number than 0.05 (as in quasi-geostrophy). The vorticity is then

$$\begin{aligned} q &= \nabla^2 \psi + Ro(\nabla^2 \psi)^2 - 4RoJ(\partial_x \psi, \partial_y \psi) \\ \psi &= p + \frac{Ro}{2}(u^2 + v^2) \end{aligned} \quad (4)$$

This system (1 & 4), which we call the generalized vorticity equation, is derived from the Navier-Stokes equation by a truncation at second order in Ro (Filatoff, 1993), and the stream function ψ is similar to a Bernoulli function. In all cases, the model conserves energy and potential enstrophy (the area integral of q^2).

Different numerical schemes are used here to solve these equations:

- for f -plane geostrophic flows, contour surgery is used, discretizing the vorticity contours into nodes which move with the Lagrangian velocity. The flow is inviscid and there is formally no dissipation operator; yet after topological modifications of the large-scale vortices, the surgery procedure discards small-scale debris.
- Secondly, for f - or β -plane geostrophic flows, a pseudo-spectral method discretizes vorticity (and stream function) on a square grid (of 128 or 256 side nodes) and advects it with the Eulerian velocity. A dissipation operator $D(\zeta) = \nu \nabla^4 \zeta$ then exists on the right-hand side of equation (1); as ν is small, this pseudo-viscosity dissipates enstrophy only weakly.
- Finally, the generalized vorticity equation on the f -plane (1 & 4) is discretized by finite differences and the nonlinear vorticity-stream function relation (4a) is solved by iteration. The resolution is 181*181 points. Enstrophy accumulation at small scales is also removed by biharmonic viscosity.

Initially the vorticity field is composed of two circular patches of piecewise constant q amplitude, at a distance d .

The merger of barotropically unstable vortices

Firstly, we investigate the effect of barotropic instability on two-dimensional vortex merger. The initial conditions are a pair of identical circular vortices with non-uniform radial profiles. For each vortex, the vorticity is unity from the center to radius a ($0 < a < 1$), and is equal to $-q$ ($q > 0$) from radius a to unity (the vortex shield). The total circulation is:

$$\Gamma = \pi(a^2 - q(1 - a^2)).$$

When $q = q_c(a) = a^2/(1 - a^2)$, the velocity is null out of the vortex and the vortex is dubbed "exactly shielded." Most vortices we consider here have a shield amplitude $q < q_c(a)$. As such vortices may be unstable, we determine the phase speed $Re(\sigma)$ and the growth rate $Im(\sigma)$ of a normal-mode perturbation with an azimuthal wavenumber m from the equation (Polvani, 1988):

$$\sigma^2 + \sigma(2m\Lambda + m - 1) + q(q - 1)a^{2m} - (q + 1 - m)(2m\Lambda + q) = 0 \quad (5)$$

where $\Lambda = \Gamma/2\pi$.

On Fig. 1, we plot the curve $\Gamma = 0$ and the boundaries of the unstable regimes for $m = 2$ and $m = 3$. Note that the unstable region lies inside the boundary for

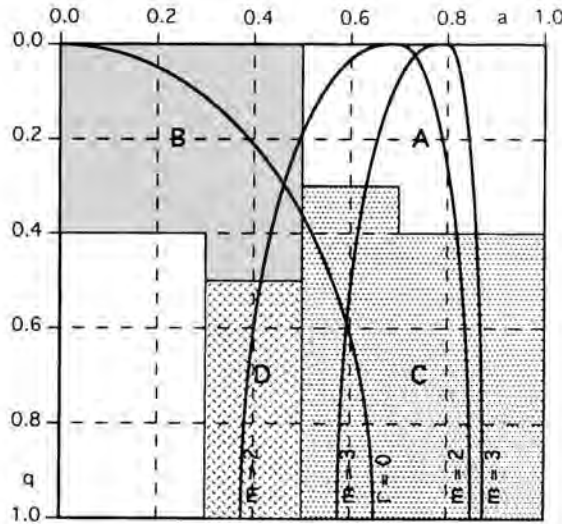


Fig. 1. Linear stability curves and nonlinear regime diagram for the merger of barotropically unstable vortices.

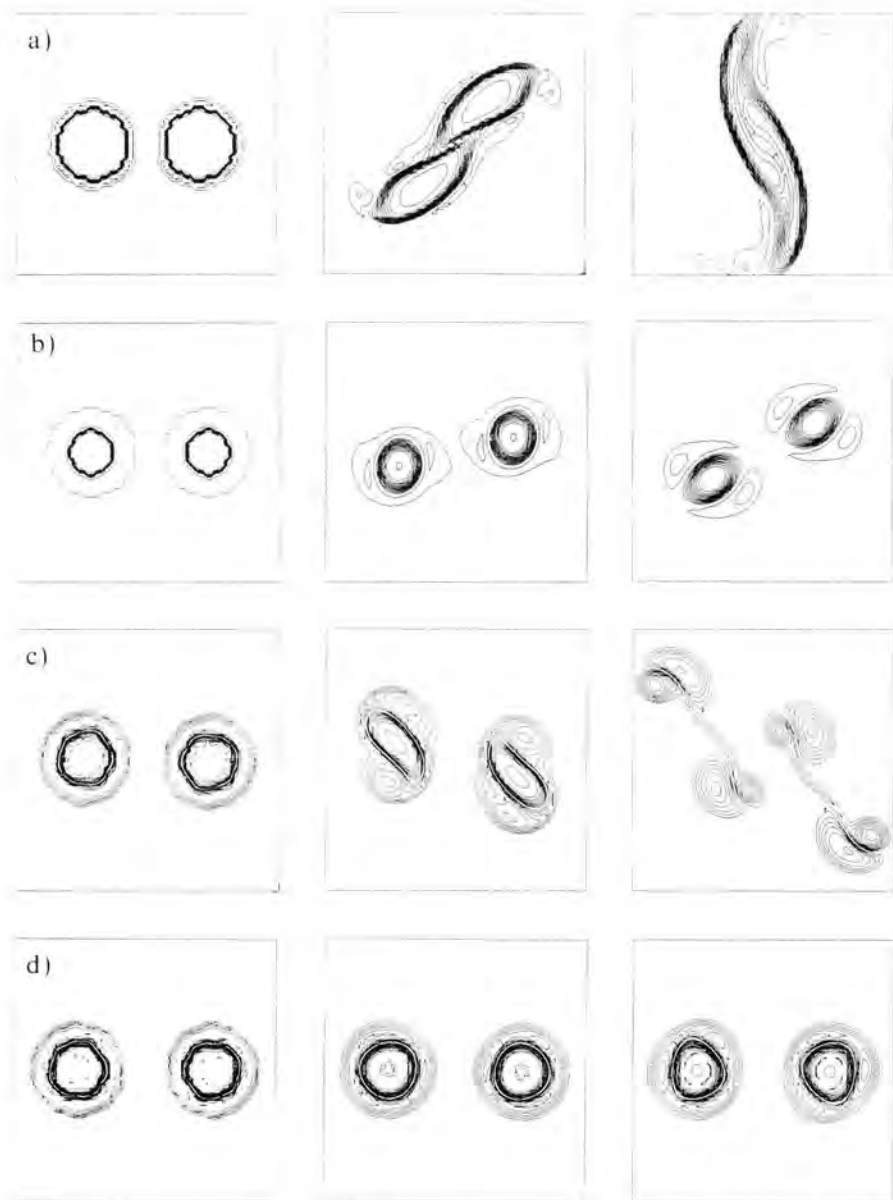


Fig. 2. Four typical regimes observed in shielded vortex merger: a) merger; b) tripole formation; c) dipolar breaking; d) transient quadrupoles.

each m . Higher modes are unstable for increasing values of a for a given q . We superimpose on this plot a nonlinear regime diagram obtained from a large number of numerical experiments (roughly 200) with the pseudo-spectral and contour surgery codes. In region A, the narrow and shallow shields only weakly influence the merger of shielded vortices. As for unshielded vortices there is a critical merger distance d_c which is observed to increase with a and $1 - q$. Vortices only marginally interact for $d > d_c$, while they merge for $d < d_c$. In region B, each vortex with a shallow and wide shield transforms into a tripole, under the influence of its companion at large distance, and rotates. For smaller initial separations, the two vortices assume the well-known figure-eight shape, characteristic of a rotating steady state. In region C, the narrow and deep shields render the vortices more sensitive to barotropic instability than in region A. Two vortices initially not in contact usually break into dipoles before they can merge, or sometimes form a pair of tripoles or quadrupoles. Close vortices merge and form a tripole with the coalesced cores and the orbiting remnants of the former shields. Finally, in region D (which has been less studied), each vortex shield is stronger than the core. An inverted merger process results where the peripheries merge and the cores are left to rotate around the final vortex.

On Fig. 2, we present a few evolutions of vorticity with time. Fig. 2a corresponds to region A with $a = 0.8$, $q = 0.2$, $d = 2.4$. A rapid merger ensues from the initial proximity of the two vortices. In region A, merger is well correlated with the non-existence of corotating steady-states (Carton, 1992). Also, the critical merger distance d_c is modified by the presence of the shield (we recall that $d_c = 3.3R$ for $q = 0$ and $a = 1.0$, with here $R = 1$). This new distance d_c can here be assessed as follows: if merger is determined initially only by the long-range influence of the companion vortex, it thus depends on F . A vortex with a narrow and shallow shield can be "seen" at some distance as an unshielded core with unit vorticity, but with a smaller equivalent radius given by $F = \pi R_{eq}^2$. It can be shown that the estimate $d_c = 3.3R_{eq}$ is in good agreement with the merger distance found experimentally (the difference varies between 2 and 5, see Carton 1992). Fig. 2b shows the formation of corotating tripoles for $a = 0.5$, $q = 0.15$, $d = 2.6$, as stated for region B. Fig. 2c presents a typical dipolar breaking event in region C ($a = 0.6$, $q = 0.8$, $d = 2.8$) under the influence of barotropic instability, while on Fig. 2d quadrupoles originate in the mode-3 component of the weak shear exerted by the other vortex ($a = 0.6$, $q = 0.6$, $d = 3.0$); here the final state is a pair of dipoles. In fact, stationary quadrupoles can form from unstable circular vortices; they possess a nonlinear (q, ψ) relation and are long-lasting multipolar vortices (Carton, 1992; Carnevale and Kloosterziel, 1994; Morel and Carton, 1994).

Vortex merger on the β -plane

In this second part, we investigate the conflict between energy concentration by geostrophic vortex merger and its dispersion into Rossby waves under the β -effect.

On the β -plane, an isolated cyclone (anticyclone) drifts to the north-west (south-west) and transfers its energy into a Rossby wave field. In the ocean as in numerical experiments, this is a slow process as vortex radii are usually much smaller than the Rhines scale $L_\beta = \sqrt{0.5U/\beta}$. For two equal cyclones, we can anticipate the effect of β : the westernmost vortex should drift to the NW but it is countered by the velocity induced by its companion; as a result, only the easternmost vortex for which the two effects cooperate should be rapidly displaced and elongated (Bertrand and Carton, 1993). Two anticyclones would evolve similarly.

Here we numerically study the merger of two cyclones initially at a distance d along the x -axis; each one has unit potential vorticity on a disk of radius unity. On Fig. 3 we sketch the various nonlinear regimes observed when varying d/R ($R=1$) and a scaled β ($=\beta*L^2/U=0.05$ to 0.1 for usual oceanic values). For low β (<0.05), corotation and then merger are observed when increasing d/R . For larger β , more complex interactions occur:

- partial merger, where the westernmost vortex tears out and absorbs part of its companion, is observed for initially close vortices $d/R < 3.6$ and intense β -effect ($\beta \geq 0.05$).
- Partial straining-out corresponds to a partial merger without vorticity absorption; it occurs for more distant vortices ($d/R \geq 3.6$) and a rather strong β -effect ($\beta \geq 0.1$) keeping the vorticity patches distant.
- An intermediate regime, dubbed differential drift, is located between corotation and partial straining-out ($d/R < 3.6$ and $0.05 \leq \beta \leq 0.1$). There, the intensity of β is sufficient to prevent merger, but its effect and the shear induced by the vortex partner are too weak to create straining-out, and the vortices drift away.

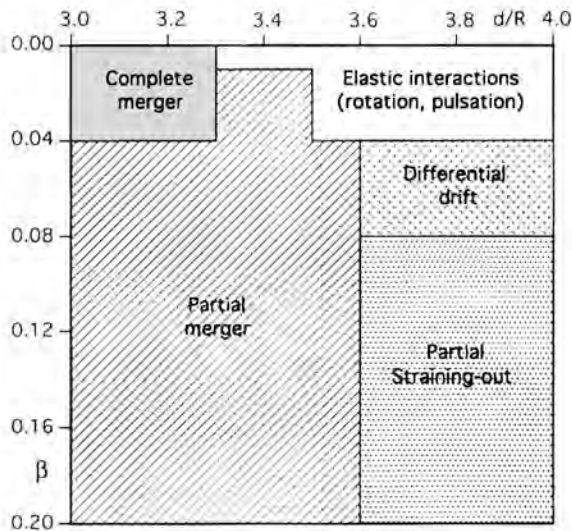


Fig. 3. Nonlinear regime diagram for two-dimensional vortex merger on the β -plane.

Note that the first two behaviors are similar to those encountered in the merger of asymmetric vortices on the f -plane (Dritschel and Waugh, 1992).

These regimes are quantified by the time evolution of the area integral of potential vorticity for each structure. In the absence of nonlinear interaction, this integral is conserved. For complete merger, the integral will double for one vortex and vanish for the other. For complete (or partial) straining-out, one integral will vanish (or decrease) while the other will not vary. Charts of vorticity are presented on Fig. 4: partial straining-out is observed for $\beta = 0.14$ and $d/R = 3.7$ on Fig. 4a, while partial merger occurs for $\beta = 0.06$ and $d/R = 3.3$ on Fig. 4b. On Fig. 4c, two vortices undergo differential drift for $\beta = 0.08$ and $d/R = 3.6$ (though the domain periodicity gives a biased representation of the phenomenon).

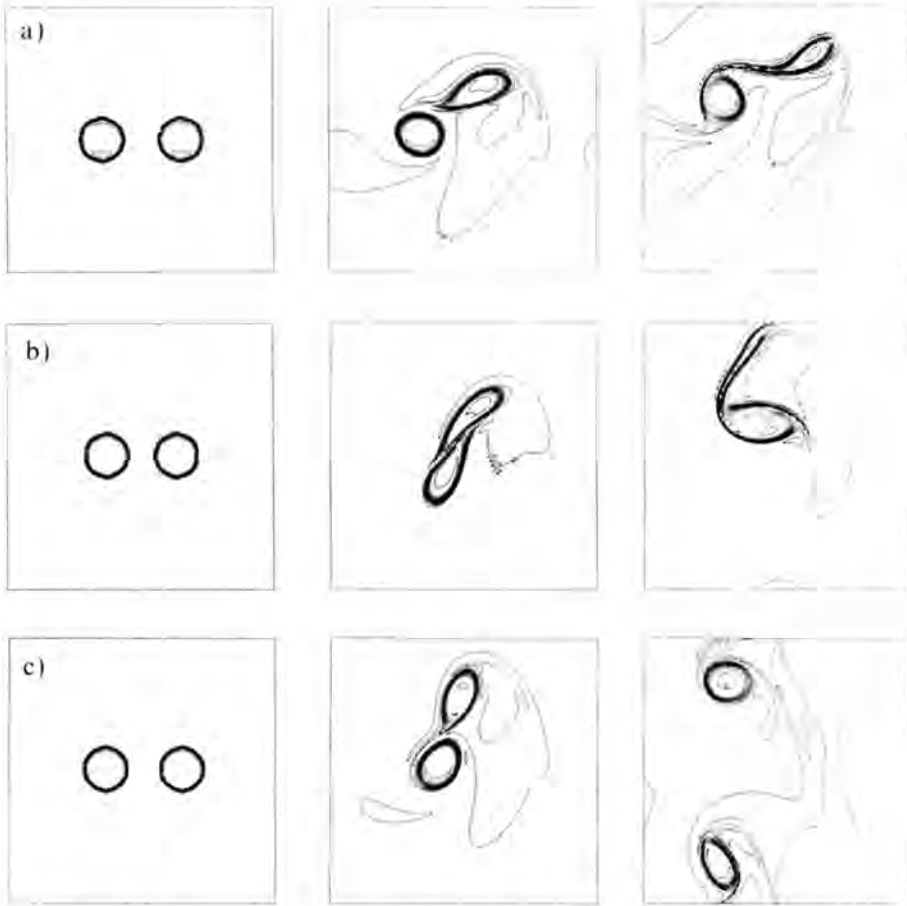


Fig. 4. Three typical regimes of β -merger; a) partial straining-out; b) partial merger; c) differential drift.

Finally, the regime boundaries are little modified when the two vortices are initially located along the y -axis if they have constant relative vorticity (RVI case), while they change noticeably for constant potential vorticity initialization (PVI case). The two vortices aligned along the x -axis correspond to a nearly mixed PVI-RVI case (as the planetary vorticity gradient across each vortex is weak). As the velocity created by one vortex on the other is proportional to its circulation, the initial motion is identical in the RVI and in the mixed RVI-PVI cases. In the PVI case, the difference in circulation between the two vortices is proportional to βd .

Ageostrophic vortex merger

In this last part, we consider vortex merger when the non-geostrophic terms become of finite-amplitude (i.e. for a gradient-wind balance rather than a geostrophic balance). The flow is then governed by equations (1 & 4) and the ageostrophic components create a difference between cyclones and anticyclones. For a given vorticity q , anticyclones cannot be found beyond a critical value of Ro (here $Ro = 0.25$ for $q = 1$), as the numerical inversion of (4a) fails.

The two vortices initially have unit radius and potential vorticity. No new finite-amplitude regime is observed when increasing Ro from zero: merger occurs

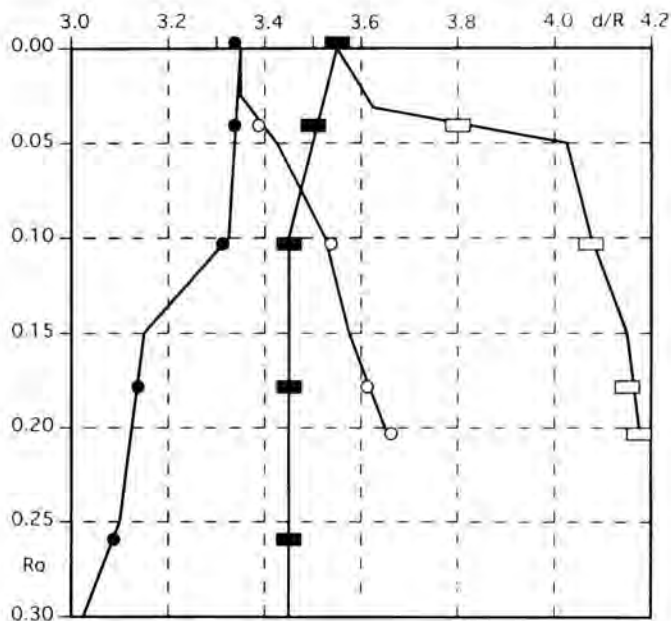


Fig. 5. Regime diagram in the $(Ro, d/R)$ plane; the black dots (rectangles) delimit cyclone merger from pulsation (pulsation from rotation); the open marks correspond to anticyclones.

for close enough vortices and increasing the initial distance results in elastic interactions. We thus do not present vorticity charts, but a regime diagram in the $Ro, d/R$ space (Fig. 5). It shows the boundaries of the merger, pulsation and rotation regimes for cyclones and anticyclones. This map is derived from more than 100 numerical experiments. The frontier between corotation and pulsation is not easy to determine by sheer visual inspection. In a flow with finite Ro , anticyclones merge more easily than cyclones and thus grow more rapidly. This result, contrary to the usual expectation that cyclones get stronger at larger Ro , is also observed in numerical simulations of two-dimensional turbulence in generalized geostrophy (Cushman-Roisin and Tang, 1990).

Conclusions

We have investigated here the influence of three antagonistic effects on two-dimensional vortex merger: barotropic instability, Rossby wave dispersion and ageostrophic effects. The novelty of this study is the richness of the interactions and end-products compared to geostrophic vortex merger on the f -plane. Here vortex sizes can decrease by dipolar breaking or wave dispersion, many fragments or complex vortex aggregates can be formed (such as tripoles or quadrupoles); partial interactions stem from conflicting influences; vortices possess intricate trajectories or finally cyclones behave differently from anticyclones. The efficiency of merger for vortex growth is degraded and a balance between vortex coalescence and decay appears which seems closer to geophysical reality. To attain complete realism, all these effects, as well as baroclinicity (Griffiths and Hopfinger, 1987; Verron and Valcke, 1994) and forcing, should be evaluated concurrently.

Acknowledgements

We gratefully acknowledge contributions by Drs L.M. Polvani and N. Filatoff and thank Dr R. Baraille for his numerical assistance. Discussions with Drs B. Legras and J.C. McWilliams proved timely and valuable. Funding and support for this project have been provided by SHOM/CMO.

References

- Bertrand, C. and X.J. Carton, 1993 - Vortex merger on the β -plane. *C. R. Acad. Sci. Paris* **t.316, Série II**, 1201–1206.
- Capéran, P. and J. Verron, 1988 - Numerical simulation of a physical experiment on two-dimensional vortex merging. *Fluid Dyn. Res.* **3**, 87–92.

- Carnevale, G.F., P. Cavazza, P. Orlandi, and R. Purini, 1991 - An explanation for anomalous vortex merger in rotating-tank experiments. *Phys. Fluids* **A3** (5), 1411-1415.
- Carnevale, G.F. and R.C. Kloosterziel, 1994 - Emergence and evolution of triangular vortices. *J. Fluid Mech.* **259**, 305-331.
- Carton, X.J., 1992 - On the merger of shielded vortices. *Europhys. Lett.* **18** (8), 697-703.
- Cushman-Roisin, B. and B. Tang, 1990 - Geostrophic turbulence and the emergence of eddies beyond the radius of deformation. *J. Phys. Oceanogr.* **20**, 97-113.
- Dritschel, D.G. and D. Waugh, 1992 - Quantification of the inelastic interaction of unequal vortices in two-dimensional vortex dynamics. *Phys. Fluids* **A4**, 1737-1744.
- Filatoff, N.G., 1993 - Le modèle intermédiaire de vorticit  g n ralis e. Internal report SHOM/CMO 92ET13.
- Griffiths, R.W. and E.J. Hopfinger, 1987 - Coalescing of geostrophic vortices. *J. Fluid Mech.* **146**, 21-43.
- Melander, M.V., N.J. Zabusky, and J.C. McWilliams, 1987 - Asymmetric vortex merger in two dimensions: which vortex is "victorious?" *Phys. Fluids* **30** (9), 2604-2610.
- Melander, M.V., N.J. Zabusky, and J.C. McWilliams, 1988 - Symmetric vortex merger in two dimensions. *J. Fluid Mech.* **195**, 303-340.
- Morel, Y.G. and X.J. Carton, 1994 - Multipolar vortices in two-dimensional incompressible flows. *J. Fluid Mech.* **267**, 23-51.
- Polvani, L.M., 1988 - Geostrophic vortex dynamics. Ph.D. thesis, MIT/WHOI, **WHOI-88-48**, 221 p.
- Verron, J. and S. Valcke, 1994 - Scale-dependent merging of baroclinic vortices. *J. Fluid Mech.* **264**, 81-106.
- Yasuda, I., 1991 - *The Evolution of a Kuroshio Warm-core Ring*, Ph.D. thesis, University of Tokyo, 219 p.

SHOM/GRGS

Centre National des  tudes Spatiales
18 Av. Edouard Belin
31055 Toulouse, France

Scale-Dependent Merging of Baroclinic Vortices

Abstract

The influence of stratification on the merging of geostrophic vortices in a two-layer stratified flow is investigated by numerical simulations. The vortices are initialized in relative vorticity (RVI) or potential vorticity (PVI) in the upper layer. The strong influence of the stratification observed in the RVI case is interpreted in terms of competitive effects between repulsing hetonic interaction and attracting barotropic vortex shape influence.

Introduction

Vortex merger is seen as a prototype mechanism for the evolution of two-dimensional turbulence which gives rise to long-lived, intense coherent vortices (Basdevant *et al.*, 1981; McWilliams, 1984). The barotropic merging process has received considerable attention through experimental, theoretical and numerical investigations (Brown and Roshko, 1974; Overman and Zabusky, 1982; Melander *et al.*, 1988).

The case of rotating stratified fluid is even more complicated and, as yet, little is known and a fortiori understood. For the two-layer case, Griffiths and Hopfinger (1987) (hereafter GH) observed, in laboratory experiments, that the merging conditions were strongly dependent on the stratification. For the same configuration, however, Polvani, Zabusky and Flierl (1989) (hereafter PZF), using contour dynamics numerical simulations, found no dependency of the merging on the stratification. Verron *et al.* (1990) showed the importance of initial conditions in the merging process and introduced the concepts of "Relative Vorticity Initialization" (RVI) and "Potential Vorticity Initialization" (PVI) (see also Verron and Valcke, 1994).

In this paper, after an introduction to the quasigeostrophic model to be used, we present our results in the PVI case and in the RVI case. Then we show how the enhanced merging tendency for a selective range of vortex scales can be interpreted as a competition between an attracting barotropic shape effect and a repulsing "hetonic" interaction. Finally, on the base of observations of real eddies, we speculate on the applicability of each initialization scheme.

Quasigeostrophic model

A standard model for the two-layer vortex dynamics is provided by the following quasi-geostrophic set of equations for the potential vorticity Q_i (Pedlosky, 1979):

$$\frac{DQ_1}{Dt} = \frac{D}{Dt} \left[\omega_1 + \frac{1}{2} \lambda^{-2} (\psi_2 - \psi_1) \right] = V_1 \quad (1a)$$

$$\frac{DQ_2}{Dt} = \frac{D}{Dt} \left[\omega_2 - \frac{1}{2} \lambda^{-2} (\psi_2 - \psi_1) \right] = V_2 \quad (1b)$$

The subscript 1 indicates the upper layer, 2 the bottom layer. ω_i is the relative vorticity and ψ_i the stream function. The internal Rossby radius λ represents the stratification and writes $\lambda = \sqrt{g'H/(\sqrt{2}f_0)}$ when the two layers are of equal depth H . The Coriolis parameter is supposed to be a constant f_0 . g' measures the density jump, $\Delta\rho$, between the two layers such that $g' = g\Delta\rho/\rho$ where ρ is the reference mean density. The dissipative terms V_i are needed, in our finite-difference numerical code, to dissipate the enstrophy which tends to accumulate at the small scales not resolved by the model. They take the form of a high-order viscosity term $V_i = -A_4 \nabla^4 \omega_i$.

Potential Vorticity Initialization

If one considers the upper vortices as equal circular patches of uniform potential vorticity Ω , i.e. having a profile of the Rankine type (designated R_a), the initial conditions for the set of equations (1) may be written as follows:

$$Q_{10} = \sum_{k=1,2} R_a^k \quad (2a)$$

$$Q_{20} = 0 \quad (2b)$$

The summation $k=1, 2$ on R_a^k indicates a pair of Rankine vortices. Their radius is denoted R and their initial distance centre to centre is d . This provides us with the so-called Potential Vorticity Initialization (PVI).

In this case, PZF found that the critical merging distance, d_c , which is the greater distance between the vortex centres below which the vortices merge, was insensitive to stratification. In our study, however, further consideration of viscous effects led us to conclude that the concept of the critical merging distance is sometimes misleading and/or inapplicable. Because of the small numerical viscosity A_4 introduced in the model, it was observed that vortices eventually merge for all initial separations d .

Additional simulations with different values of A_4 showed that for $d/R \leq 3.3$ the value of A_4 has little influence on t_c/T , the time of merging non-dimen-

sionalized by the vortex turnover period, $T = 2\pi/\Omega$, which is always less than 5. These mergings are real “convective” mergings. For $d/R \geq 3.6$, t_c/T increases drastically and is strongly dependent on the value of A_4 . On a convective timescale, the vortices are stable and the merging is induced by the viscosity on a longer viscous timescale. In these cases, we classified the interaction as non-merging from an inviscid point of view.

Taking into account the temporal dimension of merging evolution, the critical distance of merging can therefore be understood as the boundary between merging and no merging on a convective timescale. However, we have found that in practice this distinction is difficult to make. For this reason, we have decided to consider the time required for merging, t_c/T , as the relevant vortex interaction factor.

Concerning the influence of the stratification, our simulations showed that, in the PVI case, t_c/T is independent of the stratification. This result is analogous to PZF’s conclusion about an independent critical distance of merging.

Relative Vorticity Initialization

If we now assume that the bottom layer is at rest and that the initial vortices are defined in relative vorticity as two Rankine profiles of radius R in the upper layer, the initial flow fields will be $\psi_{20} = 0$ and ψ_{10} given by

$$\nabla^2 \psi_{10} = \sum_{k=1,2} R_a^k$$

Consequently, the initial potential vorticity in the two layers is

$$Q_{10} = \sum_{k=1,2} R_a^k - \frac{1}{2} \lambda^{-2} \psi_{10} \quad (3a)$$

$$Q_{20} = +\frac{1}{2} \lambda^{-2} \psi_{10} \quad (3b)$$

This is the Relative Vorticity Initialization (RVI) as introduced by Verron *et al.* (1990).

Figure 1 shows the Q_{10} profiles. These profiles are dependent on the background stratification expressed by λ/R . In particular, we see that as λ/R diminishes, the vortex acquires an increasingly pronounced “skirt” shape because of the vorticity stretching term, $1/2 \cdot \lambda^{-2} \psi_{10}$, coupling the two layers.

In the RVI case, merging was found to be strongly dependent on background stratification, as can be seen in Figure 2. It shows the isocurves for the time of merging $t_c/T = 5, 15, 30, 45$ and ∞ as a function of the initial distance d/R and of the stratification parameter λ/R .

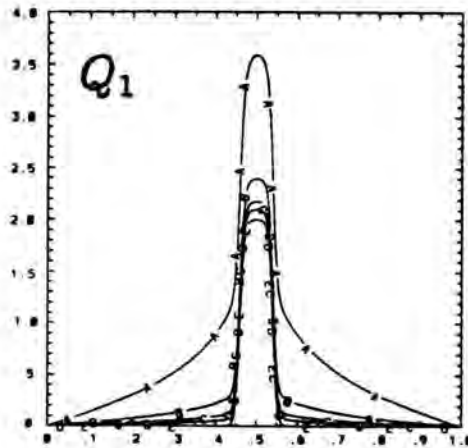


Fig. 1. Initial upper-layer potential vorticity (s^{-1}) in the RVT case for $\lambda/R=1$ (A), 2 (B), 3 (C), 4 (D), ∞ (E).

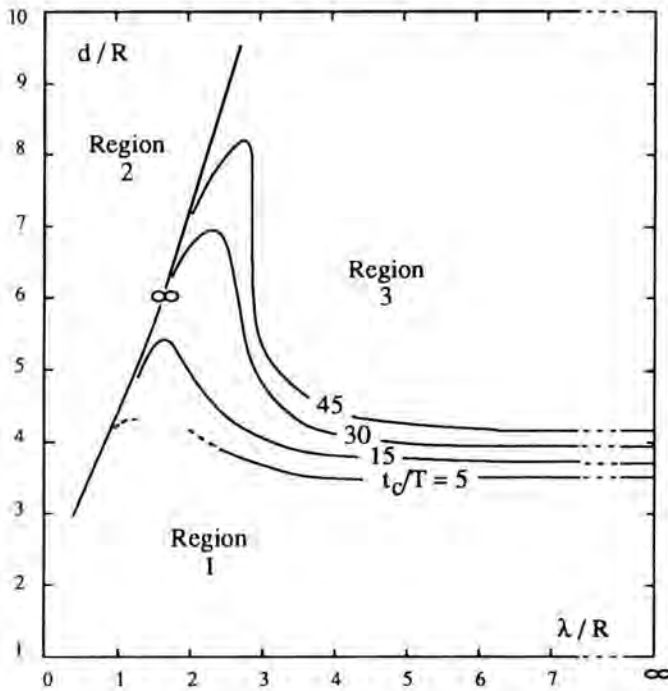


Fig. 2. Isocurves of t_c/T for the RVT simulations with $A_4/\Omega R^4 = 10^{-4}$.

Three regimes of vortex interaction may be roughly identified. Region 1 corresponds to where merging occurs on a convective timescale. The interesting point is that a marked peak subregion can be identified where merging occurs in a much shorter time than is the case for other values of λ/R . For example, for an initial distance d/R as large as 5.5, and when $\lambda/R \simeq 1.7$, merging can be obtained after a time t_c/T of around only 15, while it is 3 times longer when stratification parameter is $\lambda/R = 3.2$. Merging is therefore very much favoured for a restricted range of λ/R , between around 1.5 and 3. In Region 2, on the other hand, the vortices do not merge and the distance separating them increases with time. The merging time, t_c/T , was therefore set at ∞ . In Region 3, the vortices are stable on a convective timescale.

The appearance of a peak in Region 1 and of inhibited merging in Region 2 is an important feature of vortex interaction in the RVI case. Unlike the PVI situation, stratification appears to have a marked influence on merging here. In the next sections, we propose an explanation to this phenomenon as a competitive process between attracting barotropic shape effect and repulsing hetonic effect.

Barotropic shape effect

Let us first assume, in the case of strong stratification, that the dynamical effect of the stretching term is negligible,

$$\frac{D}{Dt} \left[\frac{1}{2} \lambda^{-2} (\psi_2 - \psi_1) \right] \ll \frac{D\omega_1}{Dt}$$

Equations (1) will reduce to

$$\frac{DQ_i}{Dt} = \frac{D\omega_i}{Dt} = 0$$

still assuming the same initial conditions (3).

Note that the term $1/2 \cdot \lambda^{-2} \psi_{10}$, corresponding to the initial interface deformation, is kept in the initial definition of the potential vorticity profile in the two layers, but it is assumed to play no further role on the dynamics. The merging problem for the upper layer reduces to a purely barotropic problem in which the initial profile of vorticity is subject to the above initial conditions (3a). The distinction between relative and potential vorticity has no further significance. Since stratification is no longer dynamically present, λ/R is no longer a measure of the Rossby radius but it becomes simply an initial vortex shape factor.

We studied the barotropic merging problem for the upper layer as the initial vortex shape varies as in (3a). The results are presented in Figure 3. In Region 1, the vortices merge rapidly on a convective timescale and in Region 3, they do not, as before. For each particular value of d/R , t_c/T decreases as λ/R decreases.

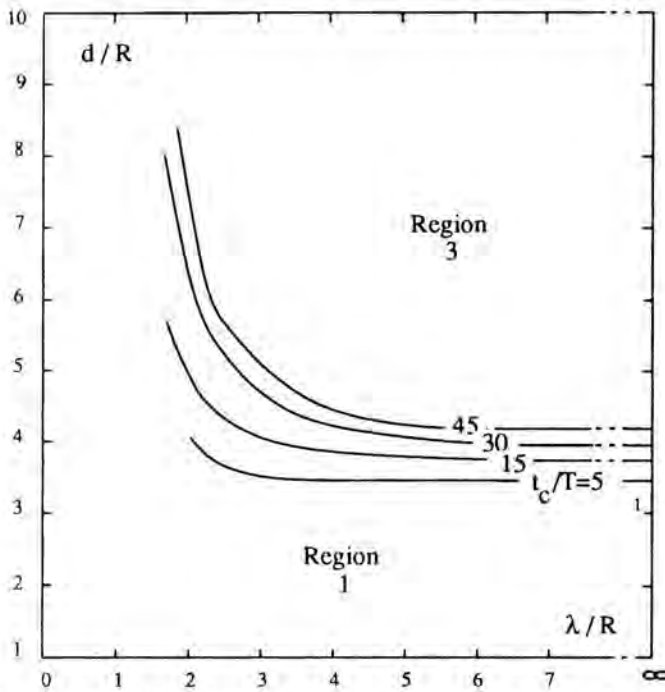


Fig. 3. Isocurves for $t_c/T = 5, 15, 30, 45$ as a function of d/R and of the shape factor λ/R for barotropic simulations with $A_4/\Omega R^4 = 10^{-4}$.

We may therefore conclude that the more pronounced the “skirt” shape is, the greater is the tendency for vortices to merge. This is not really surprising if one considers that the influence of the vortices on each other increases as the vorticity profile extends from their core.

The interesting point is that the isocurves for $t_c/R = 5, 15, 30, 45$ in Figures 2 and 3 coincide with one another almost perfectly for $3.2 < \lambda/R < \infty$ and, in both cases, the tendency to merge continues to increase strongly. This means that, in the RVI case, the pure effect of the shape of the upper-layer vortices is likely to be the principal reason for the increased tendency to merge when λ/R decreases from ∞ to about 3, but no significant baroclinic dynamics is subsequently required.

Heton interaction

Let us now consider the two-layer system in the RVI case for small values of λ/R . In the expression of the RVI initial potential vorticity (3), the stretching term $\lambda^{-2}\psi_{10}$ is now relatively large. For each vortex initialized in the upper layer, there is a corresponding one of opposite sign in the lower layer associated with this stretching term. The dynamical effect of these lower-layer vortices can no

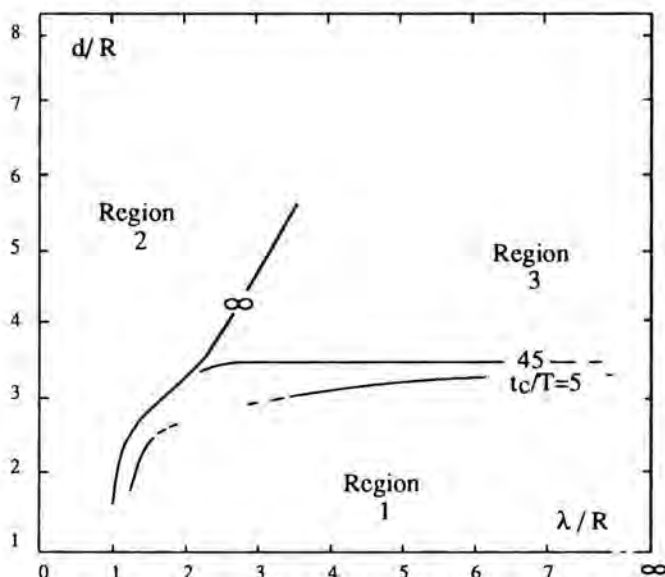


Fig. 4. Isocurves for $t_c/T = 5, 45$ and ∞ as a function of d/R and λ/R for finite-core hetons with $A_4/\Omega R^4 = 2 \cdot 10^{-5}$.

longer be neglected. The RVI situation becomes equivalent to the initialization of two vortices in the upper layer and two vortices of opposite sign in the lower layer.

This is analogous to an initial configuration of two hetons as described by Hogg and Stommel (1985) (hereafter HS). HS originally defined a heton as a pair of opposite-sign point vortices in opposite layers. In the present case, the major difference is that the vortices have a finite core with specific shape defined by equations (3) instead of being point vortices.

To understand better the concept of hetons, we investigated the interactions between two equal finite-core hetons in which all vortices (positive or negative) are of the Rankine type and have same intensity. The results of this particular study, shown on Figure 4, are presented with more details in Valcke and Verron (1993).

In Region 1, the vortices merge on a convective timescale, while in Region 3 they do not. In Region 2, the behaviour of the vortices is typical of a hetonic configuration. Initially, each heton is split by the other, but, once the two vortices of each heton are horizontally separated, the main coupling occurs across the interface between these two vortices of opposite-sign. The hetons begin to self-propel in opposite directions.

The most interesting conclusion concerns this Region 2: for $\lambda/R < 2$ approximately, the divergence motion of the hetons is strong enough to increase the distance between the same-layer vortices even when d/R is such that they would normally undergo convective merging. Their tendency to merge is therefore very much countered.

These results lead us to conclude that the divergence behaviour typical of Region 2 in the RVI case can be explained by the heton effect. For a weak stratification, the dynamical effect of the lower-layer vortices inhibits merging of the upper-layer vortices.

These considerations lead to the general conclusion that, as far as merging is concerned, the RVI behaviour, and in particular the increased tendency to merge for $1.5 < \lambda/R < 3$, is the result of two competing effects, one of *attraction* and one of *repulsion*. The attracting effect results from a pure barotropic shape influence and tends to promote merging as λ/R decreases because of the growth of the vorticity "skirt". The repulsing effect is caused by a heton-specific type of baroclinic interaction which, in a weakly stratified regime, tends to make the same-layer vortices diverge from each other. The peak area in the curves is the result of these competing effects.

Real vortices

Relatively little is known about the detailed structure of eddies in the ocean which, undoubtedly, have horizontal and vertical structures much more complicated than the simple representations discussed above.

A relevant question is now whether the "real" eddies have a signature in potential vorticity all along the vertical, as in the RVI case, or only at the surface (for example only above the thermocline), as in the PVI case.

It is first almost certain that the laboratory eddies created by GH are not totally PVI. In fact, their merging showed a strong dependency on the stratification which contradicts PVI results. However, it is not possible to assert that they are totally RVI even if their merging behaviour is qualitatively similar to our RVI results.

Observations by Olsen (1980) of Gulf Stream rings show that the ring can be clearly identified by an anomaly in potential density and potential vorticity in the area between the surface and about 1500 m. The interesting point here is that the velocity field, also clearly stronger above 1500 m, shows a reversal in sign below 1000 db. The author suggests that this feature, reminding one of the hetonic configuration associated with the RVI, could be common in the Gulf Stream cyclonic rings.

Arhan and Colin de Verdière (1985) presented a detailed analysis of field measurements taken during the Tourbillon Experiment in a region of the North East Atlantic. The relative vorticity of the eddy observed was of the same sign throughout the whole water column but was clearly intensified above the main pycnocline (850 m). The eddy potential vorticity seemed to be confined to the upper 1000 meters. Based on their findings, one is tempted to suggest that the eddy observed corresponds more to a PVI situation.

It is difficult, from the above examples, to reach a conclusion on the relevant "initialization" for real eddies, especially on their deep structure because of the

lack of observations. However, it is likely that the physical mechanisms of eddy generation act, not only to induce potential vorticity anomalies above the thermocline, but also to alter the deep potential vorticity. Complex interactions may therefore result, from which pvi behaviour with regard to merging might be an illustrating prototype.

Acknowledgements

Calculations were made using the numerical facilities of the Centre de Calcul Vectoriel pour la Recherche in Palaiseau.

References

- Arhan, M. and A. Colin de Verdière, 1985 - Dynamics of eddy motions in the eastern North Atlantic. *J. Phys. Oceanogr.* **15**, 153–170.
- Basdevant, C., B. Legras, R. Sadourny and M. Beland, 1981 - A study of barotropic model flows: intermittency, waves and predictability. *J. Atmos. Sci.* **38**, 2305–2326.
- Brown, G.L. and A. Roshko, 1974 - On density effects and large structures in turbulent mixing layers. *J. Fluid Mech.* **64**, 775–816.
- Griffiths, R.W. and E.J. Hopfinger, 1987 - Coalescing of geostrophic vortices. *J. Fluid Mech.* **178**, 73–97.
- Hogg, N. and H. Stommel, 1985 - The heton, an elementary interaction between discrete baroclinic geostrophic vortices and its implications concerning eddy heat-flow. *Proc. R. Soc. Lond. A* **397**, 1–20.
- Melander, M.V., N.J. Zabusky and J.C. McWilliams, 1988 - Symmetric vortex merger in two dimensions: causes and conditions. *J. Fluid Mech.* **195**, 303–340.
- McWilliams, J.C., 1984 - The emergence of isolated coherent vortices in turbulent flow. *J. Fluid Mech.* **146**, 21–43.
- Olson, D.B., 1980 - The physical oceanography of two rings observed by the cyclonic ring experiment. Part II: Dynamics. *J. Phys. Oceanogr.* **10**, 514–528.
- Overman, E.A. and N.J. Zabusky, 1982 - Evolution and merger of isolated vortex structures. *Phys. Fluids* **25**, 1297–1305.
- Pedlosky, J., 1979 - *Geophysical Fluid Dynamics*, Springer-Verlag, Berlin.
- Polvani, L.M., N.J. Zabusky and G.R. Flierl, 1989 - Two-layer geostrophic vortex dynamics. Part 1. Upper layer V-states and merger. *J. Fluid Mech.* **205**, 215–242.
- Valcke, S. and J. Verron, 1993 - On interactions between two finite-core hetons. *Phys. Fluids* **A5** (8), 2058–2060.
- Verron, J., E.J. Hopfinger and J.C. McWilliams, 1990 - Sensitivity to initial conditions in the merging of two-layer baroclinic vortices. *Phys. Fluids* **A2**(6), 886–889.

Verron, J. and S. Valcke, 1994 - Scale-dependent merging of baroclinic vortices.
J. Fluid Mech. **264**, 81–106.

Institut de Mécanique de Grenoble,
B.P. 53X,
38041 Grenoble Cédex, France.

A Hamiltonian Approach to the Dynamics of Long, Nonlinear Frontal Waves

Abstract

A mathematical method is described which can be used to construct dynamical equations for the motion of fronts in fluids. It is applied to the $1\frac{1}{2}$ -layer rotating shallow-water equations to obtain the first order in a long-wave (or narrow-front) expansion for the motion of a front (here, a discontinuity of potential vorticity, i.e. of the ratio of the vorticity and the upper-layer fluid depth).

Introduction

In a previous paper (Nycander *et al.* 1993, hereafter ‘NDS’), we found that the modified Korteweg-deVries (mKdV) equation,

$$\kappa_t = \gamma \left(\kappa_{sss} + \frac{3}{2} \kappa^2 \kappa_s \right) \quad (1)$$

with the curvature $\kappa(s, t)$, a function of arc-length s and time t serving as the dependent variable, governs the dynamics of a narrow-front in the $1\frac{1}{2}$ -layer rotating shallow-water system (the ‘SWE’):

$$\mathbf{u}_t + \mathbf{u} \cdot \nabla \mathbf{u} + f \mathbf{e} \times \mathbf{u} = -g \nabla h \quad (2a)$$

$$h_t + \nabla \cdot (h \mathbf{u}) = 0 \quad (2b)$$

(\mathbf{u} is velocity in the upper layer (the lower layer is infinitely deep and stagnant), h is the upper-layer depth, f is the Coriolis parameter (taken to be a constant), and g is the reduced gravity). The constant γ in Eq. (1) depends essentially on the value of the *uniform* potential vorticity (‘PV’)

$$q \equiv \frac{\omega + f}{h}; \quad \omega = v_x - u_y, \quad (3)$$

on each side of the front. The front is narrow in the sense that variations along the front are much weaker than variations across it.

In NDS, we determined the constant γ in (1) from simple considerations, using only the linear dispersion relation for long waves on a straight front, as opposed to a laborious direct expansion of (1) (Cushman-Roisin *et al.* 1993; Yoshimori 1993). It seemed remarkable that one could obtain a fully-nonlinear equation just from the linear dispersion relation.

We now understand why, after coming across some mathematical results for the dynamics of 2D curves (Goldstein & Petrich 1991, 1992, hereafter 'GP'). Starting from the two-dimensional Euler equations (the "2DEE")

$$\mathbf{u}_t + \mathbf{u} \cdot \nabla \mathbf{u} = -\rho^{-1} \nabla p \quad (4a)$$

$$\nabla \cdot \mathbf{u} = 0 \quad (4b)$$

(ρ is the constant density and p is the pressure) for the special case of piecewise-constant vorticity ω , they showed that the mKdV equation is the leading-order, nonlinear equation for the dynamics of long waves on vortex patches. More significantly, they obtained the mKdV coefficient γ from the energy of a straight front, that is no explicit consideration of disturbance behaviour was necessary.

The appearance of the mKdV equation for the SWE suggested a connection. We demonstrate this connection below. This is nontrivial since the two equation systems, the SWE and the 2DEE, are fundamentally different: in the 2DEE, the instantaneous distribution of vorticity ω determines all the dynamical fields, but in the SWE there is no such principle, owing to the possibility of gravitational oscillations of the fluid depth h .

Working by analogy

We next derive (1) by mathematical analogy with the 2DEE. For the 2DEE, the vorticity determines everything, and since the 2DEE is a Hamiltonian system (see GP), the dynamics is formally obtained from a functional derivative of the Hamiltonian with respect to vorticity,

$$\frac{\delta \mathcal{H}}{\delta \omega}, \quad (5)$$

which is in fact equal to $-\psi$, where $\psi(x, y, t)$ is the stream function (as usual, the velocity components are $u = -\partial\psi/\partial y$ and $v = \partial\psi/\partial x$). The Hamiltonian \mathcal{H} is the "excess" energy (the energy minus an infinite constant proportional to the total conserved circulation), and it is given by

$$\mathcal{H} = -\frac{1}{2} \iint \omega \psi \, dx \, dy. \quad (6)$$

For a vortex patch, the vorticity is uniform within a region \mathcal{R} , and for definiteness, we take the bounding contour \mathcal{C} (on which $\mathbf{x} = (x, y)$) to be right-handed

and denote $\Delta\omega$ as the inward jump in vorticity ($\Delta\omega = \omega_i - \omega_o$). For the patch (see GP), the variational derivative with respect to ω goes over to a variational derivative with respect to the coordinate locally normal to \mathcal{C} :

$$\frac{\delta}{\delta\omega} \rightarrow \frac{1}{\Delta\omega} \hat{\mathbf{n}} \cdot \frac{\delta}{\delta\mathbf{r}}, \quad (7)$$

i.e. $\hat{\mathbf{n}}$ points inwards (into \mathcal{R}). The dynamics of \mathcal{C} —“the front”—is then completely determined by the velocity normal to the front, viz

$$v_{\perp}(s, t) = -\frac{\partial}{\partial s} \left(\frac{\delta\mathcal{H}}{\delta\omega} \right) = -\frac{1}{\Delta\omega} \frac{\partial}{\partial s} \left(\hat{\mathbf{n}} \cdot \frac{\delta\mathcal{H}}{\delta\mathbf{r}} \right) \quad (8)$$

From v_{\perp} , one chooses the as yet arbitrary along-frontal velocity component v_{\parallel} to ensure that t and s derivatives commute (this is possible because only v_{\perp} changes the shape of the front; see NDS),

$$\frac{\partial v_{\parallel}}{\partial s} = \kappa v_{\perp}, \quad (9)$$

and then from geometrical considerations (see GP or NDS), the intrinsic dynamics is obtained from

$$\kappa_t = \left(\frac{\partial^2}{\partial s^2} + \kappa^2 \right) v_{\perp} + \frac{\partial}{\partial s} (\kappa v_{\parallel}). \quad (10)$$

The remaining task is to find the dependence of v_{\perp} on κ and its arc-length derivatives. Here, a perturbation procedure is introduced based on the assumed smallness of the ratio ε of the across-frontal scale and the along-frontal scale; we make a long-wave expansion in which κ and $\partial/\partial s$ are $O(\varepsilon)$. This permits the excess energy or Hamiltonian \mathcal{H} to be expanded as follows:

$$\mathcal{H} = \oint_{\mathcal{C}} ds (a + c\kappa^2 + e\kappa^4 + f\kappa_s^2 + \dots). \quad (11)$$

The leading-order coefficient a can thus be obtained from the excess energy of a straight front ($\kappa = 0$), while the next-order coefficient c can be obtained from the excess energy of a large circular front ($\kappa_s = 0$). Once this is done (we do it for the SWE below), one uses the following results for functional derivatives

$$\hat{\mathbf{n}} \cdot \frac{\delta}{\delta\mathbf{r}} \oint_{\mathcal{C}} ds = \kappa \quad (12a)$$

$$\hat{\mathbf{n}} \cdot \frac{\delta}{\delta\mathbf{r}} \oint_{\mathcal{C}} \kappa^2 ds = \kappa^3 + 2\kappa_{ss} \quad (12b)$$

to obtain (from (8))

$$\begin{aligned} v_{\perp} &= \frac{1}{\Delta\omega} \frac{\partial}{\partial s} (a\kappa + c(\kappa^3 + 2\kappa_{ss}) + \dots) \\ &= \frac{1}{\Delta\omega} \left(a\kappa_s + 2c \left(\kappa_{sss} + \frac{3}{2} \kappa^2 \kappa_s \right) + \dots \right) \end{aligned} \quad (13)$$

from which one can show (via (9) and (10)) that the constant γ in (1) is simply $-a/\Delta\omega$.

Now we work by analogy to get the corresponding result for the SWE. We take the premise that the PV q , like ω in the 2DEE, determines everything. Our premise, in mathematical terms, is that the frontal dynamics (to some order) can be deduced from $\delta\mathcal{H}/\delta q$. Again we consider a vortex patch with interior PV q_i and exterior PV q_o , and so just as before (cf. (7)),

$$\frac{\delta}{\delta q} \rightarrow \frac{1}{\Delta q} \hat{\mathbf{n}} \cdot \frac{\delta}{\delta \mathbf{r}}, \quad (14)$$

where $\Delta q = q_i - q_o$. The Hamiltonian is the total energy,

$$E = \frac{1}{2} \iint h(|\mathbf{u}|^2 + gh) dx dy, \quad (15)$$

minus infinite constants proportional to the total mass M on either side of the front, i.e.

$$\mathcal{H} = E - \frac{1}{2} c_i^2 M_i - \frac{1}{2} c_o^2 M_o \quad (16)$$

with

$$M_{i,o} = \iint_{\mathcal{H}_{i,o}} h dx dy \quad (17)$$

(here $c_{i,o}^2 \equiv gh_{i,o}$, and $h_{i,o} = f/q_{i,o}$ are the layer depths far from the front).

We need next an expression like (8) for the velocity normal to the front. In the SWE there is an additional field, h , which is not directly linked (like the pressure p in the 2DEE) to the velocity field. Hence, the analogous form of (8) must involve not only v_{\perp} but also \bar{h} . From (3) and (15), dimensional considerations and the requirement that mass be conserved (i.e. $dM_{i,o}/dt = \oint ds(\bar{h}v_{\perp}) = 0$) lead to

$$\bar{h}v_{\perp} = -\frac{1}{\Delta q} \frac{\partial}{\partial s} \left(\frac{1}{\bar{h}} \hat{\mathbf{n}} \cdot \frac{\delta \mathcal{H}}{\delta \mathbf{r}} \right). \quad (18)$$

Equations (9) & (10) are unchanged for they hold for any 2D curve.

Now we consider the long-wave expansion explicitly. The external length scales $L_{i,o} = c_{i,o}/f$ provide a natural across-frontal scale. The largest of these two scales L_o is associated with the deeper fluid, and we assume that κL_o and $L_o \partial/\partial s$ are small and of the same order of smallness. The Hamiltonian expands as

$$\mathcal{H} = \oint_{\mathcal{C}} ds (a + b\kappa + c\kappa^2 + d\kappa_s + \dots) \quad (19)$$

and includes new terms, κ and κ_s , not present in the case of the 2DEE (cf. (11)). These new terms arise because of the difference in depth h on either side of the front. However, neither term contributes to the frontal dynamics because their variational derivatives vanish. The leading-order coefficient a can again be obtained from the excess energy of a straight front ($\kappa=0$), while c can likewise be obtained from the excess energy of a large circular front ($\kappa_s=0$).

To see how to do this, we take note of the velocity and depth fields associated with a straight front. Let y be the coordinate perpendicular to the front (pointing into \mathcal{R}_i), and u be the velocity component along the front (in the direction of increasing s ; the across-frontal velocity is of course zero). From (3) (see NDS), we have

$$u = (c_o - c_i) e^{-|y|/L_{i,o}}, \quad h = h_{i,o} + (\bar{h} - h_{i,o}) e^{-|y|/L_{i,o}} \quad (20)$$

where $\bar{h} = (h_i h_o)^{1/2}$ is the depth of the front. Now, to obtain a , all one has to do is insert these fields into (16) (using (15) and (17)), performing only the integration over y . The result is

$$a = -\frac{1}{6g} (c_o^2 - c_i^2)(c_o^3 - c_i^3). \quad (21)$$

Since to leading-order \bar{h} is a constant, from (18) we have

$$v_{\perp} = \gamma \kappa_s \quad \text{with} \quad \gamma = -\frac{a}{\bar{h}^2 \Delta q} = \frac{c_o^3 - c_i^3}{6f^2}. \quad (22)$$

γ is the same coefficient that appears in (1) (and, of course, agrees with previous analyses).

Conclusions

Including more terms in the long-wave expansion is a simple task; results will be reported in a paper in preparation. The surprise in this case is that the apparently more complicated dynamical equations at higher order reduce again to the mKdV equation if one re-positions the front on the curve of maximum velocity (this corresponds with the jump in pv only at lowest order).

References

- Cushman-Roisin, B., L.J. Pratt and E. Ralph, 1993 - A general theory for equivalent barotropic thin jets. *J. Phys. Oceanogr.* **23**, 91–103.
- Goldstein, R.E. and D.M. Petrich, 1991 - The Korteweg-de Vries hierarchy as dynamics of closed curves in the plane. *Phys. Rev. Lett.* **67**, 3203–3206.
- Goldstein, R.E. and D.M. Petrich, 1992 - Solitons, Euler's equation and vortex patch dynamics. preprint.
- Nycander, J., D.G. Dritschel and G.G. Sutyrin, 1993 - The dynamics of long frontal waves in the shallow water equations. *Phys. Fluids A* **5**, 1089–1091.
- Yoshimori, A., 1993 - Path equation for a thin jet. preprint.

* Department of Applied Mathematics and Theoretical Physics
University of Cambridge
Silver Street, Cambridge CB3 9EW
England

+ Department of Technology
Uppsala University
Box 534, S-751 21 Uppsala
Sweden

° P.P. Shirshov Institute of Oceanology
Russian Academy of Sciences
23 Krasikova Street, 117218 Moscow
Russia

Hamiltonian Dynamics, Conservation Laws and the Vortex Stability-Instability Problem

Abstract

The concept of a Hamiltonian system is described and illustrated with three different types of models: shallow water equations with or without horizontal inhomogeneities and frontal geostrophic dynamics. Noether's Theorem relates symmetries and integrals of motion, and the latter are then used to obtain sufficient stability conditions -or necessary instability ones- suitable for the study of vortex dynamics.

Hamiltonian dynamics

This subject provides a **geometric** description of certain dynamical systems, thereby rendering some results (like the link between symmetries and conservation laws or the existence of extremal integrals of motion) less mysterious (see for instance Salmon, 1988, and Shepherd, 1990).

We start by imagining the state of the system at time t as a point φ in the state space E . In practice one has a particular set of fields $\varphi^a(\mathbf{x}, t)$ $\mathbf{x} \in \mathcal{D} \subset \mathbb{R}^n$ (e.g. depth and velocity components, for the shallow water equations), but an advantage of the Hamiltonian formalism is its manifest covariance under change of variables. An important object are the *functionals* $\mathcal{F}: E \rightarrow \mathbb{R}$, e.g.

$\mathcal{F}[\varphi, t] = \int F(\varphi^a, \nabla \varphi^a, \dots; \mathbf{x}, t)$, where “ \int ” represents an integration over the whole domain \mathcal{D} and ∇ is the nabla operator in \mathbb{R}^n . Given any functional \mathcal{F} , the *covector* $D\mathcal{F}[\varphi]$ represents its gradient at φ (in practice, an array of functional derivatives), defined such that the first variation of \mathcal{F} from φ to $\varphi + \delta\varphi$ is given by the linear expression $\delta\mathcal{F} = D\mathcal{F} \cdot \delta\varphi$, where the dot implies an integration in \mathcal{D} and, probably, its boundary $\partial\mathcal{D}$. More precisely

$$\mathcal{F}[\varphi + \delta\varphi, t] = \mathcal{F}[\varphi, t] + D\mathcal{F}[\varphi, t] \cdot \delta\varphi + D^2\mathcal{F}[\varphi, t] \cdot (\delta\varphi, \delta\varphi) + O(\delta\varphi)^3. \quad (1)$$

A key ingredient of a Hamiltonian system is the Poisson tensor $\mathbb{J}[\varphi]$, used to construct the *vector* $\mathbb{J} \cdot D\mathcal{F}$ from the the covector $D\mathcal{F}$. The *Poisson bracket* of two functionals \mathcal{F} & \mathcal{G} is then defined by

$$\{\mathcal{F}, \mathcal{G}\} := D\mathcal{F} \cdot \mathbb{J} \cdot D\mathcal{G}. \quad (2)$$

(I will discuss the properties of \mathbb{J} below.) The other key ingredient is a particular functional: the Hamiltonian $\mathcal{H}[\varphi, t]$, such that the evolution equations take the form

$$\partial_t \varphi = \mathbb{J}[\varphi] \cdot D\mathcal{H}[\varphi, t]. \quad (3)$$

The total time derivative of an arbitrary functional of state $\mathcal{F}[\varphi, t]$ is then given by $\partial_t \mathcal{F} + \{\mathcal{F}, \mathcal{H}\}$, i.e. the sum of the local one (keeping φ fixed) plus the contribution due to the flow through state space.

Time is a parameter external to state space. Therefore, the functionals of state $\mathcal{F}[\varphi, t]$ may also be functions of time but the Poisson tensor \mathbb{J} cannot have an explicit dependence in t (although \mathbf{x} and ∇ may appear in its definition); $\{\cdot, \cdot\}$ gives the *structure* of state space.

Let us see a few examples, using in all of them polar coordinates $\mathbf{x} = (r, s)$, more suitable for vortex dynamics, and a uniform Coriolis parameter f . Consider first the classical **shallow water equations**, but allowing for horizontal inhomogeneities (Ripa, 1993b). The dynamical fields are the buoyancy ϑ , the layer depth h , and the radial u and azimuthal v velocity components. The evolution equations are

$$\begin{aligned} \partial_t \vartheta &= -\mathbf{u} \cdot \nabla \vartheta, \quad \partial_t h = -\nabla \cdot (h\mathbf{u}), \\ \vartheta, \mathbf{u} &= -(f + \chi) \hat{\mathbf{z}} \times \mathbf{u} - \nabla h + \frac{1}{2} h \nabla \vartheta, \end{aligned} \quad (\text{a-d})$$

where $h := \vartheta h + u^2/2 + v^2/2$ is the Bernoulli head, $\chi := (\partial_r(rv) - \partial_s u)/r$ the relative vorticity and $\hat{\mathbf{z}}$ the vertical unit vector. These equations can be derived from the following Hamiltonian and Poisson bracket:

$$\mathcal{H}[\vartheta, h, u, v] := \frac{1}{2} \int h(u^2 + v^2 + \vartheta h) \quad (4e)$$

and

$$\{\mathcal{F}, \mathcal{G}\} := \int \left[\frac{1}{h} \nabla \vartheta \cdot \frac{\delta \mathcal{F}}{\delta \mathbf{u}} \frac{\delta \mathcal{G}}{\delta \vartheta} - \frac{\delta \mathcal{F}}{\delta h} \nabla \cdot \frac{\delta \mathcal{G}}{\delta \mathbf{u}} + q \frac{\delta \mathcal{F}}{\delta u} \frac{\delta \mathcal{G}}{\delta v} \right] - (\mathcal{F} \leftrightarrow \mathcal{G}). \quad (4f)$$

Indeed, the first variation of (4e) gives $D\mathcal{H}[\vartheta, h, u, v] = (h^2/2, b, hu, hv)$, which in (4f) and (3) yields the system (4a-d). \square

This Hamiltonian corresponds with the total energy and it is conserved because $\partial_t \mathcal{H} = 0$. The potential vorticity $q := (f + \chi)/h$, satisfies

$$\partial_t q + \mathbf{u} \cdot \nabla q = J(h, \vartheta)/2h, \quad (5)$$

where $J(A, B)$ is the Jacobian $r^{-1}(\partial_r A \partial_s B - \partial_s A \partial_r B)$.

The standard shallow water model belongs to the submanifold of E represented by $\vartheta = \text{constant}$ ($=: g$, say), which is consistent with (4a). This equation is then no longer needed and the last term on the right hand side of (4c, d) disappears. The evolution equations in the reduced state space can be obtained from

the same Hamiltonian (4e) and the Poisson bracket (4f) but without the first term. Notice that in this case, the right hand side of (5) vanishes, *i.e.*, potential vorticity is conserved. The two systems considered so far are the simplest examples of *inhomogeneous* and *homogeneous layers primitive equations* models; *ILPEM* & *HLPEM* for short (Ripa, 1993b).

Finally consider the **frontal geostrophic dynamics (FGD)** proposed by Cushman-Roisin (1986). For this model it is assumed that the local accelerations may be neglected in the slow manifold, *i.e.* (4c, d) may be approximated by $(f + \chi) \mathbf{u} = \hat{\mathbf{z}} \times \nabla h$. This balance means that u & v are no longer independent variables but, rather, functionals of h . To second order in ∇h it is indeed found that

$$\mathbf{u} = \hat{\mathbf{z}} \times \nabla \left(\mu h + \frac{\mu^2}{2f} \nabla h \cdot \nabla h \right) - \frac{\mu^2}{f} \nabla^2 h \hat{\mathbf{z}} \times \nabla h, \quad (6)$$

where $\mu := g/f$. Finally, upon substitution in (4b), and using $\nabla \cdot (B \hat{\mathbf{z}} \times \nabla A) = J(A, B)$, it is obtained

$$\partial_t h = \frac{\mu^2}{f} J(h \nabla^2 h + \frac{1}{2} \nabla h \cdot \nabla h, h). \quad (7a)$$

This evolution equation may be obtained from the following Hamiltonian and Poisson bracket:

$$\mathcal{H}[h] := \frac{1}{2} \mu^2 \int h \nabla h \cdot \nabla h \quad (7b)$$

and

$$\{\mathcal{F}, \mathcal{G}\} := - \int (h/f) J(\delta \mathcal{F} / \delta h, \delta \mathcal{G} / \delta h). \quad (7c)$$

In fact, (7b) gives $D\mathcal{H}[h] = -\mu^2(\nabla h \cdot \nabla h/2 + h \nabla^2 h)$; using this in (7c) and (3), the system (7a) is easily obtained. \square

Notice that \mathcal{H} equals the kinetic energy due to the geostrophic velocity field, first term in the right hand side of (6), but that h is changed by the advection and divergence of the ageostrophic part.

So far I have shown that the evolution equations for the three different systems can be written in the Hamiltonian form (3), with suitable chosen \mathcal{H} and \mathbb{J} , providing a common geometric description of them. (The form (3) is not enough to guarantee that a dynamical system is Hamiltonian: the Poisson tensor must also have certain general properties which I will point out in a short while.)

Of course there is more to Hamiltonian dynamics than equation (3). For instance, any functional $\mathcal{H}[\varphi, t]$ may be used to define an infinitesimal transformation with parameter s , by

$$\partial_s \varphi = -\mathbb{J}[\varphi] \cdot D\mathcal{H}[\varphi, t]. \quad (8)$$

It is more illustrative to work with the effect of the transformation on an arbitrary functional $\mathcal{F}[\varphi, t]$, rather than φ . Let $R(\Delta s)$ denote the operator that performs a *finite* transformation; from (8) it follows $\delta_s \mathcal{F} = -\{\mathcal{F}, \mathcal{H}\} \Delta s$ and therefore $R\mathcal{F} = \mathcal{F} - \{\mathcal{F}, \mathcal{H}\} \Delta s + \{\{\mathcal{F}, \mathcal{H}\}, \mathcal{H}\} \Delta s^2/2 + O(\Delta s)^3$. (If s is the azimuth, like in the models above, then \mathcal{H} is the angular momentum and R a finite rotation.)

The operator $T(\Delta t)$ for a finite time evolution is similarly found to give $T\mathcal{F} = \mathcal{F} + (\partial_t \mathcal{F} + \{\mathcal{F}, \mathcal{H}\}) \Delta t + \Delta t^2 + O(\Delta t)^3$.

Now let us combine both operations and ask what is the difference between making the s -transformation and then letting the time run and vice versa. The answer is

$$(RT - TR) \mathcal{F} = -(\{\mathcal{F}, \partial_t \mathcal{H}\} + \{\{\mathcal{F}, \mathcal{H}\}, \mathcal{H}\} - \{\{\mathcal{F}, \mathcal{H}\}, \mathcal{H}\}) \times \Delta s \Delta t + O(\Delta s, \Delta t)^3. \quad (9)$$

This is an appropriate place to point out the properties that the Poisson tensor must have in order for (3) to be a Hamiltonian system: antisymmetry and Jacobi identity, *i.e.*

$$\mathbb{J} \left\{ \begin{aligned} &\{\mathcal{F}, \mathcal{G}\} = -\{\mathcal{G}, \mathcal{F}\} \\ &\{\{\mathcal{F}, \mathcal{G}\}, \mathcal{I}\} + \{\mathcal{G}, \{\mathcal{I}, \mathcal{F}\}\} + \{\mathcal{I}, \{\mathcal{F}, \mathcal{G}\}\} = 0 \end{aligned} \right. \quad (10)$$

for any pair or triad of *admissible* functionals of state (sufficiently smooth and satisfying appropriate boundary conditions). All the Poisson tensors mentioned above satisfy these conditions (see Ripa, 1993b).

By using the antisymmetry in the right hand side of (9) we get $\{\{\mathcal{F}, \mathcal{H}\}, \mathcal{H}\} - \{\{\mathcal{F}, \mathcal{H}\}, \mathcal{H}\} = \{\mathcal{H}, \{\mathcal{F}, \mathcal{H}\}\} + \{\mathcal{H}, \{\mathcal{H}, \mathcal{F}\}\}$, which by the Jacobi identity is then equal to $-\{\mathcal{F}, \{\mathcal{H}, \mathcal{H}\}\}$. Using this in (9) it is then found

$$(RT - TR) \mathcal{F} = -\{\mathcal{F}, \partial_t \mathcal{H} + \{\mathcal{H}, \mathcal{H}\}\} \Delta s \Delta t + O(\Delta s, \Delta t)^3. \quad (11)$$

A **symmetry** is a statement in the sense that it is equivalent to let the time run and then make the transformation $R(\Delta s)$ than vice versa, $(RT - TR) \mathcal{F} \equiv 0 \forall \Delta s, \Delta t, \mathcal{F}$, *i.e.* the dynamics is invariant under the transformation R . In such a case, does (11) imply $\partial_t \mathcal{H} + \{\mathcal{H}, \mathcal{H}\} = 0$ (*i.e.* that \mathcal{H} is an integral of motion)?

In order to answer this question we need to solve $(\{\mathcal{F}, \mathcal{Z}\} = 0 \forall \mathcal{F})$ for \mathcal{Z} , *i.e.* to investigate the general solution of $\mathbb{J} \cdot D\mathcal{Z} = 0$. For a canonical system \mathbb{J} is represented by a constant non-singular matrix and therefore $\mathbb{J} \cdot D\mathcal{Z} = 0$ implies that \mathcal{Z} does not depend on φ , *i.e.*, it is but a number (or a function of time). However, for the three examples discussed above, the operator \mathbb{J} is singular, in the sense that there are non-trivial solutions of $\mathbb{J} \cdot D\mathcal{Z} = 0$.

Recall that \mathbb{J} does not depend explicitly on time, so we define a **Casimir** as a non-trivial solution of

$$\mathbb{J}[\varphi] \cdot D\mathcal{C}[\varphi] = 0, \quad (12)$$

in which t does not appear explicitly. (Notice that the Casimirs are a property of the Poisson bracket, *i.e.* of the geometrical structure of E , independent of the Hamiltonian.) The general solution of $\mathbb{J} \cdot D\mathcal{F} = 0$, called a *distinguished functional*, is but a function of the Casimirs and time.

If R represents a symmetry, $RT = TR$, then (11) implies that $\partial_t \mathcal{M} + \{ \mathcal{M}, \mathcal{H} \}$ is, at most, equal to a distinguished functional. However redefining \mathcal{M} by subtracting from it the time integral of this functional, the infinitesimal transformation (8) is not altered and the redefined functional is conserved. In sum

$$RT - TR = 0 \Rightarrow \partial_t \mathcal{M}' + \{ \mathcal{M}', \mathcal{H} \} = 0, \quad (13)$$

where $\mathcal{M}' = \mathcal{M}$ up to the addition of an appropriate distinguished functional. This is Noether's Theorem for singular Hamiltonian systems. Notice that for its derivation one needs to assume neither $\partial_t \mathcal{M} = 0$ nor $\partial_t \mathcal{H} = 0$ (*i.e.* the Hamiltonian may not be conserved).

For the shallow water equations represented by (4) the angular momentum and the Casimirs are given by

$$\mathcal{M} = \int hrv + hfr^2/2, \quad \mathcal{C} = \int h(A(\vartheta) + qB(\vartheta)), \quad (14)$$

where $A(\vartheta)$ & $B(\vartheta)$ are arbitrary. At the hypersurface $\vartheta = g$ the latter is essentially $\int h$ or $\int hq$; however, if the state is restricted to this submanifold ($\vartheta = g$ & $\delta\vartheta = 0$) then there are more Casimirs, namely $\mathcal{C} = \int hF(q)$ with arbitrary $F(\vartheta)$.

For the FGD model, on the other hand, the angular momentum and the Casimirs are given by

$$\mathcal{M} = \int hfr^2/2, \quad \mathcal{C} = \int C(h), \quad (15)$$

where $C(\vartheta)$ is arbitrary. The leading term of $\int hrv$ in (14) vanishes here (because of geostrophy) and $\int hF(q)$ becomes $\int C(h)$ because in the region of validity of FGD the potential vorticity is $\tilde{q}f/h$.

Notice that the potential energy $\int gh^2/2$ is but a Casimir, which could be added to the Hamiltonian (7b), without any change in the evolution equations. Indeed, any Casimir -with the appropriate units- can be added to \mathcal{H} or \mathcal{M} without any change in equations (3) and (8).

Lyapunov stability

Let the *basic state* Φ be some exact solution of (3) and let us study the free evolution of a perturbation from it, $\delta\varphi = \varphi - \Phi$. Stability of Φ represents some statement on the inability of $\delta\varphi$ to grow. The weakest definition is that of **normal modes stability**, in which it is assumed that the linearized perturbation has

a **coherent evolution for all** $\mathbf{x} \in \mathcal{D}$. The strongest concept corresponds to **nonlinear stability**, for which some measure $\|\delta\varphi\|$ is always bounded by a multiple of its initial value (this stability depends on the definition of the metric $\|\cdot\|$).

Somewhere in between is **Lyapunov stability**, based upon the existence of a functional $\mathcal{I}[\varphi, t]$ which (i) is an integral of motion, $\partial_t \mathcal{I} + \{\mathcal{I}, \mathcal{H}\} = 0$, and (ii) has a vanishing first variation from the basic state, $D\mathcal{I}[\Phi, t] = 0$. This condition implies, with (1), a quadratic restriction on the evolution of the linearized perturbation, namely

$$D^2 \mathcal{I}[\Phi, t] \cdot (\delta\varphi, \delta\varphi) = \text{constant} \quad \forall \delta\varphi. \quad (16)$$

Furthermore, (iii) if this second variation is sign definite, then the basic state is Lyapunov (or formally) stable. This concept is stronger than normal modes stability because the perturbation may have arbitrary shape and a time dependence not necessarily exponential. However, unlike the finite dimensional cases, formal stability does not necessarily imply normed stability.

It may seem a formidable task to find integrals of motion that satisfy (ii) at some basic state. However, here is where the Hamiltonian formalism comes to our rescue: If the basic state is steady, $\partial_t \Phi = 0$, and/or s -symmetric, $\partial_s \Phi = 0$, then equations (3) and (8) imply that $\mathbb{J}[\Phi] \cdot D\mathcal{H}[\Phi, t] = 0$ and/or $\mathbb{J}[\Phi] \cdot D\mathcal{M}[\Phi, t] = 0$. Except for some pathological cases, (12) then shows that the desired functional \mathcal{I} will be \mathcal{H} and/or \mathcal{M} plus some distinguished functional. In the examples above \mathcal{H} & \mathcal{M} are not explicit functions of t , and therefore

$$\mathcal{I} = \begin{cases} \mathcal{H} + \mathcal{C}_E: \text{pseudoenergy,} & \text{if } \partial_t \Phi = 0, \\ \mathcal{M} + \mathcal{C}_M: \text{pseudomomentum,} & \text{if } \partial_s \Phi = 0. \end{cases} \quad (17)$$

This is Arnol'd's method to find the extremal functional $\mathcal{I}[\varphi]$.

Let me now illustrate the construction of these extremal integrals of motion, in the case of the *FGD*, i.e. for $h = H + \delta h$. If the basic state H is a steady solution of (7a), then it must satisfy

$$H\nabla^2 H + \frac{1}{2}\nabla H \cdot \nabla H = \Psi(H). \quad (18)$$

Let $\mathcal{I} = \mathcal{H} + \mathcal{C}_E$ (pseudoenergy): $D\mathcal{I}[H] = 0 \quad \forall \mathbf{x}$ requires $dC_E(h)/dh = \mu^2 \Psi(h)$. The second variation is then found to be

$$D^2 \mathcal{I} \cdot (\delta\varphi, \delta\varphi) = \frac{1}{2} \mu^2 \int H(\nabla \delta h)^2 + (\Psi(H)' - \nabla^2 H) \delta h^2. \quad (19)$$

Clearly if $\Psi(H)' > \nabla^2 H \quad \forall \mathbf{x}$ then the basic state is formally stable.

Now assume that the basic state is also axial-symmetric, $H = H(r)$; we may use $\mathcal{I} = \mathcal{H} + \mathcal{C}_E - \alpha(\mathcal{M} + \mathcal{C}_M)$, where α is arbitrary. A positive definite second

variation is now guaranteed if $\exists \alpha |\mu^2 \Psi(H)' > \mu^2 \nabla^2 H - \alpha f r / H(r)' \forall \mathbf{x}$. Using (18) the stability condition can be written in terms of $H(r)$ and its derivatives:

$$\text{If } \exists \alpha \left| \frac{V_0(r) - \alpha r}{fH(r)'} < 0 \quad \forall r \quad (20)$$

then the basic state is formally stable, where

$V_0(r) := (\mu^2/f)(H\nabla^2 H)' - (\mu^2/fr)(H')^2$. A necessary instability condition is that inequality (20) must be violated $\forall \alpha$. [For a parallel basic state $H = H(y)$, the stability condition is $(U_0(y) - \alpha)/fH(y)' > 0 \quad \forall y$ and some α , where $U_0(y) := (\mu^2/f)(HH'')'$.]

If one uses the second variation of the pseudomomentum alone, then only the term proportional to α is obtained: a sufficient stability condition is that $H(r)$ be monotonous. [The same is true for $H(y)$ in the parallel case.]

The stability conditions for the shallow water equations with a homogeneous layer are two (Ripa, 1991): $(V(r) - \alpha r)/Q(r)' > 0$ & $(V(r) - \alpha r)^2 < gH(r)$, whereas the quasi-geostrophic model (Ripa, 1992a, 1993a) and the FGD one (for which $Q' \sim fH'/H^2$) have only the first one. This is not surprising, because violation of the second condition, by some unstable flow, results in growing perturbations which are Poincaré-like, and these modes are absent in models of the slow manifold. Notice, however, that V_0 in (20) is *not* equal to the azimuthal velocity V .

Conclusions

Hamiltonian dynamics provides a unified description of diverse models of interest in geo-hydrodynamics, represented by evolution equations in the form (3) and infinitesimal transformations of the form (8); equations (10) & (12) describe the geometry of state space. This representation is manifestly covariant under a change of state variables, in the same sense that equation (4), written in vectorial notation, is coordinate independent.

Given a steady basic state, it is possible to construct a conserved pseudoenergy, $\mathcal{I}_E = \mathcal{H} + \mathcal{C}_E$, quadratic to lowest order in the deviation $\delta\varphi$ from this state. A conserved pseudomomentum, $\mathcal{I}_M = \mathcal{M} + \mathcal{C}_M$, is similarly constructed given a symmetric basic state. This might seem rather "miraculous":

$D\mathcal{I}_E = 0$ for the *ILPEM* represents the annihilation of four fields (at every point) by means of the choice of two functions of one variable. However, this is no miracle but a result from Hamiltonian dynamics.

Consider the problem linearized in $\delta\varphi$: The original Hamiltonian is not appropriate for this problem, in the sense that the first variation of (3) gives $\partial_t \delta\varphi = \mathbb{J} \cdot \delta D\mathcal{H} + \delta \mathbb{J} \cdot D\mathcal{H}$ and the last term is non-Hamiltonian. However, because of (12) \mathcal{I}_E may be used instead of \mathcal{H} in (3), and then it is $\partial_t \delta\varphi = \mathbb{J}[\Phi] \cdot \delta D\mathcal{I}_E$ because $D\mathcal{I}_E = 0$ by construction. Furthermore $\delta D\mathcal{I}_E \equiv D\mathcal{H}_C$, where $\mathcal{H}_C := D^2\mathcal{I}_E[\Phi] \cdot (\delta\varphi, \delta\varphi)$ is an appropriate Hamiltonian for the

linearized problem. Similarly, $\mathcal{H}_C := D^2 \mathcal{J}_M[\Phi] \cdot (\delta\varphi, \delta\varphi)$ is a momentum. Finally $\mathcal{H}_C - \alpha \mathcal{H}_C$ is the Hamiltonian in a frame rotating with speed α relative to the f -plane.

The link between symmetries and conservation laws given by Noether's Theorem was found useful in the search for extremal integrals of motion \mathcal{J} , but that relationship also represents a formidable limitation on the class of Arnol'd stable states: $D^2 \mathcal{J}[\Phi] \cdot (\delta\varphi, \delta\varphi) > 0 \forall \delta\varphi$ implies that the basic state Φ must have the same symmetries of whole system (Andrew's Theorem).

Moreover, this method for the derivation of sufficient stability conditions has not had much success in models with more physical breadth, e.g. the *ILPEM* have no stability conditions at all (Ripa, 1993b). However, the condition $D^2 \mathcal{J}[\Phi] \cdot (\delta\varphi, \delta\varphi) = 0$ for the unstable manifold may be used to characterize the types of instability modes (Ripa, 1992b). On the other hand, the limitations of Arnol'd's method may be overcome by restricting the class of $\delta\varphi$ in $D^2 \mathcal{J}[\Phi] \cdot (\delta\varphi, \delta\varphi)$ (e.g. see Kloosterziel & Carnevale 1992).

The most important limitation in using the Hamiltonian formalism is the lack of dissipative processes, although some progress has been made in that sense (e.g. Kaufman 1984 or Morrison 1986).

Acknowledgement

This work was supported by CONACyT (México) through grant 1282 – T9204.

References

- Cushman-Roisin, B., 1986 - Frontal geostrophic dynamics. *J. Phys. Oceanogr.* **16**, 132–143.
- Kaufman, A.N., 1984 - Dissipative Hamiltonian systems: A unifying principle. *Phys. Lett.* **100**, 419–422.
- Kloosterziel, R.C., and G.F. Carnevale, 1992 - Formal stability of circular vortices. *J. Fluid Mech.* **242**, 249–278.
- Morrison, P.J., 1986 - A paradigm for joined Hamiltonian and dissipative systems. *Physica* **18D**, 410–419.
- Ripa, P., 1991 - General stability conditions for a multi-layer model. *J. Fluid Mech.* **222**, 119–137.
- Ripa, P., 1992a - Wave energy-momentum and pseudo energy-momentum conservation for the layered quasi-geostrophic instability problem. *J. Fluid Mech.* **235**, 379–398.
- Ripa, P., 1992b - Instability of a solid-body-rotating vortex in a two layer model. *J. Fluid Mech.* **242**, 395–417.
- Ripa, P., 1993a - Arnol'd's second stability theorem for the equivalent barotropic model. *J. Fluid Mech.* **257**, 597–605.
- Ripa, P., 1993b - Conservation laws for primitive equations models with inhomogeneous layers. *Geophys. Astrophys. Fluid Dyn.* **70**, 85–111.

Salmon, R., 1988 - Hamiltonian fluid mechanics. *Ann. Rev. Fluid Mech.* **20**, 225-256.

Shepherd, T.G., 1990 - Symmetries, conservation laws, and Hamiltonian structure in geophysical fluid dynamics. *Adv. Geophys.* **32**, 287-338.

Centro de Investigación Científica y
de Educación Superior de Ensenada (CICESE)
22800 Ensenada, B.C.; México.
E-mail: pedror@cicese.mx

Stability of 2-D Circular Vortices

Abstract

The second variation of a linear combination of energy and angular momentum is used to investigate the stability of circular vortices. For the simplest model of an isolated vortex the linear stability regime is found to coincide with the formal stability regime. The method uses Lagrangian displacements of vorticity contours and can be applied to vortices consisting of several nested rings of piecewise constant vorticity.

Introduction

With regard to the stability of planar circular vortices in an ideal, incompressible and unbounded fluid, Rayleigh's inflection-point theorem (Drazin & Reid, 1981) states that a sufficient condition for linear stability is that the vorticity gradient does not change sign anywhere, i.e. no inflection-point in the azimuthal velocity profile. Rayleigh's theorem is of little use when one considers isolated vortices, i.e. vortices with zero circulation and finite energy. Such vortices always have at least one inflection-point, but this does not guarantee instability, and the question arises whether in some cases they are actually stable. Linear stability, i.e. stability with respect to vanishingly small perturbations, can be established with normal-modes analysis, but here, however, a method is discussed to establish a stronger form of stability, i.e. formal stability. A stationary flow is called formally stable if there is a conserved quantity such that the first variation of this quantity (i.e. the lowest order change due to arbitrary infinitesimal perturbations) is zero while the second variation is sign-definite. In finite dimensional systems formal stability implies nonlinear stability whereas in infinite dimensions it is a necessary prerequisite for nonlinear stability.

The present method was developed after it was noted that Arnol'd's (1966) method cannot be applied to isolated vortices. It is applied here to the simplest possible model of an isolated vortex and the single, circular vortex patch (Rankine vortex). Details can be found in Kloosterziel & Carnevale (1992).

Variations of conserved quantities

For an ideal incompressible fluid, the area enclosed by a material curve Γ is a constant of the motion, as well as the kinetic energy E and angular momentum L . The dependence of E and L on the vorticity distribution $q(x, y)$ is

$$E = \frac{1}{2} \int \int_{\mathcal{C}} q \psi \, dx \, dy, \quad (1)$$

$$L = \int \int_{\mathcal{C}} (x^2 + y^2) q \, dx \, dy, \quad (2)$$

where the stream function ψ is

$$\psi(\mathbf{r}) = -\frac{1}{2\pi} \int \int_{\mathcal{C}} q(\mathbf{r}') \log|\mathbf{r} - \mathbf{r}'| \, dx' \, dy'. \quad (3)$$

Consider the case of a circular vortex, which is a steady state. In particular, the models to which our analysis are most easily applied are circular vortices with piecewise constant vorticity, i.e. vortices with (in polar coordinates (r, θ))

$$\begin{aligned} q &= q_1 & (0 < r < d_1), \\ &= q_2 & (d_1 < r < d_2), \\ &= q_j & (d_{j-1} < r < d_j), \quad \text{etc.} \end{aligned}$$

At each radial position $r = d_i$ the vorticity jumps by $\Delta q_i = q_{i+1} - q_i$. The vortex is perturbed by slightly deforming the circular vorticity contours without breaking or folding them. Energy, angular momentum and area enclosed by each contour are conserved during the subsequent evolution. It appears plausible therefore that the flow cannot develop towards a radically different state if it can be shown that a further growth of the perturbation amplitude would violate a conservation law. Such is the case if at $O(\varepsilon)$, with ε some measure for the perturbation amplitude, energy and angular momentum are unchanged while the second order variation of some combination of them is sign-definite, in other words, in the case that the particular functional has a maximum/minimum at the stationary state with respect to area preserving perturbations.

In order to apply classical calculus of variations, one expands all functionals involved in a power series in ε . First, however, one has to prescribe the perturbation. For instance, in polar coordinates a perturbed circular contour could be written as $d_i + \varepsilon \delta r_i(\theta)$, with d_i the radius of the circle and $\varepsilon \delta r_i$ the perturbation (with $|\delta r_i|$ at most $O(1)$). The index i labels the particular contour under consideration here. The change in area is $\varepsilon \int_0^{2\pi} d_i \delta r_i(\theta) \, d\theta + \frac{1}{2} \varepsilon^2 \int_0^{2\pi} \delta r_i(\theta)^2 \, d\theta$, and although at $\mathcal{O}(\varepsilon)$ area conservation can be satisfied, it cannot at $\mathcal{O}(\varepsilon^2)$. A more general perturbation is introduced

$$r_i(\theta) = d_i + \varepsilon \delta r_{i,1}(\theta) + \frac{1}{2} \varepsilon^2 \delta r_{i,2}(\theta) + \dots,$$

and for given $\delta r_{i,1}$ area can now be conserved at orders higher than one also by an appropriate choice of the $\delta r_{i,m}$ ($m=2, 3, \dots$). The area enclosed by the perturbed circle is

$$A(\Gamma_i + \delta\Gamma_i) = A_{i,0} + \varepsilon A_{i,1} + \frac{1}{2} \varepsilon^2 A_{i,2} + \dots,$$

where $A_{i,0} = \pi d_i^2$ and

$$A_{i,1} = \int_0^{2\pi} d_i \delta r_{i,1} d\theta = \int_0^{2\pi} dA_{i,1}(\theta),$$

$$A_{i,2} = \int_0^{2\pi} (\delta r_{i,1}^2 + d_i \delta r_{i,2}) d\theta = \int_0^{2\pi} dA_{i,2}(\theta).$$

Area conservation means $A_{i,1} = A_{i,2} = \dots = 0$. In a similar vein changes in stream function, energy and angular momentum are expanded

$$\begin{aligned} \psi &= \psi_0 + \varepsilon \psi_1 + \frac{1}{2} \varepsilon^2 \psi_2 + \dots, \\ E &= E_0 + \varepsilon E_1 + \frac{1}{2} \varepsilon^2 E_2 + \dots, \\ L &= L_0 + \varepsilon L_1 + \frac{1}{2} \varepsilon^2 L_2 + \dots. \end{aligned} \quad (4)$$

first variations

After some calculations (see Kloosterziel & Carnevale, 1992) the following first variations are found:

$$\begin{aligned} L_1 &= -\sum_i \Delta q_i d_i^2 \int_0^{2\pi} dA_{i,1}(\theta), \\ E_1 &= -\sum_i 2\Delta q_i \psi_0(\Gamma_i) \int_0^{2\pi} dA_{i,1}(\theta). \end{aligned}$$

The unperturbed vortex is a steady flow and therefore the stream function ψ_0 is constant on each contour Γ_i . It is thus seen that under area preserving perturbations, i.e. $\int dA_{i,1} = 0$, the first variations of energy and angular momentum are zero. It can be shown more generally that the first variation of energy is zero for any stationary flow, while for angular momentum it is zero only when the flow is circularly symmetric.

second variations

For the second variations it is convenient to introduce the variable ϕ_i defined as $\phi_i(\theta) = d_i \delta r_{i,1}(\theta)$. First order area conservation is then equal to $\int \phi_i d\theta = 0$. Also the real inner product on $L^2[0, 2\pi]$ is introduced $\langle f, g \rangle = \int_0^{2\pi} fg d\theta$, and the norm $\|\cdot\|$ in L^2 , i.e. $\|f\| = \langle f, f \rangle^{1/2}$. If one imposes second order area con-

servation, one finds, using the notation introduced above, the following expressions for the second variations

$$L_2 = -2 \sum_i \Delta q_i \|\phi_i\|^2, \quad (5)$$

$$E_2 = \sum_i \frac{2v_\theta(d_i)}{d_i} \Delta q_i \|\phi_i\|^2 - \sum_i \sum_j \Delta q_i \Delta q_j \langle \mathcal{L}_{i,j} \phi_i, \phi_j \rangle. \quad (6)$$

Here v_θ is the azimuthal velocity of the unperturbed vortex at the indicated radial position and $\mathcal{L}_{i,j}$ is an integral operator

$$\mathcal{L}_{i,j} \phi(\theta) = \frac{1}{\pi} \int_0^{2\pi} \log|d_j e^{i\theta} - d_i e^{i\theta'}| \phi(\theta') d\theta'. \quad (7)$$

It can be shown that the eigenvalues of $\mathcal{L}_{i,j}$ are

$$\lambda_n(i,j) = -A_{i,j}^n \quad (n = 1, 2, \dots), \quad (8)$$

with

$$A_{i,j} = \min \left\{ \frac{d_i}{d_j}, \frac{d_j}{d_i} \right\}, \quad (9)$$

and eigenfunctions $\cos n\theta$ and $\sin n\theta$.

Rankine vortex

The Rankine vortex is a single circular 'patch' of constant vorticity q_1 . For this case the second variation of angular momentum is according to (5) simply (there is only one contour $r = d_1$)

$$L_2 = 2q_1 \int_0^{2\pi} \phi_1^2 d\theta. \quad (10)$$

This expression is sign-definite for any perturbation $\phi_1(\theta) = d_1 \delta r_{1,1}(\theta)$, and it is seen that the Rankine vortex minimizes angular momentum when q_1 is positive, and is therefore formally stable.

Moreover, equation (5) shows that a vortex with, say, maximum positive vorticity at the centre, which decays monotonically with increasing radius (all $\Delta q_i < 0$), is also formally stable. Nonlinear stability for this case has been proven by Dritschel (1988), also by essentially using the angular momentum invariant and the area constraint. Similar vortices with smooth, monotonically decreasing vorticity can be shown to be nonlinearly stable with Arnol'd's method (Carnevale & Shepherd, 1990).

For vorticity distributions that have both positive and negative Δq_i (this corresponds to vortices with inflection points), it appears necessary to use energy in addition to angular momentum. Before turning to this more complicated case, it is first shown here that formal stability of the Rankine vortex can also be inferred from a consideration of the energy. For this the perturbation is expanded in the eigenfunctions of the operator \mathcal{L}

$$\delta r_1(\theta) = \sum_{k=1}^{\infty} a_k \cos k\theta + b_k \sin k\theta,$$

where no $k=0$ component has been allowed so that area conservation at $\mathcal{O}(\varepsilon)$ is not violated. After substitution in (6) one gets

$$E_2 = -\pi q_1^2 d_1^2 \sum_{k=1}^{\infty} \left(\frac{k-1}{k} \right) \{a_k^2 + b_k^2\}, \quad (11)$$

where we have used $v_\theta(d_1) = \frac{1}{2} q_1 d_1$. It is seen that E_2 is sign-definite except for the case of a pure wavenumber 1 perturbation (in polar coordinates the perturbations are proportional to $\exp(ik\theta)$, where k is the wavenumber). Such a perturbation corresponds to a displacement of the vortex, and as expected this does not change the energy. This proves that the Rankine vortex with, say, positive vorticity, is a local maximum in energy with respect to all area preserving perturbations (modulo translations).

An isolated vortex

A simple example of an isolated vortex is one for which the azimuthal velocity increases monotonically from the centre until it reaches a maximum at some finite radius, and then falls off to zero monotonically. A velocity profile is then called 'steeper' than another, similar one, when the velocity falls off to zero faster in this outer region. Laboratory observations (Kloosterziel & van Heijst, 1991), numerical analysis (Gent & McWilliams, 1986; Carton & McWilliams, 1989) and analytical studies (Flierl, 1988) indicate that an isolated vortex of this type is unstable if steep enough. The simplest model for such vortices consists of a core of constant vorticity $q_1 = 1$ within the non-dimensional radius $r = 1$ plus an annulus of oppositely-signed vorticity $q_2 = -q < 0$ between $r = 1$ and $r = d$. These vortices all have vanishing circulation at $r = d$ if one takes $q = 1/(d^2 - 1)$. A steeper vortex corresponds here to larger q and correspondingly smaller d .

Normal-modes analysis shows (Flierl, 1988) that for large enough d (small q) they are linearly stable to all wavenumber perturbations. In the notation introduced above one has $d_1 = 1$, $d_2 = d$, $\Delta q_1 = -(1 + q)$ and $\Delta q_2 = q$. Substitution in (5) and (6) yields

$$L_2 = (1 + q) \|\phi_1\|^2 - q \|\phi_2\|^2, \quad (12)$$

$$E_2 = -(1+q)\|\phi_1\|^2 - (1+q)^2 \langle \mathcal{L}_{1,1} \phi_1, \phi_1 \rangle - q^2 \langle \mathcal{L}_{2,2} \phi_2, \phi_2 \rangle - 2q(1+q) \langle \mathcal{L}_{1,2} \phi_1, \phi_2 \rangle. \quad (13)$$

It is clear from (12) that angular momentum is not sign-definite, and stability can no longer be inferred from it alone.

As an aside it may be noted here that the structure of unstable normal-modes can be uncovered using these expressions. The reason for this is the following. It turns out that the linearized equations of motion, from which the normal-modes equations follow, conserve both L_2 and E_2 . This implies that unstable modes can only correspond to those cases for which $L_2 = E_2 = 0$, because a growing normal-mode would otherwise violate the conservation law (E_2 and L_2 are proportional to the square of the amplitude of the mode). So, by putting (12) and (13) equal to zero, one has two equations in two unknowns: the ratio of the perturbation amplitudes on the inner and outer boundary, and the phase difference between the two (see Kloosterziel & Carnevale, 1992). For a normal-mode one has

$$\begin{aligned} \phi_1(\theta) &= d_1 \delta r_{1,1}(\theta) = r_1 \cos m\theta \\ \phi_2(\theta) &= d_2 \delta r_{2,1}(\theta) = r_2 \cos(m\theta + m\theta_0), \end{aligned}$$

where θ_0 is the phase difference between the perturbation on the inner and outer circle.

For instance, for $m=2$ one has, after using (12) to eliminate the occurrence of $\|\phi_1\|$ in E_2 ,

$$E_{2,m=2} = q\|\phi_2\|^2 \left\{ -\frac{1}{2} + q - q\sqrt{\frac{q}{1+q}} \cos 2\theta_0 \right\}.$$

Depending on the choice of θ_0 , $E_{2,m=2}$ varies between

$$-\frac{1}{2} + q - q\sqrt{\frac{q}{1+q}} \leq E_{2,m=2}/(q\|\phi_2\|^2) \leq -\frac{1}{2} + q + q\sqrt{\frac{q}{1+q}}.$$

It follows that if the upper and lower bound are of the same sign, the vortex is linearly stable to wavenumber 2 perturbations. This happens only for $q < q_{\text{crit}} = 1/3$, and then E_2 is negative definite. The situation can be interpreted as that all small $m=2$ perturbations lead to an increase in energy. This critical value was previously found by Flierl (1988) by means of a normal-modes analysis of the linearized equations of motion. With q above the critical value the phase difference for a possible unstable, wavenumber-2 mode is determined by the relation

$$\cos 2\theta_0 = \frac{(q-\frac{1}{2})\sqrt{1+q}}{q\sqrt{q}},$$

while (12) determines the ratio of the amplitudes of the normal mode on the inner and outer boundary, i.e.

$$\frac{\|\phi_1\|^2}{\|\phi_2\|^2} = \frac{q}{1+q}.$$

Formal stability is proven if one can show that along the manifold defined by $L_2 = 0$, E_2 is sign definite, or vice versa. The same is accomplished in an elegant fashion if one can find a Lagrange multiplier μ such that the quadratic form $E_2 + \frac{1}{2}\mu L_2$ is sign definite. The calculations are rather involved, and the reader is referred to Kloosterziel & Carnevale (1992) where it is shown that such a μ exists whenever $0 \leq q \leq 1/3$. This is exactly the linear stability range as found with normal-modes analysis, but with wavenumber 1 perturbations excluded. Such perturbations correspond to imparting linear impulse to the system and lead to a translating vortex (see Stern, 1987). Modulo translations, it is thus concluded that the isolated vortex with $0 \leq q \leq 1/3$ is formally stable.

Final remarks

In this paper only two cases have been discussed, i.e. the Rankine vortex and the simplest possible model of an isolated vortex, but clearly with (5) and (6) formal stability of other cases can also be investigated. Furthermore, by taking the limit of ever smaller vorticity jumps and closer and closer jump positions, one can derive the equivalent expressions for continuous vorticity distributions too.

A major question to be answered in the future is whether if formal stability is found for an isolated vortex, one can also find a proof of normed, nonlinear stability. For this the remainder of the Taylor series expansion has to be estimated and many technical complications surface. But, in view of many observations of long-lived, stable isolated vortices such a proof appears not impossible. It has been found that the above analysis proceeds along exactly the same lines when, instead of the variable $r(\theta)$, the variable $y(\theta) = r(\theta)^2/2$ is introduced. Angular momentum is then exactly quadratic in this variable, and the remainder of the functional $E + \frac{1}{2}\mu L$ beyond second order stems from just the energy functional. Unlike in Arnol'd's stability, this remainder can be of both signs, depending on the amplitude of the perturbation, for instance, and the type of stability to be expected can only be conditional, i.e. stability with respect to perturbations that are 'small enough' initially. Arnol'd's stability is unconditional, i.e. applies to perturbations of any size. It is similar to the finite-dimensional case of a marble in an infinitely-deep well. The case of conditional stability, however, is similar to that of a marble in a well of finite depth, surrounded by more 'holes' or planes. In this case a large-enough perturbation may take the marble far from its original location.

Acknowledgements

This research has been supported in part by National Science Foundation grant OCE 91-21998 and Office of Naval Research grant N00014-93-1-0459.

References

- Arnol'd, V.I., 1966 - On an a priori estimate in the theory of hydrodynamic stability. *Izv. Uchebn. Zaved. Matematika* **54**, no. 5, 3-5. [English translation: *Amer. Math. Soc. Transl., Series 2* **79**, 267-269 (1969)].
- Batchelor, G.K., 1967 - *An Introduction to Fluid Dynamics*. Cambridge University Press, Cambridge.
- Carnevale, G.F. & T.G. Shepherd, 1989 - On the interpretation of Andrew's theorem. *Geophys. Astrophys. Fluid Dyn.* **51**, 1-17.
- Carton, X.J. & J.C. McWilliams, 1989 - Barotropic and baroclinic instabilities of axisymmetric vortices in a quasi-geostrophic model. In *Mesoscale/Synoptic Coherent Structures in Geophysical Turbulence* (eds. J.C.J. Nihoul & B.M. Jamart), pp. 225-244. Elsevier.
- Drazin, P.G. & W.H. Reid, 1981 - *Hydrodynamic Stability*. Cambridge University Press, Cambridge.
- Dritschel, D.G., 1988 - Nonlinear stability bounds for inviscid, two-dimensional, parallel or circular flows with monotonic vorticity, and the analogous three-dimensional quasi-geostrophic flows. *J. Fluid Mech.* **191**, 575-581.
- Flierl, G.R., 1988 - On the instability of geostrophic vortices. *J. Fluid Mech.* **197**, 349-388.
- Gent, P.R. & J.C. McWilliams, 1986 - The instability of circular vortices. *Geophys. Astrophys. Fluid Dyn.* **35**, 209-233.
- Kloosterziel, R.C. & G.F. Carnevale, 1992 - Formal stability of circular vortices. *J. Fluid Mech.* **242**, 249-278.
- Kloosterziel, R.C. & G.J.F. van Heijst, 1991 - An experimental study of unstable barotropic vortices in a rotating fluid. *J. Fluid Mech.* **223**, 1-24.
- Stern, M.E., 1987 - Horizontal entrainment and detrainment in large-scale eddies. *J. Phys. Oceanogr.* **17**, 1688-1695.

* University of Hawaii

School of Ocean and Earth Science and Technology

Department of Oceanography

Honolulu, Hawaii 96822, USA

° Scripps Institution of Oceanography

La Jolla, CA 92093, USA

Stability of Shielded Vortex Dipoles

Abstract

In this study we consider a Lamb dipole and a shielded dipole with the same linear relationship between the vorticity ω and the stream function Ψ . In the second case the vorticity distribution is that of a Lamb dipole surrounded by an oppositely-signed vorticity layer. Direct simulations for moderate values of the Reynolds number have shown that the Lamb dipole maintains its structure while the shielded dipole breaks down. A numerical study of the evolution of small vorticity perturbations has shown that in the Lamb dipole the disturbance is convected far from the main structure, whereas in the shielded dipole the disturbance remains trapped within the vortical structure and grows in time.

Introduction

Vortex dipoles are common features of geophysical flows, and they are believed to play an important role in the general large-scale circulation, since they provide an important mechanism in the transport of various physical properties. In the ocean, dipolar vortices may be generated as a result of shedding from unstable coastal currents or due to localized wind forcing. In the atmosphere, dipolar flow structures may occur in the form of blocking systems which tend to have a stabilizing influence on the local weather. Within the context of the stability of such flow structures it is of importance to know whether the structure, once perturbed, relaxes towards its initial (stable) state. It is easy to show that any functional relationship $\omega = f(\Psi)$ between the vorticity ω and the stream function Ψ satisfies $J(\omega, \Psi) = 0$ and thus represents a stationary solution of the Euler equations. An interesting query is whether this functional relationship indicates stability or not.

In a previous study (Cavazza *et al.*, 1992) we considered the behaviour of a Lamb dipole (with $\omega = k^2\Psi$, see Lamb 1932) when subjected to different types of small perturbations (here we refer to the vortex structure as 'Lamb dipole', although the name 'Chaplygin-Lamb dipole' might be more appropriate, see Meleshko & van Heijst, 1994). In the numerical simulations it was observed that during the first stages of the flow evolution the dipole generally ejects patches of vorticity, while the finally remaining dipole attained a structure with the same

linear relationship but with a slope $k' = k/a'$, with a' the radius of the new dipole.

In the present study we address the question whether the linear relationship is the only condition necessary to show that the dipole has reached a stable state. To this purpose we have considered both the Lamb dipole and the shielded dipole, *i.e.* a Lamb dipole surrounded by an oppositely-signed vorticity layer. The stream functions Ψ and Ψ_s of the Lamb dipole and the shielded dipole, respectively, are given by

$$\Psi = -2U \frac{J_1(kr)}{kJ_0(ka)} \sin \theta, \quad 0 \leq r \leq a \quad (1)$$

$$\Psi_s = -2U \frac{J_1(kr)}{kJ_0(kb)} \sin \theta, \quad 0 \leq r \leq b \quad (2)$$

with U the translation velocity of the Lamb dipole, J_0 and J_1 the zeroth and first order Bessel functions of the first kind, respectively, and $ka = 3.832$ and $kb = 7.016$ the first and second zeros of J_1 , respectively. The 'shield' of the shielded dipole lies in the ring $a \leq r \leq b$, and contains a dipolar vorticity distribution of polarity opposite to that of the dipole core $0 \leq r \leq a$. Although this shielded dipole is a solution of the stationary Euler equation, the numerical simulations to be described below indicate that this structure is unstable.

Numerical simulation

The stability of these vortex structures has been studied numerically by solving the vorticity equation

$$\frac{\partial \omega}{\partial t} + J(\omega, \Psi) = \frac{1}{Re} \nabla^2 \omega \quad (3)$$

where J is the Jacobian operator and Re is the Reynolds number based on the dipole radius a and translation speed U . The numerical finite differences scheme has been described in Orlandi (1990) and Orlandi & van Heijst (1992), and its performance has been tested both by grid-refinement checks and by changing the location of the symmetry boundary conditions. Here it suffices to briefly describe the main characteristics of the numerical method. The system of equations is second order accurate in time and space, and the convective terms have been discretized by the Arakawa scheme (Arakawa, 1966) that conserves, in the inviscid limit, total energy and enstrophy, and maintains the skew symmetry of the Jacobian. This conservation property ensures not only the stability of the calculation but also the correct energy transfer. The advancement in time of the solution has been obtained by a third-order Runge-Kutta scheme calculating the nonlinear terms explicitly and the viscous terms implicitly. The large stability limit $CFL \leq \sqrt{3}$ allows a large Δt . Periodic boundary conditions in one direction

permit the use of FFT's and thus the stream function is obtained by a direct solver.

The calculations presented here were performed on a uniform 193×193 grid on the half-plane $-4.6 < x < 4.6$, $0 < y < 7$ (in view of the flow symmetry about $y = 0$), with periodic boundary conditions in the x -direction.

Apart from the numerical simulations of the regular and shielded Lamb dipoles given by (1) and (2), respectively, additional simulations were performed in which the dipolar vortex structures were locally perturbed in the area of maximum vorticity gradients, *i.e.* in a narrow band along the radius $r = a$. This vorticity perturbation, that is superimposed on the basic vorticity distribution, was taken as

$$\omega'(r, \theta) = \varepsilon \exp \left\{ -\frac{(1 - r/a)^2}{\sigma^2} \right\} \sin 4\theta, \quad (4)$$

with ε the perturbation amplitude and σ a parameter that controls the width of the perturbation band around $r = a$. The amplitude ε was set at a nondimensional value $\varepsilon = 0.05$, which is small compared to the peak value 11.08 of the unperturbed Lamb dipole, whereas the width parameter was set at $\sigma = 0.15$. The structure of the vorticity perturbations of the unshielded and shielded dipoles are shown in Figure 1.

Results

The numerical solution of (3) for the Lamb dipole with the initial stream function (1) revealed that the dipole maintains its shape for a long time and that,

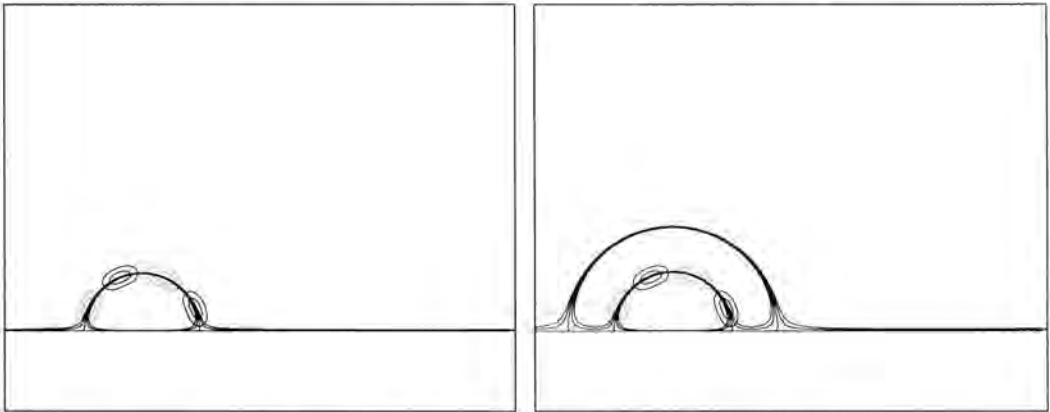


Fig. 1. Graphs showing the distribution of the initial perturbation vorticity (— positive, negative) for (a) the regular and (b) the shielded Lamb dipole (only the upper halves $0 \leq \theta \leq \pi$ are shown). The structure of the dipoles is shown by the unperturbed separatrices and a few neighbouring streamlines.



Fig. 2. The evolution of the unperturbed Lamb dipole for $Re = 1000$ from $t = 0$ to $t = 5$ (in non-dimensional time units) shown by vorticity contours $\Delta\omega = 0.5$; only the upper half-plane is shown.

depending on the Reynolds number, the peak vorticity decreases in time. Some results for $Re = 1000$ are shown in Figure 2: at $t = 5$ (the time is scaled with U and $2a$) has travelled approximately 5 dipole diameters and the cusp-shaped vorticity contour indicates a distortion of the initial dipole structure in the wake, *i.e.* near the rear stagnation point. In contrast, the shielded vortex loses its original shape very quickly, see Figure 3. In comparison with the unshielded dipole, the structure shows an initial tendency to move in opposite direction. This may be surprising at first glance, but in fact it is explicitly given by the solutions (1) and (2) which have different signs since $J_0(ka) = -0.4027\dots$ and $J_0(kb) = +0.3001\dots$

The other vorticity patch is seen to be split into two parts, one being left behind near the symmetry axis, while the other pairs with the original positive core patch in order to form an asymmetric dipole that slowly moves away from the symmetry axis. This behaviour may be understood from the fact that the net negative vorticity contained in the shell is larger than that in the positive core. Besides, the position of extreme negative vorticity in the shell lies closer to the vorticity maximum in the positive core half than that of the negative core half. Apparently, the combination of these effects leads to a redistribution of the vorticity in the outer band and a separation of both inner core halves. From these simulations it thus appears that the outer band of oppositely-signed vorticity is

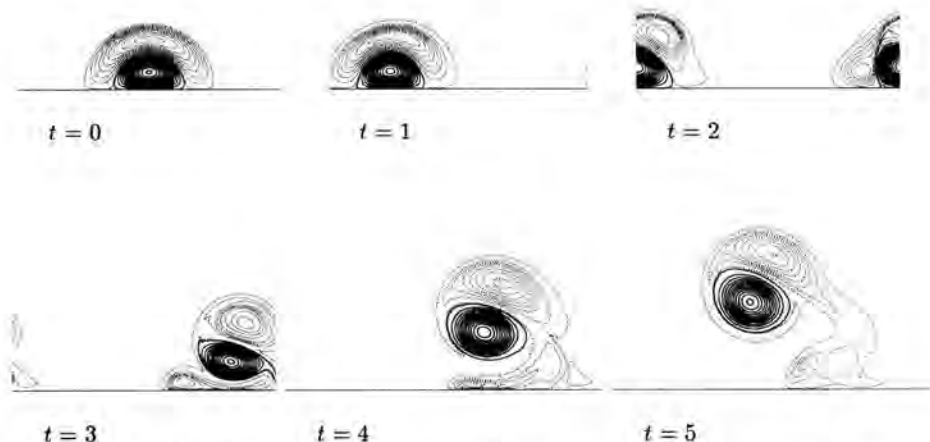


Fig. 3. The evolution of the unperturbed shielded dipole for $Re = 1000$ from $t = 0$ to $t = 5$ shown by vorticity contours $\Delta\omega = \pm 0.5$ (— positive, negative); only the upper half-plane is shown.

not just a passive shield around the dipolar core: the outer vorticity shell is dynamically important and affects the behaviour of the dipole core to a high degree.

In order to gain some insight in the behaviour of the shielded dipole in comparison with that of the regular dipole, we studied the evolution of the vorticity perturbation (4) by numerically solving the 'linearized' vorticity equation

$$\frac{\partial \omega'}{\partial t} + J(\omega', \Psi_0) + J(\omega_0, \Psi') = \frac{1}{Re} \nabla^2 \omega' \quad (5)$$

in which the prime denotes perturbation quantities, whereas the subscript 0 refers to the nonperturbed dipole solutions (1) and (2). The calculations have been performed for $Re = 5000$, so for the case of slight viscosity. The distributions of the perturbation vorticity after 15 time units for both the regular and the shielded dipole are shown in Figure 4. For the Lamb dipole, a considerable portion of the perturbation vorticity is expelled, and thus dissipated in the wake, while only some weak effects of the perturbation remain in the dipole's interior. In contrast, in the case of the shielded dipole most of the perturbation vorticity remains trapped within the structure, see Figure 4b, while only a negligible amount is left behind in the wake. Moreover, one observes the formation of larger regions of positive and negative ω' within the two recirculation regions of the shielded dipole half, thus resulting in an increased distorting effect. This remarkable difference in the evolution of the perturbation vorticity may give a clue to the observed instability of the shielded dipole, see Figure 3.

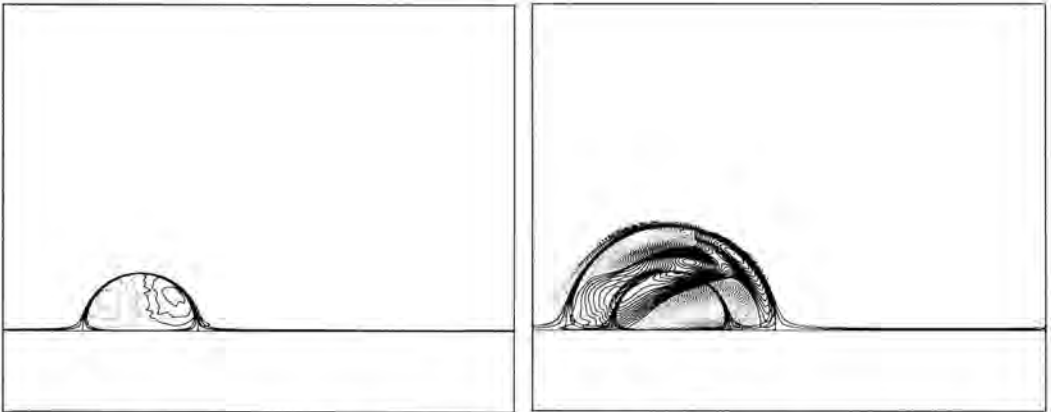


Fig. 4. The distribution of the perturbation vorticity at $t = 15$ for (a) the regular dipole and (b) the shielded dipole. The structure of the unperturbed dipole is shown by the unperturbed streamlines as in Figure 1.

Discussion

The numerical simulations of the regular and shielded dipoles have shown remarkable differences in their evolution. In order to gain insight in the flow evolution it is useful to consider the topological flow structure of both dipoles. As schematically shown in Figure 5, the topological structure of the Lamb dipole is characterized by a circular separatrix Ψ_a and two stagnation points (*i.e.* hyperbolic points) at the intersections of the separatrix and the symmetry streamline $\Psi_{0,\pi}$. The shielded dipole has an outer separatrix Ψ_b with two stagnation points S_{b1} and S_{b2} , and an inner separatrix Ψ_a with stagnation points S_{a1} and S_{a2} . It is known from previous studies on a perturbed point-vortex dipole, which has the same topology, that small perturbations introduced inside or at the separatrix generally result in the 'opening' of the dipole atmosphere at the rear stagnation point, here S_{a2} (*cf.* Rom-Kedar *et al.* 1990 and Velasco Fuentes & van Heijst 1994). In general this results in fluid exchange between the dipole interior and the exterior, *i.e.* in detrainment and entrainment at the dipole's rear. Most likely this mechanism is responsible for the effective 'leaking' of the perturbation vorticity ω' from the Lamb dipole interior, as observed in the numerical simulation (see Figure 4a). As indicated in Figure 5b, the topological structure of the shielded dipole is essentially different: any small perturbations introduced near the inner separatrix Ψ_a will quickly leak into the outer shell (near the inner stagnation point S_{a1}) according to the same mechanism as described above. The recirculation in the outer shell results in a quick spreading of the perturbation vorticity over the entire vortex domain (see Figure 4b), while initially hardly any mass exchange between the dipole and its exterior occurs. Obviously, internal perturbations remain trapped within the shielded dipole, thus leading to changes in the internal vorticity structure. This internal redistribution mechanism is most likely the reason for the break-up of the shielded dipole as observed in the simulations (Figure 3). Although these simulations were carried out for an unperturbed shielded dipole, it may be expected that diffusion of vorticity (being most effective at locations of maximum vorticity gradients, *i.e.* at both separatrices) results in a similar perturbation vorticity field as described artificially by (4).

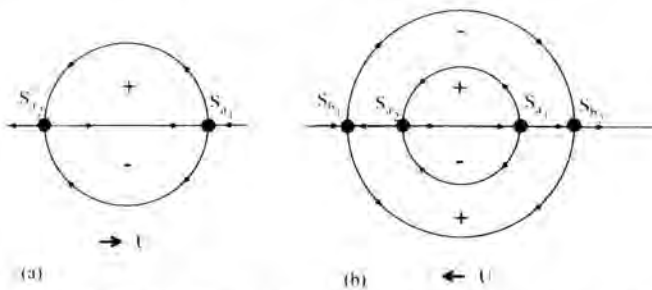


Fig. 5. Schematic drawing of the topological inviscid flow structure of (a) the Lamb dipole and (b) the shielded dipole, seen in a frame co-moving with velocity U .

In view of their different evolutions, the question arises whether the regular Lamb dipole and the shielded dipole possibly contain different amounts of *enstrophy*. The enstrophy is here

$$G = \int \int \frac{1}{2} \omega^2 dA = \frac{1}{2} k^4 \int_0^{2\pi} \int_0^R \Psi^2 r dr d\theta, \quad (6)$$

with R the dipole radius and Ψ the stream function given by (1) or (2). The integrals are easily evaluated, and one derives (with the index S referring to the shielded dipole):

$$G = \pi a^2 k^2 U^2, \quad G_S = \pi b^2 k^2 U^2. \quad (7)$$

Although the *total* enstrophy of the shielded dipole is larger than the total enstrophy of the Lamb dipole by a factor of $(b/a)^2 \simeq 3.37$, the enstrophy *per unit area* is the same for both vortex structures:

$$G' = \frac{G}{\pi a^2} = k^2 U^2, \quad G'_S = \frac{G_S}{\pi b^2} = k^2 U^2. \quad (7)$$

Apparently, this does not provide any further clues. Figure 6 shows the evolution of G' and G'_S as calculated numerically for $Re = 1000$ (the corresponding evolutions of the spatial vorticity distribution are presented in Figures 2 and 3). Both G' and G'_S show a gradual decrease, although G'_S decreases at a higher rate. The decrease of the enstrophy is entirely due to the removal of weak, small-scale low-amplitude vorticity (less than 10^{-6}) in the exterior flow field during the numerical simulations. The different decay rates indicate that the slightly viscous Lamb dipole shows only little 'leaking' of vorticity in comparison with the shielded dipole, which by breaking up soon loses its coherent character.

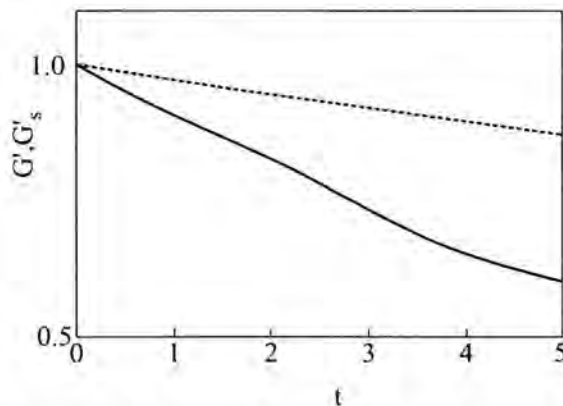


Fig. 6. Evolution of the enstrophies G' and G'_S calculated numerically for $Re = 1000$. The dotted curve represents the Lamb dipole (G'), while the solid curve represents the shielded dipole (G'_S).

Conclusions

In this numerical study we have provided evidence that the shielded Lamb dipole, although governed by the same linear relationship between the vorticity and the stream function as the regular Lamb dipole, is unstable for moderate values of the Reynolds number. It is believed that the explanation for this instability lies in the flow topology of the vortex structure: small internal vorticity perturbations (either artificially generated or arising from diffusion of vorticity) are seen to remain trapped within the shielded dipole, whereas they are quickly detrained in the case of a regular Lamb dipole.

References

- Arakawa, A., 1966 - Computational design for long term numerical integration of the equations of fluid motion: Two-dimensional incompressible flow. Part I. *J. Comput. Phys.* **1**, 119–143.
- Cavazza, P., G.J.F. van Heijst & P. Orlandi, 1992 - The stability of vortex dipoles. Proc. 11th Australasian Fluid Mech. Conf., Hobart, Australia.
- van Heijst, G.J.F., R.C. Kloosterziel & C.W.M. Williams, 1991 - Laboratory experiments on the tripolar vortex in a rotating fluid. *J. Fluid Mech.* **225**, 301–331.
- Lamb, H., 1932 - *Hydrodynamics*. Cambridge University Press.
- Meleshko, V.V. & G.J.F. van Heijst, 1994 - On Chaplygin's investigations of two-dimensional vortex structures in an inviscid fluid. *J. Fluid Mech.* **272**, 157–182.
- Orlandi, P., 1990 - Vortex dipole rebound from a wall. *Phys. Fluids A2*, 1429–1436.
- Orlandi, P. & G.J.F. van Heijst, 1992 - Numerical simulations of tripolar vortices in 2D flows. *Fluid Dyn. Res.* **9**, 179–206.
- Rom-Kedar, V., A. Leonard & S. Wiggins, 1990 - An analytical study of transport, mixing and chaos in an unsteady vortical flow. *J. Fluid Mech.* **214**, 347–394.
- Velasco Fuentes, O.U., G.J.F. van Heijst & B.E. Cremers, 1994 - Chaotic advection by dipolar vortices on a β -plane. *J. Fluid Mech.* (submitted.) Also: B.E. Cremers & O.U. Velasco Fuentes, 1994 - Chaotic advection by dipolar vortices on a β -plane. *This issue*.

* Università di Roma "La Sapienza"
Dipartimento di Meccanica e Aeronautica
Via Eudossiana 18, 00184 Rome, Italy

+ Fluid Dynamics Laboratory
Eindhoven University of Technology
P.O. Box 513, 5600 MB Eindhoven, The Netherlands

Dynamics of Dipole Vortices

Abstract

Simulations of unsteady dipole vortices on the β -plane are compared with the predictions of an ideal model equation. The most striking discrepancy is the relaxation to eastward propagation in the simulations. This effect can be understood theoretically and incorporated into the model, which results in a qualitative agreement with the simulations.

Introduction

Although dipole vortices are observed more seldom than monopole vortices in natural flows, there are reasons to believe that they are important. They consist of two close counter-rotating vortices that push each other forward. This self-propelling mechanism gives the dipole vortex an arbitrary intrinsic velocity. (The drift of monopole vortices, on the other hand, is mainly determined by gradients in the background parameters, such as topography or the β -effect). Combined with the fact that they always carry trapped fluid, this means that dipole vortices are probably more important for transport than their sheer number would indicate. Also, their intrinsic velocity and nonzero linear impulse give them a very different (and richer) dynamic behaviour than monopole vortices.

Ideal theory

The discussion will here be confined to flows described by the equivalent barotropic vorticity equation, which is called the Hasegawa-Mima equation in plasma physics (Hasegawa *et al.* 1979):

$$\frac{\partial}{\partial t}(\phi - \nabla^2 \phi) - \beta \frac{\partial \phi}{\partial x} - J(\phi, \nabla^2 \phi) = 0 \quad (1)$$

where the stream function ϕ represents the perturbation of the fluid depth, $J(,)$ the Jacobian, and β the gradient of the Coriolis parameter. We denote the relative potential vorticity $\nabla^2 \phi - \phi$ by q . The absolute potential vorticity, $q = \beta y$,

is a Lagrangian invariant, i.e. it is conserved in each fluid element moving with the velocity $\mathbf{v} = \hat{\mathbf{z}} \times \nabla \phi$.

Exact dipole vortex solutions of eq. (1) travelling with the velocity $\mathbf{U} = \hat{\mathbf{x}}U$ were found by Larichev and Reznik (1976):

$$\begin{aligned}\phi &= U \frac{\rho^2}{\kappa^2} \left[a \frac{J_1(\kappa r)}{J_1(\kappa a)} - r \left(\frac{\kappa^2}{\rho^2} + 1 \right) \right] \sin \theta, & r < a \\ \phi &= -Ua \frac{K_1(\rho r)}{K_1(\rho a)} \sin \theta, & r > a\end{aligned}\quad (2)$$

where $\rho^2 = (U + \beta)/U$, a is the radius of the separatrix, and κ is found as the first root of the equation

$$K_2(\rho a)/\rho a K_1(\rho a) = -J_2(\kappa a)/\kappa a J_1(\kappa a)$$

For the solution to be localized, U must be outside of the interval of possible phase velocities for the linear Rossby waves. (This is a general condition for localized and steadily propagating structures: their velocity should not coincide with the phase velocity of linear waves. Otherwise they radiate linear waves and gradually lose energy). Thus, there are two kinds of steady dipole vortices: those propagating eastward, i.e. $U > 0$ (ETD's), and those propagating westward and faster than the Rossby waves, i.e. $U < -\beta$ (WTD's).

Similar solutions exist for a large number of two-dimensional fluid models, both in fluid dynamics and in plasma physics, while localized monopole vortices exist in fewer cases. The underlying physical reason for this difference is that dipole vortices have an intrinsic velocity. Since this velocity is arbitrary, it can always be outside the region of linear phase velocities.

In (2) the separatrix is circular, and the absolute potential vorticity depends linearly on the stream function, both inside and outside the separatrix (but with different coefficients). However, it is clear that there also exist steady solutions with a noncircular separatrix, and a nonlinear functional dependence in the inner region. Such solutions have been found numerically (McWilliams and Zabusky 1982, Boyd and Ma 1990), and by perturbation analysis, using (2) as the zeroth order solution (Nycander 1988). Rigorous existence proofs for nonlinear dipole vortex solutions of the Euler equation have also been given by Norbury (1975) and Burton (1988). In the theory below, nothing will be assumed about the functional relationship or the shape of the separatrix.

If the direction of propagation of a dipole vortex is not exactly eastward or westward, it is not steady. In order to describe the dynamics in this case, we first define $M = \int q \, dx \, dy$, which will be referred to as "mass" or "total charge", and

$$\Omega = \frac{1}{2} \int q^2 \, dx \, dy,$$

which is called "enstrophy", or "pseudo-momentum" (since it is the difference

between the linear impulse and the quadratic Casimir integral). Both M and \mathcal{Q} are conserved integrals. Another important relation is

$$\frac{d\mathbf{R}_c}{dt} = -\beta\hat{x}, \quad (3)$$

which determines the velocity of the "centre of mass", defined by

$$\mathbf{R}_c = (1/M) \int q\mathbf{r} \, dx \, dy.$$

The derivation of the approximate equation of motion for dipole vortices by Nycander and Isichenko (1990) will now be briefly repeated. The basic assumption is that β is small. If $\beta = 0$ a dipole vortex with $M \neq 0$ moves on a circle around the fixed centre of the mass, cf. (3), as has been observed both in simulations and laboratory experiments (Flierl *et al.* 1983, Couder and Basdevant 1986). To find the radius of this circle we define the dipole moment

$\mathbf{P} = \int q\mathbf{r} \, dx \, dy = M\mathbf{R}_c$. The value of \mathbf{P} generally depends on the choice of the origin. Defining the "intrinsic dipole moment" \mathbf{P}_d as the value obtained with the origin at its centre, the radius of the circle is given by $R_c = P_d/M$. Using the usual expression for the centripetal acceleration of circular motion, this result can formally be written as an equation of motion:

$$\frac{d\mathbf{U}}{dt} = \hat{z} \times \mathbf{U} \frac{MU}{P_d}. \quad (4)$$

Here \mathbf{U} is the velocity of the vortex, and $U = |\mathbf{U}|$ is defined to be always positive, unlike in (2). M is the "mass" or "total charge" associated with the vortex itself, excluding the contribution from the far field.

The main modification of (4) on the β -plane is that M is no longer constant. The conservation of absolute potential vorticity in the trapped fluid inside the separatrix implies that $M = -S\beta y$, where y is the position of the vortex, S the area inside the separatrix, and we have chosen the coordinate system so that $M = 0$ at $y = 0$. Inserting this into (4) we obtain:

$$\frac{d\mathbf{U}}{dt} = \mathbf{U} \times \hat{z} y \beta U \frac{S}{P_d}, \quad (5)$$

which is the ideal equation of motion for dipole vortices in an inhomogeneous medium. Both S and P_d are assumed to be constant parameters.

Steady solutions of (5) are given by $y = U_y = 0$. If $U_x > 0$ the trajectory is stable. The frequency of small oscillations around it is given by $\omega^2 = U^2 \beta S / P_d$. The steady solutions with $U_x < 0$ are unstable.

Eq.(5) can be solved completely in terms of elliptic integrals, noting that U and

$$p_x = U_x - \beta(S/P_d) U(y^2/2) \quad (6)$$

are both constants of motion. The frequency of oscillations with arbitrary amplitude can then easily be calculated:

$$\omega^2 = \frac{U^2 \beta S}{P_d} \left(\frac{\pi}{2K(k)} \right)^2, \quad (7)$$

where K is a complete elliptic integral of the first kind, $k = |\sin(\alpha/2)|$, and α is the maximum angle between the trajectory and the positive x-axis.

Simulations

A series of simulations were performed by Hesthaven *et al.* (1993) in order to test the theory described above. They were done with a pseudospectral code with 128 by 128 Fourier modes. A simple cutting technique was applied to remove the wake field behind the vortex before it collided with it because of the periodic boundary condition. This was seen to be crucial for the long-term behaviour of the vortices.

One would not expect the theory to work well when the radius of curvature of the trajectory is of the same order as the size of the vortex. In this case the cyclonic and anticyclonic parts have very unequal strength, and the separatrix is not well defined. Thus, we only expect a good agreement when $\beta \ll U$, and when the vortex is propagating at a small angle to the x-axis, close to the steady eastward case.

For a short time the agreement between the simulations and eq. (7) is surprisingly good, even outside the expected region of validity. Fig. 1 shows the frequency of initially symmetric dipole vortices that started at different angles to the x-axis, and with different values of β . (The initial condition was the exact solution (2) with $U > 0$, but rotated by α degrees). The frequency was estimated at the first maximum of the oscillation - after a quarter of a period. If β was larger than U and the angle too large, the vortex soon disintegrated, but before that happened the deviation from the ideal theory was not large even in this case. The agreement was good also for other quantities, such as the maximum displacement of the dipole vortex in the y -direction.

There was, however, a significant discrepancy in the region where the best agreement was expected $\beta \ll U$ and small α . In this case the first period was anomalously long. The frequency then increased and stabilized, and after one or two periods agreed well with the predicted value. Scatter plots showed that the functional relationship between the stream function and the absolute potential vorticity changed during the first period, and then settled down to a nonlinear profile. This effect was stronger when α was small. Apparently, the initial discrepancy is caused by some internal transient process.

The long-term development of a dipole vortex, however, is not well described by the ideal theory above. Instead, either of two things happens. Either it dis-

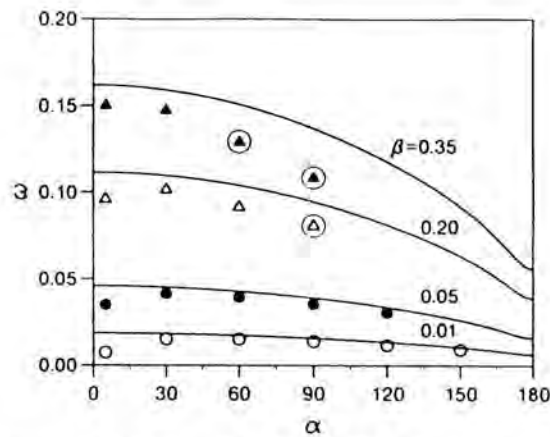


Fig. 1. Oscillation frequency ω as a function of the initial propagation angle α . The theoretical curves were calculated from eq. (7) using the solution (2). Disintegrating dipole vortices are encircled. Here and in all subsequent figures $a = 1.0$ and $U = 0.1$. (Reproduced from Hesthaven *et al.* 1993)

integrates (this usually happens rather quickly), or it relaxes to an eastward propagating, almost steady dipole, as seen in Figs. 2 and 3. (In Fig. 3 the vortex is initially propagating close to westward, but swings around and starts propagating eastward). The general rule is that it disintegrates if β is too large (i.e. if the amplitude of the vortex is too small) and the initial angle is too large.

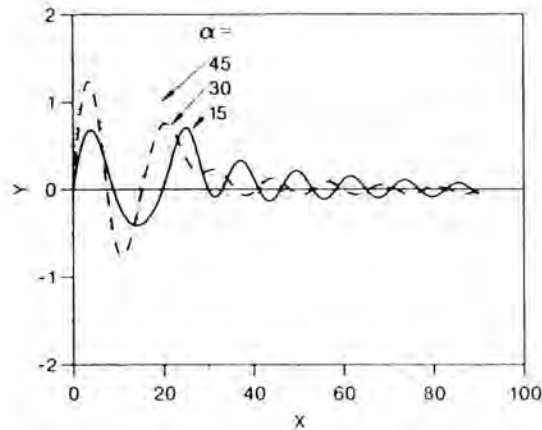


Fig. 2. Trajectories of tilted ETD's, i.e. U in eq. (2) is positive; $\beta = 0.05$. (Reproduced from Hesthaven *et al.* 1993)

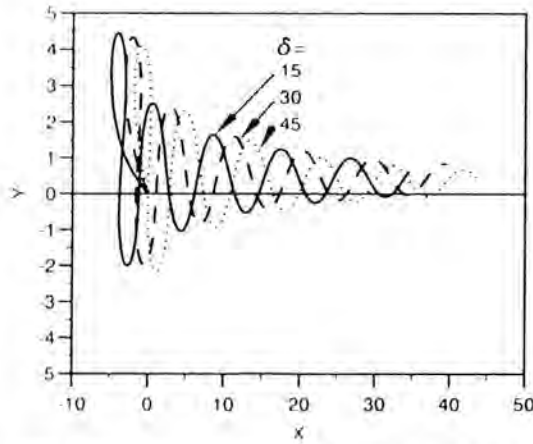


Fig. 3. Trajectories of tilted WTD's, i.e. U in eq. (2) is negative. δ is the angle between the initial propagation direction and the negative x -axis; $\beta = 0.05$. (Reproduced from Hesthaven *et al.* 1993)

Relaxation mechanism

The relaxation of dipole vortices to eastward propagation is associated with inviscid loss of enstrophy from the vortex to the surrounding fluid. It is possible to identify two loss mechanisms. The first one is displacement of outer fluid. If the vortex propagates northward, it displaces the fluid outside the separatrix southward as it passes by. Because of the conservation of absolute potential vorticity, the displaced fluid acquires some relative vorticity of the order $q_w \approx \beta \lambda \sin \theta$, where θ is the propagation angle of the vortex and λ its diameter. Thus a wake field appears behind the vortex, and the enstrophy lost to this wake field can be estimated as

$$\frac{d\Omega}{dt} \approx -\frac{1}{2} q_w^2 \lambda U \approx -\frac{1}{2} \beta^2 \lambda^3 U \sin^2 \theta. \quad (8)$$

It should be possible to calculate this loss more exactly for a linear dipole vortex with a circular separatrix, since the velocity field outside the separatrix is then known. One would then assume that θ changes little during the time it takes for a typical fluid parcel to be displaced by the vortex.

The other mechanism is "breathing", i.e. regular trapping and untrapping of fluid as the cyclonic and anticyclonic parts of the vortex shrink and grow during the oscillations. Since the fluid elements are not released at the same value of y as where they were trapped, they acquire some relative vorticity. This mechanism is generally weaker than the displacement of outer fluid, since the amount of displaced outer fluid is much larger than the amount of trapped and untrapped fluid, while the magnitude of the displacement is comparable in both

cases. (Contrary to what was stated by Nycander and Isichenko, this is true even when θ is small. They assumed that the fluid is released at a random point on the periphery, but in fact the trapping and untrapping always takes place near the stagnation points).

To understand why the enstrophy loss leads to a decreasing propagation angle (i.e. the observed relaxation) we again invoke the conservation of absolute potential vorticity. For the amplitude q in the vortex to decrease in magnitude, the cyclonic part must move a little northward, and the anticyclonic one a little southward. If the internal structure is unchanged so that the distance between them is constant (this appears to be approximately the case), the propagation angle then decreases.

To express this effect qualitatively, we calculate the increase in enstrophy of the dipole vortex as it is artificially rotated away from exactly eastward, which is the position of minimum enstrophy. Assuming that the relative change of q is small (this is always true if $\beta\lambda$ is much smaller than the characteristic amplitude q_0), we obtain

$$\Delta\Omega = \int_S q \Delta q \, dx \, dy = -\beta \int_S q \Delta y \, dx \, dy, \quad (9)$$

where Δy is the displacement of each fluid element due to the rotation, and the integral is taken over the surface inside the separatrix. The integral on the right-hand side of eq. (9) is just the change of the y -component of the dipole moment. Thus, the vortex enstrophy Ω_d may be written as a function of the propagation angle θ :

$$\Omega_d = \Omega_o - \beta P_d^{\text{in}} \cos \theta, \quad (10)$$

where Ω_o is a constant, and P_d^{in} the dipole moment inside the separatrix.

The second term in (10) is analogous to the potential energy $-\mathbf{p} \cdot \mathbf{E}$ of an electric dipole in an external electric field \mathbf{E} . Just like the dipole vortex, the oscillations of an electric dipole are damped if there is some loss mechanism (for instance radiation), until it is aligned with the external field.

From eqs. (8) and (10) it is possible to estimate the rate of rotation caused by the loss:

$$\left(\frac{d\theta}{dt} \right)_{\text{loss}} \approx -\frac{\lambda^3 \beta}{2P_d^{\text{in}}} U \sin \theta.$$

Using the relation $d\mathbf{U}/dt = \hat{\mathbf{z}} \times \mathbf{U} \, d\theta/dt$ this can be expressed as an acceleration. Adding this term to eq. (5) we obtain the modified equation of motion

$$\frac{d\mathbf{U}}{dt} = \mathbf{U} \times \hat{\mathbf{z}} \left(\beta U \frac{S}{P_d} y + \frac{\lambda^3 \beta}{2P_d^{\text{in}}} U_y \right). \quad (11)$$

It is easy to see that the new term in (11) indeed represents damping. The ideal constant of motion p_x , defined in (6), now increases monotonously, and it can be seen that it is maximum for eastward propagation. The linearized equation for small perturbations around this steady solution is the usual equation for a damped oscillator, and the ratio between the damping coefficient and the frequency can be estimated as $(\beta\lambda/q_0)^{1/2}$. This indicates that the damping during one period is insignificant in the limit of small β , which supports the consistency of the theory. (Notice that one should not compare the enstrophy loss with the total enstrophy of the vortex, as was done by Nycander and Isichenko (1990). The loss has a significant effect if it is comparable to the second term in (10), which is smaller than the total enstrophy).

In Fig. 4 the solution of eq. (11) is shown, using the same parameter values as in Fig. 2, with $\alpha = 45^\circ$. The coefficient of the damping term in (11) was divided by four in order to improve the agreement with the simulation in Fig. 2. Such an adjustment is possible, since the derivation above only determined this term up to a factor of order unity.

However, regardless of the value of this coefficient, the solution of eq. (11) differs from the observed trajectory in two ways. The first is that eq. (11) is obviously incapable of describing the irregular behaviour during the first few periods which is particularly apparent for $\alpha = 15^\circ$ and 30° in Fig. 2. Secondly, the damping of the observed trajectory is relatively stronger when the amplitude is large, and weaker when the amplitude is small, as compared with solutions of eq. (11). This is particularly clear from Fig. 3. To model this a nonlinear damping term would have to be added to the right hand side of eq. (11), for instance a term proportional to U_y^3 . However, no motivation for this or any other particular form of a nonlinear damping term has been found.

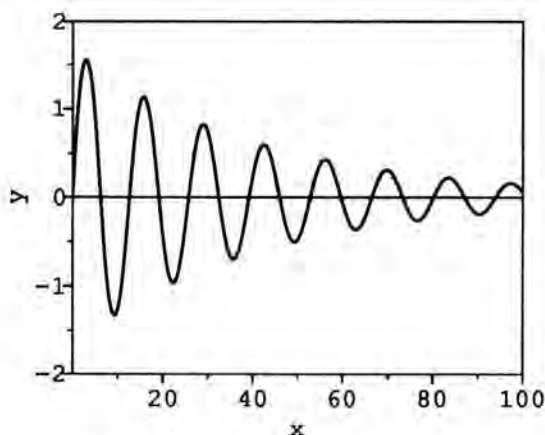


Fig. 4. Theoretical trajectory of dipole vortex calculated from eq. (11). It should be compared with the dotted curve in Fig. 2.

The cutting technique made it possible to measure the loss of enstrophy from the vortex to the surrounding fluid directly in the simulations. It was found that the enstrophy decrease is smaller than indicated by eq. (10), except when θ is small. Probably some of the "free enstrophy" made available by the decrease of θ is absorbed by internal oscillations, instead of being lost to the surrounding fluid. There were also direct numerical indications of such internal oscillations in the dipole vortex when the initial launch angle was large, with a frequency a few times larger than the oscillation frequency of the trajectory.

It is tempting to guess that what appears as nonlinear damping of the trajectory is caused by excitation of such internal oscillations, and that the rather irregular trajectories during the first two periods in Fig. 2 are the result of an interplay between the internal dynamics and the macroscopic motion of the dipole vortex.

Conclusion

The simple ideal model equation (5), which is conservative and can be written in Hamiltonian form, was compared with numerical simulations of dipole vortices. For a short time the agreement was good, but in the long run the motion is strongly affected by effects not included in the ideal model, such as inviscid loss of enstrophy to the surrounding fluid, and excitation of internal oscillations in the vortex. The result is that all dipole vortices either quickly disintegrate, or relax to steadily propagating ETD's.

The enstrophy loss can rather easily be incorporated into the model. The main mechanism is displacement of surrounding fluid by the dipole vortex. Estimating this effect up to a factor of order unity (as mentioned above, it should be possible to sharpen this estimate), the modified equation of motion (11) was obtained. Solutions of this equation qualitatively resemble the relaxing trajectories in the simulations, cf. Fig. 4, but a good quantitative agreement is still lacking. This is true regardless of the value of the coefficient of the damping term.

Thus, we are reaching the limits of what can be done without taking the internal dynamics into account. Its effects on the vortex trajectories can be seen in several places in the simulations: in the irregularities during the first few periods in Fig. 2, in the anomalous behaviour during the first period when both α and β are small in Fig. 1, and, probably, in what appears as nonlinear damping in Figs. 2 and 3, in contrast to the linear damping in the theoretical Fig. 4.

One way of approaching the problem of the internal dynamics might be to use the linear eigenmodes of the dipole vortex, if, indeed, any localized eigenmodes exist. However, virtually nothing is known about the linearized problem for small perturbations of a dipole vortex. There has been a number of attempts to prove linear (and nonlinear) stability, but they have all been shown to be invalid (Nycander 1992). The anomalous behaviour in Fig. 1 when α and β are small indicates that the regular oscillations of perturbed ETD's do not correspond to linear eigenmodes.

Another approach might be to use the point vortex model. One should then use at least two point vortices for the cyclonic part and two for the anticyclonic part of the dipole vortex, as was done by Zabusky and McWilliams (1992). However, it is uncertain whether this kind of model is at all suited for describing the internal dynamics of a dipole vortex.

Acknowledgement

The main part of this work was done in collaboration with Jan Hesthaven and Jens-Peter Lynov while I was visiting Risø National Laboratory.

References

- Boyd, J.P. and H. Ma, 1990 - Numerical study of elliptical modons using a spectral method. *J. Fluid Mech.* **221**, 597–611.
- Burton, G.R., 1988 - Steady symmetric vortex pairs and rearrangements. *Proc. Roy. Soc. Edinburgh* **108A**, 269–290.
- Couder, Y. and C. Basdevant, 1986 - Experimental and numerical study of vortex couples in two-dimensional flows, *J. Fluid Mech.* **173**, 225–251.
- Flierl, G.R., M.E. Stern, and J.A. Whitehead, 1983 - The physical significance of modons: laboratory experiments and general integral constraints. *Dyn. Atmos. Oceans* **7**, 223–263.
- Hasegawa, A., C.G. MacLennan, and Y. Kodama, 1979 - Nonlinear behavior and turbulence spectra of drift waves and Rossby waves. *Phys. Fluids* **22**, 2122–2129.
- Hesthaven, J.S., J.P. Lynov, and J. Nycander, 1993 - Dynamics of nonstationary dipole vortices. *Phys. Fluids A* **5**, 622–629.
- Larichev, V.D. and G.M. Reznik, 1976 - Two-dimensional solitary Rossby waves. *Dokl. Akad. Nauk SSSR* **231**, 1077–1079.
- McWilliams, J.C. and N.J. Zabusky, 1982 - Interactions of isolated modons. I. Modons colliding with modons. *Geophys. Astrophys. Fluid Dyn.* **19**, 207–227.
- Norbury, J., 1975 - Steady vortex pairs in an ideal fluid. *Comm. Pure Appl. Math.* **28**, 679–700.
- Nycander, J., 1988 - New stationary solutions of the Hasegawa-Mima equation. *J. Plasma Phys.* **39**, 413–430.
- Nycander, J., 1992 - Refutation of stability proofs for dipole vortices. *Phys. Fluids A* **4**, 467–476.
- Nycander, J. and M.B. Isichenko, 1990 - Motion of dipole vortices in a weakly inhomogeneous medium and related convective transport. *Phys. Fluids B* **2**, 2042–2047.
- Zabusky, N.J. and J.C. McWilliams, 1982 - A modulated point vortex model for geostrophic, β -plane dynamics. *Phys. Fluids* **25**, 2175–2182.

Department of Technology, Uppsala University
Box 534, 751 21 Uppsala, Sweden

Laboratory Experiments on Dipolar Vortices in a Rotating Fluid

Abstract

The behaviour of dipolar vortices on a β -plane is investigated in the laboratory using a rotating fluid with a varying depth. Dipoles initially directed under a certain angle relative to the west-east axis showed meandering or cycloid-like trajectories. For East-travelling dipoles (ETD's) a small deviation from zonal motion results in small oscillations around the equilibrium latitude. For West-travelling dipoles (WTD's) small deviations result in large displacements in meridional direction. ETD's increase in size and eventually split into two independent monopoles.

Introduction

Large scale motions in the oceans and in the atmosphere, being two-dimensional in a first approximation, are characterized by the emergence of coherent vortices. After the monopolar vortex the dipole is the most commonly occurring vortex structure. The dipolar vortex has two remarkable properties: it possesses a separatrix and it has a non-zero linear momentum. Therefore this vortex structure provides an efficient mechanism for the transport of mass and momentum over large distances. In particular, oceanic dipolar vortices are believed to play an important role in the transport of scalar properties such as heat, salt, nutrients and other biochemical components.

The dynamics of geophysical flows is further influenced by the gradient of the Coriolis parameter in the latitudinal direction, usually referred to as the β -effect. A similar gradient of the ambient vorticity can be caused by variations of the depth of the fluid. When these variations are linear and small, the result is equivalent to a gradient of the Coriolis parameter (with the direction of steepest bottom slope corresponding with the northern direction). This effect is sometimes called "topographic β -effect".

There are several dipolar solutions, also called modons, which can exist in such inhomogeneous media (see Flierl, 1987). One common characteristic of these modons is that they are either stationary or they translate steadily along lines of equal ambient vorticity. An important question concerns the existence of similar structures that propagate transversally to these isolines.

One approach to this problem has been the representation of the dipole by a couple of point vortices. During the evolution the relative circulation changes to preserve potential vorticity. Kawano and Yamagata (1977) first found three "regimes" in the motion of the couples: i) eastward meandering, ii) westward cycloid-like trajectories, and iii) the "non-propagating" mode, in which the couple moves along an 8-shaped curve fixed in space. Zabusky and McWilliams (1982) presented calculations of a point-vortex couple and a dipole represented by two pairs of point vortices. These point-vortex calculations showed good agreement with numerical simulations of a modon solution for the first oscillation.

Makino *et al.* (1981) used "tilted" modons as initial conditions for numerical simulations. They found that the modons survive as coherent structures, moving along meandering trajectories in eastward direction or along cycloid-like paths in westward direction, depending on the tilting angle. Using a perturbation technique, Nycander and Isichenko (1990) also found these two regimes as well as the "non-propagating" mode. They also showed that the decay due to generation of relative vorticity was negligible during one oscillation of the dipole.

The results reported here concern flow measurements and visualizations of the evolution of dipoles propagating transversally to the lines of equal ambient vorticity.

Point-vortex model

On a β -plane every column of fluid is assumed to conserve potential vorticity during the evolution, i.e. $q = \omega + \beta y$ is constant, where ω is the relative vorticity and β is the gradient of ambient vorticity in the northern direction y . On a rotating sphere $\beta = 2\Omega \cos \phi_0 / R$, with Ω the angular velocity, ϕ_0 a reference latitude and R the sphere's radius. On a "topographic β -plane" $\beta = 2\Omega s / h_0$, with s the gradient of the fluid depth and h_0 the reference depth.

This principle can be implemented in the point-vortex model under the assumption that a point vortex represents a small patch (with area πL^2) of uniform vorticity $\bar{\omega}$. Using conservation of potential vorticity, the point-vortex's circulation ($\kappa = \bar{\omega} \pi L^2$) can be expressed as a function of the position:

$$\kappa = \kappa_0 + \pi L^2 \beta (y_0 - y)$$

where y_0 represents the initial latitude, at which the vortex has strength κ_0 .

The motion of a point-vortex dipole on the β -plane can be described by a couple of ordinary differential equations (see e.g. Velasco Fuentes and van Heijst, 1994). In the case of a weak β (more precisely $\beta d L^2 / \kappa_0 \ll 1$, with d the distance between the point-vortices) the evolution is described by:

$$\frac{d^2 \alpha}{dt^2} + \frac{L}{d} \beta U \sin \alpha = 0$$

where α is the angle of the dipole's velocity vector with respect to the lines of equal ambient vorticity and $U = \kappa_0/2\pi d$ is the initial translation velocity of the dipole. Initial conditions are $\alpha'(0) = 0$ and $\alpha(0) = \alpha_0$.

This equation is identical to the simple pendulum equation and can be solved in terms of elliptical integrals. The condition $\alpha'(0) = 0$ ensures that all the solutions represent oscillations in the dipole's direction of propagation. The stability properties of the dipole trajectory can be immediately established: an ETD ($\alpha_0 = 0$) performs small oscillations when its trajectory is perturbed, whereas any small perturbation causes the WTD ($\alpha_0 = \pi$) to make a big loop.

Experimental arrangement

The experiments were carried out in a rectangular tank of horizontal dimensions $100 \times 150 \text{ cm}^2$ and 30 cm depth mounted on a rotating table. In most experiments the angular speed of the system was $\Omega = 0.56 \text{ s}^{-1}$, so that the Coriolis parameter $f = 1.12 \text{ s}^{-1}$. The working depth of the fluid was varied from 15 to 20 cm, and a false bottom was raised 4 to 8 cm along one of the long sides to provide the topographic β -effect. With these parameter settings the equivalent value of β measured approximately $0.25 \text{ m}^{-1} \text{ s}^{-1}$.

Once the fluid was in solid body rotation a columnar dipole vortex was generated by slowly moving a small, bottomless cylinder of 8 cm diameter horizontally along a straight line relative to the rotating tank, while slowly lifting it out of the fluid. The vorticity generated by the motion of the cylinder accumulates in a dipolar structure in the wake of the cylinder. After typically 1–2 rotation periods the organization of the vortex flow is completed. The Rossby number for the resultant dipolar structure, defined as $R_\rho = U/2\Omega r$ with U as the maximal velocity and r as the radius of the dipole, is of order 0.1 to 0.2.

In a first series of experiments dye was added to the fluid within the small cylinder before generating the dipole. Photographs of the evolving dipole were taken at intervals of typically 5 to 15 sec by a camera mounted in the rotating frame about 150 cm above the free surface of the fluid.

Flow measurements were made from photographic streaks of small (1 mm diameter) paper particles floating on the free surface. The velocity field is measured from the lengths and orientations of particle streaks. Then the velocity field is interpolated onto a regular grid using cubic splines. The relative vorticity ($\omega = v_x - u_y$) is calculated analytically from the interpolating polynomials and the stream function is obtained by numerically inverting the Poisson equation $\nabla^2 \psi = -\omega$.

Meandering dipoles

A typical trajectory of a dipole initially moving towards shallower parts of the tank ("north") is shown in Figure 1a. In this case the dipole was initially directed

at some angle to the topography gradient, approximately to the “north-east”. Due to the background rotation the two dipole halves experience asymmetric effects: the cyclonic vortex becomes weaker while the anticyclonic one becomes stronger, resulting in a trajectory curved in clockwise sense. The clockwise rotation brings the dipole southwards, and the asymmetry gradually diminishes. The dipole recovers its zero net circulation when it crosses the equilibrium line (where the height of the fluid column is equal to its initial value). Because of its own momentum the dipole moves further into deeper regions (“south”), so that the column of fluid is stretched further. Owing to this stretching, the cyclonic half becomes stronger and as a result the dipole’s trajectory curves in anti-clockwise sense. After reaching its southernmost position the dipole moves back to its equilibrium latitude. At this stage the dipole has decayed and its propagation speed is reduced to almost zero.

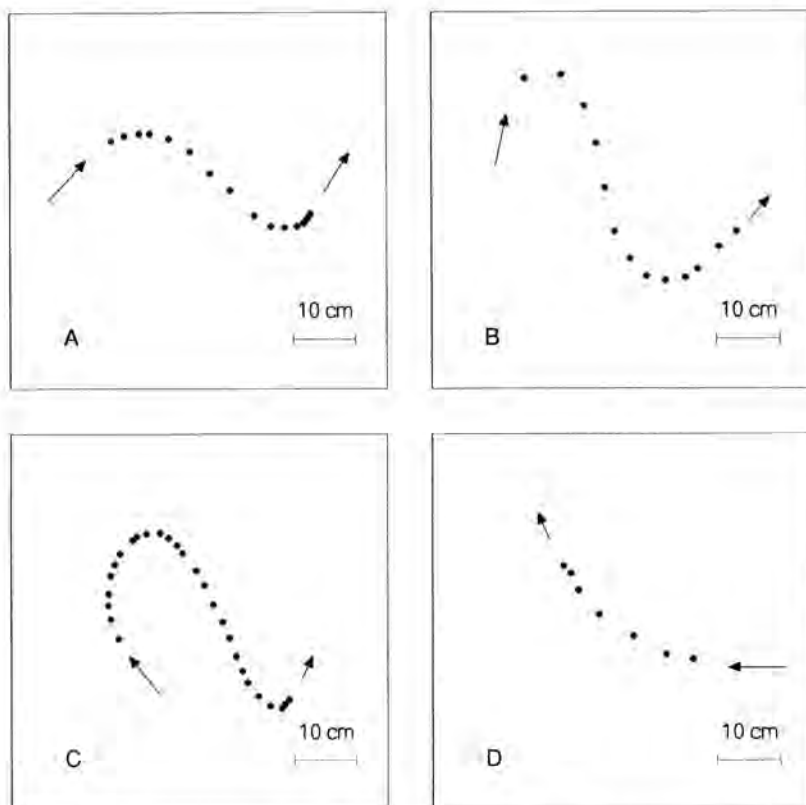


Fig. 1. Observed dipole trajectories for different initial direction of propagation: (A) northeast, (B) north, (C) northwest, and (D) west. The arrows indicate initial and final directions of the observed dipole translation. Since the medium depth h_0 of the fluid in the dipole evolution varies from one experiment to another (in the range 15 to 18 cm) the β -effect changes accordingly in the range $0.25\text{--}0.3\text{ m}^{-1}\text{ s}^{-1}$.

This squeezing and stretching mechanism is active for every initial orientation of the dipole axis. However, its effect is very different on dipoles moving initially at angles greater than $\pi/2$ (i.e. dipoles with a westward component in their motion) and on dipoles moving at angles smaller than $\pi/2$ (dipoles with an eastward component). When the initial angle is less than $\pi/2$ the dipole acquires

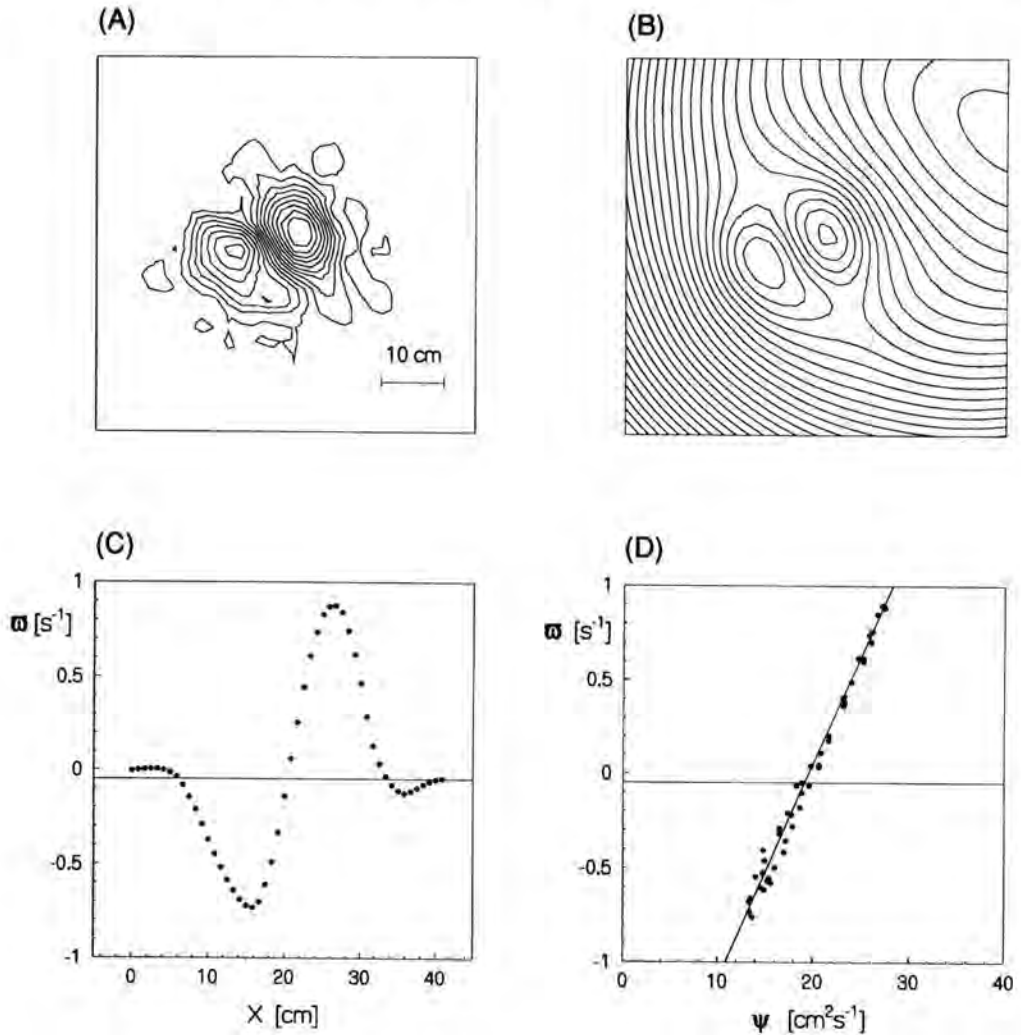


Fig. 2. Measured flow characteristics of a dipolar vortex on a β -plane at $t = 1.77T$, with $T = 11.3$ s the rotation period of the turntable. The dipole moved initially to the south and subsequently described a meandering path. The graphs represent (a) vorticity contours (contour interval $CI = 0.1 \text{ s}^{-1}$), (b) stream function contours ($CI = 2 \text{ cm}^2 \text{ s}^{-1}$) corrected for the observed motion of the dipole, (c) distribution of vorticity along a line crossing the points of extremal vorticity values and (d) ω - ψ relation, obtained by plotting the vorticity value against the stream function value of every grid point in the interior of the dipole. Experimental parameters: $f = 1.11 \text{ s}^{-1}$, $h_0 = 0.17 \text{ m}$, $s = 0.23$, $\beta = 0.26 \text{ m}^{-1} \text{ s}^{-1}$.

an asymmetry of the proper sign to pull it back to its equilibrium latitude. The smooth oscillation of a dipole with initial north-east motion appears in Figure 1a, and a similar trajectory can be seen in Figure 1b for a dipole released in northward direction. Dipoles with tilting angles greater than $\pi/2$ move initially away from the equilibrium latitude along a big loop before finally returning to it (see Figure 1c for an example of a dipole initially moving north-westward). Figure 1d shows an example of the trajectory instability of a West-travelling dipole (WTD). In this case the dipole moves northward and breaks up before being able to return to its initial latitude.

Flow measurements were done in the case of a dipole initially directed southward. When it reaches a mature state at time $t = 1.77$ (in units of the rotation period $T = 11.3$ s), the dipole moves in an approximate south-east direction. The cyclonic half is stronger, resulting in an anti-clockwise deflection of the dipole's trajectory. The density of the vorticity and stream function contours in Figures 2a,b shows a clear asymmetry between the two dipole halves. The centre of the dipole's rotational motion at this stage is also visible in the upper right corner of Figure 2b (note that both vorticity and stream function have been corrected for the motion of the dipole).

A remarkable feature in the cross-section of vorticity is the presence of a small ring of oppositely-signed vorticity around the dipole (see e.g. the small humps in the vorticity cross-section, Figure 2c). The shielding ring is caused by the advection of ambient fluid in meridional direction and leads to a widening of the dipole. At the earlier stages of the dipole motion the vortex structure was found to be characterized by a linear relation between ω and ψ , see Figure 2d. As a result of entrainment of passive fluid, at later stages a weak nonlinearity in the ω - ψ relation is developed.

Break-up of an ETD

Besides the asymmetry of stability properties a few more differences were observed between eastward and westward travelling dipoles. The ETD's were always larger and slower than the WTD's, which were compact and travelled relatively fast. These different types of behaviour can be explained by the secondary vorticity field generated in the fluid exterior to the vortex dipole (Velasco Fuentes and van Heijst, 1994). The magnitude of the secondary vorticity is of order βr , where r is the radius of the dipole. As β is increased the value of the generated vorticity gets closer to the values of the dipole's vorticity itself, thus producing a faster growth and eventually a break-up of the ETD. In the WTD the tendency to become compact and fast vanishes rapidly due to the instability of the westward trajectory.

In order to investigate the splitting of an ETD in more detail, an experiment was carried out using a strong β -effect ($\beta = 0.52 \text{ m}^{-1} \text{ s}^{-1}$). The formation of the dipolar structure was completed approximately 4–5 revolution periods after the lifting of the generating cylinder. In comparison with the previously shown

dipole (Figure 2), the size of the dipolar vortex was relatively large in this case, and the two halves were not compactly attached as before. At a later stage ($t = 14.5$) the separation between the two halves had increased significantly (Figures 3a,b) and a weak *westward* drift of the two halves was observed.

The vorticity distribution along the line joining the vortex centres (Figure 3c) shows an almost complete break-up of the dipole and it resembles that of two

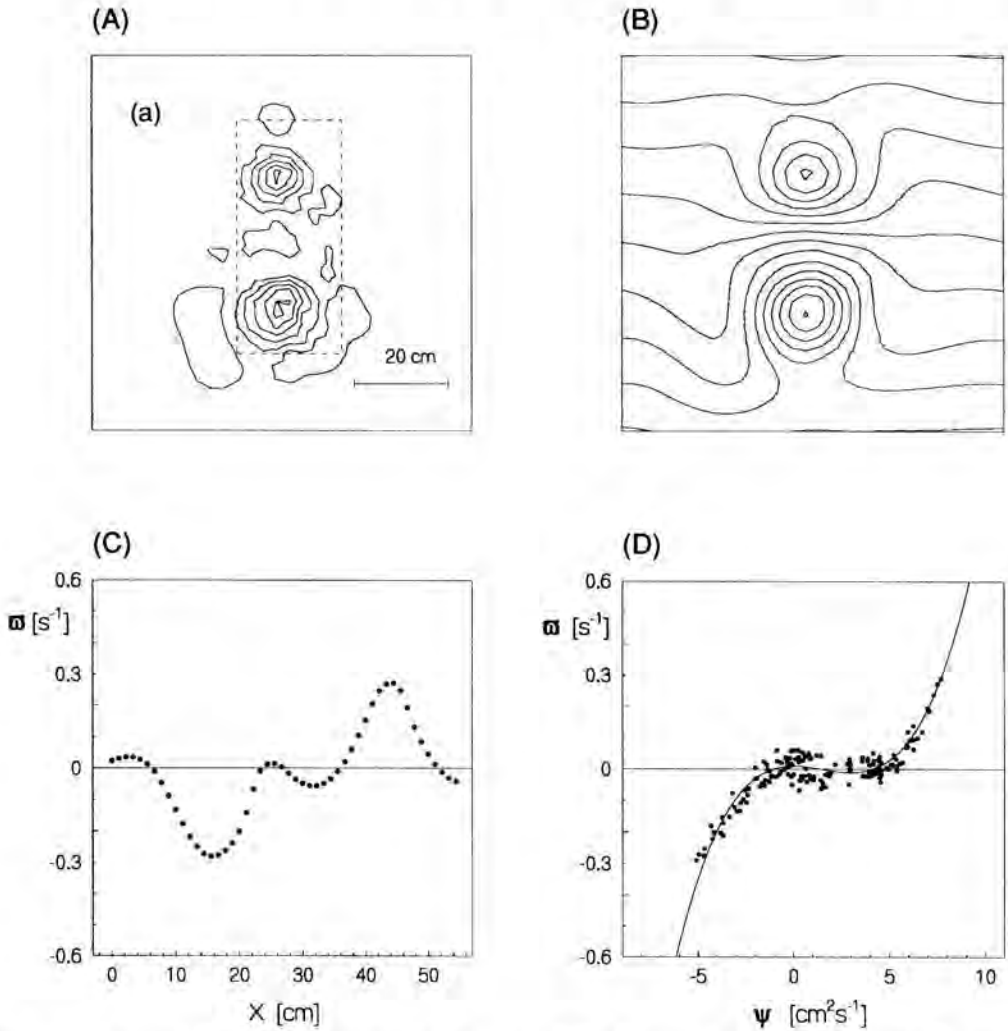


Fig. 3. Measured flow characteristics of the ETD after the splitting has been completed (at time $t = 14.5$ T): (a) vorticity contours ($CI = 0.06$ s⁻¹), (b) stream function contours ($CI = 1$ cm² s⁻¹) corrected for the observed westward motion of the monopolar vortices, (c) vorticity distribution along a line intersecting the points of extremal vorticity, and (d) the ω - ψ plot obtained from the grid points in the rectangular area indicated by the broken line in (a). Experimental parameters: $f_0 = 1.1$ s⁻¹, $h_0 = 0.16$ m, $s = 0.42$, $\beta = 0.52$ m⁻¹ s⁻¹.

(oppositely signed) isolated monopolar vortices placed close together (see e.g. Kloosterziel and van Heijst, 1992). The ω - ψ relation shows two antisymmetric branches which are reasonably approximated by a cubic polynomial (Figure 3d). Comparison with the ω - ψ relationship of an isolated monopolar vortex (e.g. van Heijst *et al.*, 1991), confirms that the ω - ψ plot in Figure 3d indeed represents a combination of a cyclonic and an anticyclonic shielded monopolar vortex. The considerable scatter can be attributed to the different meridional drift components of the vortices (which can not be simultaneously corrected for), and also to the non-steadiness of the individual vortices: as shown by e.g. Carnevale *et al.* (1991), the shielded monopolar vortex on a β -plane is not quasi-stationary, and loses vorticity while drifting.

Conclusions

In a series of dye experiments dipoles were initiated at different angles with respect of the isobaths. The trajectories of dipoles with an eastward component in their motion are in good agreement with theoretical predictions (Kawano and Yamagata, 1977; Makino *et al.*, 1981). Dipoles with a westward component agree only in the perturbation enhancement mechanism but do not show the 8-shaped path or the cycloid-like mode.

Flow measurements show variations of the relative vorticity that are in qualitative agreement with the predictions of the point-vortex model and numerical calculations. A functional relation is observed between vorticity and stream function, being linear at the first stages and becoming nonlinear at later stages.

Generation of relative vorticity by advection of ambient fluid in meridional direction causes ETD's to grow and to translate slower, while WTD's become compact and fast-moving during the first stages (before the development of the trajectory instability). The rate of growth of the ETD is determined by the gradient of ambient vorticity (β). A strong β -effect leads to the break-up of the ETD. After the separation of the dipole into two monopolar vortices, each vortex drifts independently under the β -plane dynamics, namely: the cyclonic half moves in northwestern direction and the anticyclonic vortex travels to the southwest.

Acknowledgement

O.U.V.F. gratefully acknowledges financial support from the Stichting voor Fundamenteel Onderzoek der Materie (FOM).

References

- Carnevale, G.F., R.C. Kloosterziel & G.J.F. van Heijst, 1991 - Propagation of barotropic vortices over topography in a rotating tank. *J. Fluid Mech.* **233**, 119-139.

- Flierl, G.R., 1987 - Isolated eddy models in geophysics. *Ann. Rev. Fluid Mech.* **19**, 93–530.
- van Heijst, G.J.F., R.C. Kloosterziel & C.W.M. Williams, 1991 - Laboratory experiments on the tripolar vortex in a rotating fluid. *J. Fluid Mech.* **225**, 301–331.
- Kloosterziel, R.C. & G.J.F. van Heijst, 1992 - The evolution of stable barotropic vortices in a rotating free-surface fluid. *J. Fluid Mech.* **239**, 607–629.
- Kawano, J. & T. Yamagata, 1977 - The behaviour of a vortex pair on the beta plane. *Proc. Oceanogr. Soc. Japan* **36**, 83–84 (in Japanese).
- Makino, M., T. Kamimura & T. Taniuti, 1981 - Dynamics of two-dimensional solitary vortices in a low- β plasma with convective motion. *J. Phys. Soc. Japan* **50**, 980–989.
- Nycander, J. & M.B. Isichenko, 1990 - Motion of dipole vortices in a weakly inhomogeneous medium and related convective transport. *Phys. Fluids* **B2**, 2042–2047.
- Velasco Fuentes, O.U. & G.J.F. van Heijst, 1994 - Experimental study of dipolar vortices on a topographic β -plane. *J. Fluid Mech.* **259**, 79–106.
- Zabusky, N.J. & J.C. McWilliams, 1982 - A modulated point-vortex model for geostrophic, β -plane dynamics. *Phys. Fluids* **25**, 2175–2182.

Fluid Dynamics Laboratory
 Eindhoven University of Technology
 P.O. Box 513
 5600 MB Eindhoven
 The Netherlands

Chaotic Advection by Dipolar Vortices on a Topographic β -Plane

Abstract

Dipolar vortices on a topographic β -plane meander around lines of equal ambient vorticity (i.e. equal fluid depth). During this motion exchange of mass takes place between the interior and the exterior fluid of the dipole as well as between the two dipole halves. This exchange is caused by a variation of the distance between the vortices due to stretching and squeezing of the dipole as well as by a variation of the strength of the vortices due to conservation of potential vorticity. The exchange process is simulated using a point-vortex model. The amount of mass exchange and the residence time of fluid particles is evaluated using recent techniques for transport in dynamical systems.

Introduction

The basic dynamics of dipolar vortices on the β -plane can be understood using a point-vortex model, with the vortices' circulations changing in order to preserve potential vorticity (see e.g. Velasco Fuentes and van Heijst, 1994a, hereafter called VFvH). Using this approach, it is found that the motion of the couple displays three regimes: (i) eastward meandering, (ii) westward cycloid-like trajectories, and (iii) non-propagating, 8-shaped trajectory.

The gradient of the Coriolis parameter on the Earth can be mimicked in the laboratory by variations in the depth of a rotating fluid, when these variations are linear and small. This effect is usually referred to as the "topographic β -effect". On a topographic β -plane the direction of decreasing depth of the fluid corresponds to 'north'. VFvH studied analytically and experimentally the dynamics of dipolar vortices on a topographic β -plane. They found that the dipolar vortex meanders around isolines of ambient vorticity (i.e. lines of equal depth of the fluid), when the angle between the initial direction of the dipole and the 'east' direction is not zero. It is also observed that during this meandering motion fluid is exchanged between the dipole and the surroundings as well as between the two dipole halves.

In this particular case transport of fluid is dominated by a convective process so that the relative motions of fluid parcels is important. The study of particle motion ('Lagrangian' view) can be started if the velocity field of the flow

('Eulerian' view) is known for all times. Using the point-vortex approach, and given a particular set of initial conditions, the positions and strengths of the point vortices are known for all times. Therefore, the motion of individual particles, which is far more complex than the motion of the couple itself, can be extensively analysed using recent developments in the theory of transport in nonlinear dynamical systems (Wiggins, 1992). In particular, some of these methods can be used to calculate physically measurable quantities such as the amount of exchange across certain boundaries and the residence times of particles in chaotic regions of the flow. Rom-Kedar *et al.* (1990) used the latter approach to study chaotic particle motion due to a point-vortex dipole embedded in an oscillating strain-rate field. This work should be consulted by readers interested in a detailed discussion of the techniques used in following sections.

Theory

The equations describing the trajectory of a fluid particle in an incompressible two-dimensional flow are

$$\frac{dx}{dt} = \frac{\partial \Psi}{\partial y}, \quad \frac{dy}{dt} = -\frac{\partial \Psi}{\partial x} \quad (1)$$

where Ψ is the stream function of the flow. This is a Hamiltonian system with Ψ playing the role of the Hamiltonian. If the flow is steady (Ψ time independent) particle motions are integrable, the trajectories being simply the streamlines. Time dependent flows, however, can produce chaotic particle trajectories, at least in some regions of the flow.

A dipolar vortex can be modelled, in a first approximation, by a couple of point vortices of (initially) equal but opposite strengths $\kappa_1 = 1$ and $\kappa_2 = -1$, separated by a constant distance $d = 1$. With dimensionless time defined as $t^* = t/2\pi$, the point vortices move along a straight line with a constant velocity $V_0 = 1$. The stream function of the flow induced by this unperturbed dipole (with the vortices in $y = \pm d/2$) in a frame moving with the structure is

$$\Psi = -\kappa_1 \ln(x^2 + (y - d/2)^2) - \kappa_2 \ln(x^2 + (y + d/2)^2) + C \quad (2)$$

where the correction term $C = -y$.

With the models introduced in the following section, it will be necessary to write $\Psi = \psi_u(x, y) + \varepsilon \psi_p(x, y, t)$ and to change C accordingly to obtain a stationary frame; here, ψ_u represents the unperturbed, steady state and ψ_p the time-periodic perturbation.

For time-periodic flows a significant simplification of the description of particle motion is achieved by using the Poincaré map—the map of the particle location $(x(t_0), y(t_0))$ to the location one period later $(x(t_0 + T), y(t_0 + T))$. For

$\varepsilon = 0$, a point and its mapping lie on the same streamline. There exist two fixed points p_+ and p_- corresponding to the front and rear stagnation points of the dipole, respectively. Both are of hyperbolic type so that there is a collection of orbits forming a line that approaches p_- as $t \rightarrow +\infty$, called the stable manifold, and a collection of orbits that emanates from p_+ (i.e. approaches p_+ as $t \rightarrow -\infty$), called the unstable manifold. In the unperturbed case the unstable manifold of p_+ and the stable manifold of p_- coincide and correspond to the separatrix (figure 1a).

For $\varepsilon \neq 0$ the fixed points persist and the unstable manifold of p_+ smoothly emanates from p_+ as before, but in this case undergoes strong oscillations as it approaches p_- . A fluid mechanical analogy illustrates the numerical computation of the unstable manifold: a circle of tracers is placed around the stagnation point and as times progresses the small circle will be stretched in the direction of the unstable manifold. The stable manifold is constructed in a similar way, but the integration now backwards in time.

The structure which results from the intersection of the manifolds of the two hyperbolic points is called a heteroclinic tangle (figure 1b). The intersecting manifolds create a mechanism for transport of fluid between the interior and the exterior of the vortex dipole in the following way. Note that the area ABCD in figure 1c maps to the area A'B'C'D'. This is because (i) the points A,B,C,D lie on (at least) one manifold and therefore they map to points on the same manifold; and (ii) the Poincaré map preserves orientation (see Wiggins, 1992). If the upper half of the trapped fluid is redefined as that enclosed by p_+ C on the

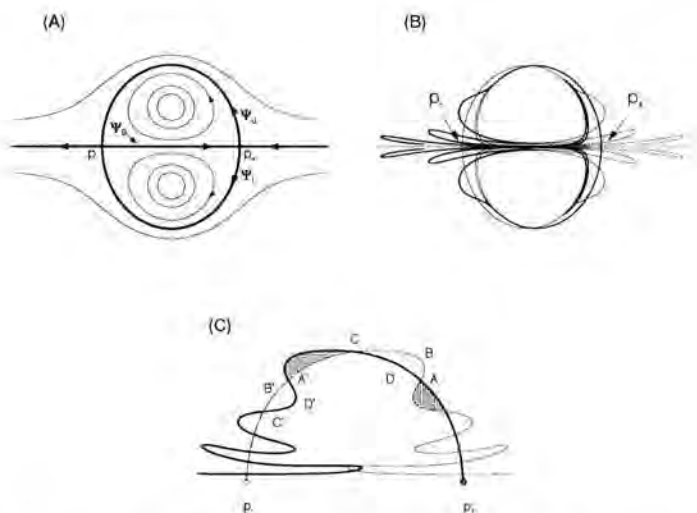


Fig. 1. (a) Streamlines of an unperturbed point-vortex dipole. (b) The heteroclinic tangle in the perturbed case. The thick line is the unstable manifold (the observable structure in flow visualization) and the thin line is the stable manifold. (c) The transport mechanism in the heteroclinic tangle. Region ABCD is mapped to A'B'C'D' (see text).

unstable manifold of p_+ , and Cp_- on the stable manifold of p_- and p_+p_- on the x -axis, then the area ABCD represents the fluid that will be entrained in the next cycle. Similarly, the dotted area near A represents the fluid that will be detrained in the next cycle. Since the flow is incompressible, the area entrained is equal to the area detrained in every cycle.

The exchange of mass can be evaluated directly from the discrete set of points defining the manifolds. Once a single lobe is identified the area follows from $\mu = \int x dy$ along AB-BA. This method is valid for every amplitude of perturbation ε .

For small ε , one can obtain an $O(\varepsilon)$ approximation for the area of a lobe by using the Melnikov function (Rom-Kedar *et al.* 1990). The area of a lobe is given by

$$\mu = \varepsilon \int_{t_{01}}^{t_{02}} M(t_0) dt_0 + O(\varepsilon^2) \quad (3)$$

where t_{01} and t_{02} are two adjacent zeros of the Melnikov function $M(t_0)$ (i.e. they correspond to adjacent intersections of the unstable and stable manifolds). $M(t_0)$ is defined as

$$M(t_0) = \int_{-\infty}^{\infty} \|\vec{U}(\vec{x}_u(t)) \times \vec{u}(\vec{x}_u(t), t + t_0)\| dt \quad (4)$$

Here $\vec{U} = (\partial\psi_u/\partial y, -\partial\psi_u/\partial x)$ is the unperturbed flow; $\vec{u} = (\partial\psi_p/\partial y, -\partial\psi_p/\partial x)$ is the time-periodic perturbation; and $\|\cdot\|$ denotes the magnitude of a vector. The coordinates of points belonging to the unperturbed manifold $\vec{x}_u = (x_u(t), y_u(t))$ are expressed as a function of the parameter t .

Analytical and numerical results

Strengths perturbations

As described by e.g. VFvH, the evolution of a symmetric point-vortex dipole on the β -plane is governed by a second order ordinary differential equation for the dipole's direction of propagation. In the limit of small β -effect with respect to the vortex circulation ($\beta r L^2/\kappa_0 \ll 1$) and small initial deviation from eastward propagation ($\alpha_0 \rightarrow 0$), the following equations can be used for the vortex circulation (κ), the meridional position of the dipole's centre (ξ) and the direction of propagation (α)

$$\kappa_{1,2} = \pm 1 - \beta \xi \quad (5)$$

$$\frac{d\xi}{dt} = \alpha \quad (6)$$

$$\frac{d\alpha}{dt} = -2\beta\xi \quad (7)$$

Initial conditions are $\xi(0) = 0$, and $\alpha(0) = \alpha_0$. Therefore, the perturbation of the vortices' strengths is approximately given by:

$$\kappa_1(t) = 1 - \varepsilon_1 \sin \omega t \quad (8)$$

$$\kappa_2(t) = -1 - \varepsilon_1 \sin \omega t \quad (9)$$

where $\varepsilon_1 = \alpha_0 \sqrt{\beta/2}$, and $\omega = \sqrt{2\beta}$.

Because of the varying asymmetry of the vortices, the vortex pair neither moves along a straight line nor rotates around a fixed point. The motion of the vortex can be described as a rotation with varying angular speed

$\Omega(t) = -2\varepsilon_1 \sin \omega t$ around a point lying on the line defined by the two point vortices and located at a varying distance $R(t) = (\varepsilon_1 \sin \omega t)^{-1/2}$ from the dipole's centre. A steady stream function results from substitution of κ_1 , κ_2 and the correction term $C = \Omega(t)[x^2 + (y - R(t))^2]/2$ in (2).

Because of the asymmetries present in the dipolar flow structure not only the outer manifolds, but also the middle manifold will break up. As a consequence, besides entrainment and detrainment of fluid, exchange of mass between the two dipole halves will occur.

Two dimensionless parameters characterize the perturbation: the perturbation amplitude ε_1 and the ratio between the (dimensionless) perturbation period

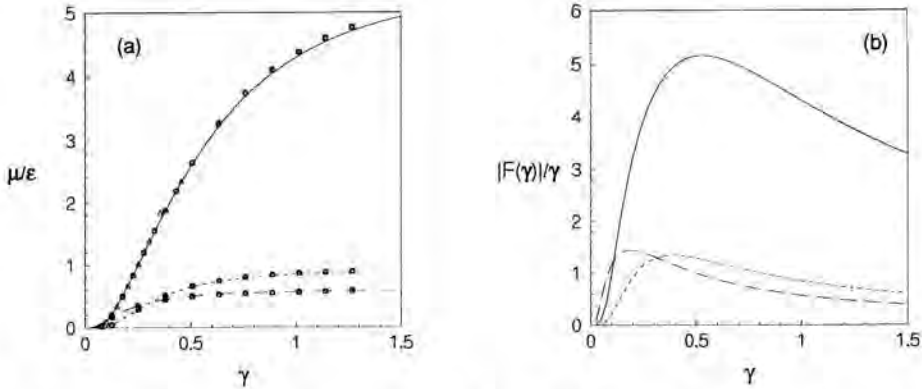


Fig. 2. Transport in the perturbed point-vortex dipole: (a) lobe area μ (normalized by the perturbation amplitude ε), and (b) exchange rate $\mu^* = F(\gamma)/\gamma$ as a function of γ . The lines indicate the Melnikov function calculations, and the markers denote results from direct numerical integration of the advection equations.

$T = \omega^{-1}$ and a timescale associated with the dipole's translation d/V . The latter parameter is defined to be $\gamma = (2\beta)^{-1/2}$.

The lobe area according to the Melnikov function is $\mu = \varepsilon_1 F(\gamma) + O(\varepsilon_1^2)$, where $F(\gamma)$ is the numerically computed function shown in figure 2a. The dotted line represents the exchange of mass between interior and exterior and the broken line exchange between the dipole's halves. In the same figure the markers show the lobe areas evaluated by direct numerical integration for $\varepsilon_1 = 0.01, 0.05$ and 0.1 .

Size perturbations

The meandering trajectory of a dipolar vortex on a topographic β -plane causes the water column to be alternately stretched and squeezed. As a result the distance between the vortex centres will decrease as the dipole moves into deep water and increase as the dipole moves towards shallower water. This effect is modelled using the same point-vortex dipole but imposing on it a sine-like variation of the distance between the vortices: $d = d_0(1 + \varepsilon_2 \cos \omega t)$. The point vortices have constant circulation κ_0 and $-\kappa_0$, respectively. Because of symmetry about the x-axis the middle manifold remains unaffected and no exchange of fluid can occur between the two halves of the vortex dipole.

In figure 2a the solid line represents the absolute value of the function $F(\gamma)$ obtained with the Melnikov function and the markers show the lobe areas (divided by the perturbation amplitude) obtained from direct numerical integration of the advection equations for $\varepsilon_2 = 0.01, 0.05$ and 0.1 .

Perturbation of the dipole's size produces stronger entrainment/detrainment than perturbation of the strengths. For strength perturbation, the exchange of fluid between the two halves of the vortex pair is more than the exchange of fluid between the interior and the exterior of the vortex pair up to $\gamma = 0.3$. For greater values of γ , the relation is reversed. For all three ways of exchange of fluid, the function $F(\gamma)$ increases with γ . This can be understood because a larger period allows for more fluid to be exchanged. However, this behaviour changes for the exchange rate (mass exchanged per unit of time). As can be seen in figure 2b, the exchange rate is maximal where $F(\gamma)/\gamma$ is maximal. In the case of size perturbation, we found this to occur for $\gamma = 0.528 \pm 0.001$. For strength perturbation, the exchange rate between interior and exterior fluid is maximal for $\gamma = 0.386 \pm 0.001$ and the exchange rate between the two halves of the vortex pair is maximal for $\gamma = 0.189 \pm 0.001$.

Particle transport

All fluid detrained during the first cycle is originally "interior fluid"; this is, however, not necessarily the case for later cycles. Some of the detrained fluid will be "exterior fluid": fluid parcels originally located outside the dipole, later being entrained and finally, after a few cycles are returned to the surroundings.

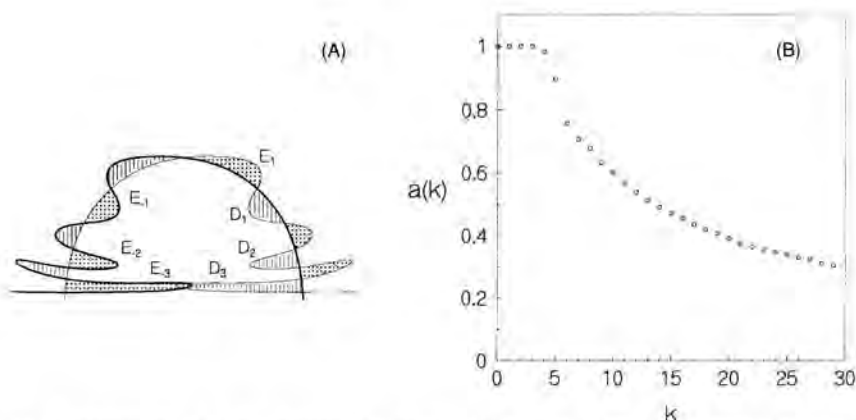


Fig. 3. (a) Intersection of detrainment (D_3) and entrainment lobes (E_{-3}) provides information about residence times and transport of species (see text) (b) Fraction a of the detrainment lobe formed by "interior fluid", as a function of the number of perturbation cycles k .

The determination of the amount of interior fluid that is detrained in cycle k is highly simplified by the knowledge of the lobe geometry. In particular by the intersections of the entrainment (E) and detrainment (D) lobes, as shown in figure 3a. A positive subindex indicates in which cycle, forward in time, the lobe will change the region; a negative subindex indicates the cycle, backwards in time, in which the lobe changed of region. The intersection of E_{-3} and D_3 that will be detrained during the third cycle represents fluid that was located outside the dipole three cycles before. Thus in general $D_i - D_i \cap E_{-j}$ gives the area of interior fluid that escapes the dipole in the $k = i + j$ period of the perturbation. In figure 3b the fraction of interior fluid that is detrained after k cycles is shown for the case $\varepsilon_2 = 0.1$ and $\kappa = 0.15$.

Experiment

For comparison, laboratory observations and a numerical simulation that matches the parameters used in the experiment are shown. For details on the experimental technique see VFvH. The experimental parameters are: period of the rotating table $T = 11$ s; fluid depth $h_0 = 18$ cm; and gradient of the sloping bottom is 0.04. With these parameters the topographic β -effect measured $\beta = 0.247 \text{ m}^{-1} \text{ s}^{-1}$ (see VFvH). In this experiment the dipole was started at an angle $\alpha_0 = \pi/4$. The angular frequency of the perturbations and the amplitude of strength perturbation can be computed directly from the experimental parameters: $\varepsilon_1 = \alpha_0 \sqrt{\beta/2}$, $\gamma = (2\beta)^{-1/2}$; and the amplitude of the size perturbation is measured directly from the experiment, yielding $\varepsilon_2 = 0.1$.

Three stages in the dipole's evolution are shown in figure 4. One lobe has been formed when the dipole reaches its northermost position (figure 4a) by detrainment of fluid from the negative half (upper side in the picture). A second lobe

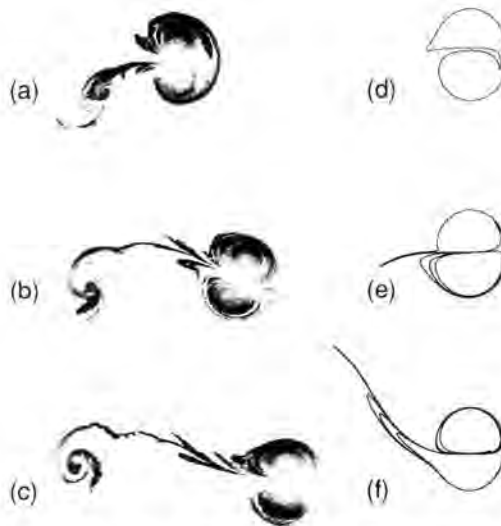


Fig. 4. The formation of lobe-like structures in the fluid transported by a dipolar vortex on a topographic β -plane. Experimental images (a)-(c) and numerical calculations (d)-(f) are shown at $T/4$, $T/2$ and $3T/4$, with T the period of the dipole's oscillatory motion.

is formed on the negative half when the dipole returns to its equilibrium position (figure 4b). Both lobes are stretched along the tail (figure 4c).

The deformation of the patch of dye is simulated numerically by following the evolution of the initial separatrix. In figure 4d–4f we can see the deformation of the separatrix in a frame moving with the vortex pair at stages corresponding with the experimental figures. While the distance between the two vortices increases and the negative vortex becomes stronger, fluid is entrained into the dipole and begins to circle around the negative vortex (figure 4d). Detrained fluid is left behind from the positive half of the vortex dipole and forms a long tail. After this stage fluid is also entrained into the positive vortex (figure 4e) and fluid is detrained from the negative half, forming a second lobe (figure 4f).

Qualitatively, similar features can be recognized such as entrainment and detrainment of fluid and the associated formation of lobes. Note that the long tail in the experiment is formed during the generation of the dipolar vortex and is not primarily a result of fluid detrainment. In general, not all the dye lies initially within the vortex (see VFvH). In the numerical simulation, however, the advected line corresponds with the original separatrix.

Conclusions

The exchange of fluid induced by a dipolar vortex on a topographic β -plane is investigated. The dipole meanders around lines of equal ambient vorticity if

it initially travels transversally to those lines. During the meandering, the dipole shows a variation in size (due to squeezing and stretching as the dipole moves between the shallow and deep sides of the tank) and a variation in the intensity of the individual vortices (due to conservation of potential vorticity). Consequently there is a continuous exchange of mass between the interior and the exterior fluid of the dipolar vortex, and between the two dipole halves.

The two exchange mechanisms have been studied independently using a point-vortex model, which has been shown to describe reasonably well the meandering of the dipole (see VFvH). The exchange of fluid due to the strengths perturbation is studied in the linear limit (α_0 small) of the modulated point-vortex dipole and the effect of size perturbation is studied by prescribing a periodic variation of the distance between the point vortices.

Recent developments in the theory of transport in dynamical systems (lobe dynamics, see Rom-Kedar *et al.* 1990) have been applied to these particular problems. For small amplitudes of perturbation the area of a lobe evaluated using direct numerical integration corresponds well with the results obtained using the Melnikov function.

For equal amplitudes of perturbation (i.e. the same percentual variation with respect to the unperturbed value), the size variation causes more exchange of fluid than the variation of strength.

Although the total exchange of fluid increases with increasing perturbation period, the exchange rate shows a maximum for a specific value of the period of perturbation. This value is different for each mass exchange mechanism.

The analysis of the transport of species (particles with a particular origin, e.g. interior or exterior regions of the dipole) is simplified by the knowledge of the lobe geometry. For a specific set of parameters, this is illustrated by the computation of the fraction of detrained fluid that was originally within the dipole.

Numerical simulations of the deformation of the separatrix using size and strength perturbation is compared with laboratory observations of dye patterns produced by a dipolar vortex on a topographic β -plane. Good qualitative agreement exists. The observed differences are likely due to: (i) the discrete representation of the original vorticity distribution (ii) the absence in the model of relative vorticity generated by advection of ambient fluid.

Acknowledgement

O.U.V.F. gratefully acknowledges financial support from the Stichting voor Fundamenteel Onderzoek der Materie (FOM).

References

- Rom-Kedar, V., A. Leonard, and S. Wiggins, 1990 - An analytical study of transport, mixing and chaos in an unsteady vortical flow. *J. Fluid Mech.* **214**, 347-394.

- Velasco Fuentes, O.U. and G.J.F. van Heijst, 1994a - Experimental study of dipolar vortices on a topographic β -plane. *J. Fluid Mech.* **259**, 79–106. See also: Velasco Fuentes, O.U. and G.J.F. van Heijst, 1994b Laboratory experiments on dipolar vortices in a rotating fluid. This issue.
- Wiggins, S., 1992 - *Chaotic Transport in Dynamical Systems*. Springer.

Fluid Dynamics Laboratory
Eindhoven University of Technology
P.O. Box 513
5600 MB Eindhoven
The Netherlands

The February 1989 Pacific Block as a Coherent Structure

Abstract

Throughout the latter part of January and most of February 1989 a large-scale intense blocking event occurred over the Northeast Pacific Ocean. During its lifetime the block exhibited two distinct spatial configurations corresponding to Omega and dipole shapes, respectively. A time series of scatter diagrams of 5-day-averaged 500 mb geostrophic stream function versus potential vorticity is computed. It is suggested that both the Omega and dipole forms may correspond to free modes. It is shown that as the block develops the contribution of the gravest, quasi-barotropic mode dramatically increases and forms the dominant mode.

Introduction

Over the past decade, attempts have been made to model atmospheric blocking using idealized solutions of the quasi-geostrophic equations that can persist for times comparable to blocking durations. Because the timescale associated with a block (on the order of about 10 days; see Rex (1950)) and the horizontal amplitudes are larger than that typically associated with transient baroclinic disturbances, a reasonable conjecture is that blocking may correspond to the atmospheric attempting to configure itself into a localized, finite-amplitude free-mode that is rather stable to smaller eddy disturbances. In quasi-geostrophic dynamics, a free-mode is characterized formally by a functional relation $q = q(\psi)$, where q is the potential vorticity and ψ the stream function.

One way of testing whether or not a particular observed flow pattern is developing into a free-mode is to examine the *geostrophic scatter diagrams* for the flow (see Read *et al.*, 1986). Scatter diagrams are simply two-dimensional scatter plots of the observed stream function versus the observed potential vorticity from many points within a given geographical region at a given height.

Read *et al.* (1986) presented a technique for computing the area associated with a given scatter diagram. For a free mode, the scatter plot collapses onto a

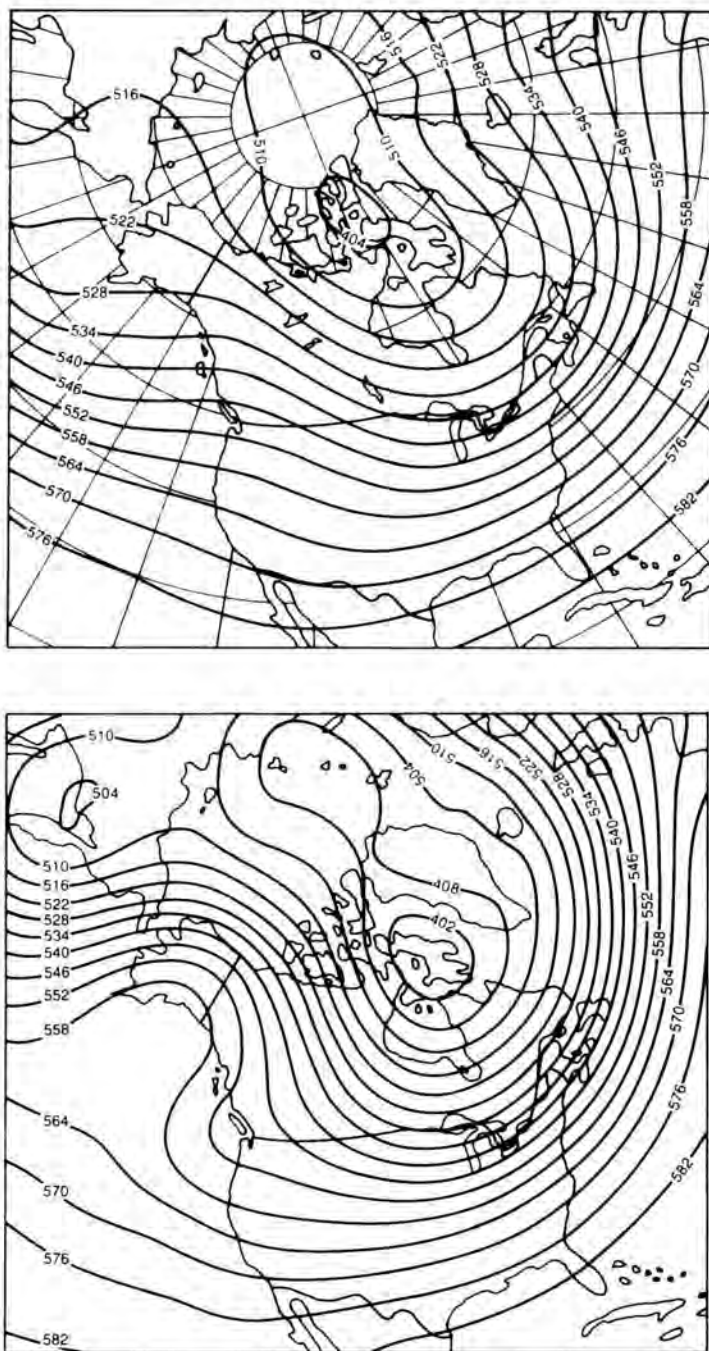


Fig. 1. Mean 500 mb geopotential height [dam.] for February; (a) climatological average; (b) February 1989. Adapted from Canadian Meteorological Centre, *Monthly Review*, May 1989.

curve, and the area *must* be identically zero because the integrated or net flux of vorticity is zero. The *observed* scatter diagram area can therefore be viewed as a measure of the degree of departure of the observed flow from a quasi-geostrophic free-mode state.

Butchart *et al.* (1989) presented a theoretical and diagnostic study of an atmospheric block over central Europe. One of the most important conclusions of their study was the clear indication of the development of a simple non-analytic pattern in the scatter diagrams which had a striking resemblance to the scatter diagram for a geostationary modon solution. The principle purposes of this extend abstract is to very briefly present the results of a similar study for a blocking episode over the Northeast Pacific Ocean (see Figure 1). The reader is referred to Ek and Swaters (1993) for a complete description of our methods, analysis and conclusions.

The time series of 5-day-averaged scatter diagrams that we present shows a tendency for the scatter diagram area to decrease as the block develops; strongly suggesting that the blocking configuration observed is more free-mode like than either the pre- or post-block configurations. The baroclinic evolution of the block is also examined. Our results show a tendency toward a quasi-barotropic configuration as the block develops. This barotropic configuration is maintained throughout the life of the block. However, immediately prior to the formation of the dipole block we can identify a brief period with a slight increase in baroclinic activity associated with a transient cyclone. It is interesting to speculate that this baroclinic activity is associated with the eddy-straining process proposed by Shutts (1983, 1986) as a mechanism for driving atmospheric blocks into a dipole configuration.

The data set

The data (supplied by the Canadian Meteorological Centre) consist of objectively-analyzed archived data on a latitude-longitude grid, at a two-degree spacing. The full grid extends from 30°N to 80°N and westward from 20°W to 120°E (see Figure 2). Five levels were used: 850, 700, 500, 400, and 250 mb. At each level, 3 data fields were used: The geopotential height of the pressure surface denoted as Z ; the temperature denoted as T ; and the dew-point depression given by $T - T_d$. There are normally four data-sets for each day (one for every 6 hours), running for 39 days from 21 January through to 28 February, 1989. The initial preparation consisted of time-averaging (at each grid point) each data field, over the four synoptic periods per day. This smoothed out the smallest-scale disturbances.

The geostrophic stream function was calculated at each grid point (i, j) as $\psi_{i,j} \equiv f_0^{-1} g Z_{i,j}$, where f_0 is the Coriolis parameter at 60°N, g is the gravitational acceleration, and $Z_{i,j}$ is the geopotential height of the isobaric surface. The vertical component of absolute vorticity was calculated as $\nabla^2 \psi_{i,j} + f$, using a centred finite difference scheme for the Laplacian term. We used a β -plane approxima-

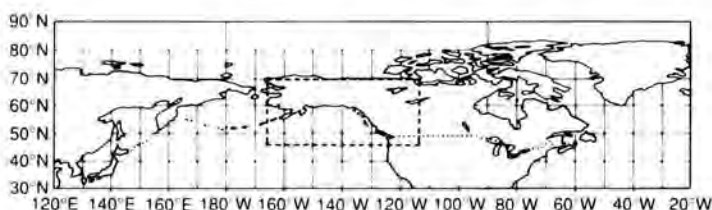


Fig. 2. The region covered by the data. The box over the Gulf of Alaska approximates the block's interior.

tion throughout our work. The baroclinic stretching term in the potential vorticity was computed using a finite-difference approximation.

We applied first a spatial and then a temporal smoother to the vorticity and stream function fields. The spatial smoother is a simple 5-point smoother, weighted to take into account the variable zonal grid spacing. The fields were then time-averaged over 5 days, with equal weights. All calculations in this paper begin with the 5-day mean fields, each centred on the date listed.

Throughout this study, the region occupied by the block was approximated by a horizontal box-shaped area, bounded by the latitudes 46°N and 70°N , and longitudes 114°W and 166°W . This box-shape was subjectively chosen to surround, as closely as possible, the portion of the block having closed stream function and vorticity contours, on as many days as possible.

Scatter diagrams and free modes

A means of testing the applicability of free modes to blocking originates with an interesting result of Read *et al.* (1986). Suppose that we pick an arbitrary, simple horizontal curve enclosing a region $\mathcal{R}_{(x,y)}$, in physical (x, y) space. The net flux of vorticity across the curve, $\partial\mathcal{R}_{(x,y)}$, due to the geostrophic wind, can be written as

$$F_q \equiv \oint_{\partial\mathcal{R}_{(x,y)}} q \vec{v}_g \cdot \hat{n} dl, \quad (1)$$

where $\vec{v}_g \equiv \hat{k} \times \nabla\psi$ is the geostrophic wind, \hat{n} is the outward unit normal vector to the curve $\partial\mathcal{R}_{(x,y)}$, dl is the differential arc-length, \hat{k} is the unit vector pointing vertically upward, and $\nabla = (\partial/\partial x, \partial/\partial y)$.

A positive flux entails a net export of cyclonic vorticity. We can apply the two-dimensional divergence theorem to (1) to get

$$\begin{aligned} F_q &= \iint_{\mathcal{R}_{(x,y)}} \nabla \cdot [q(\hat{k} \times \nabla\psi)] dx dy \\ &= \iint_{\mathcal{R}_{(x,y)}} J(\psi, q) dx dy. \end{aligned} \quad (2)$$

The second integral in (2) may be directly transformed into an integral over the corresponding region $\mathcal{R}_{(\psi, q)}$ in (ψ, q) space as follows:

$$\begin{aligned} F_q &= \int \int_{\mathcal{R}_{(x, y)}} \text{sign}[J(\psi, q)] |J(\psi, q)| dx dy, \\ &= \int \int_{\mathcal{R}_{(\psi, q)}} \text{sign}[J(\psi, q)] d\psi dq. \end{aligned} \quad (3a)$$

The sign of the Jacobian is positive if the curve in (ψ, q) space is closed off in the same sense as the corresponding (x, y) space curve, which we take to be counter-clockwise. The sign is negative for (ψ, q) curves that are closed off in the

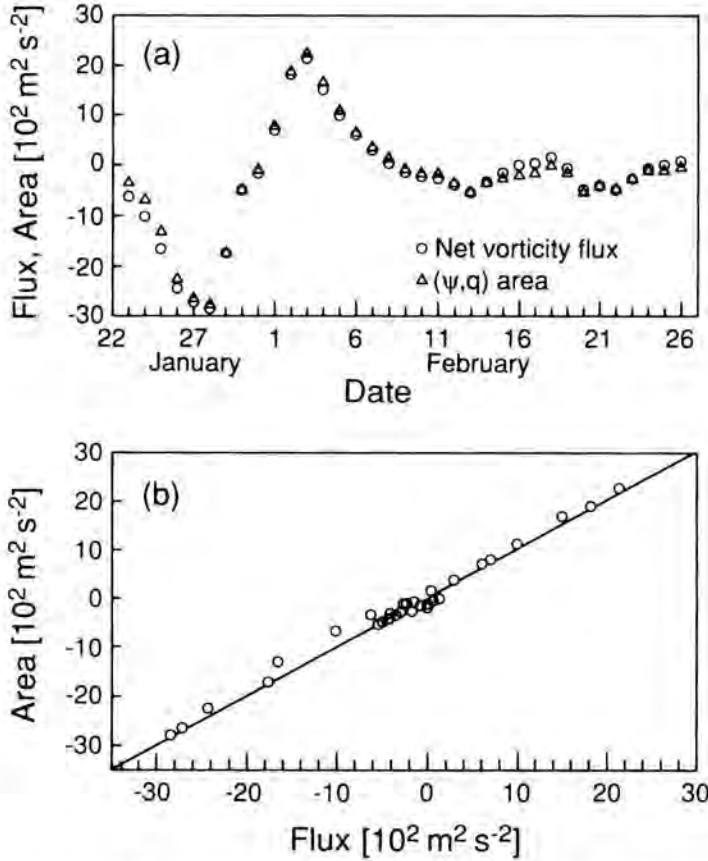


Fig. 3. (a) Time series of the area of the 500 mb net vorticity flux across the box bounded by latitudes 46° – 70°N and longitudes 114° – 166°W as computed directly from cartesian coordinate and q/ψ – scatter diagram representations, respectively. (b) The same variables as (a): net vorticity flux calculation in cartesian coordinates plotted against the q/ψ – scatter diagram calculation.

clockwise sense. Alternatively, we can relate the area of the q/ψ - scatter diagram, denoted by $A_{(\psi, q)}$, to the Jacobian as follows:

$$\begin{aligned} A_{(\psi, q)} &\equiv \iint_{\mathcal{R}(\psi, q)} d\psi dq \\ &= \iint_{\mathcal{R}(x, y)} |J(\psi, q)| dx dy. \end{aligned} \quad (3b)$$

In the case of a free mode formally defined by $q = q(\psi)$, we have $J(\psi, q) = 0$, and both the area of the (ψ, q) region, and F_q , must vanish. It is evident that either of the two quantities, F_q or $A_{(\psi, q)}$, may be thought of as a measure of the *departure* of the system from *any* free mode of the form $q = q(\psi)$.

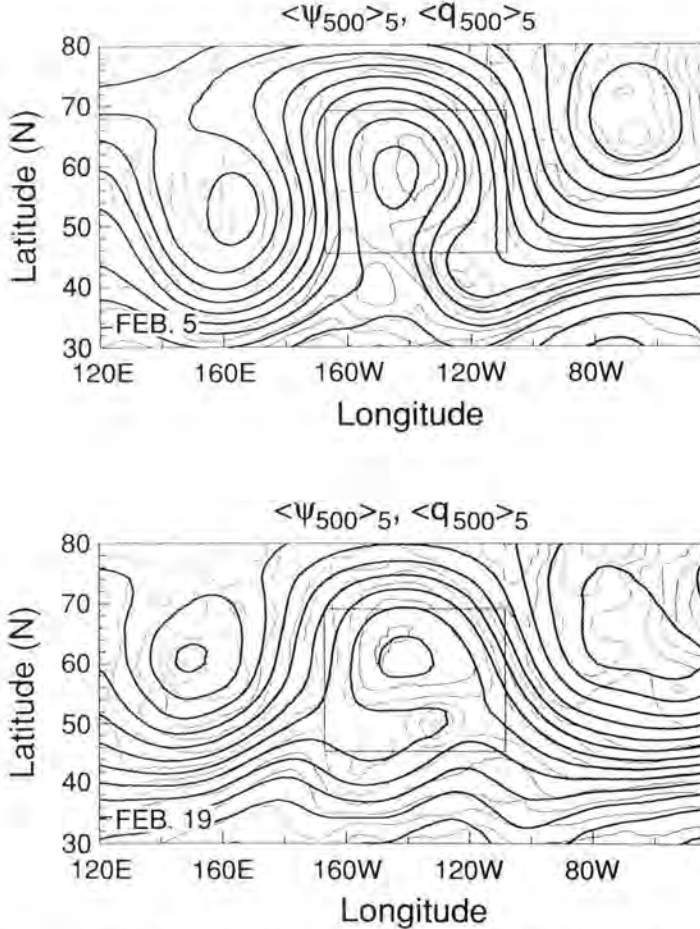


Fig. 4. Five-day mean 500 mb geostrophic stream function, ψ (solid contours), and potential vorticity, q (light dashed contours). Contour intervals are $6 \times 10^6 \text{ m}^2 \text{ s}^{-2}$ for ψ and $2 \times 10^{-5} \text{ s}^{-1}$ for q . a) Feb. 5, b) Feb. 20, 1989.

In Figure 3 we present time-series of the computed net vorticity flux using the cartesian representation (1) and the q/ψ - scatter diagram area representation (3a), respectively. The two quantities are in quite good agreement, as they should be, from which we conclude that it is possible to calculate the net vorticity flux using either representation as suggested by Read *et al.* (1986), and that our data are reasonably consistent. Repeating the calculations using a slightly larger box (Ek, 1992) produces nearly identical results, suggesting that the sensitivity to our choice of boundary, in this case, is not too severe.

The time series of the net flux clearly shows that it remains near zero values for the lifetime of the block. This suggests that the block is very near to an inertial free mode of the quasi-geostrophic equations, in the geostationary reference frame. The vorticity flux time series does not seem to distinguish between the dipole and Omega blocking configurations.

Based on the complete series of 5-day mean 500 mb charts, we may subjectively consider the block to have evolved between two states. From about February 1 to 14, the flow pattern had the familiar 'Omega' (Ω) shape (see Figure 4a). During the second, shorter period, February 18 to 21, shortly before it broke down, the block developed a discernible dipole-like form (see Figure 4b). The full series of 500 mb charts is given in Ek (1992).

Baroclinic structure

In order to study the baroclinic evolution of the block we computed a time-series of spectral coefficients for the blocking stream function (defined to be the total dynamic stream function minus the stream function associated with the background zonal flow) associated with the orthonormalized vertical modes given in terms of pressure coordinates by (see Ek and Swaters (1993) for details of the derivation)

$$\frac{d}{dp} \left(\frac{1}{\sigma_r} \frac{d\Psi_n}{dp} \right) + f_0^{-2} (\gamma_n - A_0) \Psi_n = 0, \quad (4a)$$

$$\frac{d\Psi_n}{dp} - \frac{dU(p)/dp}{U(p)} \Psi_n = 0, \quad (4b)$$

on $p = p_r$ (250 mb) and $p = p_h$ (850 mb), respectively, and where

$$A_0(p) \equiv \left[f_0^2 \frac{d}{dp} \left(\frac{1}{\sigma_r} \frac{dU}{dp} \right) - \beta \right] / U, \quad (4c)$$

where $U = U(p) > 0$ is the eastward background zonal flow, and where σ_r , f_0 , and β are the static stability, and constant Coriolis and beta parameters, respectively.

In order to be able to compare the average contribution of each mode to the

vertical structure of the blocking eddy, we computed the root-mean-square (RMS) value of each coefficient, defined as

$$\langle a_n \rangle_{\text{RMS}} = \left[\frac{\sum_{x,y}^{(N \text{ points})} [a_n(x,y)]^2}{N} \right]^{1/2},$$

where the sum is understood to be over each horizontal grid point and $a_n(x,y)$ is the spectral coefficient associated with the n^{th} vertical mode.

Figure 5 presents a time-series for the first four root-mean-square coefficients. We can see that as the block develops, there is a significant increase in the relative contribution of $\langle a_0 \rangle_{\text{RMS}}$ suggesting a quasi-barotropic configuration.

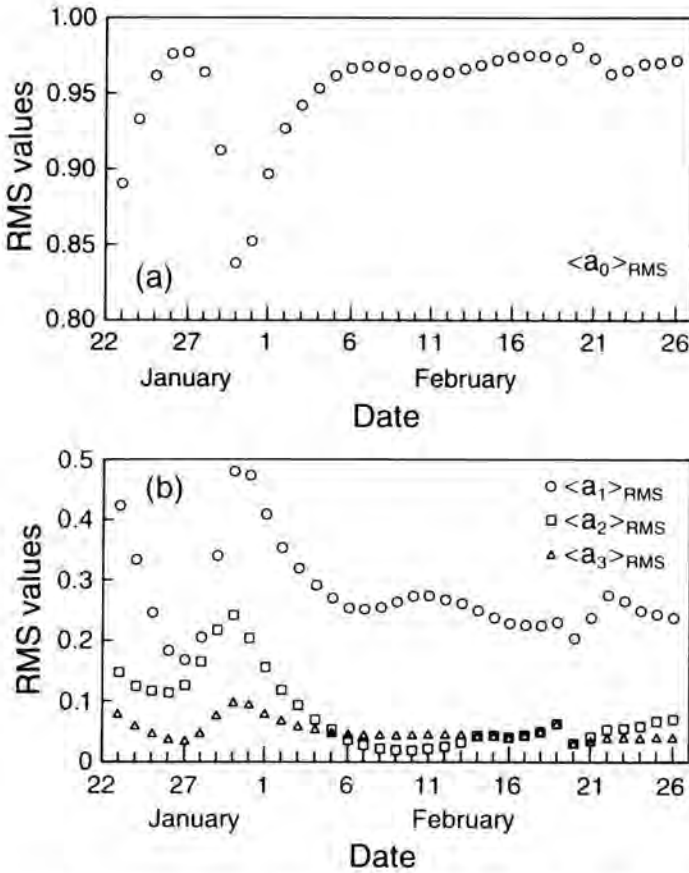


Fig. 5. Time series of normalized Root-Mean-Square (RMS) Fourier coefficients of the four gravest vertical normal modes. (a) Gravest mode. (b) First, second, and third modes. Normalizations are such that the sum of the squares of each day's four RMS values is unity.

Acknowledgement

Preparation of this manuscript was supported in part by research grants awarded by the Natural Sciences and Engineering Research Council of Canada and by the Atmospheric Environment Service of Canada.

References

- Butchart, N., K. Haines, and J.C. Marshall, 1989 - A theoretical and diagnostic study of solitary waves and atmospheric blocking. *J. Atmos. Sci.* **46**, 2063–2078.
- Canadian Climate Centre, 1989 - *Clim. Pers.* **11**, nos. 1–9.
- Canadian Meteorological Centre, 1989 - *Mon. Rev.* May, 1989.
- Ek, N.R., 1992 - Geostrophic scatter diagrams and the applicability of free mode theory to a Northeast Pacific Blocking Episode. M.Sc. Thesis, Division of Meteorology, Department of Geography, University of Alberta, Edmonton, Alberta, Canada, T6G 2G1, 123 pp.
- Ek, N.R., and G.E. Swaters, 1993 - Geostrophic scatter diagrams and the application of quasi-geostrophic free mode theory to a Northeast Pacific blocking episode. Submitted to *J. Atmos. Sci.*
- Read, P.L., P.B. Rhines, and A.A. White, 1986 - Geostrophic scatter diagrams and potential vorticity dynamics. *J. Atmos. Sci.* **43**, 3226–3240.
- Rex, D.F., 1950 - Blocking action in the middle troposphere and its effect upon regional climate. I. An aerological study of blocking action. *Tellus* **2**, 196–211.
- Shutts, G.J., 1983 - The propagation of eddies in diffluent jetstreams: eddy vorticity forcing of 'blocking' flow fields. *Quart. J. Roy. Meteor. Soc.* **109**, 737–761.
- Shutts, G.J., 1986 - A case study of eddy forcing during an Atlantic blocking episode. *Adv. Geophys.* **29**, 135–161.

Applied Mathematics Institute
University of Alberta
Edmonton, Alberta, Canada T6G 2G1

Stability of Isolated Compound Vortices

Abstract

The stability of the members of a class of isolated vortices is discussed. Two well-known examples of stable isolated flows are the dipole and tripole. The existence of an even more complicated stable isolated flow is demonstrated here. Like the dipole and tripole, it is also a compound vortex and consists of a core vortex surrounded by three satellite vortices of opposite sign. The core of this 'quadrupole' is triangular in shape and the satellites are semicircular. The stability of this flow is inferred from high-resolution numerical simulations and analysis of point-vortex models. Further consideration suggests that all higher order n -poles will be unstable to merger of the satellite vortices.

Introduction

Isolated two-dimensional vortices are models for the localized flow structures that are prevalent in geophysical flows. By isolated we mean a vortex whose net circulation is zero so that the velocity field induced by the vortex falls off faster than $1/r$ in the far field, where r is the distance measured from the center of the vortex. Such vortices are created, for example, by topographic forcing of islands or mountains, instabilities of major current systems such as the Gulf Stream, and strong localized wind forcing on the ocean surface. Two-dimensional models provide a first approximation to such vortices and have been extensively studied.

A simple model for circularly symmetric isolated flows consists of a core of single-signed vorticity surrounded by an annulus of vorticity of opposite sign, with amplitudes such that the total circulation vanishes. There have been numerous studies of the stability and evolution of such vortices. If the annulus is sufficiently narrow, so that the fall off of vorticity from its maximum to minimum value is sufficiently steep, then the flow is unstable. Numerical simulations and laboratory experiments (cf., Carton & McWilliams 1989, Kloosterziel & van Heijst 1991, Carnevale & Kloosterziel 1994) show that under these conditions the vorticity regions can break up and reassemble into more complex, yet more stable, structures. One common scenario is the formation of a tripole. In that case the core becomes elliptical in shape while the annulus clumps and separates into two distinct vortices that remain as satellites of the core. The entire com-

pound vortex simply rotates, as in solid-body rotation, at a constant angular rate about the centre of the core. Another common scenario, called dipole splitting, results if the initial profile is even steeper than for the case which produces the tripole. The instability then proceeds initially as in the case of tripole formation, but eventually the satellites shear apart the core, which then rolls up into two new vortices. This results in two dipoles that propagate away from each other.

The dipole consists of two oppositely-signed vortices that advect each other, and it appears to be a very stable structure. The well-known analytic model for this flow was given by Lamb (1932), and many writers, therefore, refer to it as the Lamb dipole. Recently, reference to an earlier publication (Chaplygin, 1903) of this analytic model has been made, but we have not yet seen a copy of this work.[†] This dipole model has been of considerable interest since it can be used to represent various geophysical phenomena such as mushroom vortices (cf., Federov 1989). Furthermore, this dipole has a generalization to a similar isolated flow on the β -plane, called the modon, and as such has generated considerable interest due to its possible relevance in the phenomenon of atmospheric blocking (cf., Stern 1975, McWilliams 1980). In numerical simulations and laboratory experiments, the dipole appears to be very stable. Diagrams summarizing the stability of the modon to various types of perturbations have been published by McWilliams *et al.* (1981) and Carnevale *et al.* (1988a). It is hard to give a precise stability range because much depends on the exact form of the perturbation, but it seems that modons are most sensitive to forcing on length-scales comparable to their own diameter and that perturbations of greater than 10%, relative to its unperturbed strength, are necessary for destruction. The usual instability by which the modon is destroyed involves a separation of the two regions of oppositely-signed vorticity (Carnevale *et al.* 1988b). Similar studies of the Lamb dipole show essentially the same results as in the modon case (unpublished). Although there have been many attempts at proving the stability of dipoles, an uncontested proof remains elusive (cf., Carnevale *et al.* 1988c, Nycander 1992).

An even more complicated isolated flow is the tripole. It consists of a central core of vorticity of one sign and two satellites of opposite sign, all co-linear and all rotating at constant rate about the center. Although this compound vortex appeared in a published numerical simulation of turbulence (Sadourny, 1985), it was not noted in that paper or any other, to our knowledge, until the work of Legras *et al.* (1988), in which the tripole was clearly pointed out as being a very stable element in an otherwise turbulent flow. Publications of laboratory work which also showed this tripole quickly followed (van Heijst & Kloosterziel, 1989). In that work, the tripole was produced as a result of the breakdown of a circularly symmetric flow as discussed above. Oceanic observations of a tripole were reported by Pingree & LeCann (1992). Laboratory studies (van Heijst *et al.* 1991) and numerical simulations (Polvani & Carton 1990) attest to the

[†] Note added in proof: Chaplygin's work is described in a recent paper by Meleshko & van Heijst (1994), *J. Fluid Mech.* **272**, 157–182.

stability of these structures. Unfortunately, there is no analytic model of tripoles with continuous vorticity. Models using three point vortices have been successful at simulating many of the properties of the tripole under external perturbations, and nonlinear stability of this three point model with respect to displacements of the satellites can be proven (Kloosterziel, 1990).

At this point, it is natural to consider whether there may be a hierarchy of more complicated stable n -poles consisting of a core vortex surrounded by $n_s = n - 1$ satellites of opposite sign. In fact, laboratory experiments on the instabilities of circularly symmetric vortices in a rotating tank (Kloosterziel & van Heijst 1991) have shown the natural evolution of a quadrupole consisting of a triangular core vortex surrounded by three semi-circular satellites of vorticity of opposite sign. Although never observed in other than a transitory state in the laboratory, subsequent numerical simulations and point vortex models led us to believe that this kind of structure can also be stable if prepared in a sufficiently symmetric way. This is further discussed in the next section.

As for the existence of compound vortices even more complicated than the quadrupole, our investigations indicate that there are none. The instability of the higher-order structures is discussed in a separate section below.

The quadrupole or triangle vortex

In rotating-tank experiments, the quadrupole is observed to break apart rather rapidly after it has formed (see Kloosterziel & van Heijst 1991, Carnevale & Kloosterziel 1994). The instability begins with two of the satellites moving closer together. One of these satellites moves in between the other satellite and the core. The two satellites are then close enough together to merge into a single vortex in the same way that two like-signed vortices merge in isolation (cf. Melander *et al.* 1988). This results in a transitory tripole stage, which then proceeds to double-dipole splitting as described above. Orlandi & Van Heijst (1992) were able to capture this formation and transitory existence of the quadrupole in numerical simulations. This encouraged us to explore more fully the mechanisms involved in this evolution, using spectral simulations and point-vortex models.

Orlandi & van Heijst (1992) used the following vorticity profile as their unperturbed basic state:

$$\zeta = -\left(1 - \frac{1}{2}\alpha r^2\right)\exp(-r^2), \quad (1)$$

where r is the radial distance from the centre of the vortex. Distances have been non-dimensionalized by L , the horizontal length-scale of the vortex, and velocities by U . This is the same profile as used in several earlier studies (e.g., Carton & McWilliams, 1989). Note that increasing α makes the vorticity in the core more uniform, the width of the annulus smaller, and the slope of the vor-

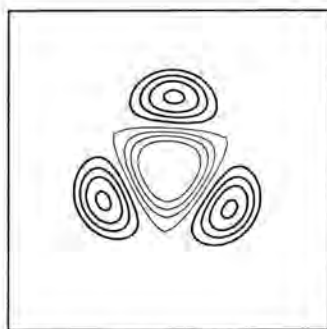


Fig. 1. Vorticity contour plot of a quadrupole vortex. Thick (thin) contours indicate positive (negative) relative vorticity. The contour level values are chosen to have increments of $\Delta\zeta = 0.2 \text{ s}^{-1}$. The dimensional velocity and length scales used in the initialization were $U = 20 \text{ cm/s}$ and $L = 11 \text{ cm}$, and the length of a side of the computational domain was 90 cm (although here we have only plotted the field over an inner square of 54 cm on a side).

ticity as a function of r steeper between the core and annulus. We will refer to α as the steepness parameter. This family of profiles is a reasonable model for the types of isolated vortices created in the tank. Orlandi & van Heijst (1992) used an initial condition in which the basic state in equation (1), with $\alpha = 5$, is perturbed with a randomly generated vorticity field defined by

$$\zeta' = \eta \exp\left(\frac{-(\alpha r^\alpha - 2)^2}{2\sigma^2}\right) - c. \quad (2)$$

Here $\eta(x, y)$ is a random number uniformly generated on the range $(-\eta_0, \eta_0)$ for each grid-point, and c is a constant chosen to ensure that the spatially integrated value of ζ' (i.e. the circulation of the perturbation) vanishes. This perturbation is concentrated at the radius where the unperturbed vorticity field changes sign, and σ can be adjusted to make the perturbation penetrate the core and annulus to any desired degree.

In Carnevale & Kloosterziel (1994), we examined the stability of the vorticity distribution (1) for a range of α -values, subject to perturbations of single azimuthal modes given by

$$\zeta' = \mu \cos(m\theta) \exp\left(\frac{-(\alpha r^\alpha - 2)^2}{2\sigma^2}\right), \quad (3)$$

where μ is a constant amplitude and m is the mode number. The results of a linear stability analysis showed that the behaviour observed in the laboratory experiments and the random initial condition simulations could be understood as a combination of the simultaneous growth of both azimuthal modes $m = 2$ and $m = 3$. Furthermore, setting $\alpha = 6$, we found that if modes other than mode 3 are sufficiently weak initially, a symmetric quadrupole can form and persist.

In a simulation with an initially pure mode-3 perturbation and with viscosity

appropriate to the rotating-tank conditions used in the laboratory experiments, we found that a fairly symmetric triangular core forms by the end of the first rotation. It also takes about one rotation for the triangle to form in the purely inviscid case but the rotation period is about 15% shorter. Figure 1 shows the triangle structure in the viscous simulation after about two full rotations. The fact that it is not perfectly three-fold symmetric is due to asymmetries associated with the finite resolution of the grid which have amplified during the evolution. This quadrupole persisted unchanged in form although becoming somewhat broader in scale due to the effect of the Laplacian diffusion. During the course of the simulation the amplitude of the vorticity field decayed by three orders of magnitude under the influence of Ekman drag and molecular diffusion. This indicates that it should be possible to create a triangle vortex in the laboratory which would simply decay in amplitude.

To test the inviscid stability of the quadrupole, we began with the quadrupole shown in figure 1 as an initial condition and simulated forward in time with no viscosity. In figure 2, we show the initial stream function in the reference frame co-rotating with the quadrupole. If the state were perfectly stationary, then these streamlines would be aligned with those of the vorticity. Since there is some difference, this quadrupole deviates from an ideally symmetric one that would be steadily rotating; nevertheless, we followed the inviscid evolution of this vortex for over twenty of its rotations without observing any evidence that it would break down. This was verified at both resolutions 64×64 and 128×128 . Although there was some variation of its form over that long period, the basic structure did not change significantly. Thus it appears possible that, for inviscid flow, the symmetric quadrupole is a stable structure. The difficulty in finding a stable triangle vortex experimentally or in the corresponding random-perturbation simulations must be due to the fact that it is only stable for perturbations with amplitude below some small threshold value.

To examine how large the tolerance for perturbations is, we performed two different kinds of stability tests. In the first, we perturbed the strength of the

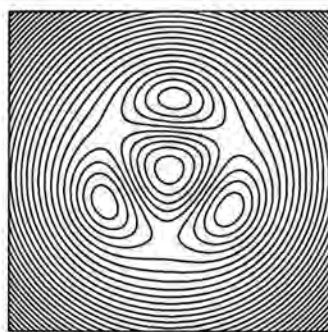


Fig. 2. Stream function contour plot of quadrupole vortex. The stream function is evaluated in the co-rotating frame with rotation period 81s. The contour increment was taken as $\Delta\psi = k^{-2} \Delta\zeta$, where $k = j_1^1/a$ with $j_1^1 = 3.83$ and where $a = 12$ cm is approximately the radius of the semicircular satellites.

satellite vortices while leaving the inner triangular core unperturbed. This type of perturbation was suggested by an analysis of point-vortex models and by experience from the experiments and simulations. It seemed that the triangle is sensitive to variations in the strengths of the outer satellites. Such asymmetries would lead to variations in the rate of revolution of the satellites about the core and thus permit a collision of a pair of satellites. The perturbation was prepared by taking the state shown in figure 1 and multiplying the vorticity field of the satellites by the factors $1 + \delta$, $1 - \delta$, 1, respectively, in one set of experiments, and by factors $1 + \delta$, $1 - \delta/2$, $1 - \delta/2$, in a second series. All of the stability simulations were run with no bottom drag and no Laplacian viscosity; however, in order to avoid the build up of enstrophy in the smallest scales during the long runs, hyperviscosity was used.

In figure 3, we plot the time it takes until a merger occurs between two of the satellites in each of these series of experiments. The time is given in units of the rotation period of the unperturbed vortex and the simulations were terminated after 20 rotation periods even if no breakdown had occurred. For perturbations less than 2 percent, the triangle remains intact for more than 20 rotation periods. There is a steep fall off of the time to merger or breakdown between perturbations of 2 and 4 percent. Defining a stability boundary based on simulations requires some arbitrary choice of how to define the stable regime since numerical noise will eventually contaminate the results. For practical purposes, we can take our stability boundary to be approximately where the lifetime, as a function of the perturbation amplitude, becomes very large. Thus the stability boundary is around 3 percent. This is much smaller than the rough estimate of about 10% for dipoles as mentioned above.

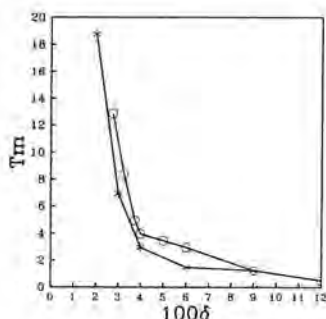


Fig. 3. Stability plot for the quadrupole. We show the time to merger of two of the satellites for the perturbed triangle vortex as a function of the strength of the perturbation. The data points marked by asterisks (circles) correspond to the case in which the initial satellite vortex strengths are multiplied by $1 + \delta$, $1 - \delta$, 1 ($1 + \delta$, $1 - \delta/2$, $1 - \delta/2$). The merger time is expressed in units of the unperturbed vortex rotation period (81 s).

In the second kind of stability study, we added a randomly generated homogeneous isotropic vorticity field to the vortex shown in figure 1. This perturbation field was created by adding contributions from all wavevectors with wavenumbers between two fixed limits, $k_0 \leq k_1$, in such a way that the energy spectrum of the perturbation was independent of wavenumber in that band. The real and imaginary parts of the complex amplitude for each wave number were generated from a Gaussian distribution. The perturbation amplitude is measured as the ratio of the rms velocity of the perturbation to the rms velocity of the triangular vortex. The rms averages are taken only over the area within an imaginary boundary of an idealized structure consisting of the triangle surrounded by three semicircles. The length scale of the perturbation is defined as $\lambda \equiv L_B / (L_A \bar{k})$, where L_B is the size of the periodic computational box, $L_A = 2a$ is the length of one side of the triangle vortex, and $\bar{k} = (k_1 + k_0)/2$. Thus the value $\lambda = 1$ corresponds approximately to the scale of the triangular vortex. The circles on the plot in figure 4 indicate the simulations in which the triangle vortex survives for more than ten rotation periods, and the asterisks indicate the simulations in which the triangle breaks up before that time limit is reached. Again the definition of a stability boundary is somewhat fuzzy. But we may conclude that the triangle vortex is most unstable to perturbations of length scale close to its own, and the minimum strength of the perturbation needed to destabilize it is about 3 percent measured in rms velocity. The structure appears very stable to large-scale perturbations, which for the most part simply advect it, and also to small-scale perturbations, which are quickly sheared out to even smaller scales to be eventually dissipated by hyperviscosity.

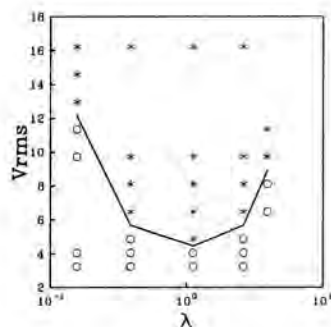


Fig. 4. Stability plot for the quadrupole. The graph shows the results from a stability study in which a random velocity field of length scale λ and amplitude V_{rms} was added to the triangle vortex. Asterisks mark the experiments in which merger occurred between two of the three satellites before ten rotations periods of the unperturbed structure had elapsed. Circles mark those simulations in which the vortex system was still intact after ten rotation periods. The perturbation amplitude V_{rms} is given in multiples of the rms velocity of the triangle vortex, and λ is defined so that $\lambda = 1$ corresponds to the size of one side of the triangle vortex (see text).

Higher order n -poles

Since the mode 3 instability of the initially circularly symmetric vortex leads through nonlinear saturation to the triangular vortex, we went on to test whether the mode 4 instability would lead to a square vortex. We performed a series of experiments with values of α running from 3 to 8, both with and without viscosity. To the unperturbed state we added a perturbation as defined by equation (3) with azimuthal wavenumber 4 only, with amplitudes varying from $\mu = 0.1$ to 0.5 and with a length-scale $\sigma = 1$ in the initial condition. A further exploration of the parameter space was not performed since we found that these somewhat arbitrary choices did lead to the formation of square vortices for $\alpha > 5$. For example, in figures 5 and 6, we show the vorticity and stream function plots of a square vortex which formed for a steepness parameter $\alpha = 8$. The simulation which produced this vortex was run with Ekman decay time and molecular viscosity set to the values that agreed with our laboratory experiment that produced quadrupoles (i.e., $T_E = 132$ s and $\nu = .01$ cm²/s). The basic structure developed by time $t = 10$ s and by time 72 s, the structure reached the state shown in the figure. The vorticity distribution is shown in figure 5 and the stream function, in the co-rotating frame of the vortex system, is given in figure 6.

In all the simulations in which the square vortex formed, the structure broke down before at most 3.5 rotations were completed. The longest-lived square vortex was achieved for $\alpha = 8$, starting with a perturbation amplitude of $\mu = 0.5$, with only hyperviscosity dissipation acting. In all cases, these square vortices, which have satellites of equal strength, broke down through the simultaneous merger of their satellites in two pairs on opposite sides of the square core.

In figure 7, we show the instability that destroys the square vortex. The conditions for the simulation were again set to match those in our rotating tank experiments. The initial vortex in this simulation was created with $\alpha = 8$, and a

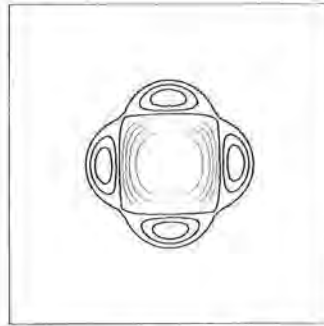


Fig. 5. Vorticity contour plot of a square vortex. Thick (thin) contours indicate positive (negative) relative vorticity. The contour level values are chosen to have increments of $\Delta\zeta = 0.3$ s⁻¹ (other parameters are as in figure 1).

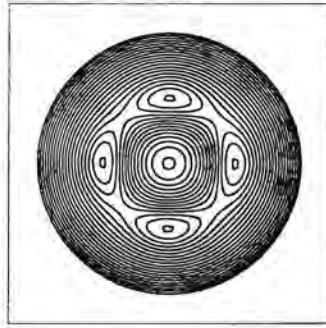


Fig. 6. Stream function contour plots of a square vortex. The stream function is evaluated in the co-rotating frame with rotation period 44.8 s. Beyond a certain value, the high level contours were not drawn because of 'bleeding' between the lines. The contour increment was taken as $\Delta\psi = k^2 \Delta\zeta$, where $ka = j_1^1$ and $a = 8.3$ cm is approximately the radius of the semicircular satellites (other parameters are as in figure 1).

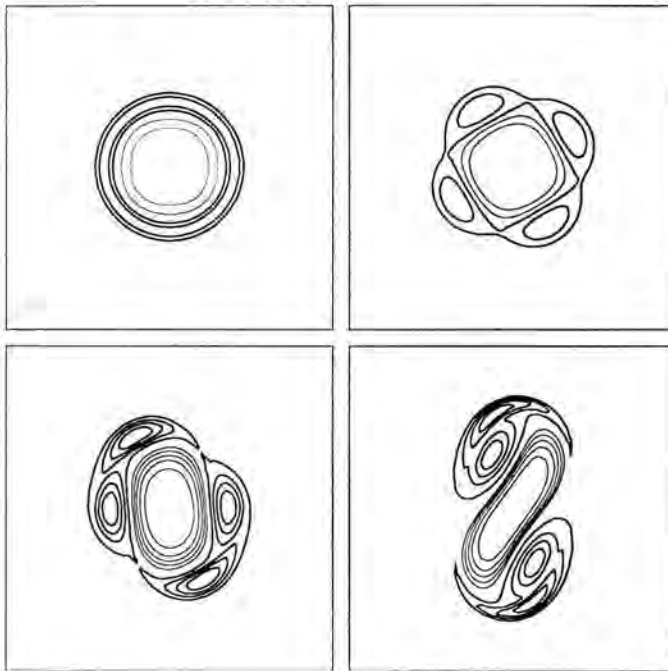


Fig. 7. Vorticity contour plot showing the evolution of the square vortex. For this simulation we used a kinematic viscosity and bottom drag with an Ekman decay time typical of the values corresponding to our rotating tank experiments. Thus this simulation demonstrates the possibility of producing a transitory square vortex in the rotating-tank under conditions similar to those in which the triangle was produced. The dimensional velocity and length scales and box size are as in figure 1. Thick (thin) lines represent positive (negative) contour levels. Panels are ordered from left to right, top to bottom, corresponding to times $t = 0.80, 130$, and 140 s, and they have contour value increments of $\Delta\zeta = 0.8, 0.4, 0.12$, and 0.11 s^{-1} , respectively.

wavenumber 4 perturbation of amplitude $\mu = 0.125$. The square vortex formed after about 10 seconds. Unlike the triangle vortex which lasted indefinitely under the same conditions, this square vortex broke down after about two and a half rotations. The double satellite merger begins in the lower left panel. This led to an intermediate tripole state (lower right panel) which then broke down through the familiar double dipole instability. We also performed simulations in which the square vortex shown in figure 5 was perturbed by strengthening one satellite while correspondingly weakening another to preserve the total circulation. In those cases, only two satellites merged at first, leading to a temporary triangle vortex. Then another merger took place leading to the tripole state, and then finally the double-dipole instability took over. From these results, we conclude that it should be possible to observe a square vortex emerge from a nearly circularly symmetric vortex in rotating-tank experiments if the initial perturbation is made sufficiently close to a pure mode-4 perturbation. However, it is also clear that it would only appear as a transitory state.

We have also been able to create a pentagon vortex in a numerical simulation by a wavenumber-5 perturbation on an $\alpha = 8$ profile. Although strong satellites do form rapidly, the structure breaks down after executing only about half a rotation. The breakdown began with the nearly simultaneous merger of two pairs of satellites which produced a roughly triangular system. Another merger followed, producing a tripole state. The tripole finally broke up into a dipole and monopole.

Point – vortex models

Finally, we turn to the stability of the higher-order geometrical vortices, the square, the pentagon, etc., from the point of view of point-vortex models. Specifically, we consider here only the zero-circulation, steadily-rotating configurations, consisting of $n_s = n - 1$ equal strength point vortices symmetrically placed on a circle centred on a point vortex of opposite sign. It can be shown that the case $n = 3$, a model for the tripole, is nonlinearly stable to displacements (Kloosterziel 1990), and in Eckhardt (1988) it is shown that the case $n = 4$, the model of the triangular vortex, is also nonlinearly stable. Morikawa & Swenson (1971) performed a linear stability analysis on these models for all n . The perturbations they considered were small displacements in the initial positions. Consistent with the later nonlinear stability results, they found that the cases $n = 3$ and $n = 4$ are linearly stable, but more importantly, they proved that for all cases $n \geq 5$ the configurations are linearly unstable. For the cases $n = 5$ and $n = 6$, the models of the pentapole and hexapole, we have performed simulations that show that a 1% or less perturbation in the radial position of the satellites away from symmetry will result in the close approach of two of the satellites within one rotation period. This is the same form of instability that led to the close approach and merger of satellites in our simulations of the continuous pentapole

and hexapole vortices. This should be contrasted with the case of the point-vortex model of the triangle, where perturbations of even 20% in the positions of the satellites can still be stable (Carnevale & Kloosterziel, 1994). In view of the results of Morikawa & Swenson (1971), we anticipate that all higher-order coherent continuous vortices are also unstable.

Conclusion

We have considered a hierarchy of isolated compound vortices in which the Lamb dipole and the tripole are the first two elements. The stability of these two structures is well known from experiments and simulations. Here we have reviewed evidence that the next element in this hierarchy, the quadrupole, is also stable, but with a much smaller instability threshold than the two lower-order structures. It seems that these three elements, dipole, tripole and quadrupole, are the only stable ones in the whole hierarchy. All of the higher-order compound vortices are expected to show the close approach and merger of two of the satellites, and subsequent breakup of the whole structure.

All of our simulations were performed with continuous vorticity profiles on a doubly periodic domain using a spectral code. Morel & Carton (1994) have performed a similar study based on contour dynamics, that is, simulations involving regions of piecewise constant vorticity. They also have found that the quadrupole is stable while higher order n -poles are not, thus adding to the weight of evidence for our conclusion.

Acknowledgements

This research has been supported in part by National Science Foundation grant OCE 91-21998 and Office of Naval Research grant N00014-93-1-0459. The numerical simulations were performed at the San Diego Super Computer Center. The laboratory experiments were performed in the Applied Mechanics and Engineering Sciences department at the University of California, San Diego.

References

- Carnevale, G. F., M. Briscolini, R. Purini, & G.K. Vallis, 1988a - Numerical experiments on modon stability to topographic perturbations. *Phys. Fluids* **31**, 2562-2566.
- Carnevale, G. F., Vallis, G.K., Purini, R., & Briscolini, M. 1988b Propagation of barotropic modons over topography. *Geophys. Astrophys. Fluid Dyn.* **41**, 45-101.

- Carnevale, G.F., G.K. Vallis, R. Purini, & M. Briscolini, 1988c - The role of initial conditions in flow stability with applications to modons. *Phys. Fluids* **31**, 2567–2572.
- Carnevale, G.F., J.C. McWilliams, Y. Pomeau, J.B. Weiss, & W.R. Young, 1991 - Evolution of vortex statistics in two-dimensional turbulence. *Phys. Rev. Letters* **64**, 2735–2737.
- Carnevale, G.F., & R.C. Kloosterziel, 1994 - Emergence and evolution of triangular vortices. *J. Fluid Mech.* **259**, 305–331.
- Carton, X.J., & J.C. McWilliams, 1989 - Barotropic and baroclinic instabilities of axisymmetric vortices in a quasi-geostrophic model. In: *Mesoscale/ Synoptic Coherent Structures in Geophysical Turbulence* (eds. J.C.J. Nihoul & B.M. Jamart), pp. 225–244, Elsevier.
- Carton, X.J., G.R. Flierl, & L.M. Polvani, 1989 - The generation of tripoles from unstable axisymmetric isolated vortex structures. *Europhys. Lett.* **9**, 339–344.
- Eckhardt, B., 1988 - Integrable four vortex motion. *Phys. Fluids* **31**, 2796–2801.
- Federov, K.N., & A.I. Ginsburg, 1989 - Mushroom-like currents (vortex dipoles): one of the most widespread forms of non-stationary coherent motions in the ocean. In: *Mesoscale/ Synoptic Coherent Structures in Geophysical Turbulence* (eds. J.C.J. Nihoul & B.M. Jamart), pp. 1–14, Elsevier.
- van Heijst, G.J.F., & R.C. Kloosterziel, 1989 - Tripolar vortices in a rotating fluid. *Nature* **338**, 569–561.
- van Heijst, G.J.F., R.C. Kloosterziel, & C.W.M. Williams, 1991 - Laboratory experiments on the tripolar vortex in a rotating fluid. *J. Fluid Mech.* **225**, 301–332.
- Kloosterziel, R.C., 1990 - *Barotropic Vortices in a Rotating Fluid*. PhD thesis, University of Utrecht, The Netherlands (209 pp.)
- Kloosterziel, R.C., & G.J.F. van Heijst, 1991 - An experimental study of unstable barotropic vortices in a rotating fluid. *J. Fluid Mech.* **223**, 1–24.
- Lamb, H., 1932 - *Hydrodynamics*. Cambridge University Press, 738 pp.
- Legras, B., P. Santangelo, & R. Benzi, 1988 - High-resolution numerical experiments for forced two-dimensional turbulence. *Europhys. Lett.* **5**, 37–42.
- McWilliams, J.C., 1980 - An application of equivalent modons to atmospheric blocking. *Dyn. Atmos. Oceans* **5**, 43–66.
- McWilliams, J.C., G.R. Flierl, V.D. Larichev & G.M. Reznik, 1981 - Numerical studies of barotropic modons. *Dyn. Atmos. Oceans* **5**, 219–238.
- Melander, M.V., N.J. Zabusky, & J.C. McWilliams, 1988 - Symmetric vortex merger in two-dimensions: causes and conditions. *J. Fluid Mech.* **195**, 303–340.
- Morel, Y.G., & X.J. Carton, 1994 - Multipolar vortices in two-dimensional incompressible flows. *J. Fluid Mech.* **267**, 23–51.
- Morikawa, G.K., & E.V. Swenson, 1971 - Interacting motion of rectilinear geostrophic vortices. *Phys. Fluids* **14**, 1058–1073.
- Nycander, J., 1992 - Refutation of stability proofs for dipole vortices. *Phys. Fluids A* **4**, 467–476.
- Orlandi, P., & G.J.F. van Heijst, 1992 - Numerical simulation of tripolar vortices in 2D flow. *Fluid Dyn. Res.* **9**, 170–206.

- Pingree, R.D., & B. LeCann, 1992 - Three anticyclonic Slope Water Oceanic eddies (SWODDIES) in the Southern Bay of Biscay in 1990. *Deep Sea Res.* **39**, 1147-1175.
- Polvani, L.M., & X.J. Carton, 1990 - The tripole: a new coherent vortex structure of incompressible two-dimensional flows. *Geophys. Astrophys. Fluid Dyn.* **51**, 87-102.
- Sadourny, S., 1985 - Quasi-geostrophic turbulence: an introduction. In: *Turbulence and Predictability in Geophysical Fluid Dynamics and Climate Dynamics* (M. Ghil ed.), North Holland, Amsterdam, pp. 133-158.
- Stern, M.E., 1975 - Minimal properties of planetary eddies. *J. Mar. Res.* **33**, 1-13.

⁺ Scripps Institution of Oceanography
La Jolla, CA 92093, USA

[□] University of Hawaii
School of Ocean and Earth Science and Technology
Department of Oceanography
Honolulu, Hawaii 96822, USA

Characterization and Numerical Calculation of Plane Vortex Structures

Abstract

A variational characterization is given for coherent vortices in plane fluid flows. We characterize isolated vortices, such as mono-, di- and tripolar vortices, as (relative) equilibrium states of the dynamical equation. To calculate the vortices numerically, an iteration scheme is constructed to solve the variational problems. The Lagrange multipliers and the free boundary are solved implicitly in the iteration process, which makes it possible to calculate the complex vorticity configurations with distributed vorticity.

Confined vortices in two-dimensional fluid flow

The Euler equations which give the evolution equations for incompressible, homogeneous and inviscid fluid flow, are a dynamical system with a special structure, called a Poisson structure. In vorticity formulation the Euler equations for purely two-dimensional flow are given by:

$$\begin{cases} \partial_t \omega + \nabla \omega \cdot J \nabla \psi = 0 \\ \omega = -\Delta \psi \end{cases} \quad (1)$$

which are the vorticity equation and the Poisson equation; here ω denotes the scalar vorticity, ψ the stream function and J the skew-symmetric matrix $J = \begin{pmatrix} 0 & 1 \\ -1 & 0 \end{pmatrix}$.

For this dynamical system there exists a natural invariant functional, the Hamiltonian H , which is the kinetic energy of the system:

$$H(\omega) = \frac{1}{2} \int \psi \omega \, dx \, dy \quad (2)$$

Together with other invariant functionals the Hamiltonian determines special solutions of the evolution equation. Critical points of the Hamiltonian on level sets of the invariant integrals are called relative equilibria. They are equilibrium solutions of the equation (1).

For an arbitrary function f of ω , the invariant functional:

$$C(\omega) = \int f(\omega) dx dy \quad (3)$$

is a Casimir integral, called the generalized enstrophy. A special case is given by the circulation or total vorticity:

$$\Gamma(\omega) = \int \omega dx dy \quad (4)$$

which is indeed a constant of the motion, as was shown by Kelvin. Besides the invariants given by the Casimirs C , the system admits constants of the motion given by the momentum integrals (linear and angular momentum), if the flow domain is translationally or rotationally symmetric.

We can find time-independent solutions by looking for relative equilibria, solving variational problems of the following type:

$$\text{extr}_{\omega \in L_2} \{H(\omega) | C(\omega) = \gamma\} \quad (5)$$

The Lagrange multiplier rule supplies a constant λ such that an extremizing solution ω (depending on γ) satisfies:

$$\delta H(\omega) = \lambda \delta C(\omega) \quad (6)$$

or similarly:

$$\psi = \lambda f'(\omega) \quad (7)$$

This yields an explicit functional relationship between stream function and vorticity, which is directly related to the choice of integral constraints $C(\omega)$ in the variational principle.

Denoting by M a momentum integral (either linear or angular momentum), steadily translating or rotating solutions can be found from the variational principles:

$$\text{extr}_{\omega \in L_2} \{H(\omega) | C(\omega) = \gamma; M(\omega) = m\} \quad (8)$$

We are interested in finding confined vortices, i.e. vorticity distributions with compact support, surrounded by irrotational flow. To find confined solutions, the function $f'(\omega)$ in (7) must be multivalued in $\omega = 0$. To achieve this multivaluedness, we use non-differentiable constraints given by the positive and negative circulations:

$$\Gamma_+(\omega) = \int (\omega)_+ \quad \text{and} \quad \Gamma_-(\omega) = \int (\omega)_- \quad (9)$$

where $(\omega)_+ = \max(\omega, 0)$, $(\omega)_- = \min(\omega, 0)$.

Related to the confinement of the vorticity distributions is the free boundary of the vortex support. The vorticity distribution and consequently the domain of non-zero vorticity have to be found from the variational inequalities for the vorticity.

We look at an algorithm that solves the variational inequality for the vorticity. The algorithm is able to find the multipliers and to adapt the free boundary within the process. First it is observed that the Lagrange multipliers satisfy a variational characterization (see also Eydeland and Van Groesen, 1989). Secondly the method by Eydeland *et al.* (1988, 1990) for non-convex optimization is applied, by linearizing the non-convex part of the functionals around the previous iteration step.

Instead of the variational inequality that has to be satisfied outside the vortex support, we use the Laplace equation for the stream function, with $\Delta\psi = 0$ and ψ sufficiently smooth over the boundary of the vortex domain.

The iteration scheme and some calculations are shown for mono-, di-, tri- and quadrupolar vortices.

Variational principle for Lagrange multipliers

Suppose a family of equilibrium solutions is parametrized by the value of γ in the following variational problem for the energy:

$$\text{extr}_{\omega} \{ H(\omega) \mid C(\omega) = \gamma \} \quad (10)$$

If H and C are sufficiently smooth, there exists a constant $\lambda \in \mathbb{R}$ such that:

$$\delta H(\omega) - \lambda \delta C(\omega) = 0 \quad (11)$$

The value of λ depends on the specified value of the constraint, $\lambda = \lambda(\gamma)$, and the variational problem can be written as: $\text{extr}_{\omega} H(\omega) - \lambda C(\omega)$. The multiplier λ can be found from the following variational principle:

$$\text{extr}_{\lambda} \text{extr}_{\omega} H(\omega) - \lambda(C(\omega) - \gamma) \quad (12)$$

The extremum for ω , denoted by $\omega(\lambda)$, satisfies (11) and the remaining critical value problem for λ yields the value for λ for which $C(\omega(\lambda)) = \gamma$. In this way the constrained variational problem is transformed to an unconstrained problem. Without any restriction this can be generalized to variational problems with a family of constraints. After substitution of the extremizer $\omega(\lambda)$ into (12), the finite dimensional optimization problem for the multiplier(s) can be solved by a steepest descent method. The optimization for ω in (12) is infinite dimensional and the functional $H(\omega) - \lambda(C(\omega) - \gamma)$ might be non-convex in ω . We implement a numerical optimization method for non-convex functionals by Eydeland *et al.* (1988, 1990).

The iteration process

An iteration scheme is constructed, combining the non-convex optimization and the optimization for the Lagrange multipliers. Consider the variational principle (10). Choose a starting value for the vorticity ω_0 with corresponding stream function ψ_0 . At iteration step k , with stream function ψ_k , the linearization of the energy functional is given by: $\int \delta H(\omega_k) \omega = \int \psi_k \omega$. If we define for each iteration step the functional:

$$\mathcal{L}_k(\omega, \lambda) = \int \psi_k \omega - \lambda(C(\omega) - \gamma) \quad (13)$$

the iteration process is given by:

$$\begin{cases} \omega_{k+1}(\lambda) = \arg \text{extr}_{\omega} \mathcal{L}_k(\omega, \lambda) \\ \lambda_{k+1} = \arg \text{extr}_{\lambda} \mathcal{L}_k(\omega_{k+1}(\lambda), \lambda) \end{cases} \quad (14)$$

From ω_{k+1} one finds ψ_{k+1} by application of a Laplace solver for the Poisson equation:

$$-\Delta \psi_{k+1} = \omega_{k+1} \quad (15)$$

with suitable boundary conditions for ψ_{k+1} . At each iteration step the multipliers are found such that the constraints are satisfied. This means that no distraction takes place from the level sets of the integrals.

The method is applied to steadily rotating vortices in the plane and to dipolar vortices in a bounded domain with periodic boundary conditions.

Calculation of confined vortices

Rotating vortices in the plane, with continuous and distributed vorticity, can be found from the following variational problem:

$$\text{extr}_{\omega \in S} \{H(\omega) - \alpha P(\omega)\} \quad (16)$$

with the constrained set S given by:

$$\{W(\omega) = w; \Gamma_+(\omega) = \gamma_+; \Gamma_-(\omega) = \gamma_-\} \quad (17)$$

The fixed value of α corresponds to the rotation rate of the vortices. Here $H = \frac{1}{2} \int \psi \omega$ denotes the kinetic energy, $P = \frac{1}{2} \int r^2 \omega$ the angular momentum, $W = \frac{1}{2} \int \omega^2$ the enstrophy or squared vorticity and Γ_+ and Γ_- the positive and negative circulations (9).

We simulate the vortices in the plane by considering a numerical spatial domain D , with boundary condition imposed upon the stream function given by either $\psi(\mathbf{x}) = 0$ or:

$$\psi(\mathbf{x}) = -\frac{\Gamma(\omega)}{2\pi} \log|\mathbf{x}|, \quad \mathbf{x} \in \partial D \quad (18)$$

The variational inequality for a maximizer of (16) reads:

$$\begin{cases} \psi - \frac{1}{2}\alpha r^2 = \mu\omega + \sigma_+, & \text{if } \omega > 0 \\ \psi - \frac{1}{2}\alpha r^2 = \mu\omega + \sigma_-, & \text{if } \omega < 0 \\ \sigma_- \leq \psi - \frac{1}{2}\alpha r^2 \leq \sigma_+, & \text{if } \omega = 0 \end{cases} \quad (19)$$

Here μ , σ_+ , σ_- are the multipliers associated to W , Γ_+ , Γ_- respectively. We linearize the energy (with the correction for the rotation), and define the functional \mathcal{L}_k at iteration step k by:

$$\begin{aligned} \mathcal{L}_k(\omega, \mu, \sigma_+, \sigma_-) = & \int \left(\psi_k - \frac{1}{2}\alpha r^2 \right) \omega - \mu \left(\frac{1}{2} \int \omega^2 - w \right) \\ & - \sigma_+ \left(\int (\omega)_+ - \gamma_+ \right) - \sigma_- \left(\int (\omega)_- - \gamma_- \right) \end{aligned} \quad (20)$$

Given ψ_k at step k , the next iteration step reads with $\mu > 0$:

$$\omega_{k+1} = \frac{1}{\mu} \left(\psi_k - \frac{1}{2}\alpha r^2 - \sigma_+ \right)_+ + \frac{1}{\mu} \left(\psi_k - \frac{1}{2}\alpha r^2 - \sigma_- \right)_- \quad (21)$$

Substitution of ω_{k+1} into \mathcal{L}_k yields $\mu_{k+1} = \arg \text{extr}_\mu \mathcal{L}_k(\omega_{k+1}, \mu, \sigma_+, \sigma_-)$ and after substitution of μ_{k+1} into \mathcal{L}_k the problem reduces to a convex minimization, of a function $\mathcal{L}_k(\sigma_+, \sigma_-)$.

Numerical results

We chose the numerical domain $D = [-1, 1] \times [-1, 1]$. The calculations are performed on a 64x64 equidistant grid.

Monopolar vortices:

By taking $\gamma_- = 0$ in the variational principle (16), the extrema are positive monopolar vortices surrounded by irrotational flow. Figures 1 and 2 show typical vorticity distributions for maximization and minimization, respectively. The parameter values are: $w = 20$, $\gamma_+ = 4$, $\gamma_- = 0$ for the calculations on the monopolar vortices.



Fig. 1. Spatial plot of the vorticity solution of (16) for $w=20$, $\gamma_+=4$, $\gamma_-=0$, $\alpha=7$.



Fig. 2. Spatial plot of the vorticity solution of (16) for $w=20$, $\gamma_+=4$, $\gamma_-=0$, $\alpha=-7$.

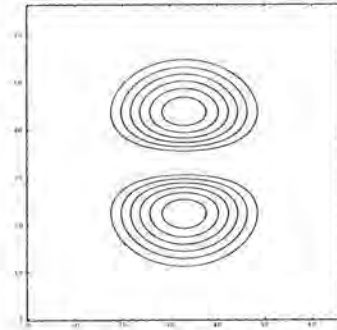


Fig. 3. Contour plot of the vorticity solution of (16) with $w=3.2$, $\gamma_+=1.6$, $\gamma_-=-1.6$, $\alpha=0.0$.

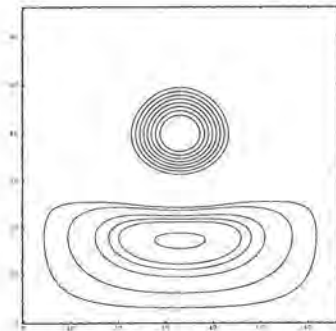


Fig. 4. Contour and spatial plots of the vorticity solution of (16) with $w=3.2$, $\gamma_+=1.6$, $\gamma_-=-1.3$, $\alpha=0.0$.

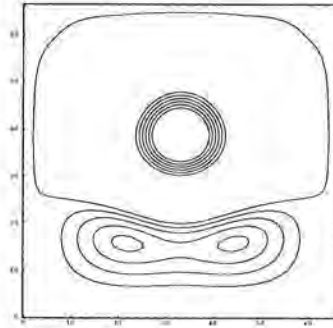


Fig. 5. Contour plot of the vorticity solution of (16) with $w = 3.2$, $\gamma_+ = 1.6$, $\gamma_- = -1.15$, $\alpha = 0.0$.

Non-symmetric dipolar vortices:

By taking $\alpha = 0$ in the variational principle (16) and $\psi = 0$ on ∂D we find a characterization of dipolar vortices on a periodic domain. We chose parameter values $w = 3.2$ and $\gamma_+ = 1.6$ and different values for γ_- in the neighbourhood of $\gamma_- = -1.6$. Figure 3 shows the vorticity in a contour plot for $\gamma_- = -1.6$. For this choice of parameter values there exists a solution which is a confined and symmetric dipolar vortex. The multipliers σ_+ and σ_- satisfy $\sigma_+ = -\sigma_-$.

There exists a branch of confined dipolar solutions, parametrized by the value of γ_- . In a neighbourhood of $\tilde{\gamma}_- = -\gamma_+$ non-symmetric, confined solutions of (16) are found. In figure 4 a non-symmetric dipole is shown for $\gamma_- = -1.3$. In figure 5 we show the result of the calculations with $\gamma_- = -1.15$. For this value of γ_- the value of the multiplier σ_- has become positive, such that the vorticity solution is not confined.

Tripolar and quadrupolar vortices:

For special choices of the parameter values we find tripolar and even quadrupolar vortical structures. The structures rotate as a whole around the center of vorticity (the origin). We chose parameter values $w = 10$, $\gamma_+ = 1$, γ_- in the neighbourhood of $\gamma_- = -1$ and α in \mathbb{R} .

We show the vorticity at different stages in the iteration process in figures 6 and 7. It is observed that the symmetries of the initial vortex configuration are not necessarily conserved. The succeeding iterates form no approximation of any real dynamics.

In the experiments by Van Heijst and Kloosterziel (1989, 1990) only tripolar vortices have been observed with positive core and negative satellites rotating counter-clockwise (corresponding to α negative). The sign of rotation corresponds with the sign of vorticity of the vortex core. For most confined tripoles that are found by our numerical calculations, the rotation corresponds to the vorticity in the core. However, also tripoles are found that rotate in the

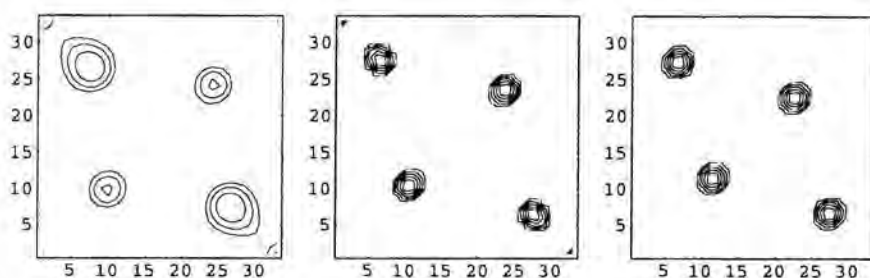


Fig. 6. Contour plots of the vorticity at different stages in the iteration. The calculation is performed with $w=10$, $\gamma_+ = 1$, $\gamma_- = -1$, $\alpha = -0.04$.

other direction. In fact, tripolar and quadrupolar vortices are found with rotation rates positive, negative or even zero. Also in numerical simulations by Polvani and Carton (1990) tripolar vortices have been found with positive, negative or no rotational velocity.

With the chosen parameter values, the regions of vorticity are not far from the boundary of the numerical domain. This means that the imposed boundary condition on the square domain has a large influence on the solutions. It might be possible to find vorticity distributions that are confined to a small neighbourhood of the origin, by changing the parameter values for w , γ_+ , γ_- , p and α . This however needs further investigation.

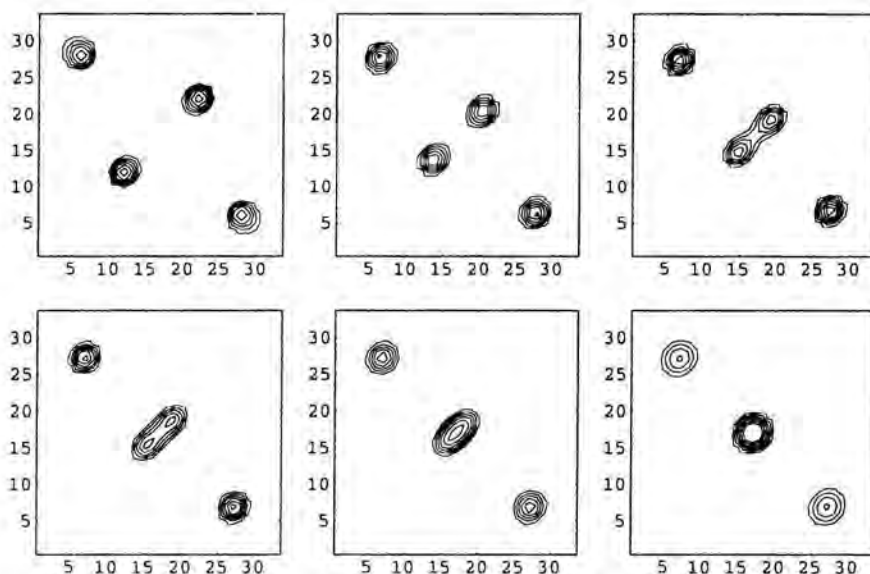


Fig. 7. Contour plots of the vorticity at different stages in the iteration. The calculation is performed with $w=10$, $\gamma_+ = 1$, $\gamma_- = -1$, $\alpha = -0.08$.

References

- Eydeland, A. and E. van Groesen, 1989 - An extended self-organisation principle for modelling and calculating the dissipation of 2D confined vortices. *Nonlinearity* **2**, 459–475.
- Eydeland, A. and J. Spruck, 1988 - The inverse power method for semilinear elliptic equations. *Nonlinear Diffusion*, 1, MSRI series vol. 12, Springer-Verlag.
- Eydeland, A., J. Spruck and B. Turkington, 1990 - Multiconstrained variational problems of nonlinear eigenvalue type: new formulations and algorithms. *Math. of Comp.* **55**, 509–535.
- Eydeland, A. and B. Turkington, 1988 - A computational method of solving free-boundary problems in vortex dynamics. *J. Comp. Physics* **78**, 194–214.
- van de Fliert, B.W. and E. van Groesen, 1992 - Monopolar vortices as relative equilibria and their dissipative decay. *Nonlinearity* **3**, 473–495.
- van de Fliert, B.W., E. van Groesen, R. de Roo and R.W. de Vries, 1992 - Numerical algorithm for the calculation of non-symmetric dipolar and rotating monopolar vortex structures. Submitted to *J. Comp. and Appl. Math.*
- van Heijst, G.J.F. and R.C. Kloosterziel, 1989 - Tripolar vortices in a rotating fluid. *Nature* **340**, 212–215.
- van Heijst, G.J.F., R.C. Kloosterziel and C.W.M. Williams, 1990 - Laboratory experiments on the tripolar vortex in a rotating fluid. *J. Fluid Mech.* **225**, 301–331.
- Polvani, L.M. and X.J. Carton, 1990 - The tripole: a new coherent vortex structure of incompressible two-dimensional flow. *Geophys. Astrophys. Fluid Dyn.* **51**, 87–102.

Department of Applied Mathematics
Twente University
PO Box 217, 7500 AE Enschede
The Netherlands

Topography-Induced Modulation of a Tripolar Vortex in a Rotating Fluid

Abstract

Laboratory experiments on the tripolar vortex generated at some distance off the rotation axis of a rotating free-surface fluid have revealed a remarkable unsteady behaviour: the tripole becomes asymmetric, and its evolution follows a repetitive dipole-monopole interaction scenario. This unsteady behaviour is caused by a modulation of the core and satellite vortices due to the parabolic topography of the free fluid surface. It is shown that the main characteristics of the tripole evolution are quite well described by a simple modulated point-vortex model. In addition to describing the trajectories of the individual vortices, this model is also capable of describing the advection of fluid elements.

1. Introduction

A tripolar vortex can be concisely defined as a compact, symmetric linear arrangement of three patches of distributed vorticity, with the elongated central vortex being adjoined at its longer sides by two weaker satellite vortices of oppositely signed vorticity. The symmetric tripolar vortex performs a steady rotation as a whole in the direction defined by the circulation of the central vortex. Initially, the tripole was observed in numerical studies of 2D flows (Legras *et al.* 1988; Carton *et al.* 1989; Orlandi & van Heijst 1992) and in laboratory experiments on vortices in rotating and stratified fluids (van Heijst & Kloosterziel 1989; van Heijst *et al.* 1991; Flór *et al.* 1993). Recent satellite observations have yielded evidence that the tripolar vortex may also exist in the ocean (Pingree & Le Cann 1992a,b).

In the present study the attention is focussed on the behaviour of the asymmetric tripole. In particular, we will consider the effect of perturbations associated with a gradient in the ambient vorticity.

2. Laboratory experiments

As described by van Heijst *et al.* (1991), a tripolar vortex can be generated in a rotating fluid by stirring the fluid in a thin-walled bottomless cylinder of small diameter, placed in the tank, and then lifting the cylinder quickly: one thus produces an isolated monopolar vortex in the uniformly-rotating ambient fluid. Under certain conditions this vortex becomes unstable, resulting - when cyclonic - in the gradual formation of a tripolar vortex. In previous experiments the vortex was released at the rotation axis, and the evolving tripole performed a quasi-steady rotation, while remaining symmetric. When the tripole is created at some distance from the rotation axis, however, it soon loses its initial symmetry, and a somewhat more complicated evolution is observed, see Figure 1. In the first stage of this evolution, one observes a 'kink' in the tripole axis (between Figs. 1a and 1b), upon which the characteristic monopole-dipole interaction scenario follows: one of the satellite vortices pairs with the core vortex and this newly formed asymmetric dipole (the core vortex is stronger than each of the satellites) moves along a curved trajectory, leaving behind the other satellite (see

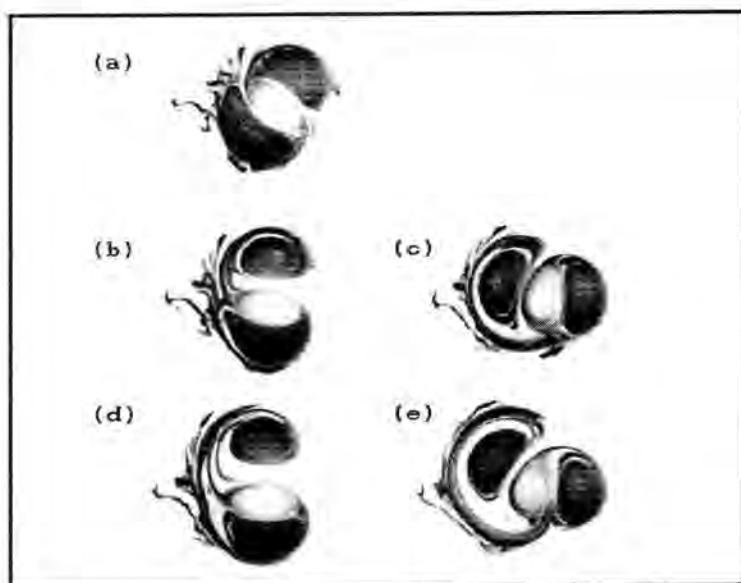


Fig. 1. Laboratory observations of a tripolar vortex in a rotating fluid generated at some distance from the rotation axis. The tripole has lost its symmetry and shows repeated partner exchange between the core vortex and the two satellite vortices. The sequence of pictures shows the tripole in the stages of aligned vortices (b,d) and maximum kink of the axis (c,e).

Fig. 1b). Somewhat later, after performing its looped excursion, the dipole returns and momentarily the tripole structure is re-established, although again with a kinked axis (see Fig. 1c). The core vortex now pairs with the other satellite vortex (*i.e.* partner exchange occurs), thus forming an asymmetric dipole that moves away along a curved path (see Fig. 1d). This process is repeated many times, although the amplitude of the looping dipole excursions gradually increases (*cf.* Figs. 1b and 1d). Also the kink in the tripole axis at the stage of re-unification becomes more pronounced during the course of the experiments (*cf.* Figs. 1c and 1d).

Another feature of the experiment worth noting is the complicated distribution of the dye. Each time a dipolar structure is formed, it leaves behind a tail of dye, which is wrapped around the remaining satellite (Fig. 1b), somewhat later around the newly formed dipole (Fig. 1c), and so on (Figs. 1d and 1e). Close inspection of the dye tails reveals the occurrence of alternating dyed and undyed filaments, indicating that some distance from the individual vortex centres originally 'interior' and 'exterior' fluid are stirred. The evolution of the dye filaments also shows signs of repeated stretching and folding, thus suggesting chaotic advection of the passive tracers in some parts of the flow domain.

3. The asymmetric point-vortex tripole

The simplest description of the tripolar vortex is obtained by representing each of the three vorticity patches by a point vortex of appropriate strength. As was shown by van Heijst *et al.* (1991), the gross features of the symmetric tripole are captured by a point-vortex model consisting of two satellite vortices with strength $-\gamma$ at the same distance a from the central vortex, whose strength is 2γ (see Fig. 2a). This configuration performs a steady rotation with angular velocity $\omega_o = 3\gamma/(4\pi a^2)$, which corresponds with the observed rotation speed, provided that the quantities γ and a are correctly estimated. Also, the shape of the separatrix (in which mass is trapped) corresponds very well with the laboratory observations.

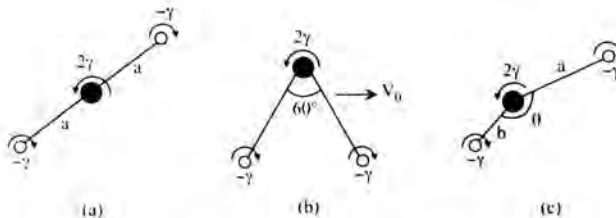


Fig. 2. Unmodulated tripolar point-vortex configurations with net zero circulation: (a) the steadily rotating symmetric tripole, (b) the steadily translating equilateral tripole, and (c) the general asymmetric configuration with $a_o \neq b_o$ and $\theta_o \neq \pi$.

When the point vortices are placed at the corners of an equilateral triangle (Fig. 2b), the structure performs a steady *translation* at speed $V_o = \gamma \sqrt{3}/(2\pi a)$ in a direction parallel to the line through the satellite vortices.

In the general case, schematically shown in Fig. 2c, however, the three-vortex configuration performs a complicated non-steady motion: the tripole geometry changes continuously in time, and the separation distances and the kink angle are essentially time-dependent, *i.e.* $a = a(t)$, $b = b(t)$ and $\theta = \theta(t)$. The motion of this asymmetric point-vortex tripole has been analysed by taking a linear initial arrangement with $\theta(t=0) = \theta_0 = \pi$, $a(t=0) = a_o$ and $b(t=0) = b_o$. This (initial) configuration is similar to that visible in Fig. 1a. It was found that, depending on the ratio $c = b_o/a_o$, different scenarios of vortex motion are possible. In all cases, however, the motion is periodic, *i.e.* the vortices take their initial relative positions after some period T . The frequency $f = 1/T$ of the motion was calculated as a function of the initial distance ratio c by measuring the time T that it takes to the vortices to return to their initial (relative) configuration. The results are represented by the thick line in Fig. 3. In this graph one easily recognizes two régimes of motion. Régime I ($0 < c \lesssim 0.3$) corresponds with the case of one of the satellites rotating around the core, while the far satellite performs a small-amplitude ‘wobbling’ motion. In régime II ($0.3 \lesssim c < 1$) the three point vortices move according to the same monopole-dipole interaction scenario as observed in the laboratory experiment (Fig. 1), in which the central vortex alternately pairs with one of the satellite vortices. It thus appears that a weak initial asymmetry is sufficient to bring the tripole in this mode of repeated partner exchange. In the limiting case $c = 1$ the tripole is symmetric and rotates steadily with frequency $\omega_o/(2\pi) = 3\gamma/(8\pi^2 a^2) \simeq 0.038\gamma/a^2$; this value is indicated by the horizontal line in Fig. 3.

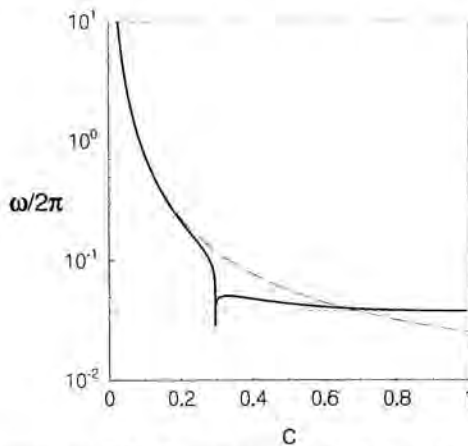


Fig. 3. Graphical representation of the frequency $\omega/2\pi$ in the motion of the asymmetric tripole as a function of the initial distance ratio $c = b_o/a_o$. The initial distances are normalized as $a_o + b_o = 2$ and the frequency has been scaled by γ/a^2 . The solid line represents calculated values, the horizontal line denotes the limiting frequency $\omega_o/2\pi$ of the symmetric tripole ($c = 1$), whereas the curved broken line represents the frequency (1) for the limiting case $c \rightarrow 0$.

In the limiting case $c \rightarrow 0$ the frequency should correspond with the rotation frequency of the rotating dipole, which is equal to $\omega_{dipole} = \gamma/(2\pi h_o^2)$. The initial distances are here normalized as $a_o + h_o = 2$, so that $h_o = 2c/(1+c)$. One thus obtains

$$f_I = \frac{\omega}{2\pi} = \gamma \left(\frac{1+c}{4\pi c} \right)^2, \quad (1)$$

which is shown graphically by the broken curve in Fig. 3. Apparently, this predicted limiting frequency corresponds very well with the actual frequency of the point-vortex system in régime I for $0 < c \lesssim 0.2$. Although this model captures some characteristic features of the observed asymmetric tripole evolution (*i.e.* the repeated partner exchange in régime II), the motion is purely periodic and does not show the increasing dipole excursions and the increasing maximum kink angle as observed in the experiment.

4. The modulated point-vortex tripole

The tripole evolution as shown in Fig. 1 is only observed when the tripolar vortex is generated at some distance from the rotation axis. Apparently, the curved free surface is responsible for this remarkable behaviour, even though the height differences across the tripole diameter are small compared to the total fluid depth (in the experiment shown in Fig. 1 this height difference is typically 2 mm, while the average fluid depth was 17 cm). When a vortex is moved in radial direction the topography of the free surface causes stretching or squeezing of the vortex tube, and therewith leads to changes in its strength: the vortex strength is modulated by the topography. This topography effect not only breaks the symmetry of the initial tripole, but also affects its dynamics during the subsequent evolution.

The topography-induced modulation can be incorporated in the point-vortex model in a similar way as was done by Kono & Yamagata (1977) and Zabusky & McWilliams (1982) for the β -effect. For this purpose the “point” vortex is replaced by a columnar Rankine-type vortex with a circulation γ given by

$$\gamma = \bar{\omega} A, \quad (2)$$

with $\bar{\omega}$ the relative vorticity averaged over the cross-sectional area A . Changes in the local fluid depth $H(\mathbf{x})$, with \mathbf{x} the horizontal position vector, results in squeezing or stretching of the vortex tube, which must be compensated by changes in A in order to satisfy conservation of volume:

$$A(\mathbf{x}) H(\mathbf{x}) = A_o H_o = \text{constant}, \quad (3)$$

where the subscript o refers to a reference state. Conservation of potential vorticity implies

$$\frac{2\Omega + \bar{\omega}(\mathbf{x})}{H(\mathbf{x})} = \frac{2\Omega + \bar{\omega}_o}{H_o}, \quad (4)$$

with Ω the rotation speed of the fluid system. Combination of (3)-(5) yields the following expression for the topography-modulated point-vortex strength

$$\gamma(\mathbf{x}) = \gamma_o + 2\Omega A_o \left[1 - \frac{H_o}{H(\mathbf{x})} \right]. \quad (5)$$

In the present experiments the undisturbed fluid depth is given by

$$H(r) = H(0) + \frac{\Omega^2 r^2}{2g} \quad (6)$$

where r is the radial coordinate measured from the rotation axis and g is the magnitude of the gravitational acceleration. Because $\Omega^2 r^2 / 2g \ll 1$ we can use a Taylor expansion of $H_o/H(r)$ to obtain the following relation for the modulated strength:

$$\gamma(\mathbf{x}) = \gamma_o - \frac{\Omega^3 A_o}{g H_o} (r_o^2 - r^2) \quad (7)$$

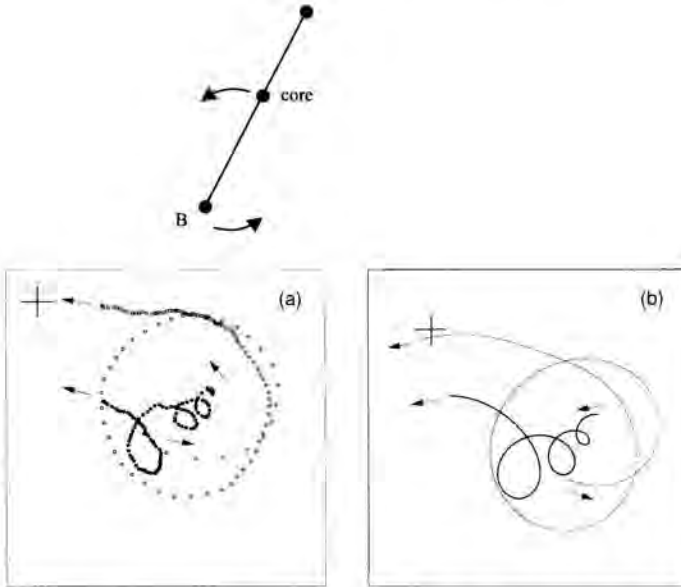


Fig. 4. Trajectories of the centres of the core vortex and one of its satellites (a) as measured in a laboratory experiment in a rotating free-surface fluid and (b) as predicted by the modulated point-vortex tripole model initialized with the experimental data.

where second order terms have been neglected. This equation is equivalent to that describing the strength modulation of a vortex on the gamma plane, which approximates the variation of the Coriolis parameter close to the poles of a rotating planet.

Numerical simulations have been performed for a point-vortex tripole with strength modulation according to (7), the fluid depth being given by (6). Such a set of three modulated point vortices forms a parametrically excited dynamical system that is no longer integrable, so that complicated (chaotic) behaviour is to be expected. An example of the trajectories of the centres of the core vortex and one of its satellites as measured in a typical laboratory experiment is shown in Fig. 4a. It is seen that the core vortex moves along a spiral-shaped path, while the satellite orbits around it. The corresponding trajectories according to the modulated point-vortex model (initialized with the experimental data) are shown in Fig. 4b, and the agreement with the observed tracks is striking.

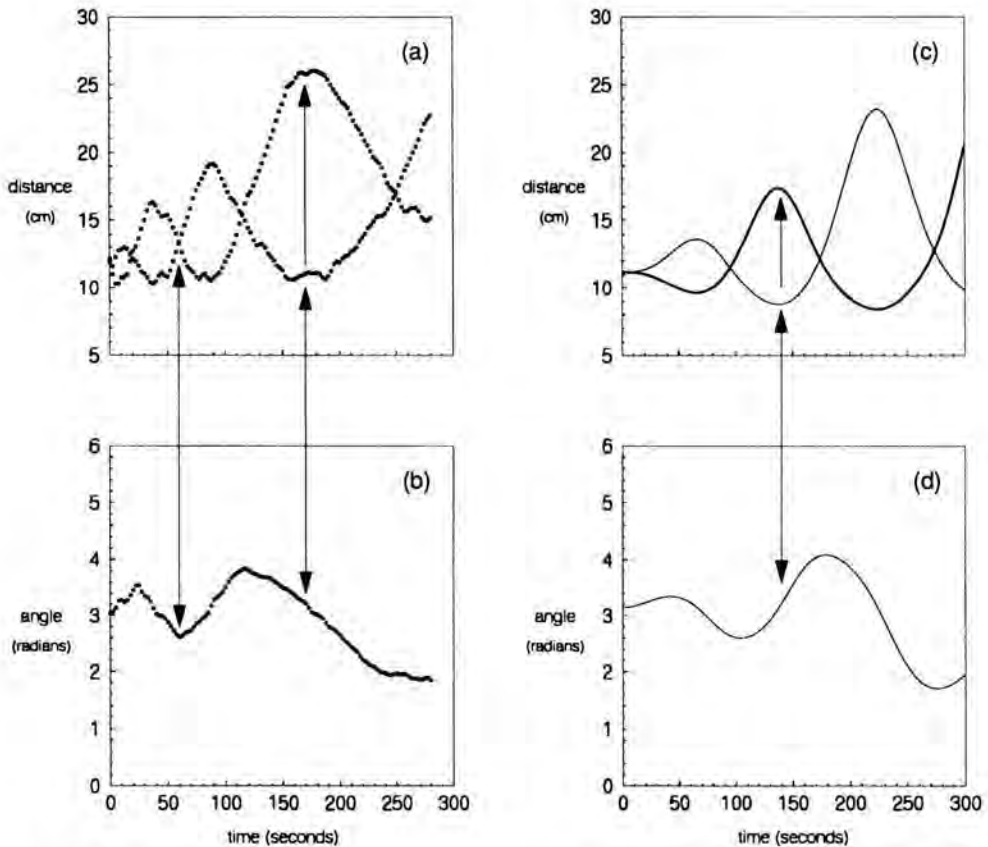


Fig. 5. Graphical representation of the distances $a(t)$ and $b(t)$ and the kink angle $\theta(t)$ as a function of time (a,b) as measured in the laboratory experiment and (c,d) as predicted by the modulated point-vortex tripole. The experiment corresponds with that shown in Figs. 1 and 4.

For the same experiment the measured distances $a(t)$ and $b(t)$ of the satellite centres to the centre of the core vortex as well as the kink angle $\theta(t)$ are presented as a function of time t in Fig. 5a,b. It is seen that the curves of $a(t)$ and $b(t)$ are exactly out of phase: a relative maximum of $a(t)$ corresponds with a relative minimum of $b(t)$ and *vice versa*. At such a local extreme value of $a(t)$ or $b(t)$, the angle $\theta(t)$ is equal to π , which corresponds to a linear arrangement of the vortex centres as visible in Figs. 1b and 1d, when the core-satellite dipole is at a maximum distance from the other satellite before the re-establishment of the tripole takes place. This is the case when $a(t) = b(t)$, for which the kink angle $\theta(t)$ apparently reaches an extreme value. During the course of the experiment the relative extremal values of the distances a and b and the angle show a significant increase, which was not predicted by the unmodulated model discussed in section 3. The modulated point-vortex tripole, initialized with the experimental values, however, predicts this behaviour quite well, see Fig. 5c,d.

An important question concerns the advection of passive scalars induced by the perturbed tripole. Seen in the co-rotating frame, the unperturbed symmetric tripole has a separatrix that does not change shape, and fluid remains trapped within it. Laboratory experiments on a perturbed tripolar vortex, however, show increasingly complicated filamentary distributions of dye that was initially contained within the compact tripole structure, see Fig. 1.

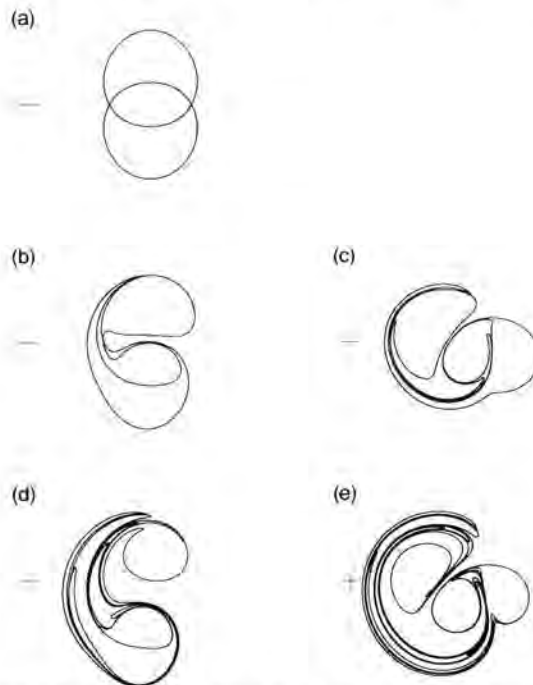


Fig. 6. Sequence of plots showing the evolution of passive tracers originally placed on the separatrix (a) of the initial (modulated) point-vortex tripole. The plots are drawn for the stages of aligned vortices (b,d) and maximum kink angle (c,e), corresponding with those shown in Fig. 1.

In order to investigate the advection properties of the modulated point-vortex tripole, the evolution of passive markers located on the separatrix of the initial, symmetric tripole was computed numerically, and the results are shown in Fig. 6. A total of 100 markers were evenly distributed over the initial separatrix, which clearly shows the separate core and satellite regions (Fig. 6a). The new marker positions, connected by straight line elements, are shown in Figs. 6b-e for four subsequent stages of the tripole evolution that correspond with aligned vortices (b,d) and maximum kink angle (c,e), similar to those shown in Fig. 1.

A comparison with the dye distributions in the laboratory experiment reveals a striking agreement between the model and the laboratory observations. This result stresses the power of the (modulated) point-vortex model: not only the motion of the vortex positions is accurately described, the model is also capable of describing into remarkable detail the advection of passive scalars induced by the vortex motions.

A more extensive description of this work will be published elsewhere (Velasco Fuentes, van Heijst and van Lipzig 1994).

Acknowledgement

One of us (O.U.V.F.) gratefully acknowledges financial support from the Stichting voor Fundamenteel Onderzoek der Materie (FOM).

References

- Carton, X.J., G.R. Flierl and L.M. Polvani, 1989 - The generation of tripoles from unstable axisymmetric vortex structures. *Europhys. Lett.* **9**, 339-344.
- Flór, J.B., W.S.S. Govers, G.J.F. van Heijst and R. van Sluis, 1993 - Formation of a tripolar vortex in a stratified fluid. *Appl. Sci. Res.* **51**, 405-409.
- van Heijst, G.J.F. and R.C. Kloosterziel, 1989 - Tripolar vortices in a rotating fluid. *Nature* **338**, 569-571.
- van Heijst, G.J.F., R.C. Kloosterziel and C.W.M. Williams, 1991 - Laboratory experiments on the tripolar vortex in a rotating fluid. *J. Fluid Mech.* **225**, 301-331.
- Kono, J. and T. Yamagata, 1977 - The behaviour of a vortex pair on the beta-plane. *Proc. Oceanogr. Soc. Japan* **36**, 83-84 (in Japanese).
- Legras, B., P. Santangelo and R. Benzi, 1988 - High-resolution numerical experiments for forced two-dimensional turbulence. *Europhys. Lett.* **5**, 37-42.
- Orlandi, P. and G.J.F. van Heijst, 1992 - Numerical simulation of tripolar vortices in 2D flow. *Fluid Dyn. Res.* **9**, 179-206.
- Pingree, R.D. and B. Le Cann, 1992a - Three anticyclonic Slope Water Oceanic EDDIES (SWODDIES) in the Southern Bay of Biscay in 1990. *Deep - Sea Res.* **39**, 1147-1175.

- Pingree, R.D. and B. Le Cann, 1992b - Anticyclonic Eddy X91 in the Southern Bay of Biscay, May 1991 to February 1992. *J. Geophys. Res.* **97**, 14,353–14,367.
- Velasco Fuentes, O.U., G.J.F. van Heijst and N.P.M. van Lipzig, 1994 - Unsteady behaviour of a topography-modulated tripolar vortex. *J. Fluid Mech.* (submitted).
- Zabusky, N.J. and J.C. McWilliams, 1982 - A modulated point-vortex model for geostrophic, β -plane dynamics. *Phys. Fluids* **25**, 2175–2182.

Fluid Dynamics Laboratory
 Department of Physics
 Eindhoven University of Technology
 P.O. Box 513, 5600 MB, Eindhoven
 The Netherlands

Maintenance of Continental Boundary Layer Shear through Counter Gradient Vorticity Flux in a Barotropic Model

Abstract

The use of a classical eddy parametrization in the analysis of continental boundary currents leads to the diffusion of momentum and vorticity and fails to recognize that the relevant eddies are dominated by the conservation of potential vorticity, which in turn may produce an increase in the mean relative vorticity. To illustrate this effect, we examine a non-inflected barotropic shear flow destabilized by the cross-stream variation in the bottom topography of a continental slope. The increase in maximum mean vorticity is computed for various values of the Rossby number and the topographic elevation.

Introduction

Continental boundary currents often exhibit a region of relatively strong cyclonic shear on their inshore side as is the case for the Gulf Stream (Brooks and Niiler 1977) where mean shear of the order of the Coriolis parameter can be observed over the continental slope. The shelf break region is also the site of strong eddy activities leading to the exchange of water with different properties between the deep and the shelf regions. Stern (1991, 1993) proposed that the inshore shear of a boundary current could be maintained by counter-gradient vorticity fluxes at the steep continental slope, rather than by a classical eddy diffusive parametrization, and the particular mechanism investigated involved a net cross-slope mass flux produced by down-stream topographic variations.

A different kind of topographic mechanism is discussed here, *viz.* that which is due to the instability of a laminar shear flow along a continental slope. Collings and Grimshaw (1984) have shown that cross-stream topography can destabilize non-inflected barotropic currents which are otherwise stable.

An illustration is provided by the flow in figure 1 which extends across the continental slope and onto a limited part of the shelf, with the relative vorticity decreasing monotonically to zero. Suppose that the corresponding cross-stream decrease in bottom depth is strong enough at the shelf break to produce the necessary potential vorticity maximum for a barotropic instability. If the condition is also sufficient, there will be a net eddy transport of water with maximum

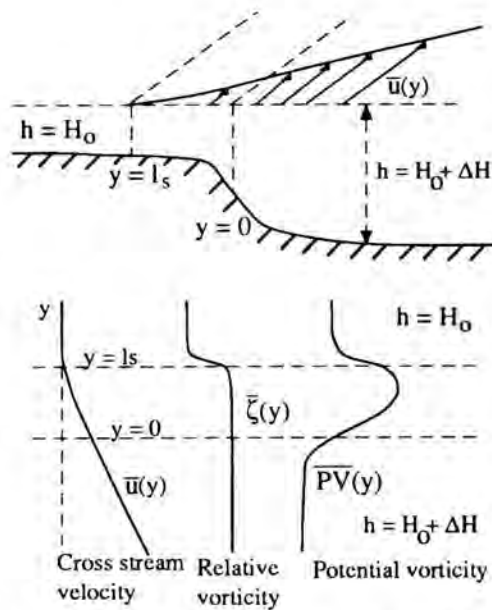


Fig. 1. A laminar shear flow $\bar{u}(y)$ with monotonic vorticity $\bar{\zeta}(y)$ at the edge of a continental slope of depth $h(y)$ which changes rapidly at the shelf break such that the potential vorticity of this current has an extremum. Top diagram is a perspective view.

potential vorticity into the deep water, thereby increasing the maximum mean vorticity in the shear flow by stretching of fluid columns displaced across the steep topography. Therefore any small tendency for lateral eddy diffusion of relative vorticity can be compensated by these topographically dominated effects at the continental slope.

For simplicity, we will consider a piecewise constant shear flow $\bar{u}(y)$ and a step-like topography ($h = H_0$, $y > 0$; $h = H_0 + \Delta H$, $y < 0$). In this model, a layer of width l_s of high potential vorticity on the shelf separates lower potential vorticity fluids on the semi-infinite shelf from the semi-infinite deep region (having the same relative vorticity on the other side of the escarpment ($y = 0$)). The evolution of the disturbance is quantitatively similar to the roll up of cores in the classical inflected shear flow problem (Pozrikidis and Higdon 1985), but now a qualitatively different effect on the mean vorticity occurs, *viz.* vorticity can be transported up the mean gradient.

The presence of cross-stream topography in continental boundary currents has a profound effect on the eddies and the velocity profile. In fact, as we will show, the restoring topographic force prevents the current from diffusing to the beach, and the conservation of potential vorticity increases or maintains the maximum mean vorticity. The nonlinear stability calculation uses the well known contour dynamical method with a novel feature presented by the topography which requires the computation of the appropriate Green's function.

Topographic Green's function

It can be shown (Bidlot and Stern 1994) that in the case of a step-like topography (at $y = 0$) the appropriate Green's function is made of the contribution of the classical two-dimensional barotropic point vortex (ξ, η) with strength Γ , and an image given by

$$G_1(x, y) = \frac{\Gamma}{4\pi} \frac{E}{2 + E} \operatorname{sgn}(y) [(x - \xi)^2 + (|y| + |\eta|)^2]$$

where $E = \Delta H/H_0$ and

$$\operatorname{sgn}(y) = \begin{cases} +1 & y > 0 \\ -1 & y < 0 \end{cases}$$

Note that the field G_1 is equivalent to the field produced in a uniform depth fluid by a point vortex of strength $\Gamma E/(2 + E) \operatorname{sgn}(y)$, located at a point $(\xi, -\eta \operatorname{sgn}(\eta) \operatorname{sgn}(y))$.

Using this Green's function, a contour dynamical code was constructed to follow the evolution of the two potential vorticity interfaces in our simplified shelf break model (Fig. 1). Special attention was given to the discontinuity in the normal velocity of a parcel crossing $y = 0$.

Numerical results

The initial perturbation is the most unstable normal mode of the linear theory for given Rossby number $Ro = \bar{\zeta}/f$ and cross-stream topographic change E . In that which follows, either l_s or the wavelength λ may be taken as the unit of nondimensional distance, and the other is prescribed by the maximum growth rate of the linear analysis. The initial amplitude of the disturbance was small enough to allow a comparison of the numerics with the linear theory, but no significant differences were noticed if somewhat different values are chosen; this will only alter the time required for the nonlinearities to be noticeable.

When $Ro = E$, the potential vorticity of the irrotational ($y > l_s$) and deep region ($y < 0$) are equal (Fig. 2), and the early evolution (Fig. 2a) is as predicted by the linear theory with the crest and trough of each interface growing exponentially with time. Consistent with this growth is the phase shift between L_1 and L_2 , which ensures that the positive vorticity anomalies in the L_1 -crest induce a net 'upward' (amplifying) motion on the nearest L_2 -crest and *vice versa*. As the disturbance gets larger (Fig. 2b), straining by the mean shear causes interfacial steepening ahead of the L_1 trough and behind the L_2 ridge, leading to the roll up and core formation ($t > 30$), as in the classical Kelvin-Helmholtz problem (Pozrikidis and Higdon, 1985). Figure 2c clearly shows the accumulation of high potential vorticity into well defined cores along the escarpment,

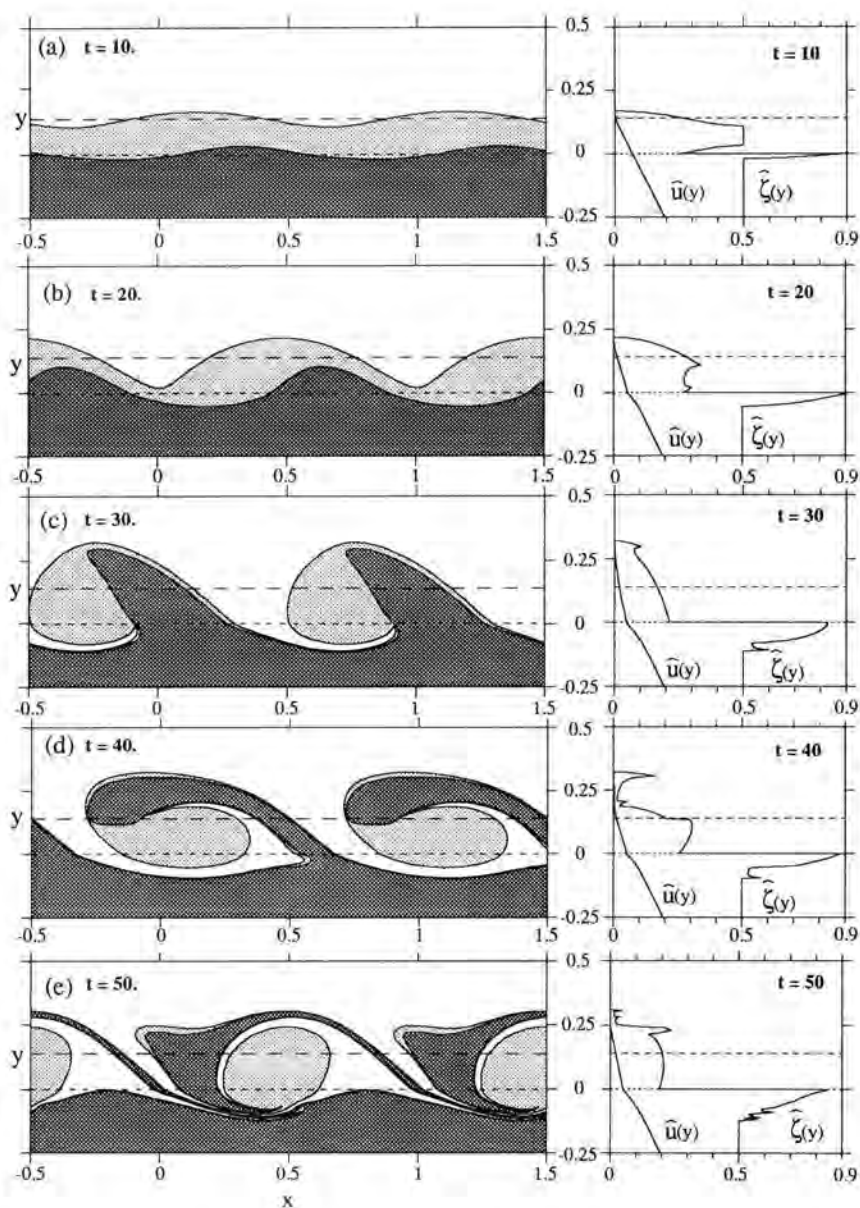


Fig. 2. Nonlinear evolution of the fastest growing mode for $E = .5$ and $R\sigma = .5$ with $\lambda = 1$ as the length unit (corresponding to $l_s = .14$). $1/f$ is the time scale. The light shaded strip contains the maximum potential vorticity and separates the deep water (dark shaded area) from the irrotational shelf water (white area). The dashed lines represent the undisturbed frontal positions. The cross-stream vorticity as well as the along-escarpment velocity averaged over one wavelength are also shown.

whereas the maximum penetration of the disturbance in adjacent regions is limited. The emerging state, even though not strictly steady, seems to consist of cores of maximum potential vorticity, around which tongues of lesser potential vorticity fluid from the deep as well as from the irrotational shallow region wind (Fig. 2d-e). Also shown in figure 2 is the x -averaged relative vorticity distribution $\zeta(y)$, and the corresponding mean velocity distribution. The amount of different water "types" (fluid with different shading and potential vorticity) transported across the escarpment was also computed. Note that the pinching-off of the interfaces tends to transport 'deep' water on the shelf ($y > 0$). This water is partially replaced by high potential vorticity core water whose stretching accounts for the region of maximum mean vorticity at $y < 0$. This illustrates how a countergradient vorticity flux can maintain a maximum shear and oppose any type of diffusive action tending to reduce the peak value. The topographic instability in figure 2 strongly suggests a new statistically steady state with maximum mean vorticity increased by 70%, and the small positive $\zeta(y)$ at $y > l_s$ implies that deep water will always ($t > 0$) occupy the upper shelf region. Likewise filaments from this region are entrained near $0 < y < l_s$, wound around the core and advected with the mean field far downstream from its place of origin on the upper shelf.

Many other cases were investigated for different values of Ro and E as indicated in figures 3a,b which show the entrained volume of irrotational water per eddy into the shear layer as well as the volume transport of deep water across the shelf break as a function of those two parameters with $l_s = 1$ and $H_o = 1$ as horizontal and vertical length unit. The entrained volume was defined and computed as follows (Bidlot and Stern 1994). The branch of L_1 in the ridge of the amplifying wave winds counterclockwise around the core, and approaches the trailing branch of L_1 in the trough of the wave. When close contact of the L_1 -branches occurs, a "cut" is made to form a multiconnected L_1 . One portion of this constitutes a "new" shear flow interface, outside of which is purely irrotational fluid and inside of which are the cores plus the entrained irrotational fluid (Fig. 3a).

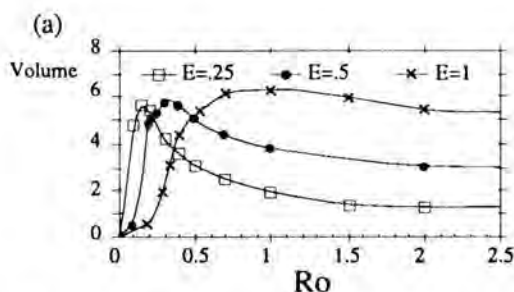


Fig. 3a. Nondimensional entrained volume per wavelength of irrotational shelf water into the shear flow as a function of Ro and E for the fastest growing mode with l_s and H_o as length unit.

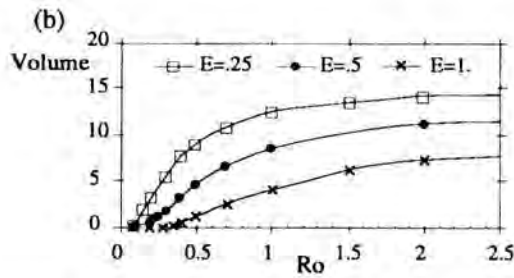


Fig. 3b. Nondimensional volume transport per wavelength of deep water across the shelf break as a function of Ro and E for the fastest growing mode when l_s and H_o as length unit.

Similarly, each ridge of the amplifying L_2 -wave is squeezed at its base ($y=0$) between two consecutive wedges of shelf water winding around the cores. This leads to the pinching-off of a finite volume of deep water on the shelf. A cut was made in a manner similar to L_1 when the neck was fully formed above $y=0$ and the entrained volume defines the transport of deep water across the shelf break (Fig. 3b).

Figure 3a shows that for any given geometry, an increasing shear increases the amount of originally irrotational fluid that is trapped inside the shear layer until a maximum is reached, followed by slower decrease. On the other hand (Fig. 3b), the exchange between the deep and the shelf region increases monotonically with the back-ground shear.

A useful measure of the nonlinear finite amplitude is the width of the high vorticity region δ , defined as the distance from $y=0$ to the point $y < 0$ where the x -average total vorticity returns to its background value. A longtime average $\bar{\delta}$ was computed and figure 4 summarizes its dependence on the parameters.

Conclusions and suggestions

We have computed the finite amplitude evolution of a non-inflected shear flow destabilized by a cross-stream variation of topography, in order to illustrate an

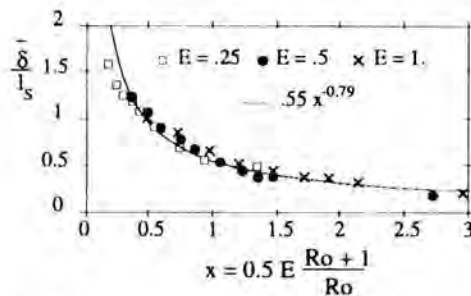


Fig. 4. Average value of δ/l_s as a function of Ro and E . The curve is the best power fit.

apparently ubiquitous effect in continental boundary currents, *viz.* the countergradient vorticity flux which increases the maximum mean vorticity. This effect is to be contrasted with the rapid diffusion of mean vorticity which would occur in any classical (diffusive) parametrization of the effect of the eddies on the mean flow.

The applicability of our model to real continental boundary currents is limited by the absence of stratification and other kinds of topographic effects. However, the oceanic isopycnals (in the Florida Current, for example) tend to have a similar cross-stream variation as the isobaths. It is therefore conceivable that cross-stream motion along these isopycnals will generate vorticity in a similar manner as illustrated above, so that the countergradient vorticity flux may also occur in the baroclinic case. It is suggested that those potential vorticity conserving effects maintain such strong inshore lateral shear as is observed in the Gulf Stream.

The simple escarpment model has also been used to illustrate the cross-slope transfer of conservative water mass properties like potential vorticity, temperature, salinity and nutrient in the more realistic oceanic case. Figure 2 shows how an instability leads to the formation of a "new" potential vorticity interface across which there has been an entrainment of the "inshore water mass", and figure 3 documents some of the volumetric transfers.

References

- Bidlot J.-R. and M.E. Stern, 1994 - Maintenance of continental boundary-layer shear through counter gradient vorticity flux in a barotropic model. *J. Fluid Mech.* **271**, 55-85.
- Brooks I.H. and P.P. Niiler, 1977 - Energetics of the Florida current. *J. Mar. Res.* **35**, 163-191.
- Collings S.I. and R. Grimshaw, 1984 - Stable and unstable barotropic shelf waves in a coastal current. *Geophys. Astrophys. Fluid Dyn.* **29**, 179-220.
- Pozrikidis C. and J.J. Higdon, 1985 - Nonlinear Kelvin-Helmholtz instability of a finite vortex layer. *J. Fluid Mech.* **157**, 225-263.
- Stern M.E., 1991 - Countergradient vorticity flux generated in continental boundary currents. *J. Phys. Oceanogr.* **21**, 1622-1630.
- Stern M.E., 1993 - Topographic jetogenesis and transitions in straits and along continents. *J. Phys. Oceanogr.* **23**, 846-854.

J.-R. Bidlot and M.E. Stern
Department of Oceanography
Florida State University
Tallahassee, FL 32206-3048
USA

Evolution of a Rotating Barotropic Modon in a Primitive Equation Model

Abstract

An analytic solution for a rotating barotropic modon, which is an exact solution to the quasigeostrophic potential vorticity equation, is used as an initial condition for a series of numerical experiments describing two-layer primitive equation flow over an isolated seamount in a periodic channel. For the case with no topography, the upper and lower layers evolve in exactly the same way, resulting in a rectilinear dipole translating to the west. For cases with finite topography, the upper layer dipole drifts away from the seamount, while the lower layer dipole expands to cover the entire seamount, and undergoes a change in rotation direction. These results indicate that modons may be robust in a primitive equation environment.

Introduction

Coherent vortex motions are observed quite commonly in the open and coastal oceans, as is evident from many remote sensing images. These flows arise naturally on a rotating earth, because the Coriolis force is horizontal but also perpendicular to the velocity vector. Their ability to transport mass, momentum, and energy makes a knowledge of their dynamics crucial to an understanding of the balances of these quantities in the ocean. For this reason, and because their dynamics are intrinsically interesting, research into single eddies and multiple vortex systems has flourished within the past two decades. Of particular interest is the study of dipoles, two oppositely-signed vortices linked together to form a single entity. Dipoles have been observed with increasing frequency through remote sensing, laboratory experiments, and numerical simulation.

In a remote sensing context, vortex pairs have been observed in a broad range of scenarios. For example, Johannessen *et al.* (1989) have noted the presence of dipoles in AVHRR imagery of the Norwegian Coastal Current system, and attributed their genesis to an instability in the flow. Fedorov and Ginzburg (1986) have showed extensive evidence of dipole eddies in ice imagery and state that these paired vortices appear to be the ocean's universal long-term response to a momentum impulse which injects vorticity of both signs into the near-

surface ocean. In an apparently related vein, Sheres and Kenyon (1989) observed a dipole emerging from the Santa Barbara Channel, and attributed its existence to an abrupt changes in wind stress. But perhaps the richest population of remotely-sensed dipoles was shown by Ahlnas *et al.* (1987) who discovered well over a dozen such structures in the Alaska Coastal current, although the precise cause for their origin is uncertain.

The occurrence of dipole vortices is not limited to observations of their remote imagery, however. Laboratory simulations have provided another opportunity to study their behaviour. Flierl *et al.* (1983) have used an impulsive injection of fluid at the boundary of a tank of homogeneous fluid to generate a stable vortex pair that traveled along a curved trajectory, while van Heijst and Flor (1989) used a similar technique to generate dipoles. Their study also gave an indication of the robustness of these forms as they emerged essentially intact after enduring collisions with other dipoles. Using an equivalent impulsive-generation mechanism in a rotating tank, Kloosterziel *et al.* (1993) studied trajectories generated by vortex pairs which were allowed to propagate onto a slope.

While the analysis of laboratory and remote-sensing data is a useful tool for understanding the behavior of dipolar vortices, the scope of the phenomena available is necessarily limited to either what is observable in nature or feasible in the laboratory. Numerical simulation affords us the opportunity to examine a potentially far richer ensemble of generation and propagation conditions. For example, McWilliams and Flierl (1979) used a two-layer quasigeostrophic (QG) model to demonstrate that an axisymmetric, pure-baroclinic monopole will evolve to produce a rectilinear dipole modon. Mied and Lindemann (1979) showed that a qualitatively similar result could be obtained using a primitive equation (PE) model as well. Furthermore, at least one other mechanism exists for the creation of dipoles from monopoles. McWilliams (1983) found that two propagating, oppositely-signed beta-plane monopoles could collide, merge, and propagate as a stable dipole modon.

Numerical simulations have also allowed a more extensive investigation of Fedorov and Ginzburg's (1986) suggestion that dipole eddies are a common response to short-term momentum inputs to the near-surface ocean. Mied *et al.* (1991) have investigated the fate of a variety of momentum patches used as initial conditions in a reduced gravity PE calculation. They found that dipoles can result from patches having many Rossby numbers and length scales. Similarly, Ikeda (1991) reported that a uniform wind stress field, acting over anomalies in ice cover thickness in a coupled ice-ocean system, can produce differential Ekman transport that results in paired eddies with the vortices having opposite sign. And finally, Haidvogel *et al.* (1991) and Hofmann *et al.* (1991) have shown deflection of the near-shore flow by a cape on the coast of California can produce a large-scale dipole. Signell and Geyer (1991) showed that the separation of a flow oscillating with tidal frequency past a cape could result in an injection of high vorticity lateral boundary layer fluid into the interior of the flow, which can sometimes assume a dipole form.

Of interest in the context of the present work are the observations of dipoles over isolated topographic features. Johnson (1978) showed that steady flow over an isolated topographic feature produced a dipole at finite Rossby number. Nof (1990) used a circular gamma plane model (reminiscent of paraboloid bottom topography) to show that an asymmetric, steady modon-like solution could result, while Reznik (1985) showed that a similar dipolar modon could stably orbit on infinite parabolic relief along a line of constant topographic height. And finally, Mied *et al.* (1992) exhibited solutions to the QG equations of motion which can rotate steadily over isolated paraboloid topography.

Although the work of Mied *et al.* (1992) documents the existence of an infinity of radial and azimuthal modes, we shall focus on the dipoles to understand the viability of these barotropic, QG solutions in a more realistic oceanic environment. Accordingly, we describe the results of numerical experiments which use these exact solutions as initial conditions in a PE model. Their stability is investigated over a flat bottom topography, and modifications to their behavior are observed as the topographic height is increased to finite amplitude.

Experiment description

These experiments examined the evolution of an exact, QG rotating modon solution in a PE periodic zonal channel over an isolated seamount of varying height. The initial condition for each simulation was the analytic barotropic rotating modon solution described by Mied *et al.* (1992). For a modon of radius r_a and a seamount with base radius r_b , the nondimensional stream function for each of the three regions defined for the small modon case ($\alpha^{1/2} = r_a/r_b \leq 1$) is given by:

$$\begin{aligned}\Psi^I &= Q + \omega(r^2/2 - 2\beta) + AJ_0(\beta^{-1/2}r) + G_T(r) + b_n^I J_n(\beta^{-1/2}r) \sin n\theta, \quad r \leq \alpha^{1/2} \\ \Psi^{II} &= I(r) + b_n^I \alpha^{n/2} J_n(a) r^{-n} \sin n\theta, \quad \alpha^{1/2} \leq r \leq 1 \\ \Psi^{III} &= b_n^I \alpha^{n/2} J_n(a) r^{-n} b_n^I \sin n\theta, \quad 1 \leq r\end{aligned}\quad (1)$$

where r and θ represent position in polar coordinates, with the origin located at the seamount centre. J_n is the order n Bessel function of the first kind, ω represents the modon rotation rate, and b_n^I is an arbitrarily specified amplitude for the azimuthal solution part. Also, β is the separation parameter associated with the separation of variables solution, and, for azimuthal mode n and radial mode p , a is the p th root of the eigenvalue relation given by:

$$J_{n-1}(a) = 0$$

In equations (1), $G_T(r)$, $I(r)$, Q , and A are defined in Mied *et al.* (1992) in terms of the above quantities, an arbitrary axisymmetric rider amplitude Ψ_0 , and γ , the ratio of seamount centre height h_m to undisturbed ocean depth H :

$$\gamma = h_m/H$$

Equations (1) are applicable only to cases where the seamount is a paraboloid, with the bottom topography given by:

$$h(r) = h_m [1 - (r/r_h)^2] S(1 - r/r_h) \quad (2)$$

where $S(x - a)$ is the Heaviside step function such that $S = 1$ for $x < a$ and $S = 0$ for $x > a$.

Note that equations (1) are an exact solution of the QG potential vorticity equation in which both stream function and radial velocity are required to be continuous throughout the domain, while relative vorticity may be discontinuous at the modon boundary.

The initial condition modon geometry and amplitudes were the same for all experiments. Our intent was to focus on the dynamics of rotating dipoles, so the first radial and azimuthal modes were chosen ($n = p = 1$). The modon radius r_a was 20 km, and the azimuthal amplitude b'_n was set to 0.1. The arbitrary rider amplitude Ψ_0 was chosen to be zero.

The shallow water equations for a two-layer Boussinesq fluid on an f -plane are:

$$\begin{aligned} \partial u_i / \partial t + u_i \partial u_i / \partial x + v_i \partial u_i / \partial y - f v_i &= -\partial p_i / \partial x + A_H \nabla^2 u_i \\ \partial v_i / \partial t + u_i \partial v_i / \partial x + v_i \partial v_i / \partial y + f u_i &= -\partial p_i / \partial y + A_H \nabla^2 v_i \\ \partial h_i / \partial t + \partial h_i u_i / \partial x + \partial h_i v_i / \partial y &= 0 \\ \nabla p_2 &= \nabla p_1 - g' \nabla h_1 \end{aligned} \quad (3)$$

where subscripts $i = 1, 2$ represent upper and lower layer variables, respectively. The x and y velocities are represented by u_i and v_i , while h_i and p_i represent the layer thicknesses and Boussinesq pressure. A_H is the horizontal viscosity coefficient and g' is the reduced gravity. If the undisturbed layer thicknesses are H_1 and H_2 , the interface displacement is described as $h = H_1 - h_1 = h_2 - H_2$.

To describe the modon's evolution, equations (3) were solved numerically on a rectangular grid, with periodic boundary conditions at the boundaries oriented north-south, and free slip boundary conditions at the east-west oriented boundaries. The fluid surface was prescribed to be a rigid lid, and the kinematic viscosity was chosen to simulate nearly inviscid flow conditions while maintaining numerical stability.

For all experiments, the channel width was 240 km, with an upper layer undisturbed depth of 1000 m, and a lower layer undisturbed depth of 4000 m. The bottom topography consisted of a single isolated seamount with a circular base 80 km in diameter, located at the center of the computational grid.

To initialize the PE calculation, the layer velocities and the interface displacement must be specified. Since the analytic solution was barotropic, the velocities in each layer were initially specified to be equal and were set to the modon

velocities. Modon velocities were obtained by calculating the stream function value at each grid point from the analytic solution, and then calculating velocities numerically using a second order finite difference scheme. The initial interface displacement was specified to be zero at each grid point.

These experiments examined the effects of increasing seamount height on the evolution of the initial modon. Four different seamount heights were examined. In each experiment, γ for the analytic solution initial condition was matched with the actual seamount centre height in the PE model. Note that the analytic modon rotation rate depends on γ , so that the expected initial rotation rate was different for each experiment.

Results

Flat bottom case ($\gamma = 0$)

For the first experiment, an analytic modon solution with $\gamma = 0$ is used as an initial condition for a PE calculation with model topography set to zero. The calculation represents a time interval of 40 inertial periods.

Figure 1 shows a time series of lower layer relative vorticity from inertial period (IP) 0 to IP 40. Each panel shows only part of the computational domain, from -100 km to 100 km along the X axis, and from -70 km to 70 km along the Y axis. The dipole appears to undergo an initial adjustment process between IP 0 and IP 2, during which the vorticity becomes more uniformly distributed, with smaller vorticity gradients near the dipole boundary.

For this experiment, the anticipated dipole rotation rate is zero, based on the rotation rate for the analytic modon initial condition. From Figure 1 it is clear that, although no rotation develops in either layer, the dipole seems to evolve rapidly to a rectilinear form translating to the west. Estimates of the movement of the dipole centre indicate an approach to a steady translation rate.

Note that although the strength of the vorticity maxima within the dipole decreases steadily, the relative vorticity field continues to show a clear dipolar structure up to IP 40.

The time series of upper layer relative vorticity is not shown, since it is identical to the lower layer for this experiment.

Finite topography experiments ($\gamma > 0$)

For the remaining three experiments, analytic modon solutions with finite topography ($\gamma = 0.1, 0.2, 0.3$) were used as the initial conditions for calculations with model topography described by equation (2) and $h_m = 400, 800$, and 1200 m, respectively. For each experiment, the calculation was performed for a time interval of 40 inertial periods.

Figure 2 shows a time series of upper layer relative vorticity from IP 0 to IP 40 for the $\gamma = 0.2$ ($h_m = 800$ m) case. The circle in each panel represents the

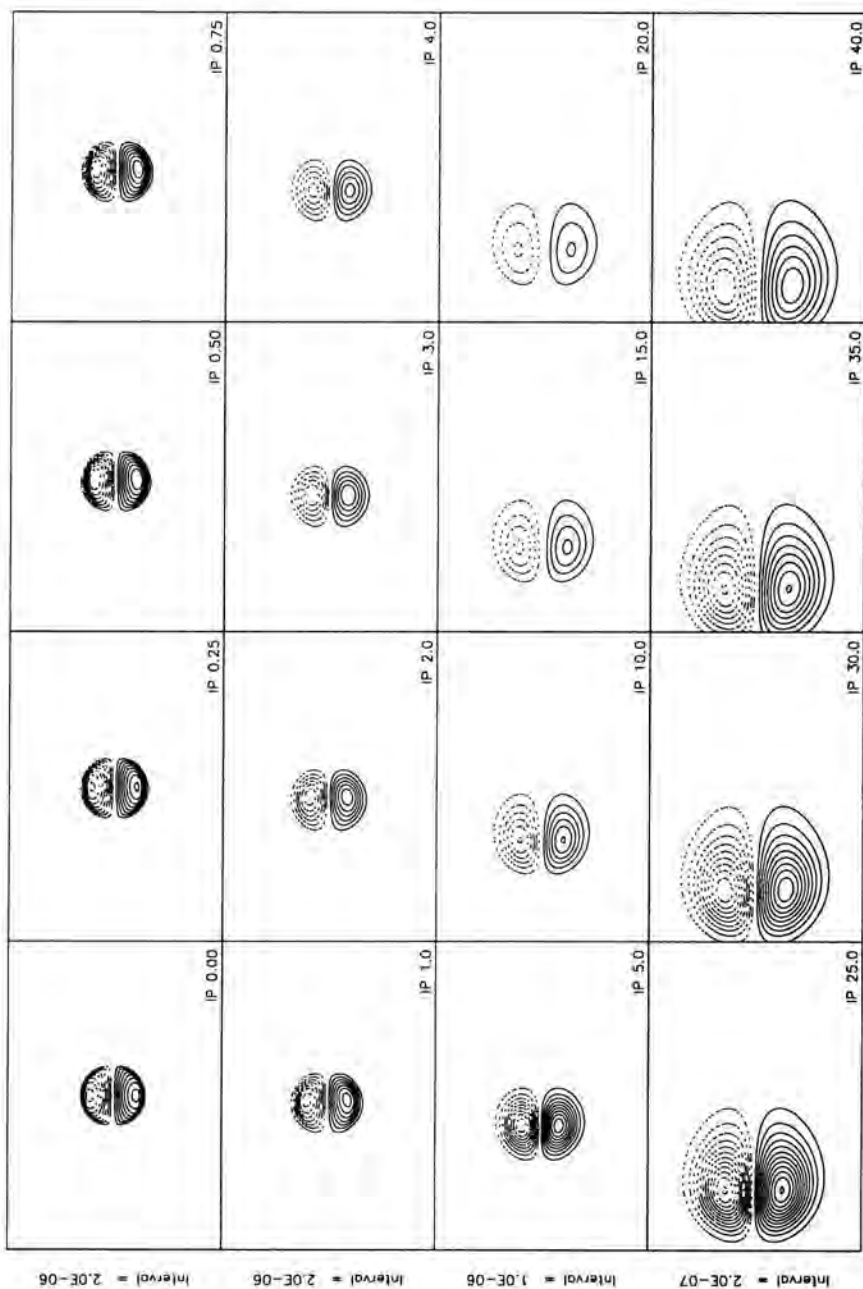


Fig. 1. Lower layer relative vorticity for the flat bottom case. Time (in inertial periods) is shown at lower right in each panel. Solid contours show positive vorticity, and dotted contours show negative vorticity. Contour intervals (in rad/sec) for each row are shown at left margin.

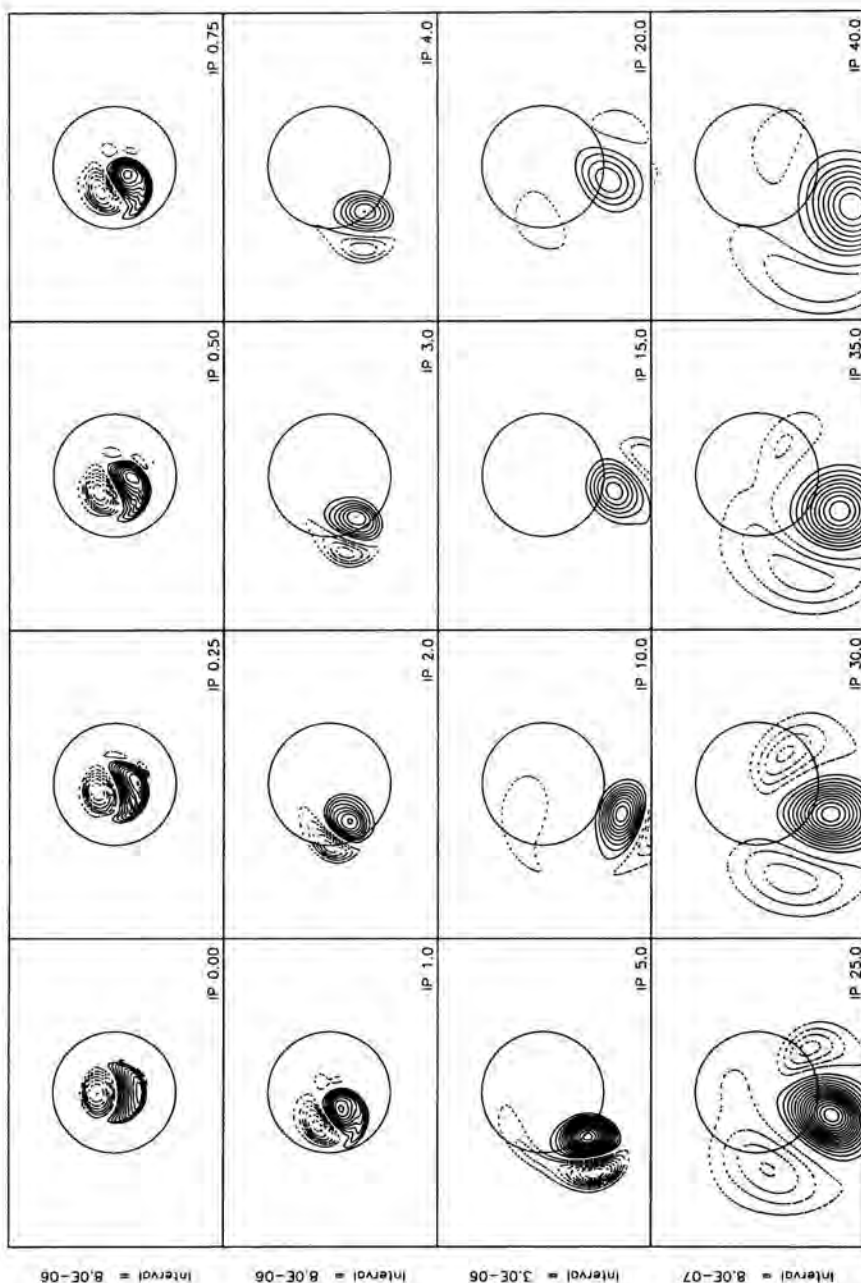


Fig. 2. Upper layer relative vorticity for the $h_m = 800$ m case. Time (in inertial periods) is shown at lower right in each panel. Solid contours show positive vorticity, and dotted contours show negative vorticity. Contour intervals (in rad/sec) for each row are shown at left margin.

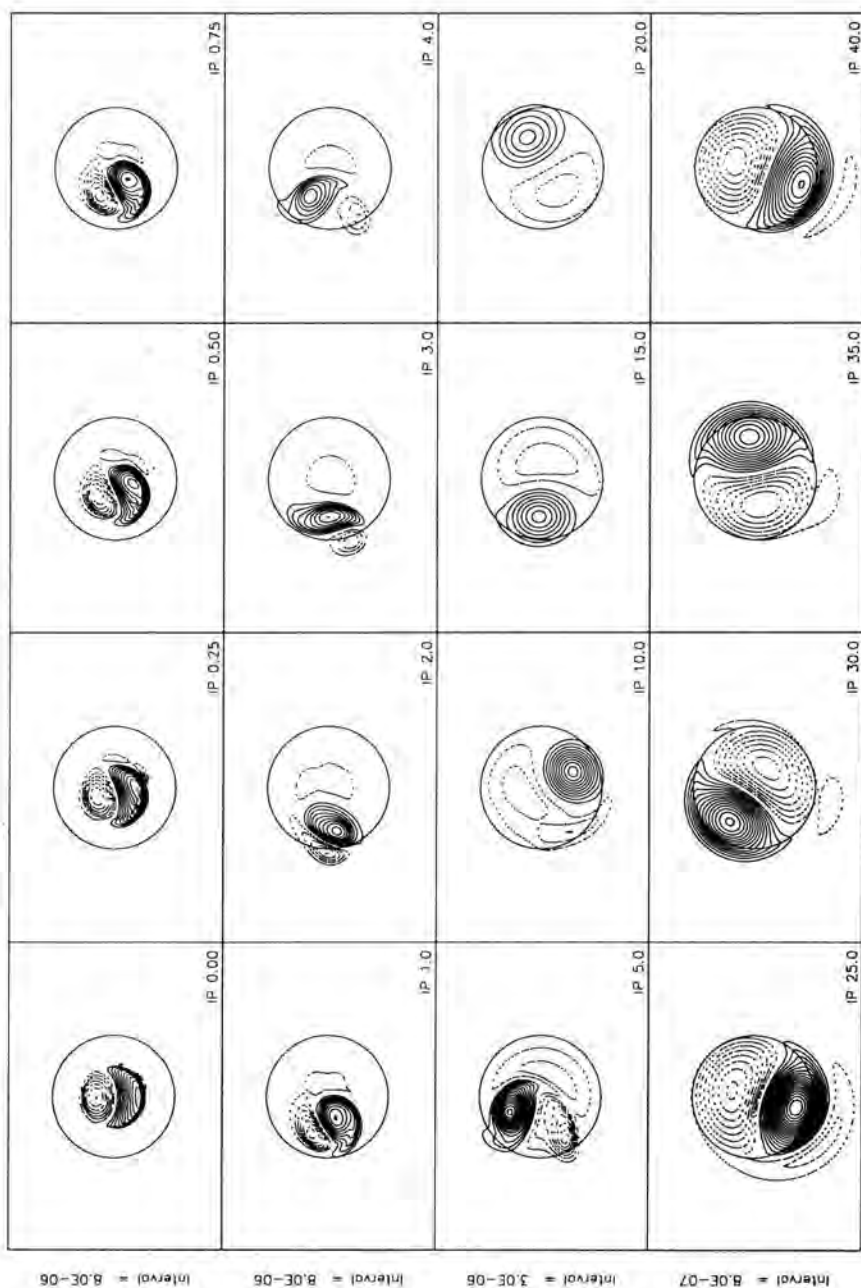


Fig. 3. Lower layer relative vorticity for the $h_m = 800$ m case. Time (in inertial periods) is shown at lower right in each panel. Solid contours show positive vorticity, and dotted contours show negative vorticity. Contour intervals (in rad/sec) for each row are shown at left margin.

seamount base, and the horizontal scales associated with each panel are the same as in Figure 1.

With $\gamma = 0.2$, there is an initial mutual westward advection while the shape of the vorticity patches changes. By IP 2 the vorticity gradients at the modon boundary are noticeably reduced. For this case, the anticipated dipole rotation rate is 6.63×10^{-6} rad/sec, based on the initial condition analytic solution. Figure 2 shows that, from IP 0 to about IP 20, the dipole does rotate in a positive sense, but this rotation is accompanied by translation along a curved trajectory.

Figure 3 shows a time series of lower layer relative vorticity from IP 0 to IP 40 for the $\gamma = 0.2$ case. The lower layer dipole undergoes an initial mutual advection and vorticity adjustment similar to the upper layer. Again, the anticipated dipole rotation rate is 6.63×10^{-6} rad/sec. From IP 0 to IP 5, the dipole does indeed rotate in a positive sense. After IP 5, however, the negative vorticity lobe is redistributed, and the dipole that emerges begins to rotate in a negative sense, opposite from the anticipated rotation rate. Between IP 10 and IP 40, the dipole maintains a relatively constant negative rotation rate.

Figure 3 also reveals some interesting changes in the size of the lower layer dipole. Although the changes in contour interval between rows of panels in Figure 3 makes precise estimates of the dipole's size difficult, it is clear that the modon boundary, initially located 20 km from the seamount centre, gradually moves outward until, at IP 40, the dipole extends over the entire seamount.

The results for the $\gamma = 0.2$ case in each layer are qualitatively similar to those for $\gamma = 0.1$ and 0.3 , so that results from these two experiments will not be shown. In both of these experiments, the upper layer dipole moves off of the seamount, and exhibits unsteady rotation, while the lower layer dipole gradually grows in

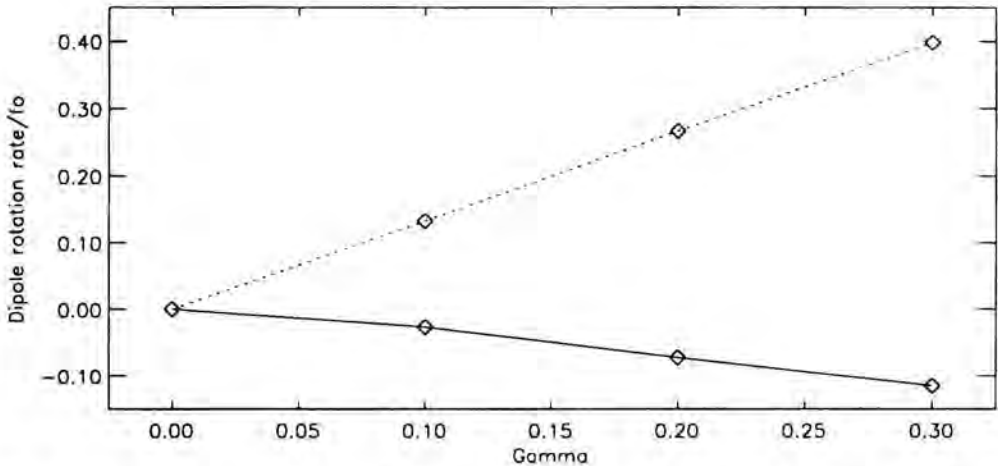


Fig. 4. Comparison of lower layer dipole rotation rate after inertial period 30 (solid line) with modon rotation rate anticipated from the analytic solution (dotted line). Rotation rates are scaled by f_0 .

size to cover the entire seamount and undergoes a vorticity adjustment process, emerging as a dipole rotating in a sense opposite to that anticipated from the analytic solution. Figure 4 compares lower layer dipole rotation rate (after 30 inertial periods) with the anticipated rotation rate from the analytic initial condition as a function of topographic height. It is clear that the lower layer dipole undergoes a significant adjustment process, and in all cases with non-zero topography, emerges with a rotation rate that is drastically different from that predicted by the initial condition.

Conclusions

In this work, we have examined the viability of rotating barotropic dipolar modons. The analytic model of Mied *et al.* (1992) indicates that exact solutions to the QG equation of motion can exist as steadily rotating vortex pairs over paraboloid topography of limited horizontal extent. Since the real ocean includes non-QG effects, it seems important to test the behaviour of the analytic QG solution in a more realistic environment. Accordingly, we use these barotropic dipoles to initialize a PE two-layer numerical model, thus allowing for non-QG effects (e.g., interfacial Poincaré waves) and possible modal coupling between the initial barotropic mode and the baroclinic mode available in a two-layer system. In addition, these calculations allow for an assessment of the effects of finite amplitude topography.

With these objectives in mind, we have used a single, representative barotropic modon with zero axisymmetric rider ($\Psi_0 = 0$) and a non-zero azimuthal strength ($b'_n = 0.1$); topographic height lies in the interval $0.0 \leq \gamma \leq 0.3$. Although both similarities and differences were noted between the experimental and analytic results, none of the experimental results could be anticipated from the analytic solution.

The flat bottom case ($\gamma = 0$) is perhaps the most surprising. With no axisymmetric rider, the expected rotation rate is zero, but the numerical results differ from the anticipated behaviour in several significant ways. Specifically, we find that:

- Viscosity acts to redistribute the vorticity, diminishing the sharp vorticity gradient at the edge of the modon.
- The modon evolves to a rectilinear, translating form which propagates stably away from its initial position.
- The dipole approaches a steady translation rate after thirty inertial periods.

The results for the finite topography cases are qualitatively different from those for the flat bottom case. Specifically, we find that:

- Mutual advection of the vortices occurs while vorticity is redistributed.
- In the upper layer, the dipole moves off the seamount.

- In the lower layer, the vorticity patches expand, but are confined to the region over the seamount.
- Although the initial analytic modon rotates in a positive (anticlockwise) sense, the lower layer dipole changes rotation direction before IP 10, and develops an approximately steady negative rotation rate (clockwise).

We conclude by noting that the analytic modon forms of Mied *et al.* (1992) may be weakly unstable in a more realistic baroclinic ocean possessing finite-amplitude topography. In the presence of viscosity, the dipoles evolve to a new morphology. In the upper layer, the dipole moves away from the seamount. However, in the lower layer, these unanticipated forms remain modon-like, possessing at least two characteristics of rotating modons: a spatially compact vorticity distribution (with zero vorticity just outside the seamount) and steady rotation. These results suggest that there may be many rotating modon configurations and argues strongly for a tractable analytical formulation that mirrors the resulting, steady-state numerical results.

Acknowledgments

B.L. Lipphardt, Jr. acknowledges the Department of Defense National Defense Science and Engineering Graduate Fellowship program. R.P. Mied and G.J. Lindemann acknowledge support from the Naval Research Laboratory Project 72-5512-04. A.D. Kirwan, Jr. acknowledges the support of ONR Grant N00014-91-J-1560 (Office of Naval Research) and the Samuel L. and Faye M. Slover endowment to Old Dominion University.

References

- Ahlnas, K., T.C. Royer, and T.H. George, 1987 - Multiple dipole eddies in the Alaska Coastal Current detected with Landsat Thematic Mapper data. *J. Geophys. Res.* **92**, 13041–13047.
- Fedorov, K.N. and A.I. Ginzburg, 1986 - "Mushroom-like" currents (vortex dipoles) in the ocean and in a laboratory tank. *Annales Geophysicae* **4**, 507–516.
- Flierl, G.R., M.E. Stern, and J.A. Whitehead, 1983 - The physical significance of modons: Laboratory experiments and general integral constraints. *Dyn. Atmos. Oceans* **7**, 233–263.
- Haidvogel, D.B., A. Beckmann, and K.S. Hedstrom, 1991 - Dynamical simulations of filament formation and evolution in the coastal transition zone. *J. Geophys. Res.* **96**, 15017–15040.
- van Heijst, G.J.F. and J.B. Flór, 1989 - Dipole formation and collisions in a stratified fluid. *Nature* **340**, 212–215.

- Hofmann, E.E., S. Hedstrom, J.R. Moisan, D.B. Haidvogel, and D.L. Mackas, 1991 - Use of simulated drifter tracks to investigate general transport patterns and residence times in the coastal transition zone. *J. Geophys. Res.* **96**, 15041-15052.
- Ikeda, M., 1991 - Wind-induced features in a coupled ice-ocean system. *J. Geophys. Res.* **96**, 4623-4629.
- Johannessen, J.A., E. Svendsen, S. Sandven, O.M. Johannessen, and K. Lygre, 1989 - Three-dimensional structure of mesoscale eddies in the Norwegian Coastal Current. *J. Phys. Oceanogr.* **19**, 3-19.
- Johnson, E.R., 1978 - Trapped vortices in a rotating flow. *J. Fluid Mech.* **86**, 209-224.
- Kloosterziel, R.C., G.F. Carnevale and D. Philippe, 1993 - Propagation of barotropic dipoles over topography in a rotating tank. *Dyn. Atmos. Oceans*, **19**, 65-100.
- McWilliams, J.C., 1983 - Interactions of isolated vortices. II. Modon generation by monopole collision. *Geophys. Astrophys. Fluid Dyn.* **24**, 1-22.
- McWilliams, J.C. and G.R. Flierl, 1979 - On the evolution of isolated, nonlinear vortices. *J. Phys. Oceanogr.* **9**, 1155-1182.
- Mied, R.P., A.D. Kirwan, Jr., and G.J. Lindemann, 1992 - Rotating modons over isolated topographic features. *J. Phys. Oceanogr.* **22**, 1569-1582.
- Mied, R.P. and G.J. Lindemann, 1979 - The propagation and evolution of cyclonic Gulf Stream rings. *J. Phys. Oceanogr.* **9**, 1183-1206.
- Mied, R.P., J.C. McWilliams, and G.J. Lindemann, 1991 - The generation and evolution of mushroom-like vortices. *J. Phys. Oceanogr.* **21**, 489-510.
- Nof, D., 1990 - Modons and monopoles on a gamma-plane. *Geophys. Astrophys. Fluid Dyn.* **52**, 71-87.
- Reznik, G.M., 1985 - Exact solution for two-dimensional topographic Rossby solution. *Dok. Akad. Nauk. SSSR* **282**, 981-985. (in Russian)
- Sheres, D. and K.E. Kenyon, 1989 - A double vortex along the California coast. *J. Geophys. Res.* **94**, 4989-4997.
- Signell, R.P. and W.R. Geyer, 1991 - Transient eddy formation around headlands. *J. Geophys. Res.* **96**, 2561-2575.

B.L. Lipphardt, Jr. and A.D. Kirwan, Jr.,
Center for Coastal Physical Oceanography
Old Dominion University
Norfolk, VA 23529, USA

R.P. Mied and G.J. Lindemann,
Naval Research Laboratory
Remote Sensing Division, Code 7250
Washington, D.C. 20375, USA

Stirring of an Inviscid Fluid by Interacting Point Vortices

Abstract

The purpose of this paper is to discuss quantitatively some stirring properties of a two-dimensional, ideal fluid induced by two and three point vortices. Special attention is given to the mixing process associated with the periodic interaction between a vortex pair and a monopole.

Introduction

Interest in the advection of two-dimensional (2D) motion of Lagrangian particles in an inviscid incompressible fluid with a prescribed Eulerian velocity field dates from quite a long time ago. The Hamiltonian structure of the equations of motion of an individual fluid particle led Gibbs (1902) to the idea of considering the 2D motion of some coloured area of liquid as an analogue for an ensemble of points in an abstract phase space. In particular, he introduced the term "stirring of incompressible liquid" for a pure mechanical displacement of the coloured regions. This idea was further developed by Welander (1955), who presented some pictures showing the deformation of a tracer pattern in a 2D atmosphere due to a strong monopolar vortex. In recent times the analysis of 2D coherent vortex structures is increasingly attracting the attention of many fluid dynamicists. The emergence of these structures is a characteristic feature of quasi-geostrophic or two-dimensional flows, and coherent vortices have indeed been observed abundantly in the oceans (Robinson, 1983) and the planetary atmospheres (Scorer, 1978).

An important question in the study of vortex structures concerns their stirring and mixing properties, in particular when smaller or larger perturbations are introduced by, for example, instability or interaction with other vortices. Experiments on interacting vortex dipoles by van Heijst and Flór (1989), have revealed the complicated nature of the advection of passive tracers during the interaction process, in which some fluid initially trapped in the atmospheres of the original dipoles may be left behind via detrainment, while some surrounding fluid may be caught in the newly formed structures (entrainment).

Some essential features of the dynamics and the associated advection of these coherent vortices can be modelled by a simplified model in which the coherent

vortex structures are represented by point vortices. Comparison of numerical simulation results of this point-vortex approach (see Meleshko *et al.*, 1992) with available experimental observations (van Heijst and Flór, 1989) shows reasonably good quantitative agreement. The main aim of present paper is to use this model to a quantitative analysis of stirring processes in some typical cases of periodic interactions of two and three point vortices.

The two-dimensional problem of the interaction of three point vortices of strength κ_α and position (x_α, y_α) in the unbounded (x, y) -plane of an inviscid fluid consists in solving the following nonlinear system of first order differential equations

$$\dot{z}_\alpha^* = \frac{1}{2\pi i} \sum_{\beta=1}^3 \frac{\kappa_\beta}{z_\alpha - z_\beta}, \quad \alpha = 1, 2, 3, \quad (1)$$

with initial conditions $z_\alpha = z_\alpha^{(0)}$ at $t=0$. Here $z_\alpha = x_\alpha + iy_\alpha$, the dot, asterisk and accent indicate time derivative, complex conjugation, and the omission of the term corresponding with $\beta = \alpha$, respectively. The system (1) has four first integrals, these being:

$$Q + iP = \sum_{\alpha=1}^3 \kappa_\alpha z_\alpha, \quad I = \sum_{\alpha=1}^3 \kappa_\alpha |z_\alpha|^2, \quad H = -\frac{1}{4\pi} \sum_{\alpha, \beta=1}^3 \kappa_\alpha \kappa_\beta \ln|z_\alpha - z_\beta|. \quad (2)$$

It is known due to Gröbli (1877) (see also Aref, 1979 and Aref *et al.*, 1992) that this problem is integrable. Therefore, using the invariants (2) the solutions $z_\alpha(t)$ to equation (1) can be obtained in an analytical form containing, in general, some quadratures.

The equation of the passive advection of an individual Lagrangian fluid particle induced by the point vortices may be obtained by considering a marker at $Z = X + iY$ as a point vortex of zero strength, namely

$$\dot{Z}^* = \frac{1}{2\pi i} \sum_{\beta=1}^3 \frac{\kappa_\beta}{Z - z_\beta}, \quad (3)$$

with $Z = Z^{(0)}$ at $t=0$.

Hence, the advection by two interacting point vortices forms an integrable problem because a fluid particle may be considered as point vortex of zero strength. Rom-Kedar *et al.* (1990) have found that in the presence of a periodic strain-rate velocity field at infinity the whole picture is radically changed, namely depending on initial conditions fluid particles can appear either in regular or in chaotic regions. Then the following question arises: what will the behaviour of a cloud of fluid particles look like for the case of periodic interactions of two and three vortices?

Results

We will consider two typical examples of point vortex motion. For both of them the strengths of vortices and their initial positions are chosen in such a way that $P=0$, $Q=0$ in (2). For the first example with two vortices we put $(\kappa_i, x_i^{(0)}, y_i^{(0)})$ as $(2\kappa, 0, (f-b)/2)$ and $(-\kappa, 0, f-b)$ for $i=1, 2$, respectively. For the second example with three vortices we put $(\kappa_i, x_i^{(0)}, y_i^{(0)})$ as $(\kappa, 0, f-b)$, $(-\kappa, 0, f+b)$ and $(\kappa, 0, -2b)$ for $i=1, 2, 3$, respectively. In other words, we will consider the changes in the stirring process due to splitting of the "big" vortex of intensity 2κ into two vortices of equal intensity κ , located at a distance $d=3b-|f|$ from each other, see Fig. 1.

It is well known that for the case of two point vortices of strength κ_1 and κ_2 , the distance d between them remains constant and the two vortices move in circular paths (Fig. 1a) around the centre of vorticity with the same angular velocity $\Omega = (\kappa_1 + \kappa_2)/2\pi d^2$ and period $T_{12} = 4\pi d^2/(\kappa_1 + \kappa_2)$.

For the case of three vortices Gröbli's (1877) solution provides the positions of the vortices in a polar coordinate system as following

$$z_\alpha(t) = r_\alpha(t) e^{i\theta_\alpha(t)}, \quad \alpha = 1, 2, 3, \quad (4)$$

where $r_\alpha(t)$ represents periodic functions of period

$$T = \frac{16b^2}{\kappa\zeta_1\sqrt{1-\zeta_2}} \left\{ (1+2\lambda) \mathbf{K} - \frac{1+4\lambda}{1-\zeta_1} \mathbf{E} \right\} \quad (5)$$

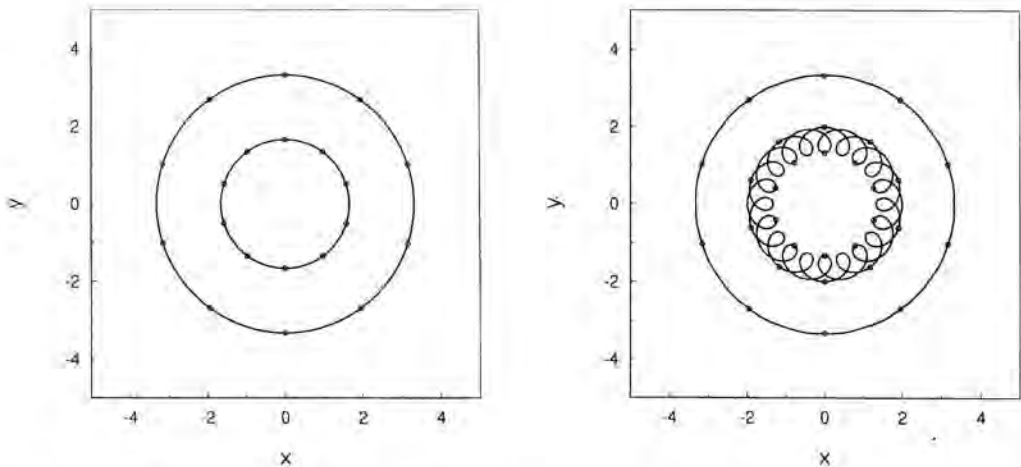


Fig. 1. Periodic trajectories of two and three point vortices of strengths $\kappa_1 = 2\kappa$, $\kappa_2 = -\kappa$ (a) and $\kappa_1 = \kappa$, $\kappa_2 = -\kappa$, $\kappa_3 = \kappa$ (b), respectively. The dots show the positions of the vortices at intervals of $0.1T$, with T being the full period (T_{12} and T_{123} , respectively).

with E and K the complete elliptical integrals of the first and the second kind with modulus $k^2 = (\zeta_1 - \zeta_2)/(1 - \zeta_2)$. Here ζ_1, ζ_2 are the roots of the polynomial $\zeta^2 - 4(\lambda^2 - \lambda)\zeta + 4\lambda^2$ and the governing parameter $\lambda = (f + 3b)^2/4b(f + b)$.

For $-0.25 < \lambda < 0$ the motion of the vortices appears to be bounded: neither vortex 1 nor vortex 3 can form a vortex pair with vortex 2 and escape to infinity. During the period T the radial distances of the vortices from the origin change between the limits

$$\sqrt{\lambda^2 - 2\lambda} + \lambda \leq \frac{r_1}{B}, \frac{r_3}{B} \leq \sqrt{\lambda^2 - 2\lambda} - \lambda,$$

$$2\sqrt{\lambda^2 - 2\lambda} \leq \frac{r_2}{B} \leq \sqrt{2 - 4\lambda} - 2\sqrt{1 + \lambda}$$

with $B = 2b|f + b|/|f + 3b|$ and the angles θ_α increase with the same value

$$\theta = \frac{2}{\sqrt{1 - \zeta_2}} \left\{ (1 - 2\lambda) K - \frac{2\lambda}{\zeta_2} \Pi \right\} \quad (6)$$

where Π is the complete elliptical integral of the third kind with the moduli k^2 and $\mu = \zeta_1/\zeta_2 - 1$.

The case when $2\pi/\theta$ is a rational number m/n is of special interest. For such a case the motion of the three vortices are exactly periodical: after time mT all vortices is exactly at their initial positions after n turns around the origin. The trajectories of the vortices for $\lambda = -0.0856$, $f = -2.3261b$, $\theta = \pi/5$, $T = 1.7578b^2/\kappa$ with $m = 10$, $n = 1$ are presented in Fig. 1b. Vortices 1 and 3 form a local interacting pair while vortex 2 moves at almost constant speed around the origin. At the time intervals $t_k = kT$ the relative positions of the vortices, marked by circles, are the same as in the initial configuration. As a first approximation one may consider the motion of the three vortices as a motion of two vortices, *viz.* by replacing vortices 1 and 3 into one "big" vortex 1 + 3 with intensity 2κ at distance $(|f| + b)/2$ from the origin on the negative y -axis. Such a "pair" will also rotate uniformly with dimensionless period

$T_{(1+3)2} = \pi(1 + |f|/b)^2/2$. The whole picture of motion can be considered as a superposition of two rotations with different time scales: a "rapid" rotation of two identical vortices 1 and 3 and "slow" rotation of the asymmetric dipolar vortex (1 + 3) and 2 around the origin (see Fig. 1b). The calculated period $T_{(1+3)2}$ of this slow rotation agrees reasonably well with the period $T_{123} = 10T$.

These apparently similar motions of the vortices result, however, in different stirring of the surrounding fluid. In order to gain some insight in the mixing behaviour of the fluid, we considered the particles in 3 different regions, *i.e.* areas enclosed by closed contours. Two of these regions are circles of radii $r_0 = b$ and $r_0 = 0.1b$ located far from and quite near to the initial positions of the vortices, respectively (Figs. 2a and 3a). The third area is enclosed by a kidney-shaped contour that is constructed by Poincaré mapping of a single marker initially

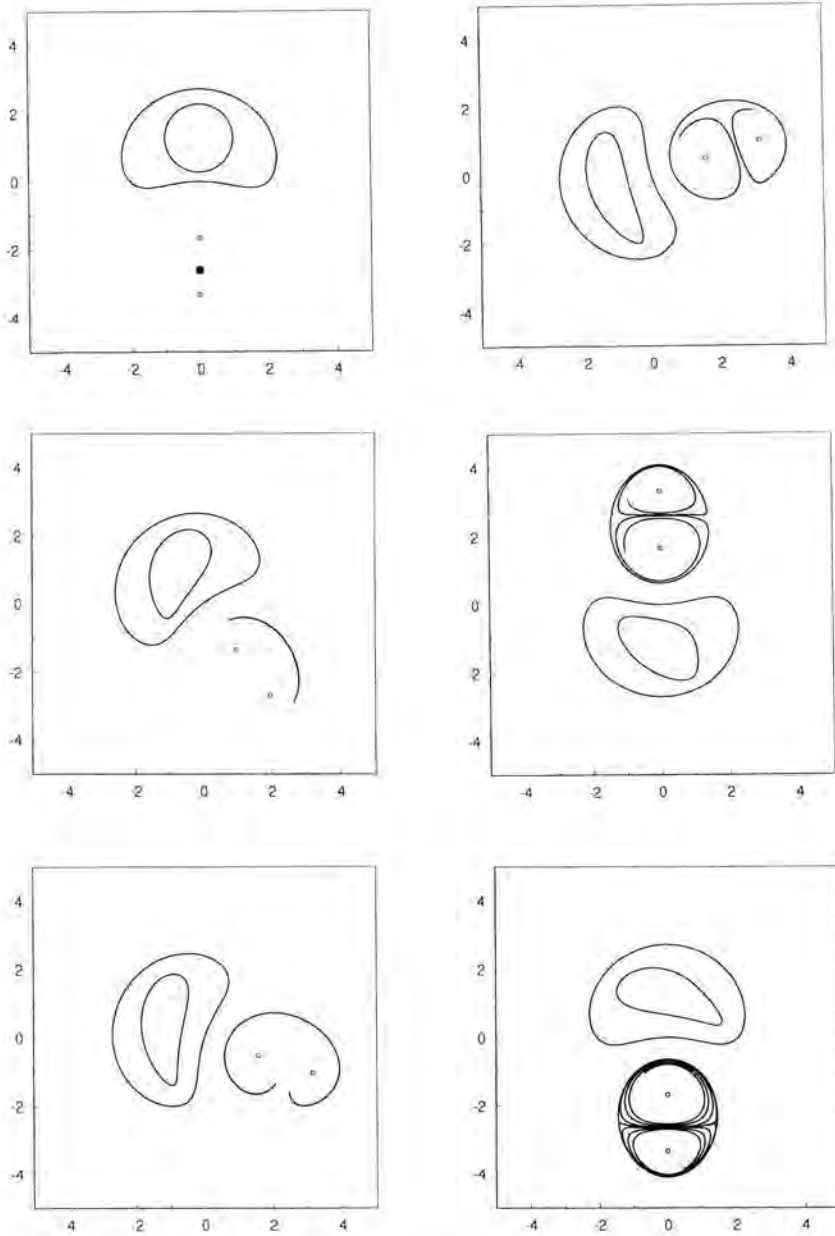


Fig. 2. The evolution of three regions of passive tracers (indicated by the black dot and the two closed curves) from time $t=0$ to time $t=T_{12}$ for the nonsymmetric dipole $(2\kappa, -\kappa)$. The relative length $l(t) = L(t)/L(0)$ of the boundary of the dark blob is: $t=0$, $l=1$, (a); $t=0.1T_{12}$, $l=12$, (b); $t=0.2T_{12}$, $l=29$, (c); $t=0.3T_{12}$, $l=48$, (d); $t=0.5T_{12}$, $l=88$, (e); $t=T_{12}$, $l=187$, (f).

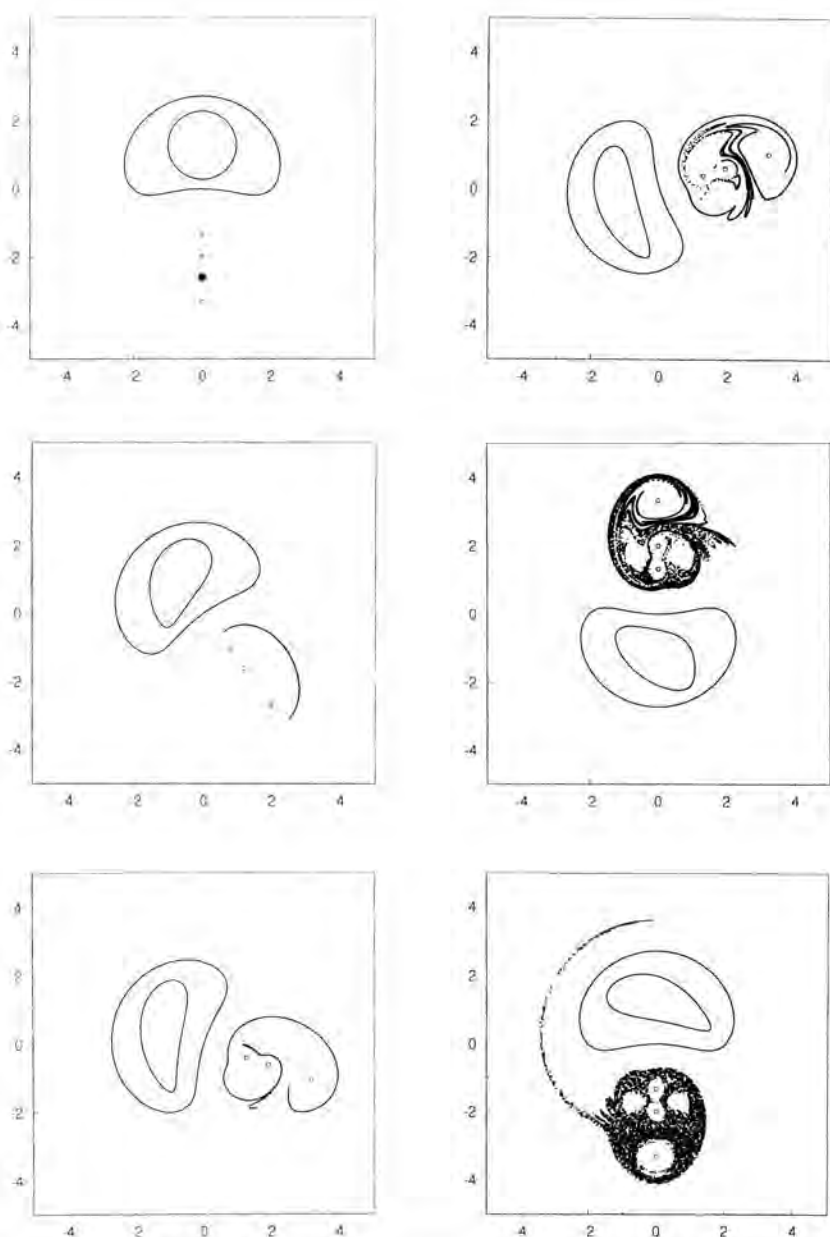


Fig. 3. The evolution of three regions of passive tracers (indicated by the black dot and the two closed curves) from time $t=0$ to time $t=T_{123}$ for the three vortices $\kappa_1=\kappa$, $\kappa_2=-\kappa$, $\kappa_3=\kappa$. The relative length $l(t)=L(t)/L(0)$ of the boundary of the dark blob is: $t=0$, $l=1$, (a); $t=0.1T_{123}$, $l=12$, (b); $t=0.2T_{123}$, $l=44$, (c); $t=0.3T_{123}$, $l=232$, (d); $t=0.5T_{123}$, $l\approx 5\cdot 10^3$, (e); $t=T_{123}$, $l\approx 7\cdot 10^5$, (f).

located at the origin. This region corresponds to a large elliptic island connected with a periodic point $(0, 1.44h)$. It is important to note that the phase plane used in the Poincaré section method for the case of 2D periodical fluid motion is the actual physical plane. So, if a regular sequence of Poincaré mappings tends to create some sufficiently simple closed curve, it is clear that during *one* period of motion this curve must exactly return to its initial position.

Results of the numerical simulations (for a detailed discussion of the numerical procedure see Meleshko *et al.*, 1992) for the same moments of dimensionless time in terms of the whole periods of rotation T_{12} and T_{123} , respectively, are presented in Figs. 2 and 3. The process of deformation of tracer lines in the regular domain is very similar in both cases. Moreover, lines formed by Poincaré mappings return exactly into their *initial* positions after one full period. At the same time Figs. 2 and 3 clearly show the difference that is induced by splitting one vortex into two vortices. At the initial stages (Figs. 2b and 3b) the blob is only stretched and the process of stirring is the same in both cases of vortex interaction. For two vortices this line continues to stretch (Figs. 2c-e) and after one period it forms the boundary of the "atmosphere" of the nonsymmetric dipole $(2\kappa, -\kappa)$, see Fig. 2f.

For three vortices, however, folding occurs (Fig. 3c) and after the full period (Fig. 3f) the line is stretched and folded to such a degree that it is impossible to follow the whole line as a continuous curve without any self-intersections. For this reason Figs. 3d-e only show the positions of 4000 markers which were initially located on the circumference of the black circle. After one full rotation of three-vortex system the points of the initial blob are located mainly inside some bounded domain and produce a few lobes in the wake, but again, none of them appear in the circular regions around the vortices. Not intending to enter all the details of chaotic stirring by three vortices, we would like to explain only the appearance of two additional elliptical islands inside the domain which are connected with positions of the vortices. This explanation naturally leads to the important notion of the "atmosphere" of the two point vortices.

Discussion

In order to gain insight in the stirring process let us consider the topological structure of the flow generated by two point vortices. W. Thomson (1867) was the first to show that a vortex pair (two point vortices of equal but oppositely-signed intensities) in its steady motion in an unbounded plane is also accompanied by an "atmosphere", *i.e.* a fixed closed volume of fluid particles. This motion can be generalized to the case of any set of two point vortices of strengths κ_1 and κ_2 . If their initial positions are $z_1^{(0)} = x_1^{(0)} + iy_1^{(0)}$ and $z_2^{(0)} = x_2^{(0)} + iy_2^{(0)}$, each of the vortices rotates uniformly around the point

$z_c = x_c + iy_c = (\kappa_1 z_1^{(0)} + \kappa_2 z_2^{(0)})/(\kappa_1 + \kappa_2)$ with a constant angular velocity $\Omega = (\kappa_1 + \kappa_2)/(2\pi|z_1^{(0)} - z_2^{(0)}|^2)$. In other words, the expressions

$$z_1(t) = z_c + (z_1^{(0)} - z_c) \exp(i\Omega t), \quad z_2(t) = z_c + (z_2^{(0)} - z_c) \exp(i\Omega t) \quad (7)$$

are the solutions to equations (1).

The advection of fluid particles surrounding such a uniformly rotating pair can be analyzed by searching for a solution to equation (3) of the form

$$Z(t) = z_c + (\zeta(t) - z_c) \exp(i\Omega t). \quad (8)$$

It is easy to verify that the new function $\zeta(t) = \xi(t) + i\eta(t)$ satisfies the differential equation

$$\dot{\zeta}^* = \frac{1}{2\pi i} \left(\frac{\kappa_1}{\zeta - z_1^{(0)}} + \frac{\kappa_2}{\zeta - z_2^{(0)}} \right) + i\Omega(\zeta^* - z_c^*) \quad (9)$$

where the right hand side does not depend implicitly on time. Equation (9) can be transformed into the autonomous Hamiltonian form

$$\dot{\xi} = \frac{\partial \psi}{\partial \eta}, \quad \dot{\eta} = -\frac{\partial \psi}{\partial \xi} \quad (10)$$

where

$$\begin{aligned} \psi(\xi, \eta) = & -\frac{\kappa_1}{4\pi} \ln[(\xi - x_1^{(0)})^2 + (\eta - y_1^{(0)})^2] \\ & -\frac{\kappa_2}{4\pi} \ln[(\xi - x_2^{(0)})^2 + (\eta - y_2^{(0)})^2] + \frac{\Omega}{2} [(\xi - x_c)^2 + (\eta - y_c)^2]. \end{aligned} \quad (11)$$

Thus in the (ξ, η) -system rotating uniformly around the point z_c , the particle motion is steady and the streamlines $\psi(\xi, \eta) = C$ coincide with pathlines of fluid particles.

Choosing the initial positions of the vortices on the y -axis, with $z_1^{(0)} = ib$ and $z_2^{(0)} = -ib$, let us consider some typical vortex atmospheres. When $\kappa_1 \kappa_2 < 0$ the best known is the vortex pair atmosphere, with $\kappa_1 = -\kappa_2 = \kappa$ and $z_c = \infty$, $\Omega = 0$. Two types of streamlines are formed, *viz.* a system of closed lines and a system of non-closed lines, see Fig. 4a. The streamline $C = 0$ defines a fixed, closed region of fluid, and its shape is approximately an ellipse with axes $1.73b$ and $2.09b$ and area $S = 3.61\pi b^2$; this is the "atmosphere", which moves permanently with the vortex pair. The equation of the atmosphere boundary (the lines Ψ_u , Ψ_l) was already obtained by W. Thomson (1867) as

$$\xi^2 = 2\eta b \coth \frac{\eta}{2b} - b^2 - \eta^2. \quad (12)$$

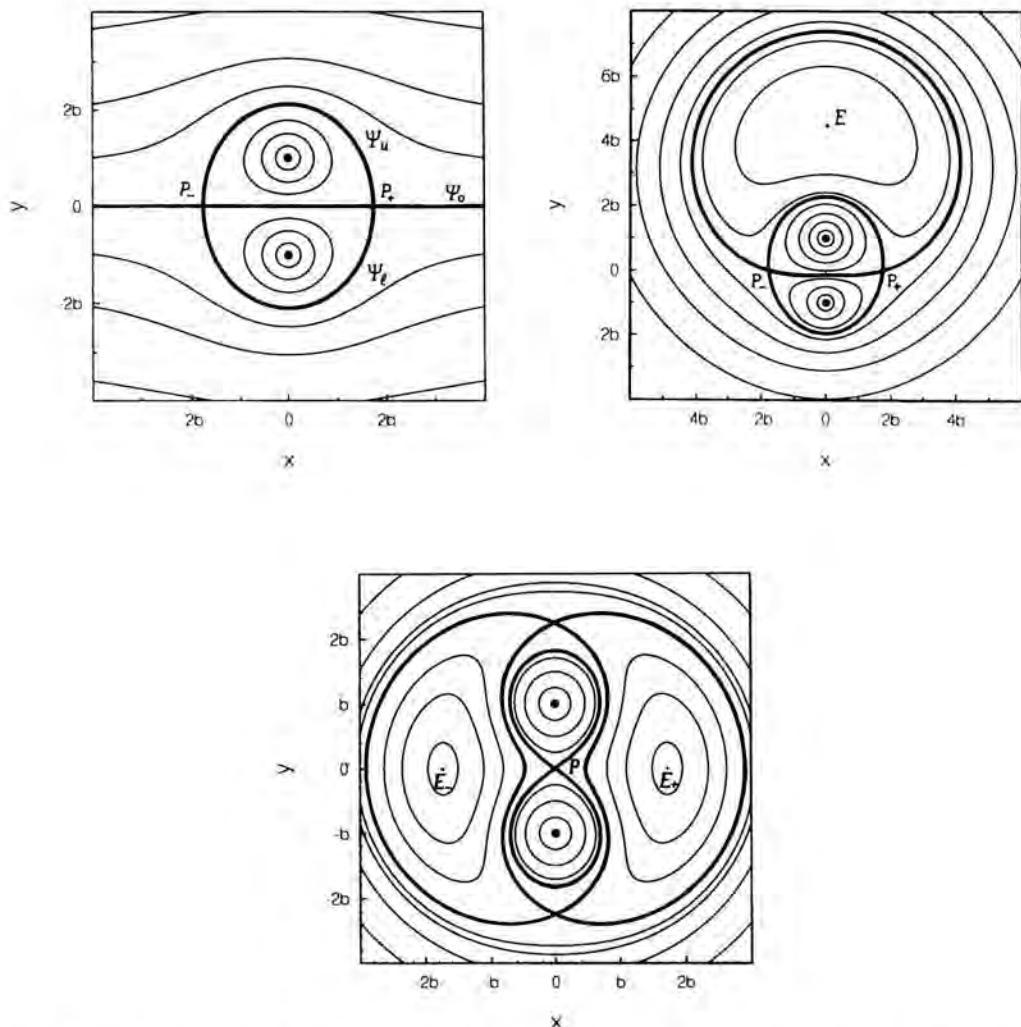


Fig. 4. Streamlines, separatrices (Ψ_ℓ , Ψ_u , Ψ_0 and bold lines), elliptical points (E_+ , E_- , E) and hyperbolic points (P_+ , P_- , P) of flow, seen in a co-moving (co-rotating) frame for: the symmetrical vortex pair, $\kappa_1 = \kappa$, $\kappa_2 = -\kappa$, (a); the nonsymmetric dipole, $\kappa_1 = 2\kappa$, $\kappa_2 = -\kappa$, (b); and two identical vortices, $\kappa_1 = \kappa$, $\kappa_2 = \kappa$, (c).

The atmosphere does not change essentially for the case of nonequal strengths (in absolute sense) of the vortices. The atmosphere for $\kappa_1 = 2\kappa$, $\kappa_2 = -\kappa$, ($z_c = 3ib$, $\Omega = \kappa/8\pi b^2$) is shown in Fig. 4b. It can be shown that the coordinates of the hyperbolic points P_+ and P_- , where the velocity according to (9) is equal to zero, do not depend on κ_1 and κ_2 . They are $\xi_{P_+} = b\sqrt{3}$, $\eta_{P_+} = 0$ and $\xi_{P_-} = -b\sqrt{3}$, $\eta_{P_-} = 0$. At the same time, the line Ψ_0 transforms now into the closed separatrix, which encloses an elliptic point E at $\xi_E = 0$, $\eta_E = 4.54b$.

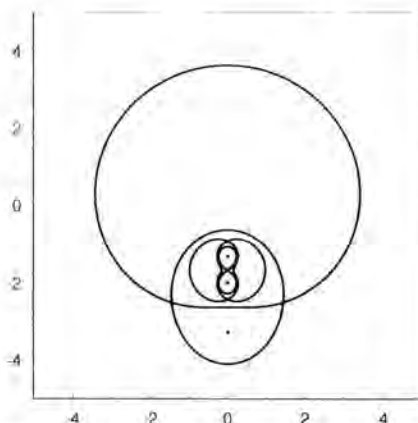


Fig. 5. Schematic picture of the superposition of separatrices of the flow due to the nonsymmetric dipole and that due to two identical vortices.

When $\kappa_1 \kappa_2 > 0$ the pattern of streamlines is somewhat more complicated. A typical picture for $\kappa_1 = \kappa_2 = \kappa$, ($z_c = 0$, $\Omega = \kappa/4\pi b^2$) is presented in Fig. 4c. It is seen that there are now three systems of closed streamlines surrounding one, two or none of the vortices, and which are divided by separatrices. Besides the hyperbolic point P at $(0, 0)$ for this case there exist also two elliptic points E_+ and E_- at $(\pm \sqrt{3}, 0)$.

Thus, in all the cases two steadily translating or rotating point vortices catch with them some fluid within separatrices, *i.e.* within the atmosphere, while these large coherent structures move without any changes.

If we now put together the separatrices of Fig. 4b and Fig. 4c on a proper scale for our case of the three-vortex system, we obtain a schematical picture as shown in Fig. 5. Therefore, the appearance of two additional large elliptical islands is connected with the topological structure of the flow near the two equal vortices. This explanation, of course, is only approximate because the "ideal" pattern of separatrices is destroyed during the periodic interaction of three vortices. It does provide, however, some insight into the qualitative and, in some respects, quantitative nature of the stirring by three point vortices.

Conclusions

In the present analytical and numerical study we have provided evidence that two and three point vortices, although having in some cases similar trajectories under periodical interaction, induce stirring of surrounding fluid that is in some respects similar, while in other respects different. In spite of the nonintegrability of the Hamiltonian system for advection of fluid by three point vortices there are large regions of nonstirred fluid particles which conserve their identity after a whole period of vortex interaction. These regions are formed by Poincaré

mapping of a single marker located initially within a regular domain. The stirring of a dyed blob initially placed in the region between the vortices results in a redistribution of fluid inside the atmosphere of the vortex system. For the case of three vortices such a region contains two additional islands. The appearance of these islands is connected with the topological properties of the flow structure associated with two point vortices of the same strengths.

Acknowledgement

The final version of this paper was written while the authors were visiting the Fluid Dynamics Laboratory, Eindhoven University of Technology within the framework of a collaboration project that is financially supported by the Netherlands Organization for Scientific Research (NWO). The authors gratefully acknowledge this support.

References

- Aref, H., 1979 - Motion of three vortices. *Phys. Fluids* **22**, 393–400.
- Aref, H., N. Rott & H. Thomann, 1992 - Gröbli's solution of the three-vortex problem: a case study of graduate work in the 1870's. *Ann. Rev. Fluid Mech.* **24**, 1–20.
- Gibbs, J.W. 1902 - *Elementary Principles in Statistical Mechanics*. Yale University Press, New Haven.
- Gröbli, W., 1877 - Specielle Probleme über die Bewegung geradliniger paralleler Wirbelfäden. *Vierteljahr. Naturfor. Gesellsch. Zürich* **22**, 37–81, 129–165.
- van Heijst, G.J.F. & J.B. Flór, 1989 - Dipole formation and collisions in a stratified fluid. *Nature* **340**, 212–215.
- Meleshko, V.V., M.Yu. Konstantinov, A.A. Gurzhi & T.P. Konovaljuk, 1992 - Advection of a vortex pair atmosphere in a velocity field of point vortices. *Phys. Fluids* **A4**, 2779–2797.
- Robinson, A.R., Ed., 1983 - *Eddies in Marine Science*. Springer, Berlin.
- Rom-Kedar, V., A. Leonard & S. Wiggins, 1990 - An analytical study of transport, mixing and chaos in an unsteady vortical flow. *J. Fluid Mech.* **214**, 347–394.
- Scorer, R., 1978 - *Environmental Aerodynamics*. Ellis Horwood, Chichester.
- Thomson, W., 1867 - On vortex atoms. *Phil. Mag.* (ser. 4) **34**, 15–24.
- Welander, P., 1955 - Studies on the general development of motion in a two-dimensional, ideal fluid. *Tellus* **7**, 141–156.

Institute of Hydromechanics
Ukrainian Academy of Sciences
252057 Kiev
Ukraine

Entropies for 2D Viscous Flows

Abstract

Previously, two-dimensional Navier-Stokes (2D NS) flow was represented as the evolution of two non-negative vorticity fields whose difference is the physical 2D vorticity, and whose overlap corresponds to the viscous dissipation of vorticity. Any physical state in 2D periodic geometry can be achieved as some rearrangement of the (conserved) fluxes of these two fields. Defining an entropy for the system is equivalent to assigning statistical weights to the possible rearrangements. Maximizing this "two fluid" entropy leads to satisfactory predictions for the turbulent decay of the embedded 2D NS flow, as indicated by numerical solutions of the two-fluid equations. The entropy defined is independent of the absolute values of the fluxes.

1. Introduction

Recent spectral-method computations (Matthaeus *et al.*, 1991a; Matthaeus *et al.*, 1991b; Montgomery *et al.*, 1992) of freely-decaying, two-dimensional, Navier-Stokes (2D NS) turbulence at high Reynolds numbers have been carried out for periodic boundary conditions. In a few hundred large-scale eddy turnover times, a two vortex final state has been achieved, and appears to decay stably thereafter. The decay is on the much slower energy decay time scale, typically more than 10,000 eddy turnover times. The dominant dynamical mechanism that achieves the two vortex state is like-sign vortex merger, repeated over and over again at increasingly larger spatial scales.

A respectable fit (Montgomery *et al.*, 1992) of the computed data to a much earlier (Joyce and Montgomery, 1973; Montgomery and Joyce, 1974) statistical mechanical theory of many ideal parallel line vortices has been noted. In particular, there is an apparent hyperbolic-sinusoidal dependence of the vorticity ω upon the stream function ψ (where $\nabla^2\psi = -\omega$) that characterizes the two vortex final state and which requires a justification going beyond the mean-field theory for the discrete-particle Hamiltonian mechanics (Onsager, 1949; Kraichnan and Montgomery, 1980) that underlie the ideal line vortex model.

Seeking a most-probable state for any system to evolve toward requires some kind of an entropy to maximize. Entropy for continua is still a controversial

topic. Here, we propose a two-fluid description, involving positive and negative vorticity fields, which contains embedded in it the 2D NS dynamics. The non-negative fluxes associated with the two vorticities are conserved, and their interpenetration is equivalent to a decay of the physical vorticity. As conserved quantities, the two non-negative fluxes adapt themselves to an information-theoretic (Jaynes, 1957) definition of entropy.

The two-fluid model is summarized in Section 2, and some supporting numerical evidence is described in Section 3, along with some closing remarks.

2. Two-fluid model

The two vorticity fields, ω^\pm , both non-negative, are taken to obey

$$\frac{\partial \omega^\pm}{\partial t} + \mathbf{v} \cdot \nabla \omega^\pm = \nu \nabla^2 \omega^\pm \quad (1a,b)$$

where the physical vorticity field is the difference, $\omega \equiv \omega^+ - \omega^-$. The fluid velocity is $\mathbf{v} = \nabla \psi \times \hat{e}_z$, where the stream function $\psi = \psi(x, y, t)$ obeys the Poisson equation, $\nabla^2 \psi = -\omega$. The kinematic viscosity is $\nu \ll 1$. For all fields, $\partial/\partial z \equiv 0$, and for simplicity we assume periodic boundary conditions in the (x, y) plane over a square box of edge 2π . Subtracting Eq. (1b) from Eq. (1a) gives the 2D NS equation in the well known vorticity representation.

For reasons which are familiar (Kraichnan and Montgomery, 1980), the energy $E = (1/2) \int (\omega^+ - \omega^-) \psi d^2x$ decays slowly, according to Eqs. (1a,b), but the enstrophy $\Omega = (1/2) \int (\omega^+ - \omega^-)^2 d^2x$ decays much more rapidly. The essence of the maximum entropy argument is to define an entropy, or measure of the likelihood of a particular state, then maximize that measure subject to the constancy of the conserved or nearly-conserved quantities that may exist. If the system exhibits ordinary statistical-mechanical behaviour, or something close to it, its time evolution should typically lead it toward that maximum-entropy state. Previously (Montgomery *et al.*, 1992), the entropy proposed was

$$S = - \int \omega^+ \ln \omega^+ d^2x - \int \omega^- \ln \omega^- d^2x,$$

the maximization of which leads to the “sinh-Poisson” equation, if only energy and fluxes are conserved, and positive-negative symmetry is assumed:

$$\nabla^2 \psi = \lambda^2 \sinh(\beta \psi)$$

where $\lambda^2 (>0)$ and $\beta (<0)$ are real constants.

An unfortunate feature of this definition of entropy is that it is dependent

upon the absolute value of the (conserved) fluxes, equal for periodic boundary conditions:

$$\int \omega^{\pm} d^2x \equiv V \langle \omega^{\pm} \rangle,$$

where V is $(2\pi)^2$, the area of the periodic box. However, both Eqs. (1) and all the other dynamics are invariant to the addition of the same positive constant to ω^+ and ω^- .

There is a more subtle way of counting states and assigning entropies that is invariant to the addition of constants to the two vorticity fields. For any pair of initial vorticities, ω^+ and ω^- , we may define four auxiliary fields by the following relations ($\langle \rangle$ means a spatial average):

$$\begin{aligned} \omega^{++} &= \omega^+ - \langle \omega^+ \rangle, & \text{if } \omega^+ > \langle \omega^+ \rangle, & \text{zero otherwise;} \\ \omega^{+-} &= -\omega^+ + \langle \omega^+ \rangle, & \text{if } \omega^+ < \langle \omega^+ \rangle, & \text{zero otherwise;} \\ \omega^{-+} &= -\omega^- + \langle \omega^- \rangle, & \text{if } \omega^- < \langle \omega^- \rangle, & \text{zero otherwise;} \\ \omega^{--} &= \omega^- - \langle \omega^- \rangle, & \text{if } \omega^- > \langle \omega^- \rangle, & \text{zero otherwise.} \end{aligned}$$

Then any other spatial redistribution of these four non-negative fluxes associated with ω^{++} , ω^{+-} , ω^{-+} , and ω^{--} can account for all possible states into which the system might evolve, and do it in a way that is invariant to the addition of constants to ω^+ and ω^- . An entropy which measures the likelihood of any such redistribution may be taken to be

$$S = - \int (\omega^{++} \ln \omega^{++} + \omega^{+-} \ln \omega^{+-} + \omega^{-+} \ln \omega^{-+} + \omega^{--} \ln \omega^{--}) d^2x. \quad (2)$$

Given the four auxiliary fields, ω^+ may for example be written as $\omega^+ = \omega^{++} - \omega^{+-} + \langle \omega^+ \rangle$ and similarly, $\omega^- = -\omega^{-+} + \omega^{--} + \langle \omega^- \rangle$.

Maximization of this S , subject to constant values of the fluxes of the four auxiliary fields and the nearly constant value of E yields, as most probable values, $\omega^{++} = \exp[-\alpha^{++} - \beta\psi]$, $\omega^{+-} = \exp[-\alpha^{+-} + \beta\psi]$, $\omega^{-+} = \exp[-\alpha^{-+} - \beta\psi]$, and $\omega^{--} = \exp[-\alpha^{--} + \beta\psi]$. Here, the α 's and β are five Lagrange multipliers, to be determined from the conservation laws. If an assumption of complete symmetry is made among the four auxiliary fields, the four α 's may be taken to be equal, and a hyperbolic-sinusoidal connection between $\omega = \omega^+ - \omega^- = \omega^{++} - \omega^{+-} + \omega^{-+} - \omega^{--}$ and ψ results. As will be seen in Section 3, this symmetry is not quite fulfilled by the computations, for reasons that are apparently rather specific to the system.

3. Numerical results

A 2D spectral-method periodic code has been written by Shan (Montgomery *et al.*, 1993) to solve Eqs. (1a,b). In the process, of course, a solution for the

2D NS equation is generated, but extra information on the two-fluid system is provided. Interpreted in terms of the 2D NS variables (ω , \mathbf{v} , ψ), the evolution is familiar (Matthaeus *et al.*, 1991a, Matthaeus, 1991b; Montgomery *et al.*, 1992). For Reynolds numbers greater than about 1000, like-sign vortex mergers occur until only one vortex of either sign remains. Here R is the large scale Reynolds number defined from the initial rms velocity $\langle \mathbf{v}^2 \rangle^{1/2}$ (typically = 1), unit length scale, and ν^{-1} which has ranged from 1000 to about 14,000 in recent runs. With these conventions, the Reynolds number is in effect ν^{-1} , and the characteristic energy decay time is also of the order of ν^{-1} . The vortex captures are typically completed in a time more than an order of magnitude less than the energy decay time.

As illustrated in Fig. 1, a scatter plot of the computed ω^+ and ω^- vs. ψ at late times is typically well fit by the maximum entropy predictions, which are the curves drawn through the scatter plots. The α 's and β for the curves are determined by a least squares fitting procedure. The symmetry requirements necessary to convert the exponentials into hyperbolic sines for ω are typically not quite so well fulfilled, for what seems to be the following rather specific reason.

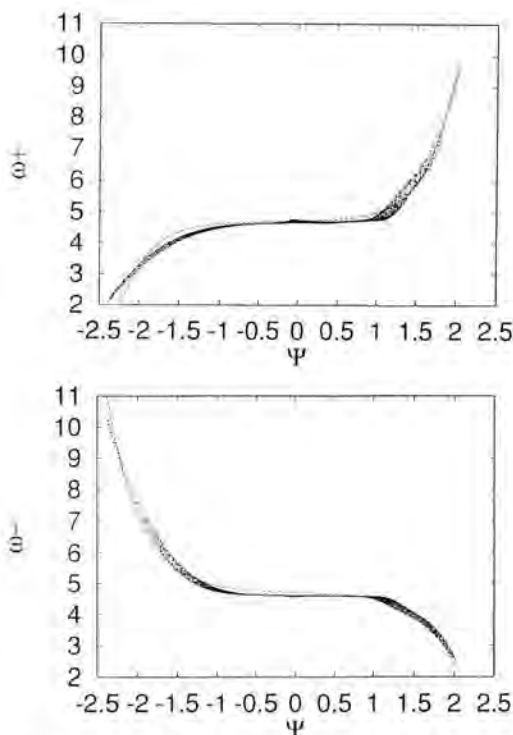


Fig. 1a,b. Scatter plots of the computed ω^+ vs. ψ and ω^- vs. ψ at $t=390$ initial large-scale eddy turnover times at $R=10,000$. The dashed lines are the least-squares fit of the maximum entropy predictions (from Montgomery *et al.* (1993)).

In the vortex merger process, there is a conservation law that guarantees that the two final-state vortices should have equal absolute values of integrated vorticity; but there is no corresponding reason why they should acquire equal energies. While a roughly equal distribution of energy might be expected, there is nothing in the dynamics of the sequence of like-sign vortex mergers leading to the final state that guarantees an equal sharing of energy. In the runs that have been done, it has been typical to have a ten percent difference in the kinetic energy associated with the half of the basic box containing the positive vortex, compared with the half containing the negative vortex, and this difference persists.

A consequence of this difference is that the structure of the positive and negative vorticity parts of the final state can be better fit separately by the two values of the reciprocal temperature β that differ by perhaps 15% than by a single common value of β . There are comparable differences in the α 's, since they are not independent of the β . The mergers seem to lead to vortices that are individually maximum entropy structures more accurately than the whole system is fit by the overall maximum entropy prediction, somewhat in the manner suggested by Smith (1991). However, the overall fit with a single maximum-entropy sinh-Poisson prediction is not a bad fit to the computed data (Matthaeus *et al.*, 1991a; Matthaeus *et al.*, 1991b; Montgomery *et al.*, 1992).

Considerable work remains, in defining entropies precisely for the three-dimensional case (Chorin, 1991). There has also been a suggestion that a maximum-entropy analysis can be made to fit the solutions of the Euler equations ($\nu=0$), which appears somewhat more problematical (Robert and Sommeria, 1992).

Acknowledgement

This work has been supported in part by the U.S. Department of Energy, NASA, and Los Alamos National Laboratory.

References

- Chorin A.J., 1991 - *Commun. Math. Phys.* **141**, 619.
- Jaynes E.T., 1957 - *Phys. Rev.* **106**, 620 and **108**, 171.
- Joyce G. and D. Montgomery, 1973 - *J. Plasma Phys.* **10**, 107.
- Kraichnan R.H. and D. Montgomery, 1980 - *Rep. Prog. Phys.* **43**, 547.
- Matthaeus W.H., W.T. Stribling, D. Martinez, S. Oughton, and D. Montgomery, 1991, - *Physica D* **51**, 531.
- Matthaeus, W.H., W.T. Stribling, D. Martinez, S. Oughton, and D. Montgomery, 1991 - *Phys. Rev. Lett.* **66**, 2731.
- Montgomery D. and G. Joyce, 1974 - *Phys. Fluids* **17**, 1139.

Montgomery D., W.H. Matthaeus, W.T. Stribling, D. Martinez, and S. Oughton, 1992 - *Phys. Fluids A* **4**, 3.
Montgomery D., X. Shan, and W.H. Matthaeus, 1993 - *Phys. Fluids A* **5**, 2207.
Onsager L., 1949 - *Nuovo Cimento Suppl.* **6**, 279.
Robert R. and J. Sommeria, 1992 - *Phys. Rev. Lett.* **69**, 2776.
Smith R.A., 1991 - *Phys. Rev. A* **43**, 1126.

¹ Dartmouth College
Hannover, NH 03755-3528
USA

² Bartol Research Institute
Newark, DE 19716
USA

On Long-lived Vortices in 2D Viscous Flows and Most Probable States of Inviscid 2D Flows

Abstract

We discuss, in contraposition to the most probable states of quasi-inviscid theories, the status of the vorticity-stream function relations satisfied by the long-lived vortices observed in some numerical simulations of decaying two-dimensional turbulence and in experiments in stratified fluids.

The emergence of large-scale, long-lived vortices in 2D, viscous, incompressible flows has been well established through numerical simulations [1, 2, 3] and laboratory observations [4, 5]. The mechanisms that lead to their emergence have been studied, see, e.g., [6], as well as the important role they play in determining the dynamics and the statistical characteristics of the flow, e.g., [7]. While viscosity is essential for the coalescence of smaller vortices into larger ones, the segregation of opposite-signed vorticity regions is a striking characteristic of the frictionless dynamics, as had been pointed out by Onsager [8], already decades before the above-mentioned investigations and was verified by Joyce and Montgomery [9]. State-of-the-art numerical calculations [10] seem to indicate that some quasi-stationary states of two-dimensional, viscous flows are characterized by a hyperbolic-sine relation between the vorticity field $\omega(x, y, t)$ and the stream function $\psi(x, y, t)$, i.e., suppressing the weak time-dependence,

$$\omega(x, y) = \omega_0 \sinh(\psi(x, y)/\psi_0). \quad (1)$$

Moreover, some quasi-stationary states observed in recent laboratory experiments in stratified fluids [11] are consistent with such an ω - ψ relationship. Taking into account the general relation between vorticity and the two-dimensional stream function of incompressible flows, i.e., $\omega \equiv -\Delta\psi$, this implies that, in these cases, the quasi-stationary stream function satisfies the following differential equation,

$$\left(\frac{\partial^2}{\partial x^2} + \frac{\partial^2}{\partial y^2} \right) \psi = -\omega_0 \sinh(\psi/\psi_0), \quad (2)$$

with $\psi = 0$ on the boundary of the domain. It should be noticed that such an ω - ψ relation is not preserved by viscous dissipation, therefore, these states can be quasi-stationary only if the Reynolds number is still large enough so that the evolution is not dominated by viscous effects.

The possibility raised by eq. (2) is interesting for a number of reasons. Firstly, as pointed out in [10], because statistical mechanical studies of inviscid two-dimensional hydrodynamics predict that the most probable equilibrium state is a stationary solution of Euler's equations, i.e., its stream function $\Psi(x, y)$ satisfies $\Delta\Psi = F(\Psi)$, with F either the hyperbolic-sine function as in eq. (2) [9] or some other similar function [12, 13, 14], see below. Secondly, because such a relation could make possible the application of powerful mathematical methods related to soliton equations. Before analysing this second aspect, some comments on the above-mentioned statistical mechanical studies are in place.

Joyce and Montgomery [9] computed the most probable state of a Hamiltonian system consisting of identical positive and negative point vortices and obtained that, in the case of vanishing total vorticity, the stream function of the equilibrium state must satisfy eq. (2), see also [15]. Their calculations can be extended, e.g., by discretizing the continuous vorticity distribution with non-identical point vortices; by doing so, one obtains most probable states that are characterized by ω - ψ relations reminiscent of but different from (2). The dependence of results upon the arbitrary discretization of the field, had already been noticed by Onsager [8].

This observation is in agreement with the more elaborate mean-field theories recently developed by two groups [12, 13, 14], see also [16], which take into account, besides the conservation of kinetic energy, momentum, etc, an infinite number of quantities conserved by the dynamics, i.e.,

$$\frac{d}{dt} \int f(\omega) dx dy = 0, \quad (3)$$

where $f(\omega)$ is an arbitrary function of the vorticity field. Due to these conservation laws, initial conditions that have, e.g., equal energy, momentum and enstrophy, but different vorticity distributions, will lead to different stationary, most probable distributions; i.e., (2) is only one possibility among many. These theories lead to partition functions $Z(\beta, \psi(x, y))$ of the following form,

$$Z(\beta, \psi(x, y)) = \int \exp(\beta\mu(a) - \beta a\psi(x, y)) da, \quad (4)$$

where the parameters β (analogous to an inverse temperature) and the function $\mu(a)$ (analogous to a chemical potential) are Lagrange multipliers chosen in such a way that the constraints on the conserved quantities are satisfied. More precisely, the value of the energy determines β and the area (density) on which the vorticity takes a value, call it a , determines the function $\mu(a)$. The integrand in (4) is proportional to the probability of observing the vorticity value a at a

position (x, y) with stream-function value $\psi(x, y)$. Consequently, the average vorticity is given by

$$\omega(x, y) = Z^{-1} \int a \exp(\beta\mu(a) - \beta a\psi(x, y)) da = -\frac{1}{\beta} \frac{\partial}{\partial \psi} \log Z(\beta, \psi). \quad (5)$$

Identifying the $\psi(x, y)$ in this equation with the average stream function, i.e., using a mean-field approximation, this equation leads to a functional relation between the average vorticity $\omega(x, y)$ and the average stream function $\psi(x, y)$; therefore, these functions correspond to stationary solutions of Euler's equations. Moreover, Robert [13] has shown that the probability distribution is sharply peaked around the most probable state. It should be noticed that these theories do not conserve all the invariants of the inviscid dynamics, for example, the connectivity of isovortical lines is not conserved and, e.g., the enstrophy of the most probable state may be less than that of the initial state [12, 14]. Therefore, I shall use the term 'quasi-inviscid' in order to characterize them.

The following examples should illustrate the many possible most probable states allowed by these quasi-inviscid theories of 2-D flows. The chemical potential $\mu(a)$ is closely related to the initial probability distribution of vorticity [12, 14]. If the initial state corresponds to a random 'turbulent' field, it makes sense to consider Poissonian and Gaussian distributions. It turns out that if the chemical potential $\mu(a)$ is given by $\exp(\beta\mu(a)) = \exp(-|a|/q)$ where q is a positive constant, i.e., a Poisson distribution of the initial vorticity values a , then one obtains

$$\nabla^2 \bar{\psi} = 2\beta q^2 \frac{\bar{\psi}}{1 - \bar{\psi}^2} \quad \text{with} \quad \bar{\psi}(x, y) = \beta q \psi(x, y) \quad \text{and} \quad |\beta q \psi(x, y)| < 1. \quad (6)$$

This functional relation fits the experimental results as satisfactorily as the hyperbolic-sine relation (2) does [11, 17], see Fig. 1; it should be noticed that a cubic polynomial does the job as well [11]. Therefore, it would be interesting to check whether it is capable of fitting also the results of the numerical simulations.

Besides regular solutions, eq. (6) allows also non-regular ones. Circular, non-regular solutions of eq. (6) behave like $\psi = 1 - r/\sqrt{2} + O(r^2)$, where r measures the distance from a cusplike singularity; such a singularity carries finite circulation and kinetic energy but has infinite enstrophy.

On the other hand, if the chemical potential is taken to be quadratic in the vorticity, $\beta\mu(a) = -(a/2q)^2$, i.e., a Gaussian distribution of initial vorticity values, then one obtains a linear relation between vorticity and stream function [12],

$$\nabla^2 \psi = \beta q^2 \psi(x, y). \quad (7)$$

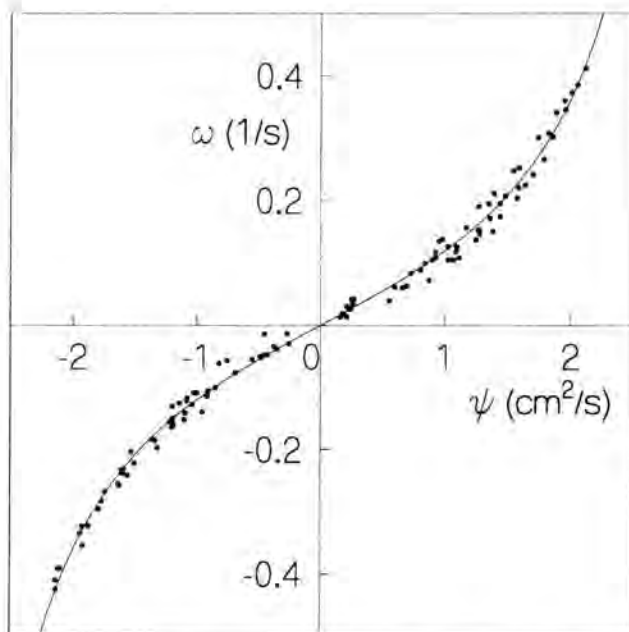


Fig. 1. The vorticity ω , in s^{-1} , as a function of the stream function ψ , in cm^2/s . The dots are experimental results from [11], the line is the best fit obtained using eq. (6) with $\beta = -1.88 (s/cm)^2$ and $q = 0.17/s$. Courtesy of Flór and van Heijst [17].

The ω - ψ relations obtained in the numerical simulations of Morel and Carton, fig. 5c of ref. [18], as well as the hyperbolic-sine relation in (2) can be obtained as follows: Consider the case

$$\exp(\beta\mu(a)) = A^2\delta(a - q_1) + B^2\delta(a) + C^2\delta(a - q_2), \quad (8)$$

with $A^2 + B^2 + C^2 = 1$ and $A^2q_1 + C^2q_2 = 0$, i.e., the initial vorticity takes only the values q_1, q_2 and 0 with probabilities A^2, C^2 and B^2 respectively, such that the total vorticity is 0; this agrees with the initial conditions used in these simulations [18]. This leads to

$$\nabla^2\bar{\psi} = -\beta A^2 q_1^2 \frac{\exp(A^2\bar{\psi}/C^2) - \exp(-\bar{\psi})}{1 + A^2(\exp(-\bar{\psi}) - 1) + C^2(\exp(A^2\bar{\psi}/C^2) - 1)} \quad (9)$$

with $\bar{\psi}(x, y) \equiv \beta q_1 \psi(x, y)$. Joyce and Montgomery's result, eq. (2) with $\beta q_1 \psi_0 = 1$ and $\omega_0 = q_1 C^2$, follows if one takes identical point vortices, i.e., the limits of $A^2 = C^2 \rightarrow 0$ and $q_1 = -q_2 \rightarrow \infty$ such that the circulation $q_1 A^2$ remains finite and $\beta \rightarrow 0$ such that $q_1 \beta$ remains finite. One sees then that it is possible to obtain $\omega(\psi)$ functions that remain finite for all values of ψ , as in eq. (9), or that diverge for $\psi \rightarrow \pm \infty$, as in eqs. (2) and (7), or that diverge at a finite value of ψ , as in eq. (6). All the above examples illustrate a point which was already

realized by Onsager [8]: in a bounded domain, localized solutions exist with $\beta < 0$, i.e., there are 'negative temperature' states.

The results briefly reviewed in the previous paragraphs, raise a number of interesting questions: What is the relation, if any, between quasi-stationary states generated by viscous flows and the most probable ones predicted by quasi-inviscid theories? Why should viscous dissipation lead into a quasi-stationary state before reaching the final stages of dissipation? Do some quasi-stationary states, out of infinitely many possibilities, actually satisfy the hyperbolic-sine relation (2)? How universal is this relation, i.e., do other initial conditions or boundary conditions lead to different quasi-stationary states? If yes, then what are the other possibilities or 'universal classes'? Does eq. (6) provide a better or worse fit of the same observations or does it correspond to another universal class? These questions still remain open; only some partial answers and conjectures have been advanced: It has been pointed out that the above-mentioned mean-field theories introduce, through coarse graining, some irreversibility and dissipation [12, 14] so that the 'dressed' vorticity distribution which measures the long-time, coarse-grained vorticity field is, in general, different from the 'bare', initial one so that, for example, the enstrophy is effectively dissipated. In fact, Pomeau has argued that such an effective dissipative behaviour should be generic to nonlinear, non-integrable classical fields [19]. Even if this were true, it remains to explain why the predictions of these quasi-inviscid theories should agree with the quasi-stationary states reached through standard viscous dissipation since other types of dissipation, like hyperviscosity or Ekman damping, could and in fact seem to lead to different quasi-stationary states [14]. Robert and Sommeria [20] have proposed a diffusive algorithm that conserves energy and all other constants of the motion and converges into the most probable stationary state; however, there is no reason why this algorithm should reproduce the actual inviscid dynamics, let alone the viscous one. Miller has shown that the most probable states predicted by the quasi-inviscid theories coincide with the maximum-energy states under the constraint of the dressed vorticity distribution [12]. Therefore, this approach can also be viewed as a generalization of the 'selective-decay' approach [27] in which only the second moment of the distribution, i.e., the enstrophy, is taken into account. This property may turn out to be the most relevant one for the possible application of this quasi-inviscid approach to viscous flows.

With respect to universal classes and their relation to initial conditions, it is worthwhile noticing that while turbulent-jet injection leads to a nonlinear ω - ψ relation similar to (2) or to (6), laminar-jet injection leads to a linear relation [11] while the initial conditions used in the numerical simulations of Morel and Carton [18] lead to a relation close to eq. (9). Also, it has been proposed by Farge and Holschneider that the presence of quasi-singularities in the initial conditions of some numerical simulations leads to the appearance of cusplike axisymmetric vortices [21].

In spite of all these uncertainties, the hyperbolic-sine relation (2) may play a role in the characterization of large vortices in decaying 2D turbulence; there

fore, it is worthwhile studying some mathematical aspects of this differential equation. This equation, known in the plasma-physics literature as the sinh-Poisson equation, is the elliptic version of the sinh-Gordon equation, i.e., in dimensionless form,

$$\left(\frac{\partial^2}{\partial t^2} - \frac{\partial^2}{\partial x^2}\right) \Psi = \sinh \Psi. \quad (10)$$

The sinh-Gordon equation, like the sine-Gordon equation, is known to be exactly solvable by the inverse scattering method, to have soliton solutions, etc [22]. Therefore, one may ask whether some of the known nice properties of this integrable equation also hold for its elliptic version, eq. (2). The desirable properties one has in mind are, e.g., 1) exact solutions expressible in terms of known functions and 2) relatively simple algorithms (like Bäcklund transformations [23] or nonlinear superposition formulas) for the generation of new solutions from known ones¹. A positive answer to these questions was given by Ting, Chen and Lee [24] who showed that, in the case of periodic boundary conditions, the exact solutions can be expressed in terms of Riemann theta functions and presented superposition formulas. Since the numerical simulations of Matthaeus *et al.* [10] were done with periodic boundary conditions, it follows that the quasi-stationary structures found by them should be described by these exact solutions, if they satisfy eq. (2), as it is claimed. In a more extended version of this work [25], it is shown that in the case of axisymmetry, the sinh-Poisson eq. (2) reduces to a particular case of the IIIrd Painlevé transcendent [26] and examples of regular solutions that vanish at infinity are presented as well as a Bäcklund transformation [23] from axisymmetric solutions into dipolar ones.

Besides continuing with the theoretical analysis, there is a clear need for more and better results obtained through numerical simulations and experiments in order to determine, e.g., the relevance of the initial conditions in the selection of quasi-stationary states and the interplay between the inviscid part of the dynamics on one hand and dissipation (and forcing) on the other hand.

Acknowledgements

I would like to thank Jan-Bert Flór and GertJan van Heijst for making Fig. 1 available prior to its publication. I greatly appreciate the hospitality offered by the staff of the Research Institute for Mathematical Sciences, University of Kyoto, where this article was completed, in particular by Prof. S. Kida and Dr. K. Ohkitani. This work was partially supported by the Japanese Ministry of Education, Science and Culture (Monbusho).

References

1. B. Fornberg, 1977 - Numerical study of 2D turbulence. *J. Comp. Phys.* **25**, 1.

¹ Both things are possible for the sinh-Gordon eq. (10).

2. C. Basdevant, B. Legras, R. Sadourny and M. B  land, 1981 - A study of barotropic model flows: Intermittency, waves and predictability. *J. Atmos. Sci.* **38**, 2305.
3. J.C. McWilliams, 1984 - The emergence of isolated coherent vortices in turbulent flows. *J. Fluid Mech.* **146**, 21.
4. Y. Couder and C. Basdevant, 1986 - Experimental and numerical study of vortex couples in 2D flows. *J. Fluid Mech.* **173**, 225.
5. J.-M. Nguyen Duc and J. Sommeria, 1988 - Experimental characterization of steady two-dimensional vortex couples. *J. Fluid Mech.* **192**, 175.
6. A. Babiano, C. Basdevant, B. Legras and R. Sadourny, 1987 - Vorticity and passive-scalar dynamics in two-dimensional turbulence. *J. Fluid Mech.* **183**, 379.
7. R. Benzi, S. Patarnello and P. Santangelo, 1987 - On the statistical properties of two-dimensional decaying turbulence. *Europhys. Letters* **3**, 811.
8. L. Onsager, 1949 - Statistical Hydrodynamics. *Nuovo Cim. Suppl.* **6**, 279.
9. G. Joyce and D. Montgomery, 1973 - Negative temperature states for the twodimensional guidingcenter plasma. *J. Plasma Phys.* **10**, 107 and D. Montgomery and G. Joyce, 1974 - Statistical mechanics of "negative temperature states". *Phys. Fluids* **17**, 1139.
10. W.H. Matthaeus, W.T. Stribling, D. Martinez, S. Oughton and D. Montgomery, 1991 - Decaying, two-dimensional, Navier Stokes turbulence at very long times. *Physica D* **51**, 531 and D. Montgomery, W.H. Matthaeus, W.T. Stribling, D. Martinez and S. Oughton, 1992 - Relaxation in two dimensions and the "sinh-Poisson" equation. *Phys. Fluids A* **4**, 3.
11. J.-B. Fl  r and G.J.F. van Heijst, Experimental study of dipolar vortex structures in a stratified fluid. *J. Fluid Mech.* **279**, 101.
12. J. Miller, 1990 - Statistical mechanics of Euler equations in two dimensions. *Phys. Rev. Lett.* **65**, 2137 and J. Miller, P.B. Weichman and M.C. Cross, 1992 - Statistical mechanics, Euler's equations and Jupiter's Red Spot. *Phys. Rev. A* **45**, 2328.
13. R. Robert, 1990 - Etat d'  quilibre statistique pour l'  coulement bidimensionnel d'un fluide parfait. *C.R. Acad. Sci. Paris* **311** (I), 575; R. Robert, 1991 - A maximum-entropy principle for two-dimensional perfect fluid dynamics. *J. Stat. Phys.* **65**, 531.
14. R. Robert and J. Sommeria, 1991 - Statistical equilibrium states for two-dimensional flows. *J. Fluid Mech.* **229**, 291; R. Robert and J. Sommeria, 1991 - Final equilibrium state of a two-dimensional shear layer. *J. Fluid Mech.* **233**, 661.
15. S. Kida, 1975 - Statistics of the system of line vortices. *J. Phys. Soc. Japan* **39**, 1395.
16. D. Lynden-Bell, 1967 - Statistical mechanics of violent relaxation in stellar systems. *Mon. Not. Roy. Astron. Soc.* **136**, 101.
17. J.-B. Fl  r and G.J.F. van Heijst, private communication.
18. Y.G. Morel and X.J. Carton, 1994 - Multipolar vortices in two-dimensional incompressible flows. *J. Fluid Mech.* **267**, 23-51.

19. Y. Pomeau, 1992 - Asymptotic time behaviour of nonlinear classical field equations. *Nonlinearity* **5**, 707.
20. R. Robert and J. Sommeria, 1992 - Relaxation towards a statistical equilibrium state in two-dimensional perfect fluid dynamics. *Phys. Rev. Lett.* **69**, 2776.
21. M. Farge and M. Holschneider, 1991 - Interpretation of two-dimensional turbulence energy spectrum in terms of quasi-singularity in some vortex cores. *Europhys. Letters* **15**, 737.
22. D.W. McLaughlin and A.C. Scott, 1978 - Perturbation analysis of fluxon dynamics. *Phys. Rev. A* **18**, 1652.
23. A.V. Bäcklund. 1876 - Ueber Flächentransformationen, *Math. Ann.* **IX**, 297.
24. A.C. Ting, H.H. Chen and Y.C. Lee, 1984 - Exact vortex solutions of two-dimensional guiding-center plasmas. *Phys. Rev. Lett.* **53**, 1348 and 1987 - Exact solutions of a nonlinear boundary problem: The vortices of the sinh-Poisson equation. *Physica* **26 D**, 37 and the references therein.
25. R.A. Pasmanter, 199. - On long-lived vortices in 2-D viscous flows, most probable states of inviscid 2-D flows and a soliton equation. *Phys. Fluids* **6**, 1236-1241.
26. P. Painlevé, 1906 - *C.R. Acad. Sc. Paris* **143**, 111 and E.L. Ince 1956 - *Ordinary Differential Equations*, Dover.
27. W.H. Matthaeus and D. Montgomery, 1980 - Selective decay hypothesis at high mechanical and magnetic Reynolds numbers, *Ann. NY Acad. Sci.* **357**, 203.

Royal Netherlands Meteorological Institute (KNMI)
P.O. Box 201, 3730 AE De Bilt
The Netherlands

Evolution of Turbulence as a Function of Initial Flows on a Beta Plane

Abstract

The evolution of the wavenumber spectra and energy balances in turbulent channel flows on a beta plane is considered using a three-layer isopycnal model. The initial conditions for the experiments are selected from an analytical study of the stability of three-layer channel flows representative of various oceanic gyre regimes. Experiments are integrated for 400 days following initialization of the various flow states with superimposed white noise perturbations. In most of the states there is an initial adjustment period which follows the linear wave growth expected from the analytical computation. This is followed by a cascade to larger scales and a filling in of the wavenumber spectra. The onset of steady inertial ranges in the model spectra occurs as an event-like shift that occurs earlier in westward flows than it does in eastward currents. For stable or near neutral initial conditions the spectra only have a limited region that might be termed inertial. These stochastically forced turbulent states without additional energy input from the mean flows exhibit low PE spectral slopes, k^{-3} or less. The higher energy runs where the turbulence is dominated by energy input from baroclinic instability exhibit steeper PE spectra, $\sim k^{-5}$. Energetics of these states are also discussed along with comparisons with observed oceanic energetics and energy spectra based on satellite altimeters.

Introduction

Spectral closure theories for turbulence following Kolmogoroff (1941) have centred attention on various inertial ranges which arise depending on the controlling factors in the flow (*cf.* Vallis, 1992 for an up to date review of 2-D theories). Spectral theories for oceanic turbulence have made various predictions concerning the wavenumber structure expected (*cf.* Charney, 1971; Rhines, 1977; Salmon, 1982). Early attempts to verify these predictions were thwarted by sampling of dynamical variables that was inadequate to span the range of spatial scales required to resolve these inertial ranges (Dantzler, 1976). Observations that did resolve an adequate range of scales were made for "passive" variables such as sea surface colour or temperature (Denman and Platt, 1980; Gower *et al.*,

1980). One might also consider using mooring data in combination with Taylor's advection hypothesis to reconstruct wave number spectra. Again, the results would at least be suspect. The availability of sea level height measurements from satellite altimeters has changed this state of affairs by providing abundant spatial data (Fu, 1983; Le Traon *et al.*, 1990; Forbes *et al.*, 1993). A representative set of spectra averaged in 10° squares in the South Atlantic from Forbes *et al.* (1993) is shown in Fig. 1. There is a broad range of spectral slopes from k^{-2} in the quieter northeastern subtropical gyre to values with slopes near k^{-4} in the Agulhas and Brazil/Malvinas regions. Individual satellite tracklines in the Brazil and Agulhas have slopes of k^{-5} (not shown). Similar results in the North Atlantic are given in Fu (1983) and Le Traon *et al.* (1990). In the present study the goal is to explore the dynamics behind this range of spectral fall-offs. This will involve both characterizing and understanding the relationship between wavenumber spectra of surface height and kinetic energy (KE) since most turbulence closure theories predict the slope of KE spectra while altimeters sample the surface height (η) variability.

A starting place is Fu's (1983) analysis and its relationship to Charney (1971, 1973). Charney's analysis explicitly suggests that both KE and PE have a k^{-3}

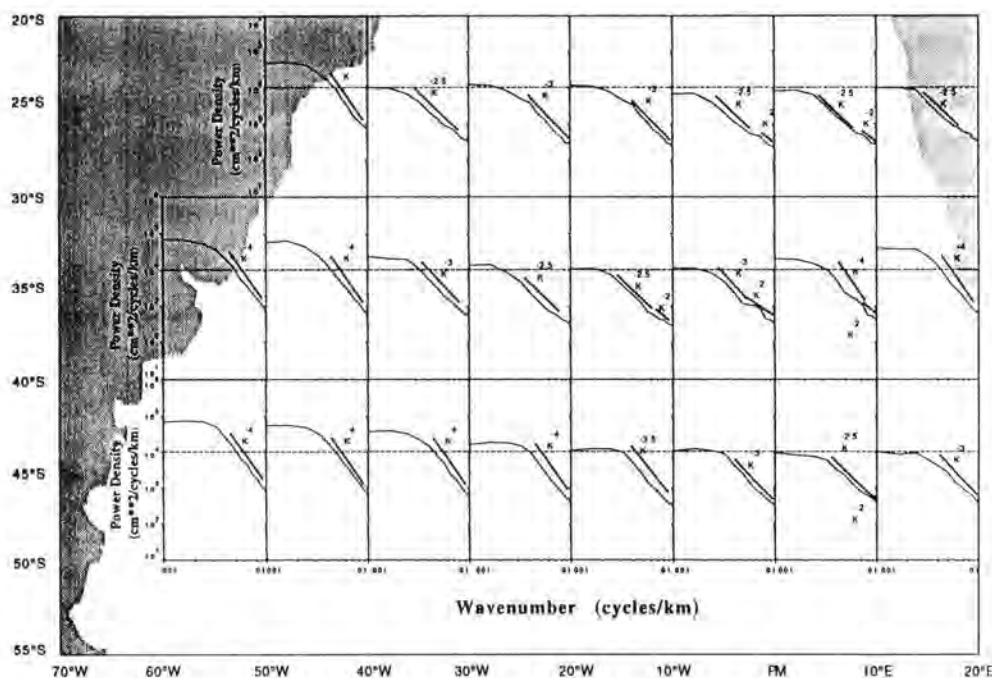


Fig. 1. Sea level height wavenumber spectra by ten degree square for the South Atlantic subtropical gyre from Forbes *et al.* (1993). Data are based on individual satellite trackline data spectra averaged over the squares shown. Altimeter sea surface height anomalies are from the GEOSAT mission. The dashed line through each spectrum indicates the 10^{-4} cm/(cycle km) energy level. Spectral slope lines are given for reference.

spectral dependence below the radius of deformation (R_D). This is concise within the bounds of quasi-geostrophic theory as demonstrated by Hua and Haidvogel (1986). In contrast, Fu's suggestion that the KE spectra should be k^{-2} times the PE spectra, *i.e.* $\eta^2 \sim k^{-5}$, is intuitively based on the geostrophic relation. More formally, if we assume that both PE and KE are locally transferred in wavenumber space in the inertial range and that the eddies are in near geostrophic balance, then $PE \propto \eta^2$ and $KE \propto k^{-2}\eta^2$ or η^2/L^2 at each eddy scale. Fu's scaling, $PE \sim k^{-2}KE$, is only consistent with Charney's assumption of equi-partition between KE and PE for $L \leq R_D$ near the radius of deformation. Charney's result is consistent with the quasi-geostrophic result that as $L \rightarrow R_D$, $KE \rightarrow PE$. For this problem the appropriate scaling parameter to consider is the Burger number, $B = R_D^2/L^2$. Quasi-geostrophic theory predicts $KE/PE \propto B$ for baroclinic motions, exactly the relationship of Fu (1983). This relationship is borne out in observations of individual rings (Olson, 1991). This scaling requires extension theoretically into more nonlinear parameter domains as suggested by Cushman-Roisin *et al.* (1992) and Tang and Cushman-Roisin (1992) and observationally to a larger range of oceanic eddies.

Theories for spectral slopes associated with different inertial ranges arise from assumptions made about the dynamical controls on turbulent cascades. The k^{-3} solution follows from the assumption that it is enstrophy dissipation that is the controlling factor (Kraichnan, 1967; Salmon, 1982). Charney's (1971) contribution is the extension of this to geophysical flows. An assumption that there is a separate range controlled by an energy flux to larger scales leads to a $k^{-5/3}$ spectrum (Salmon, 1982) which is analogous to the three dimensional turbulence result of Kolmogoroff (1941). Various other inertial ranges have been hypothesized. Rhines (1975), for example, suggests k^{-5} based on a similarity theory for turbulence on a β -plane. His treatment assumes the relevant similarity variables are the wave number and the short Rossby wave group velocity, $E = E(k, C_g)$; $C_g = \beta/2k^2$. Accepting the Rhines (1975) formulation for the kinetic energy spectra and applying the quasi-geostrophic scaling gives a k^{-7} spectra for PE. Of course, there is nothing in the Rhines case that distinguishes between PE and KE. One could assume that the similarity holds in PE and therefore $PE \sim k^{-5}$ and $KE \sim k^{-3}$. A full range of Rossby waves in spectral space would have variable KE/PE ratios under the arguments above and are expected to have dispersive dynamics. Note that an ambiguity in whether KE or PE scales to the similarity variables does not appear in the case of the k^{-3} arguments for two or quasi-two dimensional flows described in the previous paragraph. Those results are based on enstrophy arguments and therefore can be directly tied to the KE spectra. Another alternative, within the rules of the similarity arguments, would be to invoke β without any assumption of Rossby wave dynamics. Following the arguments of Nof (1981) concerning the planetary induced motion in coherent vortices, if $E = E(k, \beta)$ then by similarity $E \sim k^{-4}$. Finally as pointed out by Fu (1983), the existence of fronts must be considered. Andrews and Hoskin (1978) obtain $k^{-8/3}$ for inertial ranges in flows involving significant frontogenesis. A view of fronts as steps or "edges" in

property distributions will alternatively produce k^{-2} spectral slopes through Gibb's phenomenon (Phillips, 1971).

The wealth of different potential rationale for the spectral fall off and the altimeter observations of a range of spectral slopes in various portions of subtropical gyres (Fig. 1) suggest a division of the gyre into different dynamical regimes. These different regimes may reflect changes in the manner in which the turbulent field is forced (Hua and Haidvogel, 1986; Le Traon *et al.*, 1990). The changes across the gyre may reflect the differences between eddy fields which arise from instability of the mean flow versus areas where the eddy field is derived directly from wind forcing (Le Traon *et al.*, 1990). Here a set of numerical simulations exploring the linear stability space for various flow conditions found in ocean gyres will be explored to test the conjecture that flows forced to turbulence via local instability have higher spectral fall-off rates than flows forced either by random winds (Le Traon *et al.*, 1990), or in the present case by random initial perturbation fields superimposed on a flow.

Choice of models

The basic choice of models is meant to provide a fairly complete set of ocean-like flows while retaining some analytic capability. The analytic calculations allow the stability of various flow regimes to be addressed. These are then used to specify initial conditions for primitive equation simulations. Both computations consider a three layer isopycnic, periodic channel model with unequal layer mean thicknesses and reduced gravities typical of subtropical gyre circulations. These give radii of deformation of 30 km for the upper layer and 46 km for the second layer. The analytic solutions are from a linearized, quasi-geostrophic case (Halliwell *et al.* 1994) with the same model geometry. The linear formulation follows the development of Davey (1977, see also Pedlosky, 1979) except in the choice of unequal layer thickness. The model configuration is the minimum needed to capture the various shears across the upper interface representing the upper thermocline and the lower isopycnal surface representing the deep main thermocline. The stability space along with schematics of the isopycnal (interface) geometries for the four quadrants of the space are shown in Fig. 2. The various letters on the diagrams in Fig. 2 indicate the numerical simulations completed using the isopycnal model of Bleck and Boudra (1986) and Boudra *et al.* (1988). The numerical model is a primitive equation formulation with Lagrangian vertical coordinates. Here it is used in a zonally-periodic β -plane channel geometry, 20 km grid, and Laplacian viscosity ($K_H = 100 \text{ m}^2/\text{s}$).

The simulations are initialized with a given interface profile and then perturbed with a deformation process which sharpens the flow in the central channel (Boudra *et al.*, 1988; Halliwell *et al.*, 1994). This is followed by the addition of white noise perturbations to the meridional velocity field. The points in the stability space (Fig. 2.) are based on zonal average conditions following the deformation step. Following the initial deformation step and the addition of the

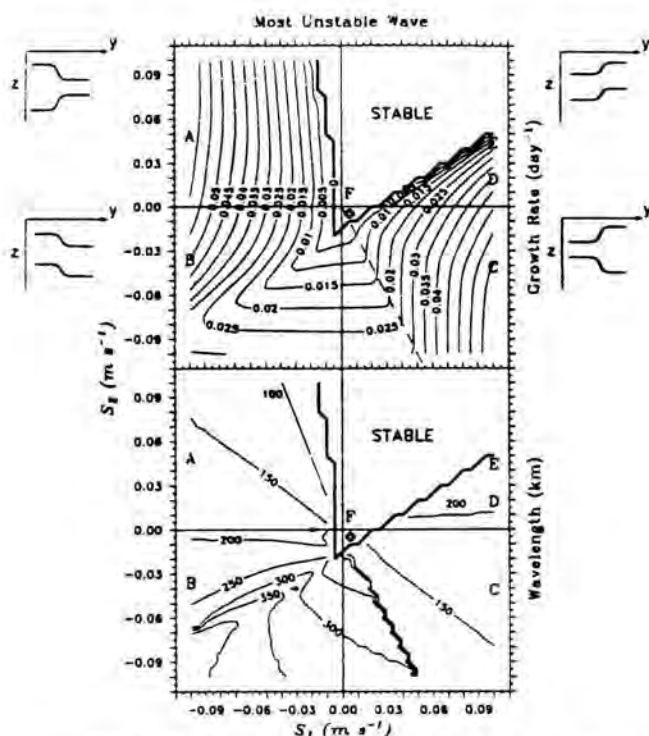


Fig. 2. The linear stability space for the initial conditions used in the numerical simulations. The axes indicate the shear in zonal velocity across the upper (S_1) and lower (S_2) interfaces. The geometry of the interface slopes for these cases are shown to the side of each quadrant in the upper diagram with contours of linear unstable wave growth rate. The lower panel shows the wavelength of maximum growth rate. The letters on the diagrams show the shears relevant for the model runs. The basic geometry of the two pycnoclines in each quadrant of the diagrams is shown schematically with the upper figure (y positive northwards). Full discussion of the linear model and its application to conditions in subtropical frontal zones (case C) can be found in Halliwell *et al.* (1994).

white noise perturbations, the simulations are no longer forced. In this sense these are spin-down experiments and can never reach a formal equilibrium state. The model simulations are integrated out to 411 days in each case. Further elaboration of both the analytic and numerical models can be found in the discussion of a set of experiments representing the subtropical convergence frontal zone in the Atlantic (Fig. 2, point C) which is the essential objective of the Halliwell *et al.* (1994) study.

Spectral evolution and energetics

While each point in the stability regime evolves differently, overall the behaviour can be broken down into points that fall in the stable or near neutral domain (E,F) and those that are unstable (A,B,C,D). The final spectra of the sea surface

height as diagnosed in the model at 411 days for each of the six points in Fig. 2 are shown in Fig. 3a. The neutral and stable conditions produce spectral peaks associated with the resonance in the channel and an underlying slope of k^{-2} in η (Fig. 3a). This would suggest under Fu's (1983) hypothesis that the kinetic energy spectrum is close to the initial perturbation spectrum and essentially white. The model, however, produces a very steep KE spectrum with slopes between -5 and -6 (Fig. 3b). For the unstable cases all of the η spectra approach $\sim k^{-5}$ in

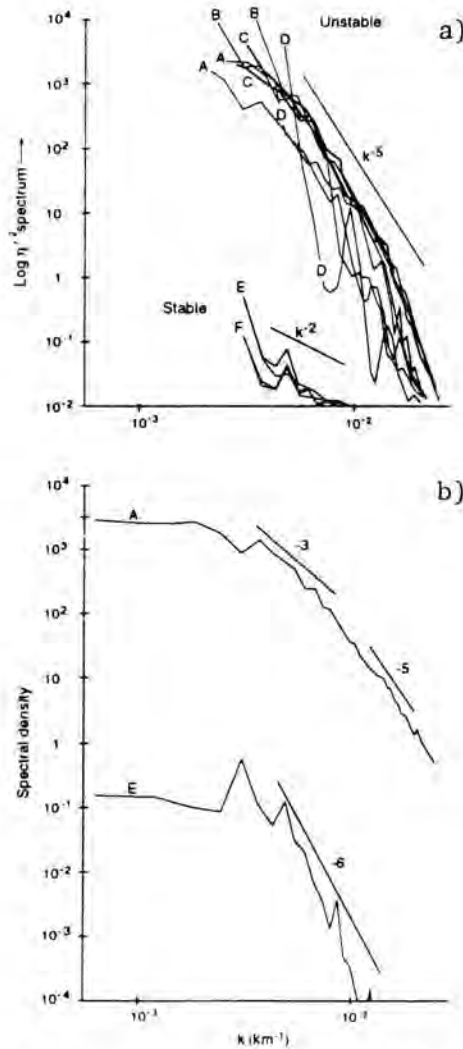
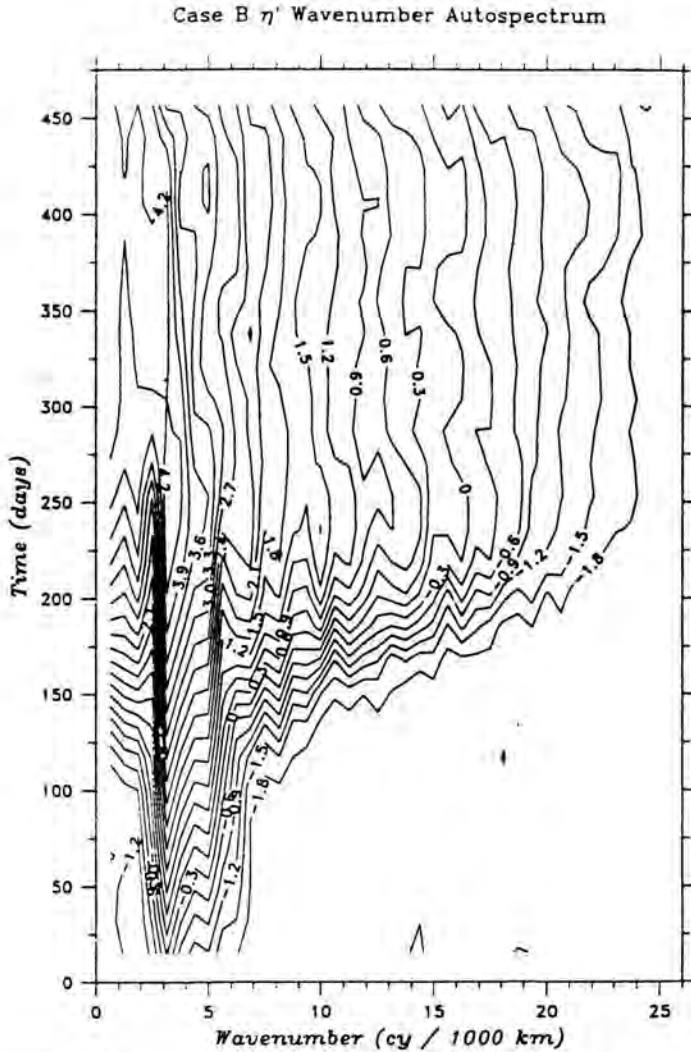


Fig. 3. a) End state surface height spectra for the various model runs for the stability space shown in Fig. 2. Data are for the last portion of each of the runs when the spectra are nearly at equilibrium (200-400 days). Two spectra approximately 100 days apart are shown for each case. b) Kinetic energy spectra on day 411 for cases A and E.

a range of wavenumbers between $k \sim 3 \times 10^{-3}$ and 10^{-2} km^{-1} (100 to 300 km). The upper portion of this wavenumber range has a KE spectral slope of -3 in the simulations (Fig. 3b). There is little indication of a $-5/3$ range in any of the cases although the model geometry may not be adequately large to allow this to develop. The spectra at smaller scales tend to fall off more rapidly as one reaches the dissipation scales in the model. The latter scale is estimated as the place in the kinetic energy spectra where the Reynolds number becomes one, *i.e.*



$R_E = UL^2/K_H = 1$. From the kinetic energy spectra in the simulations and $K_H = 100 \text{ m}^2/\text{s}$ the dissipation range corresponds to wavenumbers $k \sim 2 \times 10^{-1} \text{ km}^{-1}$ or $L \sim 30 \text{ km}$. The overall Reynolds number in these simulations exceeds 3000.

The evolution of the spectrum over time for case B is shown in Fig. 4. The less unstable case (D) has a more wave-like structure throughout the model run as compared to the more unstable cases (A,B). All of the unstable cases eventually evolve into similar near-equilibrium states although the transition to this state occurs at different times (Fig. 5). The near-neutral (E) and stable cases (F) also equilibrate but with very different final states as noted above.

The initial hundred days of each run is dominated by slow energy transfers associated with the linear growth phase and the initial onset of nonlinear but inefficient wave-wave interaction processes (Figs. 4,5). The early periods as displayed in Figs. 4 and 5 essentially follow the linear growth curves expected from theory. This is followed by a sharp transition period which is relatively short (Fig. 4) and involves peak energy transfers as shown for cases A, B and C in Fig. 5. These energy transformations involve large transfers of mean potential energy to the eddy field and the creation of significant new mean kinetic energy in the form of jets which will be discussed in more detail below. This transition period is followed by a long quasi-equilibrium period where the spectra are of nearly constant form (Fig. 4). The energetics in this final equilibrium period of cases A and C involve an end of the transition of eddy kinetic to mean flow energy and a more or less steady set of conversions of potential energy to both kinetic energy pools. Case B although it is fairly steady in spectral space is still very variable in terms of energy transformations (Fig. 5). The potential vorticity fields for cases A and B for three periods spanning transition are shown in Fig. 6.

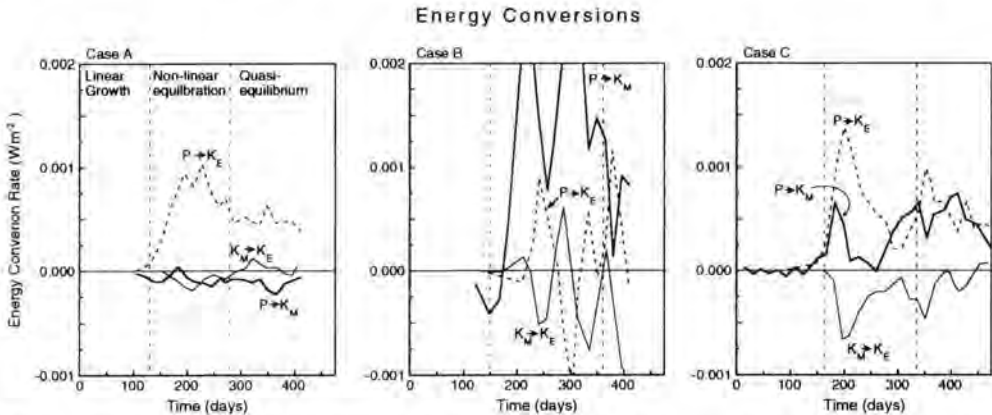


Fig. 5. Energy conversions for cases A, B, and C showing the energetics of the major periods of development as in Fig. 4. The energy conversions include conversion of potential to mean ($P \rightarrow dK_M$) and eddy ($P \rightarrow dK_E$) kinetic energy and the conversion of mean to eddy kinetic energy ($K_M \rightarrow dK_E$). Note the differences between the three cases. The influence of β in stabilizing the energy conversions in time is evident for both case A and C (eastward shear across one interface) in contrast to the sharp oscillations in the $P \rightarrow dK_E$, $K_E \rightarrow dK_M$ conversions for case B (westward shear in across both interfaces). components in case B

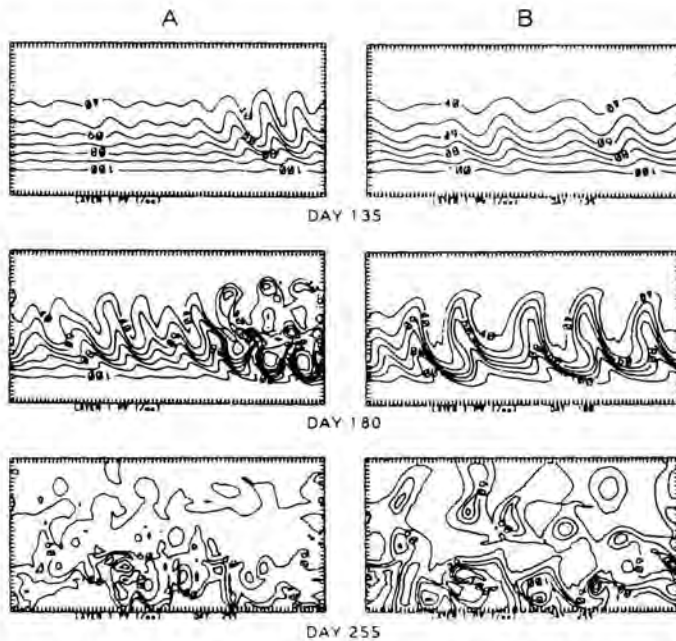


Fig. 6. Potential vorticity ($\times 10^{-8} \text{ m}^{-1} \text{ s}^{-1}$) for the upper layer in the channel at three different times spanning the transition to turbulence for cases A and B. Note the inhomogeneity along channel in both cases at the end of initial phase of flow evolution (day 135). The transition is also very different between the short wave dominated cases (A,C) and B as obvious from the selected scales at days 180 and 255. It is the zones of concentrated potential vorticity gradient, when averaged along-channel, that correspond to the surface intensified frontal jets. In this sense there are not continuous jets but net mean flows made up of a series of jet streaks. The more homogeneous regions in the potential vorticity maps are the locations of the barotropic mean zonal flows.

Transition to turbulence and the quasi-equilibrium states

The transition period in Fig. 5 is associated with a strong transfer of energy back into zonal mean flows in the channel from the eddy field and peak transformations between potential and eddy kinetic energy. Similar transitions are observed in all of the unstable cases. As noted above, the nature of these transfers varies with position in the stability space. While the different cases (A,B,C,D) all reach similar spectral forms, the route to turbulence and the energy partition between potential and kinetic in the final eddy field differs substantially. In the cases dominated by short wavelengths (A, C, D; Fig. 2; Halliwell *et al.*, 1994), coherent eddies that appear at the time of transition are near the radius of deformation. These features emerge from the flow in a localized region of the channel in case A and then slowly expand to fill the channel through interaction with a set of fronts that are produced along the channel front at the time of transition (Fig. 6). While these fronts are not continuous features they show up as velocity

jets in the along channel mean flow. The final eddy field in case A is very barotropic with a KE to PE ratio of five. Case B has slightly longer wavelengths in the initial eddy field (Fig. 2) and represents a westward flow in both of the upper layers that is not stabilized by beta. Even though the linear growth rate for B is less than either A or C, it enters the nonlinear equilibration stage (Fig. 5) at approximately the same time and the energetic conversions during this phase are considerably more intense. Case B does not settle down to a steady set of energy conversions even though the spectrum reaches a constant form suggesting a steady state cascade range that began well before the dashed line in Fig. 5. Transition in case B is marked by the breaking of a train of waves as opposed to the coherent eddy formation process in case A (Fig. 6). Case B is even more barotropic (KE to PE ratio of 7) and again has along channel fronts which lead to channel average zonal jets (Fig. 6, day 255). The other cases (not shown) are less barotropic in the eddy field and have transitions which are a mixture between the case A and B extremes in the character of transition with respect to waves versus coherent features.

The spectral character of the final states has already been shown in Fig. 3. There are several questions about these states and the manner in which they are reached that deserve further comment. First of all, how is the energy partitioned and does the scaling suggested by Fu (1983) actually work? Calculations of the kinetic energy spectra (Fig. 3b for cases A and E) as compared with the potential energy spectra agree with that predicted by the k^{-2} PE scaling hypothesized by Fu (1983) in the case A, B, C and D model runs. The neutral and stable cases (E, F) do not obey this scaling and have kinetic energy spectra that are steeper than their η spectra. The isolated peaks in these spectra suggest dominant wave numbers tied to a combination of initial conditions and the initial perturbation structure. The suggestion is that there is not a well developed inertial range in these cases. The model spectra bound those observed in the altimeter data. In fact the full set of observed spectra along GEOSAT altimeter tracklines falls exactly between -2 and -5 . The ten degree averaged spectra in Fig. 1 have a more truncated wavenumber range due to the band averaging performed.

Conclusions

This is a preliminary report on attempts to understand the nature of the ocean eddy field based on analytical stability space analysis and long spin-down mode simulations with a compatible primitive equation model. The results compared to the available observations of the ocean interior are promising in the sense that the resulting spectra bound those observed from satellite altimeters. The nature of turbulence in the locally stable domains which correspond to the low spectra fall-offs in the observations demand more work to determine to what extent the eddy variability is wind-forced or is either advected or propagated into the mid-gyre from distant unstable regions. The fact that unstable states, even in proximity to the stability boundaries in the linear problem, approach a

k^{-5} PE cascade range and a k^{-3} KE supports Fu's (1983) hypothesis. In addition all of the initial problem experiments approach Charney's (1973) case in terms of energy equi-partition and then exceed it in all unstable cases except D with the KE dominating the PE by factors of up to seven in case B. This suggests very barotropic final states for the eddy field in the very unstable cases (A, B, and C). All of the highly turbulent cases produce pronounced zonal mean flows in the channel. These intense zonal flows are marked with surface intensified jets embedded in more barotropic flows. The creation of rectified flows has long been appreciated in turbulence theory (Starr, 1968; Vallis and Maltrud, 1993) although their role in governing the transition to turbulence and the dynamics of turbulent cascades is still an important area of investigation.

The simulations presented here are preliminary and need to be followed up with a further exploration of parameter space. A set of simulations cutting across the linear stability space are currently underway. An even more relevant issue would be to consider the forced equilibrium states that can reach true equilibrium. While means of doing this without full ocean basin simulations is currently being considered, it is not simple to design such calculations.

Acknowledgements

The authors would like to thank Kevin Leaman for help with the GEOSAT spectra and the remote sensing group for basic data processing. Annalisa Griffa for constructive comments on the discussion of the turbulence theory. This research is funded by the Office of Naval Research (N00014-89-J1536, DO and GP), the National Aeronautics and Space Administration (NASA NGT-30026, CF) and the National Science Foundation (NSF OCE-9206643).

References

- Andrews, D.G. and B.J. Hoskins, 1978 - Energy spectra predicted by semi-geostrophic theories of frontogenesis, *J. Atmos. Sci.* **35**, 509-512.
- Bleck, R and D. Boudra, 1986 - Wind-driven spin-up in eddy-resolving ocean models formulated in isobaric and isopycnic coordinates. *J. Geophys. Res.* **91**, 7611-7621.
- Boudra, D., R. Bleck and F. Schott, 1988 - A numerical model of instabilities in the Florida current. *J. Mar. Res.* **46**, 715-751.
- Charney, J.G., 1971 - Geostrophic turbulence, *J. Atmos. Sci.* **28**, 1087-1095.
- Charney, J.G., 1973 - Planetary Fluid Dynamics, In: *Dynamic Meteorology*, P. Morel, ed., D. Reidel, Dordrecht, 97-351.
- Cushman-Roisin, B., G.S. Sutyrin, and B. Tang, 1992 - Two-layer geostrophic dynamics. Part I: Governing equations. *J. Phys. Oceanogr.* **22**, 117-127.

- Dantzler, H.L., 1976 - Geographic variations in the intensity of the North Atlantic and North Pacific oceanic eddy fields. *Deep - Sea Res.* **23**(9), 783-794.
- Davey, M.K., 1977 - Baroclinic instability in a fluid with three layers. *J. Atmos. Sci.* **34**, 1224-1234.
- Denman, K. and T. Platt, 1976 - The variance spectrum of phytoplankton in a turbulent ocean. *J. Mar. Res.* **34**, 593-601.
- Forbes, C., K.D. Leaman, D.B. Olson and O. Brown, 1993 - Eddy and wave dynamics in the South Atlantic as diagnosed from GEOSAT altimeter data. *J. Geophys. Res.* **98**, 12,297-12,314.
- Fu, L.L., 1983 - On the wave number spectrum of oceanic mesoscale variability observed by SEASAT altimeter. *J. Geophys. Res.* **88**, 4331-4341.
- Gower, J.F.R., K.L. Denman, and R.J. Holyer, 1980 - Phytoplankton patchiness indicates the fluctuations spectrum of mesoscale oceanic structure. *Nature* **318**, 157-159.
- Halliwell, Jr., G.R., G. Peng, and D.B. Olson, 1994 - Stability of the Sargasso Sea subtropical frontal zone. *J. Phys. Oceanogr.* **24**, 1166-1183.
- Hua, B.L. and D.B. Haidvogel, 1986 - Numerical simulations of the vertical structure of quasi-geostrophic turbulence. *J. Atmos. Sci.* **43**, 2923-2936.
- Kolmogoroff, A.N., 1941 - The local structure of turbulence in incompressible viscous fluid for very large Reynolds numbers. from *Comptes Rendus (Doklady) de l'Academie des Sciences de l' U.R.S.S.* **30**, 301-305.
- Kraichnan, R.H., 1967 - Inertial ranges in two-dimensional turbulence. *Phys. Fluids* **10**, 1417-1423.
- Le Traon, P.Y., M.C. Rouquet, and C. Boisser, 1990 - Spatial scales of mesoscale variability in the North Atlantic as deduced from GEOSAT data. *J. Geophys. Res.* **95**, 20,267-20,285.
- Nof, D., 1981 - On the beta-induced movement of isolated baroclinic eddies. *J. Phys. Oceanogr.* **11**, 1662-72.
- Olson, D.B., 1991 - Rings in the ocean. *Ann. Rev. Earth and Planetary Sciences* **19**, 283-311.
- Pedlosky, J., 1979 - *Geophysical Fluid Dynamics*. Springer-Verlag, New York, New York, 710 pp.
- Phillips, O.M., 1971 - On spectra measured in an undulating layered medium. *J. Phys. Oceanogr.* **1**, 1-6.
- Rhines, P.B., 1975 - Waves and turbulence on a beta plane. *J. Fluid Mech.* **69**, 417-443.
- Rhines, P.B., 1977 - The dynamics of unsteady currents. In *The Sea*, edited by E. D. Goldberg *et al.* **6**, Wiley Interscience, New York, 189-318.
- Salmon, R., 1982 - Geostrophic Turbulence. In *Topics in Ocean Physics*, Soc. Italiana di Fisica, Bologna, 30-78.
- Starr, V.P., 1968 - *Physics of Negative Viscosity Phenomena*. McGraw-Hill, New York, 256 pp.
- Tang, B. and B. Cushman-Roisin, 1992 - Two-layer geostrophic dynamics. Part II, Geostrophic turbulence. *J. Phys. Oceanogr.* **22**, 128-138.

- Vallis, G.K., 1992 - Problems and phenomenology in two-dimensional turbulence. In: *Nonlinear Phenomena in Atmospheric and Oceanic Sciences* G.F. Carnevale and R.T. Pierrehumbert, Eds., Springer-Verlag, New York, 1–25.
- Vallis, G.K. and M.E. Maltrud, 1993 - Generation of mean flows and jets on a beta plane and over topography. *J. Phys. Oceanogr.* **23**, 1346–1362.

Rosenstiel School of Marine and Atmospheric Sciences
University of Miami
4600 Rickenbacker Cswy.
Miami, FL 33149
USA

Toward an Optimal Description of Atmospheric Flow

Abstract

In models of the global atmospheric circulation, the vorticity field is usually expanded into series of theoretical orthogonal functions, so-called spherical harmonics. However, the atmosphere continuously generates coherent structures, which perhaps are better represented by Empirical Orthogonal Functions (EOFs) than by spherical harmonics. EOFs are calculated from observations and describe optimally fast the most energetic structures in the circulation. Therefore, we propose to project the vorticity equation onto the dominant EOFs. This approach is evaluated in the context of a barotropic model of the atmosphere.

Introduction

An unsolved problem in atmospheric modelling is how to properly describe the evolution of the turbulent atmosphere with a finite number of 'modes' or variables. It is inevitable that by using a finite number of modes the accuracy of this description is limited. The richness of circulation structures is too large to ever allow for an exact representation. A description that is not exact introduces errors in the predicted evolution of the circulation. In practice, models of the atmosphere always have some kind of parametrization to represent the interaction between the neglected scales of motion and the resolved scales. How to properly account for this effect is known as the closure problem. It is clear that a particular closure formulation will depend on which circulation structures are resolved and which are not. In this context the choice of a proper basis in phase space may be extremely important.

The most widely used descriptions are the representation of the atmospheric fields on a particular grid or the expansion of the fields in spherical harmonics, the so-called spectral representation. All features smaller than the grid size or smaller than the smallest wavelength in the spectral expansion are neglected. One could ask whether these descriptions are optimal choices. The evolution of the large scale circulation is far from random. Over and over again the same kind of structures emerge and disappear. Rather than decomposing the flow field in spherical harmonics, a description of the flow in terms of these 'coherent' structures, could have important advantages. A localized coherent structure like

a blocking ridge or a travelling cyclone projects onto many spherical harmonics, from the smallest to the very large wavenumbers. The more localized a structure, the flatter the corresponding Fourier spectrum and the more Fourier modes are involved. Since many modes are needed to describe one localized structure, the expansion is highly redundant. The spectral modes occur more or less in fixed combinations corresponding to the coherent structures of the flow. Also the interaction between two localized structures, say a blocking ridge and a travelling cyclone, is described by numerous interactions among the constituent spectral modes. Truncation of the expansion into spherical harmonics leads to a misrepresentation of this interaction. This error in the small scale details are of a large scale structure can not be described with the same parametrizations as the small scale coherent structures that play a role in cascading energy towards the viscous region. Finding a suitable closure formulation in spectral space is therefore far from trivial. A description based on the coherent structures of the atmospheric circulation could be far more efficient with respect to the number of variables needed and also might be more attractive with respect to the closure problem, as the small scales that are tied to the evolution of a large scale pattern are explicitly resolved.

How to construct such a description is far from clear. A suitable candidate is a spectral expansion in Empirical Orthogonal Functions (EOFs), since these functions optimally describe the most energetic structures in the circulation. In probability theory one refers to this expansion as the Proper Orthogonal Decomposition or Karhunen-Loève expansion. Lumley (1967, 1987) proposed its application to turbulent flows to identify coherent structures. For a review on its applications in turbulence research, see Aubry (1991). Preisendorfer (1988) contains an extensive overview of the theory and use of the EOFs in meteorology and oceanography. Several studies have been published in which models of the atmosphere are formulated in terms of EOFs (Rinne and Karhilla 1975; Schubert 1985, 1986). These studies are encouraging for the EOF modeling approach, but were restricted to the short-term behaviour of severely truncated EOF models. Furthermore, the EOFs were calculated from observations and subsequently inserted into a model of the atmosphere. The model tendencies differ from observed tendencies not only because the equations are not exactly solved due to the truncation error but also because the model equations are not exact. To investigate the effect of the truncation error, Selten (1993) did the entire analysis in the context of a model atmosphere. A two-level, quasi-geostrophic, hemispheric model was used, formulated in spherical harmonics and truncated at T5. The model consists of 30 coupled ordinary differential equations describing the evolution of the expansion coefficients. EOFs were calculated from a long model integration and evolution equations for the EOF amplitudes were derived by a Galerkin projection of the model equations onto the EOF-basis. The short and long-term behaviour of several EOF models were examined for various truncation limits. In agreement with the study by Rinne and Karhilla, he found that good short term predictions are possible with only a small number of EOFs (5 in his case). For a correct long term behaviour, at least 26 EOFs needed to be

included. An attempt was made to parametrize the effect of the neglected components, but the results were rather disappointing. The main shortcoming of the T5 model was an unrealistic spectral energy distribution. The shortest wave was dominant and the wave amplitudes were too large compared to the zonal flow. Furthermore, the stationary wave component was too small compared to the travelling component. Therefore we decided to evaluate the EOF model approach in the context of a more realistic model with much more degrees of freedom.

We implement a hemispheric barotropic model with forcing and dissipation, formulated in spherical harmonics and truncated at T21. The number of degrees of freedom is 231. The model has a realistic climate and a variability comparable to the variability of observed 10-day running mean 500hPa height fields. The aim of the present study is to investigate whether a model based on the first few dominant EOFs can adequately describe the longterm dynamics of the T21 model. Further we want to study the potential for a proper closure of the reduced system in which small scale details of large scale structures are explicitly resolved.

The experiment

The barotropic model was integrated for 30 years and the statevector was archived once every day. This dataset can be depicted as a cloud of points in the 231-dimensional phase space. We refer to this set of points in phase space as the attractor of the model, since, starting from a random point in phase space, every trajectory after some finite time, traces this same set of points. The attractor is not an isotropic and homogeneous set of points. There are directions in phase space in which the model makes large excursions. These directions correspond to preferred circulation patterns. In some regions in phase space, the density of points has a local maximum. These regions correspond to regimes, quasi-stationary circulation patterns which persist for some time. EOFs are designed to describe optimally fast the anisotropic and inhomogeneous structure of the attractor. Suppose we project the set of points onto a unit vector in phase space. The first EOF points into the direction in phase space which maximizes the projection. The second EOF points into the direction in phase space which maximizes the projection under the restriction that it must be orthogonal to the first and so on. In this way, a new set of basis vectors is constructed which optimally fast describes the attractor. Note that this set depends on the choice of an inner product in phase space. The calculation of EOFs can be written in the form of an eigen problem. The EOFs are the eigenvectors of the covariance matrix and the corresponding eigenvalues are the mean squared projections onto the EOFs.

We calculated EOFs from the 30 year dataset. The EOFs are ordered with respect to their eigenvalues. The EOF with the largest eigenvalue comes first. The eigenvalue spectrum is steep, indicating the existence of preferred circulation patterns. The first eigenvalue is very large and the corresponding EOF is almost equal to the climate. The other EOFs have virtually zero mean amplitudes and

thus describe deviations from the mean flow, represented by the first EOF. As explained in Selten (1993), the climate is retained in the expansion to allow for dynamical interactions between the climate component and the anomalous EOFs. It turns out that 99Z of the dataset projects onto the first EOF. The fractional mean squared error in the representation of anomalies is less than 5Z when the expansion includes the first 32 EOFs. Thus the state vector can efficiently be approximated by a spectral expansion into the first few dominant EOFs. A visual inspection of the EOF patterns reveals that as the eigenvalues become smaller, the scale of the structure tends to become smaller, more isotropic in the zonal direction and the patterns tend to shift toward the equator in the meridional direction. Having constructed a basis in phase space, evolution equations for the expansion coefficients are obtained by a Galerkin projection of the barotropic vorticity equation onto this basis. This procedure yields a coupled system of ordinary differential equations describing the evolution of the expansion coefficients. The general form of this system is given by

$$\frac{da_i}{dt} = \alpha_i + \beta_{ij}a_j + \gamma_{ijk}a_ja_k, \quad i = 1, \dots, T \quad (1)$$

Identical indices in a term imply a summation with the index running from 1 to the truncation limit T . The interaction coefficients are symmetric i.e. $\gamma_{ijk} = \gamma_{ikj}$. In case of spherical harmonics, the majority of the interaction coefficients, γ_{ijk} , are zero. For EOFs this is not the case. The derivation of the system (1) is unique and straightforward in case of spherical harmonics. When EOFs are used in the expansion, ambiguities arise in the derivation of (1). The reason is that spherical harmonics are eigenfunctions of the Laplace operator and EOFs are not. Choices have to be made in the derivation of the reduced system (1) which lead to different interaction coefficients and affect the integral constraints obeyed by the reduced system. It is not possible to derive a reduced system which conserves both energy and enstrophy. In this study a formulation is used which conserves only energy in the absence of forcing and dissipation. The behaviour of the EOF model (1) is evaluated at a truncation limit of 20 EOFs. The choice of this limit is rather arbitrary at this point. A thorough investigation of the behaviour as a function of the truncation is left for a future study. Both the ability to predict the evolution of the circulation of the T21 model two weeks ahead in time and the ability of simulating the T21 climatology and variability is investigated. The performance of EOF[20] model is compared with the performance of a T20 version of the T21 model. The T20 version still has 210 variables.

Results

It turned out that the mean prediction skill of the EOF[20] model of the 100 two-weeks forecasts was much better than the skill of the T20 model, both measured by anomaly correlations and RMS errors. The mean anomaly correla-

tion of the T20 forecasts dropped below 0.6 at day 7, whereas the EOF[20] model is skilful upto day 11. Apparently, a truncation in spectral space as opposed to a truncation in EOF space, seriously affects the evolution of the dominant circulation structures.

To simulate the T21 climatology, the EOF[20] model and the T20 model were integrated for 3000 days. From the last 2000 days, the mean field, the variance pattern and the mean squared amplitudes (msa) of the EOFs were calculated. The EOF model showed a substantial climate drift and a too large variability with distinctly different spatial characteristics. The msa spectrum showed an almost white distribution. The explanation for this effect is the blocked flow of energy through the EOF spectrum due to the truncation. In the mean, energy enters the model through the first EOF, which is virtually the climatological mean circulation. Energy is subsequently transported through the spectrum and is most efficiently dissipated near the end of the spectrum due to the scale selective damping. By truncating the system, energy is accumulated near the truncation limit. Also the T20 model climate differed much from the T21 climate and although the variance had about the correct magnitude, the spatial distribution was quite different. Clearly, a closure assumption is needed to account for the systematic effect of the neglected interactions.

The proposition was made, that the mean effect of the neglected interactions is merely to damp the resolved modes and that it can be adequately described by a linear damping. An extra linear damping was introduced for each component to compensate for the accumulation of energy due to the neglected interactions. The extra damping balances exactly the mean error in the energy tendency of the reduced model. The strength of the extra damping was objectively calculated for each EOF and turned out to be almost the same for each EOF. The same closure assumption applied to the T20 model did not result in reasonable values for the extra damping. Both EOF models and the T20 model were integrated again with the inclusion of the extra damping. From the integration with the EOF[20] model the climatology, the variance pattern and the spectrum of msa of the EOFs were calculated. The correspondence with the T21 model was very good. The T20 model with the same closure assumption was not capable to simulate the T21 model climate and variance.

Conclusion

The main conclusion of this study is that by using EOFs as a Galerkin basis, a significant reduction in the number of variables is possible. The reason is that EOFs efficiently describe the dominant circulation patterns and that a closure is possible for the systematic effect of the neglected interactions. In a subsequent study it is tried to model the instantaneous effect of the neglected scales as well.

References

- Aubry, N., 1991 - On the hidden beauty of the proper orthogonal decomposition. *Theoret. Comput. Fluid Dyn.* **2**, 339–352.
- Lumley, J.L., 1967 - The structure of inhomogeneous turbulent flows. In: *Atmospheric Turbulence and Radio Wave Propagation* (A.M. Yaglom and V.I. Takarski, eds.). Moscow, Nauka, pp. 166–178.
- Lumley, J.L., 1981 - Coherent structures in turbulence. In: *Transition and Turbulence* (R.E. Meyer, ed.). New York, Academic Press, pp. 215–242.
- Preisendorfer, R.W., 1988 - Principal component analysis in meteorology and oceanography (ed. C.D. Mobley). Amsterdam, Elsevier, 401 pp.
- Rinne, J. and V. Karhilla, 1975 - A spectral barotropic model in horizontal empirical orthogonal functions. *Quart. J. R. Met. Soc.* **101**, 365–382.
- Schubert, S.D., 1985 - A statistical-dynamical study of empirically determined modes of the atmospheric variability. *J. Atmos. Sci.* **42**, 3–17.
- Schubert, S.D., 1986 - The structure, energetics and evolution of the dominant frequency-dependent three-dimensional atmospheric modes. *J. Atmos. Sci.* **43**, 1210–1237.
- Selten, F.M., 1993 - Toward an optimal description of atmospheric flow. *J. Atmos. Sci.* **50**, 861–877.

Royal Netherlands Meteorological Institute
P.O. Box 201, 3730 AE De Bilt
The Netherlands

Chaotic Mixing in Tidal Residual Vortices

Abstract

Chaotic advection is studied in a model of a tidal area. The model consists of a residual flow, parametrized by a lattice of vortices, perturbed by a tidal flow. For small perturbations analytical techniques, like Melnikov's method, provide mixing coefficients. For more realistic parameter values we must rely on other techniques, like e.g. stability analysis. Using finite time Liapunov exponents we can recognize chaotic areas and quantify mixing caused by chaotic advection.

Introduction

Mixing in tidal areas is often more intense than theories predict. This is probably due to the fact that the advection of water parcels is chaotic (Ridderinkhof & Zimmerman, 1992).

We studied the advection problem of passive tracers in the Lagrangian way. The velocity field in a tidal area is assumed to be the sum of a stationary part, the residual field, and an oscillatory part, the tide. The residual field is the consequence of tide-topography interactions (Zimmerman, 1981) and therefore often organized in eddy-like structures. It is parametrized as an alternating sequence of cyclonic and anti-cyclonic vortices (see Fig. 1). The tide is parametrized as a spatially uniform time-periodic flow. The advection problem can be described in terms of 2D time-dependent Hamiltonian systems

$$\dot{\mathbf{x}} = \mathbf{f}(\mathbf{x}) + \mathbf{g}(t).$$

In general these systems are chaotic and can be studied by means of Poincaré sections. In our case the Poincaré Map is constructed in a straightforward way. The position of the particle after n tidal periods is the initial position for the calculation of the $n + 1$ -st position. We call this iterative process the Tidal Map (\mathbf{T});

$$\mathbf{x}_{n+1} = \mathbf{T}(\mathbf{x}_n).$$

We did both analytical and numerical studies to determine the amount of chaotic mixing. Mixing is quantified in terms of a dispersion coefficient and

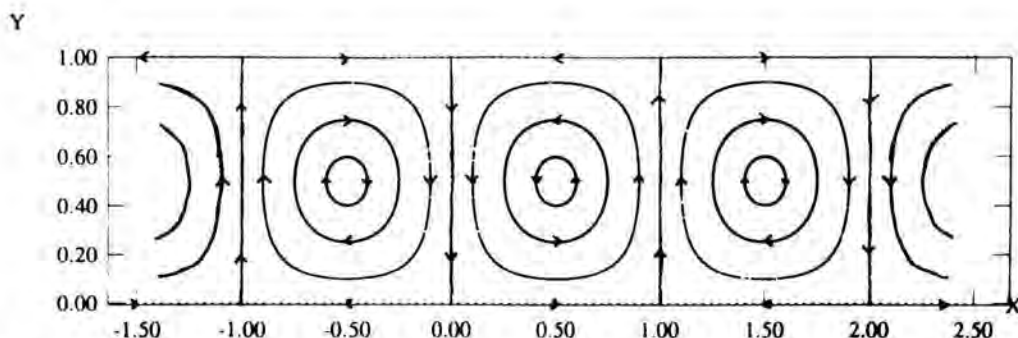


Fig. 1. The streamlines of the unperturbed velocity field. The equations of the unperturbed velocity field are given by

$$\mathbf{f}(\mathbf{x}) = \begin{cases} f_1(x,y) = v\lambda\pi \sin \pi x \cos \pi y \\ f_2(x,y) = -v\lambda\pi \cos \pi x \sin \pi y \end{cases}$$

The tidal perturbation is an oscillating flow uniform in the X-direction:

$$\mathbf{g}(t) = \begin{cases} g_1(t) = \lambda\pi \cos 2\pi t \\ g_2(t) = 0 \end{cases}$$

The following ratios are the dimensionless (chaos) parameters of the model

$$\lambda = \frac{\text{tidal excursion}}{\text{eddy diameter}} \quad \text{and} \quad v = \frac{\text{velocity in residual eddies}}{\text{tidal velocity amplitude}}$$

another coefficient, the area-fraction of the so-called mixing region. The latter is necessary because chaotic mixing is a local phenomenon and therefore high dispersion alone is not enough for good global mixing.

Analytical description of the exchange between the cells

The cells in the unperturbed system are separated by manifolds, connecting hyperbolic points of the flow. The manifold that starts in a hyperbolic point is called the Unstable Manifold (UM) and the one that ends in a hyperbolic point is called the Stable Manifold (SM). Due to the perturbation by the periodic flow, the UM and SM of the hyperbolic points no longer coincide (see Fig. 2). The cell boundary now has a complex structure. UM and SM intersect infinitely many times, forming lobes, which get longer and thinner as they reach the hyperbolic points. The cells are exchanging material in the turnstile lobes. The amount of exchanged material can be calculated for small perturbations by Melnikov's function, which is a measure of the distance between UM and SM. (Recent analytical studies of this system (Beerens *et al.* 1994) contain also the regime of strong perturbations.) The Melnikov function of the above model is given by (Bertozzi, 1988)

$$M(t) = \text{sech} \frac{1}{\lambda v} \cos 2\pi t.$$

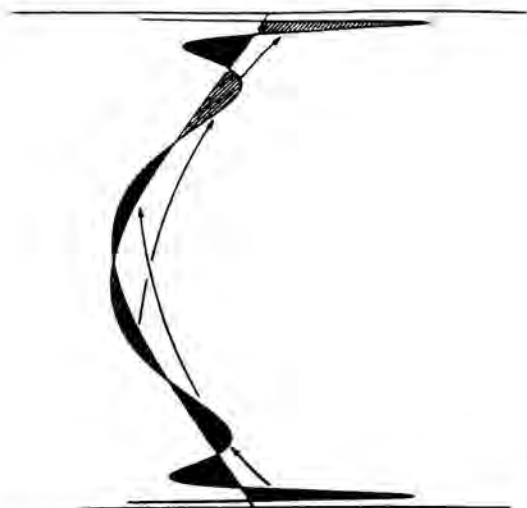


Fig. 2. This is a typical form of the perturbed manifolds near a cell boundary. The Melnikov function ($\sim \cos 2\pi t$) has infinitely many zeros, so UM and SM have infinitely many intersection points. Because the area of the lobes enclosed by UM and SM is conserved under T , the lobes get longer and thinner as they reach the hyperbolic point. In the neighbourhood of the hyperbolic point stretching and folding of material occurs, which are the fingerprints of chaos (Ottino, 1989). The arrows indicate the action of T . The two lobes in the middle act as a "turnstile"; they transport material over the boundary. The exchanged amount of material during each tidal period is exactly the area of one lobe.

Quantification of mixing

Mixing is often quantified in terms of (dimensionless) dispersion coefficients defined as

$$D = \lim_{t \rightarrow \infty} \frac{1}{2} \frac{d\sigma^2}{dt}.$$

The increase of σ^2 in a tidal period is equal to the material exchanged between a cell and its neighbours assuming that mixing in a cell is instantaneously (Ryrie, 1990). The exchanged material is contained in the area of one lobe, which can be found by contour integration of the Melnikov function between two zeros of $M(t)$;

$$D = \lambda \operatorname{sech} \frac{1}{\lambda v}.$$

Mixing is localized near hyperbolic points in the corners of the cells. Particles in the middle of the cells are trapped. They move up and down with the tide, always returning in the same cell. Therefore we want to know how much water

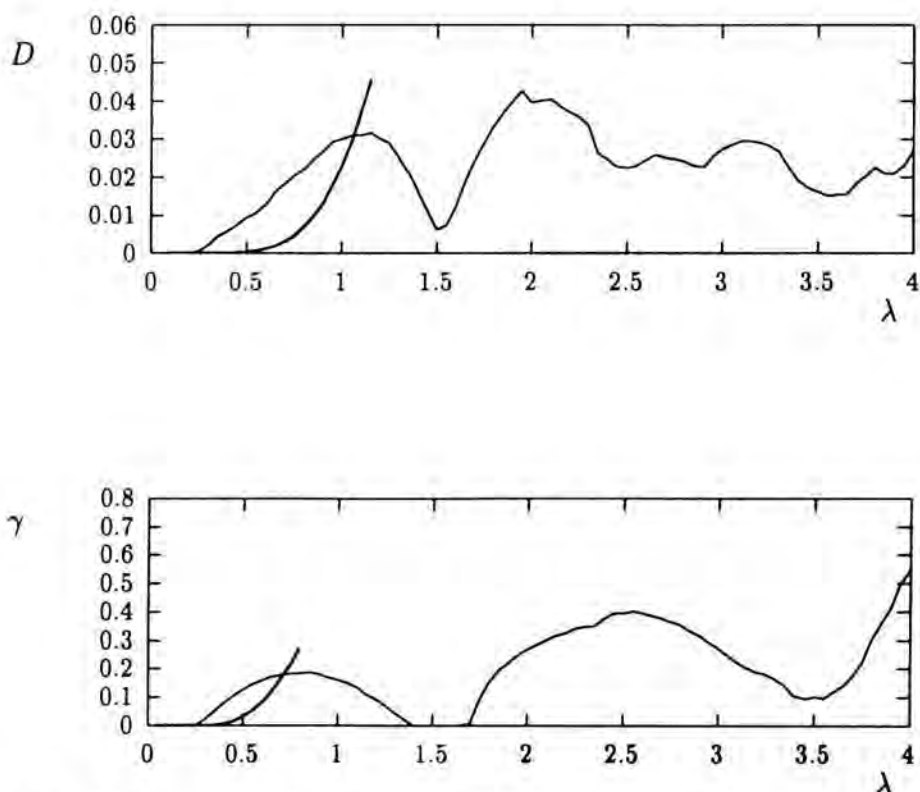


Fig. 3. D and γ versus the parameter λ for $v=0.2$. The analytical methods (smooth curves) only give reasonable approximations for relatively low λ -values (small perturbations). Note that the mixing (D and γ) does not increase monotonically with λ , but shows several maxima and minima. Typical values for the Dutch coastal waters are $\lambda \approx 2$ (North Sea) and $\lambda \approx 3$ (Wadden Sea).

is participating in the mixing process. This quantity is contained in a second mixing coefficient (γ), which is the area-fraction of the mixing region (Ryrie, 1990).

If we assume the separatrix between the mixing region and the region in which the particles are trapped to be a hyperbola, we get the following analytical expression

$$\gamma = \frac{1}{2} d \left(1 + \ln \frac{1}{2} - \ln d \right),$$

where d is the Melnikov distance in the turnstile lobe, given by:

$$d = \frac{1}{v} \operatorname{sech} \frac{1}{\lambda v}.$$

The local character of water movements in a 2D velocity field

Consider motion of water parcels in a 2D velocity field (Pierrehumbert & Yang, 1993). The equations of motion are

$$\dot{x} = u(x, y)$$

$$\dot{y} = v(x, y).$$

We are interested in the motion near a point (X, Y) , so we transform the coordinates of the system into local coordinates

$$x = X + x'$$

$$y = Y + y'.$$

The local equations of motion are up to first order (dropping the primes)

$$\dot{x} = u_x(X, Y)x + u_y(X, Y)y$$

$$\dot{y} = v_x(X, Y)x + v_y(X, Y)y,$$

which we can write in vector notation;

$$\dot{\mathbf{x}} = D\mathbf{u}\mathbf{x},$$

where $D\mathbf{u}$ is the Jacobian Matrix given by

$$D\mathbf{u} = \begin{pmatrix} u_x & u_y \\ v_x & v_y \end{pmatrix}.$$

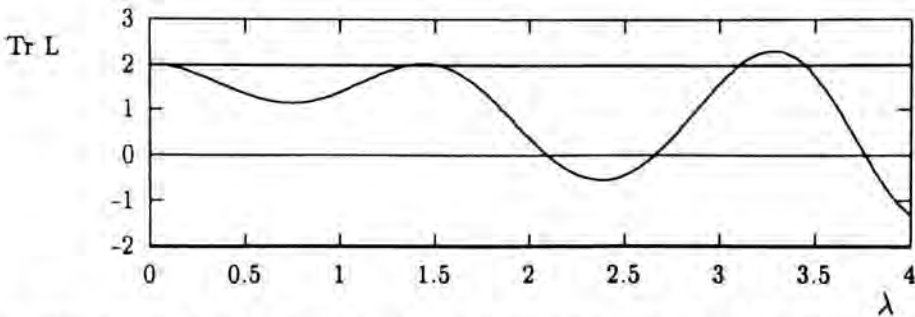


Fig. 4. Depicted is $\text{Tr}L$ in the central fixed point versus λ . Comparison with Fig. 3 learns that the plots have the same periodicity. Good mixing occurs near $\text{Tr}L = 0$. At these parameter values the (rotation of the) tidally averaged displacement is maximal. If $\text{Tr}L$ approaches the upper boundary ($\text{Tr}L = 2$) of the stability interval mixing disappears completely, because the averaged tidal displacement is 0.

The local character of the motion is determined by the eigenvalues (μ) of $D\mathbf{u}$. The eigenvalues are given by:

$$2\mu^2 = (v_x^2 + \frac{1}{2}(u_x - v_y)^2 + u_y^2) - (v_x - u_y)^2$$

where we used $\text{Tr}(D\mathbf{u}) = u_x + v_y = 0$ (mass conservation). The first term is the squared strain rate and the second is the squared vorticity. We distinguish three types of flows:

- In vorticity dominated flows the eigenvalues will be complex conjugate and the local motion is elliptic (stable).
- If the vorticity and the strain cancel the eigenvalues are 1. In this degenerate case the local motion is parabolic.
- If the strain rate dominates, the eigenvalues are real and one of them is larger than 1. The local motion is hyperbolic (unstable).

The above arguments for continuous systems also hold for discrete systems like the Tidal Map. The physical quantities, i.e. the Lagrangian velocity and vorticity are now tidally averaged. The Jacobian Matrix ($D\mathbf{u}$) is replaced by the Linearized Tidal Map (\mathbf{L}) and the eigenvalues are now given by

$$\mu_{\pm} = \frac{1}{2} \{ \text{Tr}\mathbf{L} \pm (\text{Tr}^2\mathbf{L} - 4)^{1/2} \},$$

since mass conservation for discrete systems is given by $\det(\mathbf{L}) = 1$.

Again one can distinguish between stable and unstable areas. The quantity determining this stability is the $4 - \text{Tr}^2\mathbf{L}$, which can be interpreted as the squared rotation of the tidally averaged displacement (kind of discrete vorticity).

- If $\|\text{Tr}\mathbf{L}\| < 2$ the motion in the area is stable. The orbits are elliptic and the particles remain trapped.
- If $\|\text{Tr}\mathbf{L}\| = 2$ the motion is marginally stable.
- If $\|\text{Tr}\mathbf{L}\| > 2$ the motion in the area is unstable. The orbits are hyperbolic, resulting in stretching and folding (chaos).

A plot of the $\text{Tr}\mathbf{L}$ in the fixed point in the middle of the cell, which controls most of the dynamics of the system, versus the chaos parameter λ is shown in Fig. 4. In this plot we see the importance of the stability of the central fixed point for the chaotic mixing process.

Liapunov exponents

Chaos in maps is characterized by positive Liapunov exponents

$$\sigma = \lim_{n \rightarrow \infty} \lim_{\varepsilon \rightarrow 0} \frac{1}{n} \log \frac{\|\mathbf{T}^n(\mathbf{x} + \varepsilon) - \mathbf{T}^n(\mathbf{x})\|}{\|\varepsilon\|}$$

This is not a very practical definition. The limits are hard to be taken and therefore often finite time (i.e. $n = 1$) Liapunov exponents are used (Pierrehumbert & Yang, 1993):

$$\sigma = \log \|L\|$$

Here $\|L\|$ is the norm of the matrix L . We replaced this norm by $\|\text{Tr}L\|/2$, inspired by the above analysis of local stability of fixed points. By releasing particles distributed homogeneously over a cell we can determine the character of the water movements in the whole tidal area and determine where the chaotic and regular areas are.

References

- Beerens, S.P., H. Ridderinkhof & J.T.F. Zimmerman, 1994 - An analytical study of chaotic stirring in a tidal system. *Chaos, Solitons & Fractals* **4**, 1011–1029.
- Bertozzi, A.L., 1988 - Heteroclinic orbits and chaotic dynamics in planar fluid flows. *SIAM J. Math. Anal.* **19**, 1271–1294.
- Ottino, J.M., 1989. - *The Kinematics of Mixing: Stretching, Chaos and Transport*. Cambridge University Press.
- Pierrehumbert, R.T. & H. Yang, 1993 - Global chaotic mixing on isentropic surfaces. *J. Atmos. Sci.* **50**, 2462–2480.
- Ridderinkhof, H. & J.T.F. Zimmerman, 1992 - Chaotic stirring in a tidal system. *Science* **258**, 1107–1111.
- Ryrie, S.C., 1990 - Mixing by chaotic advection in a class of spatially periodic flows. *J. Fluid Mech.* **236**, 1–26.
- Zimmerman, J.T.F., 1981 - Dynamics, diffusion and geomorphological significance of tidal residual eddies. *Nature* **290**, 549–555.

Netherlands Institute for Sea Research
P.O. Box 59, 1790 AB Den Burg
The Netherlands
E-mail: beer@nioz.nl

Decay of Monopolar Vortices in a Stratified Fluid

Abstract

This contribution describes some experimental observations of the decay of a monopolar vortex in a linearly stratified fluid. The vortex is generated by a rotating solid sphere, which is later removed. The observed decay of the planar flow in the disk-shaped vortical region is compared with three different theoretical models, and good agreement is obtained.

1. Introduction

Satellite observations have revealed the abundant occurrence of vortices in many parts of the world's oceans, see *e.g.* Robinson (1983). In addition to the surface vortices, which may be easily detected by satellite measurements of surface anomalies, oceanic vortex structures may also occur at some depth, and thus invisible for the eyes of satellites. Well-known examples of subsurface eddies are the 'Meddies', vortex structures originating from the gravitational collapse of Mediterranean Sea water that spilled over the sill in the Straits of Gibraltar. The existence of Meddies was first reported by McDowell and Rossby (1978) and later oceanographic measurements have yielded important information about the Meddies' dynamics (see *e.g.* Armi *et al.* 1989). In particular, it became clear that the Meddies occupy a relatively thin, pancake-shaped region with horizontal and vertical scales of roughly 100 km and 600 m, respectively. The relatively slow decay allows the Meddy to cross the Atlantic Ocean and reach the Bahamas after approximately one year.

This paper reports on a laboratory study of a monopolar vortex in a non-rotating, linearly stratified fluid. The flow evolution has been measured by application of digital image analysis techniques, and a comparison is made with a few simple decay models.

2. Generation and characteristics of monopolar vortices

The laboratory experiments were performed in a square perspex tank of horizontal dimensions $100\text{ cm} \times 100\text{ cm}$ and a working depth of 30 cm , which was filled with a linearly salt-stratified fluid. Monopolar vortices were generated by a solid sphere (diameter 2.5 cm), placed in the fluid at mid-depth, rotating at constant speed Ω about a vertical axis, as also described in Flór *et al.* (1993). In the experiments discussed here, the rotation speed measured 344 rev/min , and the forcing was applied during typically 30 s .

During the forcing, fluid is swept away from the sphere in radial direction, and shadowgraph visualizations have revealed that the motion in the vicinity of the sphere is definitely turbulent at this stage. Then the rotation was stopped, and the sphere was removed by carefully lifting it. During the subsequent gravitational collapse, the vertical motions are substantially suppressed and the flow soon becomes laminar: at this stage the flow takes on the appearance of a monopolar vortex confined to a thin horizontal pancake-shaped region. In most cases, this vortex was observed to be stable, while gradually decaying owing to viscous effects.

The flow was visualized by seeding the fluid with small tracer particles. Special care was taken that their density exactly matched the fluid density at the mid-level of the vortex motion. The particle motions were recorded by video, and quantitative information about the horizontal flow field was obtained by applying a digital image analysis technique. After digitization the flow was characterized by a set of velocity vectors in the nodal points of a rectangular grid covering (part of) the flow domain. As a next step, the values of the vorticity $\omega = \frac{\partial v}{\partial x} - \frac{\partial u}{\partial y}$, with $\mathbf{v} = (u, v)$ the velocity components in (x, y) -directions, and the stream function ψ (defined by $\mathbf{v} = \nabla \times \mathbf{k}\psi$, with \mathbf{k} the unit vector in vertical direction) are calculated in each grid point. Some typical results of this procedure are shown in Figure 1 for a monopolar vortex 180 s after the forcing was stopped. The graphs show (a) contours of ω , (b) contours of ψ , (c) the ω, ψ scatter plot and (d) cross-sectional distributions of ω and the azimuthal velocity v_θ , respectively. Apparently, the core of the vortex is surrounded by a ring of very weak oppositely-signed vorticity. The scatter plot reveals a linear relationship between ω and ψ in the central part of the vortex, whereas ω is almost zero for larger radii. These characteristic features of the ω, ψ -relationship remain unchanged during the subsequent flow evolution, as can be seen in Figures 2a-c: although the maximum ω -value decreases during the decay, the scatter plots indicate preservation of the linearity at least in the vortex core. For this reason it is assumed that the monopolar vortex thus produced can in good approximation be characterized by a linear ω, ψ -relationship, i.e. by

$$\omega = k^2 \psi, \quad (1)$$

with k a proportionality constant. Because of the symmetry about the horizontal mid-depth level ($z = 0$), the flow can be considered as being 2D, so that (1)

implies

$$\nabla^2 \psi = -\omega = -k^2 \psi. \quad (2)$$

The axisymmetric solution of this equation that is bounded in the origin $r=0$ is given by

$$\psi(r) = AJ_0(kr), \quad (3)$$

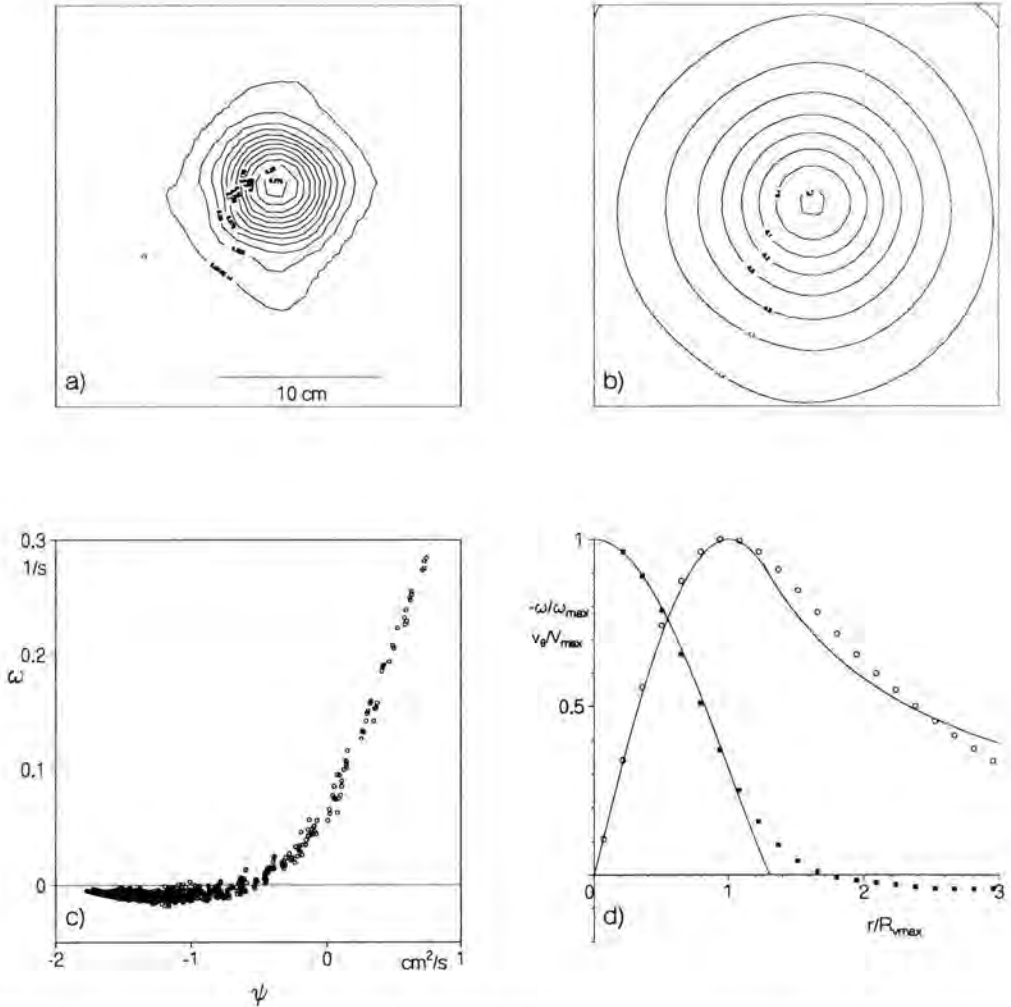


Fig. 1. Experimentally determined features of a characteristic monopolar vortex: (a) ω contours; (b) ψ contours; (c) ω, ψ scatter plot; (d) cross-sectional distributions of ω (symbol ■) and v_θ (symbol o). The profiles are scaled with their maximum values $\omega_{max} = 0.28 \text{ s}^{-1}$, $V_{max} = 0.30 \text{ ms}^{-1}$ and $R = 3.2 \text{ cm}$. The drawn lines represent the vortex model (4). These quantities were determined at mid-depth of a monopolar vortex created by a rotating sphere in a linearly stratified fluid with $N = 1.98 \text{ rad s}^{-1}$, at $t = 180 \text{ s}$ after the forcing was stopped.

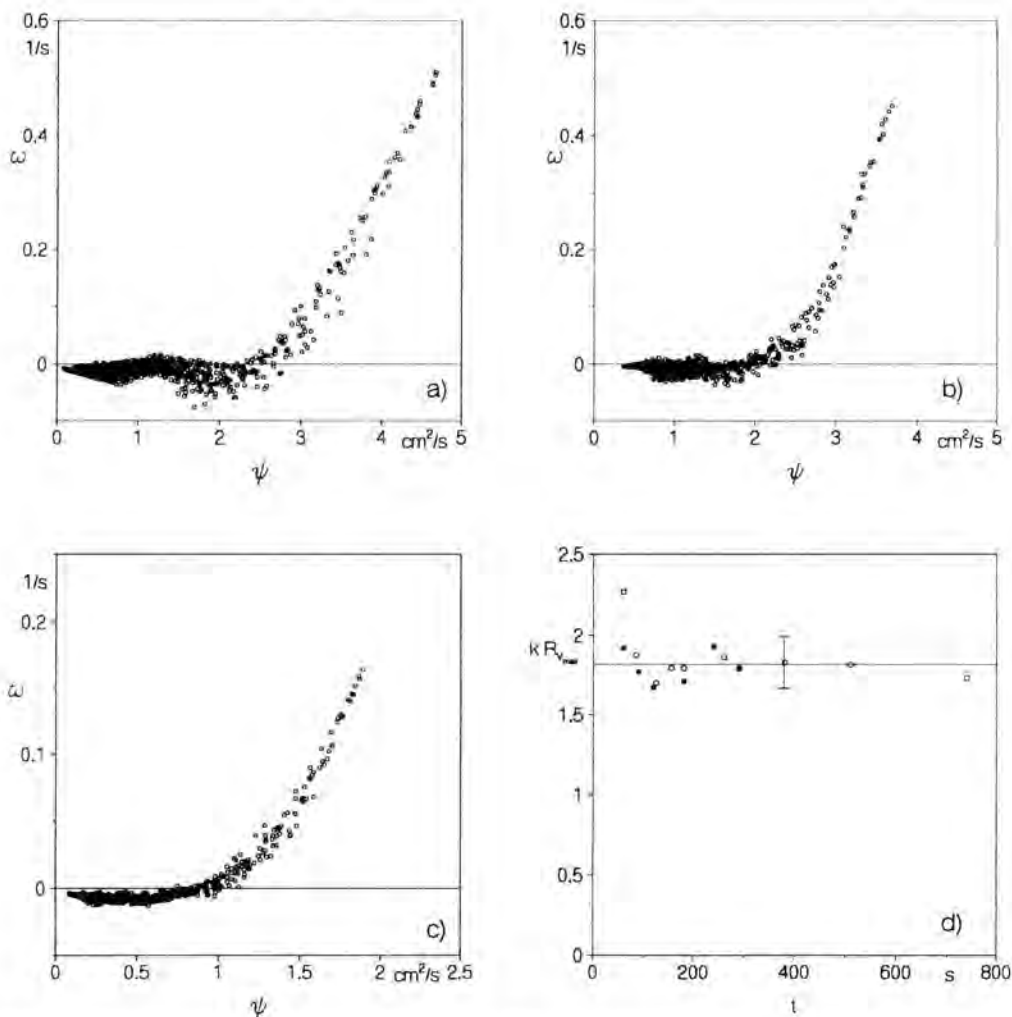


Fig. 2. Sequence of ω, ψ -plots measured at $t = 90 s$ (a), $120 s$ (b) and $240 s$ (c) after the forcing was stopped (same experiment as in Figure 1). The experimental kR -values are shown graphically for two different experimental runs as a function of time in (d), with the horizontal line representing the value $kR = 1.8$.

where J_0 is the zeroth-order Bessel function of the first kind, and A is a constant. The corresponding solutions of ω and v_θ are

$$\omega(r) = Ak^2 J_0(kr), \quad v_\theta(r) = Ak J_1(kr), \quad (4)$$

where J_1 is the first-order Bessel function of the first kind.

In view of the fact that the azimuthal motion is unidirectional, the v_θ -solution should be truncated at a radius a_1 for which $ka_1 \leq 3.83171$, this being the first

zero of J_1 . However, a single-signed vorticity distribution (as is approximately the case in the experiments, compare with Figure 1d), is obtained by truncating the solutions at the first zero of J_0 , i.e. at $ka_2 = 2.40483$. By defining a potential (outer) flow $v_\theta(r) = \frac{A}{r} k J_1(ka_2)$ for $r > a_2$ only an unphysical discontinuity occurs in ω at the radius $r = a_2$. It is shown in Figure 1d that this model gives at least a reasonable description of the flow in the central part of the vortex. The experimental kR values, k being determined from the slope of the scatter plot and R being the radius at which $v_\theta = V_{max}$, are presented for a typical vortex as a function of time in Figure 2d. According to the model, $kR = 1.84118$. Although some scatter is present in the data, the measured kR -values agree well with the value 1.8, at least within the experimental error.

During the decay, the vorticity magnitude shows a considerable decrease (see Figures 2a-c), while k and R only show a marginal change: after $t = 120s$ k decreases slowly and R increases somewhat, but in such a way that the combination kR is approximately constant (Figure 2d).

3. Decay models

In an attempt to describe some characteristic features of the decaying monopolar pancake-shaped vortex in a linearly stratified fluid, we will now consider three approximative theoretical models, in order of increasing sophistication.

(i) *purely 2D decay*

In the approximation that the decay of the planar vortex flow can be considered as purely 2D, the flow evolution is governed by the vorticity equation

$$\frac{\partial \omega}{\partial t} + J(\omega, \psi) = \nu \nabla_h^2 \omega \quad (5)$$

where ν is the kinematic fluid viscosity, ∇_h^2 the horizontal Laplacian, and J the Jacobian. Any axisymmetric vortex satisfies $J(\omega, \psi) = 0$, so that for the case of a Bessel vortex, as discussed in section 2, equation (5) takes the following form (see also Batchelor, 1967):

$$\frac{\partial \omega}{\partial t} = \nu \nabla^2 \omega = -\nu k^2 \omega \quad (6)$$

Apparently, the decaying vortex solution is

$$\omega(r, t) = \omega_o(r) \exp(-t/\tau_{2D}) \quad (7)$$

with $\omega_o(r)$ the vorticity according to the Bessel vortex, (4), and

$$\tau_{2D} = (\nu k^2)^{-1} \quad (8)$$

the 2D decay time.

(ii) *the 'constant-thickness' model*

The purely 2D decay model can be somewhat refined by taking into account the vertical structure of the planar vortex. Experiments have revealed that the vertical distribution of the horizontal velocity field is closely approximated by a Gaussian profile of the form $\exp(-z^2/2\sigma^2)$, with σ a vertical scale. It is now assumed that the thickness 2σ of the vertical region is constant during (at least) the first stages of the decay, so that in the region $z \ll \sigma$ the vorticity distribution can be approximated by

$$\omega(r, z, t) = \omega_o(r) \exp(-z^2/2\sigma^2) h(t), \quad (9)$$

with $h(t)$ a time-dependent amplitude function. Near the mid-level of the vortex region, the vorticity is close to vertical, and its evolution is described by

$$\frac{\partial \omega}{\partial t} + J(\omega, \psi) = \nu \nabla_h^2 \omega + \nu \frac{\partial^2 \omega}{\partial z^2} \quad (10)$$

Substitution of (9) into (10) yields

$$\frac{\partial \omega}{\partial t} = \nu \left(-\lambda^2 + \frac{\varepsilon^2}{\sigma^2} \right) \omega \quad (11)$$

with $\varepsilon = z/\sigma$ and $\lambda^2 = k^2 + 1/\sigma^2$. Under the restriction $|\varepsilon| \ll (1 + \sigma^2 k^2)^{1/2}$ one obtains

$$\omega(r, z, t) = \omega_o(r) \exp(-t/\tau_{cr}) \exp(-z^2/2\sigma^2) - O(\nu \varepsilon^2 t / \sigma^2) \quad (12)$$

with

$$\tau_{cr} = (\nu \lambda^2)^{-1}. \quad (13)$$

The last term in (12) is negligible as $t \ll \sigma^2/\nu \varepsilon^2$, which is easily met in most experiments as long as ε is small. Apparently, the decay is again exponential.

(iii) *the vertical diffusion model*

A more accurate model is obtained when the vertical diffusion of the (vertical) vorticity is allowed to result in an increasing thickness of the vertical region. Again limiting the validity of the model to a thin region around the midplane level $z = 0$, we put

$$\omega(r, z, t) = \omega_o(r) \gamma(z, t), \quad (14)$$

with $\omega_o(r)$ again the Bessel-vortex solution. By substitution into (10), one obtains for the amplitude function γ :

$$\frac{\partial \gamma}{\partial t} = -\nu k^2 \gamma + \nu \frac{\partial^2 \gamma}{\partial z^2}. \quad (15)$$

By the transformation $\gamma = \Phi(z, t) \exp(-\nu k^2 t)$ one obtains a diffusion equation for Φ :

$$\frac{\partial \Phi}{\partial t} = \nu \frac{\partial^2 \Phi}{\partial z^2}. \quad (16)$$

Under the assumption that initially the vorticity is confined to a thin region at midplane depth, according to $\Phi(t=0) = \Phi_o \delta(z)$, the solution of (16) is

$$\Phi(z, t) = \frac{\Phi_o}{\sqrt{t}} \exp(-z^2/4\nu t). \quad (17)$$

The solution for the vorticity is then

$$\omega(r, z, t) = \omega_o(r) \frac{1}{\sqrt{t}} \exp(-t/\tau_{diff}) \exp(-z^2/4\nu t), \quad (18)$$

with the timescale

$$\tau_{diff} = (\nu k^2)^{-1}, \quad (19)$$

and the constant Φ_o being incorporated in the amplitude of $\omega_o(r)$. Note that this timescale τ_{diff} is identical to τ_{2D} , see (8), as derived for the purely 2D decay.

4. Comparison between experimental observations and decay models

(i) *the constant-thickness model*

A useful quantity to characterize the decay of the vortex is the maximum velocity V_{max} , which is proportional to the amplitude A , see (4). Figure 3a shows the behaviour of V_{max} as a function of time for two different experiments.

was stopped was taken as $t = 0$. The graph clearly shows that the model describes a similar decay trend as the experiments. The obtained decay timescales are

	$\tau_{dif}(V_{max})$	$\tau_{dif}(\omega_{max}a)$
I	$440 \pm 26 \text{ s}$	$759 \pm 185 \text{ s}$
II	$357 \pm 17 \text{ s}$	$450 \pm 56 \text{ s}$

while the decay value $\tau_{2D} = 1/\nu k^2$ obtained from scatter plots for experiments I and II are $322 \pm 60 \text{ s}$, and $280 \pm 100 \text{ s}$, respectively. The deviation from the experimental decay values is probably due to the assumption $\omega = \omega_0 \delta(z)$ at $t = 0$ and the fact that $t = 0$ is chosen after the forcing was stopped; in reality a vortex with a certain thickness has already been formed at that time. Besides, the vortex slightly expands horizontally, an effect which is not incorporated in the model. Nevertheless, the decay timescales are of the same order of magnitude. Also, the model describes a trend in the decay that is very similar to that in the measured quantities.

Acknowledgements

One of us (J.B.F.) gratefully acknowledges financial support from the Dutch Foundation for Fundamental Research on Matter (FOM).

References

- Armi, L., D. Hebert, N. Oakey, J. Price, P.L. Richardson, T. Rossby and B. Ruddick, 1989 - Two years in the life of a Mediterranean salt lens. *J. Phys. Oceanogr.* **19**, 354–370.
- Batchelor, G.K., 1967 - *An Introduction to Fluid Dynamics*. Cambridge University Press.
- Flór, J.B., W.S.S. Govers, G.J.F. van Heijst and R. van Sluis, 1993 - Formation of a tripolar vortex in a stratified fluid. *Appl. Sci. Res.* **51**, 405–409.
- McDowell, S.E. and H.T. Rossby, 1978 - Mediterranean water: an intense mesoscale eddy off the Bahamas. *Science* **202**, 1085–1087.
- Robinson, A.R. (Ed.), 1983 - *Eddies in Marine Science*. Springer Verlag, Berlin.

Fluid Dynamics Laboratory
Department of Physics
Eindhoven University of Technology
P.O. Box 513, 5600 MB Eindhoven
The Netherlands

The Effect of Topography on the Motion of Coherent Structures

Abstract

An analytical model is derived to study the effect of a topographic slope on the propagation of intermediate layer lenses. Though the problem cannot be solved entirely, due to its nonlinearity, boundary conditions are used to obtain useful information. In particular, we find a formula for the propagation speed of the structure which depends only on the surrounding hydrological data.

Introduction

It has been conjectured that a significant part of the Mediterranean water that spreads in the Atlantic ocean forms huge bubbles of 20 to 50 km radius and 1000 m thickness. These "meddies" wander in the Atlantic basin for about 4 years and are able to transport Mediterranean water thousands of kilometers southward.

Many questions are still unanswered concerning these structures: Where and how are they generated? How can they have such a lifetime? How can we explain their southward trajectories?

McWilliams and Flierl (1979) have shown that the nonlinearity inherent to their formation (see McWilliams 1988), keeps vortices from being scattered as Rossby waves. In meddy cores, vorticity reaches 0.3 to 0.5 f; thus they are non-linear features and can resist dispersion.

As far as trajectories are concerned, only three meddies have been tracked long enough to provide a good description of their path and time dependent characteristics (Armi *et al.*, 1989; Richardson *et al.*, 1989). Coverage of the region surrounding a Mediterranean lens with SOFAR floats has shown that propagation is due to self-advection mechanisms (Richardson *et al.*, 1989). To our knowledge, at least three explanations have been proposed to account for the Robserved trajectories (Beckmann and Käse, 1989; Hogg and Stommel, 1989; Colin de Verdiere, 1992), but no-one has yet investigated the influence of bottom topography.

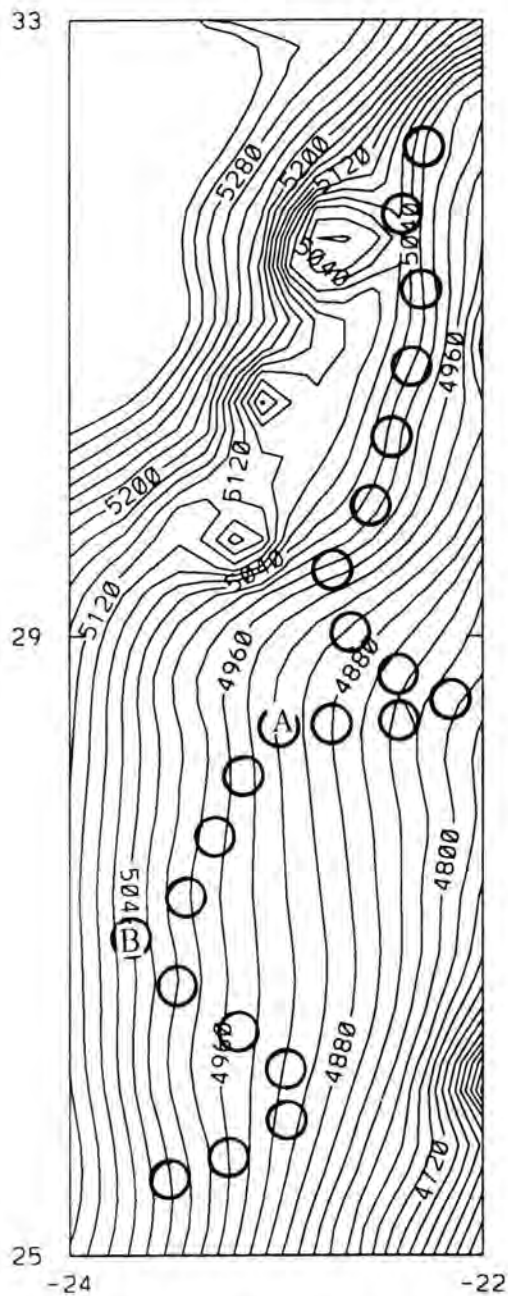


Fig. 1. Map of the bathymetry ($22-24^{\circ}W$, $25-33^{\circ}N$) and the path of a meddy observed by Armi *et al.* (1989) and Richardson *et al.* (1989). Note that the bathymetry has been smoothed down below $30^{\circ}N$. \square : Probable position of the core of the meddy. A-B: Test zone.

As intermediate lenses are baroclinic features, and as baroclinity is known to attenuate the dynamics of lower layers, topography was not thought to play a significant role in the motion of these eddies when they were above abyssal zones. Yet numerous observations seem to prove that these structures propagate along lines of constant depth; for instance, meddies always cross the mid-Atlantic ridge through Kane's fracture, while their immersion is above the seamount tops (Kostianoy and Belkin, 1989). More recently, Arhan *et al.*, 1994 have detected three meddies that seem to have been generated in the Tagus abyssal plain and travelled southward crossing the Gorringe bank over a pass. In figure 1 we have superimposed a map of the bathymetry on the trajectory of the Meddy followed by Armi *et al.* (1989). The correlations between the path and the 4900-5000 m isobaths are good, at least at the beginning. Yet, the lens propagated with deep waters on its right, whereas a barotropic model with a topographic beta predicts a translation with shallow waters on the right. In fact, this argument does not hold any more when stratification is taken into account.

We develop here an analytical model to evaluate the influence of bottom slope on the dynamics of an intermediate nonlinear eddy through dynamical coupling between the layers. The model is presented in section 2. The problem is solved and the results are analysed in section 3 and 4. Some complements are given in the last section. In particular the β -effect is added and our results on the influence of a mean upper layer velocity is briefly exposed.

The model

As the intermediate layer can be nonlinear and as the variation of this layer's thickness is thought to be as high as the thickness at rest, the simpler model to be considered is a three layer-shallow-water model on an f -plane. We also

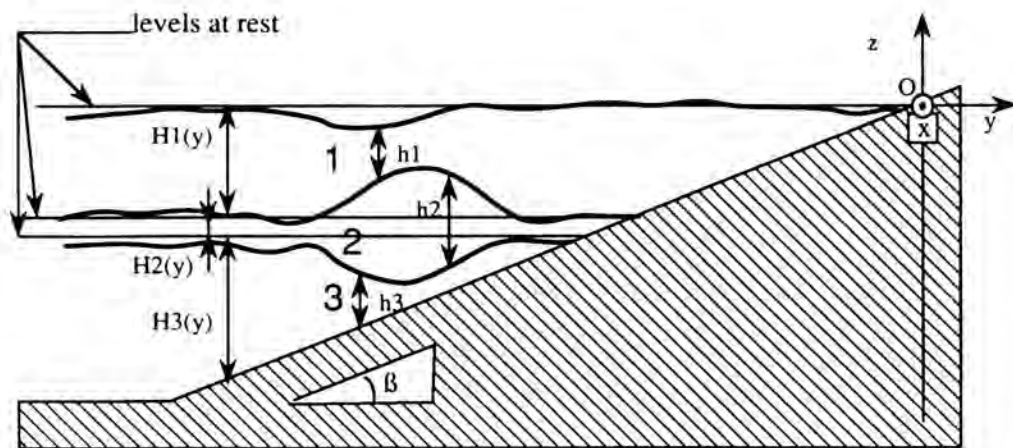


Fig. 2. Side view of the lens, $s = \tan\beta$.

assume a steadily translating axisymmetric basic state, with the second layer embedded between two quasi-geostrophic layers. For the latter, conservation of potential vorticity gives:

$$\frac{d}{dt} \frac{\zeta + f}{h} = 0 \quad \text{with} \quad \frac{d}{dt} = (\bar{u} - \bar{C}) \cdot \bar{\nabla}$$

For the basic state, using radial coordinates in a frame translating with the structure:

$$\begin{aligned} \frac{\zeta + f}{h} &= \frac{\zeta}{H} + \frac{f}{H} - \frac{f}{H^2} (\Delta h + H') \\ \zeta &= \frac{1}{\rho f} \frac{\partial_r (r \partial_r P)}{r} \quad \text{and} \quad \bar{u} = \frac{1}{\rho f} \partial_r P \bar{e}_\theta. \end{aligned}$$

where Δh is the basic axisymmetric perturbation of the thickness due to the meddy, $H' = -s r \sin \theta$ represents the bottom topography and is here an asymmetric term, and H is the thickness of the layer at the centre of the meddy.

Keeping only the higher order asymmetric terms¹, we get:

$$C \cdot \nabla \left(\frac{\zeta}{H} - \frac{f}{H^2} \Delta h \right) - \bar{u} \cdot \bar{\nabla} \left(\frac{f}{H^2} H' \right) = 0 \quad (1)$$

We can integrate this equation for each quasi-geostrophic layer ($i = 1$ and 3). We get:

$$C_y = 0 \quad C_x = C$$

$$C \left(-r \Delta h_1 + \frac{H_1}{\rho_1 f^2} \partial_r (r \partial_r P_1) \right) = 0 \quad (2)$$

$$-C r \Delta h_3 + \frac{H_3 C}{\rho_3 f^2} \partial_r (r \partial_r P_3) - \frac{1}{\rho_3 f} s r P_3 = 0 \quad (3)$$

We could also derive an equation for the intermediate layer, but we would only obtain a relationship between the basic state and higher order terms. That is why we are going to assume that $\Delta h_2(r)$ is known a-priori at first order.

¹ A more rigorous way to derive the equation is to use integral constraints to relate the order of magnitude of the asymmetric part to the axisymmetric one. We then get two small parameters that can be used to perform an asymptotic expansion: the Rossby number and $\varepsilon = C/fL$ where C is the propagation speed and is found to have order of magnitude $g's/f$ with g' the reduced gravity.

Mathematical development

To solve the previous equations we have to distinguish two cases:

$C = 0$: this is the case if and only if there is no motion in the bottom layer. Then, there exists exact axisymmetric solutions of the complete set of nonlinear equations. As meddies do translate, these exact solutions are not really of interest. However, this observation is profitable insofar as it also means that if a lens is to propagate, the bottom layer can not be at rest, whatever the mechanism of propagation, and thus our structure "feels the bottom".

$C \neq 0$: This is the most interesting case of course, and we are going to solve the equation assuming the lens does translate.

Boundary conditions

As Swaters and Flierl (1991) did in studying a cold lens on a sloping bottom, we impose isolation constraints for our lens (see also Flierl 1984):

$$v_i = 0 \quad \text{for } r \geq R,$$

where R is a radius to be determined. That constraint also means that the Δh_i are null beyond R .

We believe it is a necessary condition to have a stationary translation if we consider a "realistic" bottom. Indeed, let us assume that at $y = y_o$ the bottom becomes flat, then $\nabla H'_3 = sj$ is nul beyond y_o . In view of (1), it is necessary to impose $v_3(r) = 0$ at $y = y_o$. As v_3 only depends on r , this means that $v_3(r) = 0$ beyond a certain radius R . It also seems natural to impose such a constraint on the other layer in order to have steady propagation.

Eigenmode development

Using the hydrostatic approximation to express P_1 and P_3 in terms of Δh_1 , Δh_2 and the free surface level ζ_1 ($= \Delta h_1 + \Delta h_2 + \Delta h_3$), (2) and (3) become:

$$-r\Delta h_1 + \frac{gH_1}{f^2} \partial_r [r\partial_r \zeta_1] = 0 \quad (4)$$

$$\begin{aligned} & -r \left[(1 + \Gamma) \zeta_1 - \left(1 + \frac{\Delta \rho''}{\rho_3} \Gamma \right) \Delta h_1 \right] \\ & + \frac{gH_3}{f^2} \partial_r \left[r\partial_r \left(\zeta_1 - \frac{\Delta \rho''}{\rho_3} \Delta h_1 \right) \right] = F(\Delta h_2) \end{aligned} \quad (5)$$

$$\text{with } \Gamma = \frac{g^s}{Cf} \gg 1, \quad \Delta\rho = \rho_2 - \rho_1, \quad \Delta\rho' = \rho_3 - \rho_2, \quad \Delta\rho'' = \rho_3 - \rho_1.$$

$$F(\Delta h_2) = -r\Delta h_2 \left(1 + \frac{\Delta\rho'}{\rho_3} \Gamma \right) + \frac{\Delta\rho' g H_3}{\rho_3 f^2} \partial_r (r \partial_r \Delta h_2)$$

and the boundary conditions:

$$\partial_r \zeta_1(r=0) = \partial_r \Delta h_1 = \partial_r \Delta h_2 = 0$$

$$\zeta_1(r \geq R) = \Delta h_1 = \Delta h_2 = 0$$

$$\partial_r \zeta_1(r \geq R) = \partial_r \Delta h_1 = \partial_r \Delta h_2 = 0$$

To solve this system, we add (5) + α (4) and determine α to get two uncoupled equations. This gives:

$$\frac{gH_3 + \alpha gH_1}{f^2 \Gamma} = \frac{\Delta\rho'' g H_3}{\rho_3 f^2 (-\alpha + 1 + \frac{\Delta\rho''}{\rho_3} \Gamma)} \equiv \kappa$$

α is thus the root of a second-order equation: $\alpha^2 - (1 + \frac{\Delta\rho''}{\rho_3} \Gamma - \delta) \alpha - \delta = 0$, with $\delta = \frac{H_3}{H_1}$. The discriminant is: $A = (1 + \frac{\Delta\rho''}{\rho_3} \Gamma - \delta)^2 + 4\delta > 0$. That ensures that there are two different eigenmodes: $Z_i = \zeta_1 - \frac{\Delta\rho'' g H_3}{\kappa_i \rho_3 f^2 \Gamma} \Delta h_1$, $i = 1, 2$ and the initial system is equivalent to the following, where variables have been separated ($i = 1, 2$):

$$-rZ_i + \kappa_i \partial_r (r \partial_r Z_i) = \frac{1}{\Gamma} F(\Delta h_2) \quad (6)$$

with the boundary conditions:

$$Z_i(r \geq R) = 0$$

$$\partial_r Z_i(r=0) = 0$$

$$\partial_r Z_i(r \geq R) = 0$$

As Δh_2 and the Z_i are null beyond a certain radius R , we can decompose them using Bessel functions:

$$\Delta h_2(r) = \sum_{p=1}^{+\infty} \chi_p^2 J_p \left(\lambda_p \frac{r}{R} \right) \quad \text{for } r \leq R$$

$$\Delta h_2(r) = 0 \quad \text{for } r \geq R$$

J_p is the zeroth order Bessel function and λ_p is the p -th root of J_p . Two of the three boundary conditions are obviously satisfied, the last one can be written:

$$\sum_{p=1}^{+\infty} \gamma_p = 0 \quad \text{with } \gamma_p = \chi_p^2 \frac{\lambda_p}{R} \partial_r J_p(\lambda_p)$$

Using (6), Z_i can be written:

$$Z_i(r) = \sum_{p=1}^{+\infty} \beta_p' \chi_2^p J_0 \left(\lambda_p \frac{r}{R} \right)$$

$$\beta_p' = \frac{R^2}{\Gamma(R^2 + \kappa_i \lambda_p^2)} \left(1 + \frac{\Delta \rho'}{\rho_3} \Gamma + \frac{\Delta \rho' g H_3}{\rho_3 f^2 R^2} \lambda_p^2 \right)$$

The boundary condition for each mode can be written:

$$\left(\kappa_i \left(1 + \frac{\Delta \rho'}{\rho_3} \Gamma \right) - \frac{\Delta \rho' g H_3}{\rho_3 f^2} \right) G \left(\frac{\kappa_i}{R^2} \right) = 0 \quad \text{with} \quad G(X) = \sum_{p=1}^{+\infty} \frac{\gamma_p}{1 + X \lambda_p^2}$$

G is a function that only depends on the basic shape of the lens. Thus, if we assume that the first factor of the left hand side is not zero, our celerity and R will depend on the shape of the lens. We believe this cannot be the case because the formula we then obtain for C will not hold: $C \rightarrow 0$ when $\delta \rightarrow +\infty$. So, according to us, the right condition that determines the propagation speed C is:

$$\kappa_i \left(1 + \frac{\Delta \rho'}{\rho_3} \Gamma \right) - \frac{\Delta \rho' g H_3}{\rho_3 f^2} = 0$$

That relationship can only hold for $\alpha \leq 0$, this determines the κ_i to be chosen, and we get:

$$C = \frac{\Delta \rho' g s}{\rho_3 f} \frac{\Delta \rho}{\Delta \rho' \delta - \Delta \rho} \quad (7)$$

This formula seems consistent because:

$$C \rightarrow 0 \quad \text{when} \quad \delta \rightarrow +\infty$$

$$C \rightarrow C_{Nof} = -\frac{\Delta \rho' g s}{\rho_3 f} \quad \text{when} \quad \delta \rightarrow 0$$

(see Nof 1983).

Analysis of the results

Comments on the celerity

The striking point in formula (7) is that C can be negative (translation with shallow waters on the left) but also positive, depending on the surrounding hydrological data (in fact C is positive if H_3 is large enough):

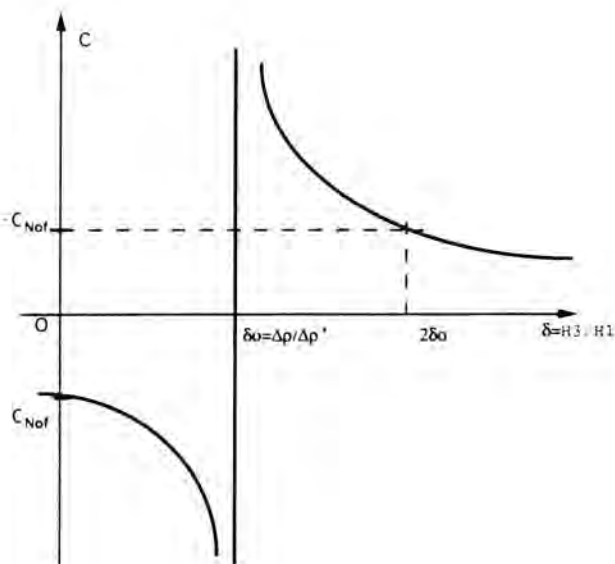


Fig. 3. Propagation speed as a function of the lower layer height.

Two constants are in fact rather difficult to estimate: the bottom slope s and the intermediate layer density ρ_2 . Indeed, Mediterranean lenses are located near the pycnocline, where density rapidly varies.

Besides, we see that even for weak slopes ($s \simeq 10^{-4}$) the translation speed is not negligible ($C \simeq 1 \text{ cm s}^{-1}$). That is why we believe bottom topography must be taken into account to study the dynamics of meddies. This study also underlines the fact that reduced gravity models are not appropriate to study such lenses. In fact Chassignet and Cushman-Roisin (1993) have shown that the conditions for neglecting lower layer dynamics are certainly never achieved in a realistic ocean.

Let us apply our formula to the meddy observed by Armi *et al.* (1989). In figure 1 we have determined a test zone where the bottom slope seems smooth and the trajectory rectilinear (A-B on fig.1). The hydrological data given by Armi *et al.* (1989) are:

$$H_1 \sim 800 \text{ m}$$

$$H_3 \sim 3600 \text{ m}$$

$$\Delta\rho \sim 0.5 \text{ kg m}^{-3}$$

$$\Delta\rho' \sim 0.5 \text{ kg m}^{-3}$$

$$f \sim 7.3 \cdot 10^{-5} \text{ s}^{-1}$$

$$s \sim 10^{-3}$$

Our formula thus gives a propagation speed of 2 cm s^{-1} southward in good agreement with the observations.

Pressure anomaly

Let us set:

$$\frac{P_1}{\rho g} = \sum_{p=1}^{\infty} P_1^p J_p \left(\lambda_p \frac{r}{R} \right) \quad \frac{P_3}{\rho g} = \sum_{p=1}^{+\infty} P_3^p J_p \left(\lambda_p \frac{r}{R} \right)$$

we get:

$$P_1^p = \frac{\Delta \rho'}{1 - \frac{\Delta \rho}{\Delta \rho' \delta} + \Delta \rho'' \lambda_p^2 r_1^2} \chi_2^p$$

$$P_3^p = \frac{1}{\delta} \frac{\Delta \rho}{1 - \frac{\Delta \rho}{\Delta \rho' \delta} + \Delta \rho'' \lambda_p^2 r_1^2} \chi_2^p$$

$$\text{with } r_1^2 = \frac{g H_1}{f^2 R^2}.$$

- if $\delta \rightarrow \infty$, $C \rightarrow 0$ and there is no motion in the lower layer ($P_3 \rightarrow 0$).
- As P_1^p , $P_3^p \sim \frac{\chi_2^p}{\lambda_p^2}$ and $\lambda_p^2 \gg 1$, we see that the intermediate layer speed is in general higher than the speed in the upper and lower layers².

Discussion

We have shown that bottom topography can be important for the propagation of an intermediate lens, even above abyssal depths. However, as a mean velocity field or the β -effect are also thought to play a role in the dynamics of these eddies, one may wonder which of these three mechanisms is essential.

It is easy to take into account the β -effect in our model, it just adds another term in the potential vorticity equation and we can solve the problem following the same pattern. The reader can verify that if the bottom slope is oriented North-South, the propagation speed C does not change! β only modifies the basic shape of the lens. On the other hand, if the slope is oriented East-West, no steadily translating motion can be achieved. In that case, we believe that for a certain range of slopes, the structure could propagate along lines of constant depths and β will just act to generate a weak loss of mass in the core of the meddy. Assuming a southward translation speed of 2 cm s^{-1} and neglecting the relative vorticity, this yields an e-folding time of 400 days ($T = f/\beta C$), which seems consistent.

² In fact χ_2^p can be chosen so that the speeds in the second layer are higher than those in the other layers.

It is also easy to take into account a mean upper layer current of the form $U = U_i$. If the mean interface slope can be neglected in front of the bottom slope, this current can also be neglected. Otherwise we get a new formula for C , depending now on the surrounding hydrological data and U .

However, these are only qualitative results and the combined effects of these three mechanisms is not clear. A thorough study to compare their respective influences seems necessary.

Finally, let us mention that in our model, as the free surface is deformed, there is an upper layer vortex. However this vortex is generated by the passage of the lens: a scaling analysis -not presented here- shows that in our model particles above the meddy do not follow it. Future measurements at sea should provide more clear-cut answers on the possible existence of such an upper layer signature in vorticity.

References

- Arhan M., A. Colin de Verdière and L. Mémery, 1993 - The Eastern boundary of the subtropical North-Atlantic. Submitted.
- Armi L., D. Hebert, N. Oakey, J.F. Price, P.L. Richardson, H.T. Rossby and B. Ruddick, 1989 - Two years in the life of a Mediterranean salt lens. *J. Phys. Oceanogr.* **19**, 354-370.
- Beckmann A. and R. Käse, 1989 - Numerical simulation of the movement of a Mediterranean water lens. *Geoph. Res. Lett.* **16**, 65-68.
- Colin de Verdière A., 1992 - On the southward motion of Mediterranean salt lenses. *J. Phys. Oceanogr.* **22**, 413-420.
- Flierl G., 1984 - Rossby wave radiation from a strongly nonlinear warm eddy. *J. Phys. Oceanogr.* **14**, 47-58.
- Hogg N. and H. Stommel, 1989 - How currents in the upper thermocline could advect meddies deeper down. *Deep-Sea Res.* **37**, 613-623.
- Kostianoy A.G. and I.M. Belkin, 1989 - A survey of observations on intrathermocline eddies in the world ocean. *Mesoscale/synoptic Coherent Structures in Geophysical Turbulence*, pp. 821-841.
- McWilliams, J. and G. Flierl, 1979 - On the evolution of isolated, nonlinear vortices. *J. Phys. Oceanogr.* **9**, 1155-1182.
- McWilliams J., 1988 - Vortex generation through balanced adjustment. *J. Phys. Oceanogr.* **18**, 1178-1192.
- Nof D., 1983 - The translation of isolated cold eddies on a sloping bottom. *Deep-Sea Res.* **30**, 171-182.
- Richardson P., D. Walsh, L. Armi, M. Schröder, and J.F. Price, 1989 - Tracking three Meddies with SOFAR floats. *J. Phys. Oceanogr.* **19**, 371-383.
- Swaters G. and G. Flierl, 1991 - Dynamics of ventilated coherent cold eddies on a sloping bottom. *J. Fluid Mech.* **223**, 565-587.

SHOM/IMG, Grenoble, France.

Merging of Cyclonic Vortices in a Rotating Fluid

Abstract

We study the interaction of two equal cyclonic vortices in a rotating fluid. A rigid lid placed on the free surface of the fluid eliminates topographic effects. Vortices initially located at a distance $d < 4R$ (R being the radius of the vortex) were observed to merge, while for initial separations $d > 5R$ the two vortices rotated around a common centre without merging. For intermediate initial separations ($4R < d < 5R$) the two vortices are strongly elongated but no single vortex is clearly formed. Two point vortices forced to approach one another simulate the main features of the early stages of the merging process. A vortex-in-cell model is used to study the interaction of vortices with more realistic vorticity distributions.

Introduction

The transfer of kinetic energy from the small scales to larger scales is a characteristic process of two-dimensional flows. It is believed that this process occurs through the merging of regions of equally signed vorticity. Although the interaction of two equal vortices embedded in irrotational flow is a strong simplification of a 2D turbulent flow, the understanding of this elementary process can illuminate the more complex processes leading to the self-organization of a two-dimensional flow.

One of the most important features in the interaction of two equal vortices is the existence of a critical distance for merging. If the vortices are initially closer than this distance they will merge into a single vortex. If the initial distance is larger the vortices will orbit around one another without forming a single vortex, while probably interchanging some outer vorticity. This merging criterion has been established using numerical simulations for different vorticity distributions in the initial vortices and simplified analytical models for patches of constant vorticity (see e.g. Melander *et al.* 1988).

Griffiths and Hopfinger (1987) studied the merging of equal vortices in a rotating, barotropic fluid and verified the existence of a critical distance for the merging of anticyclonic vortices. They observed, however, that cyclonic vortices merged for all initial distances allowed by their experimental apparatus (up to

$d = 4.5R$). The cause of this anomalous behaviour must be a three-dimensional effect since the two-dimensional vorticity equations, on which the simulations and analytical results are based, show the same behaviour with both signs of the vorticity. The natural candidates are the effect of Ekman layers (see Griffiths and Hopfinger, 1987) and the parabolic free surface (see Carnevale *et al.* 1991). Due to the Ekman pumping the radius of cyclonic vortices increases while that of anticyclonic vortices decreases. The parabolic free surface produces an effect analogous to that of the gradient of ambient vorticity in the β -plane. Cyclonic vortices move to the (local) northwest, which implies that in the case of a parabolic upper surface they spiral inwards; anticyclonic vortices move southwest, which is here equivalent to spiralling outwards. Therefore the Ekman layers as well as the free surface will enhance merging of cyclonic vortices and inhibit that of anticyclones.

The experimental results discussed here were performed using a plane rigid lid, thus the topographic effect was removed but the Ekman effect was increased (there is an additional Ekman layer at the top). The existence of a critical distance for cyclonic merger under these circumstances supports the hypothesis that the topographic effect was the cause of anomalous merger in the experiments by Griffiths and Hopfinger (1987).

Laboratory experiments

Experimental arrangement

The experiments were carried out in a rectangular tank of horizontal dimensions $100 \times 150 \text{ cm}^2$ and 30 cm depth mounted on a rotating table. The angular speed of the system was chosen to be $\Omega = 0.57 \text{ s}^{-1}$, so that the Coriolis parameter $f = 1.14 \text{ s}^{-1}$. The tank was filled up to a depth of 22 cm, and a transparent rigid lid was placed on the free surface before the rotation of the tank was started.

Vortices were generated by withdrawing some fluid during a short period of time (5 or 10 s in the experiments reported here). This was done using thin tubes (1.5 cm in diameter) with small perforations. The distance between the generating tubes (i.e. the initial distance between the vortices) was varied in the range 11.7–22.5 cm (which is equivalent to $3.3R < d < 6.3R$).

Flow measurements of a single vortex were made in absence of a rigid lid. The velocity field is measured from streak photographs of small particles floating at the free surface. Then the velocity field is interpolated onto a regular grid using cubic splines. The vorticity ($\omega = v_x - u_y$) is calculated analytically from the interpolating polynomials and the stream function is obtained by numerically inverting the Poisson equation $\nabla^2 \psi = -\omega$.

The merging experiments were all done with the use of a rigid lid and were visualized by adding dye after the generation of the vortices.

Before investigating the interaction of two equal vortices, the vorticity distribution of a single vortex generated with the sink method was measured. Figure 1 shows an example of the radial distribution of velocity (small dots) and vorticity (big dots) of a monopolar vortex. A good approximation of the vorticity distributions encountered in sink vortices is provided by the Lamb vortex (see the solid lines in figure 1):

$$\omega(r) = \frac{\kappa}{\pi R^2} \exp(-r^2/R^2) \quad (1)$$

$$v(r) = \frac{\kappa}{2\pi r} (1 - \exp(-r^2/R^2)) \quad (2)$$

where r is the radial coordinate, κ is the total circulation of the vortex and R is the position of maximal velocity. (N.B. with $R^2 = 4\nu t$ one recovers the Oseen vortex, which gives the decay of a potential point vortex with circulation κ). Note that the velocity profile resembles the Rankine model, but the vorticity distribution differs strongly from that model.

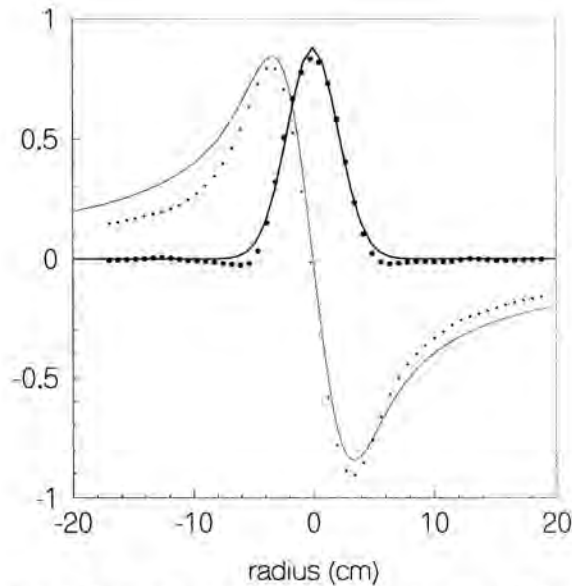


Fig. 1. Radial distribution of vorticity (thick lines and markers) and velocity (thin lines and markers) for an experimental "sink" vortex (dots) and the Lamb-vortex model (solid lines).

In a rotating fluid, the vortex evolution is affected by the Ekman layer. For cyclonic vortices, the motion in the bottom Ekman layer is directed radially inwards and leads to a 'pumping flow' into the vortex interior. To conserve mass, the axial motion will drive a weak motion in the vortex interior radially outwards. Anticyclones, on the other hand, are vertically stretched by the Ekman suction and will contract horizontally.

Following Carnevale *et al.* (1991) we derive a rough approximation for the vortex radius' rate of change produced by the Ekman effect:

$$\frac{dr}{dt} \approx \frac{1}{4} R_0 \omega E^{1/2} \quad (3)$$

with R_0 the initial radius of the vortex (≈ 4 cm), ω_0 the vorticity ($\approx 1 \text{ s}^{-1}$) and $E = \nu/\Omega H^2$ the Ekman number ($\approx 4.4 \times 10^{-5}$).

The growth of the vortex radius due to molecular diffusion follows from the Oseen model $dr/dt \approx 2\nu/R_0$. For the vortices in the present study, the effect of Ekman pumping is two orders of magnitude smaller than that of horizontal diffusion. However, the diffusion term always leads to radius increase, whereas the effect of the Ekman layer depends on the vortex being cyclonic or anticyclonic.

Topographic effect

Because of rotation, the free surface of the fluid is parabolic. This causes a gradient of ambient vorticity analogous to the β -effect. During the flow evolution a fluid parcel must conserve potential vorticity, which in this case can be expressed as $\omega - \gamma\rho^2 = \text{const.}$, where ω is the relative vorticity, ρ is the distance to the rotation axis and $\gamma = f^3/8gh$, with f the Coriolis parameter, g the acceleration due to gravity and h the depth of the fluid at the centre of the tank.

As in the β -plane case, a circularly symmetric vortex is not steady on the γ -plane (see e.g. Carnevale *et al.* 1991). A cyclonic vortex will tend to move to the local northwest, therefore making an inward spiral. In contrast, an anticyclonic vortex will tend to move to the local southwest, making an outward spiral.

Merging of cyclonic vortices

We could identify three different regimes in the interaction of two equal cyclonic vortices:

(i) when the initial distance between the vortex centres was large ($d > 5R$), the two cyclonic vortices rotated around each other. The distance alternately increased and decreased but during the whole evolution it remained close to the initial value (see curves **a** and **b** figure 2). The two vortices were slightly deformed but they conserved their almost circular shape.

(ii) for intermediate initial separations between the vortices ($4R < d < 5R$) the two vortices slowly formed a single, elongated structure. The distance between the vortices decreased almost linearly (curves c and d in figure 2). In the final stage it was still possible to recognize both vortices, which were surrounded by bands of fluid from the other vortex.

(iii) when the initial distance was small ($d < 4R$), the vortices rapidly merged into a single structure, as can be seen from the evolution of the distance in figure 2 (curves e and f). The merging process can be described as follows. Every vortex develops two cusps, one on the side of the neighbouring vortex and the other in the opposite side (figure 3a). The “exterior” cusps grow, forming the spiral arms that carry fluid out of the vortices, while the “interior” cusps also grow, thus transporting mass from one vortex to the other (figure 3b-c). The two vortices form a single, elongated structure and finally this elliptical vortex sheds more vorticity and transforms into an almost circular vortex (figure 3d).

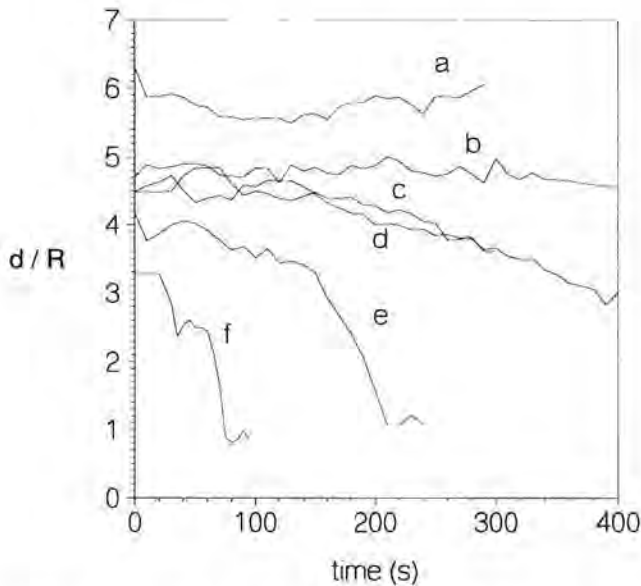


Fig. 2. Evolution of the distance between the vortices for several initial separations d/R : (a) 6.3, (b) 4.7, (c) 4.6, (d) 4.5 (e) 4.2; and (f) 3.3.

These regimes show the existence of a critical distance for merging of cyclonic vortices. In figure 2 the intersection of the curves with the line $t = 0$ gives the critical distance $d/R = 4.5 \pm 0.3$. This value seems to agree with the prediction of Carnevale *et al.* (1991), which is 4.35 ± 0.05 .

Numerical simulations

Point vortex model

The simplest model of two equal vortices consists of two point vortices of equal strength κ_0 separated by a distance d . If the two vortices evolve freely d is a constant, and the two vortices will rotate around their common centre with a constant angular speed. The stream function ψ for this rotating pair is formed by the sum of the stream functions of the initial vortices plus a correction term for the rotation of the system. For two vortices located at $(d/2, 0)$ and $(-d/2, 0)$ the stream function ψ is given by

$$\psi = -\frac{\kappa_0}{4\pi} \left[\ln((x - d/2)^2 + y^2) + \ln((x + d/2)^2 + y^2) + \frac{2}{d^2} (x^2 + y^2) \right] \quad (4)$$

To simulate the early stages of the merging process the vortices are forced to approach each other, i.e. d is a decreasing function of time. Experimentally the evolution of d was observed to be closely approximated by $d = d_{min} + a\sqrt{t_{max} - t}$, with $a = \sqrt{(d_0 - d_{min})/t_{max}}$ and d_0 is the initial distance between the vortices and t_{max} the time lapse up to the formation of a new single vortex, when $d = d_{min}$. This approximation is valid for "rapid" merger, i.e. for vortices initially separated by a distance small compared to the critical distance (see figure 2).

The equations of motion of a passive tracer in a point (x, y) in a corotating system are

$$\frac{dx}{dt} = \frac{\partial \psi}{\partial y}, \quad \frac{dy}{dt} = -\frac{\partial \psi}{\partial x} \quad (5)$$

The advection due to the approaching vortices is studied by following the evolution of the contours of two fluid parcels. The parcels are initially circular and the centre of each one corresponds with one point vortex. The number of points that define the lines increases in time as the length of the advected line increases. The time integration is performed using a fourth order Runge-Kutta scheme. Figure 3e-g show that the early evolution of the patches resembles the laboratory observations (figure 3a-c). This simple model, however, can not reproduce the transition to a single vortex as can be seen by comparing figures 3d and 3h.

Vortex-in-cell-method

In previous studies the merging process has been investigated, numerically and analytically, for vortices with uniform vorticity, i.e. Rankine vortices (or some smoothed version of this vortex). The vorticity distributions we encountered were strongly different from these vortices. Therefore, we simulated numerically the interaction of vortices with a more realistic vorticity distribution, viz. that of

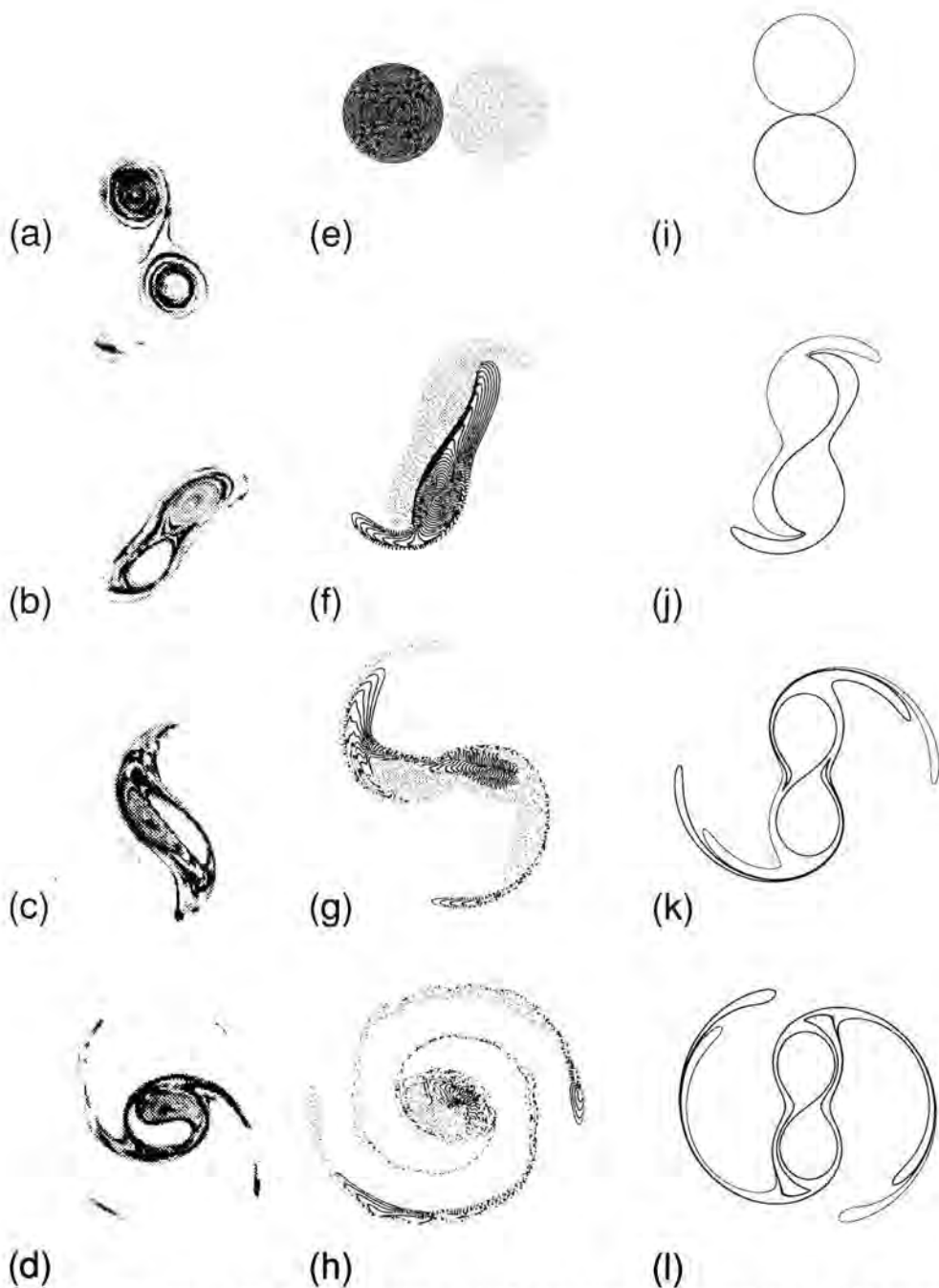


Fig. 3. Several stages in the merging process: (a)–(d) experimental observations; (e)–(h) numerical simulations of Lamb monopoles using a vortex-in-cell method; and (i)–(l) passive tracers in the velocity field of two approaching point-vortices.

the Lamb vortex, see (1). For this purpose we use a vortex-in-cell method, introduced in fluid mechanical problems by Christiansen (1973).

The initial continuous vorticity distribution is replaced by a finite set of point vortices each representing a small area, so that the uniform vorticity on that parcel times the area equals the point-vortex circulation. The region is covered by a mesh consisting of $N_x \times N_y$ cells. In the simulations reported here $N_x = N_y = 64$.

To obtain a circular vorticity region, the point vortices are distributed over m concentric circles. There are $8k$ point vortices in ring k plus 1 point vortex in the centre, yielding a total number of $N_p = 4m(m+1) + 1$ vortices. This distribution ensures equal areas for all point vortices. The number of rings used was $m = 25$ (i.e. $N_p = 2601$). For smaller numbers, the resolution is not sufficient. For higher numbers, the computation time is larger whereas the resolution does not increase significantly.

For the numerical simulations of Lamb vortices, the vorticity distribution was cut-off at a radius $r = R$ (the position of maximum velocity, as in the Rankine vortex) and $r = 2R$. The results for $r = R$ resemble those obtained for Rankine vortices: the critical distance is $d/R = 3.2$, and some exchange of vorticity occurs for $d/R = 3.4$. For $r_c = 2R$ the critical distance is $d/R = 4.2$. This difference is only due to the low-valued vorticity ring that was added.

Conclusions

Laboratory experiments have been carried out with cyclonic vortices. The vorticity distribution of this type of vortex is well approximated by a Lamb vortex, with the vorticity decreasing exponentially with the square of the radial coordinate r .

The effect of molecular diffusion on the radius of a vortex is two orders of magnitude greater than the effect of the Ekman layers. The growth influences the dimensionless parameter d/R and is therefore essential for a correct interpretation of the experimental results. Referring to the initial values the critical distance is $d/R = 4.5 \pm 0.3$. This value agrees well with the calculations of Carnevale *et al.* (1991), who found $d/R = 4.35 \pm 0.05$.

In spite of its simplicity, a point vortex model reproduces remarkably well some characteristic features of the merging process, namely the exchange of fluid between the two vortices and the formation of spiral arms.

More realistic numerical simulations have been carried out using a Lamb-vortex profile. The same features observed in the experiments are reproduced by the model. The ring of low-valued vorticity strongly influences the merging process.

Acknowledgement

O.U.V.F. gratefully acknowledges financial support from the Stichting voor Fundamenteel Onderzoek der Materie (FOM).

References

- Carnevale, G.F., P. Cavazza, P. Orlandi, and R. Purini, 1991 - An explanation for anomalous vortex merger in rotating-tank experiments. *Phys. Fluids* **A3**, 1411–1415.
- Christiansen, J.P., 1973 - Numerical simulation of hydrodynamics by the method of point vortices. *J. Comp. Phys.* **13**, 363–379.
- Griffiths, R.W. and E.J. Hopfinger, 1987 - Coalescing of geostrophic vortices. *J. Fluid Mech* **178**, 73–97
- Melander, M.V., N.J. Zabusky and J.C. McWilliams, 1988 - Symmetric vortex merger in two dimensions: causes and conditions. *J. Fluid Mech.* **196**, 303–340.

Fluid Dynamics Laboratory
Eindhoven University of Technology
P.O. Box 513, 5600 MB Eindhoven
The Netherlands

